# UNIVERSITÉ DE STRASBOURG

*ÉCOLE DOCTORALE DE PHYSIQUE ET CHIMIE PHYSIQUE*

**OBSERVATOIRE ASTRONOMIQUE DE STRASBOURG**

# THÈSE présentée par :

**Enmanuelle MOSSOUX**

soutenue le : **29 septembre 2016**

pour obtenir le grade de : **Docteur de l'université de Strasbourg**

Discipline/ Spécialité : Astrophysique

# ETUDES MULTI-LONGUEURS D'ONDE DE L'ACTIVITÉ DU TROU NOIR SUPERMASSIF SGR A* AU CENTRE DE NOTRE GALAXIE

**THÈSE dirigée par :**

| | |
|---|---|
| **M. GROSSO Nicolas** | Chargé de recherches au CNRS, université de Strasbourg |

**RAPPORTEURS :**

| | |
|---|---|
| **M. SCHARTEL Norbert** | Astronome, ESA, ESAC, Villanueva de la Cañada, Madrid, Espagne |
| **M. WILMS Jörn** | Professeur, Université de Erlangen-Nuremberg, Bamberg, Allemagne |

---

**AUTRES MEMBRES DU JURY :**

| | |
|---|---|
| **Mme DÍAZ TRIGO María** | Astronome, ESO, ALMA Regional Center, Garching, Allemagne |
| **M. GROSSO Nicolas** | Chargé de recherches au CNRS, université de Strasbourg |
| **Mme PORQUET Delphine** | Directrice de recherches au CNRS, université de Strasbourg |

# Acknowledgments

I thank my supervisor Dr Nicolas GROSSO making me discover the physics about the center of our galaxy and especially about Sgr A* which is an exciting area. I also thank him for his help during these three years.

I acknowledge the Université de Strasbourg for my IdEx PhD grant.

I was a member of the European Doctoral College of the University of Strasbourg during the preparation of my PhD, from 2013 to 2016. I had benefited from specific financial supports offered by the College and, along with my main stream research, I had followed a special course on topics of general European interests presented by international experts. I thank the European Doctoral College (CDE) for their different supports.

The research leading to the results of this Ph.D. thesis has received funding from the European Union Seventh Framework Program (FP7/2007-2013) under grant agreement n°312789. This work has also been financially supported by the Programme National Hautes Energies (PNHE).

During this Ph.D. thesis, I used the observations made by XMM-Newton. The XMM-Newton project is an ESA Science Mission with instruments and contributions directly funded by ESA Member States and the USA (NASA). This Ph.D. thesis is also based on observations made with the NASA/ESA Hubble Space Telescope (HST) obtained at the Space Telescope Science Institute (STScI) which is operated by the Association of Universities for Research in Astronomy, Inc., under NASA contract NAS 5-26555. These HST observations are associated with programs 13403 and 13316. This Ph.D. thesis is based on observations made with ESO Telescopes at the Paranal Observatory under ESO programs 092.B-0920(A), 091.B-0183(H), 093.B-0932(A), 093.B-0092(A), 093.B-0092(E), 093.B-0092(G), and 093.B-0220(B). This Ph.D. thesis is also based on observations made with the Karl G. Jansky Very Large Array (VLA) of the National Radio Astronomy Observatory is a facility of the National Science Foundation, operated under a cooperative agreement by Associated Universities, Inc.. This Ph.D. thesis is also based on observations made with the Combined Array for Research in Millimeter-wave Astronomy (CARMA). Support for CARMA construction was derived from the states of California, Illinois, and Maryland, the James S. McDonnell Foundation, the Gordon and Betty Moore Foundation, the Kenneth T. and Eileen L. Norris Foundation, the University of Chicago, the Associates of the California Institute of Technology, and the National Science Foundation. Ongoing CARMA development and operations are supported by the National Science Foundation under a cooperative agreement, and by the CARMA partner universities. This work also made use of public data from the Swift data archive, and data supplied by the UK Swift Science Data Center at the University of Leicester. Swift is supported at Penn State University by NASA Contract NAS 5-00136. This research has made use of the XRT Data Analysis Software (XRTDAS) developed under the responsibility of the ASI Science Data Center (ASDC), Italy. This Ph.D. thesis is also used data obtained from the Chandra Data Archive.

Finally, a big thank to Françoise Raucq from University of Liège (BELGIUM) and to Gaëtan Gourgue and Muriel Jadoul for their inducement.

# Table of content

# List of Tables

# List of Figures

Table 1: Table of scientific constants and unit conversions.

| Constants | | cgs units | SI units | References |
|---|---|---|---|---|
| Light velocity ($c$) | 2.99792458 | $10^{10}$ cm s$^{-1}$ | $10^{8}$ m s$^{-1}$ | a |
| Electron charge ($e$) | 1.6022 | $c\,10^{-20}$ statC | $10^{-19}$ C | c |
| Electron mass ($m_{\rm e}$) | 9.1094 | $10^{-28}$ g | $10^{-31}$ kg | c |
| Proton mass ($m_{\rm p}$) | 1.6726 | $10^{-24}$ g | $10^{-27}$ kg | c |
| Boltzmann constant ($k_{\rm B}$) | 1.3807 | $10^{-16}$ erg K$^{-1}$ | $10^{-23}$ J K$^{-1}$ | c |
| Planck constant ($h$) | 6.6261 | $10^{-27}$ erg s | $10^{-34}$ J s | c |
| Gravitational constant ($G$) | 6.6726 | $10^{-8}$ dyne cm$^2$ g$^{-2}$ | $10^{-11}$ m$^3$ s$^{-2}$ kg$^{-1}$ | c |
| Thomson cross section ($\sigma_{\rm T}$) | 6.6525 | $10^{-25}$ cm$^2$ | $10^{-29}$ m$^2$ | c |
| Fine structure constant ($\alpha$) | 7.2972 | $10^{-3}$ | $10^{-3}$ | c |
| Solar mass ($M_\odot$) | 1.9884 | $10^{33}$ g | $10^{30}$ kg | a |
| Solar radius ($R_\odot$) | 6.957 | $10^{10}$ cm | $10^{8}$ m | b |
| Solar bolometric luminosity ($L_\odot$) | 3.828 | $10^{33}$ erg s$^{-1}$ | $10^{26}$ J s$^{-1}$ | b |

**Notes:** [(a)] http://asa.usno.navy.mil/static/files/2014/Astronomical_Constants_2014.pdf; [(b)] Mamajek et al. (2015); [(c)] Huba (2013).

| Astronomical distances from Cox (2000) | | |
|---|---|---|
| 1 parsec (pc) | 3.08567758 | $10^{18}$ cm |
| 1 astronomical unit (au) | 1.495979 | $10^{13}$ cm |
| 1 light-year (ly) | 9.460530 | $10^{17}$ cm |
| 1 parsec (pc) | 2.062648 | $10^{5}$ au |
| 1 parsec (pc) | 3.2616334 | ly |

Table 2: Table of acronyms.

| | |
|---|---|
| ACIS | Advanced CCD Imaging Spectrometer (CXO) |
| ADAF | Advection Dominated Accretion Flow |
| AGN | Active Galactic Nucleus |
| APEX | Atacama Pathfinder Experiment |
| CARMA | Combined Array for Research in Millimeter-wave Astronomy |
| CCD | Charge Coupled Device |
| CCF | Current Calibration File |
| CDF | Cumulative Distribution Function |
| CXO | Chandra X-Ray Observatory |
| DSO | Dusty S-cluster Object |
| EHT | Event Horizon Telescope |
| EPIC | European Photon Imaging Camera (XMM-Newton) |
| *FWHM* | Full Width at Half Maximum |
| GBT | Green Bank Telescope |
| GRMHD | General Relativity Magneto-Hydro Dynamic |
| GTI | Good Time Intervals |
| HST | Hubble Space Telescope |
| IC | Inverse Compton |
| IR | Infrared |
| ISCO | Innermost Stable Circular Orbit |
| MCMC | Markov Chain Monte Carlo |
| MJD | Modified Julian Date |
| MOS | Metal Oxide Semi-conductor (XMM-Newton) |
| NICMOS | Near Infrared Camera and Multi-Object Spectrometer (HST) |
| NIR | Near Infrared |
| NuSTAR | Nuclear Spectroscopic Telescope Array |
| ODF | Observation Data File |
| PSF | Point-Spread Function |
| QPO | Quasi Periodic-Oscillation |
| RGS | Reflection Grating Spectrometer (XMM-Newton) |
| RIAF | Radiatively Inefficient Accretion Flow |
| SAS | Science Analysis Software |
| SGR | Soft Gamma Repeater |
| Sgr | Sagittarius |
| SINFONI | Spectrograph for INtegral Field Observations in the Near-Infrared (VLT) |
| SMA | Sub-millimeter Array |
| SMT | Sub-millimeter Telescope |
| SSC | Synchrotron Self-Compton |
| UT | Universal Time |
| VLA | Very Large Array |
| VLBA | Very Long Baseline Array |
| VLBI | Very Long Base Interferometer |
| VLT | Very Large Telescope |
| WFC3 | Wide Field Camera 3 (HST) |
| XMM | X-ray Multi-Mirror |

*« The question that I started off with was, I thought, very simple.*
*It was just: "Is there a massive black hole at the center of our Milky Way?".*
*But one of the things I love about science is that you always end up with new questions.»*
*Andrea M. Ghez*
*in Discover Magazine, May 2009, "The Frontiers of Astronomy".*

# Preface

The main messenger of information for astrophysicists is the photon. The properties of this photon (such as its wavelength and its polarization) are different according to the mechanisms of its formation and the medium it goes through. The study of the characteristics of the collected photon thus allows researchers to deduce the properties of the source and the underlying radiative processes.

The high-energy astrophysics studies mainly photons in X-rays and $\gamma$-rays, i.e., photons having energies greater than 100 eV, corresponding to wavelengths smaller than $10^{-8}$ m. The high-energy observations, available through rockets and satellites since the 1950s, have experienced exceptional growth since 1999 thanks to the increasing number of X-ray facilities such as Chandra, XMM-Newton, Swift, Suzaku and NuSTAR. Future space missions such as Athena promise a much greater number of collected photons with a better angular and spectral resolution. This will allow us to study more precisely the physical properties of the observed objects to increase the accuracy of the theoretical models.

In parallel, the software and computer development have allowed researchers to perform systematic studies of large datasets. It also allows the study and comparison of complex models with observations to better understand the properties of the emitting source.

The study of the black holes allows researchers to test the physical laws in presence of strong gravitational field that can not be reproduced in laboratory. This is also the way to test general relativity and quantum mechanics in such environment. At the Galactic Center, Sgr A* (say Sagittarius A star) is the closest supermassive black hole (SMBH) with a distance of only 8 kpc. It is thus a unique laboratory in which physical processes also relevant for nuclei of other galaxies can be studied with the higher angular resolution. However, the gas and dust on the line of sight to the Galactic Center make impossible its observation in the visible or ultraviolet making it only accessible in radio, infrared and in energies higher than about 2 keV.

Thanks to the current generation of space and ground telescopes, we are now able to detect sudden increases of flux (called flares) from Sgr A*. The flare characteristics improve our understanding of the physical processes in the vicinity of the SMBH.

My Ph.D. thesis entitled “Multiwavelength study of the flaring activity of the supermassive black hole Sgr A* at the center of the Milky Way” focuses on the study of the activity from Sgr A* mainly in X-rays and on comparisons with other wavelengths. The Chapter 1 is an overview of the current knowledge about the Galactic Center SMBH Sgr A* and the recently discovered Dusty Stellar Object (DSO) G2 object orbiting Sgr A* with a small pericenter distance. The possible increase of the Sgr A* activity due to the gravitational interaction with the DSO/G2 defines the context of my Ph.D. thesis. In this first Chapter, I also introduce the Galactic Center magnetar SGR J1745-29 which entered in burst phase in 2013 April at only 2.″5 from Sgr A*. In Chapter 2, I introduce the observational facilities I used for my studies. I then explain the different analysis methods I used and developed in Chapter 3. The results obtained for the 2011 campaign for the observations of Sgr A* in X-rays with XMM-Newton are reported in Chapter 4. The study of the multiwavelength activity from Sgr A* in Feb.-Apr. 2014, i.e., close to the DSO/G2 pericenter passage are reported in Chapter 5. In Chapter 6, I present the study of the X-ray flaring rate from Sgr A* observed with Chandra, XMM-Newton and Swift from 1999 to 2015. I finally present the conclusion and perspectives of this work in Chapter 7. Complementary informations about the radiative processes and the expanding plasmon model are given in Appendixes A and B. The observation log and the characteristics of the X-ray flares detected from 1999 to 2015 are given in Appendix C. The accepted papers reporting the results presented in this Ph.D. thesis are given in Appendix D.

# Chapter 1

# Overview of the Galactic Center and Sgr A*

In Sect. 1.1, I first set the scene with a brief description of the Milky Way before zooming towards the Galactic Center to meet Sgr A* and its closest environment. The physical characteristics, quiescent emission and flaring activity of Sgr A* are described in Sect. 1.2. A summary of these properties is given in Sect. 1.3. In Sect. 1.4, I describe the discovery and current knowledges about the DSO/G2. In Sect. 1.5, I introduce the Galactic Center magnetar SGR J1745-29 before setting the context of my Ph.D. thesis in Sect. 1.6.

## 1.1 On the way towards the Galactic Center

### 1.1.1 The structure of the Milky Way

Our solar system belongs to a bared spiral galaxy (SBc) named the Milky Way which is composed by a 15 kpc radius disk and by a central spherical bulge whose radius is 3 kpc (left panel of Fig. 1.1; Hüttemeister 2003). In the disk, there are four major spiral arms which contain the majority of gas and dust of the galaxy. The arms are composed by about 70% of hydrogen (H I, H II and $H_2$), about 30% of helium and some metals formed during supernovae explosions. Our solar system is in one of these spiral arms called the Small Orion Arm at about 8 kpc from the center of the Milky Way. The bulge is composed by an old stellar population aged of $(5-10)\times10^9$ years and gas with a total mass of $10^{10}M_\odot$.

In addition to the galactic plane components, there are the Fermi bubbles which are perpendicular to the galaxy (in violet in the right panel of Fig. 1.1). These gigantic structures, reaching 50° of latitude, emit in $\gamma$-rays with a luminosity of $4\times10^{37}$ erg s$^{-1}$ needing an exciting energy of $10^{54}$ to $10^{55}$ erg (Wardle & Yusef-Zadeh 2014). The Fermi bubbles could be explained by a past AGN (Active Galactic Nucleus) bright phase of Sgr A* (Su et al. 2010; Zubovas et al. 2011; Guo & Mathews 2012).

### 1.1.2 The central parsecs of the Milky Way

In the 1920's, Harlow Shapley and Jan Oort deduced that the center of our galaxy is located in the direction of the Sagittarius (Sgr) constellation and that the Sun is not located at the center of the Milky Way (Shapley & Curtis 1921; Oort 1930). Their discovery was done with the study of the movement of stars close to the Sun and of the position of 93 globular clusters. In 1930, thanks to a systematic study of globular clusters, Robert

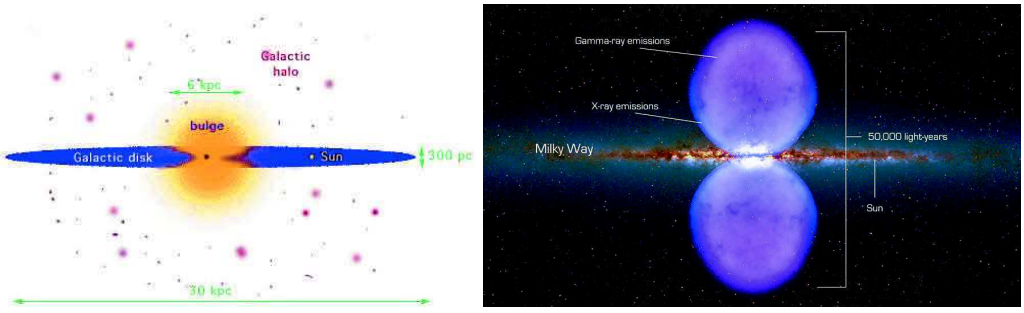


Figure 1.1: *Left panel:* Schematic view of the Milky Way (Hüttemeister 2003). *Right panel:* the Fermi bubbles (Credit: NASA's Goddard Space Flight Center).

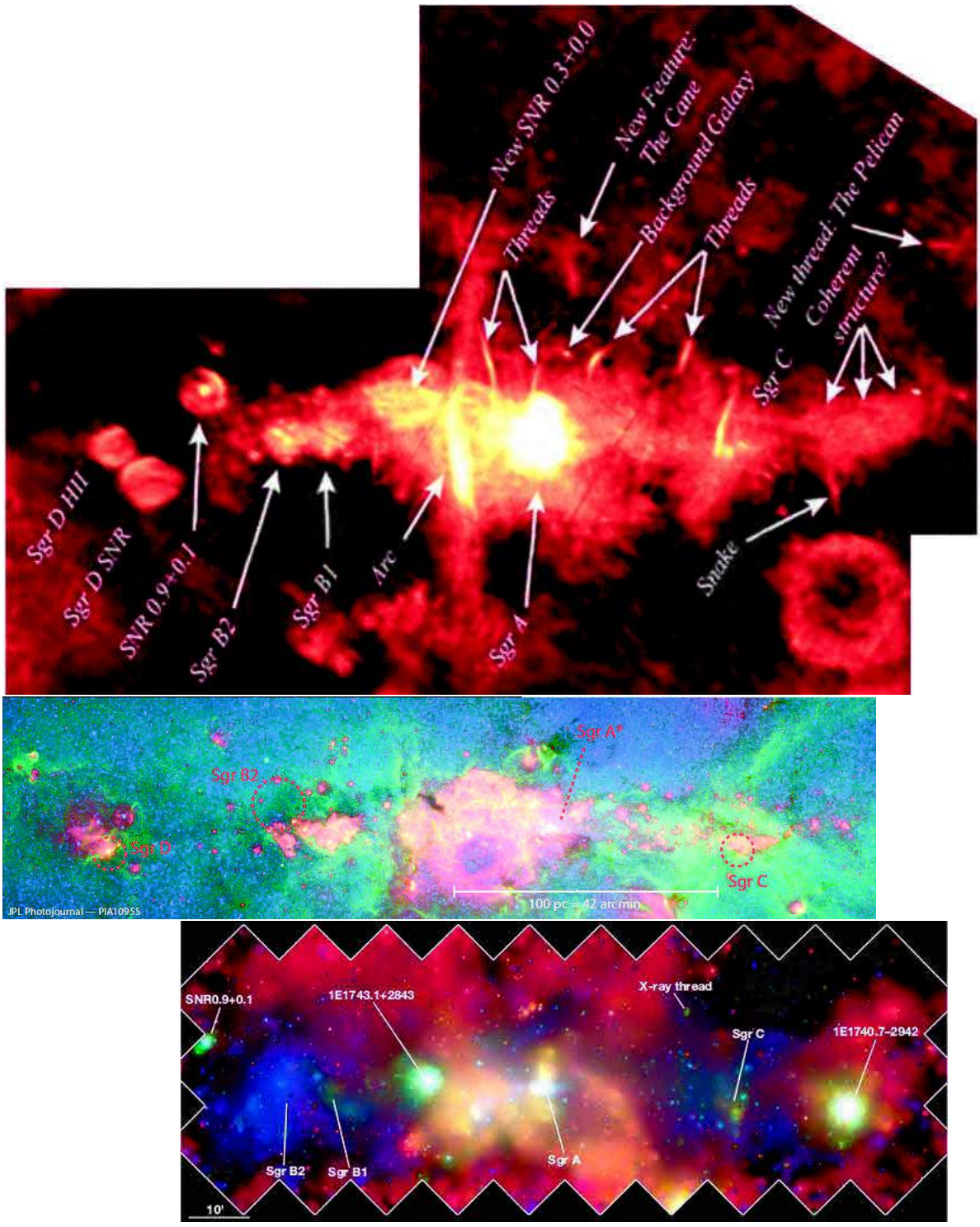


Figure 1.2: The image of the Galactic Center in radio, infrared and X-rays in galactic coordinates. The three images are shown at the same scale and aligned for an easier comparison. *Top panel:* Radio (333 MHz) image (Kassim et al. 1999) rotated and scaled to correspond to the IR and X-ray images. *Middle panel:* Spitzer image in infrared (blue = 3.6 $\mu$m, green = 8 $\mu$m and red = 24 $\mu$m). *Bottom panel:* Chandra X-ray survey between 1 and 8 keV (red = 1 − 3 keV, green = 3 − 5 keV and blue = 5 − 8 keV; Wang et al. 2002).

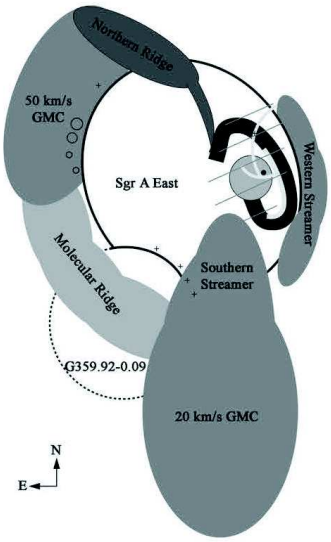


Figure 1.3: Schematic view of the Sgr A complex as seen from the Earth (Herrnstein & Ho 2005). Sgr A East fills the black ellipse. The large black band (a backwards "C" shape) is the CircumNuclear Disk. The light gray bands represent Sgr A West. The black dot is the S-cluster and the SMBH Sgr A*.

Trumpler concluded that the Galactic Center is not observable in visible light because of the dust absorption by the disk (Trumpler 1930).

Indeed, the presence of gas and dust on the light path implies that we do not receive all photons emitted by a source. This effect is called the *extinction* and is a combination of *absorption* and *scattering*. The ratio between the number of received and emitted photons is computed as $10^{-A_\lambda/2.5}$ with $A_\lambda$ the extinction at the photon wavelength $\lambda$. For the observations of the Galactic Center in radio and sub-millimeter, the galaxy is nearly transparent to all photons. For the infrared (IR) $H$-band ($\lambda = 1.637\,\mu$m), Fritz et al. (2011) found $A_\mathrm{H} = 4.21 \pm 0.10$ mag which implies that we only receive one photon on $10^{A_\mathrm{H}/2.5} \sim 100$. In optic (at 550 nm), $A_\mathrm{V} \sim 30$ mag (Rieke et al. 1989). This implies that only one photon on $10^{12}$ reaches us making impossible to observe the Galactic Center in visible light or UV. Since in IR and optic smallest wavelengths suffer more extinction, the source seems to emit more photons in longest wavelength. This phenomenon is called the interstellar reddening. In energies higher than about 2 keV, the galaxy becomes again nearly transparent to photons: more than 90% of emitted photons are received on Earth.

The center of our galaxy was observed, for the first time, in radio wavelengths at the end of the 1920s. An engineer of Bell Telephone, Karl Jansky, studied the source of noise for the phone communications with an antenna working at 20.5 MHz. He found a constant source of noise in the direction of the Sagittarius constellation (Jansky 1933). This was the first non-optic observation of the Universe. In 1959, Frank Drake observed for the first time the structure of the Galactic Center in radio with the Green Bank Telescope (Drake 1959).

A radio survey was made by Kassim et al. (1999) on a $4° \times 5°$ region with the VLA (see top panel of Fig. 1.2). Four main complexes can be seen in these wavelengths:

- Giant molecular clouds (Sgr B1, Sgr B2, Sgr C and Sgr D) forming the Central Molecular Zone;
- At the center, the 15 pc radio complex Sgr A which hosts the SMBH Sgr A*;
- Some non-thermal filaments produced by the synchrotron radiation of relativistic electrons around the magnetic field perpendicular to the galactic plane (Yusef-Zadeh et al. 1984);
- Some supernovae remnants (SNR) which have a non-thermal shell in expansion.

An infrared and X-ray image of the Galactic Center are shown in the middle and bottom panel of Fig. 1.2. The Sgr A complex is one of the most luminous object in each wavelength. In X-rays and IR, we can see two clusters of young and massive stars (the Quintuplet and Arches clusters) which create H II regions at less than 35 pc in projection from the Galactic Center. In X-rays, we can also see the center of the SNRs which are not observable in IR. The giant molecular clouds Sgr B1 and Sgr B2 are mostly seen in radio wavelengths.

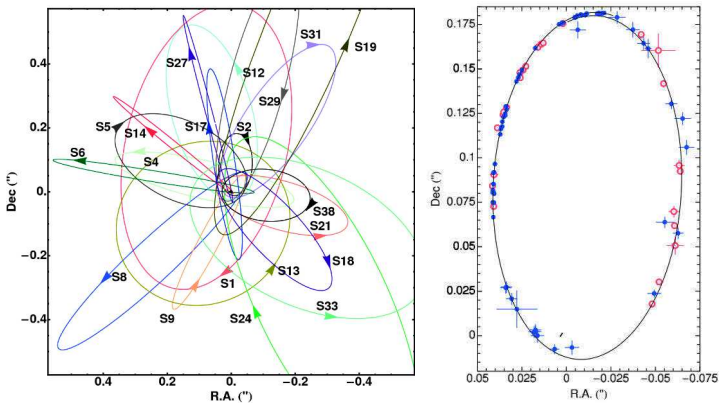


Figure 1.4: *Left panel:* Orbits of the stars in the S-cluster around Sgr A* (Gillessen et al. 2009b). *Right panel:* The S2 orbit (blue: NTT/VLT, red: Keck) from 1992 to 2009 (Gillessen et al. 2009a).

In the IR image, we observe stellar clusters, H II regions and dark clouds in silhouette against bright IR emission region.

### 1.1.3 The Sgr A complex

The Sgr A complex hosts the SMBH Sgr A* (black point in Fig. 1.3). Its structure thus influences and is influenced by Sgr A*

At 9.1 pc in projection, there is a SNR candidate named G359.92-0.09 (dotted circle in Fig. 1.3), confined by the dynamical pressure (Coil & Ho 2000).

Sgr A East (black ellipse in Fig. 1.3) is a SNR with different components: a shell dominated by synchrotron radiation which surrounds a hot plasma with X-ray thermal emission (Ekers et al. 1983). The hot ejecta in X-rays allows us to date the explosion to $10^4$ years ago (Aharonian et al. 2006).

The $10^4\ M_\odot$ tore of neutral gas named the "CircumNuclear Disk" (backwards "C" shape in Fig. 1.3) is the most luminous part of Sgr A East. It is probably fed by some molecular clouds at 10 pc in projection from Sgr A* (Eckart & Genzel 1999).

Sgr A West (light gray bands in Fig. 1.3) is composed by hot gas emitting in X-rays (Ekers et al. 1983; Sidoli & Mereghetti 1999). It hosts luminous stars which form the S-cluster (see left panel of Fig. 1.4). These stars have velocity that can reach $10^5\ \mathrm{km\,s^{-1}}$ and orbital period that can be as small as 10 years (Schödel et al. 2002; Gillessen et al. 2009a; Meyer et al. 2012).

A compact radio object was found in Sgr A West by Balick & Brown (1974) thanks to an interferometer from National Radio Astronomy Observatory (NRAO). This unresolved source was named "Sagittarius A*" by Brown (1982), the star reflecting the unresolved nature of the source, and is located at the shared focus of the Keplerian orbits of the stars from the S-cluster.

## 1.2 The Galactic Center supermassive black hole Sgr A*

### 1.2.1 The physical characteristics of Sgr A*

The mass of Sgr A* was first estimated to $2.6 \pm 0.2 \times 10^6\ M_\odot$ using the proper motion of 90 stars of the S-cluster from 1995 to 1997 (Ghez et al. 1998). Schödel et al. (2002) observed, for the first time, the pericenter passage of the $15\ M_\odot$ B0 type star S2 (also known as S0-2; Ghez et al. 1998) of the S-cluster at 124 au from Sgr A* on 2002. The orbit of this star is characterized by an eccentricity of 0.87 and an orbital period of only 15.2 years (see right panel of Fig. 1.4). Using the astrometric measurements of S2 from 1992 to 2002 (one third of the orbit), the authors constrained the mass of Sgr A* to $M = (3.7 \pm 1.5) \times 10^6\ M_\odot$. Then, the astrometric and spectroscopic measurements of S2 from 1995 to 2007 allowed Ghez et al. (2008) to constrain the mass of Sgr A* to $M = (4.1 \pm 0.6) \times 10^6\ M_\odot$ at $8.0 \pm 0.6$ kpc. Gillessen et al. (2009a) measured the orbits of 28 stars including S2 during 16 years leading to an improvement of the Sgr A* mass of $M = (4.31 \pm 0.06|_{\mathrm{stat}} \pm 0.036|_{\mathrm{dist}}) \times 10^6\ M_\odot$ at $8.33 \pm 0.35$ kpc. The discovery of a new faint star S0-102 having an orbital period shorter than S2 ($11.5 \pm 0.3$ years) allowed Meyer et al. (2012) to constrain the mass

and the distance of Sgr A* to $(4.1 \pm 0.4) \times 10^6\, M_\odot$ at $7.7 \pm 0.4$ kpc using only the orbit of the S0-102 star. This large mass thus proofs that Sgr A* is a SMBH so as the majority of massive galaxies have, at their center, a supermassive black hole whose the mass is comprised between approximately $10^5\, M_\odot$ and $10^{10}\, M_\odot$ (Maoz 2008).

The size of a black hole is defined by its Schwarzschild radius. This is the size of the event horizon where all matter and photons are gravitationally attracted by the black hole without possibility of escaping. The Schwarzschild radius is computed as

$$R_\mathrm{s} = \frac{2\,G\,M}{c^2} \approx 0.02 \frac{M}{10^6 M_\odot}\,\mathrm{au} \approx 3.0 \frac{M}{10^6 M_\odot}\,10^{11}\mathrm{cm} \tag{1.1}$$

with $M$ the black hole mass and $M_\odot$ the solar mass (Schwarzschild 1916). The gravitational radius is defined as $r_\mathrm{g} = 0.5\, R_\mathrm{s}$. The Schwarzschild radius of Sgr A* is $R_\mathrm{s} = 1.2 \times 10^{12}$ cm.

The most accurate radio position of Sgr A* was obtained with the Very Long Base Array (VLBA): RA(J2000) $= 17^\mathrm{h}45^\mathrm{m}40\overset{\mathrm{s}}{.}036 \pm 1.42$ mas, Dec(J2000) $= -29°00'28\overset{''}{.}17 \pm 2.65$ mas (Petrov et al. 2011). In near infrared (NIR), the position of Sgr A* is also known with a precision of 2 mas (Gillessen et al. 2009b).

The best constraint on the distance of Sgr A* from the Earth was given by the measure of trigonometric parallaxes and proper motions of 80 masers associated with high-mass stellar formation regions with the VLBA: $D = 8.34 \pm 0.16$ kpc $= 27.20 \pm 0.50$ kly (Reid et al. 2014).

Sgr A* has a proper motion of 20 km s$^{-1}$ in the galactic plane and 1 km s$^{-1}$ in the perpendicular direction (Reid et al. 1999; Reid & Brunthaler 2004). This is more than hundred times slower than the medium around it which proofs that it is located at the dynamical center of the Milky Way.

By abuse of language, I speak about the emission of Sgr A* instead of the emission from the matter accreted onto Sgr A*. This emission is currently described by a quiescent state (Sect. 1.2.2) with a bolometric luminosity, $L_\mathrm{bol} \approx 10^{36}$ erg s$^{-1}$ $\approx 300 L_\odot$ (Yuan et al. 2003) with episodic flaring activities (Sect. 1.2.3).

### 1.2.2 The quiescent state of Sgr A*

Considering a spherical accretion of matter, the accretion stops when the radiative force exerted by the photons on a matter element of mass $m$ ($F_\mathrm{rad} = L\,\sigma_\mathrm{T}\,m/4\,\pi\,m_\mathrm{p}\,c\,r^2$ with $r$ the distance to the attractive object center, $m_\mathrm{p}$ the proton mass and $\sigma_\mathrm{T}$ the Thomson cross section for an electron) exceeds the gravitational force undergone by this stellar matter ($F_\mathrm{G} = -G\,M\,m/r^2$). This theoretical limit on the luminosity for a black hole is defined as the Eddington luminosity:

$$L_\mathrm{Edd} = \frac{4\pi G\,M\,m_\mathrm{p}\,c}{\sigma_\mathrm{T}} \sim 3.4 \times 10^{11} \frac{M}{10^6 M_\odot} L_\odot\,. \tag{1.2}$$

For Sgr A* whose mass is about $4 \times 10^6 M_\odot$, $L_\mathrm{Edd} = 1.4 \times 10^{12} L_\odot$. Its bolometric luminosity is thus about $4.5 \times 10^{-9}\, L_\mathrm{Edd}$ which implies that Sgr A* is an extremely low-luminosity black hole.

The mass-accretion rate is linked to the bolometric luminosity by $\dot{M} = L_\mathrm{bol}/\eta\,c^2$ with $\eta$ the accretion efficiency (e.g., Czerny et al. 2013). The mass-accretion rate corresponding to the Eddington luminosity for $\eta = 0.1$ is

$$\dot{M}_\mathrm{Edd} = 2.2 \times 10^{-2} \frac{M}{10^6 M_\odot}\, M_\odot\,\mathrm{yr}^{-1}\,. \tag{1.3}$$

For Sgr A*, the Eddington accretion rate is $8.8 \times 10^{-2}\, M_\odot\,\mathrm{yr}^{-1}$. The study of X-ray quiescent emission from Sgr A* determined a mass-accretion rate $\dot{M}$ of $10^{-6}\, M_\odot\,\mathrm{yr}^{-1}$ (e.g., Baganoff et al. 2003) at the Bondi radius[1]. By measuring a rotation measure of $-5.6 \times 10^5$ rad m$^{-2}$ at the sub-millimeter bump of the spectral energy distribution of Sgr A*, Marrone et al. (2007) showed that the mass accretion rate is lower than $2 \times 10^{-7}\, M_\odot\,\mathrm{yr}^{-1}$ at about $10^{-4}$ times the Bondi radius if the magnetic field is near the equipartition. The current mass accretion rate of Sgr A* is thus several thousands of time smaller than $\dot{M}_\mathrm{Edd}$.

[1]The Bondi radius computed as $R_\mathrm{B} = GM_\mathrm{BH}/c_\mathrm{s}$ is the distance where the matter begins to be accreted (Bondi & Hoyle 1944; Bondi 1952; Shvartsman 1971). For Sgr A*, the sound velocity at infinity is $c_\mathrm{s} = 550$ km s$^{-1}$ for a plasma temperature $k_\mathrm{B}\,T = 1.3$ keV (i.e., $T = 15.1$ MK), an adiabatic index $\gamma = 5/3$ and a mean atomic weight of the gas $\mu = 0.7$ leading to $R_\mathrm{B} = 0.072$ pc $= 1\overset{''}{.}8 = 2.2 \times 10^{17}$ cm (Baganoff et al. 2003). It is about four times larger than the on-axis angular resolution of Chandra.

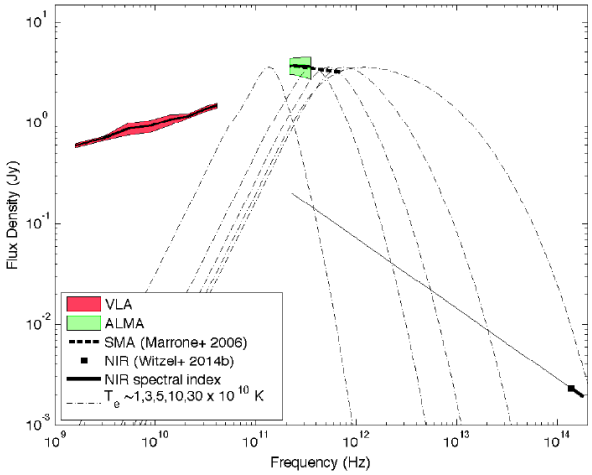


Figure 1.5: Mean SED of Sgr A* from VLA, the Atacama Large Millimeter Array (ALMA) and the Sub-millimeter Array (SMA) observations between 2012 to 2014 as shown in Bower et al. (2015).

To explain the low luminosity of Sgr A*, hot accretion flow models (for a review see Yuan & Narayan 2014 and references therein) such as the Advection-Dominated Accretion Flow (ADAF; Ichimaru 1977; Rees et al. 1982; Narayan & Yi 1994; Narayan et al. 1995, 1998) have been developed. The ADAF model invokes the decoupling between ions and electrons to explain the low luminosity with a mass-accretion rate $\dot{M}$ which is supposed to be constant over the distance. Indeed, ions are hot and advect their energy behind the event horizon before it can be radiated, while electrons are cooler than ions but radiate to produce the observed low luminosity. This model predicts a geometrically thick accretion flow which is characterized by a vertical scale similar to the horizontal scale (contrarily to the geometrically thin disk where the vertical scale is small compared to the disk radius). Yuan & Narayan (2014, and reference therein) parametrized the physical characteristics (density, magnetic field, sound speed,...) of the hot accretion flow as a function of the black hole characteristics using a self-similar and axisymmetric solution. To explain the low mass-accretion rate, they also introduced the parametrization of $\dot{M}$ with the distance with $\dot{M} = M_0(r/r_0)^s$ leading to the possibility of the presence of outflows such as winds (carrying most of mass) or jets (carrying most of energy) which eject the majority of matter captured in the Bondi radius before it reaches the black hole. The presence of such kind of mass loss is supported by the deep X-ray observations with Chandra (Wang et al. 2013) and explains the low mass accretion rate of Sgr A*.

The proximity (100 times closer that the center of M31; Schödel et al. 2002) and the large angular diameter (53 $\mu$as which is about twice larger than that of NGC 4486 in M87; Johannsen et al. 2012) of Sgr A* make it the best target to investigate such kind of models which can be applied to a majority of SMBH since these objects spend most of their lifetime in a low-luminosity state.

The quiescent luminosity of Sgr A* ($S_\nu$) may be measured at different frequencies ($\nu$) to build the spectral energy distribution (SED; see Fig. 1.5).

In the centimeter/millimeter range (typically from 1 to 100 GHz), the spectral index $\alpha$ (defined by $S_\nu \propto \nu^\alpha$) varies between 0.17 and 0.5 (Falcke et al. 1998; Bower et al. 2015) indicating that the emission is produced by an optically thick synchrotron radiation (see Appendix A.1 for further details). The quiescent emission flux in this frequency range is not constant but varies slowly with time (Zhao et al. 2001). In the sub-millimeter range (from 217 to 355 GHz), the spectral index is consistent with zero which represents a flat spectrum (Marrone et al. 2006; Bower et al. 2015). The source thus becomes optically thin in this part of the SED named the sub-millimeter bump. The intrinsic size of the quiescent emission at a certain radio/sub-millimeter wavelength can be computed thanks to the relation given in Doeleman et al. (2008) which measured a $3\sigma$ range of $37(230\,\mathrm{GHz}/\nu)^{1.44}$ $\mu$as = $4.6(230\,\mathrm{GHz}/\nu)^{1.44}$ $10^{12}$ cm. They pointed out a structure for this size which was confirmed by the observations with the Event Horizon Telescope at 230 GHz (Fish et al. 2016). These authors were able to discriminate between the two position angles of $-52°$ and $+128°$ east found by Broderick et al. (2011). The radio/sub-millimeter quiescent thus seems to be elongated with a position angle of $+128°$ east.

After the sub-millimeter bump, the spectral index in IR between the L, H, K, and M-bands (i.e., between 1.63 $\mu$m and 4.67 $\mu$m) is about $-0.6$ (Hornstein et al. 2007; Witzel et al. 2014b). This emission is produced by

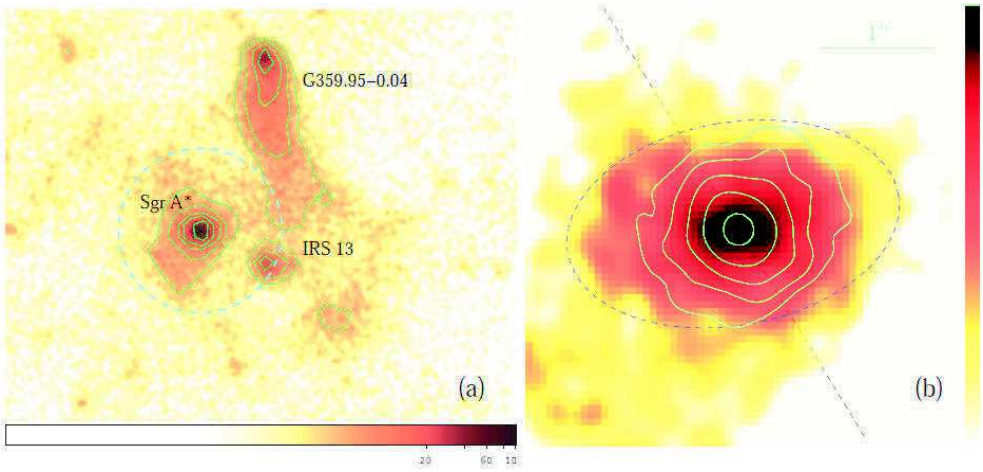


Figure 1.6: The X-ray quiescent emission from Sgr A* as seen by Chandra (Wang et al. 2013). The north is at the top and the east is on the left. *Left panel:* The dashed circle is the Bondi radius. The contours are at 1.3, 2.2, 3.7, 6.3, and $11{\times}10^{-4}$ count $s^{-1}$ arcsec$^{-2}$. *Left panel:* A zoom on the quiescent emission of Sgr A* which is decomposed into extended (colored image) and point-like (contours of 0.3, 0.6, 1.2, 2.4, and 5 counts pixel$^{-1}$) components. The dashed line is the orientation of the Galactic plane. The dashed ellipse represents the elongation of the primary massive stellar disk.

an optically thin synchrotron radiation.

The X-ray quiescent emission resolved for the first time with the ACIS-I camera on-board Chandra has a 2–10 keV unabsorbed luminosity of about $2 \times 10^{33}$ erg $s^{-1}$ (Baganoff et al. 2003). The study of the quiescent emission was then improved by Wang et al. (2013) by using the ACIS-S camera and the High Energy Transmission Grating (HETG) on-board Chandra, i.e., with an on-axis spectral resolution of the zero order of the HETG which is twice better than the previous ACIS-I study. The Chandra angular resolution allowed them to study the quiescent emission of Sgr A* without contamination by the nearby sources (see left panel of Fig. 1.6). The authors confirmed that the spectrum of the quiescent emission has several emission lines: the Fe XXV K$\alpha$ line at 6.7 keV but also the Fe XXV K$\beta$ line at 7.8 keV, Ar XVII and Ar XVIII K$\alpha$ lines at 3.1 and 3.3 keV, S XV K$\alpha$ line at 2.4 keV and Ca XIX K$\alpha$ line at 3.9 keV. They also observed a weak H-like Fe line at 6.97 keV which suggests the presence of an outflow which eject more than 99% of the accretion mass supporting the hot accretion flow model. Moreover, they found that the overall continuum spectrum is well reproduced by this model with a 2–10 keV unabsorbed luminosity of $3.4^{+0.9}_{-0.5} \times 10^{33}$ erg $s^{-1}$. The spatial distribution of the X-ray quiescent emission has an elongated shape in the east-west direction with a size of about $1'' - 1''.5$ plus a point-like contribution which represents 20% of the total quiescent emission (see right panel of Fig. 1.6) and which is an unresolved flaring emission in the X-ray light curve.

### 1.2.3 The Sgr A* multiwavelength activity

A majority of the flux coming from Sgr A* is created in the hot accretion flow with a radiatively inefficient accretion mechanism. However, several times a day, in addition to this quiescent emission, the SMBH emits a much larger number of photons from radio to X-rays during a limited period of time. These events are named "flares". Flares are important to understand the mechanism of transport and ejection of matter near Sgr A*.

***The X-ray activity***

Flares were first observed on 2000 Oct. 26 in X-rays with Chandra (Baganoff et al. 2001). During this observation, a bright flare was detected with a 2–10 keV peak unabsorbed luminosity of $L^{\rm unabs}_{2-10\,{\rm keV}} = (1.0 \pm 0.1) \times 10^{35}$ erg $s^{-1}$. On 2002 Oct. 3, a more luminous flare was detected with $L^{\rm unabs}_{2-10\,{\rm keV}} = 3.6^{+0.3}_{-0.4} \times 10^{35}$ erg $s^{-1}$ with XMM-Newton (Porquet et al. 2003). On 2012 Feb. 9, an even more bright flare was observed with Chandra ($L^{\rm unabs}_{2-10\,{\rm keV}} = 4.8^{+1.9}_{-1.1} \times 10^{35}$ erg $s^{-1}$; Nowak et al. 2012).

The 2012 *Chandra X-ray Visionary Program (XVP)* campaign of 3 Ms exposure reported by Neilsen et al. (2013) allowed the authors to detect 39 eruptions (see Fig. 1.7) and to increase the flares statistics. The flaring events brighter than $10^{34}$ erg $s^{-1}$ happen $1.1^{+0.2}_{-0.1}$ times a day. Half of the eruptions are moderate flares (with

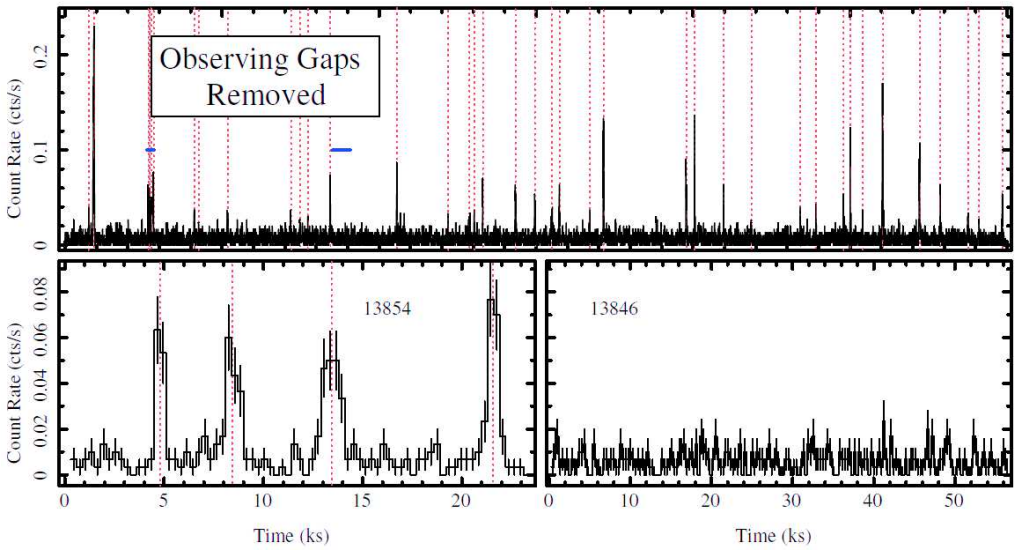


Figure 1.7: Example of X-ray light curves from Sgr A* as seen with Chandra in 2012 (Neilsen et al. 2013). The vertical dotted red lines depicts the position of the X-ray flares. The horizontal blue lines are the time range for the bottom zoomed panels.

luminosity lower than 10 times the quiescent emission) whereas bright flares (above $10^{35}$ erg s$^{-1}$) occur every 11.5 days, i.e., 0.087 times a day. The luminosity and fluence (or energy) distribution follow a powerlaw as $dN/dL \propto L^{-1.9\pm0.4}$ and $dN/dF \propto F^{-1.5\pm0.2}$, respectively. The X-ray flares last from some minutes to 3 hours.

Neilsen et al. (2013, 2015) found that 10–15% of the X-ray quiescent emission is a flaring activity undetected with Chandra. Neilsen et al. (2013) also demonstrated that the X-ray quiescent emission described in Section 1.2.2 can not be considered as only variable emission. The total X-ray emission from Sgr A* is thus composed by a detected and undetected flaring emission superimposed to the quiescent emission.

No significant quasi-periodic variability are observed in the flare light curves but some sharp drops can be detected (Porquet et al. 2003). The shortest temporal variation during an eruption was observed by Porquet et al. (2003) on 2002 Oct. 3 with a duration of 200 s. Using a supermassive black hole mass of $3 \times 10^6 M_\odot$ (leading to a Schwarzschild radius of $R_s = 8.9 \times 10^9$ m), they determined the size of the emitting source to about 7 $R_s$ for a maximum velocity equals to the light speed. From the revised Sgr A* mass of $4 \times 10^6 M_\odot$, the Schwarzschild radius increases to $R_s = 1.2 \times 10^{10}$ m leading to a maximum source size of 5 $R_s$.

The spectrum of the X-ray flares is well reproduced by an absorbed power-law with a best constrained hydrogen column density and spectral index of $16.1^{+1.9}_{-2.2} \times 10^{22}$ cm$^{-2}$ and $2.3^{+0.3}_{-0.3}$, respectively (Porquet et al. 2003; Nowak et al. 2012).

***The NIR activity***

On 2003 May 9, Genzel et al. (2003) discovered the first NIR flare from Sgr A* at 1.7 $\mu$m with NACO installed on the Very Large Telescope (VLT). Since then, infrared flares have been observed several times a day (Genzel et al. 2003; Witzel et al. 2012) with a typical duration of 40 min (Ghez et al. 2004). Quasi-periodic variabilities of several minutes are observed in the light curve of the NIR flares (Genzel et al. 2003). Substructures with a timescale of 15-25 min can be also seen in their light curves (Genzel et al. 2003; Meyer et al. 2006; Trippe et al. 2007). These timescales correspond to the period of an orbit close to the last stable orbit for a Kerr black hole, i.e., a black hole described by its mass and a non-zero spin.

The NIR flare emission comes from the synchrotron radiation (Eisenhauer et al. 2005; Eckart et al. 2006a; see Appendix A.1 for further details) and provides a huge range of flux amplitudes. An example of NIR light curves as observed by VLT/NACO is shown in Fig. 1.8.

Contrarily to X-rays, the NIR emission is considered as an overall variable emission and not a quiescent emission plus some flaring events (Meyer et al. 2014). Figure 3 of Witzel et al. (2012) shows that the distribution of the flux density observed by VLT/NACO has a maximum at 3.57 mJy. Below this amplitude, the distribution decreases because of the detection limit of VLT/NACO. Above 3.57 mJy, the distribution is highly asymmetric with a rapid decay of the frequency density followed by a long tail until 32 mJy.

General Relativity Magneto-Hydro Dynamic (GRMHD) simulations done by Chan et al. (2015) show that

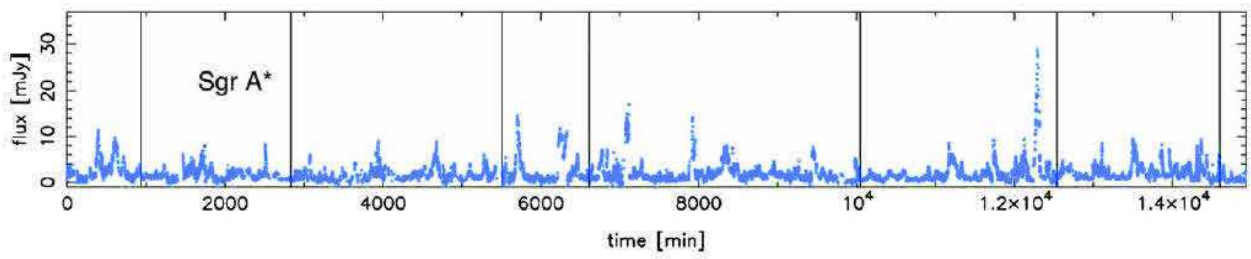


Figure 1.8: Example of NIR light curves from Sgr A* as seen with VLT/NACO (Witzel et al. 2012).

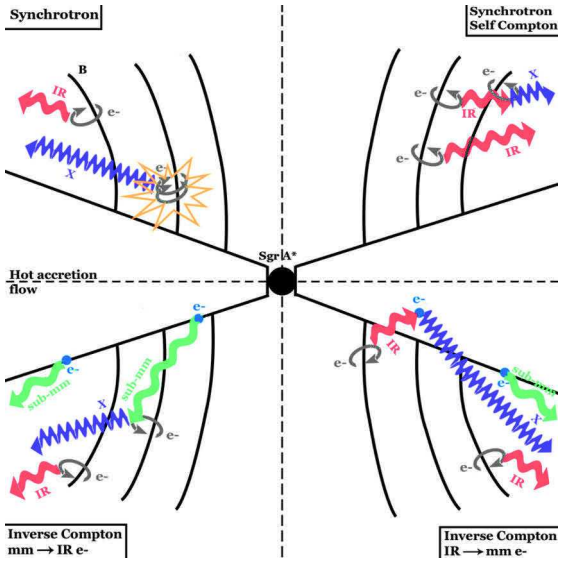


Figure 1.9: Sketch of possible radiative processes for the IR/X-ray flaring emission from Sgr A*.

an accretion flow model can reproduce the time variability and spectra of IR and millimeter flares whereas jet-dominated models produce less variability compared to observations.

The infrared eruptions show a dramatic change of polarization degree and angle during the flare: the polarization degree can increase from 10% to 40% at the flare peak and increases during the decay phase (Eckart et al. 2006b; Meyer et al. 2006; Trippe et al. 2007). Shahzamanian et al. (2015) found that, above 2 mJy, there is an intrinsic polarization degree of 20%±10% and a preferred polarization angle of 13°±15° which may be linked to the orientation of the accretion disk or jet of Sgr A*.

***The simultaneous NIR/X-ray activity***

On 2003 June 19, for the first time, a flare was observed simultaneously in X-rays and NIR (Eckart et al. 2004). The brightest NIR/X-ray flare was then observed on 2007 Apr. 4 (Porquet et al. 2008; Dodds-Eden et al. 2009). We now know that each X-ray flare has an infrared counterpart but the contrary is not true (Eckart et al. 2006a, 2008; Hornstein et al. 2007; Yusef-Zadeh et al. 2006a; Dodds-Eden et al. 2009). The delay between the maximum of the NIR and X-ray flare is lower than some minutes (Yusef-Zadeh et al. 2012).

From these simultaneous observations, three possible radiative processes involved during X-ray events are proposed (see Appendix A for details):

- Synchrotron radiation (upper left part of Fig. 1.9) emitted by relativistic electrons which gyrate around magnetic field lines. The relativistic properties of the electrons cause the emission to be collimated.

- Inverse Compton process (IC). Two different IC mechanisms can happen: in the first IC mechanism, the sub-millimeter photons from the hot accretion flow are upscattered by the non-thermal electrons producing the NIR synchrotron emission (bottom left part of Fig. 1.9). Since the hot accretion flow is optically thick to sub-millimeter photons, only photons produced near the surface of the flow are available to be upscattered. The second IC mechanism is the upscattering of infrared photons produced by accelerated electrons by the thermal electrons of the hot accretion flow (bottom right part of Fig. 1.9). Since the hot accretion flow is optically thin to the infrared photons, all these thermal electrons are

available to produce X-rays.

- Synchrotron Self Compton process (SSC; upper right part of Fig. 1.9). This radiation is the local counterpart of the IC process. The source of photons and electrons are the same, implying that the NIR photons are upscattered by the non-thermal electrons that produced them.

Several studies have been made on these radiative processes both from the theory (Yuan et al. 2003, 2004; Liu et al. 2006) and the observations (Yusef-Zadeh et al. 2006a; Marrone et al. 2008; Dodds-Eden et al. 2009; Eckart et al. 2009; Yusef-Zadeh et al. 2012; Eckart et al. 2012). At the current date, these radiative processes for the X-ray flaring emission are still debated and none of them can be ruled out.

Several mechanisms can explain the origin of eruptions in X-rays and infrared:

- A shock produced by the interaction between orbiting stars and the hot accretion flow (Nayakshin & Sunyaev 2003; Nayakshin et al. 2004). This model allowed these authors to simulate the infrared flares but their frequencies and substructures remain difficult to explain with this model. Furthermore, the hot accretion flow has to remain dense enough at large distance from Sgr A* but it is difficult to create such kind of flow with the hot accretion flow model.

- A hotspot model (Broderick & Loeb 2005; Eckart et al. 2006b; Meyer et al. 2006; Trippe et al. 2007; Hamaus et al. 2009). This model has been developed to explain the variability of the light curve during the flare event. By passing behind the black hole the observed luminosity of the source increases thanks to the gravitational lensing. Then, as the source is moving towards the observer, a second increase of the observed luminosity happens due to the Doppler boosting effect. These eruptions are generally composed by two close peaks whose the first one has a higher amplitude and a shorter duration than those of the second one. A third observed luminosity variation with an even lower amplitude can also be created when the source is located between the observer and the black hole. In this configuration, the observer also receives photons from the non visible part of the hotspot.

- A Rossby instability producing magnetized plasma bubbles in the hot accretion flow (Tagger & Melia 2006; Liu et al. 2006). These instability waves propagate inside and outside their corotational radius, where they have the same velocity than the surrounding medium. The direction of the wave depends of the sign of its specific vorticity. If the ring where the plasma bubbles are produced becomes instable, a Rossby vorticity is created and evolves non-linearly. The instability increases during several rotations and the bubble is accreted towards the center.

- An additional heating of electrons near the black hole due to processes such as accretion instability or magnetic reconnection (Baganoff et al. 2001; Markoff et al. 2001; Yuan et al. 2003, 2009).

- An increase of accretion rate when some fresh material reaches the close environment of the black hole (Yuan et al. 2003; Czerny et al. 2013).

- Tidal disruption of asteroids (Čadež et al. 2006, 2008; Kostić et al. 2009; Zubovas et al. 2012). This explanation was proposed since the luminosity released during a NIR flare corresponds to a mass of about $10^{17}$ kg for an efficiency for converting matter to energy of 10% (Genzel et al. 2003). If an asteroid larger than 10 km is disrupted by the tidal forces in the hot accretion flow of Sgr A*, the shocks and instabilities created by the fragments may produce X-rays with the required luminosity (Zubovas et al. 2012).

***The radio/sub-millimeter activity***

The radio/sub-millimeter flares from Sgr A* observed since 2003 (Zhao 2003) seems to be delayed by some tens of minutes to some hours after the infrared/X-ray flares (Marrone et al. 2008; Yusef-Zadeh et al. 2008, 2009). This behavior can be explained by an expanding plasmon with adiabatic cooling model (Van der Laan 1966; Yusef-Zadeh et al. 2006b). In this model, the IR activity comes from the synchrotron emission of a plasmon which is initially optically thin to IR and X-ray wavelengths and optically thick to the radio and sub-millimeter wavelengths leading to an occultation of a part of the hot accretion flow. As the source adiabatically

expands, the density of electrons diminishes and the source becomes optically thin to the radio and sub-millimeter wavelengths leading to an increase of observed synchrotron flux from the source and from the part of hot accretion flow that was occulted. The formula governing this model are presented in Appendix B. Other interpretations are also proposed: Brinkerink et al. (2015) supported the collimated outflow model based on the measured time lag between the sub-millimeter and radio light curves and an intrinsic size of Sgr A* at a wavelength $\lambda$ of $(0.52 \pm 0.03)\,\mathrm{mas} \times (\lambda/\mathrm{cm})^{1.3\pm0.1}$. On 2012 May 17, Rauch et al. (2016) detected a 7-mm flare which was delayed by $4.5 \pm 0.5$ h after a NIR flare with the VLBA. They localized this millimeter flare at 1.5 mas southeast of Sgr A* which provides evidence for an adiabatically expanding jet with a speed of $0.4 \pm 0.3\ c$.

## 1.3 Summary of the current knowledge on the emission from Sgr A*

For the quiescent emission, some constraints may be put on the hot accretion flow thanks to the spectral energy distribution (SED) of Sgr A* in radio/sub-millimeter, infrared and X-rays and the polarization measures observed in radio/sub-millimeter. But the parameters of the ADAF model reported in Yuan & Narayan (2014, and references therein) such as the viscosity, the mass accretion rate and the magnetic field strength are still unconstrained. Nevertheless, it is very important to understand and constrain this low-luminosity model since it could be extended to a large variety of non-active galaxies which represent the dominant extragalactic population in the local Universe. Moreover the ADAF model can be applied from stellar black hole X-ray binaries to low-luminosity AGNs.

For the flaring activity from Sgr A*, we know that the NIR flares are produced by synchrotron radiation but the radiative processes and the electrons acceleration mechanisms for the creation of the X-ray activity are still debated. In addition, we still have some difficulties to explain the range of amplitude and duration of the NIR and X-ray flares and the absence of detected X-ray activity simultaneous to some NIR flares. Moreover, the time delay between the radio/sub-millimeter activity and the NIR/X-ray flares may be explained by the expanding plasmon model but the deduced model parameters are flare-dependent. There is thus no common model parameters which explains all the radio/sub-millimeter activity yet. We thus need a higher number of simultaneous multi-wavelength observations to compare the emission models to the observations and to constrain the physical characteristics of the close environment of Sgr A* such as the magnetic field, the density, the electrons energy density,...

## 1.4 The Dusty S-cluster Object/G2

The current luminosity of the quiescent and flares characteristics from Sgr A* may change thanks to a recently-discovered object orbiting Sgr A* with a close pericenter. The orbital elements of the DSO/G2 computed in the studies presented hereafter are reported in Table 1.1.

Observations of the Galactic Center between 2004 and 2011 with VLT/NACO and SINFONI have revealed the presence of an object named G2 on an eccentric Keplerian orbit towards Sgr A* (Gillessen et al. 2012). The hydrogen Br$\gamma$ and Br$\delta$ and the He I lines were redshifted during all these observations showing that the object has not yet passed its pericenter in 2011. The first orbit estimate based on the study of the spectroscopic lines predicted a pericenter passage on mid-2013. This first study determined the nature of the G2 object as to be a dusty and ionized cloud of gas. This result was supported by two findings: the spectroscopic lines follow the proper motion seen in the $L'$-band and the Br$\gamma$ line measured in regions extracted along the predicted orbit is elongated along the orbit in a velocity-position diagram (with total luminosity of $(1.66 \pm 0.25) \times 10^{-3}\ L_\odot$). Thanks to the $M$-band observations, the authors determined that this cloud would have a gas and dust temperatures of about $10^4$ and 450 K, respectively. The deduced mass and electron density of the G2 are 3 times the Earth mass and $2.6 \times 10^5\ \mathrm{cm}^{-3}$, respectively. During the pericenter passage, the cloud would be disrupted and create a bow shock with the hot accretion flow which would be visible from radio to X-rays. The disruption of the cloud by the tidal forces of Sgr A* and the Rayleigh-Taylor and Kelvin-Helmholtz instabilities was also proposed by Morris (2012).

The formation scenario of G2 was first investigated by Burkert et al. (2012). They used the hot accretion flow model of Yuan et al. (2003) and the physical constrains given by the Chandra observations to reproduce the conditions prevailing at the Galactic Center. They deduced two possible formation scenarios according to

Table 1.1: Orbital elements of the DSO/G2.

| | a (mas) | e | i (°) | Ω (°) | $\omega$ (°) | P (yrs) | $t_0$ (yrs) | $p_0$ ($R_s$) |
|---|---|---|---|---|---|---|---|---|
| Gillessen et al. (2012)[a] | 521 ± 28 | 0.9384 ± 0.0066 | 106.55 ± 0.88 | 101.5 ± 1.1 | 109.59 ± 0.78 | 137 ± 11 | 2013.51 ± 0.04 | 3100 |
| Gillessen et al. (2013a)[b] | 666 ± 39 | 0.9664 ± 0.0026 | 109.48 ± 0.81 | 95.8 ± 1.1 | 108.50 ± 0.74 | 198 ± 18 | 2013.69 ± 0.04 | 2200 |
| Phifer et al. (2013)[a] | ..... | 0.9814 ± 0.0060 | 121 ± 3 | 56 ± 11 | 88 ± 6 | 206 ± 15 | 2014.21 ± 0.14 | 1600 |
| Gillessen et al. (2013b)[b] | 684 ± 55 | 0.9698 ± 0.0031 | 110.2 ± 1.4 | 94.5 ± 1.8 | 108.6 ± 1.2 | 276 ± 111 | 2013.72 ± 0.05 | 2000 |
| Gillessen et al. (2013b)[a] | 1048 ± 247 | 0.9762 ± 0.0074 | 118.1 ± 2.0 | 81.9 ± 4.3 | 97.2 ± 2.2 | 391 ± 66 | 2014.25 ± 0.06 | 2400 |
| Pfuhl et al. (2015)[a] | 1050 ± 250 | 0.976 ± 0.007 | 118 ± 2 | 82 ± 4 | 97 ± 2 | ..... | 2014.25 ± 0.06 | 1950 |
| Valencia-S. et al. (2015)[a] | 846.15 ± 76.9 | 0.976 ± 0.001 | 113 ± 1 | 76 ± 8 | 94 ± 8 | 262 ± 38 | 2014.39 ± 0.14 | 2032 |

**Notes:** [(a)] Br$\gamma$ based; [(b)] L'-band based.

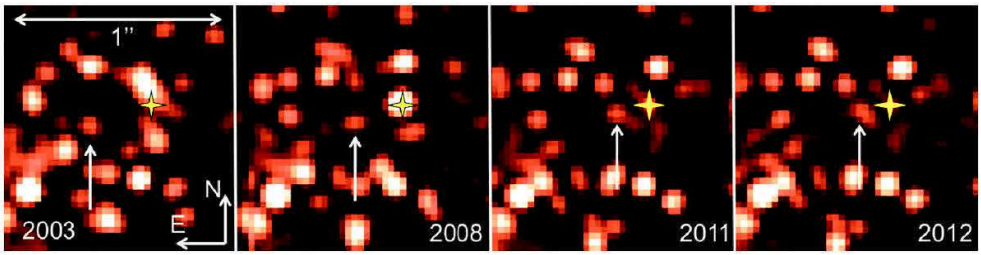


Figure 1.10: The G2's images in *L*-band from 2003 to 2012 (Gillessen et al. 2013a). The arrow points toward the G2's position. The yellow star is the position of Sgr A*.

the nature of this object: a diffuse gas cloud or a compact source. In the diffuse gas cloud model, the object was formed in 1995 thanks to the compression of the slow and cold wind of the luminous blue variable stars by the rapid and hot wind of the O and WR stars in the stellar disk surrounding Sgr A*. The cold core cools rapidly creating drops of condensed gas in the hotter medium. In this model, the G2 would be disrupted during its pericenter passage near Sgr A*. In the compact object model, the G2 is composed by a central source which is obscured by surrounding matter. The central object has to have a temperature lower than $10^{4.6}$ K and to emit most of their luminosity in UV to remain invisible. This compact object would be formed in the stellar disk but its orbit may had become highly eccentric after multiple gravitational interaction with other stars. This scenario would prevent from the disruption of the G2 at the pericenter passage.

Eckart et al. (2013) studied the compact source model and tested the nature of G2 as a star surrounded by a gas and dust disk or shell. The authors thus named G2 as a Dusty S-cluster Object (DSO) to refer to the true nature of the object. They used $L'$-, $H$- and $K_s$-bands observations from VLT/NACO between 2002 and 2012 to predict that, during the pericenter passage, only small part of matter would pass through the Lagrange point between the DSO/G2 and Sgr A*.

Additional observations in March−July 2012 with VLT/NACO lead to updated orbital parameters of the G2 (Gillessen et al. 2013a). The snapshots showing the evolution of the G2 object towards Sgr A* in *L*-band are given in Fig. 1.10. They showed that the luminosity in Br$\gamma$ is constant from 2004. The evolution of the line width of the Br$\gamma$ line still favored the gas cloud nature of G2. Some years after the pericenter passage, the spiral-in fragmented matter from the G2 would increase the accretion rate of Sgr A* with a possible reactivation the black hole in an AGN phase. This effect should be visible at all energy bands. The flares characteristics would also be different than those observed today: they would be longer, brighter and would happen more often. Furthermore, hot accretion flow around Sgr A* would become optically thin.

Phifer et al. (2013) used the W. M. Keck I and II data from 2006 to 2012 to update the orbital parameters using the Br$\gamma$ emission line and the $L'$-band observations. They did not detect emission from the $K'$-band up to 20 mag. They pointed out a bias between the orbital parameters measured with the Br$\gamma$ and in the $L'$-band since the G2 object is unresolved from the ambient gas in the $L'$-band. They also deduced that the luminosity in Br$\gamma$ and in the $L'$-band were constant within uncertainties from 2006 to 2012.

Gillessen et al. (2013b) updated the orbital parameters of G2 using the Br$\gamma$ and the $L'$-band of additional observations taken on 2013 April with VLT/NACO and SINFONI. They extracted the velocity-position diagram along the predicted orbit of G2. The elongation of G2 in the resulting velocity-position diagram still favored the interpretation of an ionized gas cloud. They also detected a blueshifted counterpart implying that a part of the cloud had passed the pericenter between the last 2012 observations and 2013 April.

Ballone et al. (2014) tested the model of a compact source with ejection of matter using hydrodynamical

Table 1.2: Rotational periods and spin-downs of the Galactic Center magnetar taken from the literature.

| References | Period (s) | Period derivative (s s$^{-1}$) | Period second derivative (s$^{-1}$) | Epoch[a] (MJD) |
|---|---|---|---|---|
| Mori et al. (2013a) | $3.7635417 \pm 80$ | ..... | ..... | 56408.0417 |
| Mori et al. (2013b) | $3.76354455 \pm 7.1 \times 10^{-7}$ | $6.5 \times 10^{-12} \pm 1.4 \times 10^{-12}$ | ..... | 56409.2657 |
| Gotthelf et al. (2013) | $3.7635603 \pm 68$ | ..... | ..... | 56415.4186 |
| Kaspi et al. (2014) | $3.763547895 \pm 2.9 \times 10^{-8}$ | $6.12 \times 10^{-12} \pm 1.2 \times 10^{-13}$ | $1.15 \times 10^{-18} \pm 1.5 \times 10^{-19}$ | 56415.42 |
| Rea et al. (2013) | $3.7635537 \pm 2 \times 10^{-7}$ | $6.61 \times 10^{-12} \pm 4 \times 10^{-14}$ | ..... | 56424.55 |
| Kaspi et al. (2014) | $3.76363824 \pm 1.3 \times 10^{-7}$ | $1.385 \times 10^{-11} \pm 1.5 \times 10^{-13}$ | $3.9 \times 10^{-19} \pm 6 \times 10^{-20}$ | 56513 |
| Coti Zelati et al. (2015) | $3.76363799 \pm 7 \times 10^{-8}$ | $1.360 \times 10^{-11} \pm 6 \times 10^{-14}$ | $3.7 \times 10^{-19} \pm 2 \times 10^{-20}$ | 56513 |
| Coti Zelati et al. (2015) | $3.7639772 \pm 1.2 \times 10^{-6}$ | $3.27 \times 10^{-11} \pm 7 \times 10^{-13}$ | ..... | 56710 |
| Mossoux et al. (2016)[b] | $3.76398106^{+2.0\times10^{-7}}_{-2.1\times10^{-7}}$ | $3.7684 \times 10^{-11}{}^{+9.9\times10^{-14}}_{-1.6\times10^{-13}}$ | ..... | 56716 |

**Notes:** [(a)] Reference epoch for the computed parameters. MJD=TJD+40000 days=JD-2400000.5 days; [(b)] The errors are the 90% confidence interval (see left panel of Fig. 5.6).

simulations. They found that the Br$\gamma$ luminosity is well reproduced by mass loss rate of the source of $8.8 \times 10^{-8}\,M_\odot\,\mathrm{yr}^{-1}$ and a wind velocity of $50\,\mathrm{km\,s}^{-1}$. This corresponds to the stellar wind of a T Tauri star, i.e., a young (pre-main sequence) low-mass star. This object would have been formed $10^6$ years ago inside the stellar disk and entered in an elliptical orbit after the encounter with a star or a massive black hole.

New observations obtained in 2014 March−August with the W. M. Keck Observatory showed that the $L'$-band emission remained constant and spatially unresolved from 2004 to 2014 with a deredened flux of 2.1 mJy which ruled out a core-less model (Witzel et al. 2014a). They deduced that the emission of G2 comes from the heating of the surrounding dust by the compact source which would be a main-sequence star (or close to the main-sequence).

Pfuhl et al. (2015) used the observations made from 2013 Aug. to 2014 July with VLT/SINFONI to deduce the new orbital parameters of the G2. They had the first observation of when the object has totally passed the pericenter passage. They computed a radial velocity change from $2700 \pm 150$ on 2013.7 to $-3300 \pm 150\,\mathrm{km\,s}^{-1}$ on 2014.3.

The best constraints on the DSO/G2 characteristics were finally provided by the study of the VLT/SINFONI observations obtained in 2014 Feb.–Sept. that I cosigned (Valencia-S. et al. 2015). The results of this study will be reported in Sect. 5.1.

## 1.5 The SGR J1745-29 magnetar

During the regular monitoring of the Galactic Center with Swift, a large increase of the X-ray luminosity was detected during the 1 ks exposure of the 2013 April 24 observation in the 10″-radius extraction region centered on Sgr A*. This luminosity was first associated to the largest flare observed from Sgr A* (Degenaar et al. 2013). Dwelly & Ponti (2013) triggered pre-approved Swift/XRT observations on 2013 April 25 at 14:38 and 15:58 UT. In these observations, an ongoing large X-ray activity was observed in the 22″-radius extraction region centered on Sgr A*. On 2013 April 25 at 19:15 UT, Swift/BAT triggered on a short (32 ms) hard X-ray (15–50 keV) burst suggesting that the large X-ray flux is produced by a new Soft Gamma Repeater (SGR) unresolved from Sgr A* (Kennea et al. 2013a). The subsequent Swift/XRT observations allowed the authors to determine the position of the SGR to RA(J2000)=$17^{\mathrm{h}}45^{\mathrm{m}}40\overset{\mathrm{s}}{.}19$ Dec(J2000)=$-29°00'28\overset{''}{.}4$ with a $2\overset{''}{.}8$ error. This SGR was named SGR J1745-29 by Gehrels et al. (2013).

On 2013 April 26, Mori et al. (2013a) observed the Galactic Center between 3 and 10 keV with the Nuclear Spectroscopic Telescope Array (NuSTAR). They found that the spectrum of the eruption is different than those measured for the X-ray flares from Sgr A*: this is a blackbody spectrum with a temperature of $kT_{\mathrm{BB}}$=0.85 keV plus a power-law spectrum with a photon index of $\Gamma = 3.2$. They measured an unabsorbed luminosity of $1.8 \times 10^{35}\,\mathrm{erg\,s}^{-1}$ for a distance of 8 kpc. They searched for a periodic signal during the eruption and found a rotational period of $P = 3.7635417(80)$ s (Table 1.2) on 2013 April 26 01:00 UT leading to a pulse profile composed by three resolved peaks.

Gotthelf et al. (2013) measured the rotational period and spin-down ($\dot{P}$) of the SGR thanks to an observation made by Swift/XRT on 2013 May 3 (Table 1.2). The spin-down measurement implies a magnetic field at the equator of $B = 3.2 \times 10^{19}\sqrt{P\dot{P}} = 3 \times 10^{14}$ G. Due to this high magnetic field, SGR J1745-29 is thus

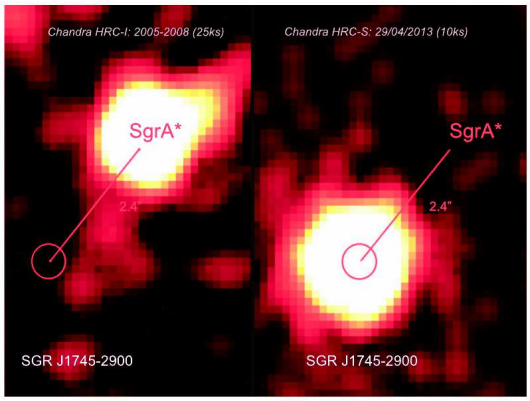


Figure 1.11: Chandra images of the Galactic Center before and after the discovery of the magnetar (Rea et al. 2013). *Left panel:* Chandra image taken with the HRC-I from 2005 to 2008 (25 ks). *Right panel:* Chandra image taken with the HRC-S on 2013 April 24 (10 ks). The magnetar is located at 2″.4 southeast of Sgr A*.

considered as a magnetar.

Kennea et al. (2013b) determined the spectral parameters of the magnetar for the Swift/XRT observation obtained on 2013 April 25 at 20:51 UT: $N_{\rm H} = 13.7^{+1.3}_{-1.2} \times 10^{22}$ cm$^{-2}$, $kT_{\rm BB} = 1.06 \pm 0.06$ keV and $\Gamma = 3.5 \pm 0.3$.

Rea et al. (2013) observed the magnetar in X-rays with Chandra/HRC on 2013 April 29 to July 2 and in radio with the Green Bank Telescope (GBT) and the Parkes Telescope from 2013 April 27 to May 4. The source completes the sample of 27 magnetars already observed whose only four display a radio emission. The rotational period and spin-down in X-rays are reported in Table 1.2. These measurements lead to a magnetic field of $1.6 \times 10^{14}$ G. They showed that the X-ray flux varies as $F(t) = F_0\, e^{-(t-t_0)/\tau}$ with $t_0$ fixed the time when the first burst was detected, $F_0 = (1.72 \pm 3) \times 10^{-11}$ erg s$^{-1}$ cm$^{-2}$ and $\tau = 144 \pm 8$ d. This is one of the smallest decay time ever measured for a magnetar. Figure 1.11 shows that SGR J1745-29 is at about 2″.4 southeast of Sgr A*. The magnetar can thus only be resolved from Sgr A* with Chandra.

The best constrain on the magnetar position was given by the Australia Telescope Compact Array (ATCA) observations on 2013 May 1 and 31: RA(J2000)= $17^{\rm h}45^{\rm m}40\overset{\rm s}{.}164 \pm 0\overset{\rm s}{.}022$, Dec(J2000)= $-29°00'29\overset{''}{.}818 \pm 0\overset{''}{.}090$ (Shannon & Johnston 2013).

The rotational measure of the magnetar may constrain the magnetic field near Sgr A* since the temporal variability of a magnetar depends on the external magnetic field. Eatough et al. (2013) computed the rotational measure (RM) of $(-6.696 \pm 0.005) \times 10^4$ rad m$^{-2}$. This is only one tenth of the RM measured at several dozens of parsec from Sgr A*. The lower limit on the magnetic field at 2″.4 in projection from Sgr A* is 50 $\mu$G. Assuming that the magnetic field increases towards Sgr A* as $r^{-1}$, the inferred magnetic field near Sgr A* is about some hundred Gauss.

Kaspi et al. (2014) used the NuSTAR observations from 2013 April 26 to August 24 to determine the change in the rotational period. Their observations were fitted using two different rotational period and spin-down before and after MJD 56450 (2013 June 7). Their results are reported in Table 1.2. The best-fit parameter of the black body model is $kT = 0.94 \pm 0.02$ keV. They also analyzed the Swift/XRT observations from 2013 April 25 to Sept. 15 to derive the evolution of the X-ray flux. They found that the flux has decreased by a factor 2 during 80 d.

The radiative and temporal properties of magnetars vary in much shorter timescale than those of pulsars. The Chandra and XMM-Newton observations from 2013 April to 2014 September used by Coti Zelati et al. (2015) showed that the blackbody temperature between 1 and 10 keV decreases linearly with time as $kT(t) = kT_0 + a\,t$ with $kT_0 = 0.85 \pm 1$ keV and $a = (-1.77 \pm 0.04) \times 10^{-4}$ s$^{-1}$. They found that the decay of X-ray flux is characterized by two exponential decay times: $\tau = 37 \pm 2$ d until 100 d after 2013 April 25 and $\tau = 253 \pm 5$ d for observations more than 100 d after 2013 April 25. They also found a change in the X-ray pulse profiles which are represented in Fig. 1.12. The updated rotational period and spin-down is given in Table 1.2.

Thanks to 18 months of Swift/XRT observations, Lynch et al. (2015) measured the exponential decay of the magnetar X-ray luminosity (see purple points in Fig. 1.13) as $F(t) = (1.00 \pm 0.06)\, e^{-(t-t_0)/(55\pm7\,{\rm d})} + (0.98 \pm 0.07)\, e^{-(t-t_0)/(500\pm41\,{\rm d})}$ with $t_0$ is the time of the peak outburst. Therefore, the X-ray flux of the magnetar was high until at least 2014 Sept. leading to a contamination of the flux observed from Sgr A* with the X-ray facilities which are not able to resolve these two close sources (e.g., XMM-Newton or Swift).

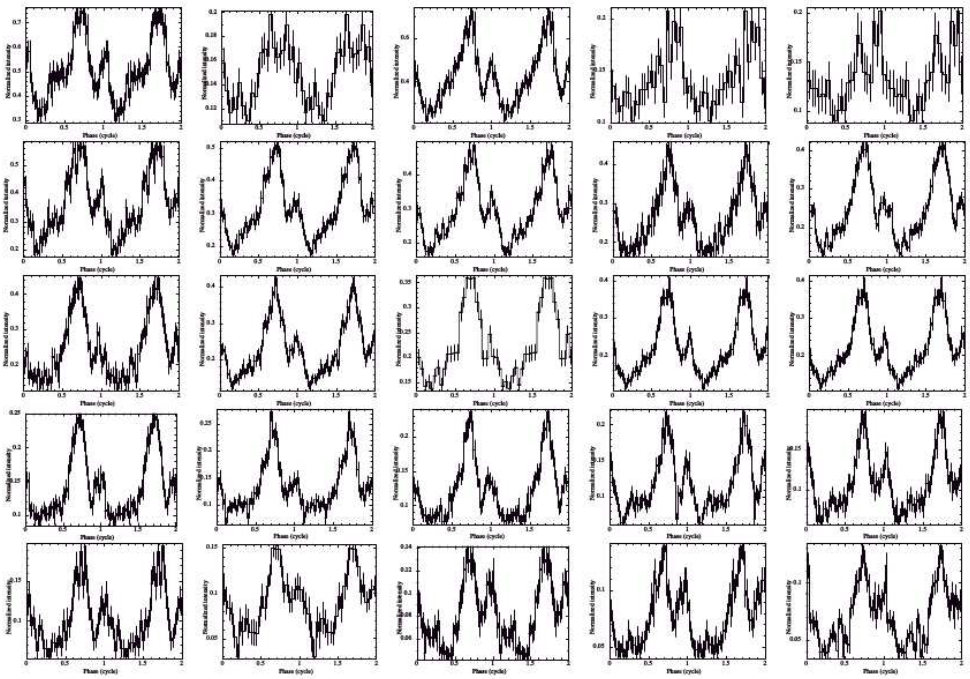

Figure 1.12: Pulse profile of SGR J1745-29 measured by Chandra between 0.3 and 10 keV at different epoch (Coti Zelati et al. 2015). The epoch increases from left to right and top to bottom.

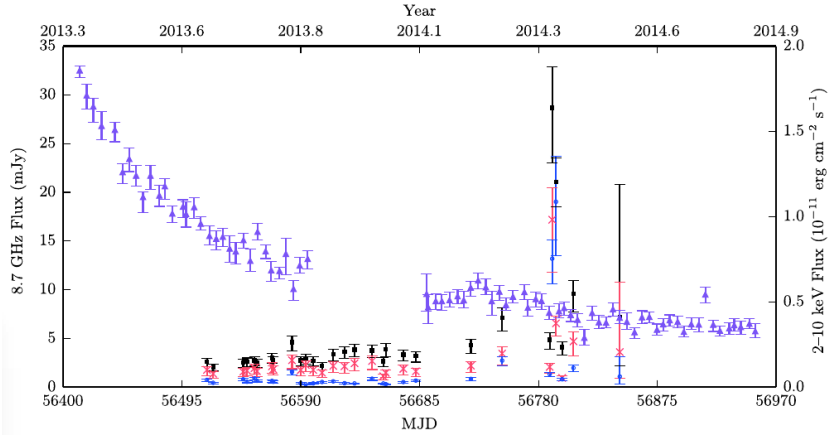


Figure 1.13: Evolution of the Galactic Center magnetar flux in X-rays (magenta; right y-axis) and radio (Lynch et al. 2015). The total radio light curve (black; left y-axis) is decomposed in the circular (blue) and linear (red) polarization.

## 1.6 The context of my Ph.D. thesis

This Ph.D. thesis held for the study of the effect of the passage of the DSO/G2 near Sgr A* on its quiescent and flaring emission. Indeed, a part of the matter from DSO/G2 may be transfered towards Sgr A* during the pericenter passage leading to a possible increase of the quiescent emission up to a few $10^{34}$ erg s$^{-1}$ due to the post-shock temperature of the cloud and to a possible increase of the accretion rate onto Sgr A* with luminosity up to $10^{37}$ erg s$^{-1}$ (Gillessen et al. 2013a). Moreover, a long-duration enhanced flaring activity and an increase of the frequency of bright flares should also be observed (Mościbrodzka et al. 2012). These possible changes of the X-ray emission depend on the physical properties of both the surrounding hot gas and the DSO/G2. It is therefore very important to monitor the X-ray activity of Sgr A* near and after its pericenter passage.

The observational facilities used in this Ph.D. thesis are described in the next Chapter 2.

I used and developed some analysis tools for the study of the X-ray observations that I describe in Chapter 3. These analysis tools were first validated using the 2011 XMM-Newton observations of Sgr A* (XMM-Newton AO-8; PI: D. Porquet) presented in Chapter 4. This campaign was designed to perform the first simultaneous observational campaign in X-rays with XMM-Newton and at 1.3 mm with the Event Horizon Telescope (EHT) order to determine the localization of X-ray flares.

An XMM-Newton large program was submitted in 2012 to obtain multiwavelength observations in order to study evolution of the flaring activity from Sgr A* close to the pericenter passage of DSO/G2 (XMM-Newton AO-12; PI: N. Grosso). Simultaneous XMM-Newton and HST observations were obtained between February and April 2014. Coordinated and simultaneous observations in NIR with the VLT were also granted in this XMM-Newton large program. Additional coordinated and simultaneous observations were also obtained in NIR with VLT and HST and in radio/sub-millimeter with VLA and CARMA. Such simultaneous multi-wavelength observations of Sgr A* during this putative accretion event, may allow us to progress in the understanding of the extremely low-luminosity accretion process onto a SMBH, where black holes are supposed to spend most of their lifetime. The results of this 2014 Feb.–Apr. campaign are presented in Chapter 5.

The overall X-ray flares from Sgr A* observed with XMM-Newton, Chandra and Swift during the 1999–2015 period were systematically detected in Chapter 6 using the tools developed here in order to determine the significance of any change in the X-ray flaring rate.

Finally, the conclusion of this Ph.D. thesis is presented in Chapter 7. I also assess the perspective on the sensitivity for the X-ray flare detection of the ESA next generation mission Athena/X-IFU observations using the tools developed here.

# Chapter 2

# Observational facilities

In this chapter I provide some overviews of the observational facilities from X-rays to infrared and radio/sub-millimeter used during my Ph.D. thesis.

As explained before, the Galactic Center is not observable in UV and optical because of the extinction. Moreover, the Earth atmosphere also absorbs photons. Only radio, sub-millimeter, optical/UV and small infrared bands can be observed from ground (see Fig. 2.1). We thus have to use space telescopes to study the Galactic Center in X-rays.

To perform radio/sub-millimeter and infrared observations, the telescopes must be placed at high altitude. The altitude is important for two points: firstly, the transmission increases with the altitude; secondly, the atmospheric turbulences are smaller at high altitude. Several ground-based telescopes also have adaptive optics working primarily in IR to correct the wave front.

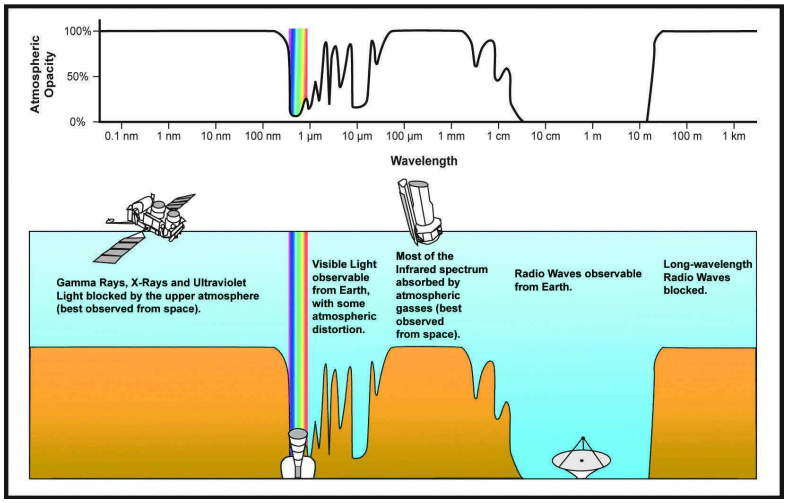


Figure 2.1: Atmospheric transmission on Earth. Credit: NASA/IPAC.

## 2.1 X-ray facilities

X-ray telescopes need a dedicated focusing system because of the great penetrating power of X-ray photons. Grazing incidence mirrors were thus designed to focus X-ray photons on the camera. A schematic view of the Wolter type I configuration for the X-ray photons focusing is shown in Fig. 2.2. The first part (on the left of this figure; first reflection) is composed by parabolic concentric mirrors whereas the last part (on the right of this figure; second reflection) contains hyperbolic concentric mirrors.

### 2.1.1 XMM-Newton

This is the telescope I used the most during my Ph.D. thesis. It is a satellite from ESA launched on 1999 Dec. 10 (Jansen et al. 2001; ESA: XMM-Newton SOC 2013). Its orbit is highly eccentric ($e = 0.72$) with a pericenter distance inside the radiation belts which imposes a stop of any observation during this passage.

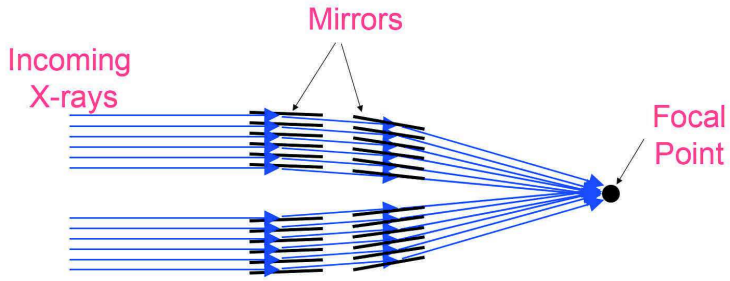


Figure 2.2: Schematic view of X-ray focusing mirrors. Credit: NASA's Imagine the Universe.

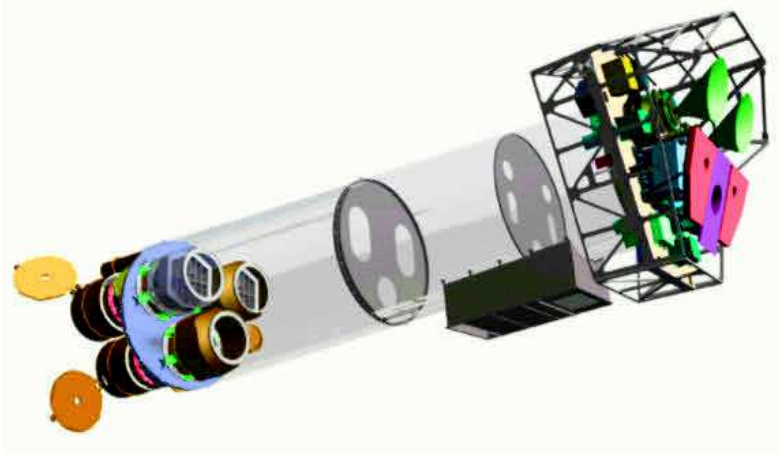

Figure 2.3: Schematic view of XMM-Newton (ESA: XMM-Newton SOC 2013).

But, thanks to the very high eccentricity, we can make very long continuous observations (about 40 h during the 48 h orbit).

In order to focus the X-ray photons, XMM-Newton has three telescopes of 58 concentric mirrors with approximately parabolic and hyperbolic shapes representing a total effective area of 4650 $cm^2$ at 1.5 keV. This is the largest effective area ever for an X-ray instrument.

XMM-Newton offers simultaneous access to X-rays and optical/UV thanks to its two distinct telescopes. It provides three types of science instruments which work independently and operate simultaneously (see Fig. 2.3):

- European Photon Imaging Camera (EPIC) with 3 CCD cameras for the X-ray imaging: 2 MOS (Metal Oxide Semi-conductor; Turner et al. 2001) cameras (7 CCD) and one pn (Strüder et al. 2001) camera (12 CCD);
- Reflection Grating Spectrometers (RGS) placed before MOS cameras leading only 50% of photons reaching the MOS CCDs. The effective areas of the two MOS cameras are thus lower than those of the pn camera;
- Optical Monitor (OM) for optical/UV imaging and grism spectroscopy.

The XMM-Newton EPIC cameras have a 30′-diameter field of view. They have a good angular resolution which does not vary over a wide energy range (0.1 − 6 keV): about 6″ and 4.″3 Point-Spread Function (PSF) Full Width at Half Maximum (*FWHM*) for EPIC pn and MOS, respectively. The MOS cameras provide a good sampling of the PSF thanks to their 1.″1 × 1.″1 pixels compared to the pn camera which has 4.″1 × 4.″1 pixels.

The EPIC background can be divided into two parts: a cosmic X-ray background and an instrumental background. The latter component may be further divided into a detector noise component, which becomes important below 300 eV, and a second component which is due to the interaction of cosmic rays with the structure surrounding the detectors and the detectors themselves.

MOS chips are front-illuminated (the photon goes through the electronic structure before being recorded), while the pn CCDs are back-illuminated (the electronic structure is not on the light path of the photon) leading

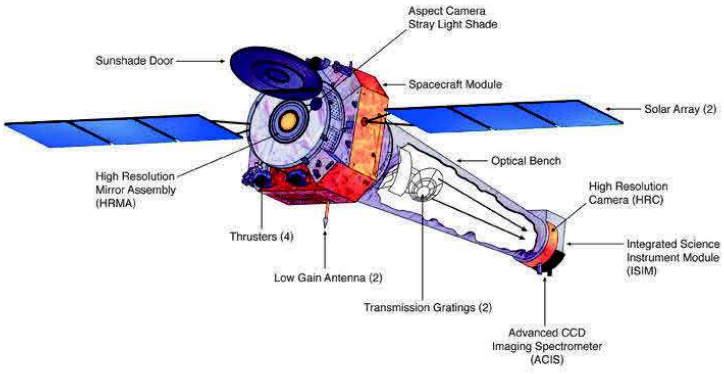


Figure 2.4: Schematic view of Chandra. Credit: Harvard-Smithsonian Center for Astrophysics/NASA.

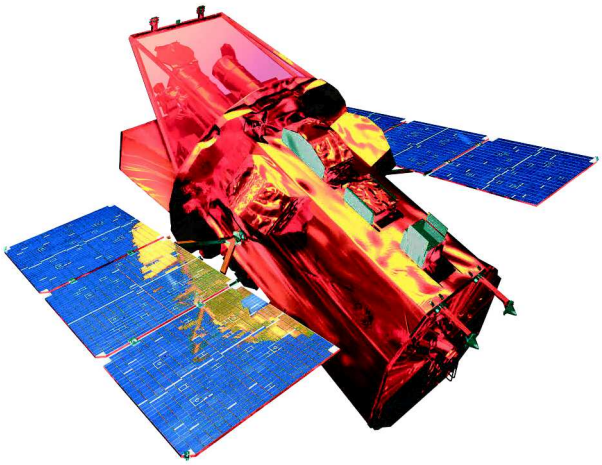

Figure 2.5: Schematic view of Swift. Credit: NASA E/PO, Sonoma State University, Aurore Simmonet.

to a better efficiency for the pn camera. The two EPIC MOS cameras are rotated by 90° with respect to each other. On 2005 Mar. 9 and 2012 Dec. 11, micrometeorite impact scattering debris were registered in the focal plane of the EPIC MOS1 instrument. Since then, MOS1 CCD6 and CCD3 do not record events anymore.

### 2.1.2 Chandra

The NASA's Chandra X-ray Observatory (Fig. 2.4) was launched on 1999 July 23 (Weisskopf 1999). Its orbit is an ellipse whose the apocenter is located at more than a third of the Earth-Moon distance leading 85% of its orbit above the radiation belts: its orbital revolution takes 64.3 h with 52 h (2.2 days) outside the radiation belts. Chandra has four concentric mirrors which represents an effective area of about 600 $cm^2$ at 1.5 keV. It hosts four scientific instruments: the Advanced CCD Imaging Spectrometer (ACIS; Garmire et al. 2003), the High Resolution Camera (HRC; Murray et al. 1998) and the High and low Energy Transmission Gratings (HETG and LETG). ACIS and HRC can not be operated simultaneously.

ACIS is composed by 10 CCD with a field-of-view of $8\farcm3 \times 8\farcm3$ for each CCD. Four of the CCD are part of the I-array (about $16' \times 16'$ field-of-view) and the others are part of the S-array (about $8' \times 24'$ field-of-view). The *FWHM* of the PSF of the ACIS camera is about $0\farcs5$ (one pixel size). ACIS can be used in conjunction with the LETG or HETG which disperse the X-rays that are emitted by all the sources on the field-of-view from 0.08 to 2 keV and from 0.4 to 10 keV, respectively.

### 2.1.3 Swift

The Swift Gamma-ray Burst Mission from NASA (Fig. 2.5) was launched on 2004 Nov. 20 (Gehrels et al. 2004). It has a low-Earth orbit (600 km altitude) with a period of about 95 min. Swift has three instruments: the Burst Alert Telescope (BAT; Barthelmy et al. 2005) to trigger the Gamma-ray Burst events, the X-ray

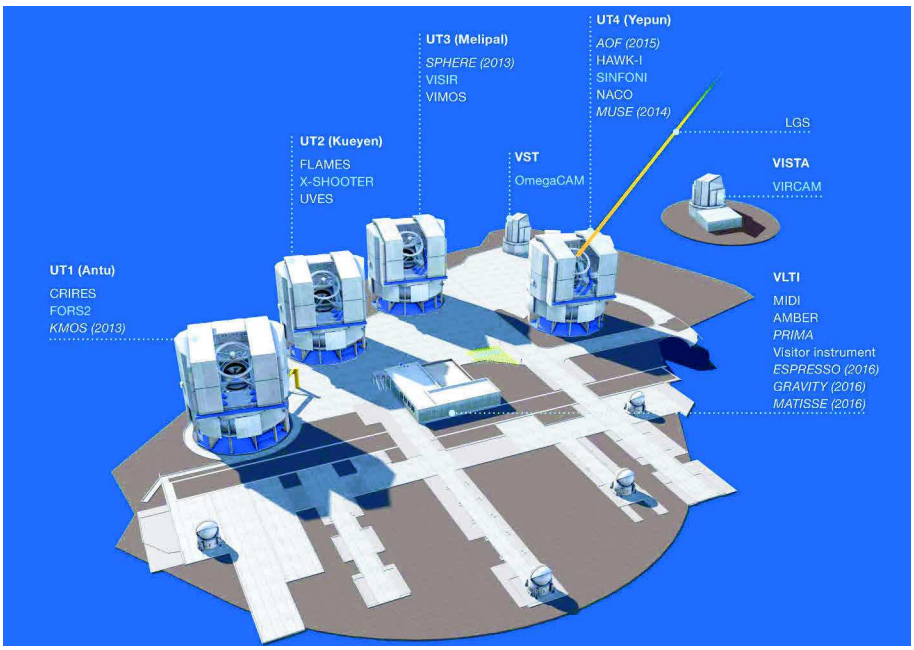


Figure 2.6: VLT. Credit: ESO.

Telescope (XRT; Beardmore et al. 2006) collecting events from the observed objects between 0.2 and 10 keV and the Ultraviolet/Optical Telescope (UVOT) observing between 170 and 600 nm. The XRT has a field-of-view of $23\farcm6 \times 23\farcm6$, an effective area of 110 $cm^2$ at 1.5 keV and an absolute-astrometry uncertainty of $3''$. The XRT CCDs have a pixel size of $2\farcs36$ and a PSF of $18''$ (half power diameter) at 1.5 keV. This camera observes in windowed timing mode or photons counting mode depending on the brightness of the source. The former observing mode uses only one dimension on the CCD to increase the timing resolution of the data whereas the latter observing mode uses the entire XRT field-of-view with a time resolution of 2.5 s.

## 2.2 Infrared facilities

### 2.2.1 VLT

The Very Large Telescope (VLT; Fig. 2.6) is an European South Observatory's (ESO) ground based telescope located at Cerro Paranal in the Atacama desert in Chile (altitude: 2635 m). This is a very good location since there are very few turbulences and the infrared transparency is high in this dry site. It is composed by four large telescopes of 8.2 m (Unit Telescope 1 to 4 named Antu, Kueyen, Melipal and Yepun, respectively) and four smaller auxiliary Telescopes of 1.8 m which can be moved to be used for interferometry. The UT telescopes are Ritchey-Chrétien type and have independent instruments.

In this Ph.D. thesis, I will speak about the NACO instrument which was largely used for the study of Sgr A*. It is composed by the Nasmyth Adaptive Optics System (NAOS; Rousset et al. 2003) working with a NIR sensor and the COudé Near Infrared CAmera (CONICA; Lenzen et al. 2003). It performs observations in the near infrared bands J, H, K, L and M. It was mounted on UT4 until Sept. 2013, then moved to UT1 but its operations had only resumed on Jan. 2015.

Since NACO was not available for the 2014 Sgr A* campaign, we used the Spectrograph for INtegral Field Observations in the Near-Infrared (SINFONI) mounted on UT4. This is a NIR integral field spectrograph operating with four gratings: J (1.10–1.40 $\mu$m), H (1.45–1.85 $\mu$m), K (1.95–2.45 $\mu$m), H+K (1.45–2.45 $\mu$m). This instrument has an adaptive optics module with an optical (450 to 1000 nm) sensor (Bonnet et al. 2004) which limits the correction performance in NIR compared to a NIR sensor as in NACO. The adaptive optics system corrects the wave front thank to a Natural Guide Star (used for Sgr A*) or the Laser Guide Star which was installed on the UT4.

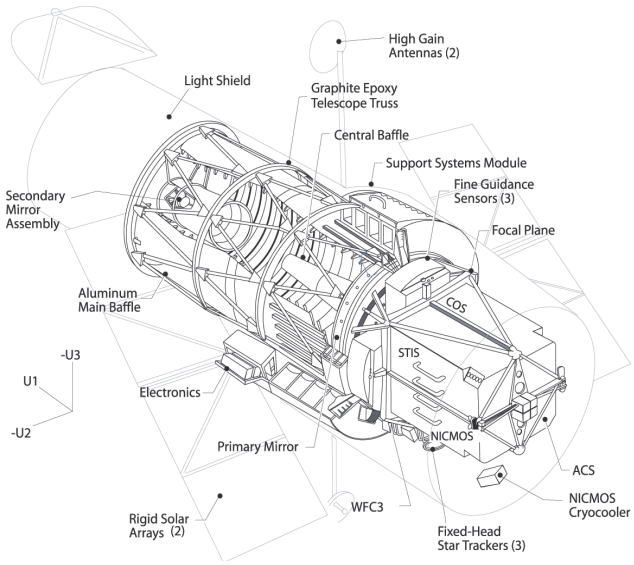


Figure 2.7: Schematic view of the HST telescope configuration since 2009 after the Servicing Mission 4 (Rose et al. 2016). U1, U2 and U3 are the spacecraft axes.

Figure 2.8: CARMA in its compact configuration. Credit: 2001–2013 CARMA.

### 2.2.2 HST

The Hubble Space Telescope (HST; Fig. 2.7) from ESA and NASA was launched on 1990 April 25. It has a 2.4 m-diameter mirror and can observe currently in infrared and optical/UV thanks to the camera WFC3 and the spectrographs STIS and COS. Its low orbit (565 km above the ground) implies repeated occultations of Sgr A* by the Earth. Moreover, the passage through the South Atlantic Anomaly imposes a limited number of consecutive 96-min orbits (generally 5–6 orbits with a maximum of 10 orbits).

The Wide Field Camera 3 (WFC3; Dressel 2012) was installed during the Servicing Mission 4 in May 2009. It has two cameras: the optical/UV camera that records photons from 0.2 to 1 $\mu$m with a field-of-view of $162'' \times 162''$ and the IR camera operating between 0.9 and 1.7 $\mu$m with a field-of-view of $136'' \times 123''$. The *FWHM* of this camera is $0\farcs151$ at 1.60 $\mu$m (1.176 detector pixels). The PSF sampling of the final image can be improved thanks to the dithering, i.e., small movements of the telescope between the exposures following a specific pattern.

The Near Infrared Camera and Multi-Object Spectrometer (NICMOS) operated between 0.8 and 2.51 $\mu$m and was stopped after the installation of WFC3. The *FWHM* of Camera 1 of NICMOS was $0\farcs16$ (3.75 detector pixels) at 1.60 $\mu$m (Yusef-Zadeh et al. 2006a). The NICMOS Camera 1 thus better sampled the PSF than the WFC3/IR.

## 2.3 Radio/sub-millimeter facilities

### 2.3.1 CARMA

The Combined Array for Research in Millimeter-wave Astronomy (CARMA) was an array of radio telescopes located in the Inyo mountains (California, USA) at 2195 m of altitude (Beasley & Vogel 2003). It was composed by 23 antennas (Fig. 2.8) with various sizes: six 10.4 m diameter antennas, nine 6.1 m diameter antennas and eight 3.5 m diameter antennas observing at 7, 3 and 1.3 mm. This telescope was shut down in April 2015.

Figure 2.9: VLA in its compact configuration. Credit: NRAO.

### 2.3.2 VLA

The Karl G. Jansky Very Large Array (VLA) of the National Radio Astronomy Observatory is a ground based radio interferometer located at the Plains of San Agustin (New Mexico, USA; 2124 m) and composed by 27 parabolic antennas of 25 m of diameter in a Y-shaped configuration (Fig. 2.9). Two of these arms measure 21 km and the other measures 19 km. Each antenna can be repositioned along a rail allowing 351 baselines for angular resolutions from 0″.2 to 0″.004 and frequency coverage from 74 MHz to 50 GHz. The extended (A) configuration allows to reach the same resolution than a 36 km-antenna. Four configurations, from extended to compact (D) are commonly used with a cycle of 16 months.

# Chapter 3

# Analysis tools for the X-ray study

In this chapter, I first explain how the data from an X-ray observation are structured and how to filter them (Sect. 3.1). I focus on the XMM-Newton satellite since it is the facility I used the most. I then present the creation of light curves of Sgr A* in X-rays (Sect. 3.2). I also explain how to generate a Poisson flux and to simulate flare light curves (Sect. 3.3). These simulations allow me to study the efficiency of the analysis tools presented in Sect. 3.4 and 3.5. I then present the creation and analyze of X-ray flare spectra from Sgr A* (Sect. 3.6).

## 3.1 The event list and data filtering for an XMM-Newton observation

The exposure time of an observation is divided into frames whose duration is composed of integration time when the events are recorded on the CCD and readout time when the CCD is read. The integration time determines the temporal resolution of the arrival time of an event. The livetime is recorded for each frame as the fraction of the frame time dedicated to the integration of events. For the pn camera, each pixel column has its own readout node implying a fast readout time of about 0.004 s with a constant integration time of 0.0687 s (in Full Frame mode). For the MOS camera, the entire CCD information are transfered in a readout storage area where the lines are read one by one leading to a longer readout time. Therefore, the frame time is about 2.69 s which is much larger than for the pn camera but the livetime is about 99% compared to 96% for the pn camera. For pn, an offset map is computed at the beginning of each pointed observation whereas the offset table values of MOS (1 and 2) are fixed which causes a delayed and shorter exposure time for pn compared to MOS.

During an ideal observation, the entire exposure would be a single Good Time Interval (GTI). But, as explained before, when XMM-Newton is close to its perigee, it passes through the radiation belts leading to a high flaring proton noise. The EPIC Radiation Monitor Subsystem monitors the radiations and, if the radiation level is too high, the CCDs record less informations on the collected photons to reduce the telemetry or, in the worst case, the observation is stopped. These time ranges of high radiation are removed from the GTI.

The characteristics of the events recorded by the cameras are stored in an event list created with the current calibration files from the first-level Observation Data File (ODF) provided to the observer using the SAS tasks `epchain` and `emchain` of the XMM-Newton Scientific Analysis Software (SAS) for the EPIC/pn and MOS, respectively. These tasks first create the attitude history file which allows us to convert of the event positions on the CCD to equatorial coordinates on the sky. They then optionally search for new bad pixels and soft protons flares. Finally, they randomize the arrival times of the events in the frame integration time, perform pattern recognition and compute the event position on the sky thanks to the attitude file. The resulting event list and GTI are recorded in a multiextension FITS file.

Following the data reduction procedure described in the XMM-Newton Users Handbook (issue 2.11; ESA: XMM-Newton SOC 2013), the event lists can be filtered on:

- CCD dead column and bad pixel using special bit masks. `FLAG == 0` is very drastic and rejects several columns/pixels around the dead column and bad pixels but also near to the edges of the CCD. This may produce a large loss of photons and thus of flux if the observed source is close to a dead column or bad pixels or close to the CCD edges. Flags that reject less columns are different for pn and MOS. For pn, this is the bit mask `#XMMEA_EP`. For MOS, we may choose between two bit masks: `#XMMEA_EM`

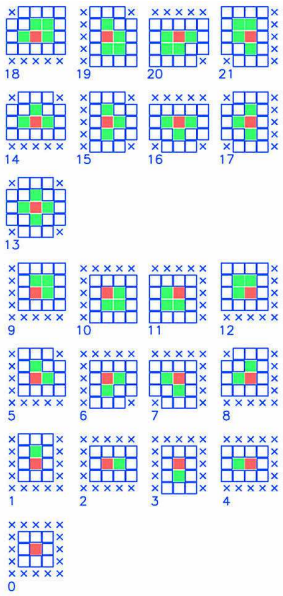


Figure 3.1: The event pattern definition for EPIC/MOS (imaging mode). Each square represents one CCD pixel. The red squares are the brightest pixels. Crosses mark pixels that are not taken into account. Credit: ESA: XMM-Newton SOC (2013).

which only rejects the dead columns, bad pixels and the edges of the camera and `#XMMEA_SM` which is intermediate between `#XMMEA_EM` and `FLAG == 0`. Following Ballet (2005), I use `FLAG == 0` for pn and `#XMMEA_SM` for MOS.

- The pattern which determines the origin of the event: X-ray photon, cosmic ray, soft proton,.... From the bottom to the top of Fig. 3.1, the single, double, triple, quadruple and quintuple events are classified with patterns 0, 1–4, 5–8, 9–12 and 13–21, respectively. To keep only events produced by X-ray photons, I select `PATTERN`$\leq$ 12 and `PATTERN`$\leq$ 4 for MOS and pn, respectively.

- Arrival time. I consider only the time ranges where the flux on the CCD field-of-view is lower or equal than 0.010 and 0.002 count $s^{-1}$ $arcmin^{-2}$ for pn and MOS, respectively. The time ranges of higher flux due to high rate of ionizing particles are removed from the existing GTI to create a new GTI file used to filter the events in time. A second arrival time filter can also be applied to select a time range of study interest (flaring activity, quiescent state,...).

- Energy. For the Sgr A* light curve creation, I consider only events with energy between 2 and 10 keV.

## 3.2 The X-ray light curve creation

Once all the filters are applied on the event lists, I can produce the light curves (histogram of the photon arrival times) using the SAS. I first select a source-plus-background (src+bkg) region centered on the observing source and a background (bkg) region which corrects the instrumental noise.

The src+bkg region is a circle of 10″-radius, corresponding to a fraction of encircled energy of about 50% at 1.5 keV on-axis and minimizing the contamination by other close sources, centered on the radio coordinates of Sgr A* (RA(J2000)=$17^h45^m40\overset{s}{.}036$, Dec(J2000)=−29°00′28″.17; Petrov et al. 2011). The absolute astrometry of EPIC cameras is 1″.2 (Guainazzi 2013) which is very small compared to the size of this extraction region and the PSF Half Power Diameter implying that I do not have to refine the EPIC coordinates. This src+bkg region also allows me to directly compare with the previous studies with XMM-Newton (e.g., Porquet et al. 2003, 2008). This region contains instrumental noise events whose rate can be estimated using a bkg region. The bkg region has to be large, located on the same CCD than the src+bkg region, and without X-ray sources. I thus search for the X-ray sources using the SAS task `edetect_chain` before filtering out those contained in the bkg region which is a square of about 3′ × 3′ at approximately 4′ north of Sgr A*.

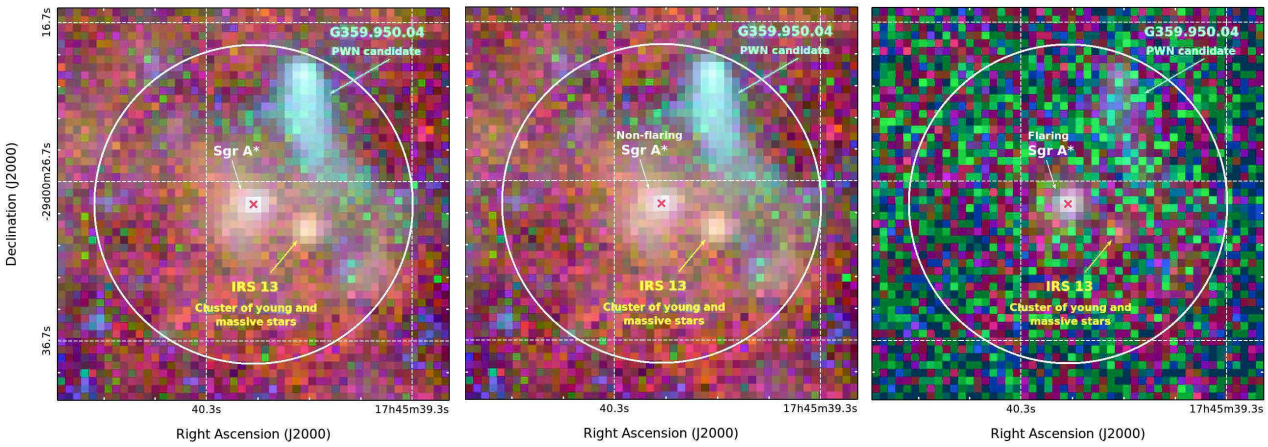


Figure 3.2: Chandra images of the Galactic Center observed from 1999 to 2012. The color coding is red=1–3 keV, green=3–5 keV, blue=5–8 keV. The image intensity (count rate) is in logarithmic scale. The pixel size is 0.″5 corresponding to the Chandra angular resolution. The blue circle represents the position of the extraction region used for the data analysis with XMM-Newton. The red cross is the radio position of Sgr A*. *Left panel:* Overall time range of 4.52 Ms. *Middle panel:* Time interval when Sgr A* is non-flaring (4.33 Ms). *Right panel:* Time interval when Sgr A* is flaring (190 ks).

In the src+bkg region, the recorded X-rays are emitted by Sgr A* but also by the cluster of massive stars IRS 13, the candidate pulsar wind nebulae G359.950.04, faint point sources and a diffuse X-ray component. Only 10% of the non-flaring level observed in this region between 2 and 10 keV comes from Sgr A* (Baganoff et al. 2003). The other sources are only resolved with Chandra since this telescope has a better spatial resolution. For illustration, I created the Galactic Center image as observed by Chandra with an angular resolution of 0.″5 with ACIS-I from 1999 to 2011 and during the 2012 *XVP* campaign with HETG/ACIS-S. The 2004 observations were skipped because of the presence of a transient low-mass X-ray binary at only 2.″9 south of Sgr A* (Muno et al. 2005a,b; Porquet et al. 2005). The observations from 2013 to 2015 were not taken into account because of the burst phase of the magnetar SGR J1745-29 (Degenaar et al. 2013; Gehrels et al. 2013, see Sect. 1.5). This results on a total exposure time of 1.53 Ms for ACIS-I and 2.98 Ms for HETG/ACIS-S. The Chandra data were reduced using the Chandra Interactive Analysis of Observations (CIAO; version 4.7) and the Calibration Database (CALDB; version 4.6.9). I reprocessed the event lists of the observations from the first-level data with the `chandra_repro` script of CIAO which creates a bad pixel file, flags afterglow events and filters the event patterns, afterglow events and bad pixels. To determine the flaring and non-flaring time ranges, I extracted the events using a src+bkg region of 1.″25-radius centered on Sgr A* and a bkg region of 8.″2-radius at 0.′54 south of Sgr A* (Nowak et al. 2012; Neilsen et al. 2013). I then applied the two-steps Bayesian blocks algorithm to automatically detect the X-ray flares with a false positive rate for the flare detection of 0.1% (corresponding to $p_1 = \exp(-3.5)$; see Sect. 3.4) and determine their start and stop times. I then divided the overall observation time into Sgr A* non-flaring and flaring time ranges. The latter is composed of 61 ks for ACIS-I and 129 ks for HETG/ACIS-S. I also divided the overall observations and the non-flaring and flaring time ranges into three spectral bands to compose an RGB image (red=1–3 keV, green=3–5 keV, blue=5–8 keV). The event lists for the three time ranges and three spectral bands were then reprojected to the Sgr A* radio position and merged together to create the nine images and their corresponding exposure maps with the CIAO task `merge_obs`. Figure 3.2 shows the resulting images for the overall (left panel), non-flaring (middle panel) and flaring (right panel) time ranges in a $24.″5 \times 24.″5$ region[1]. For the HETG/ACIS-S observations, this region only contains the zeroth order events, leading to a count rate which is about one third those observed with ACIS-I and no gratings. In the two first images, we clearly observe IRS 13, G359.950.04, faint point sources, the diffuse X-ray emission and Sgr A*. In the flaring image, Sgr A* is the dominant source in the 10″-radius region (white circle).

[1]The count rate ranges for the overall and non-flaring images are $0 - 0.072$, $5.4 \times 10^{-4} - 0.34$ and $0 - 0.20$ count ks$^{-1}$ for the red, green and blue images, respectively, corresponding to the minimum and maximum count rates observed in each energy band in the overall image. For a better clarity of the flaring image, the minima of the count rate ranges are negative while the maxima of the count rate ranges are still the maximum count rates observed in each energy band: $-8 \times 10^{-4} - 0.26$, $-8 \times 10^{-3} - 2.0$ and $-8 \times 10^{-3} - 1.3$ count ks$^{-1}$ for the red, green and blue channels, respectively.

To construct the Sgr A* light curves, I extract from the src+bkg and bkg regions the corresponding XMM-Newton event lists that will be also used for the flare detection (see Sect. 3.4). The src+bkg and bkg light curves are then created by using the SAS task `epiclccorr` which applies relative corrections, i.e., the GTI and livetime corrections. This task then corrects the src+bkg light curve from the bkg light curve scaled to the src+bkg region. I finally combine the background-subtracted (src) light curves of EPIC/pn, MOS1 and MOS2 taking the lack of observation from the pn camera at the beginning of the observation into account by computing the mean ratio between the pn count rate and the sum of the MOS count rate in the 2–10 keV energy range when the three cameras observe ($1.46 \pm 0.03$; Mossoux et al. 2016). This method for the data reduction is the same that those used by Porquet et al. (2008).

## 3.3 Simulation of Poisson flux for the synthetic light curves

It is useful to produce synthetic light curves to test analysis tools (see Sect. 3.4 and 3.5). This can be easily done by simulating photon arrival times with a Poisson flux as it is observed during an X-ray observation.

I recall that for a constant Poisson flux of mean count rate $CR$ during a total observing time $T$, the average number of recorded events is $N_c = CR \times T$ with a standard deviation of $\sqrt{N_c}$. Therefore, I first draw, with a random number generator, the total number $M$ of events in the simulated event list following a Poisson probability distribution, i.e.:

$$P(M) = \frac{N^M}{M!}\, e^{-N_c}\,. \tag{3.1}$$

I then generate $M$ values uniformly distributed between 0 and 1 that I sort by ascending order and I multiply them by $T$ to obtain the simulated arrival times.

This last step for the determination of the $M$ arrival times is equivalent to the more general inverse method based on the normalized Cumulative Distribution Function (CDF) of the count rate function:

$$CDF(t) = \frac{\int_0^t CR(x)\,dx}{\int_0^T CR(x)\,dx} = y\,. \tag{3.2}$$

The simulated arrival times are thus given by the reciprocal of this function (see Klein & Roberts 1984, Chapter 7 of Press et al. 1992 and Fig. 2 of Harrod & Kelton 2013):

$$CDF^{-1}(y) = t\,. \tag{3.3}$$

Indeed, in the simple case of constant count-rate function, these equations lead to: $CDF_c(t) = t/T = y$ and $CDF_c^{-1}(y) = t = y \times T$.

This two-steps method is equivalent to the iterative method of Klein & Roberts (1984) which determines the waiting time before the next event considering its decreasing exponential distribution until the simulated arrival time of the event exceeds the exposure time. Their resulting total number of events thus follows a Poisson distribution.

To simulate the arrival times during a flare from Sgr A*, I suppose that the flare produces above the non-flaring level a Gaussian-shape light curve peaking at $t_{peak}$ with a count rate amplitude $A_{peak}$ and normalized to $N_g$ counts:

$$N_g = A_{peak} \int_0^T e^{-\frac{(t-t_{peak})^2}{2\sigma^2}}\,dt\,. \tag{3.4}$$

The total number of events $M$ in each simulation thus follows a Poisson distribution of mean $N = N_c + N_g$. The normalized CDF of the Gaussian is

$$CDF_g(t) = \frac{A_{peak}\,\sigma}{N_g}\sqrt{\frac{\pi}{2}}\left(\mathrm{erf}\left(\frac{t_{peak}}{\sqrt{2}\,\sigma}\right) + \mathrm{erf}\left(\frac{t - t_{peak}}{\sqrt{2}\,\sigma}\right)\right) \tag{3.5}$$

with *erf* the error function and $\sigma$ the standard deviation of the Gaussian (the *FWHM* is computed as $2\sqrt{2\,\ln 2}\,\sigma$).

I combine the constant and Gaussian CDFs as

$$CDF_{c+g}(t) = CDF_c(t)\,\frac{N_c}{N_c + N_g} + CDF_g(t)\,\frac{N_g}{N_c + N_g}\,. \tag{3.6}$$

I finally draw $M$ values of $y$ uniformly distributed between 0 and 1 and sorted in ascending order. The simulated arrival times are obtained from $CDF^{-1}_{c+g}(y)$.

Figure 3.3 illustrates this method. I simulated the X-ray light curve of typical exposure of 35 ks with a non-flaring level of $CR = 0.1\,\mathrm{count\,s^{-1}}$, corresponding to those observed by XMM-Newton EPIC/pn, and a flare peaking at the exposure center with an amplitude of $A_{peak} = 0.2\,\mathrm{count\,s^{-1}}$, corresponding to the mean amplitude measured in the X-ray flares, leading to $N_g = 752$ counts. In the top panel of this figure, the red, green and blue lines are $CDF_{c+g}(t)$, $CDF_c(t)\,N_c/(N_c + N_g)$ and $CDF_g(t)\,N_g/(N_c + N_g)$, respectively. The constant and Gaussian light curve models are shown with the corresponding color in the bottom panel. The simulated arrival times are the black ticks at the top of the bottom panel of Fig. 3.3 (only one arrival time on twenty are shown here for clarity purpose). I then binned the simulated arrival times with a bin time of 100 s to create the simulated light curve shown in the bottom panel of Fig. 3.3. The Bayesian blocks computed for a false positive rate for the flare detection of 0.1% (corresponding to $p_1 = \exp(-3.5)$; see next Sect. 3.4) are also represented in this figure.

Considering the large number of counts in the typical event lists studied in this work (from several hundred to several thousand), the Poisson variation of the total number of events in the simulated event lists leads to a very small difference on the average detection efficiency. For example purpose, I compute the detection efficiency for the Chandra ACIS-I3 observations with a non-flaring level of 0.005 $\mathrm{count\,s^{-1}}$ and a typical exposure of 50 ks leading to 250 events, i.e., the lowest number of events in our simulations. I simulate 100 event lists with this two-steps method and 100 simulations where the first step is skipped (the number of counts in each event list is therefore equal to $N_c + N_g$). The difference in the detection efficiency between these two sets of simulations is larger for the faintest and shortest flares where $N_g$ is in the order of ten. However, this difference always remains lower than 1% since $N_c + N_g$ is larger than 250 counts leading to the Poisson distribution of the number of count very peaked around the average value ( $\sqrt{250} \sim 16$). I thus skipped the first step in the event list simulations for the determination of the detection efficiency.

## 3.4 The Bayesian blocks method for the flare detection

### 3.4.1 The Bayesian blocks method

In order to automatically detect flares with a given false positive rate, I use the Bayesian method proposed by Scargle (1998) and improved by Scargle et al. (2013a). Scargle et al. (2013a) provide a Matlab code of this method which was then converted in Python[2]. For ease purpose, I converted the Matlab code into the Interactive Data Language (IDL).

The Bayesian blocks method works on individual arrival times of photons. I take care to first associate the arrival time of each photon to the center of the frame during which it was recorded since the randomization of the photon arrival time in the frame time by the `epchain` or `emchain` tasks is arbitrary and not reproducible. The photons are thus separated by an integer number of frame durations. If several photons were recorded during the same frame, I consider that these $N$ photons are characterized by the same arrival time. I then filter out the frames affected by ionizing particles (i.e., the bad time intervals) by merging the GTIs to obtain a continuous photon flux. The resulting reduced time range is then divided into cells defined using the Voronoi tessellation, i.e., with cells separation located at equal distance of two frame centers containing consecutive photons. The count rate in each cell is thus the total number of photons in this cell divided by the cell length ($\Delta t$). I define the beginning and end of the first and last cell as the observation start and stop, respectively, instead of the first/last event minus/plus the half of the mean time interval between the events, as done in the Matlab code, which is arbitrary and does not use the complete GTI information.

As suggested by Scargle et al. (2013a), I also take the livetime into account by increasing the count rate of each cell by multiplying the cell length by the livetime value which is lower than 1.

The Bayesian blocks method works iteratively on the cells: it first considers the overall photon arrival times and determines if they are better described by one block with a constant count rate or by two blocks having different count rates assuming a Poisson distribution of the arrival times. If the event list is segmented into two blocks (whose separation time is called a change point), the method iterates on each on these blocks to segment them or not. The criterion for stopping the segmentation is controlled by the prior number of

[2]The Python version can be found at https://jakevdp.github.io/blog/2012/09/12/dynamic-programming-in-python.

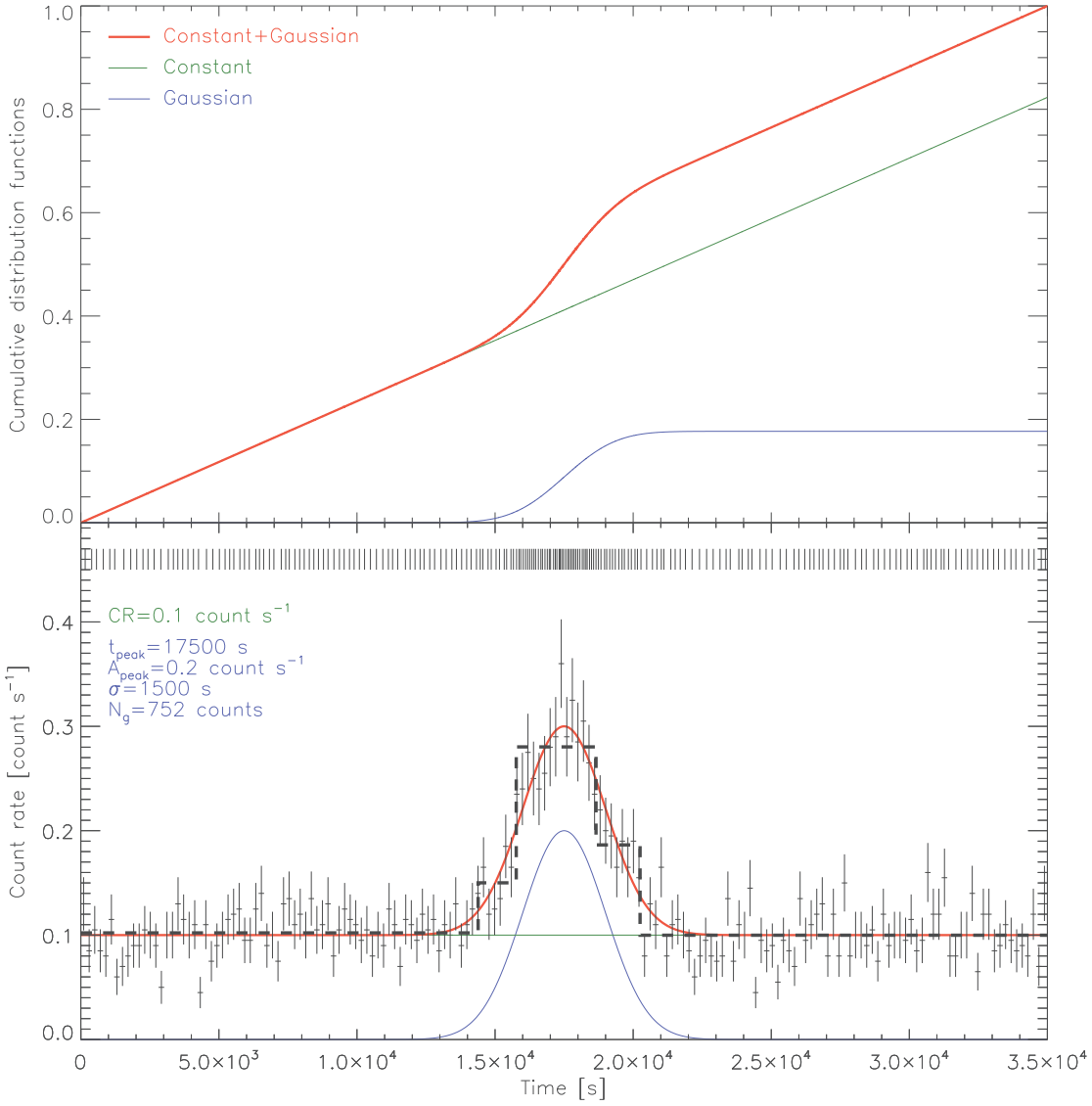


Figure 3.3: Simulation of an X-ray light curve with a flare. *Top panel:* The Cumulative Distribution Function (CDF) of a constant function (green line) representing the non-flaring emission and a Gaussian function (blue line) representing the flaring emission. The non-flaring emission has a count rate $CR = 0.1$ count s$^{-1}$. The flare is defined with a peak amplitude $A_{\rm peak} = 0.2$ count s$^{-1}$ at $t_{\rm peak} = 17500$ s and $FWHM = 3532$ s ($\sigma = 1500$ s) leading to a number of counts in the flare of $N_{\rm g} = 752$. *Bottom panel:* The constant and Gaussian light curve models are represented in green and blue, respectively. The red line is the model of the light curve with flare. The ticks at the top of this panel are 5% of the simulated arrival times. The resulting light curve and its error bars are computed for a bin time of 100 s. The results of the Bayesian block algorithm with a false positive rate for the flare detection of 0.1% (see Sect. 3.4) are shown with dashed lines.

change points, *ncp_prior*. The latter depends on two parameters: the number of events in the observation ($N$) and the false positive rate ($p_1$), i.e., the probability that a detected change point is a false one.

The result of the Bayesian blocks method is the optimal segmentation of the light curve with blocks of constant count rates separated by change points. After having computed the Bayesian blocks, I reintroduce the bad time intervals to obtain the true time of the change points. An example of segmentation of a flaring light curve is presented in Fig. 3.3. The non-flaring level is defined as the count rate of the longest block whereas flares are associated to blocks which have higher count rates. In most case, flares are defined by at least two change points (the start and end times of the flare). One of the most advantage of this method is the flare detection with a controlled false positive rate. Moreover, the start and end times of the flare are not limited by the bin size of the light curve. Indeed, with previous methods the accuracy on the beginning and end of the flares depend on the arbitrary binning of the light curve (usually 100 or 300 s). With the Bayesian blocks method the accuracy on the start and end times of a flare is equal to the distance between the two adjacent photons on either side of the change points. For the EPIC/pn camera of XMM-Newton, the mean count rate of Sgr A* is about 0.1 count $s^{-1}$ (Porquet et al. 2003, 2008) which implies an average time separation between consecutive photons of about 10 s. The timing accuracy is thus at least ten times better than in the previous methods.

Scargle et al. (2013a,c) computed a geometric *ncp_prior* estimation for data simulated with Gaussian noise of unit variance. However, their data samples contain from 8 to 1024 points which is well below the number of events recorded during an XMM-Newton observation (several thousands of events). Moreover, an X-ray observation is described with data affected by Poisson noise. I thus calibrate the *ncp_prior* for the studied XMM-Newton observations following the Scargle et al. 2013a's recipe: I simulate a large number of event lists representing the non-flaring level of the studied observation and apply the Bayesian blocks algorithm on each of these event lists with different false positive rates (see next Sect. 3.4.2).

I stress that in the Python code the geometric *ncp_prior* computed by Scargle et al. (2013a,c) is used without any care of the characteristics of the data sample. One thus needs to change this code to properly use the calibrated *ncp_prior* corresponding to the dataset.

### 3.4.2 Calibration of the prior number of blocks

I simulate 100 event lists with a constant count rate ($CR$) corresponding to the non-flaring level observed by XMM-Newton (0.1 and 0.04 count $s^{-1}$ for EPIC/pn and EPIC/MOS1 and 2, respectively; e.g., Porquet et al. 2003, 2008). I then apply the Bayesian block algorithm on each event list with a certain value of *ncp_prior* and record how many times a change point is detected. In theory, zero change point must be detected since I work with constant light curves. Each change point is thus a false positive. I test fifteen values of *ncp_prior* (from 2 to 9) and six values of number of events in the observation (from 1000 to 6000). The resulting probability of false positive is shown in the top panel of Fig. 3.4 and can be compared to the Fig. 6 of Scargle et al. (2013a). For different values of $p_1$, I report the relation between $N$ and *ncp_prior* (bottom panel of Fig. 3.4 for $p_1 = 0.05$). By combining these relations, which relies $p_1$, $N$ and *ncp_prior*, I find the calibration corresponding the observations with EPIC/pn:

$$ncp\_prior = 3.356 + 0.143 \ln(N) - 0.710 \ln(p_1) - 0.002 \ln(N) \ln(p_1) \ . \quad (3.7)$$

For $N$ lower than 1000, the last term is negligible and the relation has the same form than those found by Scargle et al. (2013a,c) but the predicted *ncp_prior* is different since the simulated models are different. As observed in the top panel of Fig. 3.4, the curves become closer as the number of counts increases. This is explained by the convergence of the *ncp_prior* towards about 7 for observations with high number of counts. This work has been reported in the appendix of Mossoux et al. (2015a) (see p. 125 of this Ph.D. thesis).

I use a fixed level of false positive rate $p_1 = \exp(-3.5)$ (Neilsen et al. 2013; Nowak et al. 2012) which allows me to deduce that one change point is real with a probability of $1 - p_1 = 96.98\%$ and two change points (one flare) are real with a probability of $1 - p_1^2 = 99.90\%$ corresponding to a false positive rate for the flare detection of 0.1%. I thus just need to simulate the event list for the actual number of events in the considered observation (leading to only one curve in the top panel of Fig. 3.4) and to report the *ncp_prior* which gives the probability of false change points corresponding to $p_1 = \exp(-3.5)$. With this method, I am sure that the detected change point has only a probability $p_1$ to be a false change point.

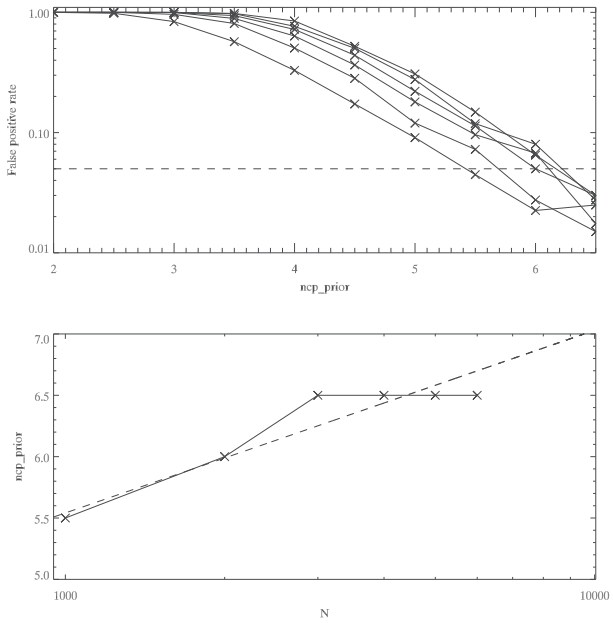


Figure 3.4: Simulations of constant light curve (Poisson signal of average 0.1 count $s^{-1}$) to calibrate the *ncp_prior* (Mossoux et al. 2015a). *Top:* False positive fraction $p_1$ vs. value of *ncp_prior* with separate curves for the values $N = 1000, 2000, 3000, 4000, 5000$, and 6000 (left to right). The points at which the rate becomes unacceptable (here 0.05; dashed line) determine the recommended values of *ncp_prior* shown as a function of $N$ in the bottom panel. *Bottom:* Calibration of *ncp_prior* as a function of the number of counts ($N$) for $p_1 = 0.05$. The dashed line is the linear fit of the simulation points.

### 3.4.3 The two-steps Bayesian blocks algorithm

As explained in Sect. 3.1, an X-ray observation is contaminated by an instrumental background. This background may reach high flaring rate especially at the beginning and end of the XMM-Newton observation because of the radiation belts. It thus has to be taken into account in order to avoid any detection of a false flare from the source.

The first method of background subtraction was proposed by Stelzer et al. (2007). The authors first computed a segmentation of their bkg and src+bkg light curves. They then randomly suppressed the normalized number of events present in each background block from the src+bkg event list. However, the random suppression of events is arbitrary and the result may therefore depend of this choice, especially when the background is high. I thus follow the recipe proposed by Scargle et al. (2013b) and described in Mossoux et al. (2015a,b): I first separately apply the Bayesian block algorithm on the src+bkg and bkg event lists. From these Bayesian blocks count rates, I compute a weight at each src+bkg photon arrival time equal to $w = CR_{\mathrm{src+bkg}}/(CR_{\mathrm{src+bkg}} - CR_{\mathrm{bkg}})$. The algorithm is then applied a second time on the src+bkg event list on which the weight is applied. With this two-steps Bayesian blocks algorithm, I keep all events from the list.

For example purpose, the results of the two-steps Bayesian blocks algorithm applied on the 2011 March 28 XMM-Newton EPIC/pn observation is shown in Fig. 3.5. In the top panel, the src+bkg event list is characterized by three blocks whose the two highest are spurious blocks due to the contribution of the high flaring background. Indeed, in the middle panel, the bkg event list is segmented with higher blocks at the end of the observation due to the increase of the ionizing particles when entering the radiation belts. After correction of the bkg with the two-steps Bayesian blocks algorithm, the src event list is described with only one block corresponding to a non-flaring light curve (bottom panel).

After the publication of Mossoux et al. (2015a), some other weights were tested by Worpel & Schwope (2015) on eclipse light curves but the two-steps Bayesian blocks algorithm appeared more stable. Indeed, we can see in Fig. 12 of Worpel & Schwope (2015) that the two-steps Bayesian blocks algorithm (labeled $h$ in this figure) correctly locates the eclipses, as well as their weighted-photon method (labeled $f$ in this figure), but with no spurious short blocks of implausibly high count-rates, by contrast to their weighted photon metod.

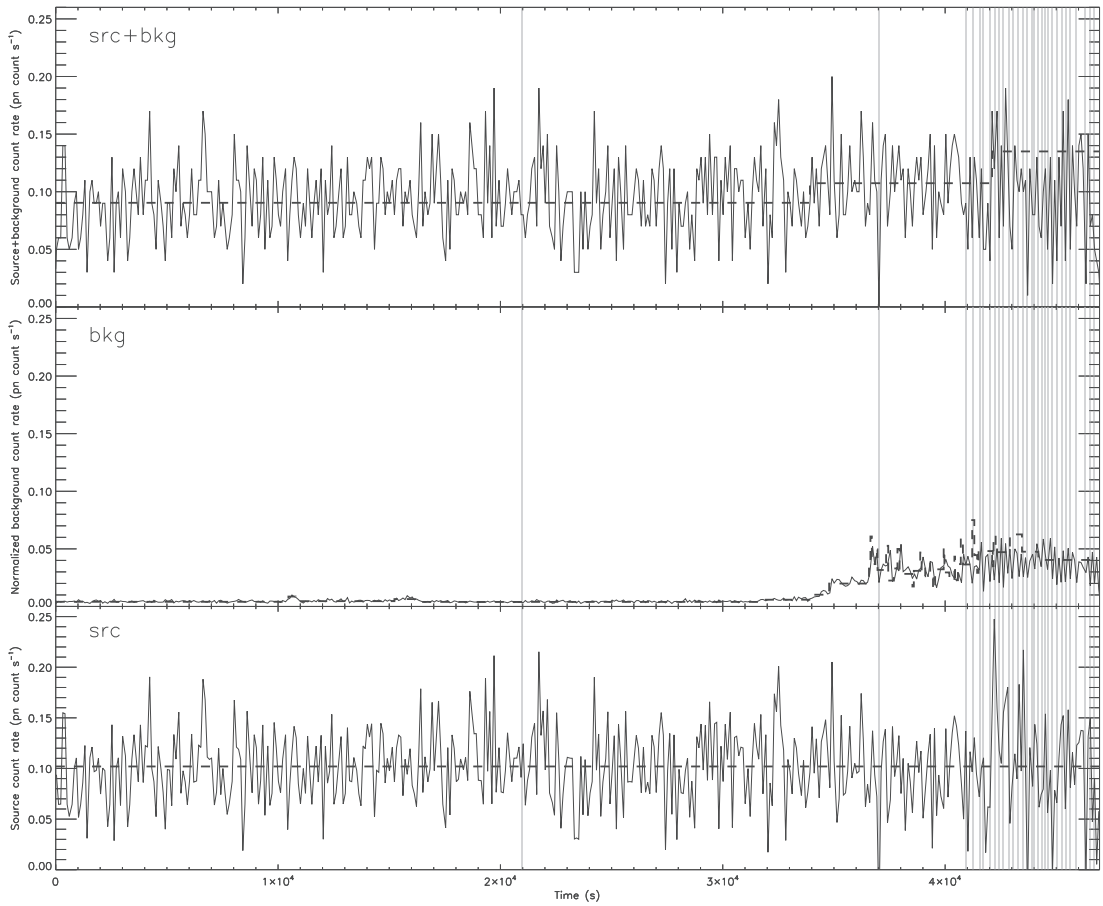


Figure 3.5: The two-steps Bayesian blocks algorithm for the background subtraction using the Bayesian block method applied on the 2011 March 28 XMM-Newton observation with EPIC/pn. The Bayesian blocks for $p_1 = \exp(-3.5)$ are represented in the dashed lines over the light curves binned on 100 s. The vertical gray boxes are the bad time intervals. *Top panel:* The source-plus-background light curve. *Middle panel:* The background light curve. *Bottom panel:* The background subtracted light curve.

### 3.4.4 Flare detection efficiency of the Bayesian blocks method

During the *Chandra XVP* campaign of 2012, 45 flares were detected using the Bayesian-blocks method during a total exposition of 2983.93 ks (Neilsen et al. 2013). Their *FWHM* ranges between 56.62 s and 1104 s and they have amplitudes from 0.015 and 0.17 Chandra count $s^{-1}$ above the constant rate. Their duration and amplitude distribution are $dN/dCR_{Ch} = 0.7\,CR_{Ch}^{-1.9}e^{-CR_{Ch}/0.3}$ and $dN/dT = 0.05T^{-0.1}e^{-T/3000}$ with $CR_{Ch}$ the peak count rate as observed by Chandra and $T$ the flare duration[3].

Using this flare demography, I investigate the detection efficiency of the flares from Sgr A* during an observation with XMM-Newton by simulating event lists (see Sect. 3.3) with a Poisson noise around the mean count rates ($CR$) of 0.1 and 0.04 count $s^{-1}$ which represent the light curves of Sgr A* observed with EPIC/pn and EPIC/MOS, respectively (Porquet et al. 2003, 2008). Above this constant light curves, I add Gaussian flares with a *FWHM* equals to 57 s, 319 s and 1104 s which are the *FWHM* minimum, median and maximum of flares from Sgr A* detected during the 2012 *Chandra XVP* campaign (Neilsen et al. 2013). I vary the amplitude of the flares in the amplitude range from the lowest to the highest amplitude measured during the 2012 *Chandra XVP* campaign. In order to convert the Chandra count rate to the XMM-Newton count rate ($CR_{XMM}$) assuming the same spectral parameters, I use the relation derived in Chapter 5 between the Chandra HETG count rate (zero and first order) of the flare peak and the unabsorbed luminosity at the peak flare, i.e., $L^{unabs}_{2-10\,keV}/10^{34}$ erg $s^{-1} = -0.031 + 136.7CR_{Ch}$. For each amplitude, I make 100 simulations and compute how many times the algorithm finds the flare for false positive rate for the flare detection of 0.1% corresponding to

[3]The cutoff value is given as a lower limit in Neilsen et al. (2013) but the specific value does not influence the result of our flare distribution because we are interested by flares characterized by small amplitude and short duration since these flares may suffer of the small detection rate.

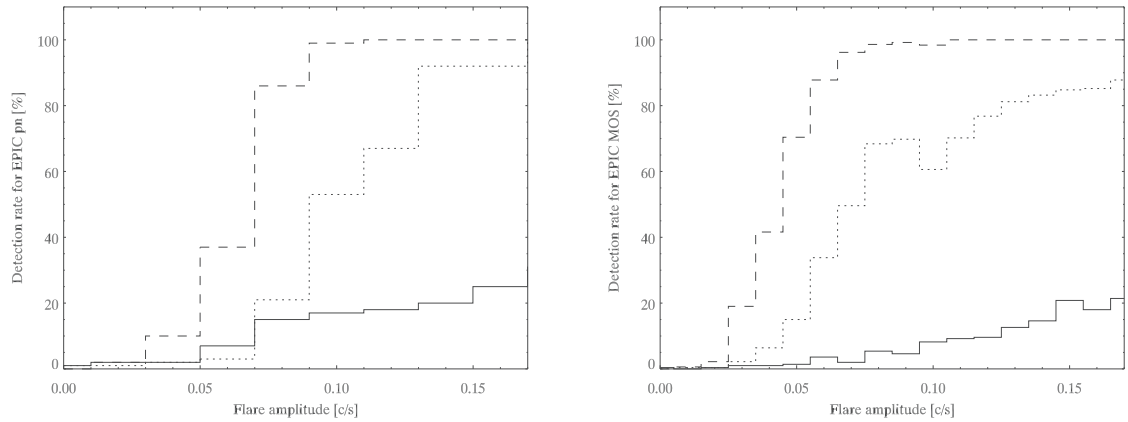


Figure 3.6: Detection efficiency of Gaussian flares by the Bayesian blocks algorithm for EPIC/pn (left panel) and MOS (right panel) (Mossoux et al. 2015a). I use $p_1 = \exp(-3.5)$ and $ncp\_prior = 6.5$. The solid, dotted and dashed lines are Gaussian with $FWHM = 57$ s, 319 s and 1104 s, respectively.

$ncp\_prior = 6.5$ for pn, MOS1 and MOS2. The result of the simulations is shown at Fig. 3.6.

For EPIC/pn and MOS, higher the amplitude and the *FWHM*, higher the detection efficiency. But, to correctly compare the detection efficiency between these two instruments for the same *FWHM*, I need to compute the relation between the unabsorbed luminosity of a flare and the count rate received by each instrument. I compute fake spectra with high unabsorbed luminosity between 2 and 10 keV, a spectral index of $\Gamma = 2$ and a hydrogen column density of $N_{\rm H} = 14.3 \times 10^{22}$ cm$^{-2}$ (Porquet et al. 2003, 2008; Neilsen et al. 2013). I determine with the ARF and RMF files of EPIC/pn and EPIC/MOS1 (see Sect. 3.6.1 for details) a count rate to unabsorbed luminosity ratio of $29.6 \times 10^{-37}$ pn count s$^{-1}$/erg s$^{-1}$ and $8.42 \times 10^{-37}$ MOS1 count s$^{-1}$/erg s$^{-1}$, respectively. For example, for an unabsorbed luminosity of flare amplitude of $2.5 \times 10^{34}$ erg s$^{-1}$, the corresponding count rate is thus 0.074 and 0.021 count s$^{-1}$ for pn and MOS1, respectively. This corresponds to a detection efficiency of 90% with pn but lower than 5% with MOS1 for $FWHM = 1104$ s. EPIC/pn is thus more efficient to detect low luminosity flares.

I also study the effect of an increase of the non-flaring level observed by XMM-Newton. During the 2014 campaign, a magnetar located at 2.″4 southeast of Sgr A* was observed in its burst phase (see Sect. 1.5 for details). Since the extraction region for XMM-Newton is a 10″-radius circle, the photons emitted by the magnetar artificially increase the non-flaring level observed in the source region which varies between 0.32 and 0.29 pn count s$^{-1}$ during the XMM-Newton observations in 2014 Feb.–Apr.. This contamination implies a decay of the detection level of the faintest and shortest flares. To assess the impact on the flare detection efficiency, I plot in Fig. 3.7 the flare detection rate of EPIC/pn presented in left panel of Fig. 3.6 versus the flare peak significance, i.e., the amplitude of the flare expressed in unit of the standard deviation of the non-flaring level. This scaling allows to comparison observations with the same instrument but different non-flaring levels. Since the non-flaring level in the 2014 Feb. 28 light curve has increased by a factor of about 3.6 by comparison with those measured by Porquet et al. (2003, 2008) and Mossoux et al. (2015a), the peak significance is divided by a factor of about $\sqrt{3.6}$. For example, if we consider a flare with an amplitude of 0.2 count s$^{-1}$ above the non-flaring level (vertical dot-dashed line in Fig. 3.7), this corresponds to a peak significance of $6.3\sigma$ without the magnetar contribution (left panel) and this flare is always detected if its *FWHM* is larger than 320 s. A flare with the same amplitude in the 2014 Feb. 28 light curve (right panel) corresponds to $3.2\sigma$ and is only detected with a probability of 53% for $FWHM = 320$ s.

The better detection efficiency is reached with the Chandra telescope. Thanks to its higher angular resolution, the source extraction region is about eight times smaller that those of XMM-Newton implying a smaller non-flaring level and a smaller Poisson noise resulting in a higher SNR of the flaring event. One can thus compare the detection efficiency of the XMM-Newton telescope on the flaring demography observed by Chandra during the 2012 *XVP* campaign. I first compute a grid of 30 flare amplitudes and 30 flare durations in the range $[0.06 - 0.4]$ count s$^{-1}$ and $[337.5 - 8100]$ s regularly distributed in the logarithmic scale. For each point of grid, I create 300 event lists of Gaussian flares characterized by the corresponding amplitude and duration (see Sect. 3.3). I then apply the Bayesian blocks algorithm on all these event lists superimposed above a non-flaring level corresponding to those of EPIC/pn (0.1 count s$^{-1}$). This allows me to have a detection

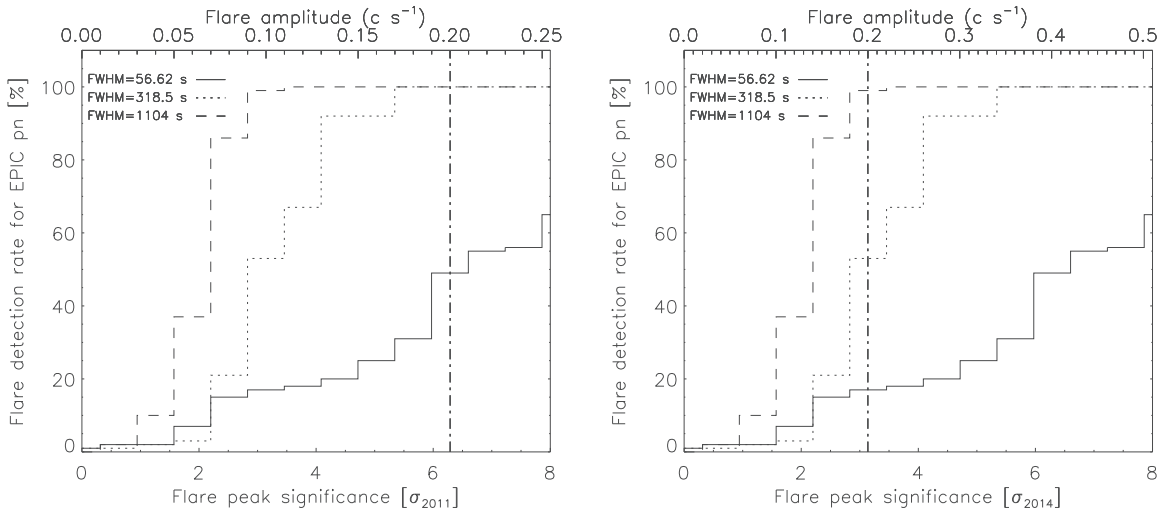


Figure 3.7: Comparison of the detection efficiency with the Bayesian blocks algorithm for the non-flaring level corresponding to those of the 2011 (*left panel*; corresponding to left panel of Fig. 3.6) and February 2014 (*right panel*) observations with EPIC/pn (Mossoux et al. 2016). The vertical doted-dashed line represents an example flare with the same amplitude above the non-flaring level for a 2011 and 2014 Feb.–Apr. observations.

efficiency for different flare amplitudes and durations with XMM-Newton.

I then normalize this probability to the duration and amplitude distribution determined during the *Chandra XVP* campaign of 2012 (Neilsen et al. 2013). Since each flare can be associated to a detection efficiency between 0 and 1, the sum of the probability for the 45 flares is the total number of flares that can be detected in average by the Bayesian-blocks method during an EPIC/pn observation with an exposure time of about 30 ks. The distribution of the flare duration and amplitude observed during the *Chandra XVP* campaign and the detection efficiency of the Bayesian-blocks algorithm are shown in the left panel of Fig. 3.8. We can detect 85.4% of the flares detected during the *Chandra XVP* campaign. The non-detected flares are the faintest and shortest ones.

In order to assess how many flares cannot be detected due to the magnetar contamination, I make the same computation as presented above to compare the 2014 EPIC/pn observation and the *Chandra XVP* campaign of 2012 (Neilsen et al. 2013). The result is shown in the right panel of Fig. 3.8. For the 2014 Feb. 28, Mar. 10, Apr. 2 and Apr. 3, we detect 79.2%, 79.4%, 80.1% and 79.8% of flares detected during the *Chandra XVP* campaign, respectively which is lower than for a non-flaring level of 0.1 count s$^{-1}$. This work can be found in Appendix A of Mossoux et al. (2016) (see p. 154 of this Ph.D. thesis).

## 3.5 Improving the light curve shape

The light curves computed with the SAS task `epiclccorr` are histograms of the photon arrival times. But, histograms have some limitations in the representation of time series:

- There is an arbitrary choice for the start of the first bin of the histogram but its shape may depend on this start point.
- The choice of the bin length is also arbitrary.
- Discontinuities between bins do not reflect the continuity of a physical phenomenon.

In order to bypass these limitations, I compute smoothed light curves by applying a density estimator (Silverman 1986; Feigelson & Babu 2012) on the event lists. This allows me to increase the accuracy on the flares characteristics such as amplitude and time of the maximum by reducing the Poisson noise and to follow the flux of the source nearly continuously. The event density is computed thanks to `quantreg` available in the R project for statistical computing[4]. This algorithm convolves the photon arrival times with a smoothing

[4] https://www.r-project.org/

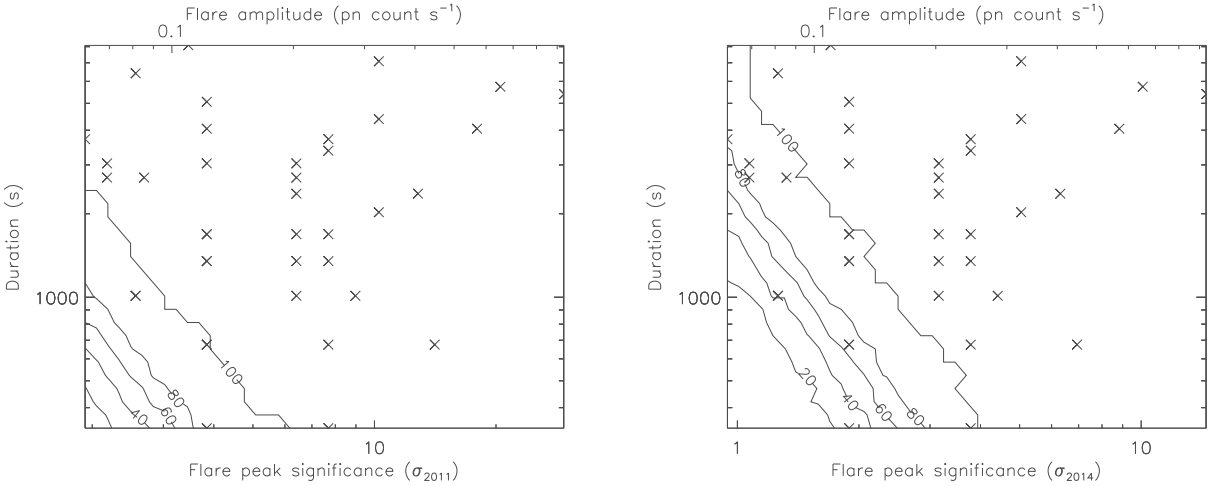


Figure 3.8: The flare distribution seen by Chandra and the detection efficiency in percent of the Bayesian-blocks algorithm during an observation with XMM-Newton (Mossoux et al. 2016). The crosses are the X-ray flares detected during the *Chandra XVP* campaign of 2012. The flare amplitude is above the non-flaring level seen by EPIC/pn (0.1 count s$^{-1}$; Porquet et al. 2003, 2008). *Left panel:* The flare amplitude above the non-flaring level seen by EPIC/pn during the 2011 campaign. *Right panel:* The flare amplitude above the non-flaring level seen by EPIC/pn during the 2014 Feb. 28 observation.

kernel. I modified this program in order to use the Epanechnikov kernel (an inverted parabola) defined as $K(x) = \frac{3}{4}\left(1 - x^2\right)$ for $|x| \leq 1$ and $K(x) = 0$ for $|x| > 1$. This kernel is more suitable since it has a *"good performance* [sic]*"* (Feigelson & Babu 2012) and it is defined on a finite support between $-1$ and 1 (unlike the Gaussian and Cauchy kernels available on the original package which are defined on an infinite support). The finite support allows me to control boundary effects (i.e., the lack of information before and after the observation start and end).

The normalized density estimator is

$$\hat{f}(t,h) = \frac{1}{N}\sum_{i=1}^{N}\frac{w(t)}{livetime} \times K\left(\frac{t - t_{\rm i}}{h}\right) \tag{3.8}$$

with $h$ the kernel window width which defines the finite support between $-h$ and $h$, $N$ the number of counts in the observations, *livetime* the correction of the integration time from the CCD readout time (see Sect. 3.1), $w(t)$ the weight which corrects the smoothed light curve from background at a time $t$ thanks to Bayesian blocks (see Sect. 3.4.3), $t_{\rm i}$ the arrival time of the event $i$ (ticks at the top of Fig. 3.9) and $t$ the time where the density is computed. A schematic view of the density estimator is given in Fig. 3.9. The red curve is the Epanechnikov kernel of window width $h = 500$ s (I suppose here that $w(t) = livetime = 1$). The time at which the density is computed is $t = 500$ s, i.e., the first point of the smoothed light curve without boundary effects. The boundary effects are controlled by rejecting times at which $t - h$ and $t + h$ are lower and higher than the first ($t_{\rm start}$) and the last ($t_{\rm stop}$) time of the event list. The density is thus defined for $t \in [t_{\rm start} + h, t_{\rm stop} - h]$. The count rate of the smoothed light curve is $CR = N \times \hat{f}(t,h)$. The error on the count rate is $\sqrt{n}$ with $n$ the number of counts in the kernel window computed as the sum of fractions of event whose arrival time is located in $[t - h, t + h]$. The resulting smoothed light curve of the event simulation presented in Sect. 3.3 is shown in Fig. 3.10 with a solid black line and gray error bars.

## 3.6 Spectral analysis of the X-ray flares from Sgr A*

Light curves allow us to make a temporal analysis of flares. But, we have a lack of information about energetics since light curves are integrated over all the energy range. We thus have to create and analyze the Sgr A* flare spectrum in order to complete our scientific investigation.

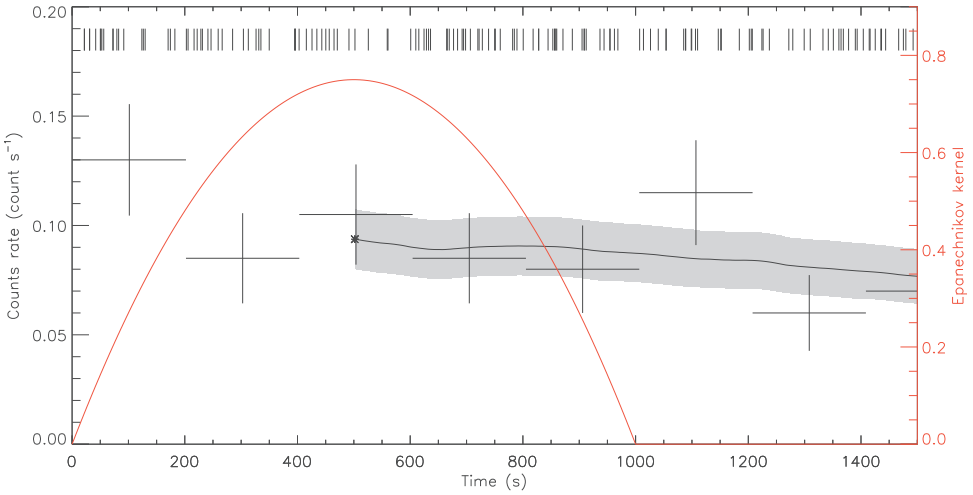


Figure 3.9: The density estimator for the light curve smoothing. The simulated arrival times are represented by the ticks at the top of this panel (see Sect. 3.3). The crosses are the first points of the simulated light curve and the error bars (see left y-axis). The red curve is the Epanechnikov kernel (see right y-axis). Here is an example for the first point of the smoothed light curve represented by an asterisk for a window width of $h = 500$ s (i.e., $t = 500$ s). The solid black curve and gray boxes are the smoothed light curve and error bars for a time interval of 5 s.

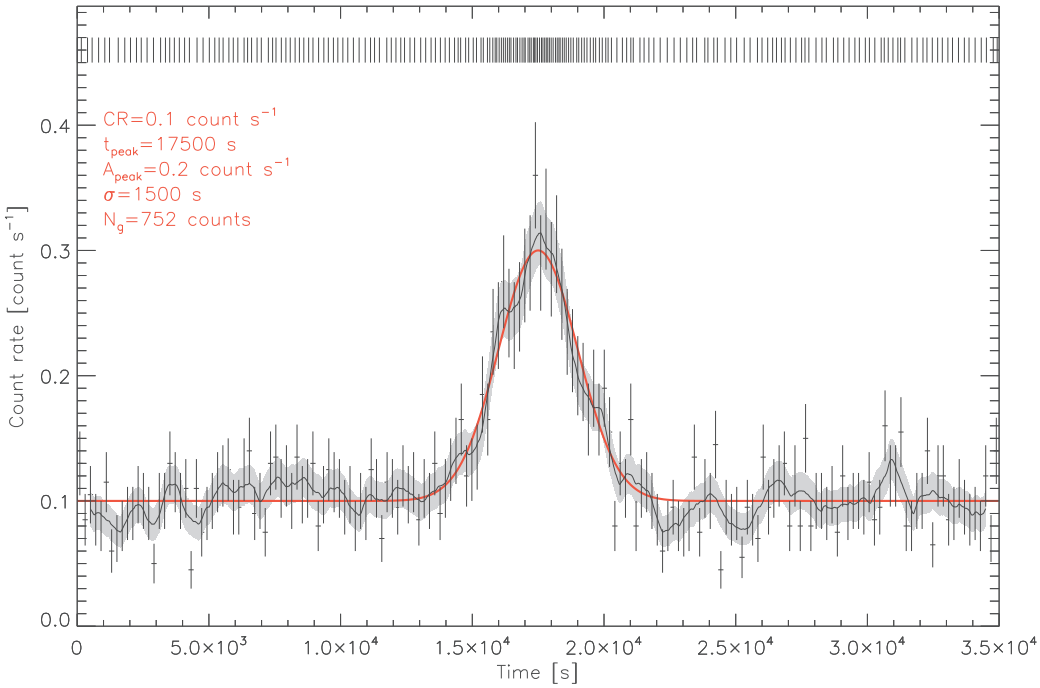


Figure 3.10: The resulting smoothed light curve of the event simulation presented in Sect. 3.3. The simulated arrival times are represented by the ticks at the top of this panel (only one arrival time on twenty are shown here for clarity purpose). The red curve is the model of the flare light curve. The crosses are the light curve points and their error bars with a bin of 200 s. The solid black curve and gray boxes are the smoothed light curve and error bars for a window width of $h = 500$ s.

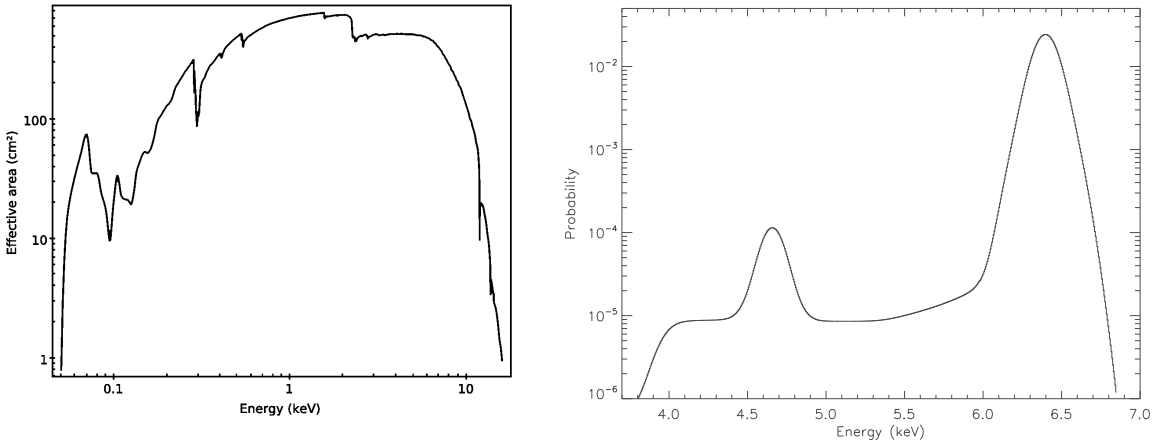


Figure 3.11: Effective area and probability distribution for EPIC/pn (medium filter, single and double events). *Left panel:* Effective area from a 10″-radius region centered on Sgr A* (ARF). *Right panel:* Probability distribution of the recorded energy of a photon with an initial energy of 6.4 keV extracted from the RMF.

### 3.6.1 Extraction of the X-ray flare spectrum

As for the creation of light curves, I have to extract the events from a source-plus-background and background region. The event extraction region for the src+bkg spectrum is a circle of 10″-radius centered on the Sgr A* radio position. Since I study the flaring spectrum, the extracted src+bkg event list is filtered to be only composed by photons recorded during the flare time interval defined with the two-steps Bayesian Blocks algorithm. Whereas the light curves are corrected from the instrumental background taking a large region different from the source region, the flare spectrum is corrected from the point sources and diffuse emission spectra contained in the 10″ source region. During the non-flaring period, the photons extracted from the 10″-radius region come from Sgr A* in its quiescent state but also from the point sources and the diffuse emission (see Fig. 3.2). I thus use the non-flaring period to correct from these contaminating sources and analyze only the Sgr A* flaring spectrum. The bkg extraction region is thus the same that the src+bkg region and the events are extracted before and after the flare with a rejection of 300 s before and after the flare start and stop to avoid any contamination of the flare spectrum in the background spectrum.

The spectra are then created from the event lists extracted from the src+bkg and bkg regions and time intervals by computing the number of events recorded in each spectral channel (4092 for XMM-Newton corresponding 0.15 to 15 keV for the nominal gain).

The src+bkg spectrum observed by an instrument is the combination of the spectrum emitted by the source, the efficiency of the instrument at each energy $E$ and the background spectrum. The number of counts observed in a spectral channel $i$ is (Eq. 7.35 of Houck 2013):

$$C(i) = T \int_0^\infty R(i,E)\, A(E)\, S(E)\, dE + B(i) \tag{3.9}$$

with $S(E)$ the source spectrum, $T$ the exposure time of the observation, $A(E)$ the effective area of the instrument, $R(i,E)$ the relation between the spectral channel and the energy and $B(i)$ is the bkg spectrum.

The effective area is the combination of the collecting area of the telescope, filter transmission, CCD quantum efficiency and PSF encircled energy fraction. This is described in the Ancillary Response File (ARF). The ARF has to be computed on the src+bkg region using the SAS task `arfgen`. The effective area from the source region centered on Sgr A* for the 2014 April 2 observation is given at the left panel of Fig. 3.11.

$R(i,E)$ is stored in the Redistribution Matrix File (RMF) which is created from the extraction region with the `rmfgen` task from the SAS package. When a photon of energy $E$ hits the CCD, there is a high probability that the recorded photon energy is $E \pm \Delta E$ but there is also a probability that the photon energy is recorded at a lower energy because of the escape peak. This is produced when the X-ray photon knocks out an inner shell electron from the detector material (Si). This atom then emits a photon of lower energy by fluorescence and the initial photon is detected with an energy $E - E_{\mathrm{Si\,K}_\alpha}$ with $E_{\mathrm{Si\,K}_\alpha} = 1.74$ keV. These escape peaks must be taken into account when fitting the spectrum. The right panel of Fig. 3.11 shows the probability distribution of

the recorded energy of a photon with an initial energy of 6.4 keV (with $\Delta E = 175$ eV) using single and double events.

The RMF and ARF may change from one observation to an other since the source position on the CCD changes from one observation to an other. The src+bkg and bkg spectrum and the corresponding RMF and ARF may be computed together for the corresponding extraction region using the SAS `especget` script.

The spectral fitting computes a theoretical model which, associated with the RMF and ARF, reproduces the observed spectrum $C(i)$.

### 3.6.2 The spectral model for X-ray flares from Sgr A*

The fitting model which best reproduces the observed spectrum of the flares from Sgr A* (Porquet et al. 2003, 2008; Nowak et al. 2012) is an absorbed powerlaw created with *TBnew* and *pegpwrlw* with a dust scattering modeled thanks to *dustscat* (Predehl & Schmitt 1995).

The *TBnew* model[5] is an improved version of the X-ray absorption model *tbabs* (Wilms et al. 2000). This model computes the absorption by photo-ionization along the line of sight of hydrogen column density $N_{\rm H}$ taking into account the cross section of each phase (dust, gas and molecules) of the ISM, $\sigma_{\rm ISM}$:

$$TB(E) = \exp\left(-\sigma_{\rm ISM}(E)\, N_{\rm H}\right) . \tag{3.10}$$

The *TBnew* model uses the updated inner and outer shells cross-sections of Verner et al. (1996) contrarily to the previous *tbabs* model which used the Band et al. (1990)'s cross section for the hydrogen, the Yan et al. (1998)'s cross section for the helium and Verner & Yakovlev (1995)'s inner shell cross sections of all other elements.

The dust scattering optical depth derived by Predehl & Schmitt (1995) using ROSAT observations of supernovae remnants was

$$\tau_{\rm scatt} = 0.486\, \frac{N_{\rm H}}{10^{22}\,{\rm cm}^{-2}} \left(\frac{E}{\rm keV}\right)^{-2} \tag{3.11}$$

with $E$ the photon energy and $N_{\rm H}$ the hydrogen column density on the line of sight. The factor 0.486 was computed using the Morrison & McCammon (1983)'s X-ray photon cross sections for photoelectric absorption and Anders & Ebihara (1982)'s abundances. However, *TBnew* uses the ISM abundances updated by Wilms et al. (2000) leading to lower metal abundances and the updated cross sections of Verner et al. (1996). Since the metal absorbs more X-ray photons than the hydrogen, the new abundances and cross sections lead to an hydrogen column density which is 1.5 times lower than previously obtained by Predehl & Schmitt (1995) as discussed in Nowak et al. (2012). The new *dustscat* model is thus

$$DS(E) = \exp\left(-\tau_{\rm scatt}\right) = \exp\left(-0.324\, \frac{N_{\rm H}}{10^{22}\,{\rm cm}^{-2}} \left(\frac{E}{\rm keV}\right)^{-2}\right) \tag{3.12}$$

### 3.6.3 Spectral fitting

Several softwares have been developed to fit the X-ray spectrum. I mainly used two of them: `ISIS` (Houck 2013) and `XSPEC` (Arnaud 1996; Arnaud et al. 2015). These two softwares may fit a binned or unbinned X-ray spectra with a user defined model using the Chi squared[6] ($\chi^2$) or Cash statistic[7]. The Cash statistic is preferred if the number of spectral bins is lower than the number of spectral parameters of fitting model or if the net number of counts in each bin is lower than 10−20 since the Poissonnian distribution of photon may not be approximated by the Gaussian distribution (Cash 1979). In order to be sure to have enough counts in each spectral bin of the background subtracted spectrum, I group the src+bkg spectrum with a minimum signal-to-noise ratio (*SNR*) using SAS task `specgroup`. In this task and the `ISIS` software, the *SNR* is computed as $(C_{\rm src} - C_{\rm bkg} \times ratio)/(C_{\rm src} + C_{\rm bkg} \times ratio^2)^{0.5}$ with *ratio* the exposure ratio multiplied by the region size ratio between the src+bkg and bkg spectrum and $C_{\rm src}$ and $C_{\rm bkg}$ the number of counts in the src+bkg and bkg spectrum, respectively.

[5] http://pulsar.sternwarte.uni-erlangen.de/wilms/research/tbabs/index.html

[6] The $\chi^2$ equation I use is normalized by the errors ($\sigma$) on the spectral bin count rate ($y_{\rm i}$): $\chi^2 = \sum_{i=1}^{n} (y_{\rm i} - M_{\rm i})^2/\sigma^2$.

[7] The Cash statistic is: $C = 2 \sum_{i=1}^{n} (M_{\rm i} - y_{\rm i} \log M_{\rm i})$.

The reliability of a fit is defined by the goodness-of-fit which measures the discrepancy between the observed and modeled spectrum and by the likelihood function which computes the probability to have this goodness-of-fit. For the $\chi^2$ statistic, the goodness-of-fit is given by the reduced $\chi^2$ ($\chi^2_{\rm red} = \chi^2/\nu$ with $\nu$ the number of degrees of freedom). The maximum likelihood is then determined with the Student's law. For the Cash statistic, we do not have access to the goodness-of-fit. `ISIS` and `XSPEC` thus make simulations of fake spectra and compute how many times the goodness-of-fit is lower than for the user data sample to define the likelihood function. The discrepancy between the observed and modeled spectrum is thus given by the maximum likelihood.

The difference between `ISIS` and `XSPEC` is the processing of the background spectrum. `XSPEC` uses the bkg spectrum scaled on the src+bkg spectrum to create a background subtracted spectrum on which the fit is applied. `ISIS` does not subtract the bkg from the src+bkg spectrum. This is the model defined as a source component plus an estimation of the background component which is fitted on the src+bkg spectrum. Moreover, `ISIS` can be parallelized for the fit error bars computations which decreases the computational time for high number of model parameters.

### 3.6.4 The Markov Chain Monte Carlo method for the spectral fitting

From the study of the 2014 campaign for the observation of Sgr A* (see Sect. 5), I used the Markov Chain Monte Carlo method (MCMC) to compute the best-fit parameters. This is an iterative method producing a set of model parameters which converges towards the target density, i.e., the marginal distribution of each parameters describing the observed spectrum. At each step, the value of the likelihood function is computed and the new set of parameters is accepted if this value is lower than the previous one. The advantage of this method is that we can easily compute, for each parameter, the marginal distribution and the associated error bar.

I use the Jeremy Sanders' `XSPEC_emcee`[8] program that allows the MCMC analysis of X-ray spectra in `XSPEC` using `emcee`[9], an extensible, pure-Python implementation of Goodman & Weare (2010)'s MCMC ensemble-sampler. Goodman & Weare (2010) proposed an affine invariant ensemble sampler for which the autocorrelation time is smaller than for the most used Metropolis-Hasting algorithm. This method uses a number of "walkers" which evolve independently from each others in the parameter space reducing the auto-correlation time. Following Foreman-Mackey et al. (2013), the number of walkers must be about 10 times the number of model parameters.

The number of steps needed to construct independent samples from the observed spectrum is given by the autocorrelation time $\tau_{\rm f}$ of the parameters which represents the covariance between samples at each step. $\tau_{\rm f}$ is computed thanks to the `acor` package (v1.1.1) available in Python[10]. It defines the "burn-in" period which is the number of steps that we do not use in the computation of the best-fit parameters. Following Foreman-Mackey et al. (2013), the "burn-in" period must be $20\,\tau_{\rm f}$ and the length of the Markov chain must be 30 times the "burn-in" period to converge towards the target density.

A proof of the convergence of the model parameters is the acceptance fraction ($a_{\rm f}$), i.e., the number of steps which are accepted since their likelihood function gives a value lower than those of the previous step. A good range (based on a huge number of simulations) is between 0.2 and 0.5 (e.g., Gelman et al. 1996; Foreman-Mackey et al. 2013). If the acceptance fraction is too low, this means that none of the set of parameters decreases the likelihood function. If it is too large, this means that the posterior probability function of the model parameters is a constant function and thus the best-fit parameters can not be computed.

The result of a fitting with the MCMC is usually represented in a triangle plot diagram (Python package `corner` v1.0.0). The marginal distribution of each parameter are the diagonal plots. They are the histograms of the values taken by all walkers at each step after the "burn-in" period. The best fitting parameters are defined by the median of the marginal distributions. The joint distributions between each couple of parameters are shown in the other plots with the confidence levels at 68, 90 and 99% (see Fig. 5.8 for an example of triangle plot published in Mossoux et al. 2016).

[8] https://github.com/jeremysanders/xspec_emcee
[9] http://dan.iel.fm/emcee/current/user/line/
[10] https://pypi.python.org/pypi/acor/1.1.1

# Chapter 4

# Constraints on the radial distance and size of the X-ray flaring region during the 2011 campaign with XMM-Newton

**Original publication**: Mossoux, E., Grosso, N., Vincent, F. H., Porquet, D., 2015, *Study of the X-ray activity of Sgr A* during the 2011 XMM-Newton campaign*, Astronomy & Astrophysics, 573, A46, p. 1–15 (see Annexe D, p. 113 of this Ph.D. thesis).

The goal of the 2011 campaign was to observe Sgr A* simultaneously for the first time in X-rays with XMM-Newton and at 1.3 mm with the Event Horizon Telescope (EHT) providing very long base interferometry in order to determine the localization of X-ray flares. Between 2011 March 18 and April 5, the merged visibility window of the 1.3 mm EHT formed by the Atacama Pathfinder Experiment (APEX) in Chile, the Sub-millimeter Telescope (SMT) in Arizona, CARMA in California and Sub-millimeter Array (SMA) in Hawaii was 10:45–15:45 UT. The observing nights of the EHT were constrained by the weather forecast. The XMM-Newton exposures have to began prior the EHT observation to detect the X-ray flares associated to the delayed millimeter counterpart. The XMM-Newton observations were planned on 2011 March 28 and 30, and April 1, 3, and 5 (XMM-Newton AO-8, 5 × 33 ks; PI: D. Porquet) for a total exposure of about 226 ks (see Table 4.1). The weather constrained EHT exposures were obtained on 2011 March 29 and 31, and April 1[1], 2, and 4. Consequently, only the EHT observation on 2011 April 1 was simultaneous with XMM-Newton observation but no X-ray flare was observed (see below). The study of the millimeter emission observed with the EHT were reported by Fish et al. (2016). The millimeter activity was not discussed in their paper but they found that the quiescent emission from Sgr A* in millimeter is elongated with a position angle of +128° east.

Table 4.1: XMM-Newton observation log for the 2011 campaign (Mossoux et al. 2015a).

| Orbit | ObsID | Start Time[a] (TT) | End Time[a] (TT) | Duration (s) |
|---|---|---|---|---|
| 2069 | 0604300601 | Mar. 28, 07:54:14 | Mar. 28, 21:13:55 | 47981 |
| 2070 | 0604300701 | Mar. 30, 08:11:26 | Mar. 30, 21:14:28 | 46942 |
| 2071 | 0604300801 | Apr. 01, 08:23:50 | Apr. 01, 19:23:59 | 39609 |
| 2072 | 0604300901 | Apr. 03, 07:56:23 | Apr. 03, 19:21:36 | 41113 |
| 2073 | 0604301001 | Apr. 05, 07:13:49 | Apr. 05, 21:11:49 | 50280 |

**Notes:** [(a)] Start and end times of the EPIC MOS camera observations in terrestrial time (TT) referential.

[1]On 2011 March 28–April 1, the timing and frequency references at CARMA was erroneously derived from a local rubidium oscillator instead of the more accurate hydrogen maser, required for very long base interferometry; however, this setup did not affect phase closure (Fish et al. 2016).

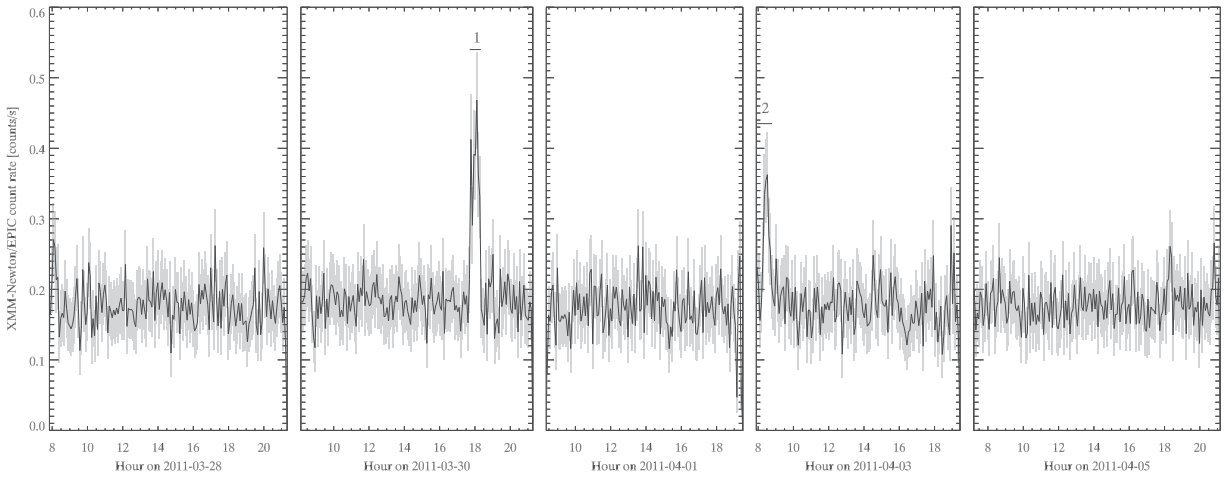


Figure 4.1: XMM-Newton/EPIC (pn+MOS1+MOS2) light curves of Sgr A* in the 2–10 keV energy range obtained in 2011 Mar.–Apr. (Mossoux et al. 2015a). The time interval used to bin the light curve is 300 s. The X-ray flares are labeled from 1 to 2. The horizontal lines below these labels indicate the flare durations.

Table 4.2: Characteristics of the X-ray flares observed by XMM-Newton/EPIC in 2011 (Mossoux et al. 2015a).

| Flare (#) | Instrument | Day (yy-mm-dd) | Start Time[a] (hh:mm:ss) | End Time[a] (hh:mm:ss) | Duration (s) | Total[b] (cts) | Peak[c] (count $s^{-1}$) | $L^{unabs}_{2-10\,keV}$[d] ($10^{34}$ erg $s^{-1}$) |
|---|---|---|---|---|---|---|---|---|
| 1 | pn | 2011-03-30 | 17:46:20 | 18:19:40 | 2000 | 211 ± 25 | 0.28 ± 0.01 | $2.7^{+2.4}_{-0.7}$ |
| – | MOS1 | ———— | 17:42:52 | 18:15:51 | 1978 | 189 ± 12 | 0.16 ± 0.04 | ..... |
| – | MOS2 | ———— | 17:39:11 | 18:20:02 | 2451 | 179 ± 13 | 0.14 ± 0.04 | ..... |
| 2 | pn | 2011-04-03 | ≤08:16:35 | 08:41:02 | ≥ 1458 | ≥ 154 ± 24 | 0.17 ± 0.01 | ≥ 2.9 |
| – | MOS1 | ———— | ..... | ..... | ..... | ..... | ..... | ..... |
| – | MOS2 | ———— | ≤07:56:23 | 08:46:15 | ≥ 2926 | ≥ 206 ± 15 | 0.16 ± 0.04 | ..... |

**Notes:** [(a)] Start and end times (TT) of the flare time interval defined by the Bayesian blocks algorithm (Scargle et al. 2013b); [(b)] Total counts in the 2–10 keV energy band obtained in the smoothed light curve during the flare interval (determined by the Bayesian blocks) after subtraction of the non-flaring level obtained with the Bayesian blocks algorithm; [(c)] Count rate in the 2–10 keV energy band at the flare peak (smoothed light curves) after subtraction of the non-flaring level; [(d)] Unabsorbed 2−10 keV average luminosity of the flare computed from the total counts collected during the flare (i.e., the average count rate) and assuming a distance of 8 kpc.

## 4.1 Analysis of the X-ray data

I follow the reduction method of the X-ray data explained in Sect. 3.1 with the SAS package version 13.5 and the calibration files of 2014 April 4 to create the XMM-Newton/EPIC (pn+MOS1+MOS2) light curves in the 2−10 keV energy range shown in Fig. 4.1. I use the two-steps Bayesian block algorithm (see Sect. 3.4) to determine the non-flaring level and detect the X-ray flares with a false positive rate of 0.1% (corresponding to $p_1 = \exp(-3.5)$). The non-flaring levels are consistent with those previously observed with XMM-Newton (e.g., Porquet et al. 2008). Table 4.2 gives the characteristics of the two X-ray flares detected on 2011 March 30 (#1) and April 3 (#2) as indicated by the horizontal lines below the labels in Fig. 4.1. I then smooth the flaring light curves of each instrument to determine the flare peak count rates. The Bayesian blocks and the smoothed light curves of the flares are shown in Fig. 4.2.

Contrarily to most of the X-ray flares already observed, the flare of 2011 March 30 (left panels of Fig. 4.2) has an asymmetric shape characterized by a short (∼458 s) and luminous subflare followed by a long (∼1542 s) and less luminous subflare with a separating time of 1000 s between the maxima. Between these two subflares, the EPIC/pn light curve recovers a level consistent with the non-flaring level. This double peaked feature is also observed in MOS1 but not in MOS2.

The flare of 2011 April 3 flare (right panels of Fig. 4.2) is only detected by the two-steps Bayesian blocks algorithm in the EPIC/pn and MOS2 event lists. The absence of detection in the MOS1 camera is due to the faintness of this flare and the lower sensitivity of the MOS cameras implying a lower detection efficiency of the two-steps Bayesian blocks algorithm (see Fig. 3.6). The change point of the Bayesian block associated to the beginning of this flare is not observed in EPIC/pn nor in MOS2 implying that this flare starts before the beginning of the XMM-Newton observation. A VLT/NACO observation was made on 2011 April 3 with

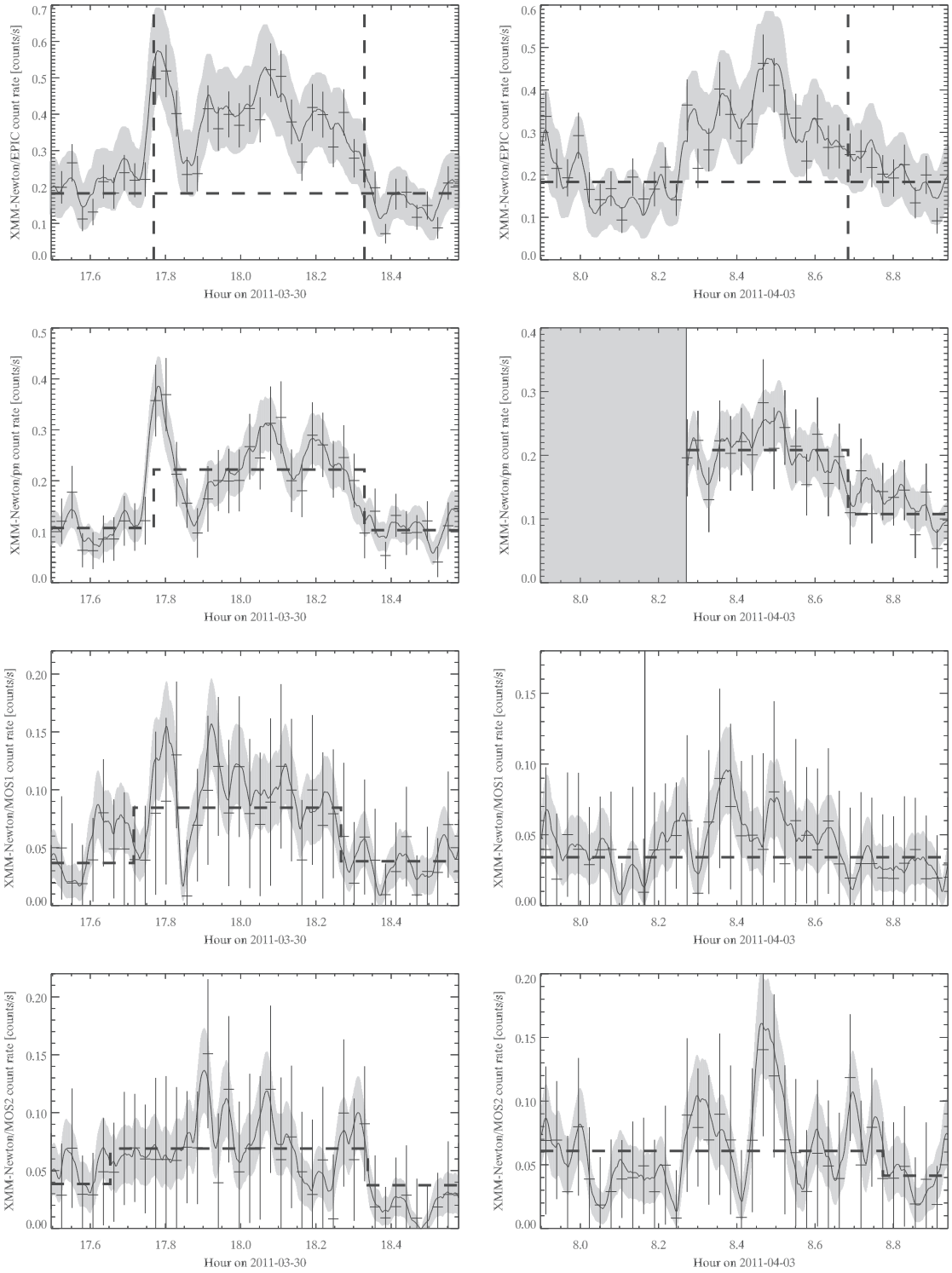


Figure 4.2: Light curves of Sgr A* in the 2–10 keV energy range obtained with XMM-Newton during the flare of 2011 March 30 (left panels) and April 03 (right panels) binned on 100 s (Mossoux et al. 2015a). The bad time intervals are shown with a light gray boxes. The dashed lines are the Bayesian blocks. The total XMM-Newton/EPIC light curves are shown in the top panels. The horizontal dashed lines are the sum of the non-flaring level in each instrument. The vertical dashed lines represent the beginning and the end of the flare determined by the two-steps Bayesian Blocks algorithm on the EPIC/pn camera. The solid lines are the smoothed light curves computed as the sum on the same time range of the smoothed light curves for each instrument. The gray curves are the errors associated with the smoothed light curves. The second, third and bottom panels represent the EPIC/pn, MOS1 and MOS2 light curves of Sgr A*, respectively.

22 min of overlap with the beginning of the observation with EPIC MOS; at the end of this observation, the rise phase of the NIR counterpart of this X-ray flare was observed (S. Gillessen, 2011, private communication).

I extract the X-ray spectrum of these two flares as explained in Sect. 3.6.1 and grouped them with a minimum signal-to-noise ratio of 4. I fit the grouped spectrum of flare #1 with the absorbed powerlaw model described in Sect. 3.6.2 with `ISIS` (v1.6.2-27). The best-fit parameters and their 90% confidence level are: hydrogen column density of $6.7^{+8.2}_{-6.7}\times10^{22}$ cm$^{-2}$, photon index of $1.5^{+1.5}_{-1.3}$, absorbed flux between 2 and 8 keV of $2.5\times10^{-12}$ erg s$^{-1}$ cm$^{-2}$ and unabsorbed flux between 2 and 10 keV ($F^{\rm unabs}_{2-10\,{\rm keV}}$) of $3.5^{+3.1}_{-1.0}\times10^{-12}$ erg s$^{-1}$ cm$^{-2}$ which is consistent with those computed for the 2002 Oct. 3 and 2007 April 4 flares observed with XMM-Newton (Porquet et al. 2003, 2008; Nowak et al. 2012). The physical characteristics of this flare (unabsorbed luminosity, unabsorbed total energy and duration) lie within the mean of the characteristics of the X-ray flares detected during the 2012 *Chandra XVP* campaign (Neilsen et al. 2013).

The flare #2 does not contains enough counts to constrain the spectral parameters. The unabsorbed flux of this flare is thus computed by fitting its spectrum with the photon index and the column density values fixed to those of the bright X-ray flare of 2002 October 3 observed with XMM-Newton (Porquet et al. 2003; Nowak et al. 2012) leading to $F^{\rm unabs}_{2-10\,{\rm keV}} = 3.91\times10^{-12}$ erg s$^{-1}$ cm$^{-2}$.

## 4.2 Discussions

### 4.2.1 Modeling the flare of 2011 March 30 with the gravitational lensing of a hotspot-like structure

The smallest waiting time between two consecutive X-ray flares observed during the 2012 *Chandra XVP* is about 3500 s (see Fig. 1 of Neilsen et al. 2013). Since the separating time observed between the two subflares of the flare #1 is smaller than this value, I consider that this flare is a single flare with a large flux variation.

The double-peaked structure of this flare may be explained by a flux variation due to the gravitational lensing effect. The gravitational lensing is due to the curvature of the space-time induced by the SMBH. The null geodesic followed by a photon is straight in a flat space-time but is bended when passing in a strong gravitational field (see Fig. 4.3). Close to the SMBH, the photon trajectory is thus deflected producing a lensing effect of the source flux. The more aligned are the observer, the lens (here the SMBH) and the source of photon, the greater is the lensing effect. If the observer is exactly aligned with the lens and the source, the deflected photons form a ring called Einstein ring (see third panel of Fig. 4.4). A consequence of the deflection of photons is an increase of the apparent source luminosity since the source photons are lensed towards the observer. This magnification can explain the first substructure with a high amplitude and short duration (which would correspond to the time that the source spends behind the SMBH). The second substructure would be explained by the Doppler relativistic boosting effect which changes the apparent luminosity of an orbiting source near a massive object. Let us consider a source orbiting at high velocity around a SMBH (Fig. 4.4). The emission of this relativistic source is beamed in the direction of the motion due to the length contraction in special relativity. This relativistic phenomenon increases the apparent luminosity of a source moving towards the observer and is maximum when the source is at the quadrature (see last panel of Fig. 4.4).

In collaboration with Frédéric H. Vincent, we constructed the light curve as it would be observed for the gravitational lensing of a hotspot orbiting Sgr A* using the ray-tracing code GYOTO (Vincent et al. 2011). The hotspot is defined as a spherical, optically thin structure, orbiting around Sgr A* with a Keplerian angular velocity and an inclination close to edge-on view. The parameters describing this structure, i.e., the hotspot radius $R$ and the orbital radius $r$ and inclination $i$, are discretized on a fitting grid. They are then constrained by a $\chi^2$ fitting of the simulated light curve to the smoothed pn light curve of the flare #1. The parameter which is easiest fitted is the orbital radius since it directly depends on the time delay between the maximum of the two peaks. The two other parameters impact both the amplitude of the first peak and the flux ratio between the two peaks. The best fitting parameters are $r = 12\,r_{\rm g}, R = 1.4\,r_{\rm g}$ and $i = 86.5°$ ($\chi^2_{\rm red} = 0.85$).

The best-fitted light curve is compared to the smoothed pn light curve in Fig. 4.5. This figure shows that the minimum between the two flares of the computed light curve is $2.5\,\sigma$ higher than the observed light curve. However, this feature is a strong characteristic of the 2011 March 30 flare since it is observed with pn and MOS1. We thus refine the hotspot model considering an elongated hotspot model whose radius varies along the orbit due to the differential Keplerian rotation and a swelling hotspot whose the volume increases linearly between the flare start and the local minimum between the two peaks. However the best-fitted light curves

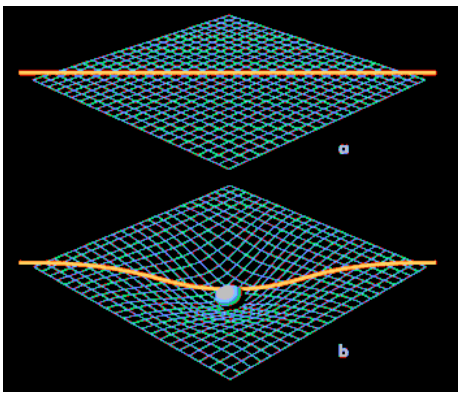


Figure 4.3: Illustration of the light bending effect. The upper image (*a*) is the trajectory of a photon in a flat space-time. The lower image (*b*) is the trajectory of a photon in a curved space-time.

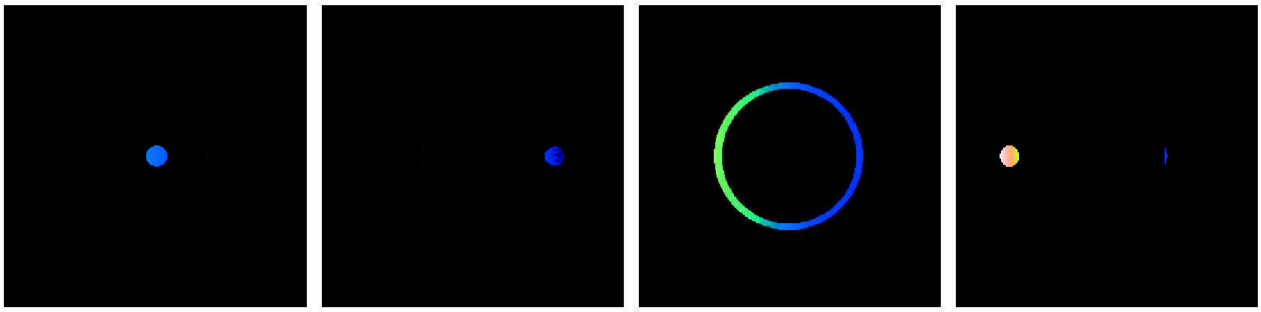

Figure 4.4: Simulation of a hotspot orbiting a supermassive black hole computed with the ray-tracing code GYOTO (F. H. Vincent, 2013, private communication). The radial distance between the optically thick hotspot is 9 $r_g$, the hotspot radius is 1 $r_g$ and the SMBH spin is null. The images from the left to the right side are when the hotspot is: in front of the SMBH, at the quadrature and moving away from the observer, behind the SMBH, and at the quadrature and moving towards the observer.

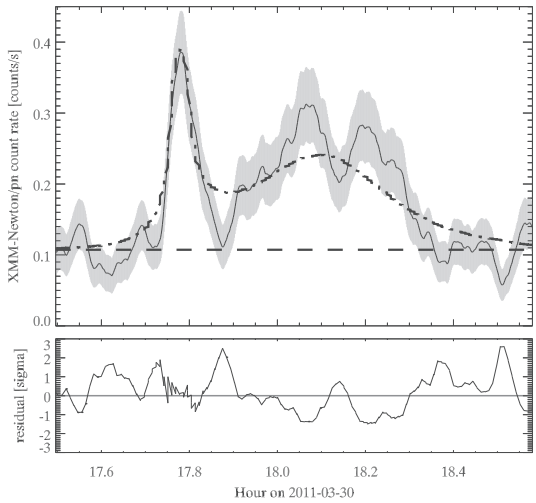


Figure 4.5: Modeling of the 2011 March 30 flare pn light curve with a rotating hotspot (Mossoux et al. 2015a). Best fitting theoretical light curve (dot-dashed line) plotted over the smoothed light curve (solid line, with 1$\sigma$-error in gray). The non-flaring level is given by the horizontal dashed line. The vertical axis is in observed units, horizontal axis is in seconds. The lower panel gives the residual in units of $\sigma$.

with these two toy models never reproduce the local minimum since the hotspot remains bright all along the orbit. We thus reject this hotspot model without adding some *ad-hoc* components which would make the model less reliable.

### 4.2.2 Constraints on the radial distance and the size of the flaring region of the first subflare of 2011 March 30

Since the 2011 March 30 flare can not be reproduced as a single flare, I consider that it is composed by two close subflares separated by about 1000 s and produced by their own population of non-thermal electrons. In this scenario, the first subflare is one of the shortest flare ever observed and the separation time between the two subflares is three times smaller than those observed between the two closest consecutive flares of the 2012 *Chandra XVP* campaign. The short duration of the first subflare allows me to constrain the size and the distance of the flaring region. I consider that this subflare is described by a rise phase during which the electrons are accelerated by the magnetic energy available in the flaring region, and a decay phase due to the synchrotron cooling of the accelerated electrons. The total luminosity emitted during the overall subflare duration is thus produced by the magnetic energy released during the rise phase.

To avoid any contamination of the non-flaring level in the computations, I consider that the start and end times of the subflare are the times when the count rate of the smoothed light curve is larger than the Poissonnian fluctuation of the non-flaring level at the 99.87% of confidence level (corresponding to a Gaussian single-sided confidence level of $3\sigma$). The end of the rise phase is the time of the maximum of the smoothed light curve. The rise and decay phase durations are thus $\Delta t_{\rm rise} = 115$ s and $\Delta t_{\rm decay} = 340$ s.

These observed durations ($\Delta t$) are shorter than the proper duration ($\Delta\tau$) due to time dilation in strong gravitational field near the SMBH. I thus compute the proper times as a function of the radial distance from Sgr A* using the Kerr metric (Kerr 1963) in Boyer-Lindquist coordinates with a dimensionless spin parameter of 1 (see Appendix C in Mossoux et al. 2015a, p. 127 of this Ph.D. thesis).

The upper limit on the radius of the flaring region is computed considering that the Alfven velocity cannot be larger than the speed of light (Dodds-Eden et al. 2009): $R < c\Delta\tau_{rise}$. The magnetic energy available in this flaring region located at a radial distance $r$ from Sgr A* is $U_{\rm B}(r) = B(r)^2 V(r)/8\pi$ with $V(r) < \frac{4}{3}\pi c^3 \Delta\tau^3_{\rm rise}(r)$ the upper limit on the volume of the region and $B(r) = B_{1R_{\rm s}} 2r_{\rm g}/r$ the magnetic field with $B_{1R_{\rm s}} = 100$ G (see Barrière et al. 2014, and references therein). The variation of the upper limit on the magnetic energy with the radial distance is represented in the top panel of Fig. 4.6 with a black solid line.

The magnetic energy is converted to the X-ray unabsorbed luminosity with a production efficiency $\eta$ ($\leq 1$). Thanks to the spectral parameters computed for the overall 2011 March 30 flare, i.e., $N_{\rm H} = 6.7 \times 10^{22}$ cm$^{-2}$ and $\Gamma = 1.5$, I determine a mean unabsorbed luminosity of $L^{\rm unabs}_{2-10\,{\rm keV}}({\rm flare}) = 5.8^{+5.7}_{-1.7} \times 10^{34}$ erg s$^{-1}$ for the first subflare. The total energy released during the first subflare is thus $L^{\rm unabs}_{2-10\,{\rm keV}}({\rm flare})\Delta\tau_{\rm flare}(r)$ with $\Delta\tau_{\rm flare}(r)$ the proper duration of the first subflare. The total energy is also represented in the top panel of Fig. 4.6 as a function of the radial distance (dashed line with gray stripes for the error bars). The conversion of magnetic energy in unabsorbed luminosity is written as

$$L^{\rm unabs}_{2-10\,{\rm keV}}({\rm flare})\Delta\tau_{\rm flare}(r) < \frac{B^2_{1R_{\rm S}}}{6}\left(\frac{2r_{\rm g}}{r}\right)^2 c^3 \Delta\tau^3_{\rm rise}\eta\,. \tag{4.1}$$

I represent $\eta = U_{\rm B}(r)/L^{\rm unabs}_{2-10\,{\rm keV}}({\rm flare})\Delta\tau_{\rm flare}(r)$ in the bottom panel of Fig. 4.6 (solid line with error bars in dotted lines) as a function of the radial distance. All the parameters except the radial distance are determined by the characteristics of the first subflare. Assuming $\eta = 1$, I obtain an upper limit on the radial distance of $r < 100^{+19}_{-29}\ r_{\rm g}$ (vertical dashed line with error bars in vertical dotted lines) corresponding to a radius of the flaring region (solid red line) of $R = 2.87 \pm 0.01\ r_{\rm g}$.

During the decay phase of the subflare, the accelerated electrons cool by emitting synchrotron radiation with a timescale (Dodds-Eden et al. 2009):

$$\tau_{\rm sync}(r) = 8\left(\frac{B(r)}{30\,{\rm G}}\right)^{-3/2}\left(\frac{\nu}{10^{14}\,{\rm Hz}}\right)^{-1/2}\ {\rm min}\,. \tag{4.2}$$

Two cooling timescales are defined according to the frequency of the photons that are created: I first consider that the X-ray photons ($\nu = 10^{18}$ Hz) are emitted by a direct synchrotron radiation. The comparison between the synchrotron cooling timescales and the duration of the decay phase ($\tau^{\rm X}_{\rm sync}(r) > \Delta\tau_{\rm decay}$) leads to a lower limit on the distance of $r > 114\,r_{\rm g}$. This latter value is inconsistent with the previously derived upper limit implying that a sustained heating must be present during the decay phase. I thus consider that the electrons accelerated by the magnetic energy emit NIR photons which are then upscattered to create the X-ray photons. The synchrotron cooling time of NIR photons ($\nu = 10^{14}$ Hz) leads to $r > 4\,r_{\rm g}$ (see Fig. 4.7).

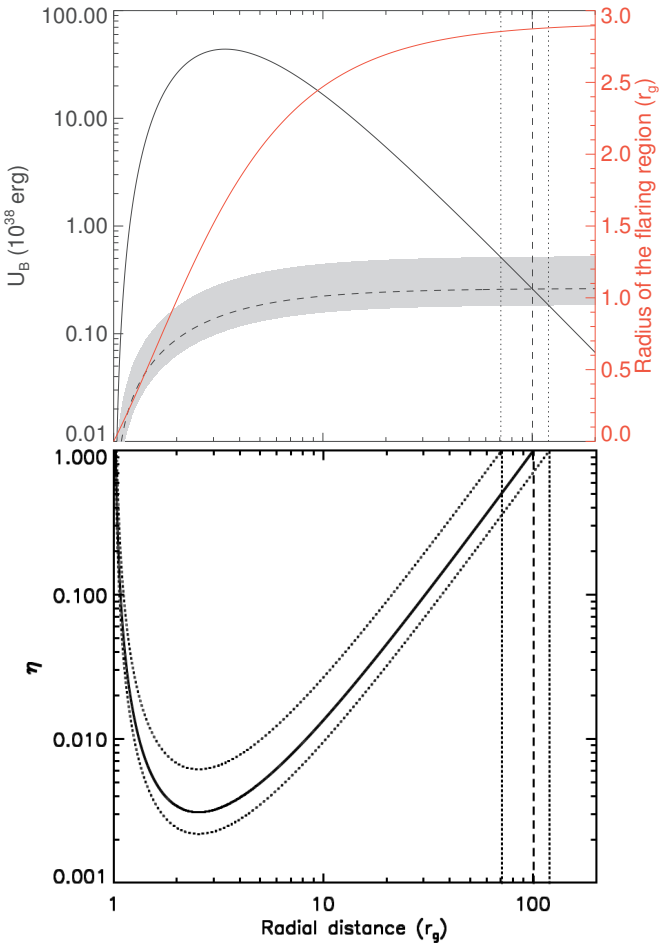


Figure 4.6: Determination of the radial distance of the flaring region (Mossoux et al. 2015a). *Top panel:* Magnetic energy vs. radial distance for a magnetic field of 100 G at 2 $r_g$ and an X-ray photon production efficiency and dimensionless spin parameter of 1. The solid black line is the distribution of the magnetic energy (see left y-axis) vs. the radial distance. The dashed line is the central value of the X-ray total energy with the gray stripes representing its error within 90% confidence level. The vertical lines are the upper limit to the distance and its error corresponding to $\eta = 1$. The solid red line is the radius of the emitting region (see right y-axis). *Bottom panel:* X-ray photons production efficiency vs. radial distance for the total energy and its upper and lower limit. The solid and dotted lines represent the efficiency for the central value of the total energy and its errors within 90% confidence level, respectively.

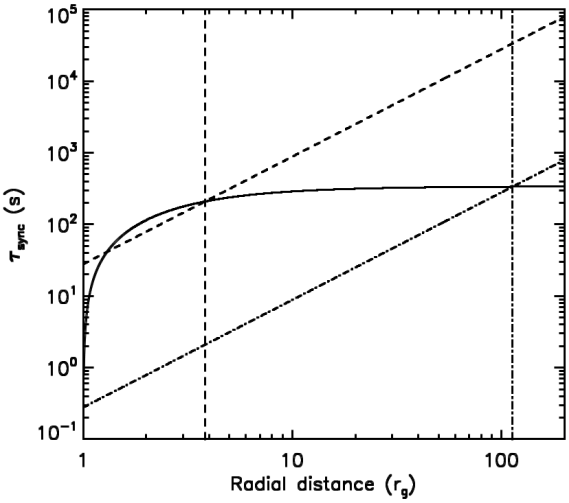


Figure 4.7: Synchrotron cooling time vs. the radial distance (Mossoux et al. 2015a). The solid line represents the proper duration of the decay phase. The dashed inclined line represents the synchrotron cooling time for infrared photons. The dotted-dashed inclined line is the synchrotron cooling time for X-ray photons. The corresponding vertical lines are the lower limit to the radial distance for each cooling timescale.

I thus constrain the radial distance of the flaring region of the first subflare to $4\,r_{\rm g} < r < 100^{+19}_{-29}\,r_{\rm g}$ for $\eta = 1$ and $B_{1R_{\rm s}} = 100\,{\rm G}$. This corresponds to a constraint on the radius of the flaring region of $1.8\,r_{\rm g} < R < 2.87 \pm 0.01\,r_{\rm g}$.

For comparison, Barrière et al. (2014) also reported a radial distance for the X-ray flare observed by NuSTAR on 2012 July 21 with a mean luminosity of $21 \times 10^{34}\,{\rm erg\,s^{-1}}$. This NuSTAR flare was characterized by a rise phase of 100 s followed by a plateau phase of about 1700 s and a decay phase of 100 s. Its was thus about four times longer and about 3.5 times more luminous than the 2011 March 30 flare but they derived a radial distance which is five times shorter than the upper limit that I derived here. However, considering their radial distance and magnetic field, i.e., $20\,r_{\rm g}$ and $B_{1R_{\rm s}} = 100\,{\rm G}$, the synchrotron cooling time is about 2500 s. Compared to the duration of the plateau phase, this implies a sustained heating during this phase or a radial distance larger than $20\,r_{\rm g}$.

Using the same method as for the first subflare of the flare #1, taking the time dilatation into account and considering only the rise and decay phase of the flare on 2012 July 21, I derive a revised value for the radial distance with an upper limit of $64\,r_{\rm g}$. If I consider also the plateau phase, this upper limit on the radial distance should be larger due to the source expansion during the supplementary 1700 s. Considering the duration of the decay phase of the 2012 July 21 flare and the synchrotron cooling time for the NIR photons, I derive a lower limit on the radial distance of $2.2\,r_{\rm g}$. For this NuSTAR flare, the direct synchrotron emission for the creation of X-ray photons is possible since the synchrotron cooling time leads to a lower limit on the radial distance of $50\,r_{\rm g}$ which is lower than the upper limit of $64\,r_{\rm g}$. I can not constrain the size of the flaring source for this flare since I do not have a strict upper limit on the distance due to the presence of the plateau phase.

# Chapter 5

# Multiwavelength study of the flaring activity of Sgr A* in 2014 February–April

**Original publication**: Mossoux, E., Grosso, N., Bushouse, H., Eckart, A., Yusef-Zadeh, F., Plambeck, R. L., Peissker, F., Valencia-S., M., Porquet, D., Cotton, W. D., Roberts, D. A., 2016, *Multiwavelength study of the flaring activity of Sgr A* in 2014 February–April*, Astronomy & Astrophysics, 589, A116, p. 1–26 (see Annexe D, p. 131 of this Ph.D. thesis).

The aim of this campaign was to study the impact of the DSO/G2 pericenter passage on the NIR/X-ray flaring activity of Sgr A*. An XMM-Newton large program was submitted in 2012 Oct. (XMM-Newton AO-12; PI: N. Grosso) to obtain joint observations with XMM-Newton, HST/WFC3 and VLT/SINFONI close to the DSO/G2 pericenter passage (based on the predictions of Gillessen et al. 2012). In order to increase the number of HST orbits simultaneous with the XMM-Newton observations, 22 additional HST orbits were requested (HST cycle 21; PI: H. Bushouse, Space Telescope Science Institute, USA).

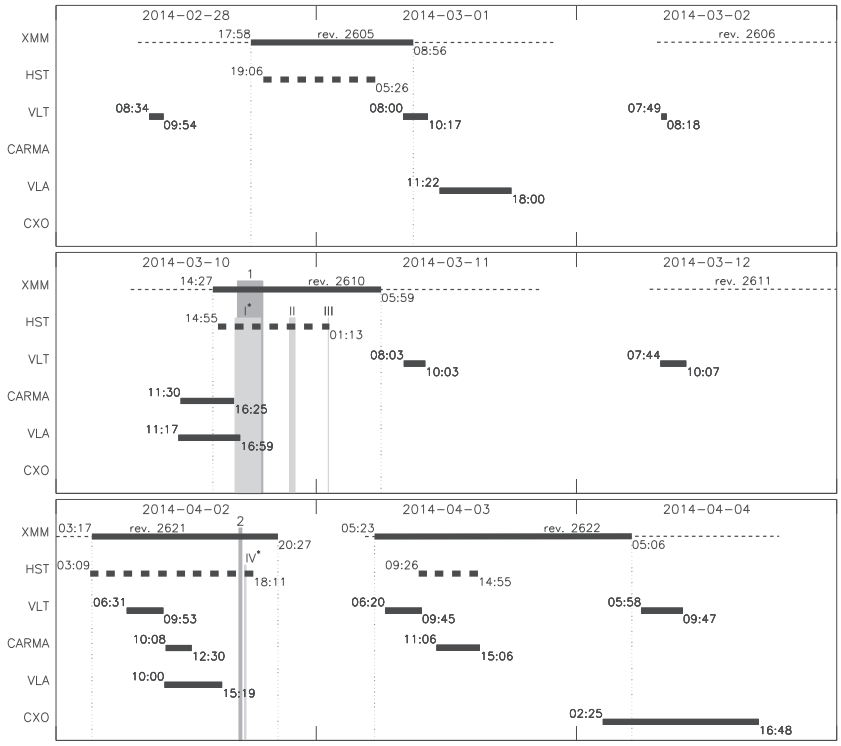


Figure 5.1: Time diagram of the 2014 Feb.−Apr. campaign (Mossoux et al. 2016). The horizontal dashed lines are the XMM-Newton orbital visibility times of Sgr A* labeled with revolution numbers. The thick solid lines are the time slot of the observations for each instrument with start and stop hours. The vertical dotted lines are the limits of the XMM-Newton observations. The vertical gray blocks are the X-ray (Arabic numerals) and NIR (Roman numerals) flares.

The XMM-Newton visibility of Sgr A* in the first semester of 2014 constrained the X-ray observations between 2014 Feb. 28 and Apr. 3. The HST/WFC3 visit scheduling was optimized to avoid the South Atlantic Anomaly (SAA) for maximizing the simultaneous observations with XMM-Newton. The three XMM-Newton observations were obtained on 2014 Feb. 28, Mar. 10 and Apr. 2 (total exposure of 170 ks) with three simultaneous HST visits of 7, 7 and 10 consecutive orbits (total exposure of 69 ks). The VLT/SINFONI observations granted in the XMM-Newton AO-12 were obtained on 2014 Apr. 2 (simultaneous with XMM-Newton) and Mar. 11, 12 and Apr. 3, 4 (for a total of 81 exposures of 400 s). We used additional VLT/SINFONI observations (ESO program 091.B-0183(H); PI: A. Eckart, Physikalisches Institut der Universität zu Köln, Max-Planck-Institut für Radioastronomie, Germany) obtained on 2014 Mar. 1 (coordinated with XMM-Newton) and Feb. 28 and Mar. 2 (for a total of 22 exposures of 400 s). We also had access to a Target of Opportunity (ToO) that was triggered to observe SGR J1745-29 with XMM-Newton on 2014 Apr. 3 (85 ks; PI: G.L. Israël, Osservatorio Astronomico di Roma, INAF, Italy). One VLT/SINFONI observation and four remaining HST orbits were simultaneous with this X-ray observation. Coordinated/simultaneous observations were also obtained with CARMA (three observations; PI: R. L. Plambeck, University of California, USA) and VLA in its A-configuration (three observations; VLA program 14A-231; PI: F. Yusef-Zadeh, Northwestern University, USA). Figure 5.1 is the time diagram of the different instruments used during the 2014 Feb.–Apr. campaign and the time ranges of the detected NIR flares (labeled with Roman numerals) and X-ray flares (labeled with Arabic numerals).

This VLT/SINFONI observing time is also very valuable to monitor the DSO/G2 and constrain its characteristics as reported in the next Sect. 5.1. I present the results of the 2014 Feb.–Apr. multiwavelength campaign for the study of the Sgr A* flaring activity in Sect. 5.2.

## 5.1 Monitoring the DSO/G2 on its orbit toward the Galactic Center Black Hole

**Original publication**: Valencia-S., M., Eckart, A., Zajaček, M., Peissker, F., Parsa, M., Grosso, N., Mossoux, E., Porquet, D., Jalali, B., Karas, V., Yazici, S., Shahzamanian, B., Sabha, N., Saalfeld, R., Smajic, S., Grellmann, R., Moser, L., Horrobin, M., Borkar, A., García-Marín, M., Dovčiak, M., Kunneriath, D., Karssen, G. D., Bursa, M., Straubmeier, C., Bushouse, H., 2015, *Monitoring the Dusty S-cluster Object (DSO/G2) on its Orbit toward the Galactic Center Black Hole*, The Astrophysical Journal, 800, 125, p. 1–21 (see Annexe D, p. 157 of this Ph.D. thesis).

VLT/SINFONI observations of the DSO/G2 with the H+K grating (1.45 – 2.45 $\mu$m) were obtained from 2014 Feb. 28 to Sept. 7 (Table 5.1). More than sixty percent of the total exposure time effectively used were granted by the XMM-Newton large program previously presented. The VLT/SINFONI observations are composed by successive exposures of 400 or 600 s on the target, preceded or followed by identical exposures on a dark cloud at 5′36″ north and 12′45″ west of Sgr A*. Data cubes are constructed for each exposure using the SINFONI pipeline. Cubes whose the *FWHM* of the two-dimensional Gaussian fitting of the S2 star is less than 83 mas (6.65 pixels) are considered as bad data cubes and are not used in the study.

The DSO/G2 spectra are extracted from 0.″05-radius aperture centered on the maximum of the Br$\gamma$ emission. Since the Br$\gamma$ line detection, *FWHM* and amplitude strongly depend on the background correction, we test different aperture sizes, positions and shapes for the background spectra extraction. The background emission at the DSO/G2 position is estimated with the third-order polynomial fitting and scaling of the background spectrum. The detected Br$\gamma$ line is not a spurious feature if it is always detected after the different background subtractions.

Before 2014 May, a redshifted Br$\gamma$ line is detected with a signal-to-noise ratio of 3.9–4.7 at about 2.185 $\mu$m corresponding to a velocity of 2700 ± 60 km s$^{-1}$. The mean *FWHM* and luminosity of the line are 720 ± 150 km s$^{-1}$ and $1.0 \times 10^{-3}\,L_{\odot}$, respectively. We stress that taking a source extraction region along the orbit as it was done in Gillessen et al. (2013b) leads to a narrower Br$\gamma$ line compared to all other extraction regions. The redshifted emission of the Br$\gamma$ line is located at 8.6 mas south and 41.5 mas east of Sgr A*. We do not detect any blueshifted emission of the Br$\gamma$ line for different positions of the source extraction regions within 200×200 mas at the southwest of Sgr A*. This absence of detection indicates that the blueshifted emissions detected by Pfuhl et al. (2015) and Gillessen et al. (2013b) are spurious lines due to the background subtraction.

Table 5.1: The DSO/G2 observations log with VLT/SINFONI.

| Date 2014 | Start Time (UT) | End Time (UT) | Number of Exposures [a] (Used/Total) | Total Exposure (s) |
|---|---|---|---|---|
| Feb. 27 [b,i] | 08:20:42 | 09:48:55 | 4/4 | 1600 |
| Feb. 28 [c,i] | 08:34:58 | 09:54:37 | 0/7 | 0 |
| Mar. 01 [c,i,j] | 08:00:14 | 10:17:59 | 0/12 | 0 |
| Mar. 02 [c,i] | 07:49:06 | 08:18:54 | 0/3 | 0 |
| Mar. 11 [b,i] | 08:03:55 | 10:03:28 | 11/11 | 4400 |
| Mar. 12 [b,i] | 07:44:35 | 10:07:45 | 13/13 | 5200 |
| Mar. 26 [c] | 06:43:05 | 09:58:12 | 8/11 | 4800 |
| Mar. 27 [c] | 06:32:50 | 10:04:12 | 8/18 | 3200 |
| Apr. 02 [d,i,k] | 06:31:39 | 09:53:52 | 16/18 | 6400 |
| Apr. 03 [d,i,k] | 06:20:46 | 09:45:02 | 18/18 | 7200 |
| Apr. 04 [d,i] | 05:58:19 | 09:47:58 | 21/21 | 8400 |
| Apr. 06 [e] | 07:51:42 | 08:43:15 | 5/5 | 2000 |
| June 09 [f] | 04:48:49 | 09:51:47 | 14/14 | 5600 |
| June 10 [f] | 04:54:21 | 09:49:49 | 5/5 | 2000 |
| Aug. 25 [g] | 23:57:46 | 04:34:49 | 4/4 | 1600 |
| Sept. 07 [h] | 00:11:08 | 04:20:07 | 2/2 | 800 |

**Notes:** [(a)] Each exposure has a duration of 400 s except for the Mar. 26 which has exposures of 600 s; [(b)] ESO program 092.B-0920(A) (PI: N. Grosso); [(c)] 091.B-0183(H) (PI: A. Eckart); [(d)] 093.B-0932(A) (PI: N. Grosso); [(e)] 093.B-0092(A) (PI: A. Eckart); [(f)] 093.B-0092(E) (PI: A. Eckart); [(g)] 093.B-0092(G) (PI: A. Eckart); [(h)] 093.B-0092(F) (PI: A. Eckart); [(i)] Also used during the 2014 Feb.–Apr. campaign for the study of the Sgr A* activity (Sect. 5); [(j)] Partially-simultaneous observation with XMM-Newton; [(k)] Simultaneous observation with XMM-Newton.

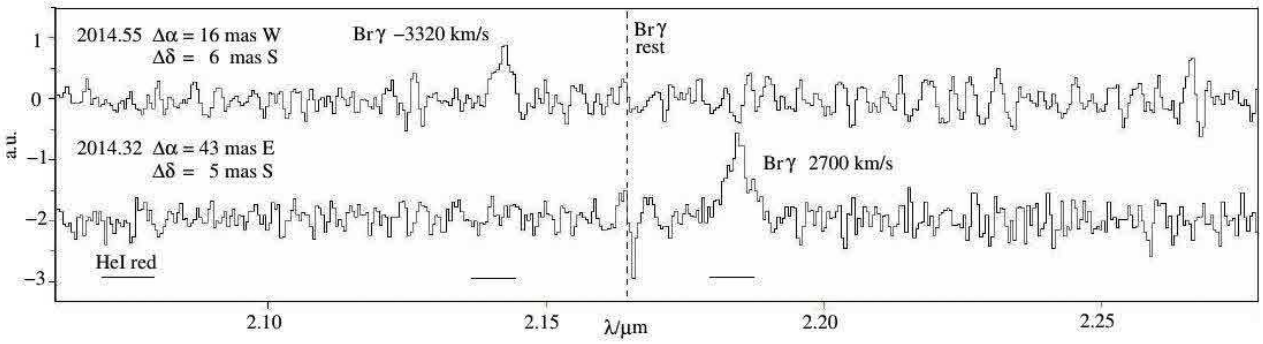


Figure 5.2: The spectra of the G2 object before the pericenter passage (2014 April; lower spectrum) and after the pericenter passage (2014 June; upper spectrum) (Valencia-S. et al. 2015). The spectra are smoothed with a Gaussian of a *FWHM* of 10 spectral resolution elements. The horizontal lines are the ranges where the emission line is detectable.

After 2014 June, a blueshifted Br$\gamma$ emission is detected with a signal-to-noise ratio of 2.5–3.1, a velocity of $-3320 \pm 60\,\mathrm{km\,s^{-1}}$, a *FWHM* of $210 \pm 1400\,\mathrm{km\,s^{-1}}$ and a luminosity of $0.4 \times 10^{-3}\,L_{\odot}$. The emission of the blueshifted Br$\gamma$ line is located at 16 mas west of Sgr A*. No redshifted emission is detected implying that the entire DSO/G2 passed the pericenter between 2014.32 and 2014.55. The spectra extracted before and after the pericenter passage are shown in Fig. 5.2.

Maps of the Br$\gamma$ emission are made before and after the pericenter passage showing that the source of emission remains compact with a size of 15 mas corresponding to 120 au for a Galactic Center distance of 8 kpc.

Using our VLT/SINFONI observations combined with the archived VLT data, the published Keck data (Meyer et al. 2014) and the Br$\gamma$ line velocities measured before and after the pericenter passage, we update the orbital parameters of the DSO/G2 as following: an ellipticity of $e = 0.976 \pm 0.001$, a half-axis length of $33.0 \pm 0.3$ Mpc, an ascending node of $76° \pm 8°$, an argument of the periapsis of $94° \pm 8°$, an inclination of

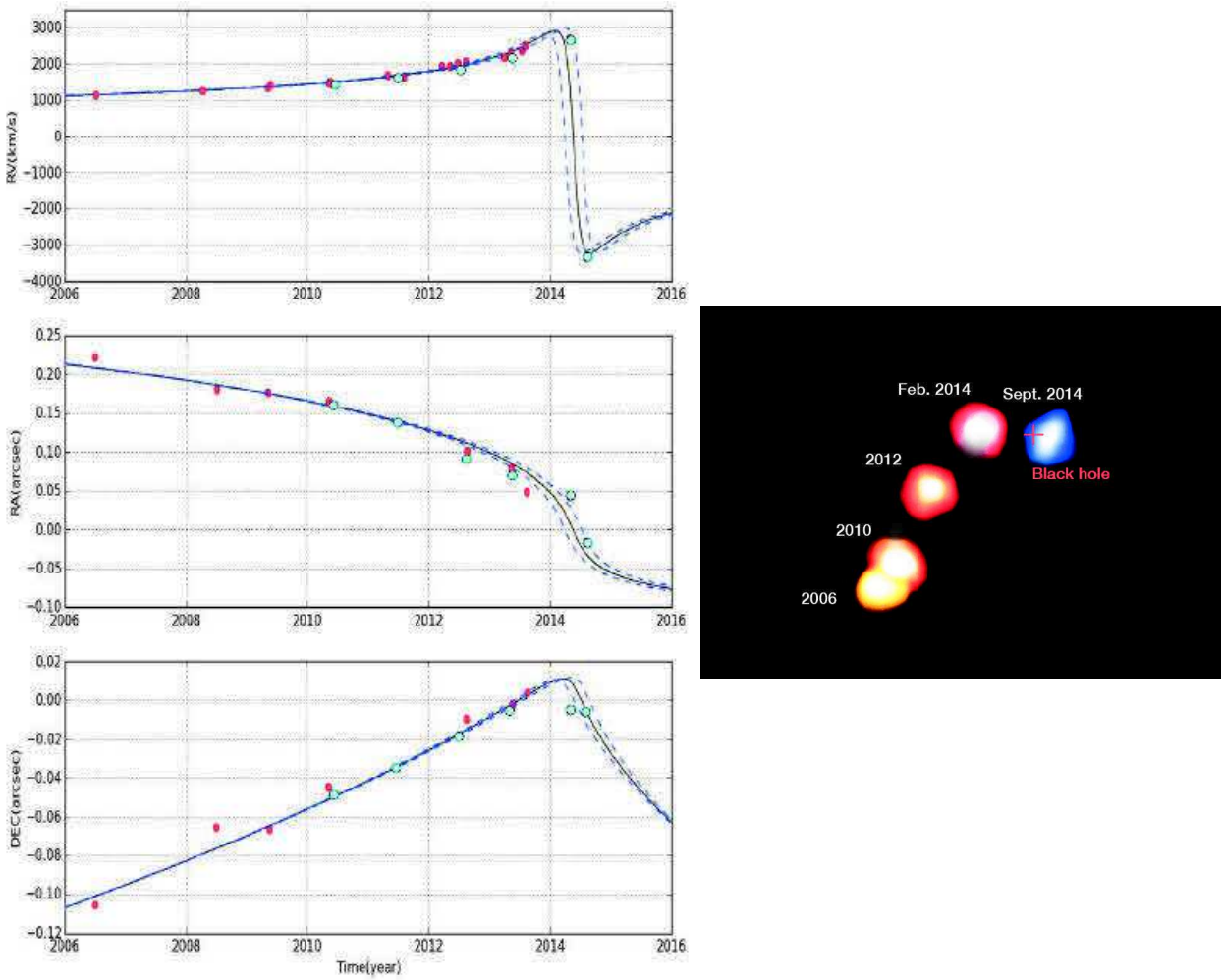


Figure 5.3: *Left panels:* The best fitted orbit of the DSO/G2 (Valencia-S. et al. 2015). From the top to bottom panels: radial velocity of the DSO/G2 and offsets from Sgr A* on the sky. *Right panel:* VLT image of the motion of the DSO/G2 from 2006 to 2014 (ESO press release eso1512 on 2015 march 26; credit: ESO, A. Eckart). The color represents the shift of the Br$\gamma$ line.

113° ± 1°, a period of 262 ± 38 yr and a pericenter passage at 2014.29 ± 0.14 corresponding to 2014 Apr. 20 (2014 Mar. 1–2014 Jun. 10) at a distance of 163 au (2032 $R_s$). This orbit and the DSO/G2 VLT's images from 2006 to 2014 are shown in Fig. 5.3.

Several results from these observations allow us to reject the purely gas cloud model:

- The absence of blueshifted and redshifted Br$\gamma$ emission before and after the pericenter passage, respectively. A purely gas cloud would be stretched near the pericenter leading the head of the cloud passing the pericenter before the tail. This also rules out the double feature observed in the velocity-position diagrams of Gillessen et al. (2013b) and Pfuhl et al. (2015).

- The compactness of the source during the pericenter passage to a size lower than 20 mas while a gas cloud model predict a size of 210–336 mas close to the pericenter passage.

- The predicted *FWHM* and the amplitude of the Br$\gamma$ line during the pericenter passage of a gas cloud are larger than those observed in our spectrum.

- Pfuhl et al. (2015) speculated that, for the gas cloud model, the G2 must have been formed between 1990 and 2000 in the mini-spiral. However, no special event have been observed in NIR or MIR in this region at these dates.

The DSO/G2 is thus considered as a pre-main sequence star with an accretion disk. We test the axisymmetric magnetospheric accretion model (see for a review Bouvier et al. 2007; see Fig. 5.4) for the emission

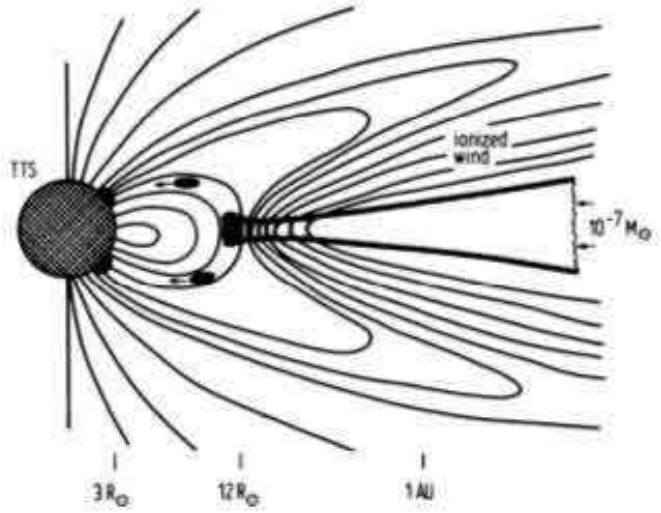


Figure 5.4: Sketch of the axisymmetric magnetospheric accretion model for a T Tauri star (Camenzind 1990). The lines are the magnetic field lines from the T Tauri star (TTS). The accretion disk of the star is represented with a thick line.

of the Br$\gamma$ line. Below the truncation radius of the accretion disk by the stellar magnetosphere, the accreted matter is driven ballistically along the closed stellar magnetic field lines towards the stellar photosphere. This forms an accretion shock close to the stellar photosphere producing emission lines such as H$\alpha$, Br$\gamma$,... Above the truncation radius, the open magnetic field lines may create winds from the accretion disk. The accretion rate, correlated to the Br$\gamma$ luminosity, is estimated to be less than $10^{-7}\,M_\odot\,\mathrm{yr}^{-1}$ while the outflow is about 10% of the accretion rate. From this simple model, an intermediate-mass star of $6\,M_\odot$ is needed to explain the *FWHM* of the Br$\gamma$ line close to the pericenter passage but this would imply an emission larger than the upper limit of $10\,L_\odot$ provided by the measurements in the $M-$band (Eckart et al. 2013). The larger *FWHM* of the Br$\gamma$ line is thus explained by the stretching of the accretion disk of an 1–2 $M_\odot$ star leading to an increase of the accretion rate onto the T Tauri star.

In this pre-main sequence star model, the matter from the accretion disk of the star is contained in the Roche lobe of the star. As the DSO/G2 approaches the SMBH, the Lagrange point between the star and Sgr A* gets closer to the star (1 au for a $1\,M_\odot$ star at the pericenter distance) and a part of the matter from the accretion disk of the star may be transferred to Sgr A* (Eckart et al. 2013). The NIR observations of Sgr A* during this campaign do not show any increase of the NIR flaring activity from Sgr A*. Therefore, the accretion of the DSO/G2 matter onto Sgr A* may still be upcoming. The absence of bow shock in the hot accretion flow of Sgr A* compared to those observed for the more distant X3 and X7 sources may be explained by the inhomogeneities in the hot accretion flow of Sgr A*.

## 5.2 The multiwavelength flaring activity from Sgr A*

### 5.2.1 Observations and data analysis

#### 5.2.1.1 X-ray data

The four XMM-Newton observations, whose total effective exposure is about 256 ks, are reduced using the SAS package version 13.5 and the 2014 Apr. 4 release of the Current Calibration files as explained in Sect. 3.1. During the last observation on 2014 April 3, MOS1 and MOS2 observed in small window requiring a bkg extraction region on the adjacent CCD at 7′ east of Sgr A*.

The X-ray light curves observed by XMM-Newton during the 2014 Feb.–Apr. campaign are shown in Fig. 5.5. The determination of the X-ray non-flaring level and the detection of the X-ray flares were made using the two-steps Bayesian algorithm presented in Sect. 3.4. The non-flaring levels on Feb. 28, Mar. 10, and Apr. 2 and 3 are $0.562 \pm 0.003$, $0.528 \pm 0.004$, $0.489 \pm 0.003$ and $0.499 \pm 0.002$ EPIC count $\mathrm{s}^{-1}$, respectively, which is about 2.5 times larger than those observed during the 2011 campaign (see Fig. 4.1) due to the contamination by the Galactic Center magnetar SGR J1745-29 (Sect. 1.5). Two X-ray flares are detected: one on 2014

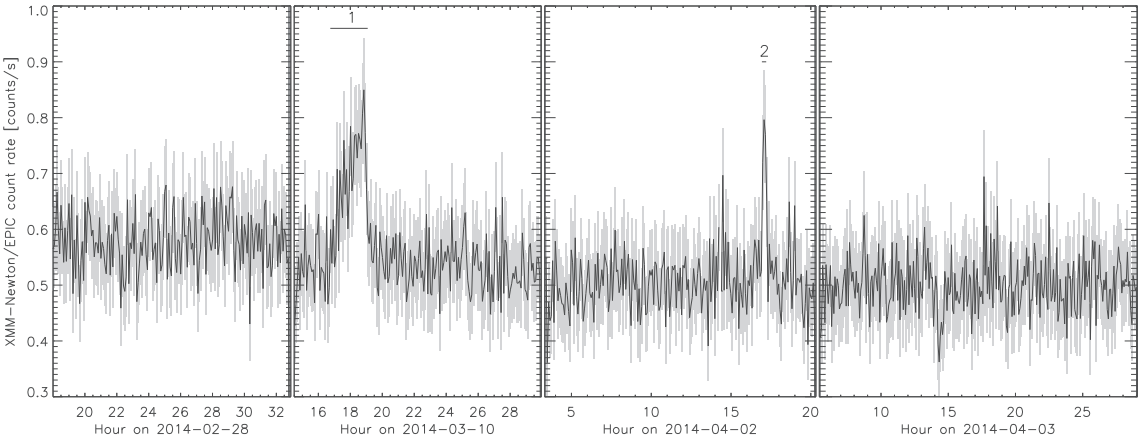


Figure 5.5: XMM-Newton/EPIC (pn+MOS1+MOS2) light curves of Sgr A* in the 2–10 keV energy range obtained in 2014 Feb.–Apr. (Mossoux et al. 2016). The time interval used to bin the light curve is 300 s. The X-ray flares are labeled with Arabic numerals. The horizontal lines below these labels indicate the flare durations.

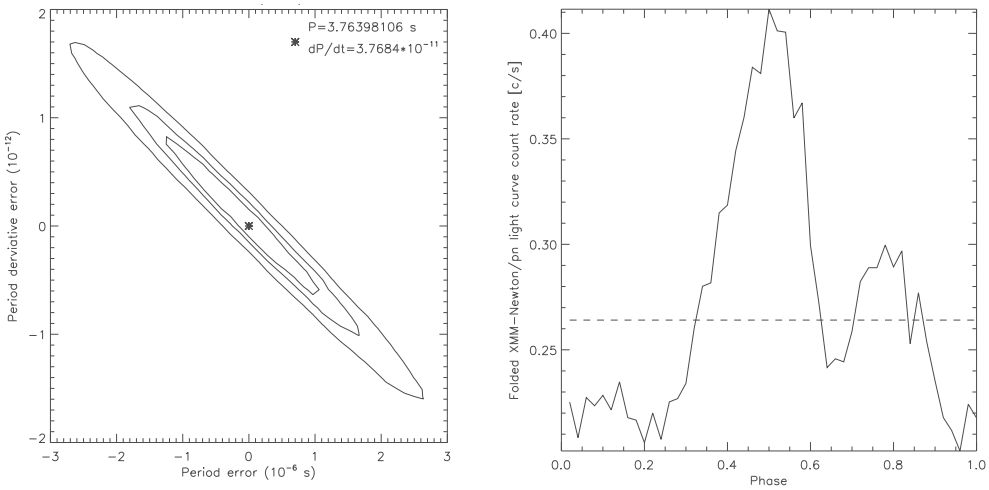


Figure 5.6: *Left panel:* $\chi^2$ distribution of the period and period derivative of the magnetar (Mossoux et al. 2016). The contours are the 68%, 90% and 99% of confidence level on the parameters. *Right panel:* Folded light curve between 2 and 10 keV on the 2014 Feb.–Apr. XMM-Newton observations with the best fit parameters (see Table 1.2).

Table 5.2: Characteristics of the X-ray flares observed by XMM-Newton in 2014 Feb.–Apr. after removing the magnetar contribution (Mossoux et al. 2016).

| Flare (#) | Instrument | Date (yy-mm-dd) | Start Time[a] (hh:mm:ss) | End Time[a] (hh:mm:ss) | Duration (s) | Total[b] (cts) | Peak[c] (count $s^{-1}$) |
|---|---|---|---|---|---|---|---|
| 1 | pn | 2014-03-10 | 16:44:48 | 19:05:07 | 8418 | 900 ± 60 | 0.159 ± 0.032 |
| – | MOS1 | ———— | 17:05:14 | 18:56:59 | 6705 | 780 ± 28 | 0.06 ± 0.02 |
| – | MOS2 | ———— | 17:33:32 | 19:01:11 | 5258 | 880 ± 30 | 0.07 ± 0.02 |
| 2 | pn | 2014-04-02 | 16:52:38 | 17:08:42 | 965 | 180 ± 12 | 0.252 ± 0.058 |
| – | MOS1 | ———— | ..... | ..... | ..... | ..... | ..... |
| – | MOS2 | ———— | ..... | ..... | ..... | ..... | ..... |

**Notes:** [(a)] Start and end times (UT) of the flare time interval defined by the Bayesian-blocks algorithm (Scargle et al. 2013b); [(b)] Total counts in the 2–10 keV energy band obtained in the smoothed light curve during the flare interval (determined by the Bayesian blocks) after subtraction of the non-flaring level obtained with the Bayesian-blocks algorithm; [(c)] Count rate in the 2–10 keV energy band at the flare peak (smoothed light curves) after subtraction of the non-flaring level.

Mar. 10 (flare 1) and one on 2014 Apr. 2 (flare 2).

As discussed in Sect. 3.4.4, any artificial increase of the non-flaring level leads to a decay of the detection efficiency of the two-steps Bayesian blocks algorithm for the faintest and shortest flares. I thus filter out the pulse phase of the magnetar to decrease the contamination level and hence increase the flares detection efficiency. I first construct the light curves from the events observed by XMM-Newton during this campaign and extracted in a 10″-radius region centered in the magnetar position. The best values of rotational period $P$ and spin-down $\dot{P}$ of the SGR J1745-29 are those which maximize the pulse shape in the magnetar EPIC/pn folded light curves. I thus apply a $\chi^2$ fitting of a constant light curve on the folded light curves and search for the values of $P$ and $\dot{P}$ maximizing the $\chi^2$. The best-fitting values and their confidence contours are show in Fig. 5.6 (left panel). The resulting folded light curve is shown in the right panel of Fig. 5.6. The pulse shapes are similar to those represented in the panel on row 4 and column 3 of Fig. 1.12 which were computed for a close epoch: the pulses amplitude ratio and phase delay are comparable. I then compute the count rate threshold on the folded light curve which removes 50% of the magnetar flux. Using the rotational period and spin-down, I create a new GTI file containing only the time ranges where the magnetar contribution is lower than the count rate threshold. I then apply the two-steps Bayesian algorithm on the filtered event lists of Sgr A*, but no more flares are found.

The characteristics of the two X-ray flares are reported in Table 5.2. The 2014 March 10 flare is described by two blocks in the EPIC/pn light curve but only with one block in MOS1 and MOS2 while the 2014 April 2 flare is only detected in EPIC/pn. The differences in the flare detection are due to the lower efficiency of the MOS cameras.

The flare 1 is one of the longest X-ray flare ever observed. Only two other flares were observed with a larger duration: the flare observed by Baganoff et al. (2001) on 2000 Oct. 26 with a duration of about 10 ks and the 2012 July 21 flare observed during the *Chandra XVP* 2012 campaign (Neilsen et al. 2013) with a duration of 7.9 ks. Moreover, the flare 1 on 2014 March 10 has a very asymmetric shape described by a long rise (about 7600 s) and a rapid decay (about 800 s).

The good PSF sampling of the MOS cameras allows us to confirm Sgr A* as the source of the 2014 March 10 flare and not the magnetar. We select the single events (`pattern=0`) since they have a better position determination and reject only the bad columns and pixels (`#XMMEA_EM`). The pixel randomization is suppressed and the position of the filtered events are associated to the center of the pixel where it was recorded with the detector sampling of 1.″1 × 1.″1 sky-pixels. We then construct two sky images corresponding to the flaring and non-flaring periods for each MOS camera (see panels a–d of Fig. 5.7). A third sky image is created for each MOS camera as the difference between the flaring and non-flaring periods leading to a representation of the count excess during the flaring period (see panels e and f of Fig. 5.7). The Bayesian method of Kraft et al. (1991) then allows us to compute the significance of this count excess in each pixel of the images assuming a Poisson statistic. The panels g and h of Fig. 5.7 show that the count-weighted barycenter of the most significant count excesses ($\geq 3\sigma$; diamonds in Fig. 5.7) is consistent with the position of Sgr A*.

For the spectral study of these two X-ray flares, I group the X-ray flaring spectrum from 2 keV with a minimum signal-to-noise ratio of 4 and 3 for the flares 1 and 2, respectively. I then fit the grouped spectrum with an absorbed powerlaw model (Sect. 3.6.2) using the MCMC method (Sect. 3.6.4) with 30 walkers and XSPEC (version 12.8.1o). The MCMC parameters and the best-fitting parameters are reported in Table 5.3 and compared to the spectral parameter obtained with the two brightest X-ray flares observed with XMM-Newton (Porquet et al. 2003, 2008; Nowak et al. 2012). The triangle plot of the resulting MCMC is shown in Fig. 5.8.

The poor constraints on the hydrogen column density is likely due to the contamination by the soft spectrum of the Galactic Center magnetar which increases the background noise in the soft spectral range.

#### 5.2.1.2 Near-infrared data

The four HST visits consist of 7, 7, 10 and 4 consecutive orbits composed by 45.5 min-exposures on Sgr A* followed by 44.5 min-occultation of Sgr A* by the Earth. We used the medium-bandwidth ($\Delta\lambda = 0.683\,\mu$m) F153M filter having an effective wavelength $\lambda_{\rm eff} = 1.532\,\mu$m (from the Spanish Virtual Observatory[1]). A 4-point dither pattern centered on Sgr A* with a spacing of 0.″6 (4 detector pixels) was used to improve the PSF sampling to $FWHM = 0.''145$ (1.136 detector pixels) at $1.50\,\mu$m. We use the predefined

[1]The website of the Spanish Virtual Observatory is: http://svo.cab.inta-csic.es/main/index.php

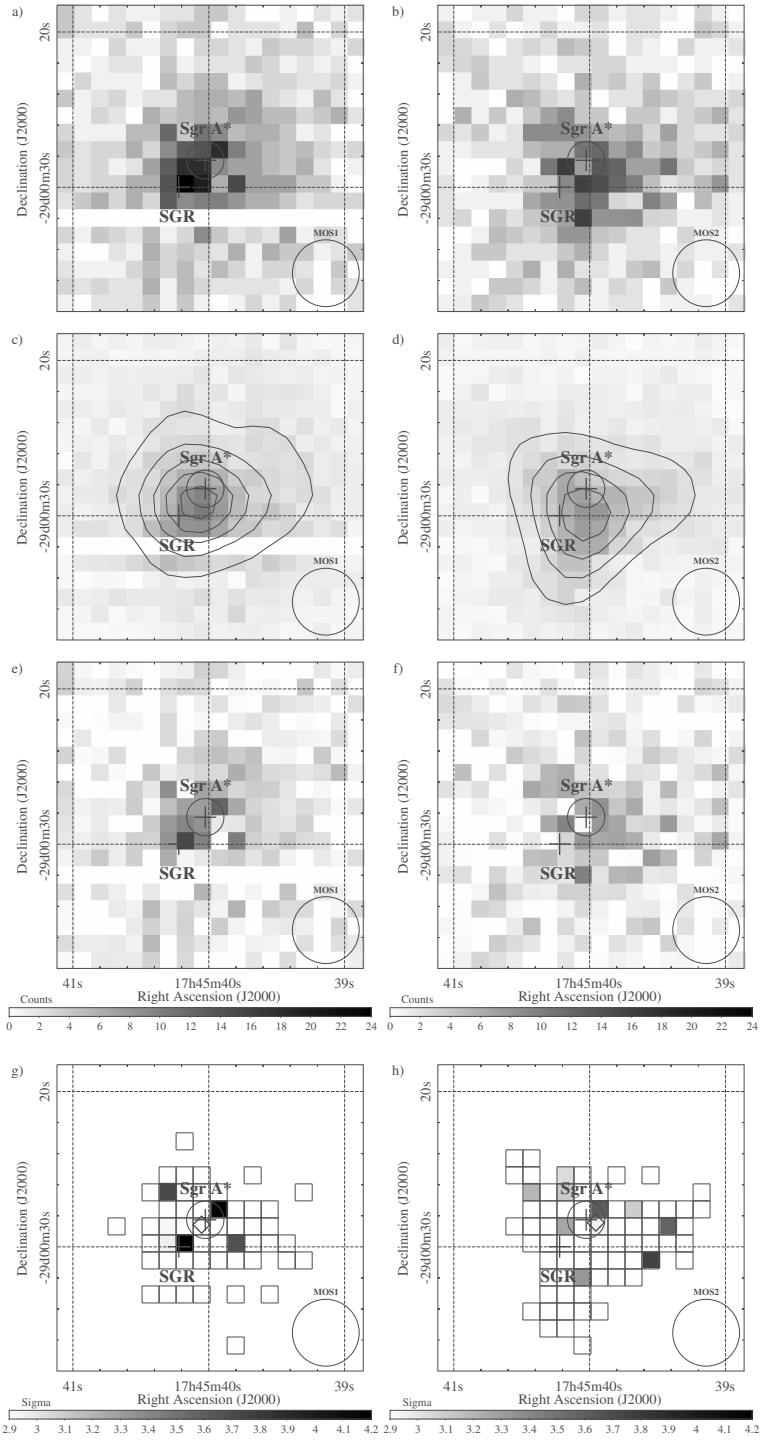


Figure 5.7: XMM-Newton/MOS1 (left column) and MOS2 (right column) images of Sgr A* on 2014 Mar. 10 (Mossoux et al. 2016). The energy range is 2–10 keV. The field of view is 20′′ × 20′′, the pixel size is 1.″1 × 1.″1. The same linear color-scale is used for Fig. a–f and Fig. g–h. In all panels, the black circle in the right-bottom corner is the instrument angular-resolution (*FWHM*); the crosses are the positions of SGR J1745-29 (Bower et al. 2015) and Sgr A* (Petrov et al. 2011), surrounded by a circle giving the absolute-astrometry uncertainty of EPIC ($1\sigma$ = 1.″2; Guainazzi 2013). *Panels a and b:* count numbers observed during the flaring period. *Panels c and d:* count numbers observed during the non-flaring period scaled-down to the flaring-period exposure. The contour map shows count numbers smoothed on four pixels with a Gaussian, starting from 2 counts with step of 1 count. *Panels e and f:* count excesses during the flaring period. *Panels g and h:* statistically significant count excesses ($\geq 3\sigma$; computed on the boxed-pixel area with the Bayesian method of Kraft et al. 1991), the diamond is the corresponding count-weighted barycenter of these detections.

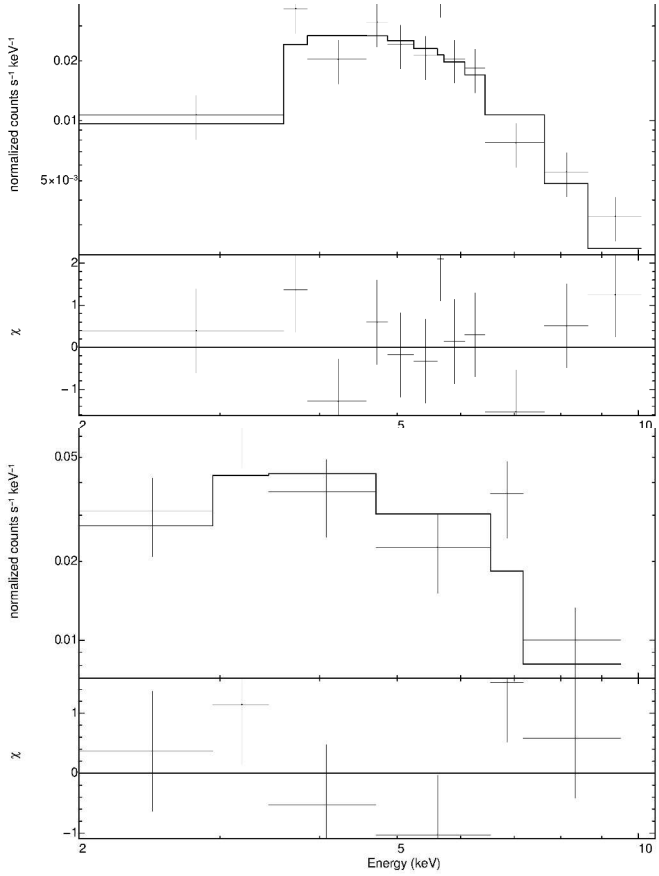


Figure 5.8: Best-fit spectral parameters of the 2014 Mar. 10 (*top*) and 2014 Apr. 2 (*bottom*) flares (Mossoux et al. 2016). The diagonal plots are the marginal density distribution of each parameter. The median values of each parameter are represented by the vertical dot-dashed lines in diagonal plots and by a cross in other panels; the vertical dashed lines define the 90% confidence interval (see Table 5.3 for the exact values). The contours are 68%, 90% and 99% of confidence levels.

Table 5.3: Spectral properties of the X-ray flares observed by XMM-Newton in 2014 Feb.–Apr. (adapted from Mossoux et al. 2016).

| Flare day (yy-mm-dd) | $N_H$ [a] ($10^{22}$ cm$^{-2}$) | $\Gamma$ [b] | $F^{unabs}_{2-10keV}$ [c] ($10^{-12}$ erg s$^{-1}$ cm$^{-2}$) | $L^{unabs}_{2-10keV}$ [d] ($10^{34}$ erg s$^{-1}$) | $\chi^2_{red}$ [g] | $\tau_f$ | *nburn* | *nstep* | $a_f$ |
|---|---|---|---|---|---|---|---|---|---|
| 2014-03-10[e] | 23.7 (14.5–37.5) | 3.1 (2.1–4.5) | 10.1 (4.9–33.5) | 7.7 (3.7–25.6) | 1.65 | 5.1 | 102 | 3060 | 0.66 |
| 2014-04-02[e] | 9.8 (2.0–23.5) | 2.2 (0.7–4.7) | 6.3 (3.5–25.7) | 4.8 (2.7–19.7) | 1.72 | 5.3 | 106 | 3180 | 0.59 |
| 2002-10-03[f] | 16.1 (13.9–18) | 2.3 (2.0–2.6) | 26.0 (22.5–30.6) | 19.8 (17.1–23.3) | ..... | ... | ... | ..... | ..... |
| 2007-04-04[f] | 16.3 (13.7–19.3) | 2.4 (2.1–2.8) | 16.8 (13.8–21.4) | 12.8 (10.5–16.3) | ..... | ... | ... | ..... | ..... |

**Notes:** [(a)] Hydrogen column density; [(b)] Photon index of the power law; [(c)] Unabsorbed average flux between 2 and 10 keV; [(d)] Unabsorbed average luminosity between 2 and 10 keV assuming a distance of 8 kpc; [(e)] Spectral properties of the EPIC/pn spectrum computed using the MCMC method. The range given between parenthesis represents the 90% confidence interval; [(f)] Spectral properties of the EPIC (pn+MOS1+MOS2) spectrum of the two brightest flares observed with XMM-Newton (Porquet et al. 2003, 2008; Nowak et al. 2012); [(g)] Reduced $\chi^2$ for 3 degrees of freedom.

readout sequence "SPARS25" with NSAMP = 12 or 13 producing one first short (2.932 s) readout of the detector, which is discarded for the data analysis, followed by 12 or 13 non-destructive readouts every 25 s throughout the ≈ 46 min exposure. The photometry of Sgr A* is extracted in a 3-pixels (about 0.″4) diameter circular aperture centered on the radio position of the SMBH. The photometry correction factor for this aperture diameter is 1.414 whereas the extinction at $\lambda_{\rm eff}$ is 5.03 ± 0.20 mag leading to a correction factor of the flux density for the WFC3 F153M filter of 103.2 ± 19.0.

The NIR light curves of Sgr A* and the reference star are computed and the flux density is corrected using the two correction factors. The NIR flares are then detected using a $3\sigma$ limit on the HST light curve. Using a $1\sigma$-clipping method, I first compute a NIR non-flaring flux density of Sgr A* of 59.3 ± 0.7, 60.1 ± 0.9, 60.8 ± 1.1 and 60.3 ± 0.8 mJy for the four HST visits. The start and stop times of the NIR flares are then defined as the $1\sigma$ limit on the flux density whose maximum amplitude is larger than $3\sigma$. Three NIR flares are observed (see left panels of Fig 5.10): two on 2014 March 10 (flares I and II) and one on 2014 Apr. 2 (flare III).

The start and stop times of the NIR flare I are delayed by about 14 min before and after the beginning and end of its X-ray counterpart (flare 1), respectively. However, the time delay between the maximum of the NIR flare I and the X-ray flare 1 is about 26 – 74 min which is one of the longest time delay ever measured between the NIR and X-ray light curves.

The NIR flare II is less luminous than the flare I and has no detected X-ray counterpart.

We only observe the decay phase of the NIR flare III since the rise phase happens during the occultation of Sgr A* by the Earth. A small increase of the NIR flux is observed just before the occultation. This could be the beginning of the rise phase of the flare III. The start and stop times of this flare enclose the time range of the X-ray flare 2.

These NIR flares belong to the 8% of the brightest NIR flares observed with VLT/NACO (Witzel et al. 2012): the flares I and III are only three times fainter than the brightest flare detected with VLT/NACO while the flare II is seven times fainter than this event.

The VLT/SINFONI data reduction is the same that in Sect. 5.1. Sgr A* was observed in the $K_{\rm s}$-band implying an extinction of $A(K_{\rm s}) = 2.46 \pm 0.03$ mag (Schödel et al. 2010).

Two NIR flares are observed in the $K_{\rm s}$ band with VLT/SINFONI: one on 2014 Apr. 3 (flare IV) and one on Apr. 4 (flare V). These flares belong to the 4% of the brightest NIR flares observed with VLT/NACO: the flares IV and V are five and six times fainter than the brightest flares observed with VLT/NACO, respectively. None of them have a detected X-ray counterpart.

The high amplitude of the detected NIR flares compared to the flux density distribution previously observed (Witzel et al. 2012) is due to the higher detection threshold of the HST/WFC3 and VLT/SINFONI compared to VLT/NACO. Therefore, no increase of the NIR flaring activity from Sgr A* is observed between 2014 February and April.

#### 5.2.1.3 Millimeter and centimeter data

Sgr A* was also observed at 3.2 mm (95 GHz) with CARMA in its C-configuration.

The flux density of Sgr A* observed at 95 GHz (3.2 mm) with CARMA on 2014 Apr. 2 increases slowly during the overall observation time (see Fig. 5.9). A bump is observed around 11.3 h, i.e., before the beginning of the observations with HST and XMM-Newton on this date implying that the NIR/X-ray early counterpart of this flare can not be observed.

The flux density measured on 2014 Apr. 3 decreases slowly and two bumps are observed at 12.4 and 13.6 h. This respectively corresponds to a delay of 4.4 and 5.6 h with the VLT flare IV observed on the same day at 7.9 h. The time delay measurements made between the NIR/X-rays and the 0.85 or 1.3 mm flares lead to time delays ranging between 1.6 and 2.7 h (Yusef-Zadeh et al. 2006b; Marrone et al. 2008; Yusef-Zadeh et al. 2008, 2009). Only one measurement was made by Yusef-Zadeh et al. (2009) between X-rays and the 7 mm flare light curves leading to a time delay of about 5.3 h. Considering the expanding plasmon model, the time delay measured between the NIR and 3.2 mm flares must be intermediate between those measured at 0.85/1.3 mm and 7 mm. This rejects the second bump as the delayed emission of the NIR flare IV since its delay is too long.

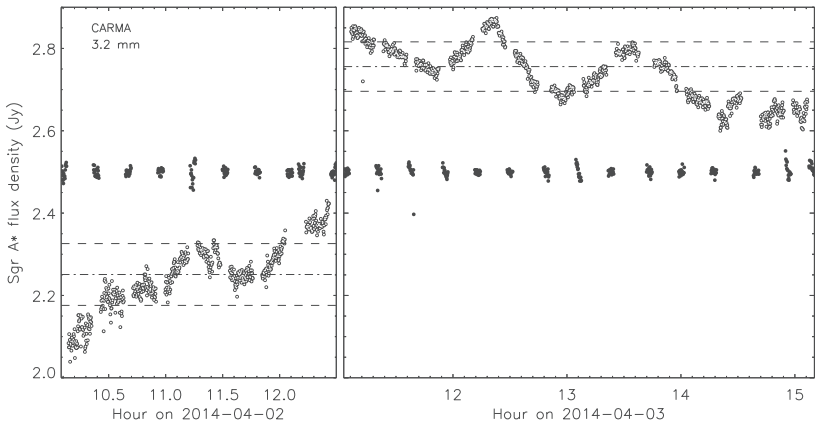


Figure 5.9: CARMA light curves at 3.2 mm (95 GHz) of Sgr A* (white filled circles) and the flux-density calibrator (black filled circles) in April 2014 (Mossoux et al. 2016). The dash-dotted line represents the mean flux density.

Sgr A* was observed at several frequency bands during the three observations with VLA in its A-configuration: the *X*−, *Ku*−, *C*−, and *L*−radio bands at 8.56, 13.37, 5.19 and 1.68 GHz.

The three VLA observations show a constant increase or decay of the flux density from Sgr A*. Only the 13.37 GHz (2.2 cm) light curve on 2014 Mar. 10 shows an obvious break in its rising flux density around $15.7 \pm 0.2$ h, with a clear increase of the rising slope. This could be the beginning of a radio flare. The break occurs before the beginning of the NIR flare I and X-ray flare 1 leading to a rejection of this radio flare as the counterpart of the observed NIR/X-ray flare. Therefore, the corresponding NIR/X-ray flare likely occurred before the beginning of the HST and XMM-Newton observations.

### 5.2.2 Constraints on the physical characteristics of the flaring region

During the 2014 Feb.–Apr. campaign, we thus observed two NIR/X-ray flares (flare I/1 and flare III/2) and three NIR flares without detected X-ray counterpart (flares II, IV and V). I now focus on each of the NIR flare to deduce the NIR–to–X-ray ratio which are needed to constrain the physical characteristics of the flaring regions.

#### 5.2.2.1 The sample of NIR flares and X-ray counterpart

***The NIR/X-ray flare I/1 on 2014 Mar. 10***

The NIR/X-ray flare I/1 on 2014 Mar. 10 is characterized by a long time delay between the flare maxima leading to a change in the NIR–to–X-ray flux ratio: between 16.5 h and 17.5 h, the NIR flux increases rapidly while the increase of the X-ray flux is slower leading to a NIR–to–X-ray flux ratio of about 0.1. Then, between 18 and 19 h, the NIR flux is fainter than during the previous orbit while the X-ray flux is still increasing leading to a NIR–to–X-ray flux ratio of about 0.01. Two interpretations could be tested to explain this change of NIR–to–X-ray flux ratio: first, the efficiency of the radiation mechanism changes between 17.5 h and 18 h to create more X-ray photons; second, the NIR/X-ray flare I/1 on 2014 Mar. 10 is composed by two close flares, produced by their own electron population.

For the first interpretation, three radiation mechanisms evolve to create the NIR and X-ray photons: the synchrotron–inverse Compton (SYN-IC), synchrotron–synchrotron (SYN-SYN) and synchrotron–synchrotron self-Compton (SYN-SSC) processes (see Annexe A for more details on these radiative processes). Yusef-Zadeh et al. (2012) found a parabolic trend between the NIR–to–X-ray amplitude ratio and the time delays between the maximum of the flares for the SYN-IC process upscattering the NIR photons on the thermal electrons in the hot accretion flow. However, considering the time delay between the maximum of the NIR and X-ray flares on 2014 March 10 of about 26 – 74 min, the theoretical NIR–to–X-ray amplitude ratio must be higher than $100\,\mathrm{mJy}/10^{35}\,\mathrm{erg\,s^{-1}}$ which is much larger than the observed NIR–to–X-ray amplitude ratio of $2.5 - 40\,\mathrm{mJy}/10^{35}\,\mathrm{erg\,s^{-1}}$. This process is thus likely excluded. The SYN-IC producing the X-ray photons by upscattering of the sub-millimeter photons from the hot accretion flow on the accelerated electrons producing the NIR photons is also rejected since the increase of the X-ray flux after 18 h would be due to a large increase

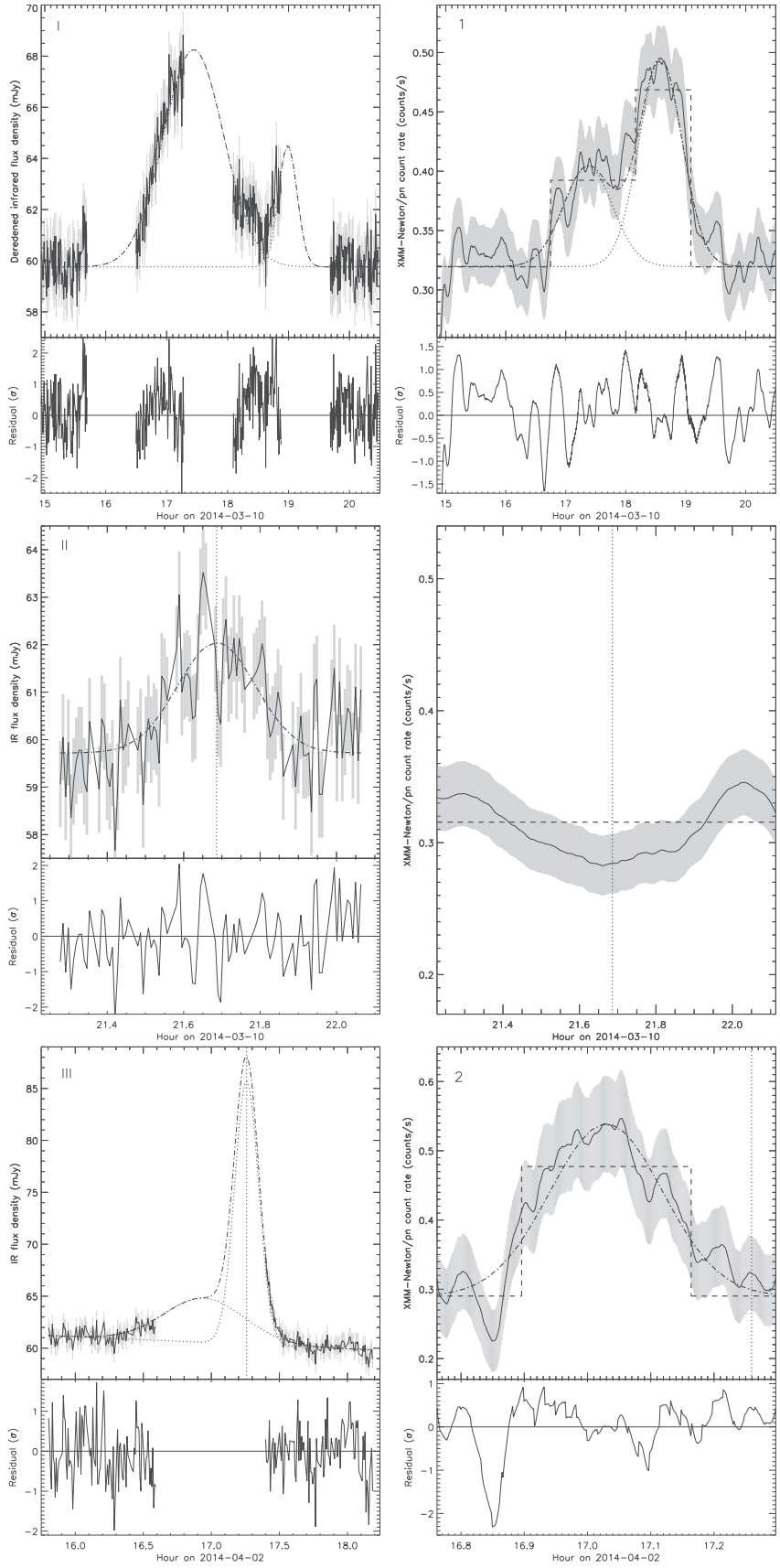


Figure 5.10: Light curve fitting of the HST NIR flares (left panels) and the X-ray (right panels) counterparts (Mossoux et al. 2016). The solid lines are the observed light curves with the error bars in gray. The dashed lines in right panels are the Bayesian blocks. The X-ray light curves are smoothed with a window width of 500 s and 100 s for 2014 Mar. 10 and Apr. 2, respectively. The dotted lines are the individual Gaussians and the dot-dashed line is the sum of the Gaussians. The vertical dotted lines are the time of the NIR flare peak when there is no detected X-ray counterpart. The residuals are in units of $\sigma$.

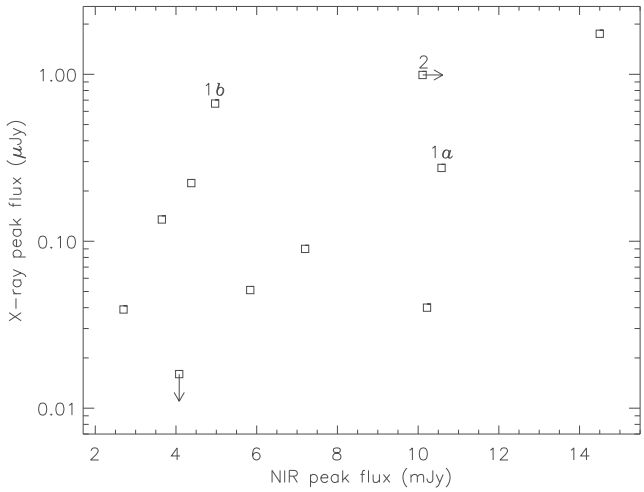


Figure 5.11: NIR-to-X-ray peak ratio vs. amplitude of the NIR flares in the $K_s$-band. Squares refer to the flares reported in Table 3 of Eckart et al. (2012). Triangles are the simultaneous NIR/X-ray flares detected on 2007 Apr. 4 and labeled *D* and *E* in Table 2 of Trap et al. (2011). Diamonds are the delayed flares of 2004 Jul. 7, 2008 Jul. 26+27 and 2008 May 5 reported in Table 2 of Yusef-Zadeh et al. (2012). The labeled points are the NIR and X-ray flares observed during this campaign.

of the sub-millimeter flux during the decay of the number of the accelerated electron explaining the decay of the NIR flux. This interpretation is thus very fine tuned. The decay of the NIR–to–X-ray flux ratio after 18 h could be explained by the SYN-SYN mechanism considering a cooling break frequency between the NIR and X-rays in the synchrotron spectrum (Dodds-Eden et al. 2009). Considering that the acceleration mechanism becomes more efficient between 18 and 19 h, more electrons from the tail of the powerlaw distribution are accelerated producing an increase of the X-ray photons production. For the SYN-SSC mechanism, the efficiency of the X-ray photons creation compared to those of the NIR photons depends on the size of the flaring source region as $R^{-\beta}$ with $\beta \equiv (8\alpha^2 + 28.392\alpha + 22.99)/(2\alpha + 5)$ with $\alpha$ the synchrotron index ($S_\nu \propto \nu^{-\alpha}$) (see for detailed computations Annexe B on p. 104 of this Ph.D. thesis). Since $\alpha$ must be positive implying $\beta > 5.4$, the increase the efficiency of the X-ray photons production by a factor of ten leads to an adiabatic decay of the radius by a factor of about 0.6 in 1.2 h. The adiabatic compression of a plasmon could occur when the plasmon goes through a bottle-neck configuration of the magnetic field. This model is preferred since it is less fine tuning than the two last radiative processes.

For the second interpretation, the NIR/X-ray flare I/1 on 2014 Mar. 10 is decomposed in two close flares (called Ia/1a and Ib/1b), each of them being produced by its own population of accelerated electrons. The HST and smoothed EPIC/pn light curves are thus fitted with two Gaussians (top panels of Fig. 5.10). The times of the NIR and X-ray maximum for each flare are now consistent with each other and the time delay between the maximum of the two flares is about 5000 s.

***The NIR/X-ray flare III/2 on 2014 Apr. 2***

The Gaussian fitting could also be applied on the HST and smoothed EPIC/pn light curves of the 2014 Apr. 2 flares. The EPIC/pn light curve is well fitted with a single Gaussian while the NIR light curve needs two Gaussians (IIIa and IIIb) to reproduce the small increase of flux at the end of the ninth HST orbit and the large flux decay at the beginning of the tenth HST orbit (see bottom left panel of Fig. 5.10). The first NIR Gaussian flare is thus simultaneous with the X-ray flare 2 while the luminous second NIR Gaussian flare has no detected X-ray counterpart (vertical dotted line in the bottom right panel of Fig. 5.10).

***The NIR flares II, IV, V without detected X-ray counterpart***

For the four NIR flares observed during the 2014 Feb.–Apr. campaign without detected X-ray counterpart, the Bayesian method of Kraft et al. (1991) allows me to determine the upper limit under a certain confidence limit (here 95%) on the amplitude of the undetected X-ray counterpart. An example of HST NIR light curve of the flare II without detected X-ray counterpart is shown in the middle panels of Fig. 5.10. I suppose that the peak of the NIR and X-ray flares are simultaneous. The time of the peak of the undetected X-ray flare is thus given

by the peak time of the Gaussian fit of the NIR flare (vertical dotted lines in Fig. 5.10). The non-flaring level at the time of the NIR maximum is given by the two-steps Bayesian blocks algorithm. For the X-ray counterpart of the NIR flare IIIb, the reference non-flaring level is given by the Gaussian fit of the X-ray flare 2 due to the short time separation between the peaks of these NIR flares. The upper limit is then computed using the posterior probability distribution function assuming a Poisson statistic.

#### 5.2.2.2 The characteristics of the flaring regions

The NIR–to–X-ray flux ratio of the overall detected NIR flares is represented as a function of the NIR amplitude in the $K_s$-band in Fig. 5.11 among the NIR/X-ray flares already observed (the amplitude of the NIR peaks are extrapolated in the $K_s$-band using the $H-L$ spectral index computed by Witzel et al. 2012). The NIR flares detected during the 2014 Feb.–Apr. campaign with an X-ray counterpart lie well within the NIR–to–X-ray flux ratio already observed. Most of the lower limit on the NIR–to–X-ray flux ratio also lie in the flux ratio range already observed. The NIR flare IIIb and its undetected X-ray counterpart is one of the brightest NIR flare ever observed and it has the largest NIR–to–X-ray flux ratio.

I use the formalism developed by Eckart et al. (2012) to constrain the physical parameters of the flaring region, i.e., the size of the emitting region ($\theta$), peak flux density at $\nu_m$ ($S_m$), number density of relativistic particles ($\rho$), and the magnetic field ($B$), from the NIR–to–X-ray flux ratio. I consider three local radiative processes involving only the electrons accelerated in the flaring region: the SYN-SYN, SSC-SSC and SYN-SSC radiation mechanisms. A radiative process is considered as dominant when the alternative emission processes are lower than 10%. The physical characteristics of the flaring region are computed for different frequencies at which the source becomes optically thin (i.e., the turnover frequency $\nu_m$) from 50 to 3000 GHz by step of 200 GHz. For the SYN-SYN and SSC-SSC cases, the synchrotron spectral index $\alpha$ is given by the NIR–to–X-ray flux ratio. For the SYN-SSC case, the spectral index in NIR does not depends on the X-ray flux. I thus use seven values of $\alpha$ from 0.3 to 1.5 by step of 0.2. The resulting physical parameters are reported in Fig. 5.12. The lower the NIR–to–X-ray flux ratio, the better constrained the physical parameters. The best constraints are thus given for the flare IIIa/2. Considering the SYN-SSC emission mechanism, the size of flaring region is $0.03-7\,R_s$ and the electron density is $10^{8.5}$–$10^{10.2}\,\mathrm{cm}^{-3}$ for a synchrotron spectral-index of $0.3-1.5$. The same method is applied using the NIR flares and the upper limit on the undetected X-ray counterpart but the physical parameters are less constrained (see Fig. 20 of Mossoux et al. 2016, p. 151 of this Ph.D. thesis).

The synchrotron–Inverse Compton emission is difficult to test since, as explained before, the relation between the NIR–to–X-ray flux ratio and the time delay between the maximum has a parabola trend. For the NIR–to–X-ray flux ratio measured for the detected NIR/X-ray flares, the predicted time delay is lower than 10 min which is below the error bars on the time of the maximum of the Gaussian fitting. The synchrotron–Inverse Compton emission is thus also a possible emission mechanism for producing X-ray flares from the NIR photons.

### 5.2.3 The observed X-ray flaring rate

The observed X-ray flaring rate (three flares during 255.644 ks) is compared to those derived during the 2012 *Chandra XVP* campaign using the Bayesian blocks algorithm for the flare detection, i.e., 1.5 flare per day (Neilsen et al. 2013). Assuming that we observe the same flare-amplitude and duration distribution during the same observational exposure than for the 2012 *Chandra XVP* campaign (2983.93 ks), the number of X-ray flares that we would observe above the non-flaring level of the 2014 Feb.–Apr. campaign is 36. This implies that 3.1 flares would have to be observe during the 255.644 ks of the 2014 Feb.–Apr. campaign. This number is consistent with the number of detected flare. I also test the null hypothesis that the flaring rate we would have to observe and the flaring rate we currently observe are the same assuming a Poisson process (Gehrels 1986; Fay 2010). The p-value for this null hypothesis is 1 implying that the flaring rate that we currently observe is consistent with those derived from the 2012 *Chandra XVP* campaign. No increase of the X-ray flaring activity is thus observed during the DSO/G2 pericenter passage.

This is well explained by the stellar nature of the DSO/G2. Indeed due to the gravitational attraction of the star, only a small part of the matter from the accretion disk of the star would have passed through the Lagrange point during the pericenter passage. Moreover, the radial transport of matter in an ADAF is characterized by

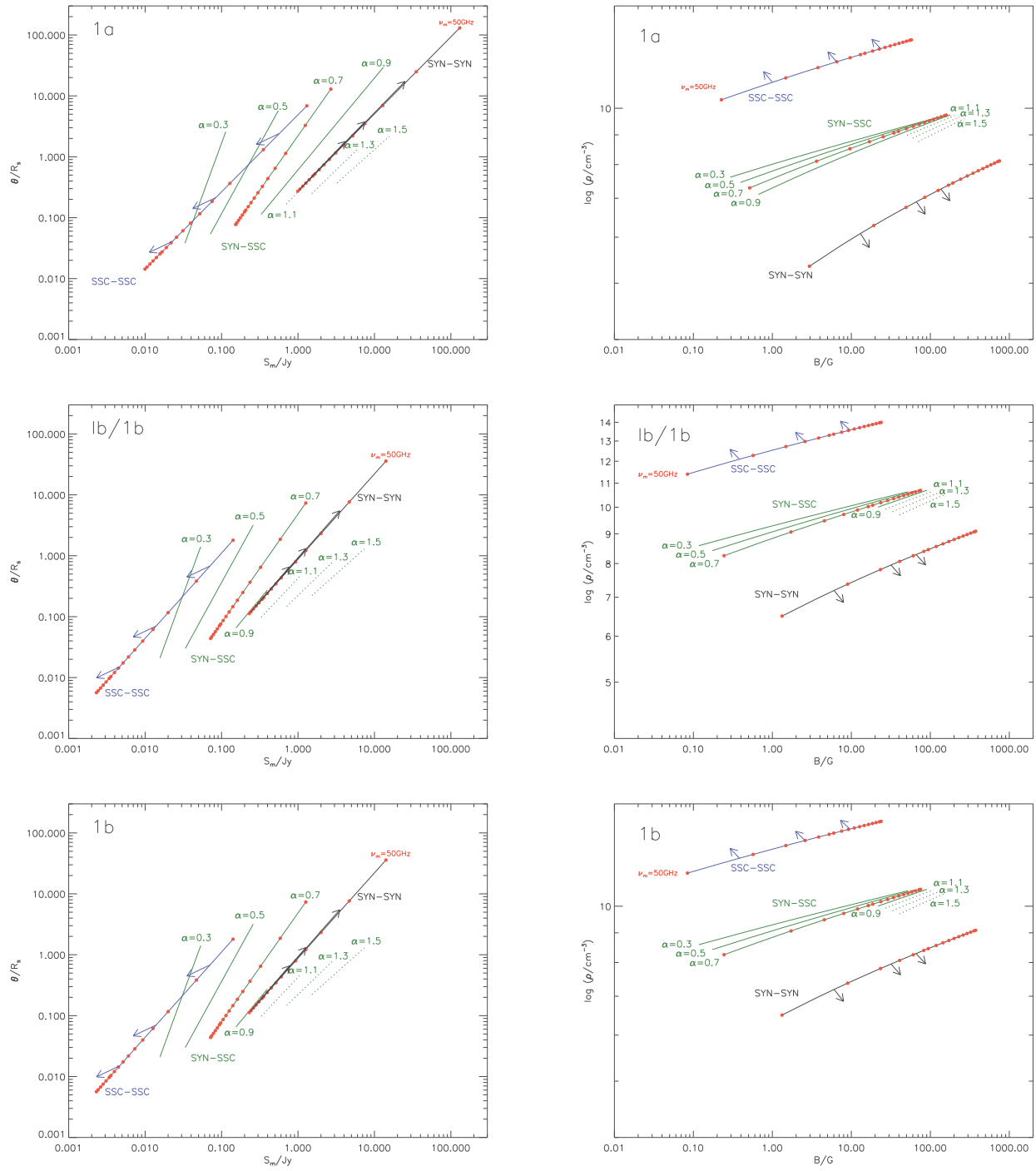


Figure 5.12: Physical parameters of the flares observed simultaneously in X-rays and NIR for the three emission models. The flare Ia/1a, Ib/1b and IIIa/2 are in the upper, middle and bottom panels, respectively. Left panels are the size of the flaring-source region ($\theta$) vs. the peak of the spectrum ($S_{\rm m}$) at the frequency $\nu_{\rm m}$. Right panels are the density of the relativistic electrons vs. the magnetic field. The locii where the Synchrotron Self-Compton−Synchrotron Self-Compton (SSC-SSC), Synchrotron−Synchrotron Self-Compton (SYN-SSC) and Synchrotron-Synchrotron (SYN-SYN) are dominant are shown in black, blue and green, respectively. The red dots represent the turnover frequencies from 50 to 3000 GHz by step of 200 GHz. The arrows show the direction of the curves if the limit on the alternative emission processes is lowered. Dotted lines are locii of SYN-SSC where the MIR emission is larger than the observed upper-limit value of 11.88 $\mu$m (Dodds-Eden et al. 2009).

the viscous timescale

$$\tau_{\rm visc} \sim 3.0 \left(\frac{r}{2000\,R_{\rm s}}\right)^{1.5} \left(\frac{\alpha}{0.1}\right)^{-1} \text{ yrs}\,. \tag{5.1}$$

with $\alpha = 0.1$ the efficiency of the mechanism of angular momentum transport introduced by Shakura & Sunyaev (1973) and $r = 2000\,R_{\rm s}$ the radial distance of the SMBH (Pfuhl et al. 2015; Valencia-S. et al. 2015) the pericenter distance. The accretion timescale with these parameters is thus about 3 years implying that we will not see any increase of the flaring activity before 2017. Moreover, the angular momentum of the matter from DSO/G2 on its eccentric orbit likely increases this estimation of the accretion timescale.

# Chapter 6

# The study of the X-ray flaring rate of Sgr A* from 1999 to 2015

Several statistical studies on the X-ray flaring rate of Sgr A* have been already made on large observational datasets. The first one was done by Neilsen et al. (2013) who used a Gaussian flare fitting on the binned X-ray light curves of Sgr A* obtained during the 2012 *Chandra XVP* campaign (3 Ms of a total exposure) to automatically detect the X-ray flares. They detected 39 X-ray flares leading to a flaring rate of $1.1^{+0.2}_{-0.1}$ flare per day but they were biased by their fitting model which supposes a Gaussian shape of the flare light curve with a minimum duration of 400 s. They also tested the Bayesian blocks method for the X-ray flare detection with a false positive rate for the flare detection of 0.1% which allowed them to detect 45 flares whose 34 were already found by their first method.

Then, Ponti et al. (2015) studied the X-ray flaring rate observed with XMM-Newton, Chandra et Swift between Sept. 1999 and Nov. 2014 with the Python Bayesian blocks algorithm. They observed an increase of the flaring rate by a factor of 9.3 for the most energetic flares (defined by an absorbed fluence larger than $5 \times 10^{-9}$ erg cm$^{-2}$ containing about 25% of the flares) starting on 2014 Oct. 30 until their last observations obtained with Swift in 2014 Nov. 2. However, the Python Bayesian blocks algorithm uses the geometric *prior* on the number of change points computed by Scargle et al. (2013a) which is not reliable for the study of the flaring rate since the flare arrival times are described by a Poissonnian flux (see Section 3.4.1); this likely leads to an inconsistency between their adopted value of the false positive rate for the change point detection (5%) and their resulting false detection probability.

Yuan & Wang (2016) also made statistical analysis of the flares observed by Chandra from 1999 to 2012. They detected the X-ray flares with a Gaussian light curve fitting directly on the event lists. The detection efficiency of their method was presented in their Fig. 3 as a function of the flare duration and fluence. Compared to this detection method, the Bayesian blocks method is more efficient for the detection of long flares and does not assume any flare shape. For the shortest and faintest flares, the method of Yuan & Wang (2016) detects more features than the Bayesian blocks method but they did not control their false positive rate.

At the time of writing this Chapter (June 2016), I have access to 392 ks of additional archival observations obtained in 2015 with XMM-Newton, Chandra and Swift. I also have access to the Swift observations obtained from 2016 Feb.–June but a new X-ray transient SWIFT J174540.7-290015 was detected at 16″ north of Sgr A* on 2016 Feb. 6 with a 2–10 keV flux of $1.0 \times 10^{-10}$ erg s$^{-1}$ (Reynolds et al. 2016). On 2016 May 28, a new X-ray transient SWIFT J174540.2-290037 was detected in the Swift observations at 10″ south of Sgr A* with an unabsorbed 2–10 keV flux of about $(7 \pm 2) \times 10^{-11}$ erg s$^{-1}$ cm$^{-2}$ (Degenaar et al. 2016). These two new transient sources having large observed X-ray flux (about six and four times larger than the burst flux of SGR J1745-29, respectively; see Sect. 1.5), they contaminate the Sgr A* light curves observed by Swift leading to a nearly impossible X-ray flare detection with Swift for the beginning of 2016 (see Table 6.1). In this Chapter, I thus use the 2015 observations with XMM-Newton, Chandra and Swift in addition to the 1999–2014 observations to investigate the significance and persistence of the high flaring rate argued by Ponti et al. (2015). I first reprocess the XMM-Newton, Chandra and Swift observations from 1999 to 2015 (Sect. 6.1) to detect the flares with the two-steps Bayesian blocks algorithm for XMM-Newton and Chandra and with the detection method of Degenaar et al. (2013) for Swift (Sect. 6.2). The unabsorbed X-ray fluxes of the detected flares are then computed with the same spectral parameters (Sect. 6.3) to construct the observed distribution of the mean unabsorbed flux and duration of the X-ray flares detected by XMM-Newton and

Chandra (Sect. 6.4.1). I then compute the detection efficiencies of the Bayesian blocks algorithm for each XMM-Newton and Chandra observation according to the observed non-flaring level (Sect. 6.4.2). I deduce the intrinsic distribution of X-ray flares fluxes and durations by correcting the observed distribution from the merged detection efficiency of Chandra and XMM-Newton (Sect. 6.4.3). This intrinsic distribution allows me to determine the detection biases in the XMM-Newton, Chandra and Swift observations. I finally apply the Bayesian blocks algorithm on the arrival times of the flares observed by XMM-Newton, Chandra and Swift to study the flaring rate corrected from these detection biases (Sect. 6.5).

## 6.1 Observations and data reduction

The observational data of XMM-Newton, Chandra and Swift are retrieved from the XMM-Newton Science Archive (XSA)[1], the Chandra Search and Retrieval interface (ChaSeR)[2] and the Swift Archive Download Portal[3]. For XMM-Newton and Chandra, I select the observations where Sgr A* was observed with an off-axis angle lower than 8′. For Swift, I take all the observations containing Sgr A* since I will correct for the effects of the off-axis angle during the data reduction. At the date of writing this Ph.D. thesis, three Chandra observations made in 2015 were not public.

### 6.1.1 XMM-Newton observations

XMM-Newton observed the Galactic Center 54 times from 2000 Sept. to 2015 Apr. with EPIC/pn, MOS1 and/or MOS2 for a total effective exposure of about 2.2 Ms. The observation starts and ends reported in Table C.1 of Appendix C in Universal Time (UT) correspond to the earliest GTI start and latest GTI stop of the three cameras. The duration of the observations is the sum of the Good Time intervals (GTI). Most of the observations were made with EPIC/pn, MOS1 and MOS2 in frame window mode with the medium filter. During the 2000 Sept. 21, 2001 Sept. 4 and 2004 Mar. 28 and 30 observations, EPIC/pn was in frame window extended mode leading to a lower time resolution (199.1 ms instead of 73.4 ms). During the 2014 Apr. 3 observation, EPIC/MOS1 and MOS2 observed in small window mode leading to a better time resolution but a smaller part of the central CCD observing. During the 2002 Feb. 26 and Oct. 3 observations, EPIC/pn observed with the thick filter while on 2008 Mar. 3 and Sept. 23, the three cameras observed with the thin filter.

I create the event lists for the MOS and pn cameras with the SAS version 14.0 and the Current Calibration files of 2015 June 13. For observations in frame window extended mode, the background region is a $\sim 3' \times \sim 3'$ region at about 4′ north of Sgr A*. For observations in small window mode, the background region is a $\sim 3' \times \sim 3'$ area at about 7′ east of Sgr A* (i.e., on the adjacent CCD).

### 6.1.2 Chandra observations

Chandra observed the Galactic Center 118 times from 1999 Sept. to 2015 May with the ACIS-I or ACIS-S cameras for a total effective exposure of about 5.7 Ms. The effective observation starts and ends reported in Table C.2 of Appendix C in UT correspond to the first GTI start and last GTI stop of the observation. The ACIS-S observations of the 2012 *XVP* campaign and the 2013 May 25, and June 6 and 9 were made with the High Energy Transmission Grating (HETG) which disperses the events on the detector. The ACIS-S observations on 2013 May 12, June 4 and after 2013 July 2 (except those on 2015 Apr. 25) were made with an 1/8 sub-array of 128 rows to decrease any pile-up by reducing the detector frame exposure. The other observations were made with ACIS-I.

I reprocess the data using the CIAO (version 4.7) script `chandra_repro` and the Calibration Database (CALDB; version 4.6.9) from the level 1 data. The `chandra_repro` script creates a bad pixel file, flags afterglow events and filters the event patterns, afterglow events and bad pixels. The bkg region is a 8.″2-radius circle at 0.′54 south of Sgr A* (Nowak et al. 2012). For observations without HETG, the src+bkg events are extracted from a 1.″25-radius disk centered on the radio position of Sgr A*. For observations with HETG, the diffraction order is determined with the CIAO task `tg_resolve_events`. I extract the zero-order events

[1] http://www.cosmos.esa.int/web/xmm-newton/xsa
[2] http://cda.harvard.edu/chaser
[3] http://www.swift.ac.uk/swift_portal

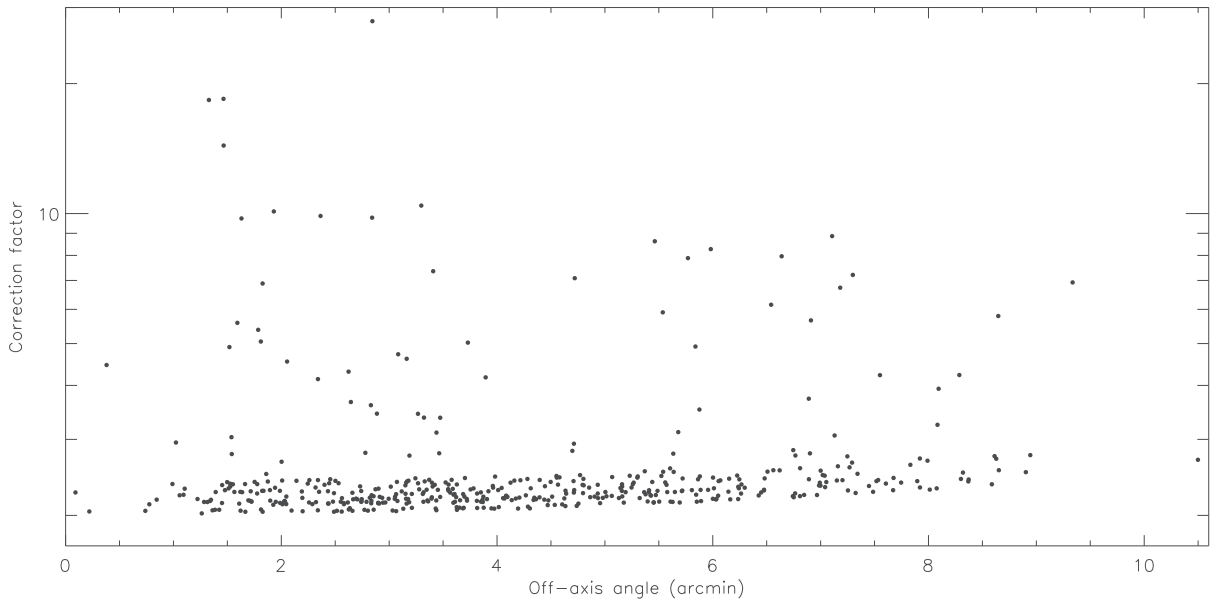


Figure 6.1: Total correction factor (bad pixels/columns, PSF extraction fraction and vignetting) for the Swift count rate of Sgr A* computed for all Swift observations of the Galactic Center from 2006 to 2015.

from the 1.″25-radius disk centered on Sgr A* and the ±1-order events from two wide rectangles of 2.″5 width centered on the Sgr A* position (Nowak et al. 2012; Neilsen et al. 2013). The position angles of the dispersed spectra are given in the region extension of the level 1 data event list.

### 6.1.3 Swift observations

Swift regularly observed the galactic center since 2006 with the XRT instrument (PI: N. Degenaar). The log of each yearly campaign is given in Table C.3 of Appendix C.

I reprocess the Swift observations made in photon counting mode from 2006 Feb. to 2015 Nov. (1.5 Ms exposure) from the level 1 data following the data reduction method of Degenaar et al. (2013, 2015). I use the HEASOFT task `XRTPIPELINE` (v0.13.1) and the calibration files released on 2014 June 12 to reject the hot and bad pixels and select the grades between 0 and 12. I then use the HEASOFT task `XSelect` (v2.4c) to extract events recorded in a disk of 10″-radius centered on the radio position of Sgr A*. Since Swift is on a low Earth orbit located below the radiation belts, the instrumental background caused by the flaring protons is negligible and I thus do not create a background extraction region.

To improve this data reduction, I correct the event losses caused by the bad pixels/columns, the PSF extraction fraction and the vignetting at 2.77 keV (the median energy observed by Swift in the 10″ extraction region) running the HEASOFT task `XRTLCCORR` (v0.3.8). This task computes the total correction factor which have to be applied on the light curve count rates for each 10 s time interval. Figure 6.1 shows the total correction factor computed for each Swift observation as a function of the off-axis angle of Sgr A*. It is different from one observation to an other, varying from about 2 to about 24, since the source position on the detector is not fixed, indeed the off-axis angle of Sgr A* can be as large as 10.′5. The correction factor is minimum on-axis with a slightly increasing trend with the off-axis angle because of the increase of the PSF width and the vignetting. The mean value of the correction factor is 2.8 but the correction factor can be as high as 24 when Sgr A* is located close to a bad column or pixel leading to a large standard deviation of the correction factor (2.1). The median value of the correction factor is 2.3 with the 5% and 95% percentiles of 2.1 and 2.4, respectively. Applying the correction factors on the count rates from Sgr A* leads to a higher non-flaring level compared to those computed in Degenaar et al. (2013): for the observations between 2006 and 2011, when there is no contamination by transient sources, I find an average count rate level of about $0.027 \pm 0.004$ counts $s^{-1}$ in the 2–10 keV energy band instead of $0.011 \pm 0.007$ counts $s^{-1}$. This increase of the corrected non-flaring level would lead to a decrease of the flare detection efficiency by the Bayesian blocks algorithm but the count rate standard deviation is 1.6 times lower than computed before since I correct the count rate bias due to the bad pixels/columns, the PSF extraction fraction and the vignetting.

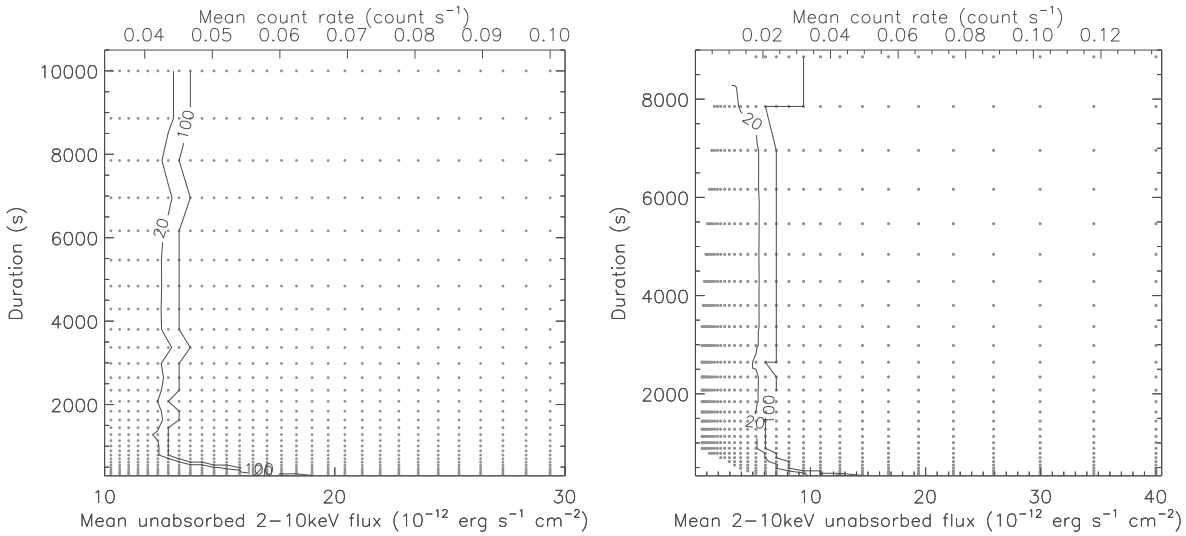


Figure 6.2: Flare detection efficiency of the Bayesian blocks algorithm (left panel) and the Degenaar et al. (2013)'s detection method (right panel) in the Swift observations. The points are the simulation grid for the Gaussian flare light curve above a non-flaring level of 0.027 counts s$^{-1}$ in the 2–10 keV energy range. The contour levels are the detection probabilities in percent.

Due to the low Earth orbit, the duration of the Swift observations are about 1 ks, which is short compared to the flare observed durations (from some hundred of seconds to more than 10 ks). I test the effect of this short exposure on the detection probability of the flares with the Bayesian blocks algorithm. I first simulate two non-flaring event lists with a typical exposure of 1 ks and a Poisson flux with a non-flaring level of 0.027 counts s$^{-1}$ in the 2–10 keV energy range. I then simulate a third event list with a Gaussian flare above this non-flaring level using for the sampling 30 mean count rates from 0.035 to 0.1 counts s$^{-1}$ and 30 durations from 300 s to 10 ks in logarithmic scale. I finally extract a time range of 1 ks from different part of the simulated flare (the center of the time range is defined to divide the flare duration in ten time ranges) to create a typical Swift event list of a flare. I apply the Bayesian block algorithm on the three concatenated event lists (non-flaring, flaring and non-flaring) and compute how many times the algorithm found two change points. The flares mean count rates are converted to mean unabsorbed fluxes using the averaged conversion factor between the mean count-rates and mean unabsorbed-flux in the 2–10 keV energy band of $293.5 \times 10^{-12}$ erg s$^{-1}$ cm$^{-2}$/count s$^{-1}$ computed for $N_{\rm H} = 14.3 \times 10^{22}$ cm$^{-2}$ and $\Gamma = 2$. The resulting detection probability, shown in the left panel of Fig. 6.2, has two different regimes with a small mean-unabsorbed-flux range where the detection probability jumps from 20% to 100%. For flare durations longer than 800 s, the X-ray flares are either nearly undetected (detection probability lower than 20%) or always detected with a mean unabsorbed flux limit of about 0.044 counts s$^{-1}$ (corresponding to $13.2 \times 10^{-12}$ erg s$^{-1}$ cm$^{-2}$). For flare durations shorter than 800 s, the flare detection efficiency decreases with the decay of the flare duration with a 100% detection probability at 0.044 counts s$^{-1}$ for a flare duration of 800 s and 0.065 counts s$^{-1}$ for a flare duration of 300 s. The Bayesian blocks algorithm is thus less efficient for observations with exposures shorter than the flare duration and detects only flares with a mean unabsorbed flux larger than $13.2 \times 10^{-12}$ erg s$^{-1}$ cm$^{-2}$ when the flare duration is larger than the observation exposure. Therefore, I use the GTI-binned method of Degenaar et al. (2013) which is optimized to detect the X-ray flares for the Swift observing setup.

To assess the detection efficiency of the Degenaar et al. (2013)'s method for the Swift observations, I simulate an event list with a Poisson flux that reproduce a Gaussian-flare light curve with different mean count rates and durations above each of the non-flaring level observed by Swift which are reported in Table 6.1. I now work on a logarithmic mean unabsorbed flux grid of 30 points between 0.6 and $40.0 \times 10^{-12}$ erg s$^{-1}$ cm$^{-2}$ and a logarithmic duration grid of 30 points between 300 s and 10.1 ks to cover the duration and flux ranges of the overall observed flares (see next sections). For each set of point, I extract ten event lists of 1 ks distributed over the flare duration to reproduce a typical flaring observation with Swift. I then apply the Degenaar et al. (2013)'s detection method to compute how many time the flare is detection. These simulations are done for each non-flaring level observed by Swift from 2006 to 2015 (Table 6.1). The resulting detection efficiencies for the 2006–2011 observations (i.e., without transient sources) are shown in the right panel of Fig. 6.2. As for

the flare detection with the Bayesian blocks method, the detection efficiency jumps from 20 to 100% in a small mean unabsorbed flux range. However, the flux limit for the 100% detection (about $7 \times 10^{-12}$ erg s$^{-1}$ cm$^{-2}$) is well below those associated to the Bayesian blocks method leading the Degenaar et al. (2013)'s detection method more efficient for the flare detection with Swift.

## 6.2 Systematic flare detection

I use the two-steps Bayesian blocks algorithm with a false positive rate for the flare detection of 0.1% to detect the X-ray flares observed with XMM-Newton and Chandra and to compute the non-flaring level for each observation[4]. The non-flaring level observed with Chandra and XMM-Newton is not constant over 1999–2015 due to the presence of contaminating transient sources (a low-mass X-ray binary at 2″.9 south and SGR J1745-29 at 2″.4 southeast of Sgr A*; see Sect. 3.2 and 1.5 ).

For the flare detection, I use the GTI-binned detection method of Degenaar et al. (2013). I filter the src events in the 2−10 keV energy band to build the Sgr A* light curves binned on each GTI. I reject the GTI whose exposure is lower than 100 s since the error bars on the count rate during this short exposure are large. For the observations between 2006 and 2012, the non-flaring level from the src event list in each yearly campaign is computed as the ratio between the number of event recorded during these campaign and the corresponding yearly exposures. A light curve bin is associated to a flare if the lower limit on the count rate in this observation is larger than the non-flaring level of the corresponding yearly campaign plus three times the standard deviation of the yearly campaign light curve. During the 2013, 2014 and 2015 Swift campaigns, the non-flaring level observed in the Sgr A* light curves has large variations due to the presence of the Galactic Center magnetar (see Fig. 1.13). The non-flaring level during these campaigns is fitted using two exponential powerlaws as it was done by Lynch et al. (2015) [5]:

$$CR = (0.246 \pm 0.009)\, e^{-\frac{t-t_0}{(66.2\pm3.5)\,\mathrm{d}}} + (0.012 \pm 0.05)\, e^{-\frac{t-t_0}{(79.0\pm9.7)\,\mathrm{d}}} + 0.027 \text{ counts s}^{-1} \tag{6.1}$$

with $t_0$ = 56406 MJD. During these three campaigns, a flare is detected if the mean count rate during the observation is larger than this count rate fit plus three times the $1\sigma$-error. The mean count rate of a flare detected with Swift is the mean count rate of the observation subtracted from the non-flaring level.

The time of the start and end of the flares observed by XMM-Newton, Chandra and Swift as well as the non-flaring levels are given in Tables C.1, C.2 and C.3, respectively, of Appendix C. In total, 102 X-ray flares were observed between 1999 and 2015: 17 flares with XMM-Newton, 77 flares with Chandra and 8 flares with Swift. The mean flare duration is 2708 s, the standard deviation is 2082 s and the median is 2027 s implying that the flare durations have a nearly homogeneous distribution without preferred value. The cumulative number of flares is given in Fig. 6.3 (blue line) as a function of time (with observing gaps) for Chandra (upper panel), XMM-Newton (middle panel) and Swift (lower panel). The flare times are computed as $(t_{\rm start} + t_{\rm end})/2$ with $t_{\rm start}$ and $t_{\rm end}$ the start and end times of the flare. I also represent in this figure the cumulative exposure (orange line) for each instrument. The cumulative flaring rate is then computed as the ratio between these two curves (black line). The total flaring rates observed by each instrument are different: $1.16 \pm 0.13$, $0.67 \pm 0.16$ and $0.45 \pm 0.16$ flare per day for Chandra, XMM-Newton and Swift, respectively. This is due to the different sensitivity of the cameras and the different non-flaring levels observed by the instruments which depends on the instrument sensitivity and the angular resolution. It is thus required to correct the detection bias due to the sensitivity in order to study consistently the flaring rate obtained by the combination of three instruments. To assess the detection efficiency for the three instruments, I use two flares characteristics that are independent of the instruments: the flare duration (already computed in this section) and mean unabsorbed flux (see next section).

[4]The *prior* number of change points is properly calibrated with the number of flare in the list (see Sect. 3.4.2) and is not the geometric *prior* estimation computed by Scargle et al. (2013a). Ponti et al. (2015) used the geometric prior coded in the Python program of the Bayesian blocks likely leading to an inconsistency between their adopted value of $p_1$ and their resulting false detection probability.

[5]I cannot directly use their fit since they did not correct from the losses caused by the bad pixels/columns, the PSF extraction fraction and the vignetting.

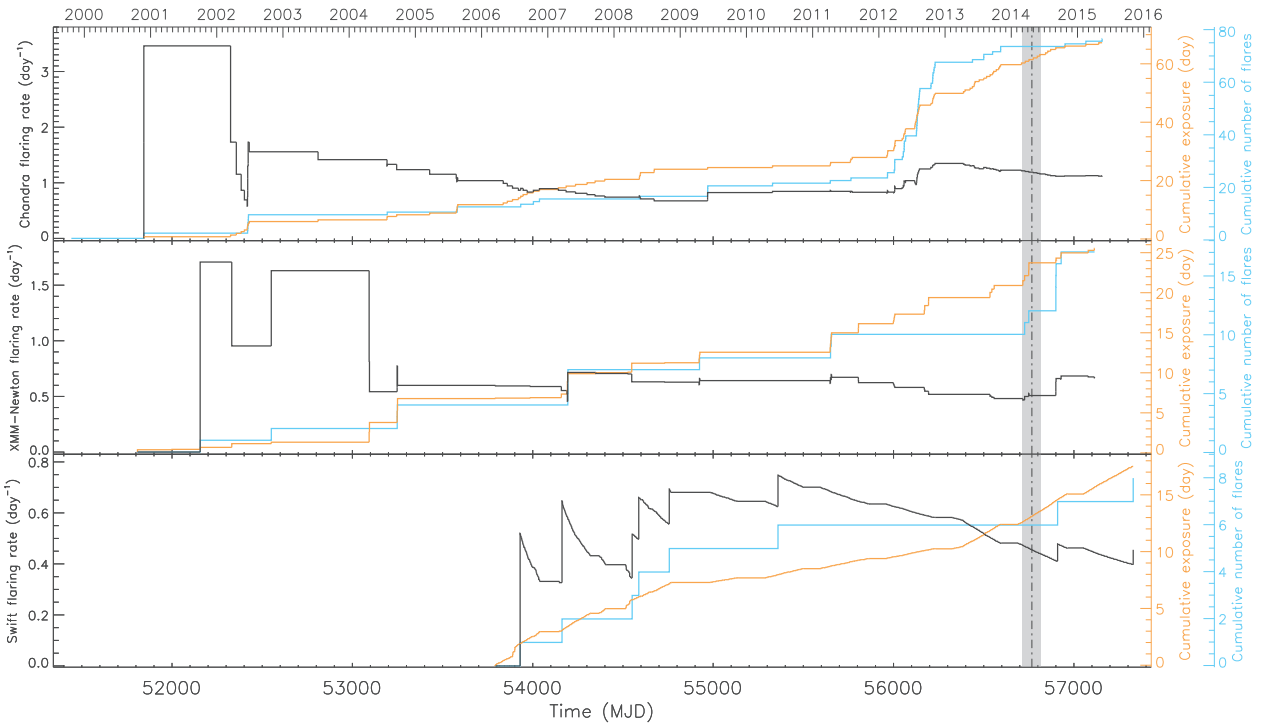


Figure 6.3: Evolution of the X-ray flaring rate from 1999 to 2015 by Chandra (top panel), XMM-Newton (middle panel) and Swift (bottom panel). The light gray box with the dot-dashed line is the time range of the DSO/G2 pericenter passage (Valencia-S. et al. 2015). The blue and orange lines are the cumulative number of flares and the cumulative observational exposure. The black line is the cumulative flaring rate computed as the ratio between the cumulative number of flares and the cumulative exposure.

## 6.3 The X-ray flare fluxes

To compute the mean unabsorbed fluxes of the X-ray flares detected by XMM-Newton and Chandra with the two-steps Bayesian blocks algorithm, I extract their spectra, ancillary files, and response matrices with the SAS script `especget` for XMM-Newton and the CIAO script `specextract` for Chandra[6]. For the Swift observations, due to the short exposure time, the flare spectra are extracted during the entire observation using the HEASOFT task `XSelect` and the corresponding arf are created using `xrtmkarf` (version 0.6.3). The rmf are taken in the Calibration Database[7]. The non-flaring spectrum is extracted from the closest surrounding observation.

I then group each spectra of the flares observed by XMM-Newton, Chandra and Swift with a minimum of one count with `grppha` to fit them using the Cash statistic (Cash 1979). For the XMM-Newton and Swift observations, I fit the spectra with the values of $N_{\rm H}$ and $\Gamma$ fixed to those computed for the two brightest X-ray flares observed with XMM-Newton and the 2012 Feb. 9 bright Chandra flare: $N_{\rm H} = 14.3 \times 10^{22}$ cm$^{-2}$ and $\Gamma = 2$ (Porquet et al. 2003, 2008; Nowak et al. 2012). Only the unabsorbed flux between 2 and 10 keV is a free parameter. The resulting mean unabsorbed fluxes of each X-ray flare are given in Tables C.1 and C.3 of Appendix C.

For the Chandra observations, the pile-up must be taken into account. The pile-up is due to the recording of more than one photon per pixel island during the same readout frame. The multiple photons are either recorded as a unique photon of merged (higher) energy or they produce the pattern (or grade) migration of the event leading this photons not classified as an X-ray event anymore. In the latter case, a dip appears in the center of the PSF image of a bright source. I use the pile-up model of Davis (2001) available in `ISIS` with the photon migration parameter $\alpha = 1$ (Nowak et al. 2012; Neilsen et al. 2013) for a PSF fraction of 95% corresponding to the 1.″25 extraction region. I fit the spectra with this pile-up model applied on the absorbed powerlaw model with the fixed $N_{\rm H}$ and $\Gamma$ reported above and a free unabsorbed flux between 2 and 10 keV.

[6] Ponti et al. (2015) used WebPIMMS to compute the mean unabsorbed flux. However, this tool considers only on-axis source with the full effective area of the facility which leads to unreliable determination of the flare mean unabsorbed fluxes.

[7] http://heasarc.gsfc.nasa.gov/FTP/caldb/data/swift/xrt/cpf/rmf/

Table C.2 of Appendix C reports the resulting mean unabsorbed flux between 2 and 10 keV.

Three flares observed with XMM-Newton and Chandra begin before the start of the observation and three other flares end after the end of the observation (see flare times in bold face in the tables of Appendix C). According to the phase of the flare which is not observed, this leads to a lower or upper limit on the mean unabsorbed flux. Indeed, assuming a Gaussian flare, if we only observe the end of the decay phase or the beginning of the rise phase, the resulting mean unabsorbed flux is a lower limit on its actual value; if we observe the end of the rise phase and the decay phase or the rise phase and the beginning of the decay phase, the resulting mean unabsorbed flux is an upper limit on its actual value. For the eight flares observed with Swift, the duration of the flares are associated to the observational exposure leading to a lower limit on the mean unabsorbed flux if the flare duration is lower than the exposure. If the flare duration is larger than the exposure, the orientation of the limit depends on the part of the flare which is observed. Hereafter, I consider these lower or upper limits on the mean unabsorbed flux as the actual value of the flare flux.

The averaged mean unabsorbed flux for the X-ray flares observed by XMM-Newton, Chandra and Swift is $8.7 \times 10^{-12}\,\mathrm{erg\,s^{-1}\,cm^{-2}}$ with a standard deviation of $10.3 \times 10^{-12}\,\mathrm{erg\,s^{-1}\,cm^{-2}}$ while the median is $4.5 \times 10^{-12}\,\mathrm{erg\,s^{-1}\,cm^{-2}}$. The observed distribution of the mean unabsorbed flux is thus peaked towards the faintest flares. However, the different detection sensitivities of the instruments according to the flare mean unabsorbed flux and duration biases the observed distribution towards the highest and longest flares. I thus need to correct from the detection sensitivities to correctly study the merged duration and mean unabsorbed flux distribution.

## 6.4 The intrinsic flare distribution

To determine the intrinsic flare distribution, I compute the flare density distribution from XMM-Newton and Chandra flare detection since the characteristics of the flares observed by Swift are not enough constrained. I then correct the observed flares density from the merged detection bias of XMM-Newton and Chandra.

### 6.4.1 The observed flare distribution

From the mean unabsorbed fluxes and durations of the X-ray flares observed by XMM-Newton and Chandra from 1999 to 2015, I construct the minimum triangulation of the Delaunay tessellation (blue lines in the top left panel of Fig. 6.4). The observed flare density is computed using the Delaunay tessellation field estimator (DTFE; Schaap & van de Weygaert 2000; van de Weygaert & Schaap 2009): the density associated to a given flare position is computed using the Delaunay triangles connected to this flare to conserve the total flare number in the reconstructed density field. I compute for each flare $i$ the area $W_\mathrm{i} = \sum A_\mathrm{k}$ with $A_\mathrm{k}$ the area of the triangle $k$ whose one of the vertex is the flare $i$ at the location $\boldsymbol{x}_\mathrm{i}$. The flare density per surface unit in the mean-unabsorbed-flux–duration plane associated to the flare $i$ is $d_\mathrm{i} = 3/W_\mathrm{i}$ . The discretized map of the flare density is linearly interpolated inside the convex hull of the observed flare set at a point $\boldsymbol{x}$ in the Delaunay triangle $m$: $d(\boldsymbol{x}) = d_\mathrm{i} + \nabla d|_\mathrm{m}(\boldsymbol{x} - \boldsymbol{x}_\mathrm{i})$. The resulting filled contour map of the observed flare density is shown in the top right panel of Fig. 6.4 with the distribution density levels of the observed flares in logarithmic scale.

### 6.4.2 The X-ray flare detection efficiency

The detection efficiency of the X-ray flares with the Bayesian blocks algorithm depends on the non-flaring level and the instrument sensitivity. During the 1999–2015 observations with XMM-Newton and Chandra, 12 different values of the non-flaring levels were recorded (see Table 6.1). I use flare durations and mean unabsorbed fluxes (and not the flare count rate amplitudes as in the previous Chapters since it is instrument dependent) to compute the local detection efficiency of the Bayesian blocks algorithm. I simulate an event list with a Poisson flux reproducing a Gaussian-flare light curve with different mean count rates and durations (defined as two times the Gaussian standard deviation) above each of these non-flaring levels as explained in Sect. 3.3. I work on a logarithmic mean unabsorbed flux grid of 30 points between 0.6 and $40.0 \times 10^{-12}\,\mathrm{erg\,s^{-1}\,cm^{-2}}$ and a logarithmic duration grid of 30 points between 300 s and 10.1 ks to cover the duration and flux ranges of the overall observed flares. The mean unabsorbed fluxes are converted into mean count rates using the count-rate–to–unabsorbed-flux ratio computed for the flares detected with each instrument, i.e., 111.3, 248.2 and $148.1 \times 10^{-12}\,\mathrm{erg\,s^{-1}\,cm^{-2}/count\,s^{-1}}$ for XMM-Newton/EPIC pn, Chandra/ACIS-

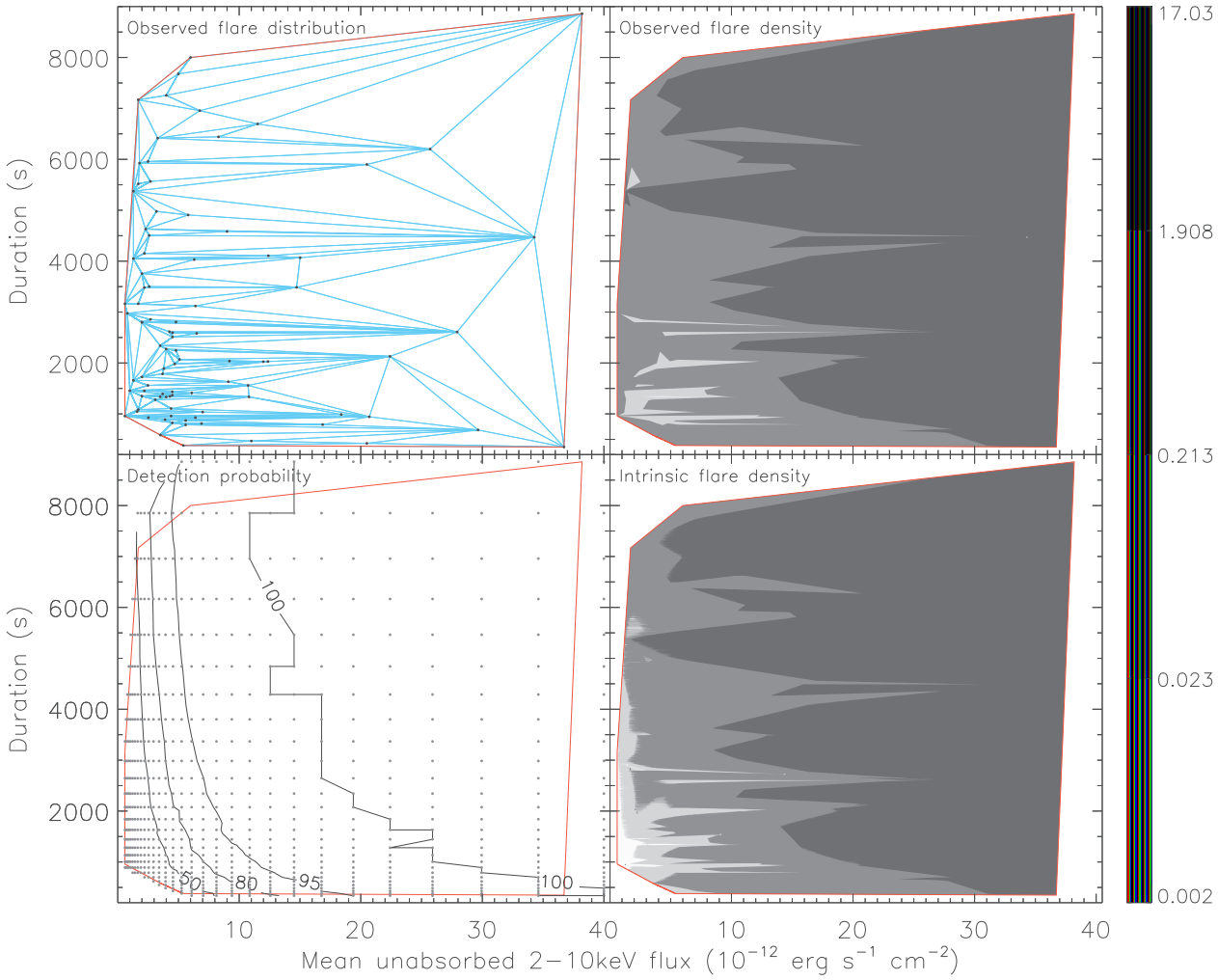


Figure 6.4: Flux–duration distribution of the X-ray flares from Sgr A*. *Top left panel:* The observed flare flux–duration distribution observed with XMM-Newton and Chandra from 1999 to 2015 (black dots) and the corresponding Delaunay's triangles (blue lines). The red lines define the convex hull. *Top right panel:* The observed flare density estimation. The filled contours are in logarithmic scale and the color bar is represented in the right hand side of the figure in unit of $10^{10}$ s$^{-1}$ erg$^{-1}$ s cm$^2$. *Bottom left panel:* The merged detection efficiency of XMM-Newton and Chandra from 1999 to 2015 in percent. The dots represent the simulation grid. *Bottom right panel:* The intrinsic flux–duration distribution in filled contour corrected from the observing bias. The filled contours are in the same logarithmic scale than in the top right panel.

Table 6.1: Average flare detection efficiency associated with the different non-flaring levels observed by Chandra, XMM-Newton and Swift.

| Telescope | Instrument | Non-flaring level (counts $s^{-1}$) | Observing dates | Total exposure[a] (ks) | $\eta^b$ (%) |
|---|---|---|---|---|---|
| Chandra | ACIS-I3 | 0.005 | 1999-09-21–2011-07-30 and 2015-04-25 | 1718.7 | 56.0 |
| ——— | ——— | 0.045 | 2013-04-06–2013-04-14 | 40.2 | 33.9 |
| ——— | ACIS-S3/HETG | 0.006 | 2012-02-06–2012-10-31 | 2983.5 | 37.6 |
| ——— | ——— | 0.009 | 2013-05-25 and 2013-06-05–2013-06-09 | 47.8 | 34.9 |
| ——— | ACIS-S3/subarray | 0.024 | 2013-05-12 | 15.1 | 27.2 |
| ——— | ——— | 0.014 | 2013-07-27–2013-08-12 and 2013-09-20 | 119.6 | 31.9 |
| ——— | ——— | 0.009 | 2013-06-04 and 2013-07-02 and 2013-08-31–2013-09-14 and 2013-10-04–2014-02-22 | 216.1 | 34.9 |
| ——— | ——— | 0.007 | 2014-03-14–2015-05-14 | 476.6 | 36.6 |
| XMM-Newton | pn | 0.100 | 2000-09-17–2002-10-03 and 2006-02-27–2012-08-31 | 1803.1 | 27.1 |
| ——— | ——— | 0.171 | 2004-03-28–2004-09-03 and 2014-08-30–2015-04-02 | 633.2 | 24.3 |
| ——— | ——— | 0.535 | 2013-08-30–2013-09-10 | 91.3 | 16.5 |
| ——— | ——— | 0.506 | 2013-09-22 | 39.4 | 16.7 |
| ——— | ——— | 0.320 | 2014-02-28 | 51.9 | 19.7 |
| ——— | ——— | 0.312 | 2014-03-10 | 54.1 | 19.8 |
| ——— | ——— | 0.287 | 2014-04-02 | 54.9 | 20.3 |
| ——— | ——— | 0.294 | 2014-04-03 | 83.5 | 20.1 |
| Swift | XRT | 0.027 | 2006-02-24–2013-04-23 and 2015-02-03–2015-11-02 | 1102.4 | 24.5 |
| ——— | ——— | 0.284 | 2013-04-24–2013-05-11 | 4.0 | 15.7 |
| ——— | ——— | 0.245 | 2013-05-12–2013-05-17 | 8.7 | 17.4 |
| ——— | ——— | 0.207 | 2013-05-18–2013-05-29 | 10.6 | 18.0 |
| ——— | ——— | 0.153 | 2013-05-30–2013-06-28 | 23.0 | 21.3 |
| ——— | ——— | 0.102 | 2013-06-29–2013-09-07 | 60.1 | 22.2 |
| ——— | ——— | 0.042 | 2013-09-08–2013-10-31 | 44.0 | 23.1 |
| ——— | ——— | 0.030 | 2014-02-03–2014-11-02 | 230.5 | 24.1 |

**Notes:** [a] Sum of the GTIs of the corresponding observations; [b] The average flare detection efficiency above the corresponding non-flaring level.

S3 subarray and Chandra/ACIS-I, respectively. For each set of point inside and close to the border of the convex hull, I simulate 100 event lists and apply the Bayesian blocks algorithm to compute how many times the algorithm detects the flare.

Since the flares are described with parameters independent from the telescope instruments, I am able to combine the local detection efficiencies of each instrument computed on the same grid. The local detection efficiencies are firstly weighted according to the total exposure time of the corresponding instrument since the impact of the detection efficiency on the number of observed flare depends on the exposure. I finally sum the weighted local detection efficiencies to determine the merged local detection efficiency of XMM-Newton and Chandra shown in the bottom left panel of Fig. 6.4 with the grid points. The merged local detection efficiency on the convex hull is computed by a linear interpolation between the merged local detection efficiency on either side of the convex hull.

### 6.4.3 Correction of the observed flare distribution

The map of flare density is finally corrected from the merged local detection efficiency XMM-Newton and Chandra to compute the intrinsic flares distribution. The observed density distribution at a point grid $\boldsymbol{x}$ is then corrected by the merged local detection efficiency XMM-Newton and Chandra $p(\boldsymbol{x}) < 1$ at each grid point $\boldsymbol{x}$ as $d_{\rm intr}(\boldsymbol{x}) = d(\boldsymbol{x})/p(\boldsymbol{x})$ (see Eq. 17 of van de Weygaert & Schaap 2009). The intrinsic flare density distribution is shown with filled contour in logarithmic scale in the bottom right panel of Fig. 6.4 with the same color scale than for the left panel of this figure. The intrinsic flare density is now highest for the faintest and shortest flares.

## 6.5 Study of the unbiased X-ray flaring rate

The overall XMM-Newton, Chandra and Swift corrected observations are then combined and the observational gaps are removed to create a continuous exposure containing the times of the 102 flares detected. The observational overlays are also removed keeping only the most sensitive instrument. Figure 6.5 shows the flares times without observing gaps over the total exposure time of 106.8 days (corresponding to 9.2 Ms). The height of each vertical line representing a flare corresponds to the mean unabsorbed flux (top panel) and fluence (mean unabsorbed flux times duration; bottom panel) between 2 and 10 keV. We thus observe 102 flares during a total exposure of 106.9 days (corresponding to 9.2 Ms) leading to a flaring rate of $0.95 \pm 0.09$ flare per day which is statistically consistent with the flaring rate of Neilsen et al. (2013) limited to the 2012

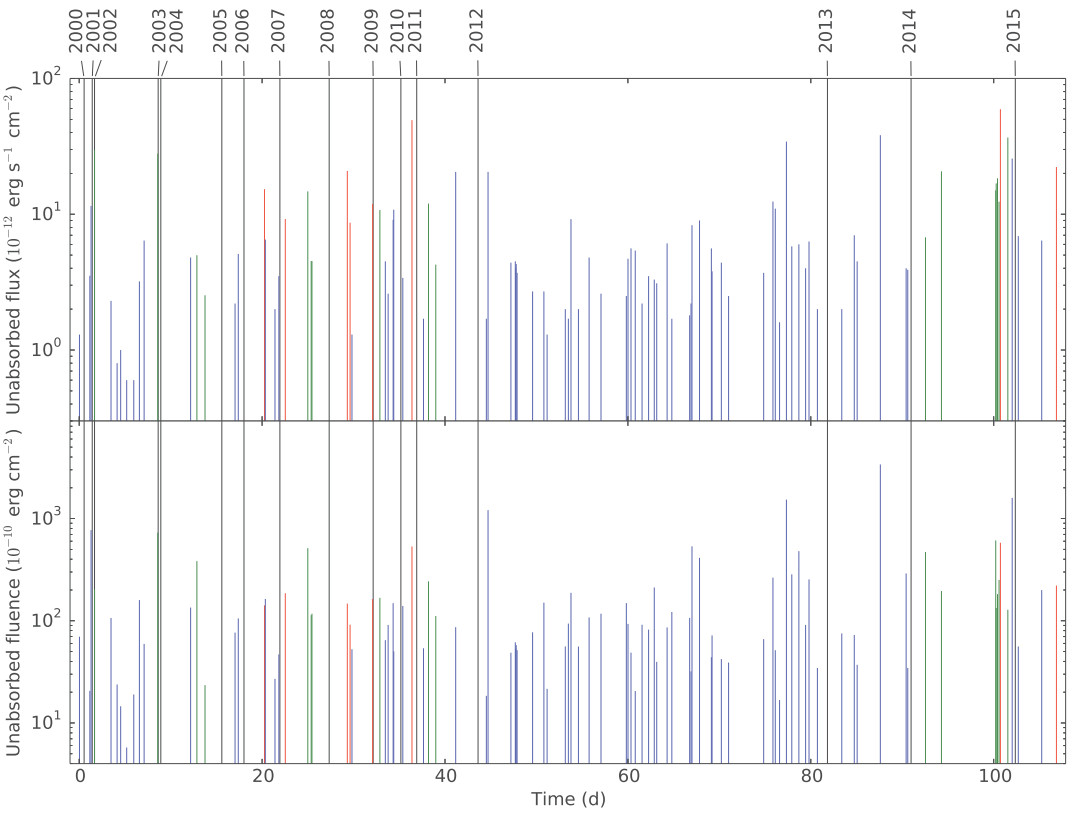


Figure 6.5: Temporal distribution of the flare fluxes and fluences. The mean flare times without observing gaps and with the correction of the average flare detection efficiency are represented by the vertical lines. The dotted lines are the time of the beginning of the first observation of the year. The blue, green and red lines are the Chandra, XMM-Newton and Swift flares, respectively. The dashed lines are only lower or upper limits on the flare flux and fluence due to the truncated flare duration when it begins/ends before/after the start/stop of the observation. *Top panel:* The mean unabsorbed flux distribution. *Bottom panel:* The mean unabsorbed fluence distribution.

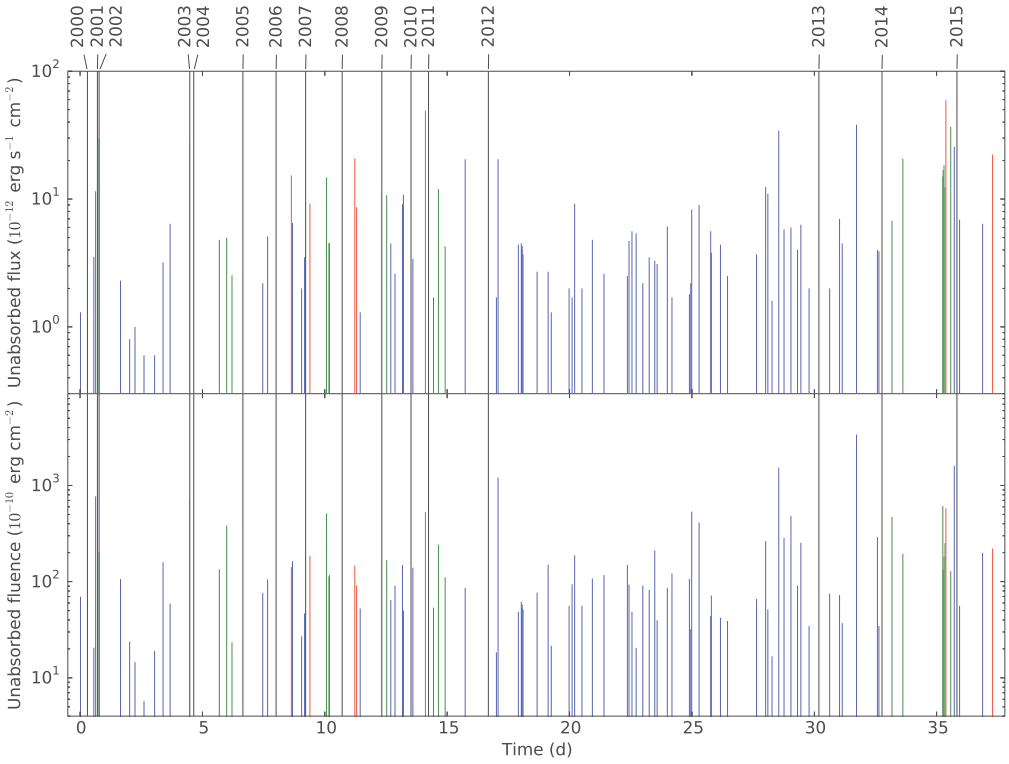


Figure 6.6: Temporal distribution of the flare fluxes and fluences corrected from the sensitivity bias. See caption of Fig. 6.5 for details.

Chandra *XVP* campaign but lower than their value since XMM-Newton and Swift are less sensitive to fainter and shorter flares. I thus need to correct the flare count rate from the flare detection bias due to the instrument sensitivities.

To do so, I apply the local detection efficiencies corresponding to each non-flaring level *nf* observed by XMM-Newton, Chandra and Swift on the intrinsic flares distribution computed above to determine the average flare detection efficiency $\eta$ for each observation. The intrinsic flare density $d_{\rm intr}(\boldsymbol{x})$ at each grid point $\boldsymbol{x}$ is affected by the corresponding local detection efficiency $p_{\rm nf}(\boldsymbol{x}) < 1$ leading only a percentage of this flare density to be observed: $d_{\rm nf}(\boldsymbol{x}) = d_{\rm intr}(\boldsymbol{x}) \times p(\boldsymbol{x})$. By computing the ratio between the 2-D integral on the convex hull of the flare density distribution affected by the local detection efficiency for a given non-flaring level and the intrinsic flare density distribution, I assess the average flare detection efficiency $\eta < 1$ corresponding to this non-flaring level (Table 6.1):

$$\eta = \frac{\int\int d_{\rm nf}(\boldsymbol{x})\, d\boldsymbol{x}}{\int\int d_{\rm intr}(\boldsymbol{x})\, d\boldsymbol{x}}\,. \tag{6.2}$$

I thus obtain a set of merged observations of XMM-Newton, Chandra and Swift, each containing $N \geq 0$ flares, with their corresponding exposure and average flare detection efficiency $\eta$ given in Table 6.1. To correct the flaring rate from the observing sensitivity, I apply the same method as used previously in Sect. 3.4.1 for correcting the event count rates in each exposure frame from the exposure livetime in the two-steps Bayesian blocks algorithm: for each observational exposure $T$, I compute the corrected observational exposure as $T_{\rm corr} = T\,\eta$ leading to a higher and unbiased flaring count rate in the corresponding observation. Figure 6.6 shows the flares times without observing gaps over the total corrected exposure time of 37.3 days.

I divide the corrected exposure time in Voronoi cells each containing one flare and whose the separation time is the mean time between two consecutive flares. I apply the Bayesian blocks algorithm on the Voronoi cells with a false positive rate for the change point detection of $p_1 = 0.05$ and the corresponding $ncp\_prior = 3.96$ obtained for an average flaring rate of 102 events during 37.3 days. The overall flaring activity is described by a constant rate of $2.74 \pm 0.27$ flares per day. This is higher than those computed by Neilsen et al. (2013) since they did not correct from the non-detection bias corresponding to their flare detection method.

I now search for any change of the flaring rate over the flux and fluence distribution. I first performed a top-to-bottom search: at each step, I remove the flare with the highest unabsorbed flux (but keeping the corresponding exposure time and updating the Voronoi cells) and apply the Bayesian block algorithm with a false probability rate of $p_1 = 0.05$ on the resulting flare list[8]. I repeat this operation until the algorithm found a flaring rate change. A change of flaring rate is detected at 32.6 days, i.e., between the two Chandra flare on 2013 Oct. 28 considering only 64 flares with a mean unabsorbed flux lower than or equal to $6.3 \times 10^{-12}$ erg s$^{-1}$ cm$^{-2}$ (the less luminous flares) with $p_1 = 0.05$ and the corresponding $ncp\_prior = 4.13$. The resulting Bayesian blocks are shown in the top panel of Fig. 6.7 where only these 64 flares are shown. The first block contains 63 flares while the second block contains only one flare. The flaring rate decreases from $1.93 \pm 0.24$ to $0.21 \pm 0.21$ flares per day. By decreasing the false probability rate, this flaring rate change is detected for $p_1 > 0.012$ leading to a significance of $1 - p_1 = 98.8\%$.

I then perform the bottom-to-top search by recursively removing the flare with the lowest unabsorbed flux and applying the Bayesian block algorithm. One change of flaring rate is found considering only 52 flares with a mean unabsorbed flux larger than or equal to $4.52 \times 10^{-12}$ erg s$^{-1}$ cm$^{-2}$ (the most luminous flares) with $p_1 = 0.05$ and the corresponding $ncp\_prior = 4.24$. The resulting Bayesian blocks are shown in the bottom panel of Fig. 6.7 where only these 52 flares are shown. The change of flaring rate happens between the two first XMM-Newton flares on 2014 Aug. 31 flares (35.2 days). The blocks contain 43 and 9 flares corresponding to flaring rates of $1.22 \pm 0.19$ and $4.44 \pm 1.48$ flares per day. There is thus an increase by a factor of $3.6 \pm 1.8$ of the flaring rate of these flares. This flaring rate change is still detected until a false positive rate of $p_1 = 0.031$ ($ncp\_prior = 4.67$) leading to a significance for this change point of $1 - p_1 = 96.9\%$.

The same study is done with the unabsorbed fluence. I first perform the top-to-bottom search: a change of flaring rate was found considering only 60 flares with an unabsorbed fluence lower than or equal to $121.9 \times 10^{-10}$ erg cm$^{-2}$ (the less energetic flares) with $p_1 = 0.05$ and the corresponding $ncp\_prior = 4.13$. The resulting Bayesian blocks are shown in the top panel of Fig. 6.8 where only these 60 flares are shown. The first block contains 58 flares while the second one contains 2 flares. The change of flaring rate happens

[8]The *ncp_prior* was calibrated at each step to be consistent with the flare number.

between the second Chandra flare on 2013 July 27 and the 2013 Oct. 28 flare also observed by Chandra (31.89 days). The corresponding flaring rates are $1.81 \pm 0.24$ and $0.37 \pm 0.26$ flares per day. This flaring rate change is detected for a decreasing false positive rate until $p_1 = 0.048$ ($ncp\_prior = 4.18$) leading to a probability that this change of flaring rate is a real one of $1 - p_1 = 95.2\%$.

For the bottom-to-top search, two changes of flaring rate are detected considering only 48 flares with a mean unabsorbed fluence larger than or equal to $107.8 \times 10^{-10}$ erg cm$^{-2}$ (the most energetic flares) with $p_1 = 0.05$ and the corresponding $ncp\_prior = 3.93$. The resulting Bayesian blocks are shown in the bottom panel of Fig. 6.8 where only these 48 flares are shown. The three blocks are described by flaring rates of $1.13 \pm 0.18$, $30.1 \pm 17.36$ and $2.59 \pm 1.16$ flares per day. They contain 40, 3 and 5 flares, respectively with the two change points between the two first XMM-Newton flares on 2014 Aug. 31 (35.26 days) and between the XMM-Newton flare on 2014 Sept. 1 and the Swift flare on 2014 Sept. 9 (35.36 days). This flaring rate change is detected for a decreasing false positive rate until $p_1 = 0.049$ ($ncp\_prior = 3.96$) leading to a probability that this change of flaring rate is a real one of $1 - p_1^2 = 99.76\%$. This increase of flaring rate for the flares having a mean unabsorbed fluence larger than or equal to $107.8 \times 10^{-10}$ erg cm$^{-2}$ corresponding occurs at the same date that the increase of the flaring rate for the most luminous flares. However, considering the flare fluences, the flaring rate is not high until the end of the observations considered here but is short-lived (from one to ten days) and the flaring rate then recovers a level consistent with those observed before 2014 Aug. 31.

In summary, no significant change of flaring rate is found with the Bayesian block algorithm considering the overall flares. However, an increase of the most luminous and most energetic flares is observed on 2014 Aug. 31, i.e., 80–181 days after the DSO/G2 pericenter passage near Sgr A*. For the most luminous flares, the flaring rate increases by a factor of $3.6 \pm 1.8$ and lasts until 2015 Nov. 2. Comparing this result to the high flaring rate argued by Ponti et al. (2015), the high level block found here contains the six flares creating the increase of flaring rate in Ponti et al. (2015) and the three additional flares observed in 2015 with Chandra (two flares) and Swift (one flare). The flaring rate for those flares is still high on 2015 Nov., i.e., at the end of the observational set considered here. The start of the higher flaring rate happened 131 days (80–181 days) after the DSO/G2 pericenter passage near Sgr A* (computed with the DSO/G2 pericenter passage determined by Valencia-S. et al. 2015). As argued in Sect. 5.2.3, if some material from DSO/G2 was accreted toward Sgr A*, the increase of flux should not be observed before the end of 2017 considering a pericenter distance of $2000\,R_s$ and an efficiency of the mechanism of angular momentum transport of $\alpha = 0.1$. Two interpretations can thus be proposed to explain this increase of flaring rate: firstly, the increase of flaring rate could be due to the accretion of matter from the DSO/G2 onto Sgr A* considering an efficiency of the mechanism of angular momentum transport of at least 0.6. Secondly, the increase of flaring rate could be explained by other mechanisms as reported in Sect. 1.2.3 which would become more efficient leading to the creation of a larger number of luminous flares.

I identified a decay of the flaring rate for the less luminous and less energetic flares. This decay occurs on 2013 Oct. 28, i.e., 185–225 days before the pericenter passage of the DSO/G2 implying that this change of flaring rate is difficult to be explained by the passage of the DSO/G2 near Sgr A*.

For the most energetic flares, the flaring rate increases by a factor of $26.6 \pm 19.6$ on 2014 Aug. 31 and lasts until 2014 Sept. 1 – Sept. 9. Interestingly, the decay of the less luminous and less energetic flares occurs before the increase of the most luminous and most energetic flaring rate. For comparison, I compute the energy lost during the decay of the flaring rate of less energetic flares between 2013 Oct. 28 and 2014 Aug. 31 and the energy gained during the increase of the flaring rate of most energetic flares. For the flares with a maximum fluence of $121.9 \times 10^{-10}$ erg cm$^{-2}$, the flaring rate decreases from 1.81 to 0.37 flare per day during 3.37 days leading an energy lost lower than $121.9 \times 10^{-10}\,(1.81 - 0.37)\,3.37 = 5.9 \times 10^{-8}$ erg cm$^{-2}$. For the flares with a minimum fluence of $107.8 \times 10^{-10}$ erg cm$^{-2}$, the flaring rate decreases from 1.13 to 30.1 flare per day during 0.10 days leading an energy gain larger than $107.8 \times 10^{-10}\,(30.1 - 1.13)\,0.10 = 3.1 \times 10^{-8}$ erg cm$^{-2}$. Therefore, the energy saved by the decrease of the number of less energetic flares during several days could be released by a few bright flares in several hours. This energy can be stored in the distortions of the magnetic field lines and then released during a magnetic reconnection event. This is reminiscent of the Earthquake behavior where stresses produce several small events during a long period of time or may accumulate before releasing in a large event. The input of fresh accreting material from the DSO/G2 is thus not needed to explain this large increase of the most luminous and most energetic flares.

This work is planned to be submitted in A&A.

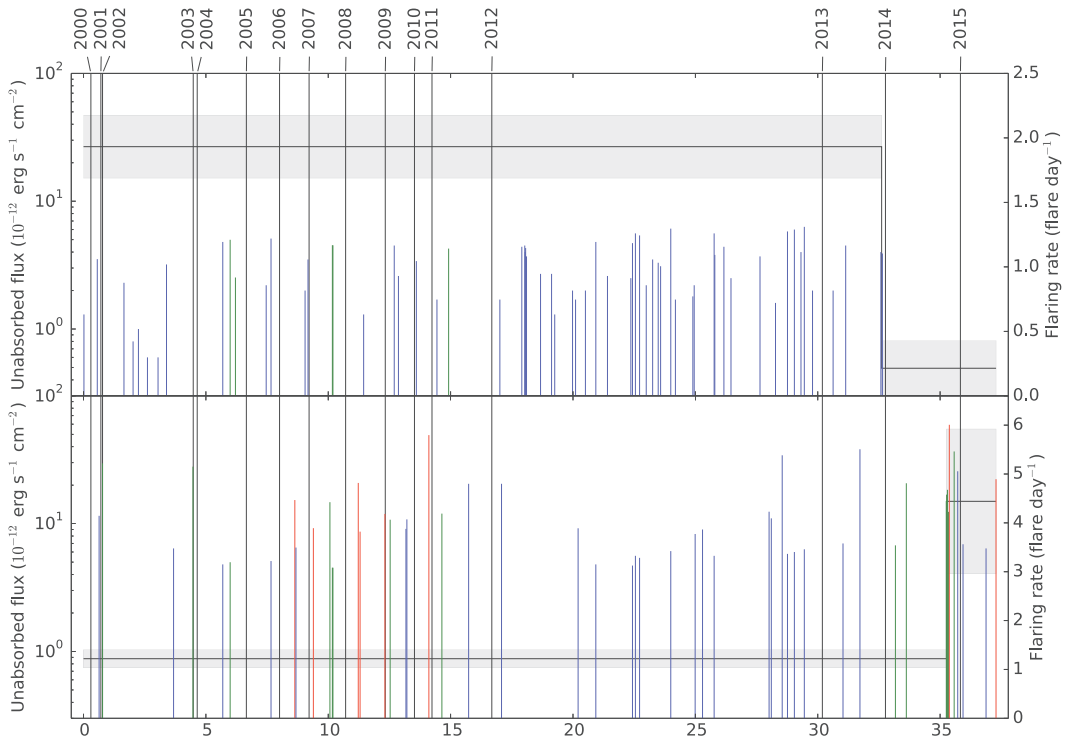


Figure 6.7: X-ray flaring rate from 1999 to 2015 computed by the Bayesian blocks algorithm in a given mean unabsorbed flux range. See caption of Fig. 6.5 for details. Only the flares used for the computation of the corresponding flaring rate are shown. The Bayesian blocks are the thick black lines. *Top panel:* The results for the top-to-bottom search. The largest mean unabsorbed flux is thus the flare flux threshold for which a change of flaring rate is found. *Bottom panel:* The results for the bottom-to-top search. The lowest mean unabsorbed flux is thus the flare flux threshold for which a change of flaring rate is found.

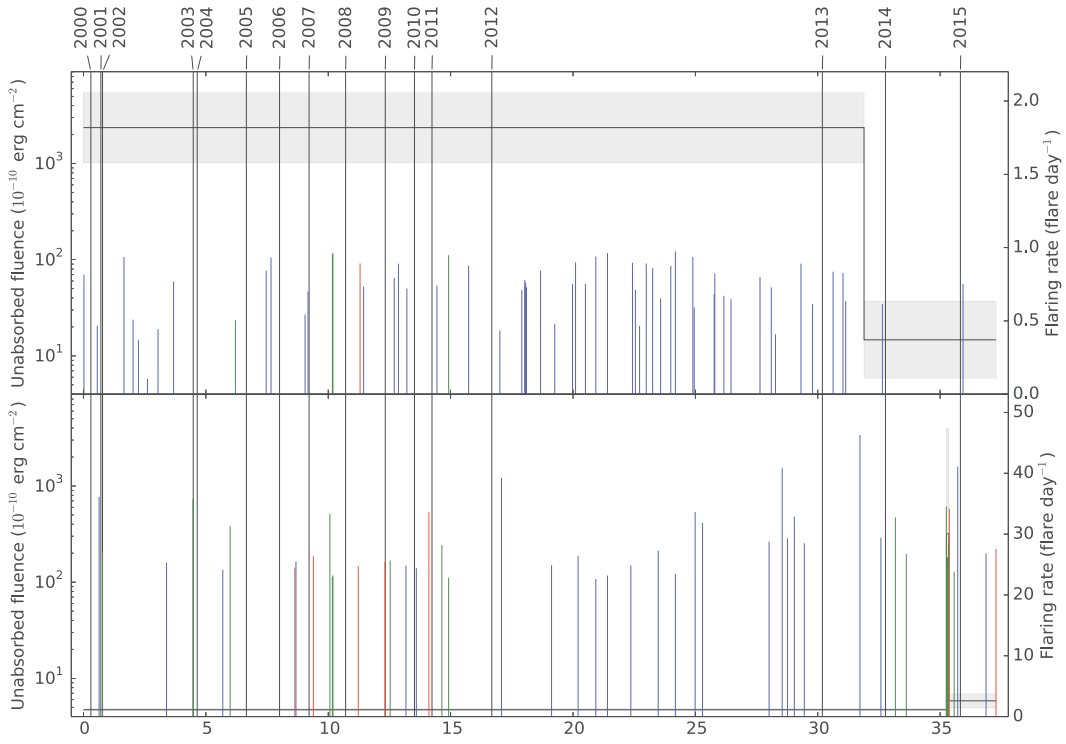


Figure 6.8: X-ray flaring rate from 1999 to 2015 computed by the Bayesian blocks algorithm in a given mean unabsorbed fluence range. See captions of Fig. 6.5 and 6.7 for details. *Top panel:* The largest mean unabsorbed fluence is thus the flare fluence threshold for which a change of flaring rate is found. *Bottom panel:* The lowest mean unabsorbed fluence is thus the flare fluence threshold for which a change of flaring rate is found.

# Chapter 7

# General conclusion and perspectives

The goal of this Ph.D. thesis was to study the impact of the DSO/G2 pericenter passage on the multiwavelength flaring activity of Sgr A*. For the X-ray analysis, I used and improved two methods for the temporal analysis (the two-steps Bayesian blocks method and light curve smoothing) and I used the Monte-Carlo Markov chains (MCMC) method for the spectral analysis. The two-steps Bayesian blocks algorithm was proposed to automatically detect X-ray flares with a given false detection probability using the source–plus–background and background event lists of an observation. As proposed by Scargle et al. (2013a), I took the CCD livetime and the recording of simultaneous events into account. I also calibrated the *prior* number of change points according to the number of events. The light curve smoothing with an Epanechnikov kernel allowed me to reduce the Poisson noise in the light curve and to increase the accuracy on the amplitude and the time of the maximum of the flares. The MCMC method is an iterative fitting method allowing to easily compute the marginal distribution and error of the spectral parameters. I used this method coded in the `XSPEC_emcee` program to fit the absorbed powerlaw model to the X-ray flare spectra.

Some progress have been made in the constraints of the physical parameters of the flaring region from Sgr A* thanks to the study of two observational campaigns: the XMM-Newton 2011 campaign and the 2014 Feb.–Apr. multiwavelength campaign. During the 2011 campaign published in Mossoux et al. (2015a), two X-ray flares were detected: one on 2011 March 30 and one on April 2. The March 30 flare had two peaks: a short and luminous peak followed by a longer and less luminous one. This flare allowed us to test the gravitational lensing model for the X-ray flux variation during a flare. But this model was rejected since it did not reproduced the dip separating the two peaks without adding some *ad-hoc* components. Considering that the 2011 March 30 flare was actually composed by two close subflares emitted by their own electrons population, the first subflare allowed me to constrain the distance and the size of the flaring region assuming that the electrons are accelerated by the magnetic field. Assuming that the luminosity observed during the overall first subflare was produced by the release of the magnetic energy (with $B = 100\,\mathrm{G}$ at $1\,R_\mathrm{s}$ and varying as the inverse of the distance to Sgr A*) during the rise phase of the subflare and that the decay phase was only due to synchrotron colling of accelerated electrons, the constrained radial distance of the flaring source from Sgr A* is $4\,r_\mathrm{g} < r < 100^{+19}_{-29}\,r_\mathrm{g}$ and the corresponding radius of the source is $1.8\,r_\mathrm{g} < R < 2.87 \pm 0.01\,r_\mathrm{g}$. I also rejected the direct synchrotron process for the creation of the X-ray photons during this first subflare.

The 2014 Feb.–Apr. multiwavelength campaign for the observation of Sgr A* was based on a XMM-Newton/HST large program which granted additional VLT, VLA and CARMA observations. These VLT/SINFONI observations were also very valuable for the study of the DSO/G2 (Valencia-S. et al. 2015). We found that the DSO/G2 is a $1 - 2\,M_\odot$ pre-main sequence star where the Br$\gamma$ emission line is produced by magnetospheric accretion of the matter from the circumstellar accretion disk on the stellar photosphere. During the pericenter passage on 2014 Apr. 20 (Mar. 1– Jun. 10) at $2032\,R_\mathrm{s}$ (163 au) from Sgr A*, the DSO/G2 was not tidally disrupted but the accretion rate on the stellar photosphere increased leading to a larger *FWHM* of the Br$\gamma$ line. The Lagrange point between Sgr A* and a star with a $1M_\odot$ mass is about 1 au leading to a possible transfer of matter from the DSO/G2 accretion disk to Sgr A*.

During the 2014 Feb.–Apr. multiwavelengths campaign published in Mossoux et al. (2016), two X-ray flares from Sgr A* were detected with XMM-Newton: one on 2014 March 10 and one on April 2. Three NIR flares were also detected with HST/WFC3 whose two had a detected X-ray counterpart. Two NIR flares were also observed with VLT/SINFONI without X-ray counterpart. We also observed the beginning of a radio flare with VLA but the NIR/X-ray counterpart could not be observed. Three other radio flares were observed

with CARMA whose the first one may be the delayed counterpart of the first VLT flare. The NIR flare on April 2 was actually composed by two close flares whose the first one was the simultaneous counterpart of the X-ray flare observed on the same date. The NIR/X-ray flare observed on March 10 has a variable NIR–to–X-ray flux ratio which could be explained by the adiabatic compression of a plasmon or the presence of two close flares produced by their own electrons population. Considering the last interpretation, we thus actually observed three X-ray flares and seven NIR flares. This X-ray flaring rate during this campaign was statistically consistent with those observed during the 2012 Chandra *XVP* campaign showing that no increase of the flaring activity occurred at the pericenter passage of the DSO/G2. Thanks to the three NIR/X-ray flares and the four NIR flares without detected X-ray emission observed during the 2014 Feb.–Apr. campaign, I put some constrains on the source size and accelerated electrons density of the flaring region for the three local radiative processes for the NIR and X-ray emission: SSC-SSC, SYN-SYN and SYN-SSC. None of these radiative processes nor the IC process could be favored or rejected for the creation of creation of X-ray photons. However to NIR/X-ray flare with the lowest NIR–to–X-ray amplitude ratio allowed me to constrain the size and the electronic density of the flaring region to $0.003 - 7\,R_{\rm s}$ and $10^{8.5} - 10^{10.2}\,{\rm cm}^{-3}$, respectively, for the SYN/SSC mechanism and a synchrotron spectral index of $\alpha = 0.3 - 1.5$. The NIR and X-ray flaring rate observed between 2014 Feb. and Apr. was consistent with those observed by VLT/NACO and the 2012 Chandra *XVP* campaign, respectively, implying that we did not observe any change of flaring rate due to the pericenter passage of the DSO/G2.

On 2015 Nov., a total of 102 X-ray flares were observed since 1999 with Swift, XMM-Newton and Chandra whose five were detected during the two campaign analyzed during this Ph.D. thesis. Thirteen of the 102 X-ray flares were observed with their NIR counterpart and three of them were discovered during the 2014 Feb.–Apr. campaign. To properly compute the X-ray flaring rate using these 102 X-ray flares, I computed the local detection efficiency for each instrument as a function of the flare mean unabsorbed flux and of the flare duration to correct from the detection bias. This allowed me to compute the intrinsic flux density and then the average flare detection efficiency for each observation. Thanks to this average flare detection efficiency, I corrected the observed flaring count rate in each observation to properly study the overall X-ray flaring rate. The observations from 1999 to 2015 were then merged and the Bayesian blocks algorithm was applied on the flare arrival times leading to an overall intrinsic flaring-rate of $2.73 \pm 0.27$ flare per day. I pointed out a decay of the flaring rate for the less luminous and less energetic flares on 2013 Oct. 28. This change of flaring rate occurred 185–225 days before the DSO/G2 pericenter passage which excludes the DSO/G2 as the origin of this change of flaring rate. There was also an increase of the X-ray flaring rate for the most luminous and the most energetic flares. The flaring rate of the most luminous increased on 2014 Aug. 31 until the end of the observations set, i.e., on 2015 Nov. 2. while those of the most energetic flares increased on 2014 Aug. 31 and decreased on 2014 Sept. 9 to recovers the flaring rate observed before 2014 Aug. 31. This increase of the flaring rate occurred 80–181 days after the DSO/G2 pericenter passage but no direct link can be done between this event and the increase of the flaring rate. Moreover, the energy balance between the decay of the X-ray flaring rate for the less energetic flares and the increase of the X-ray flaring rate for the most energetic flares suggests that the energy saved during several days by the decay of the number of the less energetic flares could be released during a few hours by a few energetic flares.

The low number of photons recorded during an X-ray flare limits the accuracy on the light curve and the spectrum of these flares. With the current X-ray facilities, we thus can not disentangle between the radiative processes producing the for the X-ray flares. The next generation X-ray satellite Athena will have an angular resolution which will be intermediate between XMM-Newton and Chandra and it will be able to record a higher number of X-ray photons.

The Advanced Telescope for High Energy Astrophysics (Athena) is the large mission of ESA which will be launched in 2028 (Nandra et al. 2013). It is composed by two instruments which operate separately: the X-ray Integral Field Unit (X-IFU; Barret et al. 2013) and Wide Field Imager (WFI; Rau et al. 2013). The WFI has a field of view of $40' \times 40'$(larger than XMM-Newton and Chandra) and covers the 0.1 to 12 keV energy band. The X-IFU is a micro-calorimeter covering the 0.3 to 12 keV energy band with a spectral resolution of 2.5 eV below 7 keV (with a goal of 1.5 eV) and increasing as $(E/{\rm keV})/2.8$ above 7 keV. Its angular resolution is $5''$ half-energy width on-axis (with a goal of $3''$) and its temporal resolution is $10\,\mu$s. The focal plane of the X-IFU is an hexagon with an equivalent diameter of $5'$ (with a goal of $7'$) and a pixel size of $4.21''$. The goal of the X-IFU CCD configuration is to oversample the inner array with $25 \times 25$ smaller pixels with a pixel size

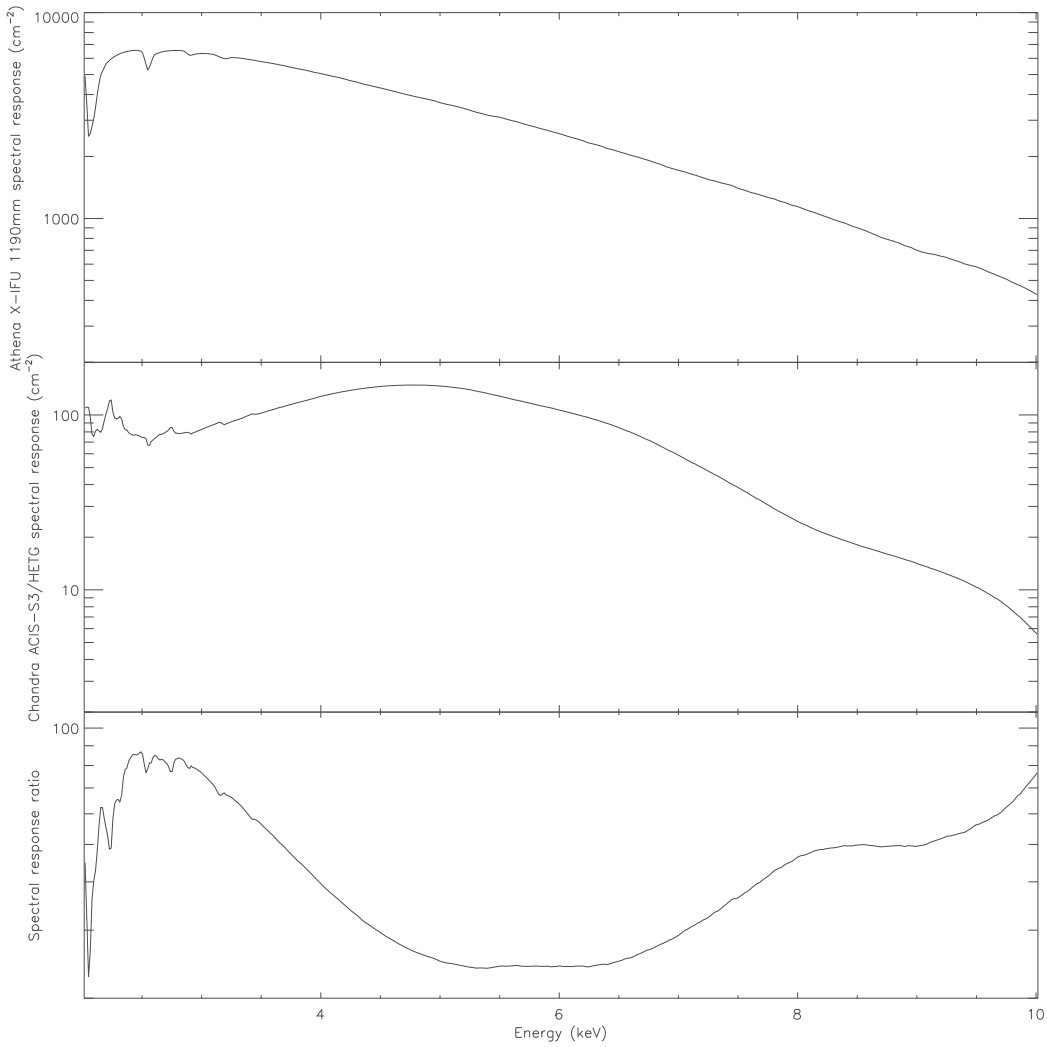


Figure 7.1: Comparison between the effective area of Athena/X-IFU and Chandra. *Top panel:* effective area of the full Athena/X-IFU focal plan for the 1190 mm mirror radii. *Middle panel:* effective area computed for Chandra HETG/ACIS-S3 on a focal plane equivalent to those of Athena/X-IFU. *Bottom panel:* effective area ratio between Athena/X-IFU and Chandra HETG/ACIS-S3.

of about 0.84″.

To compare the detection efficiency of the X-ray flares from Sgr A* with the Bayesian blocks method on the Athena/X-IFU data to those computed for XMM-Newton and Chandra, I make simulations of the Galactic Center as it would be observed by Athena/X-IFU.

I first extract the event lists of the observations made with Chandra HETG/ACIS-S3 during the 2012 Chandra *XVP* campaign and filter out the time ranges when Sgr A* was flaring as it was done in Sect. 3.2. I then create an image of the Galactic Center between 2 and 10 keV with an angular resolution of 0.″5 with these zeroth order filtered event lists (total exposure of 2.82 Ms). I extract the Chandra spectrum and the weighted arf (see middle panel of Fig. 7.1) and rmf from a region corresponding to the full X-IFU focal plane centered on Sgr A*.

To properly reproduce the source distribution at the Galactic Center with the energy, I divide this spectrum in several spectral bands and create the corresponding images. The embedded sources will thus appear only in the spectral bands of higher energy. I use nine spectral bands each containing about $2 \times 10^5$ counts from ACIS-S3 in the zeroth order of HETG: 1.0–2.0, 2.0–3.0, 3.0–3.7, 3.7–4.3, 4.3–5.0, 5.0–6.0, 6.0–7.0, 7.0–9.0 and 9.0 – 10.0 keV. I then create a Chandra image corresponding to each spectral band with an angular resolution of 0.″5.

To assess the flux of this field-of-view in each spectral band, I first compute the number of photons in each spectral band as it would be recorded by Athena/X-IFU. To do so, I use the arf and rmf computed on the full

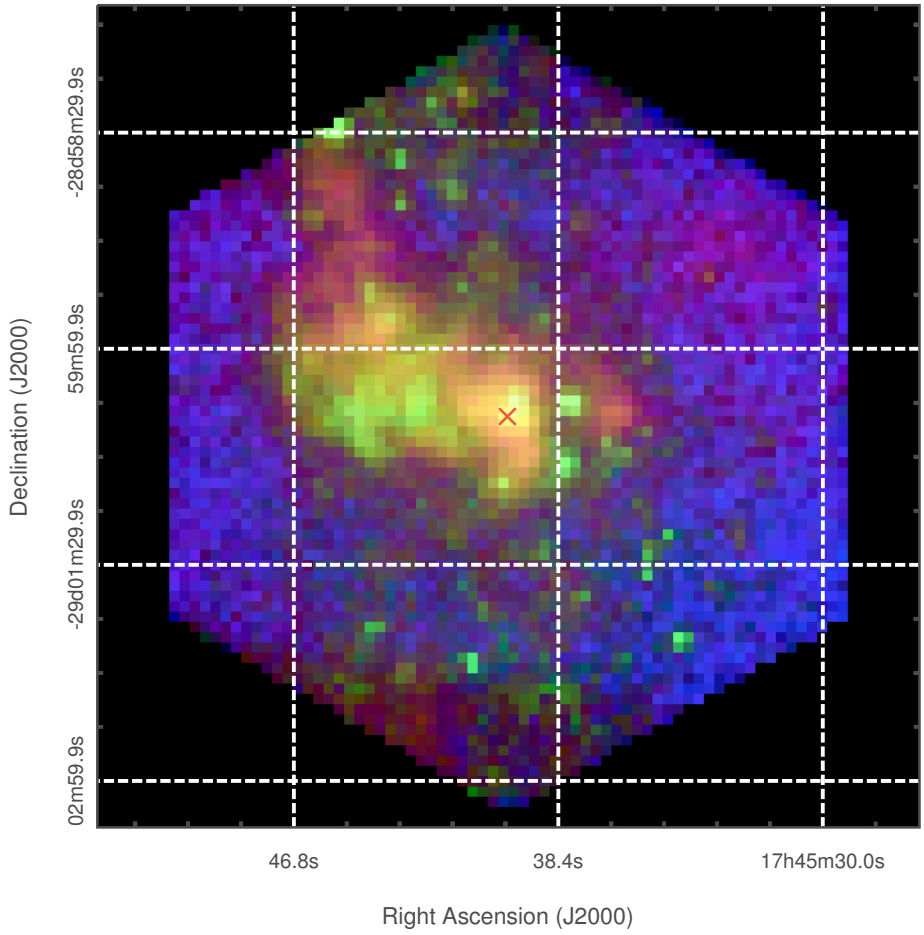


Figure 7.2: Simulated Athena/X-IFU image of the Galactic Center between 1 and 10 keV for a 100 ks exposure when Sgr A* (red cross) is in its quiescent state. The color coding is red=1–3.7 keV, green=3.7–7 keV, blue=7–10 keV. The image intensity (count rate) is in logarithmic scale. The count rate for the three images ranges from $10^{-4}$ count $s^{-1}$ to 0.12 count $s^{-1}$ (the maximum of the red channel).

X-IFU focal plane for the 1190 mm mirror radii of Athena[1] (see upper panel of Fig. 7.1). From the spectral equation (Eq. 3.9):

$$C(i) = T \int_0^\infty R(i,E)\, A(E)\, S(E)\, dE + B(i)\,, \tag{7.1}$$

where $T$ is the time exposure of the spectrum, I assume a background spectrum equal to zero ($B(i) = 0$) and a diagonal redistribution matrix ($R(i,E) = 1$ at the energy $E$ and $R(i,E) = 0$ elsewhere). I thus obtain the following spectral equations for these two instruments:

$$\begin{aligned} C_{\rm Chandra}(E) &= T\, A_{\rm Chandra}(E)\, S(E)\, \Delta E\,, \\ C_{\rm Athena}(E) &= T\, A_{\rm Athena}(E)\, S(E)\, \Delta E\,, \end{aligned} \tag{7.2}$$

with $\Delta E$ the energy width of the spectral channel for Chandra HETG/ACIS-S3 and $A_{\rm Athena}(E)$ and $A_{\rm Chandra}(E)$ the effective area of Athena/X-IFU and Chandra HETG/ACIS-S, respectively, computed for the full X-IFU focal plane. The number of count observed by Athena at an energy $E$ is thus

$$C_{\rm Athena}(E) = \frac{A_{\rm Athena}(E)}{A_{\rm Chandra}(E)}\, C_{\rm Chandra}(E)\,. \tag{7.3}$$

I thus determine the effective area ratio between Athena/X-IFU and Chandra HETG/ACIS-S in each Chandra spectral channel (see bottom panel of Fig. 7.1).

[1]The 1190 mm mirror radii corresponds to the ESA Concurrent Design Facility configuration of Athena with an effective area of the mirror of about 1.37 $m^2$ (Brand et al. 2016); the arf and rmf used here are `athena_xifu_sixte_1190_onaxis_v20150402.arf` and `athena_xifu_sixte_v20150402.rmf`.

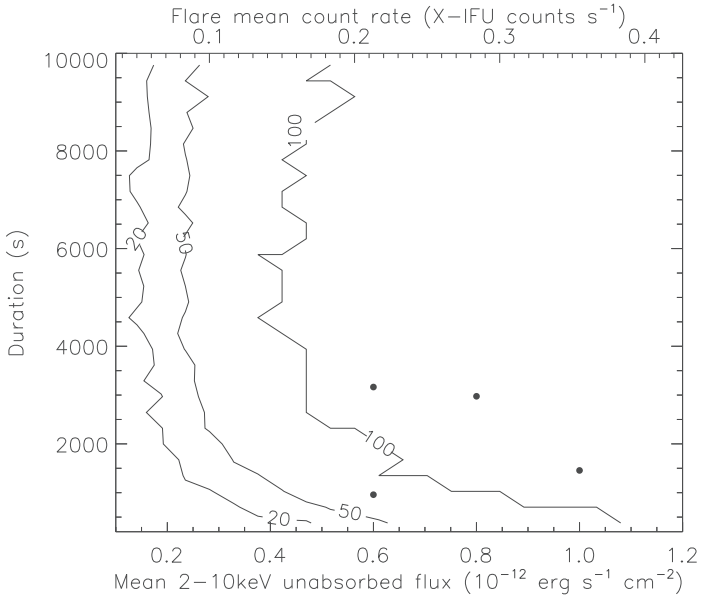


Figure 7.3: Detection efficiency of the Bayesian blocks algorithm for Athena/X-IFU. The points are the X-ray flares detected with Chandra and presented in Sect. 6.4.1.

I use the Simulation of X-ray Telescopes[2] (SIXTE; version 2.1.0 [3]) package making Monte Carlo simulations of event lists using the complete PSF, rmf and arf informations of the telescope. For each spectral band, I create a SIMulation inPUT (SIMPUT) FITS file containing the energy band, the Chandra spectrum in this energy band, the corresponding Chandra image and the flux that I first fix to an arbitrary high value. I simulate the corresponding event lists with the SIXTE task `xifupipeline`. Using the resulting number of counts in each spectral band, I then tune the input flux to match the number of counts predicted from the effective area ratio. I run again the SIXTE task `xifupipeline` on each spectral band with this correct flux. I create the Galactic Center image as observed by Athena/X-IFU by combining the images created by the SIXTE task `imgev` for each simulated event list. The resulting image between 1 and 10 keV for an exposure of 100 ks is shown in Fig. 7.2.

I then extract the src+bkg events in the 2–10 keV energy band from a disk centered on the radio position of Sgr A* with a 5″-radius which is the optimum to increase the signal-to-noise ratio of the flares with a pixel size of 4.21″; the oversampling of the inner array would allow the decay of the radius of the extraction region leading to an increase of the signal-to-noise ratio. The bkg extraction region is a square of $1' \times 1'$ at 1.′64 west of Sgr A*. The background-subtracted non-flaring level in the src+bkg extraction region is about 0.68 count s$^{-1}$ in the 2–10 keV energy range.

I also need to assess the conversion factor between the unabsorbed flux and the count-rate of the flares as observed by Athena/X-IFU. I thus create a new SIMPUT file containing the absorbed powerlaw model for the flare spectrum between 2 and 10 keV with $N_{\rm H} = 14.3 \times 10^{22}$ cm$^{-2}$, $\Gamma = 2$ and an arbitrary high unabsorbed flux. I then use the SIXTE task `xifupipeline` to create the event list corresponding to a point source with an exposure time of 1 ks. I then extract the flaring event list in the 5″-radius disk centered on the radio position of Sgr A*. The number of counts in the resulting event list gives me a conversion factor for Athena/X-IFU of 0.36 count s$^{-1}$/$10^{-12}$ erg s$^{-1}$ cm$^{-2}$.

To test the efficiency of the Bayesian blocks method, I produce synthetic light curves with a Poisson flux with a non-flaring level of 0.68 count s$^{-1}$ as explained in Sect. 3.3. I fix the exposure time to 20 ks and I simulate Gaussian flares peaking at the exposure center and with varying mean count-rates and durations in 0.0001 – 0.5 count s$^{-1}$ and 380 – 10083 s on a linear grid of 30 steps. The resulting detection probability of the Bayesian blocks algorithm is shown in Fig. 7.3 and can be directly compared to those presented in Fig. 6.4.

The overall X-ray flare distribution presented in Sect. 6 would thus be detectable with at least 80% efficiency and the intrinsic flare-flux–duration distribution determined during this Ph.D. thesis would thus

[2] http://www.sternwarte.uni-erlangen.de/research/sixte/

[3] This version 2.1.0 of SIXTE only provides the hexagonal configuration of the X-IFU field-of-view with a pixel size of 4.21″ and without the central oversampling of the inner array.

be testable with Athena X-IFU. Moreover, fainter X-ray flares could also be detected allowing the inverse Compton process to be investigated for the X-ray flare creation. Indeed, considering the NIR flares already observed with a detected X-ray counterpart (see Fig. 5.11), the median NIR amplitude is about 5 mJy in the $K_s$-band. If an X-ray counterpart of this NIR flare is detected with Athena/X-IFU, lets say with a 100% efficiency (i.e., with a mean unabsorbed flux of $10^{-12}$ erg s$^{-1}$ cm$^{-2}$), the time delay predicted by Yusef-Zadeh et al. (2012) for the IC process corresponding to this NIR/X-ray amplitude ratio is about 7 min. The error on the time of the maximum for an X-ray flare with a mean unabsorbed flux of $10^{-12}$ erg s$^{-1}$ cm$^{-2}$ as it will observed with Athena/X-IFU will only be about 2 min while those for a NIR flare as it will be observed by the European Extremely Large Telescope (E-ELT, the ground-based telescope of 39 m-diameter with first light in 2024) with the Multi-AO Imaging Camera for Deep Observations (MICADO, observing in $0.8 - 2.4\,\mu$m; Davies et al. 2016) will probably be lower than 2 min. The time delay between the NIR and X-ray flare will thus be measurable thanks to the E-ELT and Athena. For the fainter X-ray flares, the error on the time of the maximum will be larger but the time delay predicted by the IC process also increase as the square of the NIR–to–X-ray flux ratio, allowing a definitive test for the IC process.

Moreover, the higher number of collected X-ray photons will allow to increase the signal-to-noise ratio of the X-ray flares spectrum and to discriminate between the two other radiative processes for the X-ray flare creation: the synchrotron and synchrotron self-Compton. Indeed, the synchrotron self-Compton process predicts the same spectral index in the NIR and X-ray flare spectra; the higher signal-to-noise ratio of the flare spectrum will lead to a higher accuracy on the spectral index which can be compared to those determined for the NIR flare spectrum.

Finally, we will be able to study the evolution of the spectral index with the flare flux thanks to the higher signal-to-noise ratio of the flare spectrum. The evolution of the spectral index along the flare duration can also be studied. Indeed, for an average mean unabsorbed flux of $10^{-11}$ erg s$^{-1}$ cm$^{-2}$ and an average flare duration of 2700 s, the number of counts observed by Athena/X-IFU will be 9584 from the flare and 1836 from the non-flaring level. The signal-to-noise ratio will thus be about 83. We will thus easily divide the spectrum in at least three spectra, each containing the same number of counts and describing the rise, maximum and decay phase since the resulting signal-to-noise ratio will be about 50.

# Bibliography


Abramowitz, M. & Stegun, I. A. 1970, Handbook of mathematical functions : with formulas, graphs, and mathematical tables (National Bureau of Standards-Applied Mathematics Series)

Aharonian, F., Akhperjanian, A. G., Bazer-Bachi, A. R., et al. 2006, Nature, 439, 695

Anders, E. & Ebihara, M. 1982, Geochimica Cosmochimica Acta, 46, 2363

Arnaud, K., D., B., & G., C. 2015, XSPEC - An X-Ray Spectral Fitting Package - User's Guide for version 12., HEASARC - Astrophysics Science Division, NASA/GSFC, Greenbelt, MD 207

Arnaud, K. A. 1996, in Astronomical Society of the Pacific Conference Series, Vol. 101, Astronomical Data Analysis Software and Systems V, ed. G. H. Jacoby & J. Barnes, 17

Baganoff, F. K., Bautz, M. W., Brandt, W. N., et al. 2001, Nature, 413, 45

Baganoff, F. K., Maeda, Y., Morris, M., et al. 2003, ApJ, 591, 891

Balick, B. & Brown, R. L. 1974, ApJ, 194, 265

Ballet, J. 2005, Should we keep columns adjacent to bad columns for spectral analysis with the EPIC-MOS?, Tech. rep., CEA Saclay [epic-sap-jbb-02v11.ps]

Ballone, A., Schartmann, M., Burkert, A., et al. 2014, in IAU Symposium, Vol. 303, IAU Symposium, ed. L. O. Sjouwerman, C. C. Lang, & J. Ott, 307–311

Band, I. M., Trzhaskovskaia, M. B., Verner, D. A., & Iakovlev, D. G. 1990, A&A, 237, 267

Barret, D., den Herder, J. W., Piro, L., et al. 2013, ArXiv e-prints

Barrière, N. M., Tomsick, J. A., Baganoff, F. K., et al. 2014, ApJ, 786, 46

Barthelmy, S. D., Barbier, L. M., Cummings, J. R., et al. 2005, Space Sci. Rev., 120, 143

Beardmore, A. P., Godet, O., Abbey, A. F., et al. 2006, 836, 708

Beasley, A. J. & Vogel, S. N. 2003, in Proc. SPIE, Vol. 4855, Millimeter and Submillimeter Detectors for Astronomy, ed. T. G. Phillips & J. Zmuidzinas, 254–264

Blumenthal, G. R. & Gould, R. J. 1970, Reviews of Modern Physics, 42, 237

Bondi, H. 1952, MNRAS, 112, 195

Bondi, H. & Hoyle, F. 1944, MNRAS, 104, 273

Bonnet, H., Abuter, R., Baker, A., et al. 2004, The Messenger, 117, 17

Bouvier, J., Alencar, S. H. P., Harries, T. J., Johns-Krull, C. M., & Romanova, M. M. 2007, Protostars and Planets V, 479

Bower, G. C., Markoff, S., Dexter, J., et al. 2015, ApJ, 802, 69

Bradt, H. 2008, Astrophysics Processes (Cambridge University Press)

Brand, T., Dauser, T., & Wilms. 2016, Athena X-IFU response files. ECAP-XIFU-RSP-005, Tech. rep.

Brinkerink, C. D., Falcke, H., Law, C. J., et al. 2015, A&A, 576, A41

Broderick, A. E., Fish, V. L., Doeleman, S. S., & Loeb, A. 2011, ApJ, 735, 110

Broderick, A. E. & Loeb, A. 2005, MNRAS, 363, 353

Brown, R. L. 1982, ApJ, 262, 110

Burkert, A., Schartmann, M., Alig, C., et al. 2012, ApJ, 750, 58

Camenzind, M. 1990, 3, 234

Cash, W. 1979, ApJ, 228, 939

Chan, C.-k., Psaltis, D., Özel, F., et al. 2015, ApJ, 812, 103

Coil, A. L. & Ho, P. T. P. 2000, ApJ, 533, 245

Coti Zelati, F., Rea, N., Papitto, A., et al. 2015, MNRAS, 449, 2685

Cox, A. N. 2000, Allen's astrophysical quantities

Czerny, B., Kunneriath, D., Karas, V., & Das, T. K. 2013, A&A, 555, A97

Davies, R., Schubert, J., Hartl, M., et al. 2016, ArXiv e-prints

Davis, J. E. 2001, ApJ, 562, 575
Degenaar, N., Miller, J. M., Kennea, J., et al. 2013, ApJ, 769, 155
Degenaar, N., Reynolds, M. T., Wijnands, R., et al. 2016, The Astronomer's Telegram, 9109
Degenaar, N., Wijnands, R., Miller, J. M., et al. 2015, Journal of High Energy Astrophysics, 7, 137
Dodds-Eden, K., Porquet, D., Trap, G., et al. 2009, ApJ, 698, 676
Doeleman, S. S., Weintroub, J., Rogers, A. E. E., et al. 2008, Nature, 455, 78
Drake, F. D. 1959, AJ, 64, 329
Dressel, L. 2012, Wide Field Camera 3 Instrument Handbook for Cycle 21 v. 5.0 (Baltimore: STScI)
Dwelly, T. & Ponti, G. 2013, The Astronomer's Telegram, 5008, 1
Eatough, R. P., Falcke, H., Karuppusamy, R., et al. 2013, Nature, 501, 391
Eckart, A., Baganoff, F. K., Morris, M., et al. 2004, A&A, 427, 1
Eckart, A., Baganoff, F. K., Morris, M. R., et al. 2009, A&A, 500, 935
Eckart, A., Baganoff, F. K., Schödel, R., et al. 2006a, A&A, 450, 535
Eckart, A., García-Marín, M., Vogel, S. N., et al. 2012, A&A, 537, A52
Eckart, A. & Genzel, R. 1999, in The Physics and Chemistry of the Interstellar Medium, ed. V. Ossenkopf, J. Stutzki, & G. Winnewisser
Eckart, A., Mužić, K., Yazici, S., et al. 2013, A&A, 551, A18
Eckart, A., Schödel, R., García-Marín, M., et al. 2008, A&A, 492, 337
Eckart, A., Schödel, R., Meyer, L., et al. 2006b, A&A, 455, 1
Eisenhauer, F., Genzel, R., Alexander, T., et al. 2005, ApJ, 628, 246
Ekers, R. D., van Gorkom, J. H., Schwarz, U. J., & Goss, W. M. 1983, A&A, 122, 143
ESA: XMM-Newton SOC. 2013, XMM-Newton Users Handbook, Issue 2.11
Falcke, H., Goss, W. M., Matsuo, H., et al. 1998, ApJ, 499, 731
Falcke, H. & Markoff, S. 2000, A&A, 362, 113
Fay, M. P. 2010, The R Journal, 2/1, 53 [online version]
Feigelson, E. D. & Babu, G. J. 2012, Modern statistical method for astronomy with R applications, ed. Cambridge University Press (Cambridge, UK)
Fish, V. L., Johnson, M. D., Doeleman, S. S., et al. 2016, ApJ, 820, 90
Foreman-Mackey, D., Hogg, D. W., Lang, D., & Goodman, J. 2013, PASP, 125, 306
Fritz, T. K., Gillessen, S., Dodds-Eden, K., et al. 2011, ApJ, 737, 73
Garmire, G. P., Bautz, M. W., Ford, P. G., Nousek, J. A., & Ricker, Jr., G. R. 2003, in Society of Photo-Optical Instrumentation Engineers (SPIE) Conference Series, Vol. 4851, X-Ray and Gamma-Ray Telescopes and Instruments for Astronomy., ed. J. E. Truemper & H. D. Tananbaum, 28–44
Gehrels, N. 1986, ApJ, 303, 336
Gehrels, N., Barthelmy, S. D., Baumgartner, W. H., et al. 2013, The Astronomer's Telegram, 5037, 1
Gehrels, N., Chincarini, G., Giommi, P., et al. 2004, ApJ, 611, 1005
Gelman, A., Roberts, G., & Gilks, W. 1996, Efficient Metropolis jumping rules, ed. J. Bernardo (Oxford University Press)
Genzel, R., Schödel, R., Ott, T., et al. 2003, Nature, 425, 934
Georganopoulos, M., Kirk, J. G., & Mastichiadis, A. 2001, ApJ, 561, 111
Ghez, A. M., Klein, B. L., Morris, M., & Becklin, E. E. 1998, ApJ, 509, 678
Ghez, A. M., Salim, S., Weinberg, N. N., et al. 2008, ApJ, 689, 1044
Ghez, A. M., Wright, S. A., Matthews, K., et al. 2004, ApJL, 601, L159
Gillessen, S., Eisenhauer, F., Fritz, T. K., et al. 2009a, ApJL, 707, L114
Gillessen, S., Eisenhauer, F., Trippe, S., et al. 2009b, ApJ, 692, 1075
Gillessen, S., Genzel, R., Fritz, T. K., et al. 2013a, ApJ, 763, 78
Gillessen, S., Genzel, R., Fritz, T. K., et al. 2013b, ApJ, 774, 44
Gillessen, S., Genzel, R., Fritz, T. K., et al. 2012, Nature, 481, 51
Goodman, J. & Weare, J. 2010, Communications in Applied Mathematics and Computational Science, 5, 65
Gotthelf, E. V., Mori, K., Halpern, J. P., et al. 2013, The Astronomer's Telegram, 5046, 1
Guainazzi, M. 2013, XMM-Newton Calibration Technical Note; XMM-SOC-CAL-TN-0018, Calibration status document, ESA-ESAC, Villafranca del Castillo, Spain
Guo, F. & Mathews, W. G. 2012, ApJ, 756, 181
Hamaus, N., Paumard, T., Müller, T., et al. 2009, ApJ, 692, 902

Harrod, S. & Kelton, W. D. 2013, SIMULATION, 82, 147
Herrnstein, R. M. & Ho, P. T. P. 2005, ApJ, 620, 287
Hornstein, S. D., Matthews, K., Ghez, A. M., et al. 2007, ApJ, 667, 900
Houck, J. C. 2013, ISIS 1.0 Technical Manual, Chandra X-Ray Observatory Center, MIT Center for Space Research One Hampshire St. Building NE80 Cambridge, MA 021394307 USA
Huba, J. 2013, NRL PLASMA FORMULARY (Washington, DC: Naval Research Lab.)
Hüttemeister, S. 2003, The Milky Way: structure, constituents and evolution, ed. H. Falcke & F. W. Hehl (IoP, Institute of Physics), 35–71
Ichimaru, S. 1977, ApJ, 214, 840
Jansen, F., Lumb, D., Altieri, B., et al. 2001, A&A, 365, L1
Jansky, K. G. 1933, Nature, 132, 66
Johannsen, T., Psaltis, D., Gillessen, S., et al. 2012, ApJ, 758, 30
Kaspi, V. M., Archibald, R. F., Bhalerao, V., et al. 2014, ApJ, 786, 84
Kassim, N. E., Larosa, T. N., Lazio, T. J. W., & Hyman, S. D. 1999, in Astronomical Society of the Pacific Conference Series, Vol. 186, The Central Parsecs of the Galaxy, ed. H. Falcke, A. Cotera, W. J. Duschl, F. Melia, & M. J. Rieke, 403
Kennea, J. A., Burrows, D. N., Kouveliotou, C., et al. 2013a, ApJL, 770, L24
Kennea, J. A., Krimm, H., Barthelmy, S., et al. 2013b, The Astronomer's Telegram, 5009, 1
Kerr, R. P. 1963, Phys. Rev. Lett., 11, 237
Klein, R. W. & Roberts, S. D. 1984, SIMULATION, 43, 193
Kostić, U., Čadež, A., Calvani, M., & Gomboc, A. 2009, A&A, 496, 307
Kraft, R. P., Burrows, D. N., & Nousek, J. A. 1991, ApJ, 374, 344
Lang, K. R. 1999, Astrophysical Formulae, 3rd edn., Vol. 1 (Springer)
Lenzen, R., Hartung, M., Brandner, W., et al. 2003, in Society of Photo-Optical Instrumentation Engineers (SPIE) Conference Series, Vol. 4841, Instrument Design and Performance for Optical/Infrared Ground-based Telescopes, ed. M. Iye & A. F. M. Moorwood, 944–952
Liu, S., Petrosian, V., Melia, F., & Fryer, C. L. 2006, ApJ, 648, 1020
Longair, M. S. 1994, High Energy Astrophysics, ed. Cambridge University Press, Vol. 2 (Cambridge University Press)
Lynch, R. S., Archibald, R. F., Kaspi, V. M., & Scholz, P. 2015, ApJ, 806, 266
Mamajek, E. E., Prsa, A., Torres, G., et al. 2015, ArXiv e-prints
Maoz, D. 2008, Journal of Physics Conference Series, 131, 012036
Markoff, S., Falcke, H., Yuan, F., & Biermann, P. L. 2001, A&A, 379, L13
Marrone, D. P., Baganoff, F. K., Morris, M. R., et al. 2008, ApJ, 682, 373
Marrone, D. P., Moran, J. M., Zhao, J.-H., & Rao, R. 2006, Journal of Physics Conference Series, 54, 354
Marrone, D. P., Moran, J. M., Zhao, J.-H., & Rao, R. 2007, ApJL, 654, L57
Marscher, A. P. 1983, ApJ, 264, 296
Meyer, L., Ghez, A. M., Schödel, R., et al. 2012, Science, 338, 84
Meyer, L., Schödel, R., Eckart, A., et al. 2006, A&A, 458, L25
Meyer, L., Witzel, G., Longstaff, F. A., & Ghez, A. M. 2014, ApJ, 791, 24
Mori, K., Gotthelf, E. V., Barriere, N. M., et al. 2013a, The Astronomer's Telegram, 5020
Mori, K., Gotthelf, E. V., Zhang, S., et al. 2013b, ApJL, 770, L23
Morris, M. 2012, Nature, 481, 32
Morrison, R. & McCammon, D. 1983, ApJ, 270, 119
Mościbrodzka, M., Shiokawa, H., Gammie, C. F., & Dolence, J. C. 2012, ApJL, 752, L1
Mossoux, E., Grosso, N., Bushouse, H., et al. 2016, A&A, 589, A116
Mossoux, E., Grosso, N., Vincent, F. H., & Porquet, D. 2015a, A&A, 573, A46
Mossoux, E., Grosso, N., Vincent, F. H., & Porquet, D. 2015b, A&A, 580, C2
Muno, M. P., Lu, J. R., Baganoff, F. K., et al. 2005a, ApJ, 633, 228
Muno, M. P., Pfahl, E., Baganoff, F. K., et al. 2005b, ApJL, 622, L113
Murray, S. S., Chappell, J. H., Kenter, A. T., et al. 1998, in Proc. SPIE, Vol. 3356, Space Telescopes and Instruments V, ed. P. Y. Bely & J. B. Breckinridge
Nandra, K., Barret, D., Barcons, X., et al. 2013, ArXiv e-prints
Narayan, R., Mahadevan, R., Grindlay, J. E., Popham, R. G., & Gammie, C. 1998, ApJ, 492, 554

Narayan, R. & Yi, I. 1994, ApJL, 428, L13
Narayan, R., Yi, I., & Mahadevan, R. 1995, Nature, 374, 623
Nayakshin, S., Cuadra, J., & Sunyaev, R. 2004, A&A, 413, 173
Nayakshin, S. & Sunyaev, R. 2003, MNRAS, 343, L15
Neilsen, J., Markoff, S., Nowak, M. A., et al. 2015, ApJ, 799, 199
Neilsen, J., Nowak, M. A., Gammie, C., et al. 2013, ApJ, 774, 42
Nowak, M. A., Neilsen, J., Markoff, S. B., et al. 2012, ApJ, 759, 95
Oort, J. H. 1930, Bull. Astron. Inst. Netherlands, 5, 192
Petrov, L., Kovalev, Y. Y., Fomalont, E. B., & Gordon, D. 2011, AJ, 142, 35
Pfuhl, O., Gillessen, S., Eisenhauer, F., et al. 2015, ApJ, 798, 111
Phifer, K., Do, T., Meyer, L., et al. 2013, ApJL, 773, L13
Ponti, G., De Marco, B., Morris, M. R., et al. 2015, MNRAS, 454, 1525
Porquet, D., Grosso, N., Bélanger, G., et al. 2005, A&A, 443, 571
Porquet, D., Grosso, N., Predehl, P., et al. 2008, A&A, 488, 549
Porquet, D., Predehl, P., Aschenbach, B., et al. 2003, A&A, 407, L17
Predehl, P. & Schmitt, J. H. M. M. 1995, A&A, 293, 889
Press, W. H., Teukolsky, S. A., Vetterling, W. T., & Flannery, B. P. 1992, Numerical Recipes in Fortran (2nd Ed.) (New York, NY, USA: Cambridge University Press)
Rau, A., Meidinger, N., Nandra, K., et al. 2013, ArXiv e-prints
Rauch, C., Ros, E., Krichbaum, T. P., et al. 2016, A&A, 587, A37
Rea, N., Esposito, P., Pons, J. A., et al. 2013, ApJL, 775, L34
Rees, M. J., Begelman, M. C., Blandford, R. D., & Phinney, E. S. 1982, Nature, 295, 17
Reid, M. J. & Brunthaler, A. 2004, ApJ, 616, 872
Reid, M. J., Menten, K. M., Brunthaler, A., et al. 2014, ApJ, 783, 130
Reid, M. J., Readhead, A. C. S., Vermeulen, R. C., & Treuhaft, R. N. 1999, ApJ, 524, 816
Reynolds, M., Kennea, J., Degenaar, N., Wijnands, R., & Miller, J. 2016, The Astronomer's Telegram, 8649
Rieke, G. H., Rieke, M. J., & Paul, A. E. 1989, ApJ, 336, 752
Rose, S., Debes, J., & Downes, R. 2016, Tech. rep., STScI
Rousset, G., Lacombe, F., Puget, P., et al. 2003, in Society of Photo-Optical Instrumentation Engineers (SPIE) Conference Series, Vol. 4839, Adaptive Optical System Technologies II, ed. P. L. Wizinowich & D. Bonaccini, 140–149
Rybicki, G. B. & Lightman, A. P. 1979, Radiative processes in astrophysics (Wiley VCH)
Scargle, J. D. 1998, ApJ, 504, 405
Scargle, J. D., Norris, J. P., Jackson, B., & Chiang, J. 2013a, ApJ, 764, 167
Scargle, J. D., Norris, J. P., Jackson, B., & Chiang, J. 2013b, in The Bayesian Block Algorithm, 2012 Fermi Symp. Proc. – eConf C121028 [arXiv:1304.2818v1]
Scargle, J. D., Norris, J. P., Jackson, B., & Chiang, J. 2013c, ArXiv e-prints
Schaap, W. E. & van de Weygaert, R. 2000, A&A, 363, L29
Schödel, R., Najarro, F., Muzic, K., & Eckart, A. 2010, A&A, 511, A18
Schödel, R., Ott, T., Genzel, R., et al. 2002, Nature, 419, 694
Schwarzschild, K. 1916, Abh. Konigl. Preuss. Akad. Wissenschaften Jahre 1906,92, Berlin,1907, 1916, 189
Shahzamanian, B., Eckart, A., Valencia-S., M., et al. 2015, A&A, 576, A20
Shakura, N. I. & Sunyaev, R. A. 1973, A&A, 24, 337
Shannon, R. M. & Johnston, S. 2013, MNRAS, 435, L29
Shapley, H. & Curtis, H. D. 1921, Bulletin of the National Research Council, Vol. 2, Part 3, No. 11, p. 171-217, 2, 171
Shvartsman, V. F. 1971, Sov. Astron.-AJ, 15, 377
Sidoli, L. & Mereghetti, S. 1999, A&A, 349, L49
Silverman, B. W. 1986, Density Estimation for Statistics and Data Analysis, ed. C. . Hall (Chapman & Hall)
Slysh, V. I. 2008, Astronomy Reports, 52, 343
Stelzer, B., Flaccomio, E., Briggs, K., et al. 2007, A&A, 468, 463
Strüder, L., Briel, U., Dennerl, K., et al. 2001, A&A, 365, L18
Su, M., Slatyer, T. R., & Finkbeiner, D. P. 2010, ApJ, 724, 1044
Tagger, M. & Melia, F. 2006, ApJL, 636, L33

Trap, G., Goldwurm, A., Dodds-Eden, K., et al. 2011, A&A, 528, A140
Trippe, S., Paumard, T., Ott, T., et al. 2007, MNRAS, 375, 764
Trumpler, R. J. 1930, PASP, 42, 214
Turner, M. J. L., Abbey, A., Arnaud, M., et al. 2001, A&A, 365, L27
Čadež, A., Calvani, M., Gomboc, A., & Kostić, U. 2006, in American Institute of Physics Conference Series, Vol. 861, Albert Einstein Century International Conference, ed. J.-M. Alimi & A. Füzfa, 566–571
Čadež, A., Calvani, M., & Kostić, U. 2008, A&A, 487, 527
Valencia-S., M., Eckart, A., Zajaček, M., et al. 2015, ApJ, 800, 125
van de Weygaert, R. & Schaap, W. 2009, in Lecture Notes in Physics, Berlin Springer Verlag, Vol. 665, Data Analysis in Cosmology, ed. V. J. Martínez, E. Saar, E. Martínez-González, & M.-J. Pons-Bordería, 291–413
van der Laan, H. 1963, MNRAS, 126, 535
Van der Laan, H. 1966, Nature, 211, 1131
Verner, D. A., Ferland, G. J., Korista, K. T., & Yakovlev, D. G. 1996, ApJ, 465, 487
Verner, D. A. & Yakovlev, D. G. 1995, Astronomy and Astrophysics, Supplement, 109
Vincent, F. H., Paumard, T., Gourgoulhon, E., & Perrin, G. 2011, Classical and Quantum Gravity, 28, 225011
Wang, Q. D., Gotthelf, E. V., & Lang, C. C. 2002, Nature, 415, 148
Wang, Q. D., Nowak, M. A., Markoff, S. B., et al. 2013, Science, 341, 981
Wardle, M. & Yusef-Zadeh, F. 2014, ApJL, 787, L14
Weisskopf, M. C. 1999, ArXiv Astrophysics e-prints
Wilms, J., Allen, A., & McCray, R. 2000, ApJ, 542, 914
Witzel, G., Eckart, A., Bremer, M., et al. 2012, ApJS, 203, 18
Witzel, G., Ghez, A. M., Morris, M. R., et al. 2014a, ApJL, 796, L8
Witzel, G., Morris, M., Ghez, A., et al. 2014b, in IAU Symposium, Vol. 303, IAU Symposium, ed. L. O. Sjouwerman, C. C. Lang, & J. Ott, 274–282
Worpel, H. & Schwope, A. D. 2015, A&A, 578, A80
Yan, M., Sadeghpour, H. R., & Dalgarno, A. 1998, ApJ, 496, 1044
Yuan, F., Lin, J., Wu, K., & Ho, L. C. 2009, MNRAS, 395, 2183
Yuan, F. & Narayan, R. 2014, ARA&A, 52, 529
Yuan, F., Quataert, E., & Narayan, R. 2003, ApJ, 598, 301
Yuan, F., Quataert, E., & Narayan, R. 2004, ApJ, 606, 894
Yuan, Q. & Wang, Q. D. 2016, MNRAS, 456, 1438
Yusef-Zadeh, F., Bushouse, H., Dowell, C. D., et al. 2006a, ApJ, 644, 198
Yusef-Zadeh, F., Bushouse, H., Wardle, M., et al. 2009, ApJ, 706, 348
Yusef-Zadeh, F., Morris, M., & Chance, D. 1984, Nature, 310, 557
Yusef-Zadeh, F., Roberts, D., Wardle, M., Heinke, C. O., & Bower, G. C. 2006b, ApJ, 650, 189
Yusef-Zadeh, F., Wardle, M., Bushouse, H., Dowell, C. D., & Roberts, D. A. 2010, ApJL, 724, L9
Yusef-Zadeh, F., Wardle, M., Dodds-Eden, K., et al. 2012, AJ, 144, 1
Yusef-Zadeh, F., Wardle, M., Heinke, C., et al. 2008, ApJ, 682, 361
Zhao, J.-H. 2003, Astronomische Nachrichten Supplement, 324, 355
Zhao, J.-H., Bower, G. C., & Goss, W. M. 2001, ApJL, 547, L29
Zubovas, K., King, A. R., & Nayakshin, S. 2011, MNRAS, 415, L21
Zubovas, K., Nayakshin, S., & Markoff, S. 2012, MNRAS, 421, 1315

# Résumé en français

## 7.1 Contexte du travail

Une source radio non-résolue a été découverte au centre de notre galaxie en 1974. Il s'agit de Sgr A* qui est le trou noir supermassif (4 millions de masses solaire; Schödel et al. 2002; Meyer et al. 2012) le plus proche de nous (à une distance de 8 kpc; Reid et al. 2014). Sa luminosité intégrée sur toutes les longueurs d'onde est 4,5 milliards de fois plus faible que la luminosité d'Eddington attendue pour une accrétion sphérique sur un trou noir supermassif de la masse de Sgr A*. Plusieurs modèles sont proposés pour expliquer cette faible luminosité comme, par exemple, des modèles de flot d'accrétion chaud (ADAF, *Advection Dominated Accretion Flow*; Rees et al. 1982; Narayan & Yi 1994; Narayan et al. 1995, 1998) ou des modèles de jets (Falcke & Markoff 2000; Slysh 2008). Superposées à cette faible luminosité constante, appelée état quiescent, des éruptions sont détectées en infrarouge proche (NIR), rayons X et radio (millimétrique et centimétrique).

Les éruptions en NIR sont produites par le rayonnement synchrotron émis par des électrons accélérés autour des lignes de champ magnétique, tandis que l'origine des éruptions en rayons X est encore débattue. Trois interprétations sont avancées: le rayonnement direct synchrotron (SYN; Dodds-Eden et al. 2009; Barrière et al. 2014), le processus Inverse Compton (IC; Yusef-Zadeh et al. 2012) et le processus synchrotron self-Compton (SSC; Eckart et al. 2008). Le processus IC produit des photons X soit par la diffusion des photons submillimétriques continuellement produits par les électrons du flot d'accrétion sur les électrons accélérés produisant les photons NIR soit par la diffusion de ces photons NIR sur les électrons du flot d'accrétion. Ce second processus implique un délai entre le maximum des éruptions en NIR et en rayons X. Dans le processus SSC, les photons NIR sont diffusés par les électrons accélérés qui produisent ces photons NIR. Les éruptions en radio sont différées de quelques minutes à quelques heures par rapport à l'émission NIR/X. Le modèle du refroidissement adiabatique d'un plasmon en expansion permet de décrire ce délai mais les paramètres du plasmon restent difficile à contraindre. L'analyse multi-longueurs d'onde (NIR, rayons X et radio) de ces éruptions devrait nous permettre de mieux comprendre l'origine des éruptions de Sgr A* ainsi que d'autres trous noirs supermassif de faible luminosité se trouvant au centre de la plupart des galaxies massives.

Les observations du centre galactique entre 2004 et 2011 ont permis de détecter un objet appelé G2 sur une orbite très elliptique se rapprochant de Sgr A* (Gillessen et al. 2012). Les raies d'émission de G2 étaient alors décalées vers le rouge impliquant que G2 n'avait pas encore franchit son périastre. Les premières interprétations associaient cet objet à un nuage de gaz compact ou une coquille sphérique de gaz qui, à l'approche du trou noir, serait déchiqueté par les forces de marées et alimenterait Sgr A* (Burkert et al. 2012; Gillessen et al. 2013a,b). L'activité du trou noir supermassif devrait alors augmenter dans toutes les longueurs d'ondes. La possibilité d'une étoile entourée d'une coquille de poussière et de gaz (*a Dusty S-cluster Object*; DSO) a aussi été proposée (Eckart et al. 2013; Witzel et al. 2014a; Valencia-S. et al. 2015). La matière circumstellaire serait alors soumise à l'attraction gravitationnelle de l'étoile centrale et le transfert de matière vers Sgr A* serait alors plus faible.

Cette thèse a pour but d'étudier les effets du possible transfert de matière de DSO/G2 vers Sgr A* lors de son passage au périastre sur l'émission quiescente et éruptive du trou noir supermassif. Des changements d'émission pourraient nous apporter des informations sur le DSO/G2 et sur le flot d'accrétion chaud autour de Sgr A*. J'ai principalement utilisé les observations obtenues avec le satellite XMM-Newton qui est composé de trois *European Photon Imaging Camera* (EPIC/pn, MOS1 et MOS2) observant en rayons X. Les données collectées lors d'une observation en rayons X forment une liste d'événements qui donne les caractéristiques des événements enregistrés par le CCD (énergie, temps d'arrivée, position,...). Lors de cette thèse, j'ai utilisé et amélioré deux méthodes permettant une meilleure analyse temporelle des événements recueillis lors des observations en rayons X. J'ai aussi utilisé la méthode de Monte-Carlo par chaînes de Markov pour améliorer

l'analyse spectrale des éruptions.

## 7.2 Outils d'analyse pour l'étude en rayons X

### 7.2.1 L'algorithme des blocs Bayésiens pour la détection des éruptions

J'ai utilisé l'algorithme des blocs Bayésiens (blocs Bayésiens) développé par Scargle (1998) et amélioré par Scargle et al. (2013a,b) pour détecter les éruptions de manière systématique à partir des temps d'arrivée individuels des photons X sur le détecteur (résolution temporelle de 73,4 ms pour pn à 2,6 s pour MOS) tout en contrôlant la probabilité de fausse détection. Cet algorithme permet aussi d'obtenir une meilleure précision sur le début et la fin des éruptions contrairement aux méthodes de détection précédemment employées qui utilisent la liste d'événements groupés par intervalles de temps de 100 ou 300s, c'est-à-dire la courbe de lumière.

Cet algorithme permet de segmenter de manière optimale la liste de photons X en se basant sur l'inférence Bayésienne appliquée à la statistique de Poisson. Un flux de Poisson continu est obtenu à partir des temps d'arrivées des événements observés en supprimant les intervalles de temps où le détecteur est contaminé par des particules ionisantes. Des cellules de Voronoï sont ensuite créées contenant chacune un seul photon et dont le début et la fin sont définit comme la moitié de l'intervalle entre deux photons consécutifs. Le début et la fin de la première et de la dernière cellule sont définis par le début et la fin de l'observation. Le taux de comptage de chaque cellule est donc l'inverse de sa durée. L'algorithme considère d'abord l'ensemble des cellules afin de déterminer si le taux de comptage est statistiquement constant ou s'il peut être mieux décrit par deux blocs avec des taux de comptage différents et dont le temps de séparation est appelé un point de changement. Si c'est le cas, il recommence ce test sur chacun des blocs afin de les segmenter ou pas. Le résultat de cette itération est une courbe de lumière composée de blocs de taux de comptage (CR) constants.

Le *prior* du nombre de points de changement (*ncp_prior*) est contrôlé par deux paramètres: le nombre d'événements enregistrés durant une observation ($N$) et le taux de faux positif ($p_1$), c'est-à-dire la probabilité qu'un point de changement soit une fausse détection. J'ai calibré le *ncp_prior* en appliquant les blocs Bayésiens sur un grand nombre de listes de $N$ événements simulées, décrivant un flux de Poisson de moyenne égale au taux de comptage du quiescent. Le *prior* à utiliser est le *ncp_prior* le plus grand qui génère un taux de fausse détection égal à celui que je souhaite utiliser (par exemple $p_1 = 0,03$ impliquant une probabilité de faux positif pour une éruption de $p_1^2 = 9 \times 10^{-4}$; Neilsen et al. 2013; Nowak et al. 2012).

Afin de corriger du bruit instrumental du CCD, j'ai créé un algorithme en deux étapes: j'ai d'abord appliqué les blocs Bayésiens sur une liste d'événements représentative du bruit (bkg) extraite sur une large zone du CCD où les sources ponctuelles d'émission en rayons X ont été retirées, ainsi que sur la liste d'événements extraite de la région de 10″ de rayon centrée sur Sgr A* (src+bkg) qui contient donc les événements émis par Sgr A* mais aussi ceux d'autres sources non résolues et le bruit instrumental. J'ai finalement utilisé une deuxième fois les blocs Bayésiens sur les événements src+bkg en appliquant le poids $w = CR_{\mathrm{src+bkg}}/(CR_{\mathrm{src+bkg}} - CR_{\mathrm{bkg}})$ aux cellules de Voronoï.

J'ai aussi tenu compte de l'arrivée simultanée de plusieurs photons et de l'exposition effective de la caméra en appliquant un deuxième poids sur les cellules de Voronoï.

Après calibration du *ncp_prior* et application de l'algorithme en deux étapes sur les listes d'événements, nous pouvons facilement identifier l'état quiescent comme étant le taux de comptage du bloc le plus faible et le mieux contraint et les éruptions qui sont décrites par les blocs de plus grands taux de comptage.

Afin de déterminer la probabilité de détection des éruptions avec les blocs Bayésiens en fonction de leur amplitude et de leur durée, j'ai simulé un grand nombre de listes d'événements décrites par un flux de Poisson de moyenne égale au taux de comptage du quiescent plus une gaussienne représentant l'éruption avec différentes durées et amplitudes. J'ai ensuite appliqué les blocs Bayésiens sur chacune de ces listes d'événements et enregistré la probabilité qu'une éruption avec une certaine amplitude et une certaine durée puisse être détectée. Cette méthode permet aussi de comparer la probabilité de détection pour différents satellites caractérisés par différentes résolutions angulaires et différentes sensibilités impliquant différentes valeurs pour le taux de comptage du quiescent.

### 7.2.2 Amélioration de la courbe de lumière

Afin de diminuer le bruit Poissonnien de la courbe de lumière et de mieux rendre compte de la continuité des phénomènes d'émission, j'ai appliqué un estimateur de densité qui effectue une convolution des événements avec un noyau de lissage d'Epanechnikov. Ce noyau de lissage est une parabole inversée définie sur un support fini, ce qui permet de prendre en compte les effets de bord. L'exposition effective de la caméra et le bruit instrumental sont corrigés en appliquant les poids calculés précédemment.

### 7.2.3 Utilisation des chaînes de Markov pour l'ajustement des modèles spectraux

Le spectre des éruptions est créé en groupant les événements extraits de la région src+bkg par intervalle d'énergie définit par un rapport signal à bruit minimum. Je sélectionne les événements qui ont été enregistrés durant l'éruption (dont le début et la fin sont donnés par les blocs Bayésiens) afin de créer le spectre de l'éruption que je corrige du spectre enregistré durant l'état quiescent.

Le modèle ajustant le mieux le spectre de l'éruption est une loi de puissance absorbée par le gaz (absorption photoélectrique) et les poussières (diffusion) des nuages moléculaires sur la ligne de visée. L'absorption est caractérisée par une colonne d'hydrogène combinant l'effet de la diffusion par les poussières (Predehl & Schmitt 1995) et l'absorption photoélectrique par le gaz, les molécules et les poussières (Wilms et al. 2000).

Afin d'ajuster ce modèle aux spectres observés, j'ai utilisé le programme `XSPEC_emcee` de Jeremy Sanders qui permet l'analyse par la méthode de Monte-Carlo par chaînes de Markov (MCMC) des spectres en rayons X avec `XSPEC` en utilisant `emcee`, une implémentation sous `Python` de l'échantillonneur de Goodman & Weare (2010). Le MCMC utilise un ensemble de marcheurs indépendants qui évoluent dans l'espace des paramètres en convergeant vers la distribution marginale de chacun des paramètres spectraux décrivant le spectre observé. L'ajustement des paramètres spectraux s'effectue en utilisant la statistique de $\chi^2$ sur le spectre groupé. La chaîne de Markov finale contient les valeurs des paramètres qu'ont pris les marcheurs à chaque pas de l'algorithme. Après une vérification *a posteriori* de la convergence des marcheurs, la meilleure valeur de chaque paramètre est donnée par la médiane (quantile à 50%) de sa distribution marginale. L'intervalle de confiance à 90% est donné par les quantiles à 5 et 95% des distributions marginales.

## 7.3 La campagne d'observation de Sgr A* avec XMM-Newton en 2011

J'ai d'abord validé ces outils d'analyse avec la campagne d'observation de 2011. Cette campagne comprend quatre observations effectuées avec XMM-Newton pour un total de 226 ks (responsable principal, PI: Delphine Porquet, *Observatoire Astronomique de Strasbourg*). Deux éruptions ont été détectées grâce à l'algorithme des blocs Bayésiens: la première le 30 mars et la seconde le 3 avril 2011. La première éruption présente une forme particulière: elle n'est pas symétrique comme la plupart des éruptions mais présente deux pics: un long, peu lumineux précédé d'un pic court et lumineux qui fait penser à un effet de lentille gravitationnelle. La seconde éruption contient peu d'événements limitant les analyses scientifiques que l'on peut effectuer sur celle-ci.

J'ai ajusté le modèle spectral décrit précédemment (loi de puissance absorbée) aux spectres des deux éruptions et vérifié que leurs paramètres sont en accord avec ceux déterminés pour les deux éruptions les plus brillantes observées par XMM-Newton en 2002 et 2007 (Porquet et al. 2003, 2008; Nowak et al. 2012). Les caractéristiques physiques des deux éruptions de 2011 (luminosité intrinsèque, durée, énergie intrinsèque et luminosité au maximum) appartiennent à la moyenne de l'ensemble des éruptions observées en rayons X avec Chandra en 2012 (Neilsen et al. 2013).

Afin d'expliquer la forme atypique de la première éruption, nous avons simulé l'effet de lentille gravitationnelle d'un élément de matière chauffé par le trou noir en rotation solide autour de ce dernier grâce au code `GYOTO` (Vincent et al. 2011). Le premier pic serait alors expliqué par l'effet de lentille gravitationnelle lorsque la boule de gaz se trouve derrière le trou noir et le second pic serait créé par l'effet d'amplification relativiste lorsque la source se rapproche de l'observateur. Nous avons contraint la taille de la boule de gaz, le rayon de son orbite et son inclinaison en ajustant la courbe de lumière produite par ce modèle sur la courbe de lumière lissée observée par XMM-Newton. Cependant, le retour à un taux de comptage équivalent au quiescent entre les deux pics n'est pas reproduit par le modèle. En l'absence d'autres composantes *ad hoc*, cette inadéquation suffit pour rejeter ce modèle.

Nous pouvons donc considérer que l'éruption du 30 mars 2011 est composée de deux éruptions distinctes dont l'origine physique est différente. J'ai effectué une étude énergétique sur le premier pic qui fait partie des éruptions les plus courtes jamais observées (458 s) en comparant l'énergie produite et émise durant l'émission. J'ai extrait la limite supérieure sur l'énergie magnétique (proportionnelle à l'inverse de la distance au trou noir) produite dans une sphère dont le rayon est déterminé par la durée de la phase de montée du pic. Les effets de la relativité générale sur la dilatation du temps propre ont été pris en compte dans ces calculs. L'énergie totale émise durant l'éruption doit donc être, au maximum, égale à la limite supérieure sur l'énergie magnétique. Sachant que l'énergie magnétique ainsi que les durées dépendent de la distance au trou noir, nous pouvons déterminer une limite supérieure sur cette distance ($100^{+19}_{-29}$ fois le rayon gravitationnel, $r_g$, qui vaut 0,5 fois le rayon de Schwarzschild $R_s = 1,2 \times 10^{12}$ cm pour Sgr A*). De plus, supposant que la phase de décroissance est uniquement due au refroidissement synchrotron (qui dépend du champ magnétique et donc de la distance), la comparaison de l'échelle de temps du refroidissement et de la phase de décroissance nous permet de déterminer une limite inférieure sur la distance de la source ($4\,r_g$) et de rejeter l'accélération synchrotron directe pour la création des photons X durant cette éruption. Finalement, les limites inférieures et supérieures sur la distance contraignent la taille de la zone des électrons accélérés ($1,8 - 2,87 \pm 0,01\,r_g$) car cette dernière est proportionnelle à la durée de la phase de montée elle-même dépendante de la distance.

Ces résultats ont été publiés dans **Mossoux et al. (2015a, A&A, 573, A46; 2015b, A&A, 580, C2)**.

## 7.4 La campagne d'observations multi-longueurs d'onde de Sgr A* en février–avril 2014

La campagne d'observations de 2014 est dédiée au suivi de l'activité de Sgr A* lors du passage de DSO/G2 à son périastre. Un *large program* d'observations a été soumis en 2012 afin d'obtenir des observations en rayons X avec XMM-Newton et en NIR avec le *Télescope Spatial Hubble* (HST) et le *Very Large Telescope* (VLT) (XMM-Newton AO-12; PI: Nicolas Grosso, *Observatoire Astronomique de Strasbourg*). Les observations HST ont été planifiées afin de maximiser le nombre d'orbites consécutives et simultanées avec XMM-Newton. Du temps d'observations supplémentaire avec HST a aussi été obtenu pour compléter ce *large program* (HST cycle 21; PI: Howard Bushouse, *Space Telescope Science Institute, USA*). Ces observations ont été effectuées en février–avril 2014 avec XMM-Newton (170 ks), HST/WFC3 (69 ks) et VLT/SINFONI (81 expositions de 400 s). Nous avons aussi utilisé: des observations supplémentaires avec VLT/SINFONI (ESO program 091.B-0183(H); PI: Andreas Eckart, *Physikalisches Institut der Universität zu Köln, Max-Planck-Institut für Radioastronomie, Allemagne*); une *Target of Opportunity* (ToO) avec XMM-Newton déclenchée pour l'observation du nouveau magnétar au centre galactique (85 ks; PI: G.L. Israël, *Osservatorio Astronomico di Roma, INAF, Italy*); trois observations en millimétrique avec le *Combined Array for Research in Millimeter-wave Astronomy* (CARMA; Richard L. Plambeck, *Radio Astronomy Laboratory, University of California, USA*) et trois observations en centimétrique avec le *Very Large Array* (VLA; PI: Farhad Yusef-Zadeh, *Department of Physics and Astronomy, CIERA, Northwestern University, USA*).

Ces observations VLT combinées à des observations effectuées de juin à septembre 2014 nous ont permis de confirmer l'hypothèse selon laquelle le DSO/G2 serait une étoiles entourée de matière circumstellaire (Valencia-S. et al. 2015). Dans cet article, nous avons montré que l'évolution de la largeur de la raie Br$\gamma$ émise par le DSO/G2 est bien reproduite par une étoile jeune de une à deux masses solaires entourée d'un disque de gaz et de poussières qui produit des chocs d'accrétion sur la photosphère stellaire (processus d'accrétion magnétosphérique). Lors de son passage près de Sgr A*, ce disque d'accrétion serait étiré par les forces de marrée provoquant une variation du taux d'accrétion sur l'étoile expliquant la variation de la largeur de la raie Br$\gamma$. Nous avons contraint la date de passage au périastre au 20 avril 2014 (1er mars – 10 juin) avec une distance de 163 unités astronomiques. Après le passage au périastre, les raies d'émission de DSO/G2 sont entièrement décalées vers le rouge ce qui rejette l'hypothèse d'un nuage de gaz compact ou d'une coquille sphérique de gaz.

Le 24 avril 2013, un magnétar (SGR J1745-29) est entré en éruption à seulement 2,4″ au sud-est de Sgr A* (Degenaar et al. 2013; Kennea et al. 2013b). Les deux sources ne peuvent donc pas être résolues par XMM-Newton et les photons provenant du magnétar sont donc pris en compte dans la courbe de lumière de Sgr A* ce qui en augmente artificiellement le taux de comptage et diminue la probabilité de détection des éruptions. De plus, le spectre du magnétar augmente le bruit dans la bande d'énergie entre 1 et 3 keV diminuant ainsi la

précision sur la colonne de d'hydrogène du modèle spectral. J'ai calculé sa période de rotation (3,76398106 s) et dérivée première ($3{,}7684\times10^{-11}$) afin de retirer sa contribution pulsée et de vérifier que je ne perds pas d'éruptions provenant de Sgr A* lors de la détection avec les blocs Bayésiens. Deux éruptions en rayons X ont été détectées: une longue le 10 mars et une plus courte le 2 avril 2014. Nous avons pu vérifier grâce à la meilleure résolution angulaire des deux caméras MOS que l'éruption longue provenait bien de Sgr A* et non du magnétar (la seconde éruption est trop courte pour permettre cette étude). L'analyse spectrale par la méthode MCMC a montré que les paramètres spectraux sont en accord avec ceux déterminés pour les deux éruptions les plus brillantes observées par XMM-Newton (Porquet et al. 2003, 2008). L'analyse statistique du nombre d'éruptions en rayons X détectées durant cette campagne par rapport aux 39 éruptions détectées avec Chandra en 2012 montre qu'il n'y a pas eu d'augmentation d'activité en rayons X lors du passage de DSO/G2 au périastre.

Nous avons aussi détecté trois éruptions NIR avec HST dont deux se produisent en même temps que les éruptions en rayons X, deux éruptions NIR avec VLT sans contrepartie en rayons X, le début d'une éruption radio avec VLA (la contrepartie différée NIR/X est soit non-détectée, ou bien s'est produite avant le début des observations XMM-Newton et HST) et trois éruptions radio avec CARMA dont une pourrait être reliée à la première éruption vue avec VLT.

L'éruption NIR/X du 10 mars 2014 possède un profil atypique: en rayons X, elle est décrite par une phase de montée neuf fois plus longue que sa phase de descente tandis qu'en NIR elle est caractérisée par deux pics. Deux interprétations permettent d'expliquer ce profil: la première est la compression adiabatique d'une boule de gaz qui émet en NIR et en rayons X par un processus SYN-SSC; la seconde est que l'éruption du 10 mars 2014 est composée de deux éruptions distinctes mais séparées par seulement 1,2 h. Le maximum des éruptions est alors simultané en NIR et en rayons X.

Le maximum de l'éruption en NIR vue par HST le 2 avril 2014 se situe pendant l'occultation de Sgr A* par la Terre. Un ajustement Gaussien de la courbe de lumière en NIR et en rayons X m'a permis de déterminer que l'éruption en NIR est composée de deux éruptions distinctes dont la première est la contrepartie simultanée de l'éruption en rayons X. La seconde éruption possède une très grande amplitude en NIR mais pas de contrepartie en rayons X ce qui en fait l'éruption possédant le plus grand rapport d'amplitude NIR/X.

Deux éruptions en NIR ont aussi été détectées avec VLT/SINFONI le 3 et 4 avril 2014. Aucune éruption en rayons X n'a été détectée durant ces observations.

L'activité observée en NIR avec HST et VLT est comparable à celle précédemment détectée avec VLT/NACO indiquant qu'il n'y a pas eu d'augmentation de l'activité en NIR lors du passage de DSO/G2 au périastre.

J'ai utilisé la méthode de Eckart et al. (2012) pour calculer les caractéristiques physiques (taille, densité, champ magnétique et amplitude maximale de la distribution spectrale) de la zone d'électrons accélérés en considérant trois processus radiatifs pour le NIR et les rayons X: SSC-SSC, SYN-SYN et SYN-SSC. Pour les éruptions non détectées en rayons X, j'ai calculé une limite supérieure sur leur luminosité à l'aide d'une méthode Bayésienne (Kraft et al. 1991). Les caractéristiques physiques sont mieux contraintes pour la seconde éruption NIR du 2 avril 2014 sans contrepartie en rayons X mais ne permettent pas de privilégier un des processus radiatifs. Pour cette éruption et le processus SYN-SSC, la taille de la zone d'électrons accélérés vaut 0,03–7 $R_s$ et la densité d'électrons vaut $10^{8,5}$ – $10^{10,2}$ cm$^{-3}$. Le processus IC pour la création des photons X reste aussi un processus possible pour chacune des éruptions car pour les éruptions en NIR possédant une contrepartie détectée en rayons X, le délai prévu par l'IC entre les maximums en NIR et en rayons X n'est pas actuellement mesurable alors que des délais plus grands impliquent des grands rapports NIR/X et donc une faible probabilité de détection des éruptions en rayons X avec les moyens d'observations existants.

Ces résultats ont été publiés dans **Mossoux et al. (2016, A&A, 589, A116)**.

## 7.5 Étude du taux d'éruptions en rayons X de Sgr A* entre 1999 et 2015

J'ai réduit les observations effectuées avec XMM-Newton et Chandra entre 1999 et 2015 puis, j'ai utilisé l'algorithme en deux étapes des blocs Bayésiens afin de déterminer le taux de comptage hors éruption et de détecter les éruptions avec un taux de faux positif de 0,1%.

Le télescope Swift observe régulièrement le centre galactique depuis 2006 avec des observations courtes d'à peu près 1 ks effectuées entre février et novembre. J'ai utilisé la méthode de réduction des données de (Degenaar et al. 2013) tout en l'améliorant afin de tenir compte des colonnes et pixels morts du CCD ainsi

que de la variation de la fraction de la fonction d'étalement du point extraite et du vignettage en fonction de la distance au centre du CCD. La méthode des blocs Bayésiens ne peut pas être utilisée pour la détection des éruptions avec Swift car la durée des observations est courte comparées à la durée typique d'une éruption ce qui implique une faible efficacité de détection avec cet algorithme. J'ai donc utilisé la méthode de Degenaar et al. (2013) qui est optimale pour la détection des éruptions avec le mode opératoire de Swift: les courbes de lumières de Sgr A* sont crées en groupant les événement sur les temps expositions des observations. Une observation est ensuite associée à une éruption si son taux de comptage est supérieur à la limite à $3\sigma$ du taux de comptage moyen de l'année correspondante. Les observations entre 2013 et 2015 sont contaminées par le flux du magnétar SGR J1745-29. Le flux observé par Swift durant ces campagnes est donc ajusté par une somme de deux exponentielles décroissantes; une observation est ensuite associée à une éruption si son taux de comptage est supérieur au taux de comptage de l'ajustement plus trois fois son erreur. J'ai déterminé l'efficacité de détection de la méthode de Degenaar et al. (2013) pour les observations faites avec Swift en simulant des listes d'événements décrites par un flux de Poisson de moyenne égale aux différents taux de comptage hors éruption observés entre 2006 et 2015. J'ai ensuite extrait les événements contenus dans un intervalle de temps de 1 ks à différentes phases de l'éruption afin de créer une observation correspondant à une éruption observée par Swift. La méthode de Degenaar et al. (2013) est ensuite appliquée sur chacune de ces observations simulées afin de déterminer l'efficacité de détection d'une éruption avec différents taux de comptage moyens et différentes durées.

Au total, 102 éruptions on été détectées entre 1999 et 2015 avec XMM-Newton, Chandra et Swift. Le flux moyen corrigé de l'absorption de ces éruptions a été modélisé par une loi de puissance absorbée avec XSPEC en fixant les paramètres $N_{\rm H}$ et $\Gamma$ aux valeurs calculées pour les trois éruptions les plus brillante: $N_{\rm H} = 14.3 \times 10^{22}\,{\rm cm}^{-2}$ et $\Gamma = 2$ (Porquet et al. 2003, 2008; Nowak et al. 2012). Pour les éruptions détectées avec Chandra, j'ai ajouté le modèle de correction de l'empilement des photons à cette loi de puissance absorbée afin de prendre en compte les photons enregistrés simultanément dans un même ilôt de détection pendant le temps d'intégration du CCD.

J'ai ensuite calculé l'efficacité de détection de la méthode des blocs Bayésiens pour différentes éruptions caractérisées par des taux de comptage et de durées différents superposées aux différents niveau hors éruptions observés par Chandra et XMM-Newton entre 1999 et 2015. J'ai ensuite fusionnée ces efficacités de détection en pondérant par le temps d'exposition correspondant afin de créer l'efficacité de détection conjointe représentant l'ensemble des observations avec XMM-Newton et Chandra entre 1999 et 2015. A l'aide du flux moyen corrigé de l'absorption et de la durée des éruptions détectées avec XMM-Newton et Chandra entre 1999 et 2015, j'ai construit la triangulation de Delaunay dans le plan flux–durée afin de déterminer la densité d'éruptions observée avec l'estimateur de densité de la tesselation de Delaunay (DTFE; Schaap & van de Weygaert 2000; van de Weygaert & Schaap 2009). J'ai ensuite corrigé la densité d'éruptions observée de l'efficacité de détection conjointe afin de déterminer la densité d'éruptions intrinsèque.

Afin d'étudier la variation du taux d'éruptions en rayons X obtenues en combinant ces différents télescopes, j'ai dû tenir compte de l'efficacité de détection moyenne dans chacune des observations. J'ai calculé le rapport entre l'intégrale à deux dimensions de la densité d'éruptions intrinsèque pondérée de l'efficacité de détection correspondant à chacune des observations et l'intégrale à deux dimensions de la densité d'éruptions intrinsèque afin de déterminer le pourcentage de détection des éruptions. Chacun des temps expositions d'observation est finalement multiplié par l'efficacité de détection moyenne correspondante afin de corriger des biais de détection.

Ces temps d'exposition corrigés sont ensuite joints en retirant les écarts et les recouvrements entre les observations afin de créer une liste continue de temps d'arrivée des 102 éruptions observées. Le taux d'éruptions en rayons X de Sgr A* est ensuite étudié grâce à la méthode des blocs Bayésiens appliquée sur ces temps d'arrivée. Le résultat de la méthode des blocs Bayésiens appliquée sur l'ensemble des temps d'arrivées des éruptions avec $p_1 = 0{,}05$ et $ncp\_prior = 3{,}96$ est un taux d'éruptions constant à 2,74±0,27 éruptions par jour.

J'ai ensuite recherché un changement de taux d'éruptions en ne considérant que les éruptions les moins brillantes, j'ai appliqué pour cela l'algorithme des blocs Bayésiens de manière récursive sur les temps d'arrivée des éruptions en excluant, à chaque itération, l'éruption qui possède le plus grand flux moyen et ce jusqu'à ce que l'algorithme détecte un changement de taux d'éruptions (le $ncp\_prior$ est recalibré à chaque itération). Un changement de taux d'éruptions est détecté entre les deux éruptions du 28 octobre 2013 en considérant un flux moyen inférieur ou égal à $6{,}3\times10^{-12}$ erg s$^{-1}$ cm$^{-2}$ ($p_1 = 0{,}05$ et $ncp\_prior = 4{,}13$). Le taux d'éruptions est alors passé de 1,93±0,24 à 0,21±0,21 éruptions par jour. J'ai ensuite étudié le taux d'éruptions en ne

considérant que les éruptions les plus brillantes. Un changement de taux d'éruptions est détecté pour un flux moyen supérieur ou égal à $4{,}52\times10^{-12}$ erg s$^{-1}$ cm$^{-2}$ ($p_1 = 0{,}05$ et $ncp\_prior = 4{,}24$). Le point de changement est détecté entre les deux premières éruption du 31 août 2014 avec des taux d'éruptions passant de 1,22±0,19 à 4,44±1,48 éruptions par jour. Ce changement de taux d'éruptions est détecté pour un taux de faux positive plus grand que $p_1 = 0{,}031$ ($ncp\_prior = 4{,}67$). Le taux d'éruptions des éruptions brillantes reste haut jusqu'au 2 novembre 2015 et ne retourne pas à un niveau bas.

J'ai aussi étudié la variation du taux d'éruptions en fonction de l'énergie moyenne des éruptions corrigée de l'absorption (c'est-à-dire le flux moyen d'une éruption multiplié par sa durée). Une diminution du taux d'éruptions est détectée entre l'éruption du 27 août 2013 et celle du 28 octobre 2013 pour les énergies moyenne inférieures ou égale à $121{,}9\times10^{-10}$ erg cm$^{-2}$. Le taux d'éruptions est alors passé de 1,81±0,24 à 0,37±0,26 éruptions par jour. Une augmentation du taux d'éruptions a aussi été détectée pour une énergie moyenne supérieure ou égale à $107{,}8\times10^{-10}$ erg cm$^{-2}$ avec un premier changement de point entre les deux premières éruptions du 31 août 2014 et un deuxième changement de point entre l'éruption du 1er septembre 2014 et celle du 9 septembre 2014. Le taux d'éruptions passe de 1,13±0,18 à 30,1±17,36 éruptions par jour avant de redescendre à un niveau de 2,59±1,16 éruptions par jour. Cette étude confirme donc, avec une probabilité de fausse détection de $p_1 = 0{,}049$ ($ncp\_prior = 3{,}96$), l'augmentation du taux d'éruptions des éruptions les plus énergétiques mise en évidence par Ponti et al. (2015) en étudiant les observations de 1999 à 2014. Cependant, grâce aux observations de 2015, j'ai pu déterminer que cette augmentation est localisée dans le temps et qu'elle n'est observée que pour les éruptions qui ont une énergie moyenne supérieure ou égale à $107{,}8\times10^{-10}$ erg cm$^{-2}$.

Les augmentations du taux d'éruptions des éruptions les plus lumineuses et les plus énergétiques se produisent 131 jours (80–181 jours) après le passage du DSO/D2 près de Sgr A*. Cependant, le temps visqueux caractérisant le transport radial de matière située à 163 au (distance au périastre de DSO/G2) dans un flot d'accrétion chaud implique que l'on ne devrait pas voir les effets de l'accrétion de cette matière sur Sgr A* avant 2017. De plus, la diminution du taux d'éruptions des éruptions les moins lumineuses et les moins énergétiques se produit au moins 185–225 jours avant le passage du DSO/D2 près de Sgr A* ce qui implique que ce changement du taux d'éruption n'est pas la conséquence du passage du DSO/D2 près de Sgr A*. J'ai effectué un bilan énergétique montrant qu'il est possible que l'énergie économisée par la diminution du nombre d'éruptions peu énergétiques pendant plusieurs jours soit libérée en quelques heures par un surplus d'éruptions énergétiques. Cette énergie pourrait être stockée dans les distorsions des lignes de champ magnétique avant d'être libérée lors d'une reconnexion magnétique.

## 7.6 Conclusions et perspectives

Le but de cette thèse était d'étudier l'impact du passage de DSO/G2 à $2032\,R_s$ (163 au) de Sgr A* sur ses éruptions.

Grâce à l'éruption de Sgr A* en rayons X du 30 mars 2011 vue par XMM-Newton, j'ai validé l'efficacité des trois méthodes d'analyse des données en rayons X utilisées et améliorées durant cette thèse. J'ai aussi testé l'effet de lentille gravitationnelle et contraint la distance radiale et la taille de la région d'éruption à $4\ r_g < r < 100^{+19}_{-29}\ r_g$ et $1.8\ r_g < R < 2.87 \pm 0.01\ r_g$ avec $r_g$ =0,5 $R_s$ le rayon gravitationnel de Sgr A*. J'ai aussi pu rejeter le processus synchrotron direct pour la création du l'éruption en rayons X.

Entre février et avril 2012, 12 éruptions ont été détectées: sept en NIR avec HST/WFC3 et VLT/SINFONI, trois en rayons X avec XMM-Newton, une en centimétrique avec VLA (sans contrepartie en NIR ou rayons X observable) et trois en millimétrique avec CARMA (dont une pourrait être la contrepartie retardée d'une éruption vue avec le VLT). J'ai ainsi pu calculer le rapport d'amplitude des éruptions en NIR et rayons X avec un ajustement Gaussien des courbes de lumière des éruptions. Pour les éruptions en NIR sans contrepartie en rayons X, j'ai calculé un limite supérieure de l'amplitude de l'éruption X non détectée avec une méthode Bayésienne. Ces rapport d'amplitude ainsi calculés contraignent les paramètres physiques de la région d'éruption et plus le rapport rayons X/NIR est grand, plus les paramètres sont contraints. Le taux d'éruptions en rayons X et l'activité éruptive en NIR observés durant cette campagne sont compatibles avec ceux observés avant le passage du DSO/G2 au périastre. L'activité de Sgr A* n'a donc pas augmenté durant février–avril 2014.

Grâce aux 84 éruptions détectées avec XMM-Newton et Chandra par la méthode des blocs Bayésiens entre 1999 et 2015 et à l'efficacité de détection conjointe, j'ai déterminé la distribution intrinsèque des érup-

tions en rayons X de Sgr A* en fonction de leur durée et de leur flux moyen corrigé de l'absorption calculé pour $N_{\rm H} = 14{,}3{\times}10^{22}$ cm$^{-2}$ et $\Gamma = 2$. En calculant l'efficacité de détection des éruptions associée à chacune des observations avec XMM-Newton, Chandra et Swift, j'ai aussi déterminé le taux d'éruptions intrinsèque en corrigeant le taux de comptage des éruptions dans chacune des observations du biais de détection correspondant. Le taux d'éruptions instrinsèque pour les 102 éruptions observées par XMM-Newton, Chandra et Swift entre 1999 et 2015 est de 2,74±0,27 éruptions par jour. J'ai aussi étudié la variation de ce taux d'éruptions grâce à la méthode des blocs Bayésiens en considérant uniquement les éruptions dans un certain intervalle de luminosité et d'énergie des éruptions. Le taux d'éruptions des éruptions les moins lumineuses et les moins énergétiques a diminué d'un facteur 9,2 et 4,9 à partir du 28 octobre 2013 et du 27 juillet 2013, respectivement. De plus, le taux d'éruptions des éruptions les plus lumineuses et les plus énergétiques a augmenté d'un facteur 3,6 et 26,6, respectivement, à partir du 31 août 2014. Le grand taux d'éruptions des éruptions les plus énergétiques diminue à partir du 1er septembre 2014 afin de retrouver un niveau comparable à celui observé avant le 31 août 2014. Le bilan énergétique montre qu'il est possible que l'énergie économisée par la diminution du nombre d'éruptions peu énergétiques pendant plusieurs jours soit libérée en quelques heures pour créer un surplus d'éruptions énergétiques.

La distribution intrinsèque des éruptions en rayons X de Sgr A* calculée ici pourra être testée par la future grande mission de l'ESA dont le lancement est prévu en 2028: l'*Advanced Telescope for High Energy Astrophysics* (Athena). En effet, j'ai évalué l'efficacité de détection des éruptions avec l'*X-ray Integral Field Unit* (X-IFU; Barret et al. 2013) à bord d'Athena. Pour cela, j'ai d'abord créé une image du centre galactique qui devrait être observé par Athena/X-IFU en faisant une simulation Monte Carlo d'une liste d'événements entre 2 et 10 keV avec le programme SIXTE[4]. La distribution spectrale du centre galactique est extraite en huit bandes spectrales à partir des observations de 2012 faites avec Chandra HETG/ACIS-S3. La distribution spatiale des sources du centre galactique est ensuite donnée par les images faites avec Chandra HETG/ACIS-S3 (résolution angulaire de 0,5″) dans chaque bande spectrale. A partir des listes d'événements simulées pour chaque bande spectrale, j'ai extrait les événements dans un cercle de 5″ de rayon centré sur Sgr A* et calculé un taux de comptage hors éruption entre 2 et 10 keV de 0,68 coups s$^{-1}$. J'ai ensuite calculé le rapport entre le taux de comptage moyen d'une éruption vu par Athena/X-IFU et son flux moyen corrigé de l'absorption en simulant avec SIXTE une source ponctuelle dont le spectre est une loi de puissance absorbée avec $N_{\rm H} = 14{,}3{\times}10^{22}$ cm$^{-2}$ et $\Gamma = 2$. Ce rapport vaut $2{,}8{\times}10^{-12}$ erg s$^{-1}$ cm$^{-2}$/coups s$^{-1}$. J'ai finalement testé l'efficacité de détection des éruptions avec plusieurs flux moyens et plusieurs durées au dessus du taux de comptage hors éruption de 0,68 coups s$^{-1}$ avec la méthode des blocs Bayésiens. Toutes les éruptions vues avec Chandra, XMM-Newton et Swift devraient être détectées avec une efficacité proche de 100%. Cela implique que des éruptions beaucoup plus faibles pourront aussi être détectées avec une efficacité plus petite. Si ces faibles éruptions sont détectées avec leur contrepartie NIR observable avec le futur *European Extremely Large Telescope* (E-ELT) de 39 de diamètre (première lumière en 2024), le processus IC pour la création des éruptions X pourra être testé car nous serons alors capable de mesurer le délai temporel entre les maxima en NIR et rayons X dû à ce processus. Le spectre des éruptions sera aussi décrit par un rapport signal à bruit plus grand que celui observé par XMM-Newton ou Chandra ce qui permettra de mettre des contraintes sur les autres processus radiatifs.

[4] http://www.sternwarte.uni-erlangen.de/research/sixte/

# Appendix

# Appendix A

# The radiative processes evolving near Sgr A*

Here, I make a short mathematical summary of the three radiative processes debated for the creation of the X-ray flares from Sgr A*: synchrotron, inverse Compton and synchrotron self-Compton.

## A.1 The synchrotron radiation

The synchrotron radiation is emitted by relativistic electrons which gyrate around magnetic field lines. The energy of relativistic electrons is described by the Lorentz factor (or electron boosting factor) $\gamma = (1 - v^2/c^2)^{-1/2}$ where the electron velocity $v$ is always perpendicular to its acceleration. The frequency at which the electrons rotate is given by $\nu_g = eB/2\pi\gamma m_e$ with $e$ the electronic charge and $m_e$ the electron mass. The relativistic property of the electrons causes the synchrotron emission to be collimated in a beam with a semi-opening angle of $\gamma^{-1}$.

The electron energy distribution is deduced from their successive accelerations (Longair 1994). After one acceleration, the average energy of a particle is $E = \beta E_0$ and the probability that it remains in the acceleration region is $P$. Considering $k$ accelerations, $N(E) = N_0 P^k$ particles remain in the acceleration region and each particle has an energy of $E = \beta^k E_0$. The ratio of the logarithm of these two equations is $N(E)/N_0 = (E/E_0)^{\ln P/\ln\beta}$. The number of particles having an energy between $E$ and $E + dE$ is thus $N(E)\,dE = K_0\,E^{-p}\,dE$ with $p = 1 - \ln P/\ln\beta$ (Lang 1999). The spectral index $p$ can be computed considering the gain energy when the particle cross the shock ($\beta = 1 - \langle E/E_0\rangle = 1 - 4\,V'/3\,c$ with $V'$ the velocity behind the shock) and the probability to lose a particle ($P = 1 - U/c$ with $U$ the medium velocity) as it is done in Longair (1994). A spectral index value of $p = 2$ is often taken to describe synchrotron radiation without absorption for a mono-atomic and fully ionized gas of high energy particles.

The normalization parameter $K_0$ is computed assuming that the number of particles ($N_0$) into the emitting region of volume $V$ remains constant (Van der Laan 1966):

$$N_0 = V\,K_0 \int_{E_{\min}}^{E_{\max}} E^{-p}\,dE\,, \tag{A.1}$$

leading to

$$K_0 = \frac{N_0\,(1-p)}{V\left(E_{\min}^{1-p} - E_{\max}^{1-p}\right)}\,. \tag{A.2}$$

The solution of the synchrotron radiative transfer equation is

$$S_\nu = S_{\nu,0}\,e^{-\tau_\nu} + \frac{\epsilon_\nu}{\kappa_\nu}\left(1 - e^{-\tau_\nu}\right) \tag{A.3}$$

with $\epsilon_\nu$ and $\kappa_\nu$ the emission and absorption coefficients and $\tau_\nu$ the optical depth. I assume here that $S_{\nu,0} = 0$.

The energy radiated between $\nu$ and $\nu + d\nu$ by electrons with energy between $E = \gamma\,m_e\,c^2$ and $E + dE$ is

$$\epsilon_\nu d\nu = -\left(\frac{dE}{dt}\right) N(E) dE \tag{A.4}$$

with $dE = m_e\, c^2 \nu^{-1/2} d\nu / 2\nu_g^{1/2}$. The total energy loss of an ultra relativistic electron is (Longair 1994)

$$-\left(\frac{dE}{dt}\right) = \frac{3}{4}\gamma^2 \sigma_T c U_B \tag{A.5}$$

with $\sigma_T$ the Thomson cross-section and the magnetic energy density $U_B = (B\,\sin\theta)^2/8\pi$ with $\theta$ the angle between the line of sight and the direction of the magnetic field . By replacing all the terms in Eq. A.4, we have

$$\epsilon_\nu = C_\epsilon(p)\, K_0\, (B\,\sin\theta)^{(p+1)/2} \nu^{-(p-1)/2} \tag{A.6}$$

with $C_\epsilon(p)$ a constant which depends on the spectral index (Lang 1999):

$$C_\epsilon(p) = \frac{\sqrt{3}}{8\pi}\frac{e^3}{m_e\, c^2}\left(\frac{3e}{4\pi m_e{}^3 c^5}\right)^{(p-1)/2} 2^{(p-3)/2}\,\frac{p+7/3}{p+1}\,\Gamma\left(\frac{3p-1}{12}\right)\Gamma\left(\frac{3p+7}{12}\right) \tag{A.7}$$

with $\Gamma$ the Gamma function for $p > 1/3$. Considering a randomly oriented magnetic field, the integration over all angle $\theta$ leads to (Longair 1994):

$$\int_0^\infty \frac{1}{2}\sin\theta \sin^{\frac{p+2}{2}}\, d\theta = \frac{\sqrt{\pi}\Gamma\left(\frac{p+6}{4}\right)}{2\Gamma\left(\frac{p+8}{4}\right)}\,. \tag{A.8}$$

The spectrum created by such accelerated electron is characterized by a power law ($\epsilon_\nu \propto \nu^{-\alpha}$ with $\alpha = (p-1)/2$) with a polarized radiation.

However, the synchrotron emission undergoes an absorption called synchrotron self absorption. This absorption is produced by different mechanisms. First there is the Compton scattering due to the interaction between the photons and the electrons producing a change in the photon frequency. There is also the bremsstrahlung scattering due to the acceleration of an electron passing close to a proton. This acceleration produces a photon which is re-absorbed when the electron goes out of the proton field. By conservation of the momentum, a net absorption is created. The synchrotron self absorption happens at low frequency when the effective electron temperature $T_e \sim (m_e\, c^2/3k_B)(\nu/\nu_g)^{1/2}$ with $k_B$ the Boltzmann constant approaches the brightness temperature $T_b = \lambda^2\, S_\nu/2\, k_B\, \Omega$ with $\lambda$ the mean wavelength of the source and $\Omega = \pi R^2/d^2$ the solid angle with $R$ the source radius and $d$ the distance from Earth. When $T_e = T_b$, the absorption coefficient is (Rybicki & Lightman 1979)

$$\kappa_\nu = \frac{-c^2}{8\pi\,\nu^2}\int_0^\infty j(\nu, E)\frac{d}{dE}\left(\frac{N(E)}{E^2}\right)E^2 dE \tag{A.9}$$

with $j(\nu, E)$ the total emitted power per frequency:

$$j(\nu, E) = \frac{\sqrt{3} q^3\, B\sin\theta}{2\,\pi\, m\, c^2}\, F(x) \tag{A.10}$$

with $F(x) = x\int_x^\infty K_0\frac{5}{3}(\zeta)\, d\zeta$. Using Eq. 11.4.22 of Abramowitz & Stegun (1970), one may derive

$$\kappa_\nu = C_\kappa(p)\, K_0\, (B\sin\theta)^{(p+2)/2}\, \nu^{-(p+4)/2} \tag{A.11}$$

with

$$C_\kappa(p) = \frac{\sqrt{3}}{16}\left(p + \frac{10}{3}\right)\Gamma\left(\frac{3p+2}{12}\right)\Gamma\left(\frac{3p+10}{12}\right)\frac{e^3}{2\pi m}\left(\frac{3e}{2\pi m^3 c^5}\right)^{p/2}\,. \tag{A.12}$$

Finally, the resultant emission from the synchrotron radiation computed from Eq. A.3 with Eq. A.6 and A.11 is

$$S_{SYN} = \frac{C_\epsilon}{C_\kappa}\, B^{-1/2}\, \nu^{5/2}\,(1 - e^{-\tau_\nu}) \tag{A.13}$$

with the optical depth $\tau_\nu = \kappa_\nu \int_0^l dl$ and $l$ the the total distance followed by the photon in the absorbing medium.

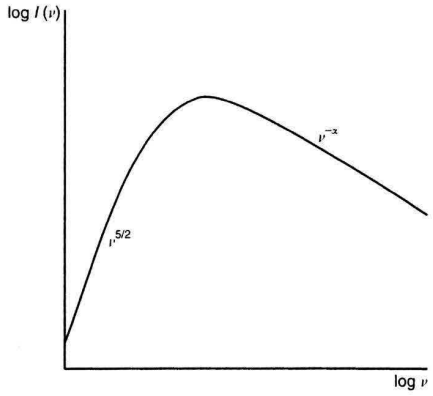


Figure A.1: Spectrum of the synchrotron radiation emitted by a powerlaw distribution of electrons of spectral index $p = 2\,\alpha + 1$.

The total synchrotron spectrum is thus composed by two power laws with a maximum flux $S_{\rm m}$ at the frequency $\nu_{\rm m}$ (see Fig. A.1):

- the first one at low frequencies (i.e., in optically thick regime): the absorption coefficient is large leading to $S_{\rm SYN} \propto B^{-1/2}\,\nu^{5/2}$.
- the second one at higher frequency (i.e., optically thin regime): $\tau_\nu << 1$ leading to $1 - e^{-\tau_\nu} \approx \kappa_\nu\,l$. The synchrotron radiation is thus reduced to $S_{\rm SYN} \propto B^{-1/2}\,\nu^{5/2}\,\kappa_\nu \propto B^{\alpha+1}\,\nu^{-\alpha}$ with $\alpha = (p-1)/2$.

The cooling time of the synchrotron radiation is computed as the ratio between the energy powered by the electrons and the energy of these electrons scaling as $B^{-2}\,\gamma^{-1}$. The synchrotron cooling timescale is $\tau_{\rm sync} = 8\ (B/30\,{\rm G})^{-3/2}\left(\nu/10^{14}\,{\rm Hz}\right)^{-1/2}$ min (Dodds-Eden et al. 2009).

## A.2 The inverse Compton (IC)

During the Compton scattering (or non-elastic Thomson scattering) process, a part of the photon energy is given to the electron since the photon energy is large compared to the electron energy. The inverse Compton scattering is the inverse process where the photon energy is increased by relativistic electrons since $\gamma\,h\nu << m_{\rm e}\,c^2$. The mean and maximum frequencies that the photon with an initial frequency $\nu_0$ acquires are $\nu = (4/3)\,\gamma^2\,\nu_0$ and $\nu_{\rm max} \sim 4\gamma^2\nu_0$, respectively.

The energy lost by the relativistic electrons in the electron reference frame is (Bradt 2008)

$$-\left(\frac{dE}{dt}\right) = \sigma_{\rm T} c\,U'_{\rm rad} \tag{A.14}$$

with $\sigma_{\rm T}$ the Thomson cross section and $U'_{\rm rad} = n_{\rm ph}\,h\nu$ the averaged photon energy density which depends on the size of the photons source and its distance to the relativistic electrons source.

The energy gained by the photon in its rest frame is

$$-\left(\frac{dE}{dt}\right) = \frac{4}{3}\sigma_{\rm T}\,c\,U_{\rm rad}\,\gamma^2\,. \tag{A.15}$$

This equation is very similar to those of synchrotron radiation (see Eq. A.5) since the acceleration processes are similar: in the case of synchrotron radiation, this is the magnetic field which accelerates electrons and in the inverse Compton mechanism, this is the sum of all electric field of the incident photon flux density. Comparing the energy losses from the synchrotron and inverse Compton radiation, we have

$$\frac{(dE/dt)_{\rm IC}}{(dE/dt)_{\rm SYN}} = \frac{U_{\rm rad}}{U_{\rm B}}\,. \tag{A.16}$$

The inverse Compton catastrophe occurs when this ratio is larger than 1 implying that each scattered photon may have a second upscattering on the relativistic electrons and produce other photons that may also be upscattered without end.

The emissivity produced by inverse Compton scattering is given in Blumenthal & Gould (1970) for a monochromatic radiation field at $\nu_0$ which is upscattered by a single electron:

$$S_{\rm IC} = \frac{3\sigma_{\rm T} c N(\nu_0)\nu}{16\gamma^4\nu_0^2}\left(2\nu\ln\left(\frac{\nu}{4\gamma^2\nu_0}\right)+\nu+4\gamma^2\nu_0-\frac{\nu}{2\gamma^2\nu_0}\right)d\nu\,. \tag{A.17}$$

For a powerlaw energy distribution of electrons $N(E)\,dE = K\,E^{-p}\,dE$ in a plasmon volume $V$, the resulting spectrum is (Georganopoulos et al. 2001)

$$S_{\rm IC} \approx C_{\rm IC}\frac{K\,V\,U_{\rm rad}}{\nu_0}\left(\frac{\nu}{\nu_0}\right)^{-(p-1)/2} \tag{A.18}$$

with $C_{\rm IC} = 4\,\sigma_{\rm T}\,c\,2^{p-1}/((1+p)(3+p))$. The inverse Compton radiation is thus proportional to $\nu^{-\alpha}$ with $\alpha = -(p-1)/2$ as for the synchrotron emission in optically thin regime. The inverse Compton cooling timescale is $\tau_{\rm IC} = m_{\rm e}c/\gamma\sigma_{\rm T}U_{\rm rad}$.

## A.3 The synchrotron self-Compton (SSC)

The SSC radiation is the local counterpart of the IC process. The source region of photons and electrons are the same implying that the photons produced by synchrotron radiation are upscattered by the electrons that produced them. Marscher (1983) computed the flux of the SSC process considering a powerlaw energy density for the accelerated electrons $N(E)\,dE = K\,E^{-p}\,dE$. The SSC radiation emitted by a source of radius $R$ is

$$S_{\rm SSC} \propto R^{-2(2\alpha+3)}\,\nu_{\rm m}^{-(3\alpha+5)}\,S_{\rm m}^{2(\alpha+2)}\,\ln\left(\frac{\nu_{\rm syn}}{\nu_{\rm m}}\right)\nu^{-\alpha} \tag{A.19}$$

with $\nu_{\rm syn}$ the cutoff frequency of the synchrotron radiation, $S_{\rm m}$ maximum flux of the synchrotron spectrum at the frequency $\nu_{\rm m}$ and $\alpha = (p-1)/2$ the spectral index. The natural logarithm in this equation may be approximated by $c_1\,(\nu_{\rm syn}/\nu_{\rm m})^{c_2}$ with $c_1 = 1.8$ and $c_2 = 0.201$ (Eckart et al. 2012).

# Appendix B

# The adiabatically expanding plasmon model

The observed time delay between the radio/sub-millimeter flares and the NIR/X-ray flares is explained with an expanding plasmon with adiabatic cooling model (Van der Laan 1966; Yusef-Zadeh et al. 2006b). In this model, the plasmon is initially optically thin to NIR and X-ray wavelengths leading to an observable NIR/X-ray flaring emission whereas it is optically thick to the radio and sub-millimeter wavelengths leading to an occultation of a part of the hot accretion flow and an unobservable flaring emission. As the source adiabatically expands, the density of electrons decreases and the source becomes optically thin to the radio and sub-millimeter wavelengths leading to an increase of observed synchrotron flux from the source and from the part of hot accretion flow which was occulted.

The velocity of the expansion is governed by the ratio between the electron energy in the plasmon $E_0$ and the mass density $\rho_0$ of the ambient medium: $V(t) = dR(t)/dt = (E_0/2\pi R(t)^3\rho_0)^{0.5}$ (van der Laan 1963). The radius of the plasmon, computed as $R(t) = R_0 + V(t)(t - t_0)$, has as an initial radius $R_0$ and a maximum radius $R_{\rm max} = (2\,E_0/B_0^2)^{1/3}$ when the expansion velocity reaches the Alfven velocity of the medium (van der Laan 1963). The total flux received by the observer is the sum of the flaring emission from the source $S_{\rm pl}(t)$, the flux emitted by the non-occulted part of hot accretion flow $(1 - f(t))\,S_{\rm q}$ with $f(t)$ the part of the hot accretion flow which is occulted and the flux from the occulted part of hot accretion flow which is transfered through the plasmon $S_{\rm occ}(t)$ (Yusef-Zadeh et al. 2010).

The initial number density of electrons in the plasmon is $n_{\rm e} = 3\,N_{\rm e}/(4\,\pi\,R_0^3)$ with $N_{\rm e}$ the constant number of electrons inside the sphere. Using the conservation of magnetic flux density density, the magnetic flux varies as $B(t) = B_0\,(R(t)/R_0)^{-2}$. Assuming that the plasmon contains ultrarelativistic particles undergoing an adiabatic cooling, we have $E(t) = E_0\,(R(t)/R_0)^{-1}$.

Considering a powerlaw distribution of electrons such as $N(E)\,dE = K_0\,E^{-p}\,dE$, $N_{\rm e}$ is computed as (see Eq. A.1)

$$N_{\rm e} = \frac{4}{3}\,\pi\,R_0^3 \int_{E_{0,\rm min}}^{E_{0,\rm max}} K_0\,E^{-p}\,dE \tag{B.1}$$

with $E_{0,\rm min}$ and $E_{0,\rm max}$ corresponding to the initial Lorentz factors $\gamma_{\rm min}$ and $\gamma_{\rm max}$. By integrating this equation, we have (as in Eq. A.2)

$$K_0 = \frac{3\,N_{\rm e}}{4\,\pi\,R_0^3}\,\frac{1-p}{E_{0,\rm min}^{1-p} - E_{0,\rm max}^{1-p}}\,. \tag{B.2}$$

The initial energy density per unit of volume in the plasmon is computed by integrating $E\,N(E)$ on the number of particles:

$$\begin{aligned} E_0 &= N_{\rm e}\,\frac{1-p}{2-p}\,\frac{E_{0,\rm max}^{2-p} - E_{0,\rm min}^{2-p}}{E_{0,\rm max}^{1-p} - E_{0,\rm min}^{1-p}} && \text{for } p \neq 2\,, \\ E_0 &= N_{\rm e}\,\frac{1-p}{E_{0,\rm max}^{1-p} - E_{0,\rm min}^{1-p}}\,\ln\left(\frac{E_{0,\rm max}}{E_{0,\rm min}}\right) && \text{for } p = 2\,. \end{aligned} \tag{B.3}$$

The electron energy is not very sensible to the value of $\gamma_{\rm max}$ whereas the value of $\gamma_{\rm min}$ varies with the distance and has a larger influence on the energy. For ultra-relativistic electrons, $\gamma_{\rm min} >> 1$.

The synchrotron emission emitted by the spherical plasmon is

$$S_{\rm pl}(t) = \frac{\epsilon_\nu(t)}{\kappa_\nu(t)} \int_0^{R(t)} \left(1 - e^{-\tau_\nu(t,r)}\right) 2\pi r\,dr\,. \tag{B.4}$$

The absorption and emission coefficients of the synchrotron emission, $\epsilon_\nu(t)$ and $\kappa_\nu(t)$, have already been described in Sect. A.1 (Eq. A.6 and A.11) at a fixed time. The parameters which depend on time in $\epsilon_\nu(t)$ and $\kappa_\nu(t)$ are $K(t) \propto R(t)^{-2-p}$ and $B(t) \propto R(t)^{-2}$.

A photon passing through the sphere travels a distance of $2(R(t)^2 - r^2)^{0.5}$ with $r \leq R(t)$ the minimum distance to the sphere center. The optical depth $\tau_\nu(t, r)$ crossed by a photon of frequency $\nu$ is thus

$$\tau_\nu(t, r) = \kappa_\nu(t)\, 2\sqrt{R(t)^2 - r^2}\,. \tag{B.5}$$

Resolving the integral B.4, we have

$$S_{\rm pl}(t) = \pi \frac{\epsilon_\nu(t)\, R(t)^2}{\kappa_\nu(t)} \left(1 - \frac{1 - e^{-2\kappa_\nu(t)\, R(t)}(1 + 2\kappa_\nu(t)\, R(t))}{2\,\kappa_\nu(t)^2\, R(t)^2}\right). \tag{B.6}$$

This equation has the same shape than those computed by Van der Laan (1966):

- In the optically thick regime: $\kappa_\nu(t)\, R(t) >> 1$ leading the term in parenthesis in the order of zero. The plasmon emission is thus proportional to $\epsilon_\nu(t)\, R(t)^2/\kappa_\nu(t) \propto B(t)^{-1/2}\, \nu^{5/2}\, R(t)^2 \propto \nu^{5/2}\, R(t)^3$.
- In the optically thin regime: $\kappa_\nu(t)\, R(t) << 1$ leading to $\frac{1-e^{-2\kappa_\nu(t)\, R(t)}(1+2\kappa_\nu(t)\, R(t))}{2\,\kappa_\nu(t)^2\, R(t)^2} \approx e^{-2\kappa_\nu(t)\, R(t)}$. The plasmon emission is thus proportional to $\epsilon_\nu(t)\, R(t)^2/\kappa_\nu(t)\,(1 - e^{-2\kappa_\nu(t)\, R(t)}) \propto B(t)^{-1/2}\, \nu^{5/2}\, R(t)^2\, \kappa_\nu(t)\, R(t)$. With the equation of the absorption coefficient, we have $K(t)\, B(t)^{(p+1)/2}\, \nu^{(1-p)/2}\, R(t)^3 \propto \nu^{(1-p)/2}\, R(t)^{-2p}$.

The flux received from the quiescent through the sphere is

$$S_{\rm occ}(t) = \frac{S_{\rm q}}{\pi R_{\rm q}^2} \int_0^{R(t)} e^{-\tau_\nu(t,r)}\, 2\pi r\, dr \tag{B.7}$$

with $R_{\rm q}$ the size of the hot accretion flow emitting with a flux $S_{\rm q}$.

$$S_{\rm occ}(t) = \frac{S_{\rm q}\, R^2}{R_{\rm q}^2} \left(\frac{1 - e^{-2\kappa_\nu(t) R(t)}(2\kappa_\nu(t) R(t) + 1)}{2\kappa_\nu(t)^2 R(t)^2}\right) \tag{B.8}$$

The total flux received by the observer is thus

$$S_\nu(t) = (1 - f(t)) S_{\rm q} + S_{\rm occ}(t) + S_{\rm pl}(t) \tag{B.9}$$

with $1 - f(t) = (R_{\rm q}^2 - R(t)^2)/R_{\rm q}^2$.

This model was tested using the equations developed in Van der Laan (1966) (i.e., without taking the evolution of the occulted accretion flow flux nor the evolution of the expansion velocity with the radius) for different delayed flares. The derived characteristics of the source are $R_0$ ranging from 0.5 to 3.2 $R_{\rm s}$, $B_0$ ranging from 10 to 76 G, $V$ ranging from 0.0028 to 0.15 $c$ and $p$ ranging from 1 to 4.6 (Yusef-Zadeh et al. 2006b; Eckart et al. 2008; Yusef-Zadeh et al. 2009).

The variation of the NIR–to–X-ray flux ratio in the observed flares may be explained by the variation of the size of the plasmon which is optically thin for the NIR and X-ray photons. Let us consider that the NIR photons are emitted by synchrotron radiation and that the X-rays are produced by synchrotron self-Compton. The optically thin synchrotron emission emitted from a spherical region is proportional to $B(t)^{\alpha+1}\, \nu^\alpha\, R(t)^3$ with $\alpha = (p-1)/2$ the spectral index. The magnetic field can be expressed as a function of $S_{\rm m}(t)$ the maximum flux of the synchrotron spectrum at the frequency $\nu_{\rm m}(t)$ and a time $t$ of the plasmon expansion (Marscher 1983): $B(t) \propto R(t)^4\, \nu_{\rm m}(t)^5\, S_{\rm m}(t)^{-2}$. This leads to

$$S_{\rm SYN}(t) \propto R(t)^{4\alpha+7}\, \nu_{\rm m}(t)^{5(\alpha+1)}\, S_{\rm m}(t)^{-2(\alpha+1)}\, \nu^{-\alpha}\,. \tag{B.10}$$

The synchrotron self-Compton emission is also given as a function of $S_{\rm m}(t)$ and $\nu_{\rm m}(t)$ in Eq. A.19. We thus have

$$\frac{S_{\rm SSC}(t)}{S_{\rm SYN}(t)} \propto R(t)^{-(8\alpha+13)}\, \nu_{\rm m}(t)^{-(8\alpha+10+c_2)}\, S_{\rm m}(t)^{4\alpha+6}\,. \tag{B.11}$$

Van der Laan (1966) computed the parameters $S_{\rm m}(t)$ and $\nu_{\rm m}(t)$ as a function of the plasmon radius: $S_{\rm m}(t) \propto R(t)^{-(14\alpha+10)/(2\alpha+5)}$ and $\nu_{\rm m}(t) \propto R(t)^{-(8\alpha+10)/(2\alpha+5)}$. Thus, $S_{\rm SSC}/S_{\rm SYN} \propto R^{-\beta}$ with

$$\beta \equiv \frac{8\alpha^2 + (30 - 8\,c_2)\alpha + 25 - 10\,c_2}{2\alpha + 5}\,. \tag{B.12}$$

For a synchrotron emission, $\alpha$ must be positive implying that $\beta > 5.4$. The variation of the NIR–to–X-ray flux ratio thus allows us to compute the variation of the flaring source size considering the adiabatically expanding plasmon model emitting the NIR photons with a synchrotron emission and the X-ray photons with a synchrotron self-Compton emission.

# Appendix C

# The observation log of Sgr A* from 1999 to 2015 and the detected X-ray flares

Table C.1: Observation log of public XMM-Newton observations and the detected X-ray flares.

| ObsID | PI | Observation start (UT) | Observation end (UT) | Duration (ks) | Non-flaring level (count $s^{-1}$) | Flare start[a] (UT) | Flare stop[a] (UT) | Flare duration (s) | Mean count rate[b] (count $s^{-1}$) | Mean flux[c] ($10^{-12}$ erg $s^{-1}$ $cm^{-2}$) |
|---|---|---|---|---|---|---|---|---|---|---|
| 112970601[d] | M. Turner | 2000-09-17 18:41:04 | 2000-09-17 19:13:58 | 2.0 | 0.102 ± 0.005 | ..... | ..... | ..... | ..... | ..... |
| 112970501[e,g] | M. Turner | 2000-09-21 09:21:08 | 2000-09-21 15:16:37 | 24.9 | 0.029 ± 0.001 | ..... | ..... | ..... | ..... | ..... |
| 112971601[e] | M. Turner | 2001-03-31 11:31:01 | 2001-03-31 12:40:31 | 4.0 | 0.038 ± 0.002 | ..... | ..... | ..... | ..... | ..... |
| 112972101[g] | M. Turner | 2001-09-04 02:34:33 | 2001-09-04 08:41:10 | 21.7 | 0.099 ± 0.003 | 08:29:45 | **08:41:10** | >685 | 0.105 ± 0.021 | 29.6 |
| 111350101[j] | B. Aschenbach | 2002-02-26 06:40:39 | 2002-02-26 17:55:35 | 40.0 | 0.105 ± 0.001 | ..... | ..... | ..... | ..... | ..... |
| 111350301[j] | B. Aschenbach | 2002-10-03 07:15:59 | 2002-10-03 11:34:19 | 15.4 | 0.100 ± 0.002 | 10:08:32 | 10:52:01 | 2609 | 0.289 ± 0.018 | 27.9 |
| 202670501[g] | A. Goldwurm | 2004-03-28 16:44:29 | 2004-03-30 03:25:39 | 105.6 | 0.200 ± 0.001 | ..... | ..... | ..... | ..... | ..... |
| 202670601[g] | A. Goldwurm | 2004-03-30 17:16:48 | 2004-04-01 03:35:08 | 107.0 | 0.187 ± 0.001 | ..... | ..... | ..... | ..... | ..... |
| 202670701 | A. Goldwurm | 2004-08-31 03:33:48 | 2004-09-01 16:05:43 | 127.5 | 0.190 ± 0.002 | 08:48:44 | 10:56:42 | 7678 | 0.075 ± 0.008 | 4.99 |
| | | | | | | 30:36:54 | 30:54:29 | 927 | 0.023 ± 0.010 | 2.53 |
| 202670801 | A. Goldwurm | 2004-09-02 03:23:36 | 2004-09-03 16:03:37 | 130.8 | 0.157 ± 0.001 | ..... | ..... | ..... | ..... | ..... |
| 302882601 | R. Wijnands | 2006-02-27 04:26:53 | 2006-02-27 05:49:46 | 4.9 | 0.109 ± 0.004 | ..... | ..... | ..... | ..... | ..... |
| 302884001 | R. Wijnands | 2006-09-08 17:18:55 | 2006-09-08 18:42:09 | 5.0 | 0.092 ± 0.003 | ..... | ..... | ..... | ..... | ..... |
| 506291201[d] | R. Wijnands | 2007-02-27 06:07:31 | 2007-02-27 16:51:07 | 38.6 | 0.048 ± 0.001 | ..... | ..... | ..... | ..... | ..... |
| 402430701 | D. Porquet | 2007-03-30 21:27:07 | 2007-03-31 06:28:47 | 32.3 | 0.121 ± 0.002 | ..... | ..... | ..... | ..... | ..... |
| 402430301 | D. Porquet | 2007-04-01 15:06:44 | 2007-04-02 17:05:07 | 101.3 | 0.111 ± 0.001 | ..... | ..... | ..... | ..... | ..... |
| 402430401 | D. Porquet | 2007-04-03 16:43:24 | 2007-04-04 19:48:15 | 86.4 | 0.105 ± 0.001 | 29:11:21 | 30:09:27 | 3486 | 0.216 ± 0.014 | 14.7 |
| | | | | | | 38:15:19 | 38:57:09 | 2510 | 0.060 ± 0.009 | 4.52 |
| | | | | | | 40:16:36 | 40:59:51 | 2595 | 0.041 ± 0.005 | 4.53 |
| 504940201 | R. Wijnands | 2007-09-06 10:27:56 | 2007-09-06 13:39:06 | 11.1 | 0.109 ± 0.002 | ..... | ..... | ..... | ..... | ..... |
| 511000301[i] | R. Wijnands | 2008-03-03 23:47:45 | 2008-03-04 01:19:25 | 5.1 | 0.111 ± 0.004 | ..... | ..... | ..... | ..... | ..... |
| 505670101 | A. Goldwurm | 2008-03-23 17:21:01 | 2008-03-24 20:17:25 | 96.6 | 0.110 ± 0.001 | ..... | ..... | ..... | ..... | ..... |
| 511000401[i] | R. Wijnands | 2008-09-23 15:53:29 | 2008-09-23 17:08:17 | 5.1 | 0.096 ± 0.004 | ..... | ..... | ..... | ..... | ..... |
| 554750401 | A. Goldwurm | 2009-04-01 01:17:45 | 2009-04-01 11:58:54 | 38.0 | 0.105 ± 0.001 | ..... | ..... | ..... | ..... | ..... |
| 554750501 | A. Goldwurm | 2009-04-03 01:55:00 | 2009-04-03 13:43:39 | 42.4 | 0.101 ± 0.001 | 08:47:39 | 09:13:39 | 1560 | 0.059 ± 0.010 | 10.7 |
| 554750601 | A. Goldwurm | 2009-04-05 03:52:26 | 2009-04-05 13:02:10 | 32.8 | 0.104 ± 0.002 | ..... | ..... | ..... | ..... | ..... |
| 604300601 | D. Porquet | 2011-03-28 08:11:53 | 2011-03-28 21:15:04 | 45.2 | 0.092 ± 0.001 | ..... | ..... | ..... | ..... | ..... |
| 604300701 | D. Porquet | 2011-03-30 09:25:00 | 2011-03-30 21:12:57 | 42.3 | 0.099 ± 0.001 | 17:42:01 | 18:15:46 | 2025 | 0.119 ± 0.010 | 11.9 |
| 604300801 | D. Porquet | 2011-04-01 09:01:06 | 2011-04-01 19:09:54 | 37.3 | 0.090 ± 0.002 | ..... | ..... | ..... | ..... | ..... |
| 604300901 | D. Porquet | 2011-04-03 08:14:00 | 2011-04-03 18:55:51 | 36.5 | 0.098 ± 0.002 | 07:51:24 | 08:34:59 | 2615 | 0.104 ± 0.008 | 4.26 |
| 604301001 | D. Porquet | 2011-04-05 07:31:48 | 2011-04-05 20:26:33 | 48.1 | 0.089 ± 0.002 | ..... | ..... | ..... | ..... | ..... |
| 658600101 | C. Darren Dowell | 2011-08-31 23:36:30 | 2011-09-01 13:04:17 | 47.6 | 0.098 ± 0.001 | ..... | ..... | ..... | ..... | ..... |
| 658600201 | C. Darren Dowell | 2011-09-01 20:25:57 | 2011-09-02 10:44:22 | 51.3 | 0.095 ± 0.001 | ..... | ..... | ..... | ..... | ..... |
| 674600601 | A. Goldwurm | 2012-03-13 04:14:14 | 2012-03-13 09:47:24 | 19.6 | 0.096 ± 0.002 | ..... | ..... | ..... | ..... | ..... |
| 674600701 | A. Goldwurm | 2012-03-15 05:09:04 | 2012-03-15 09:10:51 | 14.0 | 0.094 ± 0.002 | ..... | ..... | ..... | ..... | ..... |
| 674601101 | A. Goldwurm | 2012-03-17 03:21:30 | 2012-03-17 10:09:54 | 25.7 | 0.101 ± 0.003 | ..... | ..... | ..... | ..... | ..... |
| 674600801 | A. Goldwurm | 2012-03-19 04:14:14 | 2012-03-19 10:12:43 | 21.0 | 0.096 ± 0.002 | ..... | ..... | ..... | ..... | ..... |
| 674601001 | A. Goldwurm | 2012-03-21 03:52:26 | 2012-03-21 10:07:06 | 22.0 | 0.094 ± 0.002 | ..... | ..... | ..... | ..... | ..... |
| 694640301 | R. Terrier | 2012-08-31 11:42:07 | 2012-08-31 22:57:43 | 40.0 | 0.078 ± 0.001 | ..... | ..... | ..... | ..... | ..... |
| 694640401[e] | R. Terrier | 2012-09-02 19:09:49 | 2012-09-03 09:34:03 | 53.0 | 0.010 ± 0.0002 | ..... | ..... | ..... | ..... | ..... |
| 694641001[e] | R. Terrier | 2012-09-23 20:42:07 | 2012-09-24 09:36:52 | 46.0 | 0.015 ± 0.0002 | ..... | ..... | ..... | ..... | ..... |
| 694641101[e] | R. Terrier | 2012-09-24 10:38:50 | 2012-09-24 21:53:44 | 40.0 | 0.068 ± 0.001 | ..... | ..... | ..... | ..... | ..... |
| 724210201 | G. Ponti | 2013-08-30 20:52:40 | 2013-08-31 12:26:18 | 55.6 | 0.534 ± 0.003 | ..... | ..... | ..... | ..... | ..... |
| 700980101 | D. Haggard | 2013-09-10 04:12:07 | 2013-09-10 14:11:46 | 35.7 | 0.538 ± 0.003 | ..... | ..... | ..... | ..... | ..... |
| 724210501 | G. Ponti | 2013-09-22 21:54:32 | 2013-09-23 09:17:52 | 39.4 | 0.506 ± 0.003 | ..... | ..... | ..... | ..... | ..... |
| 723410301 | N. Grosso | 2014-02-28 18:18:41 | 2014-03-01 08:53:15 | 51.9 | 0.320 ± 0.002 | ..... | ..... | ..... | ..... | ..... |
| 723410401 | N. Grosso | 2014-03-10 14:49:09 | 2014-03-11 05:57:28 | 54.0 | 0.312 ± 0.002 | 17:07:55 | 19:03:51 | 6956 | 0.119 ± 0.008 | 6.76 |
| 723410501 | N. Grosso | 2014-04-02 03:42:35 | 2014-04-02 20:22:19 | 54.9 | 0.287 ± 0.002 | 16:53:00 | 17:08:44 | 944 | 0.200 ± 0.013 | 20.7 |
| 69044180[h] | G.L. Israël | 2014-04-03 05:48:45 | 2014-04-04 05:01:14 | 83.5 | 0.294 ± 0.002 | ..... | ..... | ..... | ..... | ..... |
| 74363020[h] | G. Ponti | 2014-08-30 20:00:24 | 2014-08-31 04:54:26 | 28.5 | 0.170 ± 0.003 | 23:46:11 | 24:53:59 | 4068 | 0.282 ± 0.023 | 15.0 |
| | | | | | | 25:06:08 | 25:19:18 | 790 | 0.116 ± 0.019 | 16.8 |
| | | | | | | 28:36:49 | 28:53:19 | 990 | 0.234 ± 0.023 | 18.4 |
| 743630301 | G. Ponti | 2014-08-31 21:03:54 | 2014-09-01 04:01:15 | 22.3 | 0.169 ± 0.003 | 25:21:16 | 25:55:05 | 2029 | 0.135 ± 0.012 | 12.4 |
| 743630401 | G. Ponti | 2014-09-27 19:47:57 | 2014-09-28 02:57:18 | 22.9 | 0.177 ± 0.002 | ..... | ..... | ..... | ..... | ..... |
| 743630501 | G. Ponti | 2014-09-28 21:42:09 | 2014-09-29 08:12:51 | 33.7 | 0.167 ± 0.002 | 30:06:58 | 30:12:47 | 349 | 0.160 ± 0.031 | 36.7 |
| 743630601 | G. Ponti | 2015-02-26 06:58:40 | 2015-02-26 15:26:25 | 27.1 | 0.152 ± 0.002 | ..... | ..... | ..... | ..... | ..... |
| 743630701[f] | G. Ponti | 2015-03-31 10:25:12 | 2015-03-31 10:26:38 | 0.1 | 0.253 ± 0.058 | ..... | ..... | ..... | ..... | ..... |
| 743630801 | G. Ponti | 2015-04-01 09:14:43 | 2015-04-01 15:55:24 | 21.5 | 0.164 ± 0.002 | ..... | ..... | ..... | ..... | ..... |
| 743630901 | G. Ponti | 2015-04-02 09:39:43 | 2015-04-02 11:35:50 | 6.23 | 0.182 ± 0.004 | ..... | ..... | ..... | ..... | ..... |

**Notes:** Flare starts and stops in bold face are those beginning or ending at the start or stop of the observation leading to a lower limit on the flare duration and a lower or upper limit on the flare mean count rate and mean flux. The flux value of these flares were taken equal to this limit in the flaring rate study. [(a)] The flare start and end times are given in hh:mm:ss since the day of the observation start; [(b)] The flare mean count rates are computed after subtraction of the non-flaring level; [(c)] Mean unabsorbed flux between 2 and 10 keV determined for $N_{\rm H} = 14.3 \times 10^{22}$ $cm^{-2}$ and $\Gamma = 2$; [(d)] For this observation, the Galactic Center was observed only with EPIC/pn; [(e)] For these observations, the Galactic Center was observed only with EPIC/MOS1 and 2; [(f)] The data transfer from XMM-Newton to the Earth during this observation was affected by the GALILEO launch and Early Orbit Phase; [(g)] Frame window extended mode; [(h)] Small window; [(i)] Thin filter; [(j)] Thick filter.

Table C.2: Observation log of public Chandra observations and the detected X-ray flares.

| ObsID | PI | Observation start (UT) | Observation end (UT) | Duration (ks) | Instrument | Non-flaring level (count $s^{-1}$) | Flare start[a] (UT) | Flare stop[a] (UT) | Flare duration (s) | Mean count rate[b] (count $s^{-1}$) | Mean flux[c] ($10^{-12}$ erg $s^{-1}$ $cm^{-2}$) |
|---|---|---|---|---|---|---|---|---|---|---|---|
| 242 | G. Garmire | 1999-09-21 02:40:30 | 1999-09-21 17:03:17 | 46.5 | ACIS-I3 | 0.0048 ± 0.0001 | 02:40:49 | 04:10:23 | 5374 | 0.004 ± 0.001 | 1.30 |
| 1561 | F. Baganoff | 2000-10-26 19:05:19 | 2001-07-14 05:56:28 | 49.9 | ACIS-I3 | 0.0059 ± 0.0008 | 26:36:54 | 26:46:39 | 585 | 0.030 ± 0.014 | 3.52 |
| | | | | | | | 28:55:12 | 30:46:46 | 6694 | 0.110 ± 0.004 | 11.5 |
| 2951 | G. Garmire | 2002-02-19 14:26:32 | 2002-02-19 18:32:35 | 12.5 | ACIS-I3 | 0.0039 ± 0.0009 | ..... | ..... | ..... | ..... | ..... |
| 2952 | G. Garmire | 2002-03-23 12:23:04 | 2002-03-23 16:10:07 | 12.0 | ACIS-I3 | 0.0053 ± 0.0007 | ..... | ..... | ..... | ..... | ..... |
| 2953 | G. Garmire | 2002-04-19 10:57:39 | 2002-04-19 14:13:34 | 11.7 | ACIS-I3 | 0.0042 ± 0.0006 | ..... | ..... | ..... | ..... | ..... |
| 2954 | G. Garmire | 2002-05-07 09:23:04 | 2002-05-07 13:18:12 | 12.6 | ACIS-I3 | 0.0047 ± 0.0006 | ..... | ..... | ..... | ..... | ..... |
| 2943 | F. Baganoff | 2002-05-22 23:17:41 | 2002-05-23 09:55:42 | 38.2 | ACIS-I3 | 0.0054 ± 0.0003 | ..... | ..... | ..... | ..... | ..... |
| 3663 | F. Baganoff | 2002-05-24 11:49:02 | 2002-05-24 22:56:10 | 38.5 | ACIS-I3 | 0.0056 ± 0.0003 | 19:06:04 | 20:23:14 | 4630 | 0.015 ± 0.002 | 2.31 |
| 3392 | F. Baganoff | 2002-05-25 15:13:52 | 2002-05-27 14:32:44 | 168.9 | ACIS-I3 | 0.0052 ± 0.0005 | 28:04:29 | 28:54:04 | 2975 | 0.018 ± 0.009 | 0.87 |
| | | | | | | | 37:37:32 | 38:01:48 | 1456 | 0.015 ± 0.009 | 1.00 |
| | | | | | | | 53:33:16 | 53:49:15 | 959 | 0.024 ± 0.008 | 0.69 |
| 3393 | F. Baganoff | 2002-05-28 05:33:33 | 2002-05-30 02:33:05 | 160.1 | ACIS-I3 | 0.0048 ± 0.0003 | 15:10:11 | 16:02:55 | 3164 | 0.081 ± 0.040 | 0.61 |
| | | | | | | | 29:40:49 | 31:03:47 | 4978 | 0.027 ± 0.012 | 3.28 |
| | | | | | | | 42:37:15 | 42:52:43 | 928 | 0.058 ± 0.016 | 6.40 |
| 3665 | F. Baganoff | 2002-06-03 01:22:29 | 2002-06-04 03:23:00 | 91.1 | ACIS-I3 | 0.0050 ± 0.0002 | ..... | ..... | ..... | ..... | ..... |
| 3549 | G. Garmire | 2003-06-19 18:26:46 | 2003-06-20 01:52:50 | 25.1 | ACIS-I3 | 0.0055 ± 0.0004 | ..... | ..... | ..... | ..... | ..... |
| 4683 | G. Garmire | 2004-07-05 22:32:02 | 2004-07-06 12:54:49 | 50.2 | ACIS-I3 | 0.0049 ± 0.0003 | ..... | ..... | ..... | ..... | ..... |
| 4684 | G. Garmire | 2004-07-06 22:27:16 | 2004-07-07 12:50:57 | 50.2 | ACIS-I3 | 0.0056 ± 0.0004 | 27:17:55 | 28:04:40 | 2805 | 0.039 ± 0.022 | 4.87 |
| 5360 | F. Baganoff | 2004-08-28 12:02:59 | 2004-08-28 13:59:10 | 5.2 | ACIS-I3 | 0.0036 ± 0.0008 | ..... | ..... | ..... | ..... | ..... |
| 6113 | F. Baganoff | 2005-02-27 06:23:57 | 2005-02-27 08:27:17 | 4.9 | ACIS-I3 | 0.0054 ± 0.0011 | ..... | ..... | ..... | ..... | ..... |
| 5950 | F. Baganoff | 2005-07-24 19:56:25 | 2005-07-25 10:05:43 | 49.2 | ACIS-I3 | 0.0052 ± 0.0003 | ..... | ..... | ..... | ..... | ..... |
| 5951 | F. Baganoff | 2005-07-27 19:06:08 | 2005-07-28 08:25:32 | 45.2 | ACIS-I3 | 0.0048 ± 0.0003 | ..... | ..... | ..... | ..... | ..... |
| 5952 | F. Baganoff | 2005-07-29 19:48:58 | 2005-07-30 09:05:36 | 45.9 | ACIS-I3 | 0.0055 ± 0.0003 | 26:31:09 | 27:29:10 | 3481 | 0.016 ± 0.002 | 2.16 |
| 5953 | F. Baganoff | 2005-07-30 19:37:18 | 2005-07-31 09:10:32 | 46.0 | ACIS-I3 | 0.0052 ± 0.0002 | 22:13:27 | 22:47:55 | 2068 | 0.043 ± 0.004 | 5.13 |
| 5954 | F. Baganoff | 2005-08-01 20:13:00 | 2005-08-02 01:16:15 | 18.1 | ACIS-I3 | 0.0042 ± 0.0005 | ..... | ..... | ..... | ..... | ..... |
| 6639 | F. Baganoff | 2006-04-11 05:31:13 | 2006-04-11 07:06:03 | 4.5 | ACIS-I3 | 0.0044 ± 0.0011 | ..... | ..... | ..... | ..... | ..... |
| 6640 | F. Baganoff | 2006-05-03 22:24:25 | 2006-05-04 00:22:07 | 5.2 | ACIS-I3 | 0.0076 ± 0.0013 | ..... | ..... | ..... | ..... | ..... |
| 6641 | F. Baganoff | 2006-06-01 16:05:47 | 2006-06-01 17:55:45 | 5.1 | ACIS-I3 | 0.0097 ± 0.0014 | ..... | ..... | ..... | ..... | ..... |
| 6642 | F. Baganoff | 2006-07-04 10:59:35 | 2006-07-04 12:51:17 | 5.2 | ACIS-I3 | 0.0070 ± 0.0012 | ..... | ..... | ..... | ..... | ..... |
| 6363 | F. Baganoff | 2006-07-17 03:56:11 | 2006-07-17 12:41:06 | 30.2 | ACIS-I3 | 0.0042 ± 0.0004 | 05:52:05 | 06:35:07 | 2516 | 0.055 ± 0.007 | 6.49 |
| 6643 | F. Baganoff | 2006-07-30 14:28:24 | 2006-07-30 16:21:53 | 5.0 | ACIS-I3 | 0.0042 ± 0.0009 | ..... | ..... | ..... | ..... | ..... |
| 6644 | F. Baganoff | 2006-08-22 05:52:40 | 2006-08-22 07:46:29 | 5.0 | ACIS-I3 | 0.0054 ± 0.0011 | ..... | ..... | ..... | ..... | ..... |
| 6645 | F. Baganoff | 2006-09-25 13:48:17 | 2006-09-25 15:41:27 | 5.2 | ACIS-I3 | 0.0061 ± 0.0009 | 14:00:33 | 14:23:03 | 1350 | 0.008 ± 0.003 | 2.07 |
| 6646 | F. Baganoff | 2006-10-29 03:27:20 | 2006-10-29 05:12:30 | 5.2 | ACIS-I3 | 0.0071 ± 0.0012 | **03:27:20** | 03:48:38 | >1338 | 0.012 ± 0.006 | 3.45 |
| 7554 | F. Baganoff | 2007-02-11 06:15:10 | 2007-02-11 08:14:16 | 5.1 | ACIS-I3 | 0.0044 ± 0.0009 | ..... | ..... | ..... | ..... | ..... |
| 7555 | F. Baganoff | 2007-03-25 22:53:57 | 2007-03-26 00:50:14 | 5.2 | ACIS-I3 | 0.0055 ± 0.0011 | ..... | ..... | ..... | ..... | ..... |
| 7556 | F. Baganoff | 2007-05-17 01:02:59 | 2007-05-17 03:11:34 | 5.0 | ACIS-I3 | 0.0060 ± 0.0011 | ..... | ..... | ..... | ..... | ..... |
| 7557 | F. Baganoff | 2007-07-20 02:25:15 | 2007-07-20 04:27:51 | 5.0 | ACIS-I3 | 0.0047 ± 0.0006 | ..... | ..... | ..... | ..... | ..... |
| 7558 | F. Baganoff | 2007-09-02 20:17:30 | 2007-09-02 22:01:29 | 5.0 | ACIS-I3 | 0.0072 ± 0.0012 | ..... | ..... | ..... | ..... | ..... |
| 7559 | F. Baganoff | 2007-10-26 10:02:16 | 2007-10-26 11:50:28 | 5.1 | ACIS-I3 | 0.0050 ± 0.0010 | ..... | ..... | ..... | ..... | ..... |
| 9169 | F. Yusef-zadeh | 2008-05-05 03:50:56 | 2008-05-05 12:05:56 | 28.0 | ACIS-I3 | 0.0055 ± 0.0005 | 10:35:14 | 11:42:44 | 4050 | 0.006 ± 0.002 | 1.27 |
| 9170 | F. Yusef-zadeh | 2008-05-06 02:58:17 | 2008-05-06 10:58:05 | 27.1 | ACIS-I3 | 0.0050 ± 0.0004 | ..... | ..... | ..... | ..... | ..... |
| 9171 | F. Yusef-zadeh | 2008-05-10 03:15:52 | 2008-05-10 11:24:06 | 28.0 | ACIS-I3 | 0.0048 ± 0.0004 | ..... | ..... | ..... | ..... | ..... |
| 9172 | F. Yusef-zadeh | 2008-05-11 03:34:30 | 2008-05-11 11:42:23 | 27.8 | ACIS-I3 | 0.0053 ± 0.0005 | ..... | ..... | ..... | ..... | ..... |
| 9174 | F. Yusef-zadeh | 2008-07-25 21:48:55 | 2008-07-26 06:25:59 | 29.2 | ACIS-I3 | 0.0044 ± 0.0003 | ..... | ..... | ..... | ..... | ..... |
| 9173 | F. Yusef-zadeh | 2008-07-26 21:18:02 | 2008-07-27 05:27:58 | 28.1 | ACIS-I3 | 0.0038 ± 0.0004 | ..... | ..... | ..... | ..... | ..... |
| 10556 | F. Baganoff | 2009-05-18 02:18:24 | 2009-05-19 10:22:34 | 114.0 | ACIS-I3 | 0.0053 ± 0.0002 | 02:34:59 | 02:58:54 | 1435 | 0.031 ± 0.007 | 4.03 |
| | | | | | | | 09:41:05 | 10:39:26 | 3501 | 0.019 ± 0.003 | 2.57 |
| | | | | | | | 23:03:43 | 23:30:56 | 1633 | 0.091 ± 0.007 | 9.07 |
| | | | | | | | 24:29:22 | 24:51:37 | 465 | 0.091 ± 0.015 | 10.8 |
| 11843 | G. Garmire | 2010-05-13 02:11:23 | 2010-05-14 00:41:47 | 80.0 | ACIS-I3 | 0.0059 ± 0.0003 | 03:30:04 | 04:38:30 | 4106 | 0.036 ± 0.026 | 3.36 |
| 13016 | F. Baganoff | 2011-03-29 10:29:11 | 2011-03-29 15:56:33 | 18.1 | ACIS-I3 | 0.0035 ± 0.0005 | 10:40:51 | 11:33:35 | 3164 | 0.009 ± 0.003 | 1.70 |
| 13017 | F. Baganoff | 2011-03-31 10:28:17 | 2011-03-31 15:58:39 | 18.1 | ACIS-I3 | 0.0047 ± 0.0005 | ..... | ..... | ..... | ..... | ..... |
| 13508 | R. Terrier | 2011-07-19 01:21:58 | 2011-07-19 10:38:44 | 31.9 | ACIS-I0 | 0.0028 ± 0.0003 | ..... | ..... | ..... | ..... | ..... |
| 12949 | R. Terrier | 2011-07-21 07:14:23 | 2011-07-22 00:19:59 | 59.2 | ACIS-I0 | 0.0030 ± 0.0001 | 18:04:31 | 18:11:33 | 422 | 0.045 ± 0.011 | 20.5 |
| 13438 | R. Terrier | 2011-07-29 05:32:16 | 2011-07-30 00:31:56 | 67.1 | ACIS-I0 | 0.0019 ± 0.0001 | ..... | ..... | ..... | ..... | ..... |
| 13850 | F. Baganoff | 2012-02-06 00:36:15 | 2012-02-06 17:53:58 | 60.1 | ACIS-S3/HETG | 0.0061 ± 0.0003 | ..... | ..... | ..... | ..... | ..... |
| 14392 | F. Baganoff | 2012-02-09 06:15:50 | 2012-02-09 23:18:07 | 59.2 | ACIS-S3/HETG | 0.0054 ± 0.0003 | 10:38:58 | 10:57:02 | 1084 | 0.016 ± 0.002 | 1.74 |
| | | | | | | | 14:25:32 | 16:03:51 | 5899 | 0.109 ± 0.004 | 20.5 |
| 14394 | F. Baganoff | 2012-02-10 03:15:10 | 2012-02-10 08:50:27 | 18.1 | ACIS-S3/HETG | 0.0065 ± 0.0005 | ..... | ..... | ..... | ..... | ..... |
| 14393 | F. Baganoff | 2012-02-11 10:12:07 | 2012-02-11 22:19:03 | 41.5 | ACIS-S3/HETG | 0.0077 ± 0.0004 | ..... | ..... | ..... | ..... | ..... |
| 13856 | F. Baganoff | 2012-03-15 08:44:14 | 2012-03-15 20:24:26 | 40.1 | ACIS-S3/HETG | 0.0055 ± 0.0004 | ..... | ..... | ..... | ..... | ..... |
| 13857 | F. Baganoff | 2012-03-17 08:56:51 | 2012-03-17 20:27:57 | 39.6 | ACIS-S3/HETG | 0.0066 ± 0.0005 | 16:04:36 | 16:23:02 | 1106 | 0.031 ± 0.006 | 4.41 |
| 13854 | F. Baganoff | 2012-03-20 10:12:19 | 2012-03-20 17:06:09 | 23.1 | ACIS-S3/HETG | 0.0081 ± 0.0011 | 11:41:40 | 12:04:27 | 1367 | 0.046 ± 0.006 | 4.47 |
| | | | | | | | 12:41:11 | 13:03:23 | 1332 | 0.047 ± 0.006 | 4.00 |
| | | | | | | | 14:03:42 | 14:26:06 | 1344 | 0.042 ± 0.006 | 4.34 |
| | | | | | | | 16:23:47 | 16:46:59 | 1392 | 0.095 ± 0.008 | 3.72 |
| 14413 | F. Baganoff | 2012-03-21 06:43:00 | 2012-03-21 11:08:58 | 14.7 | ACIS-S3/HETG | 0.0064 ± 0.0006 | ..... | ..... | ..... | ..... | ..... |
| 13855 | F. Baganoff | 2012-03-22 11:23:50 | 2012-03-22 17:29:22 | 20.1 | ACIS-S3/HETG | 0.0067 ± 0.0006 | ..... | ..... | ..... | ..... | ..... |
| 14414 | F. Baganoff | 2012-03-23 17:47:45 | 2012-03-24 00:00:18 | 20.1 | ACIS-S3/HETG | 0.0060 ± 0.0005 | ..... | ..... | ..... | ..... | ..... |
| 13847 | F. Baganoff | 2012-04-30 16:17:14 | 2012-05-02 11:37:48 | 154.1 | ACIS-S3/HETG | 0.0067 ± 0.0002 | 36:21:51 | 37:09:26 | 2855 | 0.016 ± 0.001 | 2.71 |
| 14427 | F. Baganoff | 2012-05-06 19:59:28 | 2012-05-07 18:51:38 | 80.1 | ACIS-S3/HETG | 0.0059 ± 0.0005 | 26:18:42 | 27:51:28 | 5566 | 0.015 ± 0.002 | 2.66 |
| | | | | | | | 35:16:52 | 35:44:31 | 1659 | 0.013 ± 0.003 | 1.31 |
| 13848 | F. Baganoff | 2012-05-09 12:01:48 | 2012-05-10 15:41:05 | 98.2 | ACIS-S3/HETG | 0.0066 ± 0.0002 | ..... | ..... | ..... | ..... | ..... |
| 13849 | F. Baganoff | 2012-05-11 03:17:40 | 2012-05-13 05:39:54 | 178.7 | ACIS-S3/HETG | 0.0071 ± 0.0003 | 16:37:37 | 17:24:19 | 2802 | 0.019 ± 0.003 | 2.01 |
| | | | | | | | 24:20:31 | 25:52:29 | 5518 | 0.009 ± 0.002 | 1.72 |
| | | | | | | | 31:41:37 | 32:15:35 | 2038 | 0.021 ± 0.004 | 9.20 |
| | | | | | | | 51:10:55 | 51:57:34 | 2799 | 0.041 ± 0.005 | 2.08 |
| 13846 | F. Baganoff | 2012-05-16 10:40:15 | 2012-05-17 02:18:07 | 56.2 | ACIS-S3/HETG | 0.0064 ± 0.0003 | ..... | ..... | ..... | ..... | ..... |
| 14438 | F. Baganoff | 2012-05-18 04:27:35 | 2012-05-18 12:10:09 | 25.8 | ACIS-S3/HETG | 0.0060 ± 0.0005 | ..... | ..... | ..... | ..... | ..... |
| 13845 | F. Baganoff | 2012-05-19 10:41:18 | 2012-05-21 00:48:07 | 135.3 | ACIS-S3/HETG | 0.0062 ± 0.0002 | 13:50:55 | 14:28:21 | 2246 | 0.013 ± 0.003 | 4.79 |
| | | | | | | | 44:48:29 | 46:03:33 | 4504 | 0.056 ± 0.004 | 2.62 |
| 14461 | F. Baganoff | 2012-07-09 22:33:10 | 2012-07-10 05:47:47 | 24.1 | ACIS-S3/HETG | 0.0050 ± 0.0006 | ..... | ..... | ..... | ..... | ..... |
| 14461 | F. Baganoff | 2012-07-10 23:10:04 | 2012-07-11 05:21:09 | 20.1 | ACIS-S3/HETG | 0.0051 ± 0.0005 | ..... | ..... | ..... | ..... | ..... |
| 14461 | F. Baganoff | 2012-07-12 05:47:45 | 2012-07-12 19:58:25 | 51.0 | ACIS-S3/HETG | 0.0073 ± 0.0004 | ..... | ..... | ..... | ..... | ..... |
| 13853 | F. Baganoff | 2012-07-14 00:36:15 | 2012-07-14 21:05:13 | 73.7 | ACIS-S3/HETG | 0.0057 ± 0.0003 | ..... | ..... | ..... | ..... | ..... |
| 13841 | F. Baganoff | 2012-07-17 21:05:19 | 2012-07-18 10:04:59 | 45.1 | ACIS-S3/HETG | 0.0064 ± 0.0004 | ..... | ..... | ..... | ..... | ..... |
| 14465 | F. Baganoff | 2012-07-18 23:23:20 | 2012-07-19 11:43:25 | 44.3 | ACIS-S3/HETG | 0.0057 ± 0.0004 | **23:23:20** | 25:01:37 | >5957 | 0.012 ± 0.002 | 2.51 |
| | | | | | | | 28:18:15 | 28:51:17 | 1982 | 0.012 ± 0.003 | 4.75 |

Table C.2: Continued.

| ObsID | PI | Observation start (UT) | Observation end (UT) | Duration (ks) | Instrument | Non-flaring level (count s$^{-1}$) | Flare start[a] (UT) | Flare stop[a] (UT) | Flare duration (s) | Mean count rate[b] (count s$^{-1}$) | Mean flux[c] ($10^{-12}$ erg s$^{-1}$ cm$^{-2}$) |
|---|---|---|---|---|---|---|---|---|---|---|---|
| 14466 | F. Baganoff | 2012-07-20 12:37:09 | 2012-07-21 01:32:24 | 45.1 | ACIS-S3/HETG | 0.0066 ± 0.0004 | 13:12:19 | 13:26:49 | 870 | 0.067 ± 0.009 | 5.61 |
| | | | | | | | 24:27:22 | 24:33:42 | 380 | 0.028 ± 0.008 | 5.39 |
| 13842 | F. Baganoff | 2012-07-21 11:52:09 | 2012-07-23 17:42:01 | 191.8 | ACIS-S3/HETG | 0.0059 ± 0.0003 | 28:31:33 | 29:40:45 | 4152 | 0.031 ± 0.003 | 2.21 |
| | | | | | | | 45:52:48 | 46:31:48 | 2340 | 0.049 ± 0.005 | 3.52 |
| | | | | | | | 60:14:54 | 62:01:49 | 6415 | 0.015 ± 0.001 | 3.34 |
| 13839 | F. Baganoff | 2012-07-24 07:02:13 | 2012-07-26 08:21:38 | 176.3 | ACIS-S3/HETG | 0.0067 ± 0.0003 | 09:19:45 | 09:41:03 | 1278 | 0.040 ± 0.006 | 3.11 |
| | | | | | | | 36:33:24 | 36:56:55 | 1411 | 0.066 ± 0.007 | 6.11 |
| | | | | | | | 48:07:41 | 50:07:09 | 7168 | 0.078 ± 0.005 | 1.69 |
| 13840 | F. Baganoff | 2012-07-26 20:02:14 | 2012-07-28 17:39:12 | 162.5 | ACIS-S3/HETG | 0.0069 ± 0.0002 | 59:06:44 | 60:45:28 | 5924 | 0.007 ± 0.001 | 1.80 |
| | | | | | | | 63:17:33 | 63:41:47 | 1454 | 0.014 ± 0.002 | 2.18 |
| 14432 | F. Baganoff | 2012-07-30 12:56:09 | 2012-07-31 10:12:43 | 74.3 | ACIS-S3/HETG | 0.0059 ± 0.0003 | **12:56:09** | 14:42:31 | >6442 | 0.003 ± 0.001 | 8.29 |
| | | | | | | | 32:56:20 | **34:12:43** | >4583 | 0.051 ± 0.004 | 9.08 |
| 13838 | F. Baganoff | 2012-08-01 17:28:12 | 2012-08-02 21:55:51 | 99.6 | ACIS-S3/HETG | 0.0068 ± 0.0003 | 51:18:28 | 51:31:33 | 785 | 0.024 ± 0.006 | 5.64 |
| 13852 | F. Baganoff | 2012-08-04 02:37:07 | 2012-08-05 22:37:20 | 156.6 | ACIS-S3/HETG | 0.0072 ± 0.0003 | 07:37:35 | 08:09:05 | 1890 | 0.042 ± 0.005 | 3.75 |
| | | | | | | | 32:07:01 | 32:22:59 | 958 | 0.016 ± 0.004 | 4.44 |
| 14439 | F. Baganoff | 2012-08-06 22:16:11 | 2012-08-08 05:44:50 | 111.7 | ACIS-S3/HETG | 0.0064 ± 0.0002 | 27:10:09 | 27:36:09 | 1560 | 0.009 ± 0.003 | 2.49 |
| 14462 | F. Baganoff | 2012-10-06 16:32:00 | 2012-10-08 06:19:59 | 133.4 | ACIS-S3/HETG | 0.0063 ± 0.0003 | 28:20:29 | 28:50:16 | 1787 | 0.024 ± 0.004 | 3.67 |
| | | | | | | | 52:37:38 | 53:13:08 | 2130 | 0.021 ± 0.002 | 12.4 |
| 14463 | F. Baganoff | 2012-10-16 00:50:55 | 2012-10-16 09:46:00 | 30.8 | ACIS-S3/HETG | 0.0066 ± 0.0006 | 05:46:23 | 05:54:11 | 468 | 0.102 ± 0.019 | 11.0 |
| 13851 | F. Baganoff | 2012-10-16 18:48:39 | 2012-10-18 01:03:03 | 107.1 | ACIS-S3/HETG | 0.0058 ± 0.0003 | 26:17:47 | 26:35:13 | 261 | 0.047 ± 0.007 | 1.61 |
| | | | | | | | 43:47:49 | 45:02:19 | 4470 | 0.073 ± 0.005 | 34.3 |
| 15568 | F. Baganoff | 2012-10-18 08:54:33 | 2012-10-18 19:35:13 | 36.1 | ACIS-S3/HETG | 0.0062 ± 0.0004 | 18:13:26 | **19:35:13** | >4907 | 0.006 ± 0.002 | 5.82 |
| 13843 | F. Baganoff | 2012-10-22 16:00:07 | 2012-10-24 02:07:34 | 120.7 | ACIS-S3/HETG | 0.0066 ± 0.0003 | 33:11:43 | 35:25:03 | 8000 | 0.031 ± 0.004 | 6.11 |
| 15570 | F. Baganoff | 2012-10-25 03:29:12 | 2012-10-25 23:11:05 | 68.7 | ACIS-S3/HETG | 0.0061 ± 0.0003 | 05:37:50 | 06:15:44 | 2274 | 0.027 ± 0.005 | 4.03 |
| 14468 | F. Baganoff | 2012-10-29 23:42:19 | 2012-10-31 17:01:14 | 146.1 | ACIS-S3/HETG | 0.0058 ± 0.0002 | 07:09:43 | 08:16:53 | 4030 | 0.019 ± 0.002 | 6.33 |
| | | | | | | | 37:44:54 | 38:13:41 | 1727 | 0.023 ± 0.001 | 2.01 |
| 14941 | F. Baganoff | 2013-04-06 01:21:15 | 2013-04-06 07:14:49 | 20.1 | ACIS-I3 | 0.0039 ± 0.0004 | ..... | ..... | ..... | ..... | ..... |
| 14942 | F. Baganoff | 2013-04-14 15:41:11 | 2013-04-14 21:49:30 | 20.1 | ACIS-I3 | 0.0051 ± 0.0005 | ..... | ..... | ..... | ..... | ..... |
| 14702 | N. Rea | 2013-05-12 10:36:44 | 2013-05-12 15:34:02 | 15.1 | ACIS-S3/subarray | 0.0236 ± 0.0013 | ..... | ..... | ..... | ..... | ..... |
| 15040 | D. Haggard | 2013-05-25 11:36:12 | 2013-05-25 18:48:48 | 24.4 | ACIS-S3/HETG | 0.0033 ± 0.0003 | 17:23:43 | 18:26:18 | 3750 | 0.006 ± 0.002 | 2.12 |
| 14703 | N. Rea | 2013-06-04 08:43:31 | 2013-06-04 14:27:14 | 18.6 | ACIS-S3/subarray | 0.0094 ± 0.0007 | ..... | ..... | ..... | ..... | ..... |
| 15651 | D. Haggard | 2013-06-05 21:30:38 | 2013-06-06 01:47:52 | 14.1 | ACIS-S3/HETG | 0.0032 ± 0.0005 | ..... | ..... | ..... | ..... | ..... |
| 15654 | D. Haggard | 2013-06-09 04:23:04 | 2013-06-09 07:36:37 | 9.3 | ACIS-S3/HETG | 0.0027 ± 0.0005 | ..... | ..... | ..... | ..... | ..... |
| 14946 | F. Baganoff | 2013-07-02 06:47:30 | 2013-07-02 12:43:53 | 20.1 | ACIS-S3/subarray | 0.0099 ± 0.0007 | ..... | ..... | ..... | ..... | ..... |
| 15042 | D. Haggard | 2013-07-27 01:27:10 | 2013-07-27 15:52:18 | 50.1 | ACIS-S3/subarray | 0.0141 ± 0.0006 | 03:29:36 | 03:46:53 | 1037 | 0.021 ± 0.021 | 7.01 |
| | | | | | | | 11:03:11 | 11:16:55 | 924 | 0.019 ± 0.016 | 4.47 |
| 15042 | D. Haggard | 2013-08-11 22:55:23 | 2013-08-12 13:05:40 | 49.4 | ACIS-S3/subarray | 0.0138 ± 0.0005 | ..... | ..... | ..... | ..... | ..... |
| 14945 | F. Baganoff | 2013-08-31 10:10:43 | 2013-08-31 16:26:04 | 20.1 | ACIS-S3/subarray | 0.0082 ± 0.0006 | ..... | ..... | ..... | ..... | ..... |
| 15043 | D. Haggard | 2013-09-14 00:03:23 | 2013-09-14 14:16:41 | 50.1 | ACIS-S3/subarray | 0.0090 ± 0.0006 | 02:02:00 | 04:29:39 | 8859 | 0.323 ± 0.024 | 38.2 |
| 14944 | F. Baganoff | 2013-09-20 07:00:52 | 2013-09-20 13:16:13 | 20.1 | ACIS-S3/subarray | 0.0144 ± 0.0008 | ..... | ..... | ..... | ..... | ..... |
| 15044 | D. Haggard | 2013-10-04 17:22:26 | 2013-10-05 06:58:38 | 47.1 | ACIS-S3/subarray | 0.0102 ± 0.0004 | ..... | ..... | ..... | ..... | ..... |
| 14943 | F. Baganoff | 2013-10-17 15:38:04 | 2013-10-17 21:41:46 | 20.1 | ACIS-S3/subarray | 0.0080 ± 0.0002 | ..... | ..... | ..... | ..... | ..... |
| 14704 | N. Rea | 2013-10-23 08:52:40 | 2013-10-23 20:41:18 | 40.1 | ACIS-S3/subarray | 0.0093 ± 0.0009 | ..... | ..... | ..... | ..... | ..... |
| 15045 | D. Haggard | 2013-10-28 14:30:21 | 2013-10-29 04:59:07 | 50.1 | ACIS-S3/subarray | 0.0087 ± 0.0005 | 14:47:38 | 16:48:34 | 7256 | 0.008 ± 0.004 | 3.95 |
| | | | | | | | 19:55:36 | 20:10:22 | 886 | 0.021 ± 0.016 | 3.90 |
| 16508 | D. Haggard | 2014-02-21 11:35:47 | 2014-02-22 01:23:57 | 47.9 | ACIS-S3/subarray | 0.0084 ± 0.0004 | ..... | ..... | ..... | ..... | ..... |
| 16211 | D. Haggard | 2014-03-14 10:16:20 | 2014-03-14 23:43:24 | 46.1 | ACIS-S3/subarray | 0.0052 ± 0.0003 | ..... | ..... | ..... | ..... | ..... |
| 16212 | D. Haggard | 2014-04-04 02:24:32 | 2014-04-04 16:47:09 | 50.1 | ACIS-S3/subarray | 0.0058 ± 0.0003 | ..... | ..... | ..... | ..... | ..... |
| 16213 | D. Haggard | 2014-04-28 02:42:49 | 2014-04-28 17:11:46 | 49.6 | ACIS-S3/subarray | 0.0068 ± 0.0003 | ..... | ..... | ..... | ..... | ..... |
| 16214 | D. Haggard | 2014-05-20 00:17:16 | 2014-05-20 14:46:55 | 50.1 | ACIS-S3/subarray | 0.0062 ± 0.0003 | ..... | ..... | ..... | ..... | ..... |
| 16210 | D. Haggard | 2014-06-03 02:56:53 | 2014-06-03 08:38:29 | 18.8 | ACIS-S3/subarray | 0.0063 ± 0.0006 | ..... | ..... | ..... | ..... | ..... |
| 16597 | D. Haggard | 2014-07-04 20:45:38 | 2014-07-05 02:18:48 | 18.2 | ACIS-S3/subarray | 0.0075 ± 0.0006 | ..... | ..... | ..... | ..... | ..... |
| 16215 | D. Haggard | 2014-07-16 22:41:39 | 2014-07-17 11:47:38 | 45.7 | ACIS-S3/subarray | 0.0069 ± 0.0004 | ..... | ..... | ..... | ..... | ..... |
| 16216 | D. Haggard | 2014-08-02 03:29:56 | 2014-08-02 17:07:33 | 47.1 | ACIS-S3/subarray | 0.0069 ± 0.0004 | ..... | ..... | ..... | ..... | ..... |
| 16217 | D. Haggard | 2014-08-30 04:47:01 | 2014-08-30 15:43:10 | 38.1 | ACIS-S3/subarray | 0.0097 ± 0.0006 | ..... | ..... | ..... | ..... | ..... |
| 16218 | D. Haggard | 2014-10-20 08:20:07 | 2014-10-20 19:57:00 | 40.1 | ACIS-S3/subarray | 0.0061 ± 0.0006 | 13:21:51 | 15:05:12 | 6201 | 0.127 ± 0.088 | 25.7 |
| 16963 | G. Garmire | 2015-02-13 01:00:03 | 2015-02-13 07:56:53 | 25.1 | ACIS-S3/subarray | 0.0058 ± 0.0005 | 06:03:19 | 06:16:51 | 812 | 0.033 ± 0.066 | 6.86 |
| 17236 | M. Clavel | 2015-04-25 14:09:31 | 2015-04-26 13:04:29 | 79.0 | ACIS-I3 | 0.0034 ± 0.0004 | ..... | ..... | ..... | ..... | ..... |
| 16966 | G. Garmire | 2015-05-14 08:45:36 | 2015-05-14 16:25:37 | 22.7 | ACIS-S3/subarray | 0.0034 ± 0.0004 | 12:01:25 | 12:53:24 | 3119 | 0.052 ± 0.007 | 6.44 |

**Notes:** Flare starts and stops in bold face are those beginning or ending at the start or stop of the observation leading to a lower limit on the flare duration and a lower or upper limit on the flare mean count rate and mean flux. The flux value of these flares were taken equal to this limit in the flaring rate study. [(a)] The flare start and end times are given in hh:mm:ss since the day of the observation start; [(b)] The flare mean count rates are computed after subtraction of the non-flaring level; [(c)] Mean unabsorbed flux between 2 and 10 keV determined for $N_{\rm H} = 14.3 \times 10^{22}$ cm$^{-2}$ and $\Gamma = 2$.

Table C.3: Observation log of public Swift observations and the detected X-ray flares.

| First observation (UT) | Last observation (UT) | Number of observations | Total exposure (ks) | Non-flaring level (count s$^{-1}$) | Flaring observation start (UT) | Flaring observation stop (UT) | Flare duration[a] (s) | Mean count rate[b] (count s$^{-1}$) | Mean flux[c] ($10^{-12}$ erg s$^{-1}$ cm$^{-2}$) |
|---|---|---|---|---|---|---|---|---|---|
| 2006-02-24 22:55:12 | 2006-11-02 14:22:34 | 198 | 261.7 | 0.021 ± 0.002 | 2006-07-13 21:57:36 | 2006-07-13 23:39:50 | 924 | 0.031 ± 0.007 | 15.3 |
| 2007-02-16 21:38:52 | 2007-11-02 13:52:19 | 163 | 174.6 | 0.025 ± 0.004 | 2007-03-03 00:38:21 | 2007-03-03 02:34:56 | 2018 | 0.012 ± 0.004 | 9.21 |
| 2008-02-19 23:02:24 | 2008-10-30 09:14:24 | 161 | 199.3 | 0.024 ± 0.003 | 2008-03-25 20:24:00 | 2008-03-25 23:36:58 | 707 | 0.056 ± 0.011 | 20.8 |
| | | | | | 2008-05-01 14:15:22 | 2008-05-01 20:39:50 | 1056 | 0.029 ± 0.007 | 8.66 |
| | | | | | 2008-10-17 17:15:22 | 2008-10-17 22:09:07 | 1369 | 0.036 ± 0.007 | 11.9 |
| 2009-06-04 07:23:31 | 2009-11-01 21:37:26 | 36 | 34.64 | 0.028 ± 0.009 | ..... | ..... | ..... | ..... | ..... |
| 2010-04-07 01:10:34 | 2010-10-31 10:10:34 | 62 | 70.33 | 0.030 ± 0.006 | 2010-06-12 10:23:31 | 2010-06-12 12:07:12 | 1081 | 0.127 ± 0.012 | 49.3 |
| 2011-02-04 16:53:46 | 2011-11-02 15:38:53 | 81 | 76.78 | 0.025 ± 0.006 | ..... | ..... | ..... | ..... | ..... |
| 2012-02-05 20:12:29 | 2012-10-31 23:21:07 | 79 | 73.95 | 0.020 ± 0.005 | ..... | ..... | ..... | ..... | ..... |
| 2013-02-03 22:26:24 | 2013-10-31 01:17:46 | 191 | 185.4 | 0.145 ± 0.009 | ..... | ..... | ..... | ..... | ..... |
| 2014-02-03 18:57:36 | 2014-11-02 12:56:09 | 236 | 231.4 | 0.056 ± 0.007 | 2014-09-09 11:41:17 | 2014-09-09 11:58:34 | 975 | 0.128 ± 0.013 | 59.4 |
| 2015-02-03 00:18:43 | 2015-11-02 15:14:24 | 231 | 211.1 | 0.033 ± 0.004 | 2015-11-02 14:58:34 | 2015-11-02 15:14:24 | 993 | 0.074 ± 0.009 | 22.3 |

**Notes:** [(a)] The flare duration corresponds to the corresponding observational exposure; [(b)] The flare mean count rates are background subtracted; [(c)] Mean unabsorbed flux between 2 and 10 keV determined for $N_{\rm H} = 15.46 \times 10^{22}$ cm$^{-2}$ and $\Gamma = 2.07$.

# Appendix D

# Original publications

A&A 573, A46 (2015)
DOI: 10.1051/0004-6361/201424682
© ESO 2014

Astronomy & Astrophysics

# Study of the X-ray activity of Sagittarius A* during the 2011 *XMM-Newton* campaign⋆

Enmanuelle Mossoux[1], Nicolas Grosso[1], Frédéric H. Vincent[2], and Delphine Porquet[1]

[1] Observatoire Astronomique de Strasbourg, Université de Strasbourg, CNRS, UMR 7550, 11 rue de l'Université, 67000 Strasbourg, France
e-mail: enmanuelle.mossoux@astro.unistra.fr
[2] Nicolaus Copernicus Astronomical Center, ul. Bartycka 18, 00-716 Warszawa, Poland

Received 25 July 2014 / Accepted 19 September 2014

**ABSTRACT**

*Context.* At the dynamical center of the Milky Way, there is the closest supermassive black hole: Sgr A*. Its non-flaring luminosity is several orders of magnitude lower than the Eddington luminosity, but flares can be observed in the infrared and X-rays. This flaring activity can help us to understand radiation mechanisms from Sgr A*.
*Aims.* Our aim is to investigate the X-ray flaring activity of Sgr A* and to constrain the physical properties of the X-ray flares and their origin.
*Methods.* In March and April 2011, we observed Sgr A* with *XMM-Newton* with a total exposure of ≈226 ks in coordination with the 1.3 mm Very-Long-Baseline Interferometry array. We performed timing analysis of the X-ray emission from Sgr A* using a Bayesian-blocks algorithm to detect X-ray flares observed with *XMM-Newton*. Furthermore, we computed X-ray smoothed light curves observed in this campaign in order to have better accuracy on the position and the amplitude of the flares.
*Results.* We detected two X-ray flares on March 30 and April 3, 2011, which for comparison have a peak detection level of 6.8 and 5.9$\sigma$ in the *XMM-Newton*/EPIC (pn+MOS1+MOS2) light curve in the 2−10 keV energy range with a 300 s bin. The former is characterized by two sub-flares: the first one is very short (∼458 s) with a peak luminosity of $L^{\rm unabs}_{2-10\ \rm keV} \sim 9.4\times10^{34}$ erg s$^{-1}$, whereas the second one is longer (∼1542 s) with a lower peak luminosity ($L^{\rm unabs}_{2-10\ \rm keV} \sim 6.8\times10^{34}$ erg s$^{-1}$). The comparison with the sample of X-ray flares detected during the 2012 *Chandra* XVP campaign favors the hypothesis that the 2011 March 30 flare is a single flare rather than two distinct subflares. We model the light curve of this flare with the gravitational lensing of a simple hotspot-like structure, but we cannot satisfactorily reproduce the large decay of the light curve between the two subflares with this model. From magnetic energy heating during the rise phase of the first subflare and assuming an X-ray photons production efficiency of 1 and a magnetic field of 100 G at 2 $r_{\rm g}$, we derive an upper limit to the radial distance of the first subflare of $100^{+19}_{-29}$ $r_{\rm g}$. We use the decay phase of the first subflare to estimate a lower limit to the radial distance of 4 $r_{\rm g}$ from synchrotron cooling in the infrared.
*Conclusions.* The X-ray emitting region of the first subflare is located at a radial position of $4-100^{+19}_{-29}$ and has a corresponding radius of 1.8−2.87 ± 0.01 in $r_{\rm g}$ unit for a magnetic field of 100 G at 2 $r_{\rm g}$.

**Key words.** Galaxy: center – X-rays: individuals: Sgr A* – radiation mechanisms: general

## 1. Introduction

Our Galaxy hosts Sgr A* at its dynamical center. It is the closest supermassive black hole (SMBH) at a distance of about 8 kpc (Genzel et al. 2010; Falcke & Markoff 2013). Sgr A* has a mass, $M_{\rm BH}$, of about $4 \times 10^6$ $M_\odot$, which was determined thanks to the measurements of star motions (Schödel et al. 2002; Ghez et al. 2008; Gillessen et al. 2009). The Galactic center SMBH is usually in a steady state, emitting predominately at radio to submillimeter wavelengths. Its bolometric luminosity is about $10^{36}$ erg s$^{-1}$ (Yuan et al. 2003), which corresponds to $\approx 2 \times 10^{-9}$ $L_{\rm Edd}$ with $L_{\rm Edd} = 3.3 \times 10^4 (M_{\rm BH}/M_\odot) L_\odot$. To explain this low luminosity, researchers have developed various mass-accretion flow models, such as the advection-dominated accretion flows (ADAF; Narayan et al. 1998) and jet-disk models like the ejection of magnetized plasma (Falcke et al. 1993).

Wang et al. (2013) have recently inferred the temperature and density profile of the X-ray emitting gas around Sgr A* with the help of deep *Chandra* observations. They have shown that ≤1% of the gas initially captured by the SMBH at the Bondi radius reaches the innermost region around Sgr A*; i.e, ≥99% of the gas is ejected, which is consistent with the predictions of radiatively inefficient accretion flow (RIAF) models. Therefore, Sgr A* is the ideal astronomical target for investigating the physics of mass accretion and ejection onto SMBH in the regime of a low mass-accretion rate, a state where they are supposed to spend most of their lifetime (Ho et al. 2008). This physical understanding could then be extended to the normal galaxies that dominate the population of galaxies in the local Universe.

The detections of flares from Sgr A* (first discovered in X-rays; Baganoff et al. 2001) have provided a valuable way to scrutinize accreting matter close to the event horizon. The X-ray flare frequency is 1.1 (1.0−1.3) flare per day with $L_{2-8\ \rm keV} \geq 10^{34}$ erg s$^{-1}$ (Neilsen et al. 2013), though episodes of higher X-ray flaring activity can also be observed (Porquet et al. 2008; Neilsen et al. 2013). The bulk of X-ray flares detected so far have faint-to-moderate amplitudes with factors of about 2 to 45 compared to the non-flaring luminosity ($L_{2-8\ \rm keV} \approx 3.6\times10^{33}$ erg s$^{-1}$; Baganoff et al. 2003; Neilsen et al. 2013), and three very bright flares (factors of 100−160 times the non-flaring luminosity) have

⋆ Appendices are available in electronic form at http://www.aanda.org

A&A 573, A46 (2015)

been observed to share very similar spectral properties (Porquet et al. 2003, 2008; Nowak et al. 2012). The light curves of the X-ray flares can exhibit deep drops with short duration indicating that the X-ray emission comes from a region as compact as seven Schwarzschild radii ($R_S \equiv 2GM_{BH}/c^2 = 1.2 \times 10^{12}$ cm for Sgr A*, i.e., ≈0.6 AU; Porquet et al. 2003).

When near-infrared (NIR) and X-ray flares are detected simultaneously, their light curves have similar shapes, and there is no apparent delay (<3 min) between the peaks of flare emission (e.g., Yusef-Zadeh et al. 2006; Dodds-Eden et al. 2009; Eckart et al. 2012). The current interpretation is that both X-ray/NIR flares come from a region close to the event horizon, while delayed sub-mm (e.g., ≈100 min; Marrone et al. 2008) and mm peaks (up to 5 h; Yusef-Zadeh et al. 2009) have been interpreted as the adiabatic cooling of an expanding relativistic plasma blob. While NIR flares are known to be due to synchrotron emission (Eisenhauer et al. 2005; Eckart et al. 2006), the X-ray flare emission mechanism has not been settled yet, with arguments for synchrotron (Dodds-Eden et al. 2009; Barrière et al. 2014), inverse Compton (Yusef-Zadeh et al. 2012), and synchrotron self-Compton (Eckart et al. 2008) models.

We report here the results of our Sgr A* observation campaign performed with *XMM-Newton* from March 28 to April 5, 2011 in coordination with the 1.3 mm Very-Long-Baseline Interferometry array (VLBI). In Sect. 2 we describe the *XMM-Newton* observations and data processing. In Sect. 3 we present our timing analysis of Sgr A*. In Sect. 4 we describe the spectral analysis of the two flares from Sgr A* detected during this 2011 campaign. In Sect. 5 we compare these flares with those detected in the 2012 *Chandra* XVP campaign. We also try to model the first subflare with a simple hotspot model and estimate a lower and upper limit to the radial distance of this subflare. Finally, in Sect. 6 we summarize our main results.

## 2. *XMM-Newton* observations and data processing

### 2.1. Observation set-up

These X-ray observations of Sgr A* with *XMM-Newton* (AO-8, 5 × 33 ks; PI: D. Porquet) were designed to perform the first simultaneous observational campaign in X-rays and at 1.3 mm with the VLBI (Doeleman et al. 2008), in order to constrain the location X-ray flares. Five observing nights with the 1.3 mm VLBI were planned in 2011 between March 28 and April 5, using the weather forecast each day at noon for the final optimized scheduling (PI: S. Doeleman). The merged visibility window of the 1.3 mm VLBI array formed by the Atacama Pathfinder Experiment (APEX) in Chile, the Submillimeter Telescope (SMT) in Arizona, the Combined Array for Research in Millimeter-wave Astronomy (CARMA) in California, and the Submillimeter Array (SMA) in Hawaii is 10:45−15:45 UT. Since X-ray flare peaks appear to occur before submillimeter peak (Marrone et al. 2008) and since they can last up to three hours (Baganoff et al. 2001), our *XMM-Newton* observations started about three hours before the VLBI visibility window. We observed Sgr A* with *XMM-Newton* continuously from about 07:40 UT to about 16:00 universal time (UT), which is a duration of 30 ks. The *XMM-Newton* visibility windows finally constrained the five following dates: 2011 March 28 and 30 and April 1, 3, and 5. The 1.3 mm VLBI observations were obtained on 2011 March 29 and 31 and April 1 (simultaneous with *XMM-Newton*), 2, and 4; the results of these observations will be reported elsewhere. Two complementary *Chandra* observations were obtained to extend the X-ray coverage on 2011 March 29 and March 31 from 10:29 UT to 15:29 UT (Cycle 12; PI: F. Baganoff), the former being simultaneous with VLBI. The results of these observations will be reported elsewhere.

**Table 1.** *XMM-Newton* observation log for the Spring 2011 campaign.

| Orbit | ObsID | Start time[a] (TT) | End time[a] (TT) | Duration (s) |
|---|---|---|---|---|
| 2069 | 0604300601 | Mar. 28, 07:54:14 | Mar. 28, 21:13:55 | 47 981 |
| 2070 | 0604300701 | Mar. 30, 08:11:26 | Mar. 30, 21:14:28 | 46 942 |
| 2071 | 0604300801 | Apr. 01, 08:23:50 | Apr. 01, 19:23:59 | 39 609 |
| 2072 | 0604300901 | Apr. 03, 07:56:23 | Apr. 03, 19:21:36 | 41 113 |
| 2073 | 0604301001 | Apr. 05, 07:13:49 | Apr. 05, 21:11:49 | 50 280 |

**Notes.** [(a)] Start and end times of the EPIC MOS camera observations in terrestrial time (TT) referential.

The two *XMM-Newton*/EPIC MOS cameras (Turner et al. 2001) and the *XMM-Newton*/EPIC pn camera (Strüder et al. 2001) were operated in the full frame window mode with the medium filter. EPIC pn camera starts to observe after EPIC MOS cameras and stops before them. The effective starting and end times of each observation are reported in Table 1. These times are the time of the beginning and the stop of the observation with EPIC MOS cameras in the terrestrial time (TT) referential. For this observation, the relation between terrestrial time and UT is UT = TT − 66.18s (NASA's HEASARC Tool: xTime[1]).

### 2.2. Data processing

We observed Sgr A* five times with *XMM-Newton* in early 2011 for a total effective exposure of ≈226 ks. We use the version 13.5 of the Science Analysis Software (SAS) package for the data reduction and analysis, with the latest release of the current calibration files (CCF; as of 04/04/2014). The MOS and pn event lists were produced using the SAS tasks `emchain` and `epchain`, respectively. The full detector light curves in the 2−10 keV energy range computed by these tasks reveal that the observation was only slightly affected by weak soft proton flares. The count rate of these soft protons was high only during the last four, three, one, and four hours of the 1st, 2nd, 3rd, and 4th observations, respectively.

We concentrate on analysis of the central point source, Sgr A*and, in particular, on the search for the variability of its X-ray emission. To do this, we define the source+background region as a 10″-radius disk around the VLBI radio position of Sgr A*: RA(J2000) = $17^h45^m40\overset{s}{.}0409$, Dec(J2000) = −29°00′28.″118 (Reid et al. 1999). We do not register the EPIC coordinates again because the absolute astrometry for the EPIC cameras is about 1.″2 (Guainazzi 2013). To create the light curves, we selected the events for MOS and pn with `PATTERN`≤ 12 and `#XMMEA_SM`, and `PATTERN`≤ 4 and `FLAG==0`, respectively. The contribution of the background proton flares was estimated using a ≈3′ × 3′ area with a low level of X-ray extended emission, located on the same CCD at ≈4′ -north of Sgr A*, where the X-ray emission of point sources were subtracted. This data reduction is the same as in Porquet et al. (2008).

For each observation and detector, we first built the source+background (extracted from the 10″-radius region) and the background (extracted from the 3′ × 3′ region) light curves in the 2−10 keV energy range with 300 s time bins. During this

[1] The website of xTime is: `http://heasarc.gsfc.nasa.gov/cgi-bin/Tools/xTime/xTime.pl`

operation, we used the `epiclccorr` task to apply relative corrections to those light curves. The relative corrections specify the good time intervals (GTI) of the event list according to the corresponding CCD and compute the livetime, i.e., select the time inside each CCD frame where the events were collected effectively (no FIFO reset/overflow, minimum ionizing particles, or read-out-time). Then, this task subtracts the background light curve (scaled to the same source extraction area) from the source+background light curve and scales up count rates and errors affected by the lost of exposure. Finally, the background-subtracted light curves of the three detectors were summed to produce the EPIC light curves. Any missing count rate in a detector was inferred by the one observed by the other detectors using a scaling factor between them. To do this, we calculated the scaling factor between the detectors during a time period where all three cameras were turned on. The pn count rate is 1.31 times the sum of the MOS count rates.

## 3. Timing analysis

### 3.1. Bayesian blocks analysis

To identify the flaring and non-flaring levels under a certain probability using *the unbinned* event arrival time, we used the Bayesian blocks analysis proposed by Scargle (1998) and recently improved by Scargle et al. (2013a). The Bayesian blocks analysis of an event arrival time list from one of the EPIC cameras allowed us to segment the observing period with statistically different count rate levels and created a succession of constant count rate blocks. The time defining two successive blocks is called a change point. The count rate within each block is simply the number of events it contains divided by its effective exposure (livetime). The non-flaring and flaring levels are identified as the lowest and higher blocks, respectively. The duration of the flares are determined as the time range of the Bayesian block corresponding to the elevated count rate. This algorithm gives us the duration of the flaring and non-flaring levels with better accuracy than in a binned light curve since it uses the best temporal resolution available.

The number of change points is controlled by two input parameters: the false detection probability ($p_1$) and the prior estimate of the number of change points, *ncp_prior*. We use $p_1 = \exp(-3.5)$ (Neilsen et al. 2013; Nowak et al. 2012), i.e., the probability that a found change point is a real change point is $1-\exp(-3.5) = 96.8\%$ and the probability that a flare (at least two change points) is a real flare is $1 - p_1^2 = 99.9\%$. We cannot use the geometric prior of Scargle et al. (2013a) since our data contain more events and our non-flaring level is lower than in the simulations used by Scargle et al. (2013a), see Appendix A for a detailed explanation.

We used the EXPOSU## extension (## corresponding to the CCD number where the source extraction region is located) of the event list to compute the detector live time from the nominal TIMEDEL of the corresponding instrument, i.e., the integration time without the time of the shift of a CCD line to the readout node, which is about 0.0687022 and 2.59 s for pn and MOS, respectively. The Bayesian-block algorithm is used on the list of event of the source+background and of the background in which we selected the GTI (i.e., we reject the time where the camera did not observe). It allows us to correct the light curve source+background from the flaring background following the recipe of Scargle et al. (2013b). Indeed, thanks to Bayesian blocks, we know what the background count rate is and where the high-background levels are. We can correct the source+background event list of any background contribution by applying a weight to each event, which is $w = \mathrm{CR_{src+bkg}}/(\mathrm{CR_{src+bkg}} + \mathrm{CR_{bkg}})$ with $\mathrm{CR_{src+bkg}}$ the count rate of the Bayesian blocks of the source+background event list and $\mathrm{CR_{bkg}}$ the count rate of the corresponding Bayesian block of the background that is surface-corrected[2]. Then, the Bayesian-blocks algorithm is applied a second time to this corrected source+background event lists. This method is used on the three cameras separately.

### 3.2. Smoothed light curve

We compute a smoothed light curve by applying a density estimator (Silverman 1986; Feigelson & Babu 2012) on the *unbinned* event arrival times using GTI to suppress camera switch-off. The density estimator improves the characterization of light curve features, e.g., the amplitude and the time of a local maximum or minimum. The density is computed using `quantreg` in R package, which convolves the event arrival times with a smoothing kernel. We modify `quantreg` to use the Epanechnikov kernel, which is defined as $K(x) = \frac{3}{4}(1-x^2)$ for $|x| \leq 1$ and $K(x) = 0$ for $|x| > 1$. We chose the Epanechnikov kernel since it has "good performance" (Feigelson & Babu 2012); moreover, it is defined on a finite support, which allows us to control any boundary effects. The density estimator can be expressed as

$$\hat{f}(t,h) = \frac{1}{N}\sum_{i=1}^{N} \frac{w(t)}{livetime} \times K\left(\frac{t-t_\mathrm{i}}{h}\right) \quad (1)$$

with $h$ the width of the kernel window, $N$ the number of count in the event list, $t_\mathrm{i}$ the arrival time of the event $i$ and $t$ the time at which we compute the smoothed light curve, $w(t)$ the weight that corrects the density at the time $t$ from the flaring background thanks to the Bayesian-blocks algorithm (see above Sect. 3.1) and *livetime* is the live time in the time interval $[t_\mathrm{i} - h/2,\ t_\mathrm{i} + h/2]$. The time $t$ is chose by the user. Here, we take an even time grid with point interval of 5 s[3]. We choose a constant window width of the kernel $h = 100$ s. The smoothed count rate (CR) is obtained from the density by $CR = N\,\hat{f}(t,h)$. The error of the smoothed light curve is assumed to be Poissonnian ($=\sqrt{n}$ with $n$ the number of count in the kernel window). Then, we insert observing gaps using GTIs and combine the light curves of the three instruments.

### 3.3. Results

The EPIC (pn+MOS1+MOS2) background-subtracted light curves of Sgr A* in the 2−10 keV energy range, with a time bin interval of 300 s, are shown in Fig. 1. Our Bayesian-blocks analysis of the event list for individual detectors shows that during the first exposure, no flares were detected and the activity of the source region is constant. The first flare (#1) was observed on 2011 March 30 and the last flare (#2) on 2011 April 3. The non-flaring level is determined as the count rate of the longest time interval of the Bayesian blocks of the non-flaring level,

[2] With this recipe we keep all the source+background events, sowe do not have to remove (arbitrarily) some individual events from the event list as proposed by Stelzer et al. (2007) to subtract the background events.

[3] The position of local extrema can be easily computed with required accuracy directly from the first derivative of Eq. (1).

A&A 573, A46 (2015)

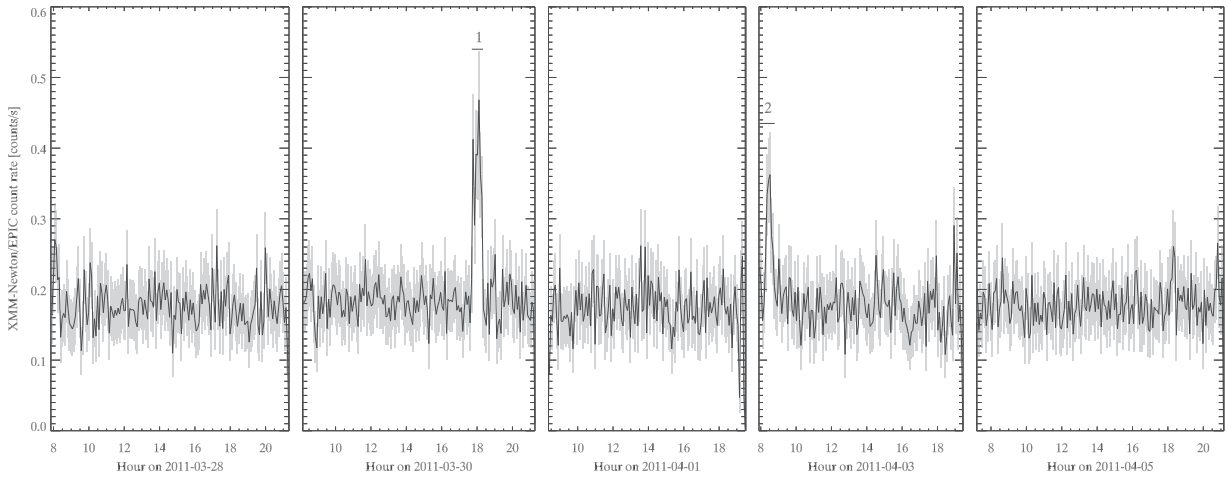


**Fig. 1.** *XMM-Newton*/EPIC (pn+MOS1+MOS2) light curves of Sgr A* in the 2−10 keV energy range obtained in Spring 2011. The time interval used to bin the light curve is 300 s. The X-ray flares are labeled from 1 to 2. The horizontal lines below these labels indicate the flare durations. The non-flaring level of Sgr A* corresponds to only 10% of the non-flaring level of these light curves (Porquet et al. 2008).

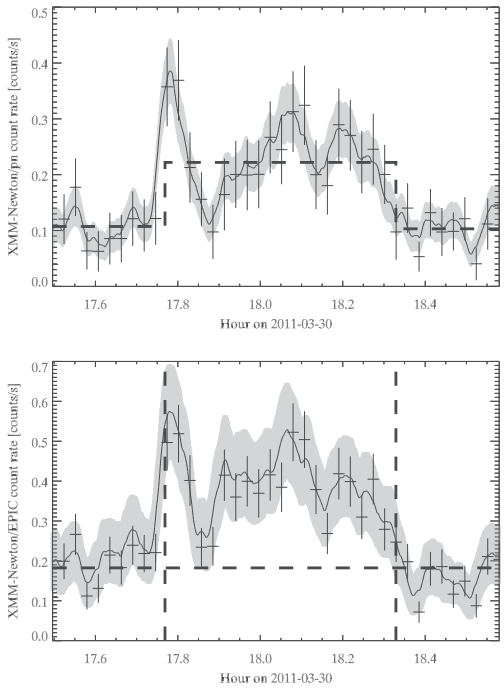


**Fig. 2.** *XMM-Newton* light curve of the 2011 March 30 flare from Sgr A* in the 2−10 keV energy range. *Top panel*: the *XMM-Newton*/EPIC pn light curve binned on 100 s. The crosses are the data points of the light curve. The horizontal dashed lines represent the non-flaring level found by the Bayesian-blocks algorithm. The vertical dashed lines show the start and stop of the Bayesian block. The solid line is the smoothed light curve. The gray curves are the errors associated with the smoothed light curve. *Bottom panel*: the *XMM-Newton*/EPIC (pn+MOS1+MOS2) light curve binned on 100 s. The horizontal dashed line represents the non-flaring level calculated as the sum of the non-flaring level in each instrument found by the Bayesian blocks. The vertical dashed lines represent the beginning and the end of the flare calculated by the Bayesian-blocks algorithm on pn camera. The solid line is the smoothed light curve, which is the sum of the smoothed light curve for each instrument (calculated on the same time range). The gray curves are the errors associated with the smoothed light curve.

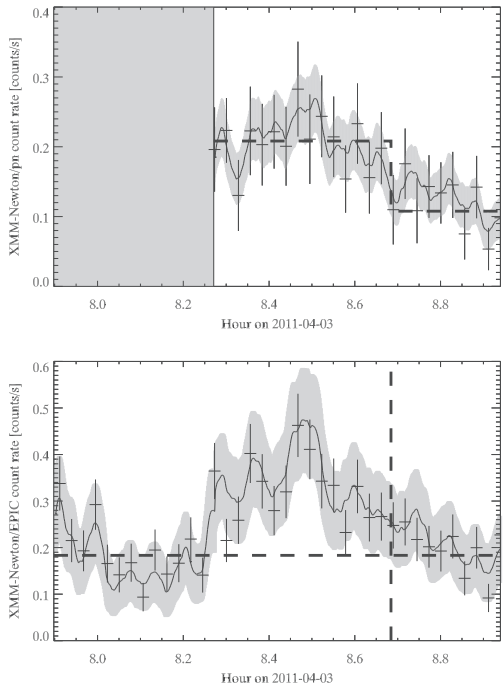


**Fig. 3.** *XMM-Newton* light curve of the 2011 April 3 flare from Sgr A* in the 2−10 keV energy range. *Top panel*: the *XMM-Newton*/EPIC pn light curve binned on 100s. The crosses are the data points of the light curve. The horizontal dashed lines represent the non-flaring level found by the Bayesian-blocks algorithm. The vertical dashed lines show the start and stop of the Bayesian block. The solid line is the smoothed light curve. The gray curve are the errors associated with the smoothed light curve. The time period during which the camera did not observe is shown with a light gray box. *Bottom panel*: the *XMM-Newton*/EPIC (pn+MOS1+MOS2) light curve binned on 100 s. The horizontal dashed line represents the non-flaring level calculated as the sum of the non-flaring level in each instrument found by the Bayesian blocks. The vertical dashed lines represent the beginning and the end of the flare calculated by the Bayesian-blocks algorithm on pn camera. The solid line is the smoothed light curve, which is the sum of the smoothed light curve for each instrument (calculated on the same time range). The gray curve are the errors associated with the smoothed light curve.

**Table 2.** Characteristics of the X-ray flares observed by *XMM-Newton*/EPIC in 2011.

| Flare (#) | Day (yy-mm-dd) | Start time[a] (hh:mm:ss) | End time[a] (hh:mm:ss) | Duration (s) | Total[b] (cts) | Peak[c] (count $s^{-1}$) | $L^{unabs}_{2-10\ keV}$ [d] ($10^{34}$ erg $s^{-1}$) |
|---|---|---|---|---|---|---|---|
| 1 | 2011-03-30 | 17:46:20.69 | 18:19:40.86 | 2000.16 | 211 ± 25 | 0.284 ± 0.013 | $2.69^{+2.4}_{-0.7}$ |
| 2 | 2011-04-03 | ≤08:16:35.65 | 08:41:02.04 | ≥1457.67 | ≥154 ± 24 | 0.165 ± 0.012 | ≥2.9 |

**Notes.** [(a)] Start and end times (TT) of the flare time interval defined by the Bayesian-blocks algorithm (Scargle et al. 2013a) on the EPIC/pn data; [(b)] total EPIC/pn counts in the 2−10 keV energy band obtained in the smoothed light curve during the flare interval (determined by Bayesian blocks) after subtractingf the non-flaring level obtained with the Bayesian-blocks algorithm; [(c)] EPIC pn count rate in the 2−10 keV energy band at the flare peak (smoothed light curves) after subtracting the non-flaring level; [(d)] unabsorbed 2−10 keV average luminosity of the flare computed from the total counts collected during the flare (i.e., the average count rate) and assuming a distance of 8 kpc, see Sect. 4 for details.

which allows very good accuracy on the count rate of the non-flaring level. On 2011 March 28, March 30, April 1, April 3, and April 5, the total non-flaring level was equal to 0.179 ± 0.003, 0, 185 ± 0.004, 0.177 ± 0.003, 0.183 ± 0.004 count $s^{-1}$, and 0.179 ± 0.003 count $s^{-1}$, respectively. It is consistent with the one previously observed with *XMM-Newton* (e.g., in 2007, Porquet et al. 2008). This non-flaring emission is a combination of emission coming from the complex of stars IRS 13, the candidate pulsar wind nebula G359.950.04, and a diffuse component, which all contribute 90% of this non-flaring level in the 2−10 keV energy range (Baganoff et al. 2003; Porquet et al. 2008) and the emission from Sgr A* which contribute only 10%. Figures 2 and 3 focus on the flare light curves obtained with EPIC (pn+MOS1+MOS2) and EPIC pn with a bin time interval of 100 s. The comparison with the EPIC MOS1 and MOS2 light curves can be found in Appendix B. We also show the Bayesian block corresponding to each camera with a dashed line. Table 2 gives the characteristics of these X-ray flares.

The first flare has two components: a short (∼458 s) and symmetrical subflare and a longer (∼1542 s) and fainter symmetrical subflare. Between these two subflares, the smoothed light curve returns at 17.87 h and during less than 100 s to a lower level, which is consistent with the non-flaring state. The first flare is seen in EPIC MOS1 camera with a shift of ≈75 s of its maximum at the first peak but the double subflare configuration is not seen in the EPIC MOS2 camera. The amplitude of the flare in the smoothed light curve corresponds to 6.8$\sigma$ (the standard deviation of the non-flaring level in the 300 s binned light curve) after subtracting the non-flaring level computed by the Bayesian-blocks algorithm.

The second flare is seen by the Bayesian-blocks algorithm in pn and EPIC MOS2 cameras but not in MOS1. This can be explained by the detection limit of the algorithm and the lower sensitivity of the MOS cameras (see details in Appendix B). The time start of this flare is lower than or equal to the start of the observation. In EPIC MOS2 camera we can see an enhancement of the count-rate level after 8.25 h on April 3 but the Bayesian block algorithm detected also an enhancement at the beginning of the observation (before 8 h). Because of the time delay of observation start of EPIC pn camera, we caught with this camera only the end of this flare[4]. The amplitude of the flare subtracted from the non-flaring level corresponds to 5.9$\sigma$.

[4] A coordinated near-infrared observation was obtained with VLT/NACO on 2011 April 3 from 06:30 to 08:18 UT (ESO's archive), which detected the rise of this flare (S. Gillessen 2011, priv. comm.), but lead to only 22 min of simultaneous observation with EPIC MOS before the flare peak that we observed in X-rays.

We also computed the hardness ratio using the 2−4.4 keV and 4.4−10 keV energy bands for all observations, but we found no significant spectral change during the flare interval. The peak count rates of the first and second flares are three and eight times less than that of the bright flare reported in Porquet et al. (2003). The durations of theses flares are 1.4 and 1.8 times shorter than this bright flare.

## 4. Spectral analysis

We did a spectral analysis of the first flare. The extraction region is the same as the one we used to construct the light curves, i.e., a circle of 10″ radius centered on the Sgr A* radio position. The spectrum analysis was only done on the pn instrument since the flare in MOS1 and MOS2 has a number of counts that is too small to constrain the spectral properties. The X-ray photons were selected with `PATTERN`≤ 4 and `FLAG==0`. The time interval of the flare was constrained by the results of the Bayesian-blocks algorithm (see Table 2). The background time interval is composed of two subintervals: the first one began at the start of the March 30 observation (see Table 1) and ended 300 s before the beginning of the flare to avoid any bias. The second one started 300 s after the end of the flare and stopped at the end of the March 30 observation.

The spectrum, response matrices, and ancillary files were computed with the SAS task `especget`. We used `ISIS` version 1.6.2−27 (Houck & Denicola 2000; Houck 2002) to fit the spectrum with X-ray emission models. The model that we used is an absorbed power law with dust scattering (*dustscat*; Predehl & Schmitt 1995). NuSTAR observations of Sgr A* confirm that this model is still a good description of the flare spectra above 10 keV (Barrière et al. 2014). We used *TBnew* for the absorption model, the interstellar medium abundances developed by Wilms et al. (2000), and the cross sections from Verner et al. (1996). These lower metal abundances and updated cross sections imply decreasing the column density (Nowak et al. 2012) input to the *dustscat* model (Predehl & Schmitt 1995) by a factor of 1.5 times. It uses the $N_H$ vs. $\tau_{scatt}$ relation obtained with *wabs* (Anders & Ebihara 1982's abundances, Morrison & McCammon 1983).

The results of the fit using 90% confidence level are hydrogen column density ($N_H$) of $6.7^{+8.2}_{-6.7} \times 10^{22}$ $cm^{-2}$, photon index ($\Gamma$) of $1.5^{+1.5}_{-1.3}$, absorbed flux between 2 and 8 keV ($F^{abs}_{2-8\ keV}$) of $2.5 \times 10^{-12}$ erg $s^{-1}$ $cm^{-2}$ and unabsorbed flux between 2 and 10 keV ($F^{unabs}_{2-10\ keV}$) of $3.5^{+3.1}_{-1.0} \times 10^{-12}$ erg $s^{-1}$ $cm^{-2}$. The extracted spectrum and best fit are shown in Fig. 4.

We can compare the spectral parameters of this flare with those of the two brightest flares detected with *XMM-Newton*, which have the better constrained spectral parameters thanks

A&A 573, A46 (2015)

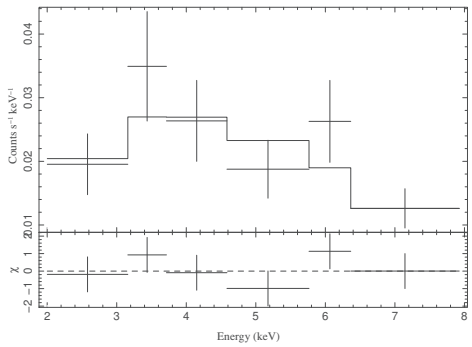


**Fig. 4.** *XMM-Newton*/EPIC pn spectrum of the 2011 March 30 flare. The data are denoted by crosses. The vertical bars is the $1\sigma$ error in the count rate and horizontal bars show the spectral bin in energy. The events have been grouped with a minimum signal-to-noise ratio of 4. *Top*: the result of the fit is shown by the continuous solid line. *Bottom*: the $\chi^2$ residual in units of $\sigma$.

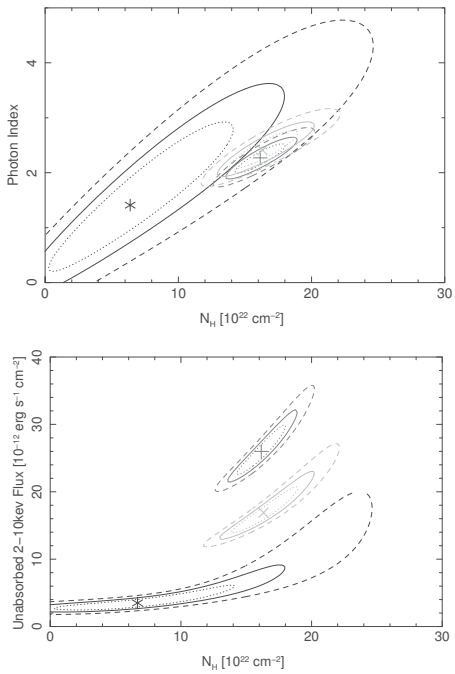


**Fig. 5.** Confidence contours for Sgr A* spectral parameters. Contours are the confidence levels of 68% (dotted line), 90% (solid line), and 99% (dashed line) for the two parameters in the graph. The three sets of confidence contours represent the 2011 March 30 flare (black lines and asterisk), the 2007 April 4 flare (light gray lines and X point), and the 2002 October 3 flare (dark gray lines and cross point).

to the high throughput and no pileup. The very bright flare of 2002 October 3 was fitted using the same modeling with $\Gamma = 2.3 \pm 0.3$, $N_{\rm H} = 16.1^{+1.9}_{-2.2} \times 10^{22}$ cm$^{-2}$ , and $F^{\rm unabs}_{2-10\ {\rm keV}} = 26.0^{+4.6}_{-3.5} \times 10^{-12}$ erg s$^{-1}$ cm$^{-2}$ (Porquet et al. 2003; Nowak et al. 2012). The bright flare of 2007 April 4 was also fitted using the same modeling with $\Gamma = 2.4^{+0.4}_{-0.3}$, $N_{\rm H} = 16.3^{+3.0}_{-2.6} \times 10^{22}$ cm$^{-2}$ and $F^{\rm unabs}_{2-10\ {\rm keV}} = 16.8^{+4.6}_{-3.0} \times 10^{-12}$ erg s$^{-1}$ cm$^{-2}$ (Porquet et al. 2008; Nowak et al. 2012). In Fig. 5, the confidence contours of these two bright flares show that these $N_{\rm H}$ and $\Gamma$ parameters are well constrained. However, those of the 2011 March 30 flare are not, since there are few events collected from this flare, which implies that the number of spectral bins with a minimum signal-to-noise ratio of 4 is small. The photon index and hydrogen column of the flare of 2011 March 30 agree with those of the flare of 2007 April 4 and 2002 October 3 within the confidence levels for two parameters of 90% and 99%, respectively.

The second flare on 2011 April 3 does not contain enough counts to constrain the spectral parameters. Its unabsorbed luminosity given in Table 2 is calculated with `ISIS` by fixing the photon index $\Gamma$ to 2 and column density to $N_{\rm H} = 14.3 \times 10^{22}$ cm$^{-2}$, i.e., to the spectral values of the 2002 October 3 flare (Porquet et al. 2003; Nowak et al. 2012). Thus, the only free parameter is the unabsorbed flux, which is $F^{\rm unabs}_{2-10\ {\rm keV}} = 3.91 \times 10^{-12}$ erg s$^{-1}$ cm$^{-2}$. The unabsorbed luminosity between 2 to 10 keV is $2.7^{+2.4}_{-0.8} \times 10^{34}$ erg s$^{-1}$ for a 8 kpc distance.

## 5. Discussions

### 5.1. The 2011 March 30 flare vs. the 2012 Chandra XVP campaign flares

We compared the spectral properties of the 2011 March 30 flare with the ones reported by Neilsen et al. (2013) from the 2012 *Chandra* XVP campaign. In this paper, the spectral properties of all *Chandra* flares have been derived by assuming the spectral parameters of the brightest flares obtained by Nowak et al. (2012): $\Gamma = 2$ and $N_{\rm H} = 14.3 \times 10^{22}$ cm$^{-2}$. We use two physical quantities given in the Table 1 of Neilsen et al. (2013): the unabsorbed 2−10 keV luminosity and the duration of the flare. We also derived two other physical quantities that are independent of the instrumental characteristics: the unabsorbed 2−10 keV fluence in erg (the product of the unabsorbed 2−10 keV luminosity with the duration) and the unabsorbed 2−10 keV peak luminosity. To compute the peak luminosity of the *Chandra* flares, we first derived the mean count rate in each flare as the pileup corrected fluence in counts (see Eq. (1) Neilsen et al. 2013) divided by the flare duration, and then we computed the linear relation between the unabsorbed 2−10 keV luminosity and the mean count rate (higher the mean count rate, higher the luminosity). We obtained $L^{\rm unabs}_{2-10\ {\rm keV}}/10^{34}$ erg s$^{-1}$ $= -0.031 + 136.7$ (CR/count s$^{-1}$) with a correlation parameter $r$ of 0.9997. Then, we applied this relation to the peak count rate given in Table 1 of Neilsen et al. (2013) to obtain the peak luminosity for each flare. The relations between these four physical quantities are shown in Fig. 6.

Since we used quantities that are independent of the instrument, we can compare flares observed with *Chandra* and *XMM-Newton*. First, we place the two brightest flare seen by *XMM-Newton* in the three diagrams. The unabsorbed 2−10 keV fluence, duration, and unabsorbed 2−10 keV luminosity are reported in Nowak et al. (2012). The unabsorbed 2−10 keV peak luminosity are computed as the ratio between the peak count rate and the mean count rate multiplied by the unabsorbed 2−10 keV luminosity in the flares (Porquet et al. 2008). We can see that these flares have high luminosities and fluences. They are thus in the upper righthand corner of the diagrams representing the unabsorbed 2−10 keV peak luminosity and the unabsorbed 2−10 keV fluence.

We also represent our first flare as a single flare (diamond) and as two distinct subflares (squares) defined as follows. The first subflare starts at the beginning of the Bayesian blocks corresponding to the 2011 March 30 flare and stops at the time corresponding to the minimum of the smoothed light curve between the two subflares. The beginning of the second subflare is the end of the first one, and its end corresponds to the end of the Bayesian block. The live time of the single flare (Table 3) is shorter than the flare duration reported in Table 2. The

**Table 3.** Characteristics of the 2011 March 3 flare and its two subflares assuming $\Gamma = 2$ and $N_H = 14.3 \times 10^{22}$ cm$^{-2}$.

| Flare (#) | Duration (s) | Live time (s) | Mean net count rate (count s$^{-1}$) | $L^{\rm unabs}_{2-10\ \rm keV}$ ($10^{34}$ erg s$^{-1}$) | Peak count rate (count s$^{-1}$) | $L^{\rm unabs}_{2-10\ \rm keV}$(peak) ($10^{34}$ erg s$^{-1}$) |
|---|---|---|---|---|---|---|
| 1 | 2000 | 1750 | 0.16 | 5.7 | 0.28 | 9.5 |
| 1.1 | 458 | 416 | 0.16 | 5.8 | 0.28 | 9.4 |
| 1.2 | 1542 | 1324 | 0.16 | 5.7 | 0.17 | 6.8 |

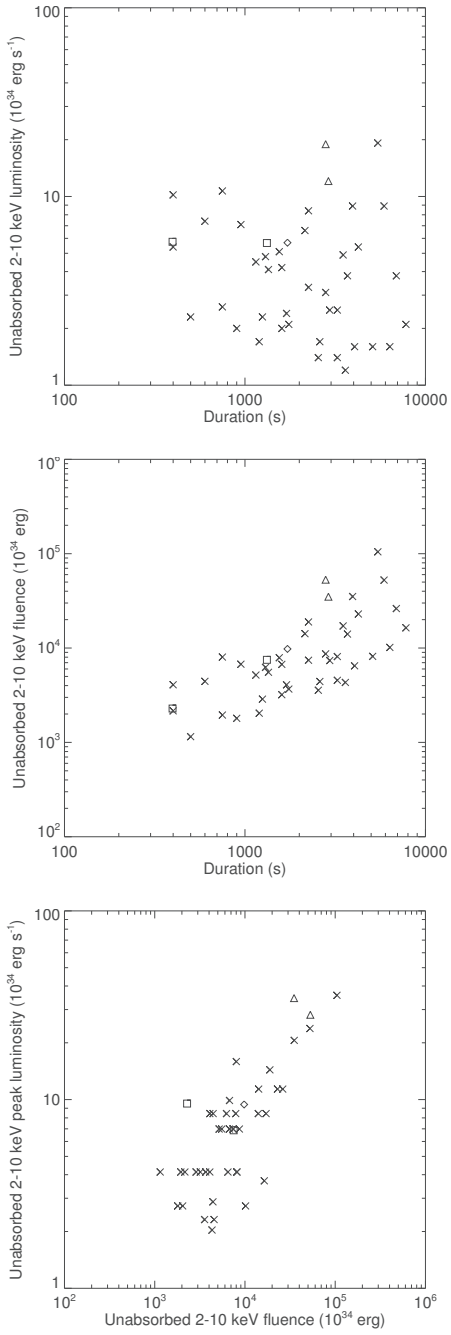


**Fig. 6.** 2011 March 30 flare vs. the 2012 *Chandra* XVP campaign flares. The X-ray flares from the *Chandra* XVP campaign (Neilsen et al. 2013) are shown by crosses, the two brightest flares seen be *XMM-Newton* are triangles, the 2011 March 30 flare is represented by a diamond, and the two subflares are shown with squares.

mean rate of the flare is given by the Bayesian-blocks algorithm. The mean rate in each subflare is the number of counts in each subflare divided by their live time. To be consistent with Neilsen et al. (2013) for direct comparison purpose, the unabsorbed 2−10 keV luminosity is computed with the same spectral parameter ($\Gamma = 2$ and $N_H = 14.3 \times 10^{22}$ cm$^{-2}$), which implies that the luminosity of the flare is slightly different than those computed with our present best fit spectral analysis (see Sect. 4). The derived quantities for the first flare (#1) and the first (#1.1) and second (#1.2) subflares are reported in Table 3.

In Fig. 6, we can see that the unabsorbed 2−10 keV luminosity of the total flare and the two subflares are nearly the same since they have more or less the same mean count rate, but the fluence of the first sub-flare is small compared to the second subflare owing to the shorter duration. Thus, the first subflare lies within the shortest and less energetic flares detected by *Chandra*, but the apparent lower detection limit of 400 s in the flare duration is probably due to the method used by Nowak et al. (2012) to identify flares in *Chandra* light curves. In fact, they use a Gaussian fit on the light curve binned with 300 s, which implies that they might missed flares whose duration is below 300 s.

We can see that, in all the diagrams, if we assume a single flare, it lies in the mean of the flares seen by *Chandra* and can then be considered as a genuine medium luminosity flare. Furthermore, if we consider the minimum waiting time between flares in the 2012 *Chandra* XVP campaign shown in Fig. 1 of Neilsen et al. (2013), we can see that the nearest flares are separated by ~3500 s. This waiting time can be considered as a lower limit for observing two distinct flares. The two subflare peaks of our first flare are separated with only 1000 s, which favors a single flare.

### 5.2. Gravitational lensing of a hotspot-like structure

We modeled the light curve of the 2011 March 30 flare with a single mechanism in order to explain the two subflares. Indeed, the very short (~458 s) first subflare and the second much longer (~1542 s) one peaking ~1000 s later but with lower amplitude can be the signature of a gravitational lensing of a hotspot-like structure. We used a hotspot model and a ray-tracing code to compute the observed intensity (Karas et al. 1992; Schnittman & Bertschinger 2004; Broderick & Loeb 2005; Hamaus et al. 2009; Dexter & Agol 2009).

#### 5.2.1. The hotspot model

We call a hotspot a spherical, optically thin structure, orbiting around the black hole with Keplerian angular velocity. The sphere is initially assumed to be in solid rotation around the black hole. No shearing or expansion of the sphere is taken into account. Such a hotspot is thus only defined by its radius $R$ and its orbital radius $r$ in gravitational radius unit ($r_g \equiv 0.5R_S$). The black hole inclination $i$ is assumed to be close to an edge-on view, i.e., $i \approx 90°$. Its actual value is a parameter of the model. The emitted spectrum of the hotspot is assumed to follow a power law, $I_\nu^{\rm em} \propto \nu^\alpha$, where $\alpha$ is a constant number, related to the photon index $\Gamma$ through $\Gamma = 2 - \alpha$. It is then straightforward to show that the observed intensity integrated over a range of

A&A 573, A46 (2015)

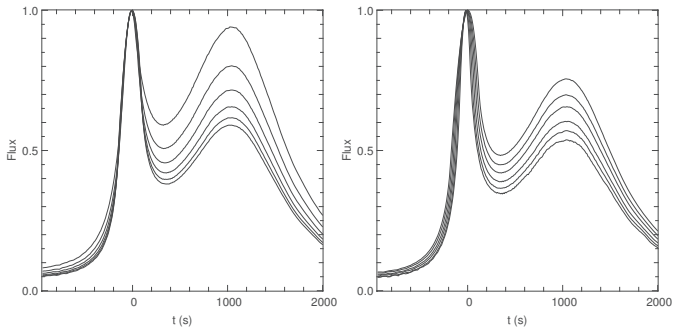


**Fig. 7.** Normalized hotspot light curves obtained for an orbital radius equal to the value of the best fit. The flux is in arbitrary units. *Left*: hotspot radius equal to the best fit value. Inclination $i$ varies over all grid values. (The range of these parameters are defined in Sect 5.2.3.) The closer the inclination to 90°, the higher the ratio between the two local maxima. *Right*: inclination fixed at its best fit value and $R$ varies over all grid values. The smaller $R$, the bigger the ratio between the two subflare peaks. The time interval between the two local maxima is the same for all curves in these two figures.

frequency $\Delta\nu_{\rm obs}$ is

$$\mathcal{I}^{\rm obs} = \int_{\Delta\nu_{\rm obs}} I_\nu^{\rm obs} {\rm d}\nu_{\rm obs} \propto g^{4-\alpha} \tag{2}$$

where $g \equiv \nu_{\rm obs}/\nu_{\rm em}$ is the redshift factor.

Maps of $\mathcal{I}^{\rm obs}$ were computed by using the open-source ray-tracing code GYOTO[5] (Vincent et al. 2011). We computed maps of $300 \times 300$ pixels over one orbital period with a time step of about $\delta t \approx 10$ s, which is close to the time sampling of the smoothed light curve. The light curve is obtained by summing each of these maps over all pixels, which boils down to integrating over all solid angles, i.e., to computing a flux.

The light curve of a hotspot seen edge-on shows a typical double-bump feature (see Fig. 7). The primary maximum ($t = 0$ s) is due to the gravitational lensing of the light emitted by the hotspot when it is on the opposite side of the black hole with respect to the observer. The secondary maximum ($t \approx 1000$ s) is due to the relativistic beaming effect: light emitted when the source is moving toward the observer is boosted.

### 5.2.2. Constraining the orbital radius of the hotspot

The orbital radius is easy to constrain because it is directly linked to the time interval between the two local maxima of the light curve, as illustrated in Fig. 7. The variation of this time interval as a function of the orbital radius $r$ evolved like this: $\delta t \approx 860$, 960, 1040, 1130, and 1230s for $r/r_{\rm g} = 10.5$, 11, 11.5, 12, and 12.5. It is clear that if the hotspot model is correct, then $r/r_{\rm g} \approx 11{-}12$.

It is not obvious to constrain the remaining parameters ($R$ and $i$) by a quick comparison to the observed data. Both of them have a strong impact on the flux ratio between the two local maxima, as well as on the flux ratio between the primary maximum and the local minimum between the two bumps.

### 5.2.3. Fitting the parameters of the hotspot model

Our hotspot model is defined by five parameters: the orbital radius $r$, the hotspot radius $R$, the black hole inclination $i$, the temporal additive shift d$t$, and the flux multiplicative scaling d$f$. The two last parameters are defined according to the following. The smoothed light curve defines the zero of time: it is by definition the time of its primary maximum. Then, each theoretical light curve is first shifted so that its zero of time corresponds to its own primary maximum. The parameter d$t$ allows the fitting of any time shift between the theoretical and the observed light curve. Each theoretical light curve is also scaled vertically. Each of them is first divided by the maximum of all fluxes computed by GYOTO (then all GYOTO fluxes are between 0 and 1). Each theoretical light curve is then again multiplied by the maximum value of the smoothed light curve, from which the non-flaring ground level was subtracted. (Then all GYOTO flux values are between 0 and $M$, the maximum of the smoothed light curve, in observed unit.) The multiplicative d$f$ fitting parameter is applied to these rescaled theoretical light curves.

The spin parameter has a low impact on the light curve, thus it is fixed to $a = 0.99$ (high spins lead to slightly smaller $\chi^2$ in the fit) and not fitted. The photon index is fixed to $\Gamma = 2$ (Porquet et al. 2003, 2008; Nowak et al. 2012; Barrière et al. 2014). Here we are interested in determining whether the hotspot model is viable or not, not in fitting in detail all the parameters.

The fitting is performed by determining the minimum of the following $\chi^2$ on a grid of parameters

$$\chi^2(r,R,i;{\rm d}t,{\rm d}f) = \sum_{t_{\rm obs}} \left( \frac{{\rm d}f \times f_{\rm Gyoto}(r,R,i;{\rm d}t;t_{\rm obs}) + f_{\rm non-flaring} - f_{\rm smooth}(t_{\rm obs})}{\sigma_{\rm smooth}} \right)^2 \tag{3}$$

where $f_{\rm Gyoto}$ is the theoretical light curve, $f_{\rm non-flaring}$ is the non-flaring level of the observed data (determined from the Bayesian-blocks analysis), $f_{\rm smooth}$ the pn smoothed light curve, $\sigma_{\rm smooth}$ the error on the smoothed flux, and the sum is performed over a subset of the range of observed times taken into account in the smoothing procedure, with a time step of about 10 s. We use conservatively only the pn smoothed light curve since pn is the most sensitive instrument. The grid that we use for the three physical parameters is $r \in [10.5, 11, 11.5, 12, 12.5]$, $R/r_{\rm g} \in [1.2, 1.4, 1.6, 1.8, 2, 2.2]$, and $i \in [81.93, 83.08, 84.22, 85.37, 86.52, 87.66]$ where radii are in units of $GM/c^2$, the inclination is in degrees, with $i = 90°$ being an exact edge-on view (i.e., maximum lensing effect). For each set of parameter values, the theoretical light curve corresponding to $(r, R, i)$ is read. It is rescaled as described above. Then the parameters d$t$ and d$f$ are fitted using the `lmfit` routine of the `Yorick` software. The set of parameters that gives the smallest $\chi^2$ following this procedure is the best-fitting set. For the fitting, the theoretical light curve is fitted to the smoothed data, interpolating linearly to determine the theoretical value at the smoothed times.

Figure 8 shows the best fit that is found for the following values of the parameters: $r = 12r_{\rm g}, R = 1.4r_{\rm g}, i = 86.5°, {\rm d}t = 11.1 \pm 4.0$ s, ${\rm d}f = 1.40 \pm 0.02$. The $1\sigma$ error on the two last parameters being computed by the `lmfit` routine. The final reduced $\chi^2$ is 0.85.

### 5.2.4. Viability of the hotspot model

The best fit illustrated in Fig. 8 clearly shows that one part of the smoothed data is not well fit by the hotspot model: the local minimum of the light curve, in between the two bumps at around $17^{\rm h}52^{\rm m}34^{\rm s}$. At this point, the observed data reach the non-flaring level while the model stays much higher, around $2.5\sigma$ distant. The remaining data is explained well by the model at the $1\sigma$ level. However, this $2.5\sigma$ inadequacy of the model at the local

[5] This code can be freely downloaded at the URL http://gyoto.obspm.fr

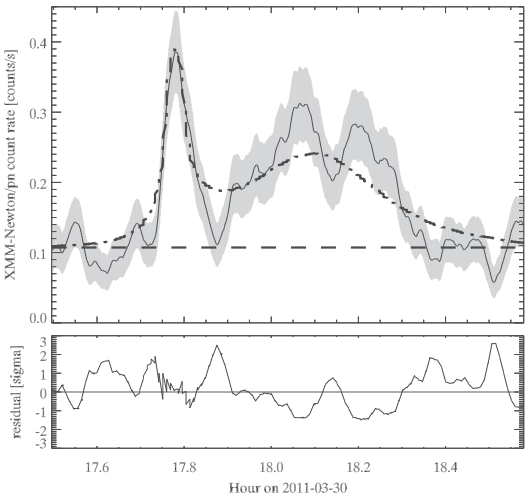


**Fig. 8.** Modeling of the 2011 March 30 flare pn light curve with a rotating hotspot. Best-fitting theoretical light curve (dot-dashed line) plotted over the smoothed light curve (solid line, with $1\sigma$ error in gray). The non-flaring level is given by the horizontal dashed line. The vertical axis is in observed units, horizontal axis is in seconds. The *lower panel* gives the residual in units of $\sigma$.

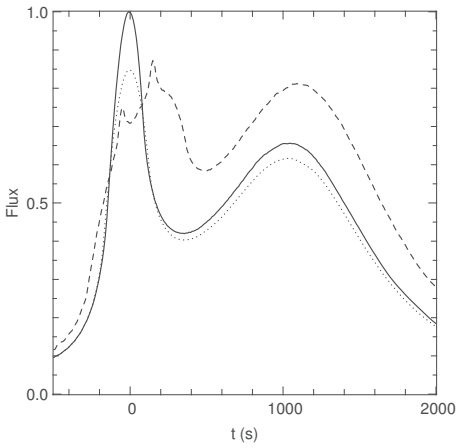


**Fig. 9.** Comparison of the best-fit light curve (solid line) with the light curve of an elongated (dashed line) and swelling (dotted line) hotspot defined by the same parameters (see text for details). The flux is in arbitrary units.

minimum is sufficient to reject the model. Indeed, a hotspot-like model will always produce a local minimum at a higher level than the non-flaring level. Indeed, this part of the light curve is associated to the part of the trajectory where the hotspot is moving from behind the black hole to the approaching side of the orbit. At this position, the relativistic beaming effect will always be significantly greater than at the receding side of the orbit, which corresponds to the minimum flux level.

To be quantitative, we compare the flux ratio between the lensing maximum and the non-flaring level and the lensing maximum and the local minimum flux level (in between the two bumps), for all light curves computed in our grid. The first ratio is always greater than ten, while the second ratio varies between 1.5 and 4. In conclusion, no set of parameters can give the same ratio for these two quantities.

### 5.2.5. Refining the hotspot model

One may wonder whether, by adding more physics to the hotspot model, this local minimum problem could be solved. To investigate this, we considered the two most natural ways of making our model more sophisticated: considering an elongated hotspot due to the shearing of the sphere by the differential Keplerian rotation and allowing the hotspot to vary in radius ($R$) along its trajectory. To model an elongated hotspot, we first computed the effect of elongation over a hotspot of initial radius $R = 1.8$ over the time elapsed between the triggering of the hotspot and the local minimum. The precise triggering time of the hotspot is not constrained, thus we assume the hotspot is created at the time that corresponds to the minimum of the theoretical light curve (thus at about $-1500$ s when $t = 0$ is set at the primary maximum). Under this assumption, the elapsed time between the creation of the hotspot and the local minimum is of $\Delta T \approx 1800$ s for the best-fitting values of parameters. This is equivalent to one third of the period. It is now straightforward to compute the difference of angular distance $\Delta\theta$ covered by the most distant (in terms of radial coordinate $r$) and least distant parts of a sphere with radius $R = 1.8$ whose center is at a radius $r = 11.5$ from the central black hole. Explicitly,

$$\Delta\theta = \frac{2\pi}{3}\, r^{3/2}\left(r_1^{-3/2} - r_2^{-3/2}\right), \tag{4}$$

where $r_1$ is the shortest distance to the black hole and $r_2$ the largest (the spin is neglected here). For the best-fitting hotspot, $\Delta\theta \approx \pi/3$. This elongation has approximately multiplied the angular extension of the initially spherical best-fit hotspot by three. Thus, we model the elongated hotspot in a simple way by considering three spherical best-fit hotspots tangent one to the next, orbiting the same orbit. The intensity emitted by each of the spheres is divided by three with respect to the standard single hotspot case in order to allow a simple comparison. Figure 9 shows the light curve associated to this elongated hotspot. Here, the hotspot is always elongated and does not change shape as a function of time.

To determine the effect of volume changing on the light curve, we have modeled a swelling, single hotspot. The swelling hotspot is modeled by requiring that the initial radius of the hotspot is the best-fitting value, $R_0 = 1.8$ and that it will increase linearly with time until it reaches $2\,R_0$ at the time corresponding roughly to the local minimum observation. The emitted intensity is inversely proportional to the sphere volume. Figure 9 shows the light curve associated to this swelling hotspot.

Both toy models show that changing the shape of the hotspot will not solve the central problem of the model: the local minimum is always significantly higher than the non-flaring level. We cannot formally exclude that a more sophisticated model, such as a non-constant density hotspot, or a trajectory not confined within the equatorial plane is able to fit our data. However, it is important to note that our hotspot model is ruled out precisely because the minimum of the flare light curve goes down to the quiescent level. Without adding some ad hoc new components to a simple hotspot model (like an obscuring component), it is clear that the flare light curve will always have a minimum above the quiescent level, since the hotspot will always be visible and make a non-zero contribution to the total intensity. As a consequence, we believe that fitting a hotspot-like model to our data would require some fine tuning using extra parameters, which would make the model less reliable.

### 5.3. Constraining the radial distance of the first 2011 March 30 subflare from magnetic energy heating and synchrotron cooling

We consider that the short duration of the rise phase of the first subflare places a limit to the size of the flaring region (e.g., Dodds-Eden et al. 2009). Following Barrière et al. (2014), we assume that the energy released during the flare is powered during the rise phase by the magnetic energy available inside the flaring region, which constrains the radial distance of the flare. By identifying the decay phase of the first subflare with synchrotron cooling, we derive a lower limit to the radial position of the first subflare.

#### 5.3.1. Timescales of the first subflare

We define the start time of the rise phase as the time when the count rate of the smoothed light curve is too high to have been produced by the Poissonnian fluctuation of the non-flaring level at the 99.87% of confidence level (corresponding to Gaussian single-sided confidence level of $3\sigma$). This threshold level is defined by $\mathrm{CR}_0 = N/h$, with $h$ the width of the kernel window ($h = 100$ s) and $N$ the lowest integer solution of the following equation:

$$\mathrm{CDF} = \sum_{n=0}^{N} \frac{(\lambda h)^n \, \mathrm{e}^{-\lambda h}}{n!} > 0.9987 \tag{5}$$

with CDF the cumulative distribution function of the Poissonnian distribution, $\lambda$ the non-flaring rate (i.e., $0.107 \pm 0.001$ pn counts s$^{-1}$). We find $\mathrm{CR}_0 = 0.23$ pn counts s$^{-1}$ at $t_{\mathrm{start}} = 17\mathrm{h}44\mathrm{m}59\mathrm{s}$ on 2011 March 30. The end time of the rise phase is the maximum of the smoothed light curve that is reached at $t_{\mathrm{max}} = 17\mathrm{h}46\mathrm{m}54\mathrm{s}$. Thus, the rise phase duration is $\Delta t_{\mathrm{rise}} = t_{\mathrm{max}} - t_{\mathrm{start}} = 115$ s. The end time of the first subflare is the time of the minimum between the two subflares: $t_{\mathrm{end}} = 17^{\mathrm{h}}52^{\mathrm{m}}34^{\mathrm{s}}$. This leads to $\Delta t_{\mathrm{flare}} = t_{\mathrm{end}} - t_{\mathrm{start}} = 455$ s.

The proper duration of any event around an SMBH is always longer than the observed duration due to time dilation in strong gravity field. Therefore, we compute the proper-to-observed time ratio versus radial position (see Appendix C). Hereafter we use a dimensionless spin parameter of one.

#### 5.3.2. Magnetic energy heating

We constrain the radius of the spherical flaring region by considering that the Alfven velocity cannot be higher than the speed of light (Dodds-Eden et al. 2009): $R < c\Delta\tau_{\mathrm{rise}}$, where $\Delta\tau_{\mathrm{rise}}$ is the proper duration of the rise phase. This leads to the upper limit to the volume of the flaring region: $V = \frac{4}{3}\pi R^3 < \frac{4}{3}\pi c^3 \Delta\tau_{\mathrm{rise}}^3$. The magnetic energy contained inside this volume is $U_B = \frac{B^2 V}{8\pi}$ with $B = B_{1R_{\mathrm{S}}} 2r_{\mathrm{g}}/r$ the magnetic field vs. the radial distance $r$ (see Barrière et al. 2014, and references therein).

We define $\eta$, the X-ray photon production efficiency, as the ratio of the flare fluence in X-rays to the available magnetic energy. The flare fluence in X-rays is the product of the unabsorbed X-ray luminosity with the duration of the first subflare (i.e., $\Delta\tau_{\mathrm{flare}}$). Indeed, we have to compute the fluence released during the whole first subflare since all the X-ray emission from this event is powered by the magnetic heating of the emitting region. We compute this luminosity with the parameters that were fitted to the flare spectrum, i.e., $N_{\mathrm{H}} = 6.7 \times 10^{22}$ cm$^{-2}$ and $\Gamma = 1.5$ (see first part of Sect. 4). The average luminosity of the first subflare is $L^{\mathrm{unabs}}_{2-10\ \mathrm{keV}}(\mathrm{flare}) = 5.8^{+5.7}_{-1.7} \times 10^{34}$ erg s$^{-1}$. As a result, $\eta = L^{\mathrm{unabs}}_{2-10\ \mathrm{keV}}(\mathrm{flare})\Delta\tau_{\mathrm{flare}}/U_B$. Therefore, the upper limit to the radial distance can be computed by the relation

$$L^{\mathrm{unabs}}_{2-10\ \mathrm{keV}}(\mathrm{flare})\Delta\tau_{\mathrm{flare}} < \frac{B^2_{1R_{\mathrm{S}}}}{6}\left(\frac{2r_{\mathrm{g}}}{r}\right)^2 c^3 \Delta\tau^3_{\mathrm{rise}}\eta. \tag{6}$$

If we assume a maximum efficiency ($\eta = 1$), the upper limit to the radial distance is $r < 100^{+19}_{-29}\ r_{\mathrm{g}}$ (see Fig. 10). The corresponding radius of the flaring region at this distance is $R = 2.87 \pm 0.01\ r_{\mathrm{g}}$.

We can neglect any magnification of the observed luminosity compared to the proper luminosity at this radial distance. Indeed in the hotspot model, the combined effects of the beaming and the gravitational redshift on the proper luminosity are small at $r = 100\ r_{\mathrm{g}}$ since the corresponding orbital period is ∼1.5 days, which implies that any magnification has a long timescale and a very small amplitude (Broderick & Loeb 2005; Hamaus et al. 2009). In the jet geometry, the Doppler factor is small owing to the small inclination and the mild velocity of the Sgr A* jet; therefore, the beaming factor, varying as the square of the Doppler factor, is also small (Barrière et al. 2014).

#### 5.3.3. Synchrotron cooling

The electrons that were accelerated by the release of the magnetic energy will cool by emitting synchrotron radiation with the following timescale: $\tau_{\mathrm{sync}} = 8 \times (B/30\ \mathrm{G})^{-3/2} \times \left(\nu/10^{14}\ \mathrm{Hz}\right)^{-1/2}$ min (Dodds-Eden et al. 2009). If the X-ray photons at $10^{18}$ Hz are the primary source of synchrotron cooling, then $\tau^{\mathrm{X}}_{\mathrm{sync}} = 0.78\,(B_{1R_{\mathrm{S}}}/100\ \mathrm{G})\left(r/2r_{\mathrm{g}}\right)^{3/2}$ s. From $\tau^{\mathrm{X}}_{\mathrm{sync}} > \Delta\tau_{\mathrm{decay}}$, we derive $r > 114\ r_{\mathrm{g}}$, which is not consistent with the previously derived upper limit. Therefore, if the X-rays are the primary source of synchrotron cooling in this subflare, sustained heating must also be present during the decay phase.

We know that X-ray flares are always associated with NIR flares (e.g., Dodds-Eden et al. 2009), which have power-law spectra consistent with synchrotron process (Eisenhauer et al. 2005). Thus, we consider the synchrotron cooling time of NIR photons ($\nu = 10^{14}$ Hz)–$\tau^{\mathrm{NIR}}_{\mathrm{sync}} = 78.9\,(B_{1R_{\mathrm{S}}}/100\ \mathrm{G})\left(r/2r_{\mathrm{g}}\right)^{3/2}$ s – which leads to $r > 4\ r_{\mathrm{g}}$ with the flaring region outside the event horizon. The evolution of these synchrotron cooling times with the radial distance is shown in Fig. 11.

We conclude that $4\ r_{\mathrm{g}} < r < 100^{+19}_{-29}\ r_{\mathrm{g}}$ in this subflare for $\eta = 1$ and $B_{1R_{\mathrm{S}}} = 100$ G. The corresponding radii of the flaring region at these distances are $1.8\ r_{\mathrm{g}} < R < 2.87 \pm 0.01\ r_{\mathrm{g}}$. The minimum distance of $r > 1.9\ r_{\mathrm{g}}$ is required to have the flaring region well outside the event of horizon.

#### 5.3.4. Comparison with previous works

The upper limit to the radial distance of the first subflare on 2011 March 30 is five times more than the one derived for the flare detected by NuSTAR on 2012 July 21 (Barrière et al. 2014). The latter was longer (1896 s) and about ∼3.5 times more luminous (mean luminosity of $21{\times}10^{34}$ erg s$^{-1}$) than the former. Moreover, the 2012 July 21 NuSTAR flare was characterized by a plateau phase of ≈1700 s between the rise and decay phases of 100 s.

Barrière et al. (2014) assume that the radius of the emitting region is constant after the rise phase. But for a radial position lower than 20 $r_{\mathrm{g}}$ and $B_{1R_{\mathrm{S}}} = 100$ G, the synchrotron cooling time of NIR photons is lower than 2500 s, which implies that the heating process is still required after the rise phase to produce

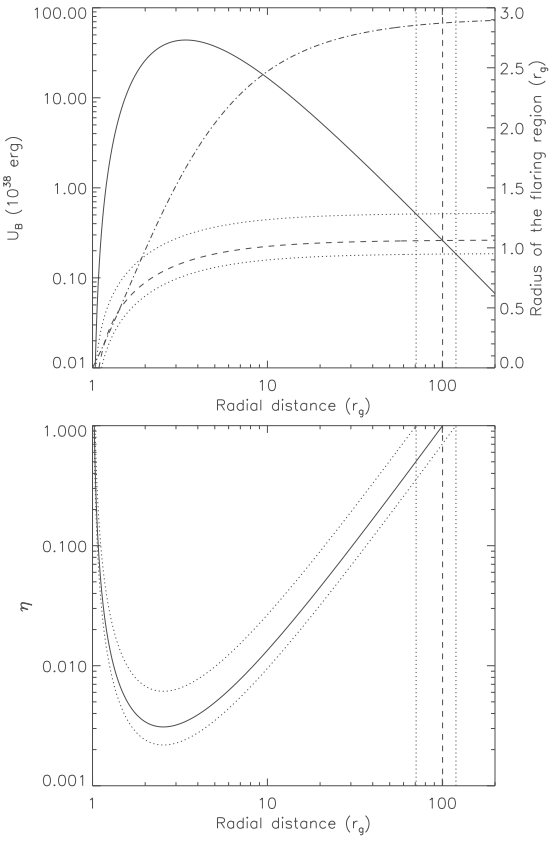


**Fig. 10.** Determination of the radial distance of the flaring region. *Top panel*: magnetic energy vs. radial distance for a magnetic field of 100 G at 2 $r_g$ and an X-ray photon production efficiency and dimensionless spin parameter of 1. The solid line is the distribution of the magnetic energy (see left *y*-axis) vs. the radial distance. The dashed and dotted lines represent the central value of the X-ray fluence and its errors with 90% confidence level, respectively. The vertical lines are the corresponding upper limits to the distance. The dashed-dotted line represents the radius of the emitting region (see right *y*-axis). *Bottom panel*: X-ray photons production efficiency vs. radial distance for the fluence and its upper and lower limit. The solid and dotted lines represent the efficiency for the central value of the fluence and its errors within 90% confidence level, respectively.

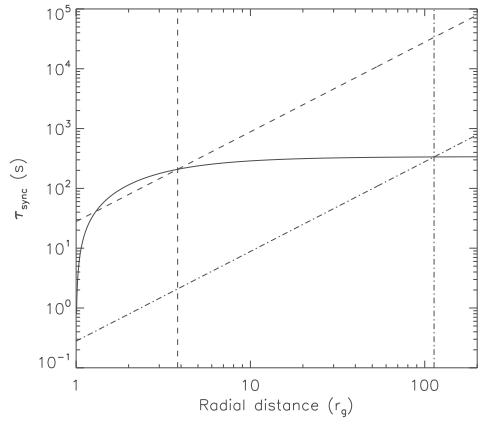


**Fig. 11.** Synchrotron cooling time vs. the radial distance. The solid line represents the proper duration of the decay phase. The dashed inclined line represents the synchrotron cooling time for infrared photons. The dotted-dashed inclined line is the synchrotron cooling time for X-ray photons. The corresponding vertical lines are the lower limit to the radial distance for each cooling timescale.

the observed plateau phase. Therefore, the radius of the emitting region of this NuSTAR flare is likely much larger than those computed by Barrière et al. (2014) from only the rise phase. If we remove the plateau phase of this NuSTAR flare, only the rise and decay phases remain, so, we can use the same method as for our first subflare.

We revise the upper limit to the radial distance of the 2012 July 21 NuSTAR flare to at least 64 $r_g$. Including the likely increase in the radius of the flaring region during the plateau phase due to sustained heating leads to an even higher value for the upper limit to the radial distance.

## 6. Summary

We have reported the data analysis of the *XMM-Newton* 2011 campaign observation of Sgr A* (five observations with a total of exposure of ≈226 ks). We used the Bayesian-blocks algorithm developed by Scargle (1998) and a density estimator with an Epanechnikov kernel to constrain the duration, the position, and the amplitude of the X-ray flares with better accuracy. The Bayesian-blocks algorithm uses the unbinned event arrival time on the EPIC cameras to identify the flaring and non-flaring period and their corresponding count-rate levels. This analysis of the event's arrival time increases the accuracy on the time of the beginning and the end of a flare in comparison with a detection above a given threshold of a binned light curve. The algorithm uses a Bayesian statistic to find the time when the count-rate level is statistically different under a given probability. We worked with a false detection probability of exp(−3.5), which implies that the detected flare is a real flare with a probability of 99.9%. We corrected the contribution of the flaring background by applying twice this algorithm on the source and the background regions. We used a density estimator to improve the determination of the characteristics of the flares. The density estimator applies a convolution between the event list corrected from the GTI and a kernel defined on a finite support in order to control any boundary effects. Thanks to the Bayesian-blocks algorithm, we could also correct the resulting smoothed light curves from the flaring background.

We observed two X-ray flares during these observations. The former occurred on 2011 March 30 and the latter on 2011 April 03. For comparison, these flares have a peak detection level of 6.8 and 5.9$\sigma$ in the *XMM-Newton*/EPIC (pn+MOS1+MOS2) light curve in the 2−10 keV energy range with a 300 s bin. The first flare is composed of two subflares: a very short-duration (∼458 s) one with a peak luminosity of $L^{\rm unabs}_{2-10\ {\rm keV}} \sim 9.4 \times 10^{34}$ erg s$^{-1}$ and a longer (∼1542 s) and less luminous one ($L^{\rm unabs}_{2-10\ {\rm keV}} \sim 6.8 \times 10^{34}$ erg s$^{-1}$ at the peak). The spectral analysis of this flare allowed us to derive these parameters: $N_{\rm H} = 6.7^{+8.2}_{-6.7} \times 10^{22}$ cm$^{-2}$, $\Gamma = 1.5^{+1.5}_{-1.3}$, $F^{\rm abs}_{2-8\ {\rm keV}} = 2.5 \times 10^{-12}$ erg s$^{-1}$ cm$^{-2}$, and $F^{\rm unabs}_{2-10\ {\rm keV}} = 3.5^{+3.1}_{-1.0} \times 10^{-12}$ erg s$^{-1}$ cm$^{-2}$. These spectral parameters are consistent with those previously found by Porquet et al. (2003, 2008) and Nowak et al. (2012) but are not really constrained.

A comparison of the physical characteristics of this flare with those reported by Neilsen et al. (2013) from the 2012 *Chandra* XVP campaign shows that it lies in the mean of the X-ray flares detected by *Chandra*, but the first subflare is one of the shortest and less luminous X-ray flares. The distribution of the minimum waiting time between two successive flares in the *Chandra* XVP campaign favors the hypothesis of a single flare.

We modeled its two subflares with a single physical phenomenon using the gravitational lensing of a hotspot-like

structure. However, the consistency of the flux level between the two subflare peaks with the non-flaring one led us to conclude that the light curve of this X-ray flare cannot satisfactorily be reproduced by a gravitational lensing event.

We also constrained the radial position of the emitting region of the first 2011 March 30 subflare by assuming that the heating energy is provided by the magnetic field available in the spherical emitting region whose radius is determined by the duration of the rise phase of this first subflare. A comparison of the duration of the decay phase of this subflare and the synchrotron cooling timescale allowed us to determine a lower limit to the radial distance. We conclude that the X-ray emitting region of the first subflare is located at a radial position of $4-100^{+19}_{-29}$ and has a corresponding radius of $1.8-2.87 \pm 0.01$ in $r_g$ unit for a magnetic field of 100 G at 2 $r_g$.

*Acknowledgements.* E.M. acknowledges the Université de Strasbourg for her IdEx PhD grant. The *XMM-Newton* project is an ESA Science Mission with instruments and contributions directly funded by ESA Member States and the USA (NASA). This work has been financially supported by the Programme National Hautes Energies (PNHE). The research leading to these results received funding from the European Union Seventh Framework Program (FP7/2007−2013) under grant agreement N° 312789.

## References

Anders, E., & Ebihara, M. 1982, Geochim. Cosmochim. Acta, 46, 2363
Baganoff, F. K., Bautz, M. W., Brandt, W. N., et al. 2001, Nature, 413, 45
Baganoff, F. K., Maeda, Y., Morris, M., et al. 2003, ApJ, 591, 891
Bardeen, J. M., Press, W. H., & Teukolsky, S. A. 1972, ApJ, 178, 347
Barrière, N. M., Tomsick, J. A., Baganoff, F. K., et al. 2014, ApJ, 786, 46
Broderick, A. E., & Loeb, A. 2005, MNRAS, 363, 353
Dexter, J., & Agol, E. 2009, ApJ, 696, 1616
Dodds-Eden, K., Porquet, D., Trap, G., et al. 2009, ApJ, 698, 676
Doeleman, S. S., Weintroub, J., Rogers, A. E. E., et al. 2008, Nature, 455, 78
Eckart, A., Baganoff, F. K., Schödel, R., et al. 2006, A&A, 450, 535
Eckart, A., Schödel, R., García-Marín, M., et al. 2008, A&A, 492, 337
Eckart, A., García-Marín, M., Vogel, S. N., et al. 2012, A&A, 537, A52
Eisenhauer, F., Genzel, R., Alexander, T., et al. 2005, ApJ, 628, 246
Falcke, H., & Markoff, S. B. 2013, Class. Quant. Grav., 30, 4003
Falcke, H., Mannheim, K., & Biermann, P. L. 1993, A&A, 278, L1
Feigelson, E. D., & Babu, G. J. 2012, Modern statistical method for astronomy with R applications (Cambridge: Cambridge University Press)
Genzel, R., Eisenhauer, F., & Gillessen, S. 2010, Rev. Mod. Phys., 82, 3121
Ghez, A. M., Salim, S., Weinberg, N. N., et al. 2008, ApJ, 689, 1044
Gillessen, S., Eisenhauer, F., Fritz, T. K., et al. 2009, ApJ, 707, L114
Guainazzi, M. 2013, XMM-Newton Calibration Technical Note; XMM-SOC-CAL-TN-0018, Calibration status document, ESA-ESAC, Villafranca del Castillo, Spain
Hamaus, N., Paumard, T., Müller, T., et al. 2009, ApJ, 692, 902
Ho, L. C., Darling, J., & Greene, J. E. 2008, ApJS, 177, 103
Houck, J. C. 2002, High Resolution X-ray Spectroscopy with XMM-Newton and Chandra, Proc. Int. Workshop, ed. G. Branduardi
Houck, J. C., & Denicola, L. A. 2000, ASPC, 216, 591
Karas, V., Vokrouhlicky, D., & Polnarev, A. G. 1992, MNRAS, 259, 569
Marrone, D. P., Baganoff, F. K., Morris, M. R., et al. 2008, ApJ, 682, 373
Morrison, R., & McCammon, D. 1983, ApJ, 270, 119
Narayan, R., Mahadevan, R., Grindlay, J. E., Popham, R. G., & Gammie, C. 1998, ApJ, 492, 554
Neilsen, J., Nowak, M. A., Gammie, C., et al. 2013, ApJ, 774, 42
Nowak, M. A., Neilsen, J., Markoff, S. B., et al. 2012, ApJ, 759, 95
Porquet, D., Predehl, P., Aschenbach, B., et al. 2003, A&A, 407, L17
Porquet, D., Grosso, N., Predehl, P., et al. 2008, A&A, 488, 549
Predehl, P., & Schmitt, J. H. M. M. 1995, A&A, 293, 889
Reid, M. J., Readhead, A. C. S., Vermeulen, R. C., & Treuhaft, R. N. 1999, ApJ, 524, 816
Scargle, J. D. 1998, ApJ, 504, 405
Scargle, J. D., Norris, J. P., Jackson, B., & Chiang, J. 2013a, ApJ, 764, 167
Scargle, J. D., Norris, J. P., Jackson, B., & Chiang, J. 2013b, 2012 Fermi Symp. Proc. – eConf C121028 [arXiv:1304.2818]
Schnittman, J. D., & Bertschinger, E. 2004, ApJ, 606, 1098
Schödel, R., Ott, T., Genzel, R., et al. 2002, Nature, 419, 694
Silverman, B. W. 1986, Density Estimation for Statistics and Data Analysis, ed. C. Hall (Chapman & Hall)
Stelzer, B., Flaccomio, E., Briggs, K., et al. 2007, A&A, 468, 463
Strüder, L., Briel, U., Dennerl, K., et al. 2001, A&A, 365, L18
Turner, M. J. L., Abbey, A., Arnaud, M., et al. 2001, A&A, 365, L27
Verner, D. A., Ferland, G. J., Korista, K. T., & Yakovlev, D. G. 1996, ApJ, 465, 487
Vincent, F. H., Paumard, T., Gourgoulhon, E., & Perrin, G. 2011, Class. Quant. Grav., 28, 5011
Wang, Q. D., Nowak, M. A., Markoff, S. B., et al. 2013, Science, 341, 981
Wilms, J., Allen, A., & McCray, R. 2000, ApJ, 542, 914
Yuan, F., Quataert, E., & Narayan, R. 2003, ApJ, 598, 301
Yusef-Zadeh, F., Roberts, D., Wardle, M., Heinke, C. O., & Bower, G. C. 2006, ApJ, 650, 189
Yusef-Zadeh, F., Bushouse, H., Wardle, M., et al. 2009, ApJ, 706, 348
Yusef-Zadeh, F., Wardle, M., Dodds-Eden, K., et al. 2012, AJ, 144, 1

Pages 13 to 15 are available in the electronic edition of the journal at http://www.aanda.org

## Appendix A: Calibration of the ncp_prior relation

We cannot use the scaling relation given in Scargle et al. (2013a) for our data set because it has different statistical properties than the simulated data set used by Scargle et al. (2013a). First, our events are affected by Poissonian noise and not by Gaussian noise. Second, our event lists with about ~4000 counts is longer than the published simulation limited to 1024 counts. To calibrate the relation between *ncp_prior* (the prior of the number of block) and the false positive rate ($p_1$), we simulate 100 constant light curves with Poisson noise around a level of 0.1 count $s^{-1}$, which is the typical non-flaring level measured by *XMM-Newton*/EPIC pn during our observations. For each sequence of 100 simulations, we increase the *ncp_prior* value from 2 to 9 by a step of 0.5 and we compute the number of change points detected. The percentage of change points detected in 100 simulations determines the $p_1$. We repeat this operation for different numbers of count $N$ in the light curve (from 1000 counts to 6000 counts by step of 1000 counts). With the $p_1$ values and the corresponding *ncp_prior*, we can create the graph presented in Fig. A.1. Then, we can take different values of $p_1$ and report the relation between the count number and *ncp_prior* that satisfied $p_1$. An example with $p_1 = 0.05$ is given in the bottom graph of Fig. A.1. The dashed line is the linear fit of the curve. Thus, we have the same number of relations between $N$ and *ncp_prior* as the number of value of $p_1$ that we choose. By combining these relations, which relies $p_1$, $N$, and *ncp_prior*, we find our calibration:

$$ncp\_prior = \begin{array}{l} 3.356 + 0.143\ln(N) - 0.710\ln(p_1) \\ -0.002\ln(N)\ln(p_1) \end{array} \quad (A.1)$$

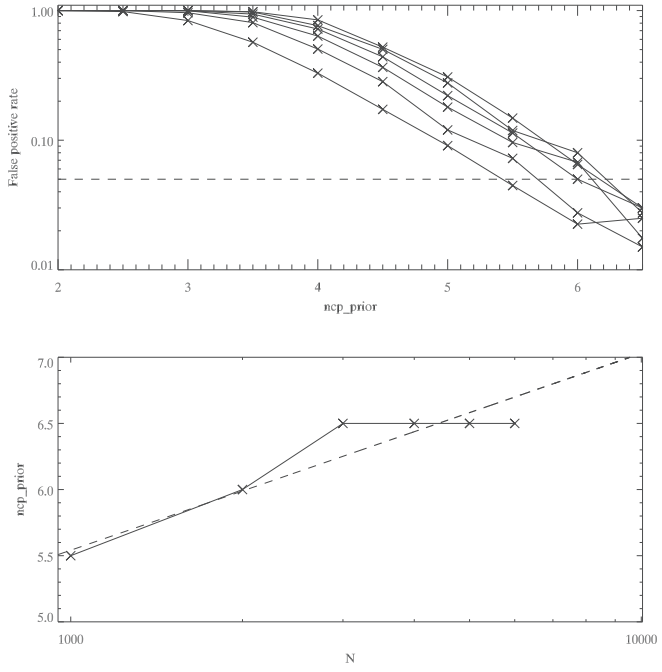


**Fig. A.1.** Simulations of point measurements (Poisson signal of average 0.1) to determine $ncp\_prior = -\log(\gamma)$. *Top*: false positive fraction $p_1$ vs. value of *ncp_prior* with separate curves for the values $N = 1000, 2000, 3000, 4000, 5000$, and 6000 (left to right). The points at which the rate becomes unacceptable (here 0.05; dashed line) determine the recommended values of *ncp_prior* shown as a function of $N$ in the bottom panel. *Bottom*: calibration of *ncp_prior* as a function of the number of counts ($N$) for a value of $p_1$ (here: 0.05). The dashed line is the linear fit of the simulation points.

with $N$ the number of events in a range of [1000:6000] counts. For $N$ lower than 1000, the last term is lower than 0.01, which is negligible. For a probability of false detection equals exp(−3.5) and $N = 4000$, ncp_prior = 7.0099.

## Appendix B: Detection rate vs. flare peak and duration

To evaluate our detection level, we simulate light curves with a Poisson signal of average 0.1 count $s^{-1}$ for EPIC pn and 0.04 count $s^{-1}$ for EPIC MOS corresponding to the non-flaring level of these cameras. This difference in the non-flaring level between the two cameras implies a difference in the Poisson noise (the higher the non-flaring level, the higher the Poisson noise), hence in the detection rate. On these constant light curves, we add a Gaussian with a FWHM equal to 1104 s, 318.49 s, and 56.62 s, which correspond to the maximum, the median, and the minimum, respectively, of the FWHM of the X-ray flares from Sgr A* detected by *Chandra* and reported by Neilsen et al. (2013). We vary the amplitude of the Gaussian between 0 and 0.17 count $s^{-1}$ above the non-flaring level. For each amplitude, we perform 100 simulations and compute the number of flare (two change points) found by the Bayesian-blocks algorithm for a false positive rate equal to exp(−3.5). The results are shown in Fig. B.1. We can see that the higher the amplitude and the FWHM of the flare, the higher the detection rate. We can also see that the main difference between the detection rate in the *XMM-Newton*/EPIC MOS and pn camera (the former has a non-flaring level that is two times lower than in pn) is that the small flares with large FWHM are more detected in MOS than in pn.

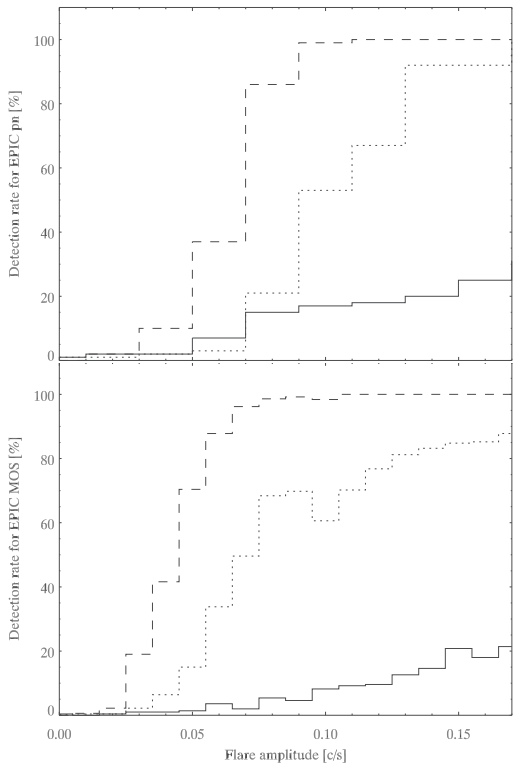


**Fig. B.1.** Detection level for different values of Gaussian amplitude and $p_1 = \exp(-3.5)$. The solid line corresponds to *FWHM* = 56.62 s, the dotted line corresponds to *FWHM* = 318.49 s, and the dashed line corresponds to *FWHM* = 1104 s.

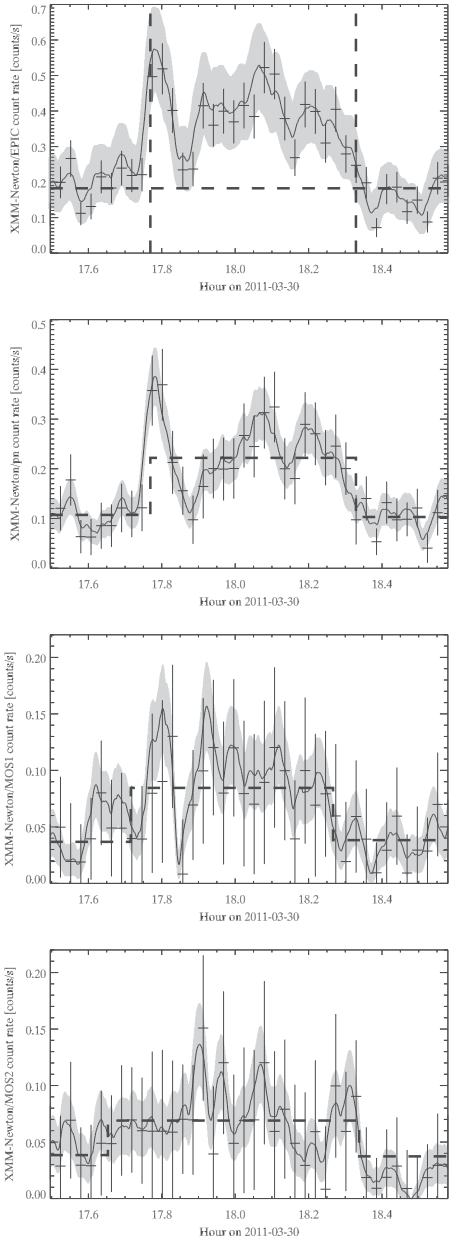


**Fig. B.2.** Light curves of Sgr A* in the 2−10 keV energy range obtained during the flare on 2011 March 30 binned on 100 s. *Top*: the total *XMM-Newton*/EPIC light curve. The horizontal dashed line represents the non-flaring level calculated as the sum of the non-flaring level in each instrument found by the Bayesian blocks. The vertical dashed lines represent the beginning and the end of the flare calculated by the Bayesian-blocks algorithm on pn camera. The solid line is the smoothed light curve that is the sum of the smoothed light curve for each instrument (calculated on the same time range). The gray curve shows the errors associated with the smoothed light curve. In all panels, the time period during which the camera did not observe is shown by a light gray box. *Second panel*: the *XMM-Newton*/EPIC pn light curve of Sgr A*. *Third panel*: the *XMM-Newton*/EPIC MOS1 light curve of Sgr A*. The vertical dashed lines represent the beginning and the end of the flare calculated by the Bayesian-blocks algorithm on MOS1 camera. *Bottom panel*: the *XMM-Newton*/EPIC MOS2 light curve of Sgr A*. The vertical dashed lines represent the beginning and the end of the flare calculated by the Bayesian-blocks algorithm on MOS2 camera.

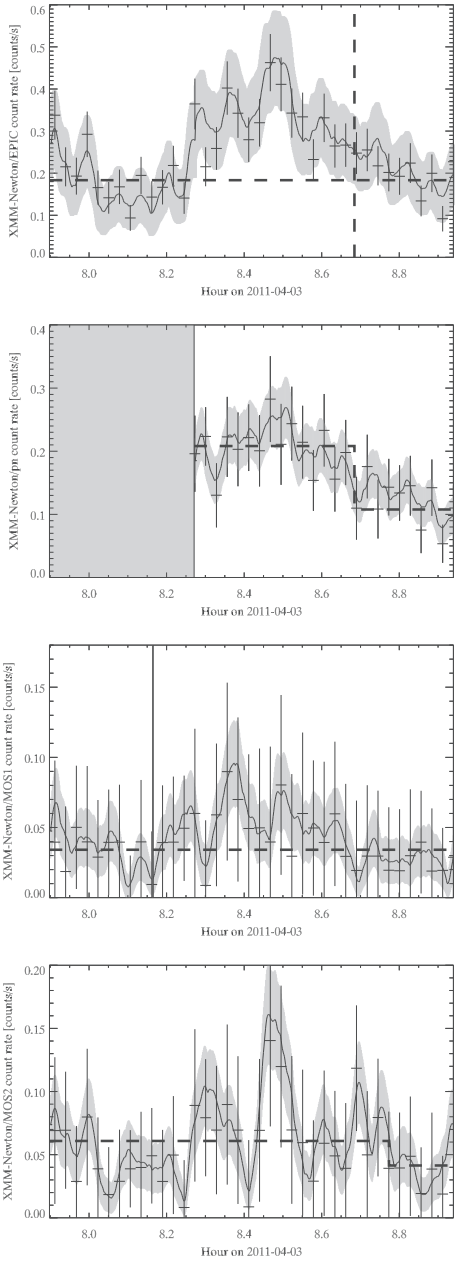


**Fig. B.3.** Light curves of Sgr A* in the 2−10 keV energy range obtained during the flare on 2011 April 3 binned on 100s. *Top*: the total *XMM-Newton*/EPIC light curve. The horizontal dashed line represents the non-flaring level calculated as the sum of the non-flaring level in each instrument found by the Bayesian blocks. The vertical dashed lines represent the beginning and the end of the flare calculated by the Bayesian-blocks algorithm on pn camera. The solid line is the smoothed light curve that is the sum of the smoothed light curve for each instrument (calculated on the same time range). The gray curve shows the errors associated with the smoothed light curve. In all panels, the time period during which the camera did not observe is shown by a light gray box delimited by vertical solid lines. *Second panel*: the *XMM-Newton*/EPIC pn light curve of Sgr A*. The dark gray box is the time during which pn did not observe. *Third panel*: the *XMM-Newton*/EPIC MOS1 light curve of Sgr A*. The light gray vertical line shows the time during which MOS1 did not observe. The vertical dashed lines represent the beginning and the end of the flare calculated by the Bayesian-blocks algorithm on MOS1 camera. *Bottom panel*: the *XMM-Newton*/EPIC MOS2 light curve of Sgr A*. The vertical dashed lines represent the beginning and the end of the flare calculated by the Bayesian-blocks algorithm on MOS2 camera.

Figures B.2 and B.3 show the flare light curves obtained with of *XMM-Newton*/EPIC observed on 2011 March 30 and April 3.

We can see that the first and second subflares on 2011 March 30 are distinguishable on *XMM-Newton*/EPIC pn and MOS1 but not in MOS2 even if a flare is detected by the Bayesian-blocks algorithm. The flare on 2011 April 3 is not detected by the Bayesian-blocks algorithm in *XMM-Newton*/EPIC MOS1. This is because the algorithm allows us to find a flare whose $FWHM \approx 900$ s in EPIC MOS camera with a probability of 95% if its amplitude above the non-flaring level is higher than 0.07 count $s^{-1}$ with a probability of false detection equal to $\exp(-3.5)$, but in *XMM-Newton*/EPIC MOS1, the flare amplitude is about 0.06 count $s^{-1}$. Since *XMM-Newton*/EPIC MOS1 and MOS2 have lower number counts than *XMM-Newton*/EPIC pn because of the RGS, it is on *XMM-Newton*/EPIC pn that the flare will have higher amplitude and thus higher accuracy on the determination of the beginning and end of the flare.

## Appendix C: Time dilatation around a Kerr black hole

We use the Kerr metric in Boyer-Lindquist coordinates:

$$\begin{aligned} \mathrm{d}s^2 = -\mathrm{d}\tau^2 = & -\left(1-\tfrac{2r}{\Sigma}\right)\mathrm{d}t^2 - \tfrac{4ar\sin^2\theta}{\Sigma}\mathrm{d}t\,\mathrm{d}\phi + \tfrac{\Sigma}{\Delta}\mathrm{d}r^2 \\ & +\Sigma\,\mathrm{d}\theta^2 + \left(r^2 + a^2 + \tfrac{2a^2 r\sin^2\theta}{\Sigma}\right)\sin^2\theta\,\mathrm{d}\phi^2 \end{aligned} \tag{C.1}$$

with $\tau$ the proper time, $t$ the observed time, $r$ the radial distance in gravitational radius, $a$ the dimensionless spin parameter, $\Sigma = r^2 + a^2\cos^2\theta$, $\Delta = r^2 - r + a^2$, and $\theta = 0$ defining the spin axis (Bardeen et al. 1972). For a direct circular orbit in the equatorial plane, we have $\frac{\mathrm{d}r}{\mathrm{d}t} = 0$, $\theta = \frac{\pi}{2}$, and $\frac{\mathrm{d}\phi}{\mathrm{d}t} = \frac{1}{r^{3/2}+a}$ (Bardeen et al. 1972). Thus, the relation between the proper time and the observed time is

$$\frac{\mathrm{d}\tau}{\mathrm{d}t} = \sqrt{1 - \frac{2}{r} - \frac{r^3 - 4ar^{3/2} + a^2 r - 2a^2}{r\left(r^{3/2}+a\right)^2}}. \tag{C.2}$$

Figure C.1 shows the time dilatation as a function of the radial distance plotted from the innermost boundary of the circular orbit, i.e., $r_g$ for $a = 1$.

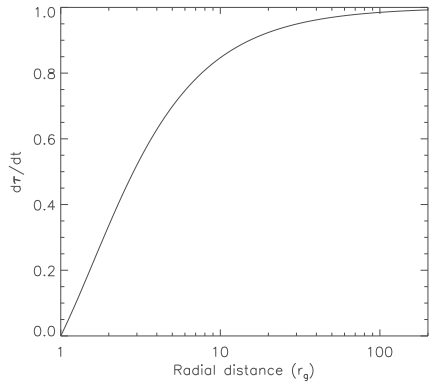


**Fig. C.1.** Ratio between the proper time and the observed time close to a Kerr black hole with a dimensionless spin parameter of 1.

A&A 580, C2 (2015)
DOI: 10.1051/0004-6361/201424682e
© ESO 2015

Astronomy & Astrophysics

# Study of the X-ray activity of Sagittarius A* during the 2011 *XMM-Newton* campaign *(Corrigendum)*

Enmanuelle Mossoux[1], Nicolas Grosso[1], Frédéric H. Vincent[2], and Delphine Porquet[1]

[1] Observatoire Astronomique de Strasbourg, Université de Strasbourg, CNRS, UMR 7550, 11 rue de l'Université, 67000 Strasbourg, France
e-mail: enmanuelle.mossoux@astro.unistra.fr
[2] Nicolaus Copernicus Astronomical Center, ul. Bartycka 18, 00-716 Warszawa, Poland

A&A 573, A46 (2015), DOI: 10.1051/0004-6361/201424682

**Key words.** Galaxy: center – X-rays: individuals: Sgr A* – radiation mechanisms: general – errata, addenda

The weight equation in Sect. 3.1 of Mossoux et al. (2015) unfortunately features a typo. The correct equation should read:

$$w = \frac{CR_{\rm src+bkg}}{CR_{\rm src+bkg} - CR_{\rm bkg}} \quad (1)$$

with $CR_{\rm src+bkg}$ the count rate of the Bayesian block of the source+background event list and $CR_{\rm bkg}$ the count rate of the corresponding Bayesian block of the background that is surface-corrected. As introduced in the first preprint version of the proceeding of Scargle et al. (2013), this weight equation adjusts the Voronoi time-interval in order to subtract the average background. The results presented in Mossoux et al. (2015) remain unchanged since they were all obtained following the recipe of Scargle et al. (2013) and using the correct equation for the Voronoi time-interval weighting.

Therefore, the "alternative" photon-weighting recently tested by Worpel & Schwope (2015) in their Sect. 4.6 ($w \equiv 1 - CR_{\rm bkg}/CR_{\rm src+bkg}$) is actually equivalent to the recipe of Scargle et al. (2013) that we used in Mossoux et al. (2015) since the photon-weighting is equal to the inverse of the Voronoi time-interval weighting. Indeed, the "alternative" photon-weighting of Worpel & Schwope (2015) is identical to those used in Eq. (1) of Mossoux et al. (2015) to compute smoothed light-curve.

## References

Mossoux, E., Grosso, N., Vincent, F. H., & Porquet, D. 2015, A&A, 573, A46
Scargle, J. D., Norris, J. P., Jackson, B., & Chiang, J. 2013, 2012 Fermi Symp. Proc. – eConf C121028 [arXiv:1304.2818v1]
Worpel, H., & Schwope, A. D. 2015, A&A, 578, A80

A&A 589, A116 (2016)
DOI: 10.1051/0004-6361/201527554
© ESO 2016

Astronomy & Astrophysics

# Multiwavelength study of the flaring activity of Sagittarius A in 2014 February–April⋆

E. Mossoux[1], N. Grosso[1], H. Bushouse[2], A. Eckart[3,4], F. Yusef-Zadeh[5], R. L. Plambeck[6], F. Peissker[3], M. Valencia-S.[3], D. Porquet[1], W. D. Cotton[7], and D. A. Roberts[5]

[1] Observatoire astronomique de Strasbourg, Université de Strasbourg, CNRS, UMR 7550, 11 rue de l'Université, 67000 Strasbourg, France
e-mail: enmanuelle.mossoux@astro.unistra.fr
[2] Space Telescope Science Institute (STScI), 3700 San Martin Drive, Baltimore, MD 21218, USA
[3] Physikalisches Institut der Universität zu Köln, Zülpicher Str. 77, 50937 Köln, Germany
[4] Max-Planck-Institut für Radioastronomie, Auf dem Hügel 69, 53121 Bonn, Germany
[5] Department of Physics and Astronomy, CIERA, Northwestern University, Evanston, IL 60208, USA
[6] Radio Astronomy Laboratory, University of California, Berkeley, CA 94720, USA
[7] National Radio Astronomy Observatory, Charlottesville, VA 22903, USA

Received 14 October 2015 / Accepted 1 March 2016

**ABSTRACT**

*Context.* The supermassive black hole named Sgr A* is located at the dynamical center of the Milky Way. This closest supermassive black hole is known to have a luminosity several orders of magnitude lower than the Eddington luminosity. Flares coming from the Sgr A* environment can be observed in infrared, X-ray, and submillimeter wavelengths, but their origins are still debated. Interestingly, the close passage of the Dusty S-cluster Object (DSO)/G2 near Sgr A* may increase the black hole flaring activity and could therefore help us to better constrain the radiation mechanisms from Sgr A*.
*Aims.* Our aim is to study the X-ray, infrared, and radio flaring activity of Sgr A* close to the time of the DSO/G2 pericenter passage in order to constrain the physical properties and origin of the flares.
*Methods.* Simultaneous observations were made with *XMM-Newton* and WFC3 onboard HST during the period Feb.–Apr. 2014, in addition to coordinated observations with SINFONI at ESO's VLT, VLA in its A-configuration, and CARMA.
*Results.* We detected two X-ray flares on 2014 Mar. 10 and Apr. 2 with *XMM-Newton*, three near-infrared (NIR) flares with HST on 2014 Mar. 10 and Apr. 2, and two NIR flares on 2014 Apr. 3 and 4 with VLT. The X-ray flare on 2014 Mar. 10 is characterized by a long rise (~7700 s) and a rapid decay (~844 s). Its total duration is one of the longest detected so far in X-rays. Its NIR counterpart peaked well before (4320 s) the X-ray maximum, implying a dramatic change in the X-ray-to-NIR flux ratio during this event. This NIR/X-ray flare is interpreted as either a single flare where variation in the X-ray-to-NIR flux ratio is explained by the adiabatic compression of a plasmon, or two distinct flaring components separated by 1.2 h with simultaneous peaks in X-rays and NIR. We identified an increase in the rising radio flux density at 13.37 GHz on 2014 Mar. 10 with the VLA that could be the delayed radio emission from a NIR/X-ray flare that occurred before the start of our observation. The X-ray flare on 2014 Apr. 2 occurred for HST during the occultation of Sgr A* by the Earth, therefore we only observed the start of its NIR counterpart. With NIR synchrotron emission from accelerated electrons and assuming X-rays from synchrotron self-Compton emission, the region of this NIR/X-ray flare has a size of 0.03−7 times the Schwarzschild radius and an electron density of $10^{8.5}$–$10^{10.2}$ cm$^{-3}$, assuming a synchrotron spectral index of 0.3−1.5. When Sgr A* reappeared to the HST view, we observed the decay phase of a distinct bright NIR flare with no detectable counterpart in X-rays. On 2014 Apr. 3, two 3.2-mm flares were observed with CARMA, where the first may be the delayed (4.4 h) emission of a NIR flare observed with VLT.
*Conclusions.* We observed a total of seven NIR flares, with three having a detected X-ray counterpart. The physical parameters of the flaring region are less constrained for the NIR flare without a detected X-ray counterpart, but none of the possible radiative processes (synchrotron, synchrotron self-Compton, or inverse Compton) can be ruled out for the production of the X-ray flares. The three X-ray flares were observed during the *XMM-Newton* total effective exposure of ~256 ks. This flaring rate is statistically consistent with those observed during the 2012 *Chandra XVP* campaign, implying that no increase in the flaring activity was triggered close to the pericenter passage of the DSO/G2. Moreover, higher flaring rates had already been observed with *Chandra* and *XMM-Newton* without any increase in the quiescent level, showing that there is no direct link between an increase in the flaring rate in X-rays and the change in the accretion rate.

**Key words.** Galaxy: center – X-rays: individuals: Sgr A* – radiation mechanisms: general

## 1. Introduction

Sgr A*, located at the dynamical center of our Galaxy, is currently a dormant supermassive black hole (SMBH) of mass $M$ about $4 \times 10^6\ M_\odot$ (Schödel et al. 2002; Ghez et al. 2008; Gillessen et al. 2009). Its bolometric luminosity ($L_{\rm bol} \sim 10^{36}$ erg s$^{-1}$) is lower than the Eddington luminosity ($L_{\rm Edd} = 3.3 \times 10^4\ M/M_\odot\ L_\odot = 3 \times 10^{44}$ erg s$^{-1}$) (Yuan et al. 2003). This low luminosity can be explained by radiatively inefficient accretion flow models (RIAF) such as advection-dominated accretion flows (ADAF; Narayan et al. 1998) and

⋆ The tables of the data used for the light curves are only available at the CDS via anonymous ftp to cdsarc.u-strasbg.fr (130.79.128.5) or via http://cdsarc.u-strasbg.fr/viz-bin/qcat?J/A+A/589/A116

A&A 589, A116 (2016)

jet-disk models. Because of its proximity ($d$ = 8 kpc; Genzel et al. 2010; Falcke & Markoff 2013), Sgr A* is the best target to study the accretion and ejection physics for the case of low accretion rate, which is a regime where SMBH's are supposed to spend most of their lifetime. Its physical understanding can be applied to a large number of normal galaxies that are supposed to host a SMBH.

Above Sgr A* quiescent emission, some episodes of increased flux are observed in X-rays, near-infrared (NIR), and sub-millimeter/radio. These flaring events from Sgr A* were first discovered in X-rays (Baganoff et al. 2001) and were then also observed in NIR (Genzel et al. 2003) and sub-millimeter wavelengths (Zhao 2003). NIR flares, which happen several times per day and have various amplitude up to 32 mJy (Witzel et al. 2012), are interpreted as synchrotron emission from accelerated electrons close to the black hole (Eisenhauer et al. 2005; Eckart et al. 2006). In the NIR, the synchrotron emission is optically thick and the spectral index between the $H$ and $L$ band is $\alpha = -0.62 \pm 0.1$ with $S_\nu \propto \nu^\alpha$ (Witzel et al. 2014b). The X-ray flaring rate is 1.0−1.3 flares per day (Neilsen et al. 2013), but two episodes of higher flaring activity in X-rays have been observed (Porquet et al. 2008; Neilsen et al. 2013). Most X-ray flares have moderate amplitude (Neilsen et al. 2013) with 2–45 times the quiescent luminosity of Sgr A* (about $3.6\times10^{33}$ erg s$^{-1}$ in 2−8 keV; Baganoff et al. 2003; Nowak et al. 2012), but brighter flares with amplitudes up to 160 times the quiescent level have also been observed (Porquet et al. 2003, 2008; Nowak et al. 2012). Several emission mechanism models are proposed in order to explain X-ray flares, such as: synchrotron (Dodds-Eden et al. 2009; Barrière et al. 2014), synchrotron self-Compton (Eckart et al. 2008), and inverse Compton (Yusef-Zadeh et al. 2006b; Wardle 2011; Yusef-Zadeh et al. 2012) emissions. During simultaneous NIR/X-ray observations, X-ray flares always have a NIR counterpart and their light curves have similar shapes, with an apparent delay less than 3 min between the peaks of flare emission (Eckart et al. 2006; Yusef-Zadeh et al. 2006a; Dodds-Eden et al. 2009). The sub-millimeter and radio flare peaks, however, are delayed several tens of minutes and hours, respectively (Marrone et al. 2008; Yusef-Zadeh et al. 2008, 2009), and are proposed to be due to synchrotron radiation of an expanding relativistic plasma blob with an adiabatic cooling (Yusef-Zadeh et al. 2006a). Considering the intrinsic size of Sgr A* at a wavelength $\lambda$ of $(0.52 \pm 0.03)\,\mathrm{mas} \times (\lambda/\mathrm{cm})^{1.3\pm0.1}$, the time lag between the sub-millimeter and radio light curves suggests a collimated outflow (Brinkerink et al. 2015). On 2012 May 17, a NIR flare was followed 4.5 ± 0.5 h later by a 7-mm flare that was observed with the Very Long Baseline Array (VLBA) and localized 1.5 mas southeast of Sgr A*, providing evidence for an adiabatically expanding jet with a speed of 0.4 ± 0.3 $c$ (Rauch et al. 2016).

Gillessen et al. (2012) reported the detection of the object named G2 on its way towards Sgr A* in an eccentric Keplerian orbit with the 2004 data from the Very Large Telescope (VLT) using the Spectrograph for INtegral Field Observations in the Near-Infrared (SINFONI) and the Nasmyth Adaptive Optics System (NAOS) and COudé Near-IR Camera (CONICA), i.e., NACO. Their observations of the redshifted emission lines Br$\gamma$, Br$\delta$, and HeI in the NIR between 2004 and 2011 allowed them to determine the pericenter passage of 2013.51 ± 0.04. They developed the first interpretation of the nature of the G2 object based on the observation of these lines: a compact gas blob. From the $M$-band they showed that G2 has a dust temperature consistent with 450 K. They predicted that, because G2 moves supersonically through the ambient hot gas, a bow shock should be created close to the pericenter passagei, which should be seen from radio to X-rays. The observation of such X-ray emission could help to put some constraints on the physical characteristics of the ambient medium around Sgr A*. The compact gas blob interpretation was still favored by Gillessen et al. (2013a) who analyzed the Br$\gamma$ line width using data from SINFONI and NACO in March−July 2012. They derived a pericenter passage of 2013.69 ± 0.04, adding their observations to those between 2004 and 2011. A velocity-position diagram of G2 was computed by Gillessen et al. (2013b) using the emission lines Br$\gamma$, HeI, and Pa$\alpha$ from SINFONI and NACO observations in April 2013. An elongation of G2 in the direction of its orbit was seen in the velocity-position diagram, which, together with the low dust temperature, favored the interpretation of an ionized gas cloud.

Two other interpretations based on the observations of these emission lines were also developed. The first one was proposed by Burkert et al. (2012): a spherical gas shell, which was supported by a simulation that reproduced the observed elongated structure in the velocity profile. They also simulated the effects of tidal shearing produced by Rayleigh-Taylor and Kelvin-Helmholtz instabilities during its approach to Sgr A* (Morris 2012). The shearing should produce a fragmentation of the envelope of G2 and provide fresh matter that would accrete onto Sgr A*. This should increase the flaring activity of Sgr A*, depending on the filling factor, or (re-)activate the Active Galactic Nuclei (AGN) phase during the subsequent years. The other interpretation is a dust-enshrouded stellar source, first developed by Eckart et al. (2013), which leads to the second name of G2: a Dusty S-cluster Object (DSO). This classification is supported by its detection in the $K_s$- and $K'$-bands in observations from NACO and the NIRC2 camera of the Keck Observatory, respectively. The $M$-band measurements showed that the integrated luminosity of this object is 5−10 $L_\odot$. Moreover, the $L$-band emission remained constant and spatially unresolved from 2004 to 2014, which ruled out a coreless model (Witzel et al. 2014a). The compact nature of the source is also supported by SINFONI observations between February and September 2014 (Valencia-S. et al. 2015). They showed that the wide range of Br$\gamma$ line widths (200−700 km s$^{-1}$) is reproduced well by the emission from a pre-main sequence star, because the magnetospheric accretion of circumstellar matter on the photosphere of these young stars emits the Br$\gamma$ line. The tidal stretching of the accretion disk around the star as DSO/G2 approaches pericenter may explain the increase of the Br$\gamma$ line width. A star with a mass of 1−2 $M_\odot$ and a luminosity less than 10 $L_\odot$ agrees with the dust temperature of 450 K found by Gillessen et al. (2012). As Valencia-S. et al. (2015) observed the blueshifted Br$\gamma$ line after 2014 May, they were able to improve the estimation of the time of the pericenter passage to 2014.39 ± 0.14 and a distance of ∼163 au (4075 gravitational radius) from Sgr A*. For comparison, the B0 spectral-type star S2 with a 15.2-year orbit around Sgr A* has a 1.3 times smaller pericenter distance (Schödel et al. 2002). The absence of a redshifted counterpart after the pericenter passage favored the interpretation of the nature of DSO/G2 as a compact object and still ruled out the coreless model.

The multiwavelength campaign presented here was designed in 2012 to study the impact of the passage of the DSO/G2 object close to the SMBH (based on the pericenter date predicted by Gillessen et al. 2012) from the NIR/X-ray flaring activity of Sgr A*. We report the results of joint observations of Sgr A* between February and April 2014 with the X-ray Multi-Mirror mission (*XMM-Newton*) and the *Hubble* Space Telescope (HST) (*XMM-Newton* AO-12; PI: N. Grosso), close to the pericenter

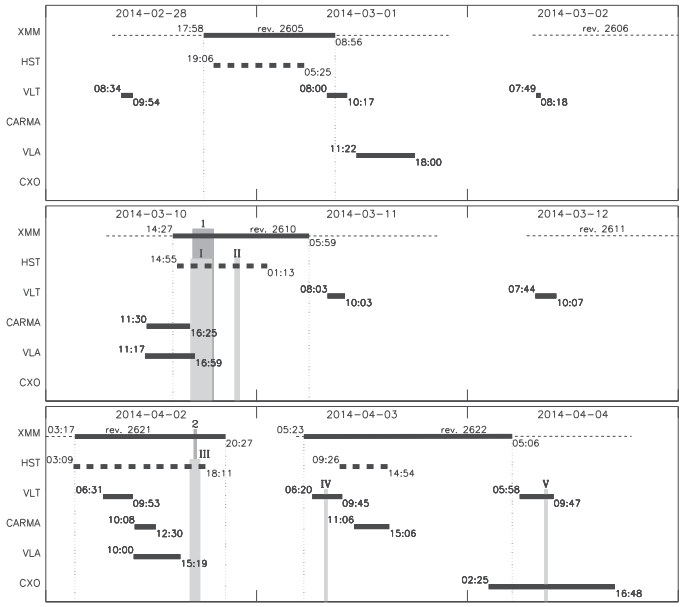


**Fig. 1.** Time diagram of the 2014 Feb.−Apr. campaign. The horizontal dashed lines are the *XMM-Newton* orbital visibility times of Sgr A* labeled with revolution numbers. The thick solid lines are the time slot of the observations for each instrument with start and stop hours. The vertical dotted lines are the limits of the *XMM-Newton* observations. The vertical gray blocks are the X-ray (Arabic numerals) and near-IR (Roman numerals) flares reported in this work.

passage of DSO/G2. We also obtained coordinated observations with the VLT, the Combined Array for Research in Millimeter-wave Astronomy (CARMA), and the *Karl Jansky* Very Large Array (VLA) to investigate NIR flaring emission and delayed millimeter/radio flaring emission. In Sect. 2 we present the observations and data reduction. In Sect. 3 we report the analysis of these observations. In Sect. 4 we determine the X-ray emission related to each NIR flare observed during this campaign. In Sect. 5 we constrain the physical parameters of the flaring region associated with the NIR flares and their X-ray counterparts. In Sect. 6 we discuss the X-ray flaring rate observed during this campaign. Finally, in Sect. 7 we summarize our main results and discuss their possible implications.

## 2. Observations and data reduction

Here we present the schedule of the coordinated observations of the 2014 Feb.−Apr. campaign (Fig. 1) followed by a description of the data reduction for each facility used during this campaign.

### 2.1. XMM-Newton observations

Table 1 reports the log of the *XMM-Newton* campaign for 2014 Feb.−Apr. (AO-12; PI: N. Grosso). The last X-ray observation is an anticipated Target of Opportunity (ToO) that was triggered to observe the new flaring magnetar SGR J1745-29 (AO-12; PI: G.L. Israël). We only use the data from the EPIC camera since the optical extinction towards the Galactic center is too high to get optical or soft X-ray photons from Sgr A* with the Optical-UV Monitor or the Reflection Grating Spectrometers.

During the first three *XMM-Newton* observations, the two EPIC/MOS cameras (Turner et al. 2001) and the EPIC/pn camera (Strüder et al. 2001) observed in frame window mode.

**Table 1.** *XMM-Newton* observation log for the 2014 Feb.−Apr. campaign.

| ObsID | Orbit | Start time (UT) | End time (UT) | Duration (ks) |
|---|---|---|---|---|
| 0723410301 | 2605 | Feb. 28, 17:59:00 | Mar. 01, 08:53:14 | 53.654 |
| 0723410401 | 2610 | Mar. 10, 14:28:16 | Mar. 11, 05:55:49 | 55.653 |
| 0723410501 | 2621 | Apr. 02, 03:18:22 | Apr. 02, 20:18:01 | 61.178 |
| 0690441801 | 2622 | Apr. 03, 05:23:33 | Apr. 04, 05:02:52 | 85.159 |

During the last observation, the two MOS cameras were in small window mode and the pn camera observed in frame window mode. All observations were made with the medium filter. The effective observation start and end times are reported in Table 1 in Universal Time (UT). During these observations, the conversion from the Terrestrial Time (TT) registered aboard *XMM-Newton* to UT is UT = TT − 67.108s (NASA's HEASARC Tool: xTime[1]). The total effective exposure for the four *XMM-Newton* observations during this campaign is ≈256 ks.

The *XMM-Newton* data reduction is the same as presented in Mossoux et al. (2015a). We used the Science Analysis Software (SAS) package (version 13.5) with the 2014 Apr. 4 release of the Current Calibration files (CCF) to reduce and analyze the data. The tasks `emchain` and `epchain` were used to create the event lists for the MOS and pn camera, respectively. The soft proton flare count rate in the full detector light curve in the 2−10 keV energy range was high (up to 0.02 count $s^{-1}$ $arcmin^{-2}$ in EPIC/pn) only during the last two hours of the third observation.

As we looked for variability of the X-ray emission from Sgr A*, we extracted events of the source+background region from a disk of 10″-radius centered on the VLBI radio position of Sgr A*: RA(J2000) = $17^h45^m40\overset{s}{.}0409$, Dec(J2000) = $-29°00'28\overset{''}{.}118$ (Reid et al. 1999). The contribution of the background events was estimated by extracting a $\approx 3' \times 3'$ region at ≈4′ -north of Sgr A* on the same CCD where the X-ray emission is low. For the last observation, the background extraction region was a $\approx 3' \times 3'$ area at ≈7′ -east of Sgr A* on the adjacent CCD because of the small window mode.

The light curves of the source+background and background regions were created from events with `PATTERN` ≤ 12 and `#XMMEA_SM` and `PATTERN` ≤ 4 and `FLAG==0` for the MOS and pn cameras, respectively. These light curves are computed in the 2−10 keV energy range using a time bin of 300 s. The task `epiclccorr` applies relative corrections to those light curves. We then summed the background-subtracted light curves of the three cameras to produce the total EPIC light curves. Missing values were inferred using a scaling factor between the pn camera and the sum of the MOS1 and MOS2 cameras. This factor was computed during the full time period where all detectors are observing and leads to a number of pn counts that is equal, on average, to 1.46 ± 0.03 times the sum of the number of MOS counts.

To perform the timing analysis of the light curves we adapted the Bayesian-blocks method developed by Scargle (1998) and refined by Scargle et al. (2013a) to the *XMM-Newton* event lists, using a two-step algorithm to correct for any detector

[1] The website of xTime is: `http://heasarc.gsfc.nasa.gov/cgi-bin/Tools/xTime/xTime.pl`

A&A 589, A116 (2016)

**Table 2.** Observation log of WFC3 on board HST for the 2014 Feb.−Apr. campaign.

| Visit | Start time (UT) | End time (UT) | Number of orbits |
|---|---|---|---|
| 1 | Feb. 28, 19:06 | Mar. 01, 05:25 | 7 |
| 2 | Mar. 10, 14:55 | Mar. 11, 01:13 | 7 |
| 3 | Apr. 02, 03:09 | Apr. 02, 18:11 | 10 |
| 4 | Apr. 03, 09:26 | Apr. 03, 14:54 | 4 |

flaring background (Mossoux et al. 2015a,b)[2]. We used the false detection probability $p_1 = \exp(-3.5)$ (Neilsen et al. 2013; Mossoux et al. 2015a) and geometric priors of 7, 6.9, and 6.9 for pn, MOS1, and MOS2, respectively. We created smoothed light curves by applying a density estimator (Silverman 1986; Feigelson & Babu 2012) and using the same method as in Mossoux et al. (2015a) to correct the exposure time and the background contribution to the source+background event list. The amplitude and time of the flare maximum were computed on the smoothed light curve with a window width of 100 s and 500 s and a time grid interval of 10 s.

### 2.2. HST observations

The NIR observations of Sgr A* were obtained with the Wide Field Camera 3 (WFC3) on HST, under joint *XMM-Newton*/HST programs 13403 (AO-12, PI: N. Grosso) and 13316 (Cycle 21, PI: H. Bushouse) in order to measure the delay between X-ray flares and their NIR counterparts. Sgr A* was observed in four visits with 7−10 consecutive HST orbits, whose observation start and end times are reported in UT in Table 2. The total effective exposure for these four HST visits during the 2014 Feb.−Apr. campaign is about 69 ks. Exposures were taken constantly during each part of these windows in which Sgr A* was visible to HST, usually resulting in an uninterrupted cadence of exposures lasting for 40−50 min at a time, and then interrupted for the remaining 40−50 min of each HST orbit in which Sgr A* is occulted by the Earth. The four visits were planned to have the maximum number of consecutive orbits before HST entered the South Atlantic Anomaly (SAA), in order to maximize the simultaneous observing time in NIR and X-ray.

Each WFC3 exposure was taken with the IR channel of the camera, which has a 1024 × 1024 pixel HgCdTe array, with a pixel scale of ∼0.″13. We used the F153M filter, which is a medium-bandwidth filter ($\Delta\lambda = 0.683$ $\mu$m) with an effective wavelength $\lambda_{\rm eff} = 1.53157$ $\mu$m (from the Spanish Virtual Observatory[3]). Each exposure used the predefined readout sequence "SPARS25" with NSAMP = 12 or 13, which produces non-destructive readouts of the detector every 25 secs throughout the exposure, and a total of 12 or 13 readouts, resulting in a total exposure time of 275−300 s after discarding the first short (2.932 s) readout. The exposures were obtained in a 4-point dither pattern centered on Sgr A*, with a spacing of ∼0.6 arcsec (∼4 pixels) per step to improve the sampling of the Point Spread Function (PSF) of *FWHM* = 0.″145 (1.136 detector pixels) at 1.50 $\mu$m (Dressel 2012)[4]. All of the WFC3 exposures were calibrated using the standard STScI calibration pipeline task `calwf3`. Once the pointing information was set for each WFC3 exposure, we could safely use the known relative position of Sgr A* for positioning a photometry aperture (Sgr A* itself cannot be easily identified in the WFC3 images because it is in the PSF wings of the star S2 located at 0.″15 during our observational epoch according to the orbital elements of Gillessen et al. 2009).

The absolute coordinates of HST exposures are limited by uncertainties in the positions of the guide stars that are used to acquire and track the target. We therefore used the radio position of IRS-16C (also known as S96; Yusef-Zadeh et al. 2014), a star near Sgr A*, as an astrometric reference to accurately register the pointing of each WFC3 exposure. The radio position of IRS-16C came from VLA observations in February 2014, which is nearly co-eval with the HST observations.

The accumulating, non-destructive readouts of each calibrated exposure were "unraveled" by taking the difference of adjacent readouts, which results in a series of independent samples taken at 25 s intervals, thereby increasing the time resolution for the subsequent photometric analysis. Photometry of Sgr A* was performed with the IRAF routine `phot`, using a 3-pixel (∼0.4 arcsec) diameter circular aperture centered on the known radio coordinates of Sgr A* (Petrov et al. 2011; Yusef-Zadeh et al. 2014).

Initial analysis of the photometry results for Sgr A* and other stars in the field revealed an overall tendency for the fluxes of individual sources to gradually decrease on the order of ∼3% during the course of each individual exposure (i.e., across the span of multiple readouts). We believe this effect is due to persistence within an individual exposure, as the total signal level reaches fairly high levels by the end of each ∼5 min exposure. We measured this trend for stars near Sgr A* and applied the results to the Sgr A* photometry to remove the effect. When applied to other stars in the field, the corrected photometry was constant, on average, throughout each exposure. The error on the photometry obtained in each of the four visits, within an individual 25 s readout interval, is 0.0044, 0.0046, 0.0022, and 0.0042 mJy, respectively, which has been estimated from the standard deviation of the flux density of a reference star. For comparison, similar observations obtained in the past using NICMOS camera 1 have an uncertainty within a bin of 32 s of 0.002 mJy at 1.60 $\mu$m (Yusef-Zadeh et al. 2006b).

Aperture and extinction corrections were also applied to the Sgr A* photometry. The aperture correction was determined by measuring the curves of growth of several isolated stars in the field, using a series of apertures of increasing size. The correction factor for an aperture diameter of 3 pixels is 1.414. The

[2] Worpel & Schwope (2015) tested different photon-weighting in order to subtract the background during observations of bursting and eclipsing objects in X-rays. The equation for the Voronoi time-interval weighting used in Mossoux et al. (2015a,b) follows the recipe of Scargle et al. (2013b), which is identical to the "alternative" photon-weighting described in Sect. 4.6 of Worpel & Schwope (2015) since the photon-weighting is equal to the inverse of the Voronoi time-interval weighting. We can see in Fig. 12 of Worpel & Schwope (2015) that the method of Mossoux et al. (2015a,b) (labeled *h* in this figure) locates the eclipses, as well as their weighted-photon method (labeled *f* in this figure). As noticed by Worpel & Schwope (2015), their weighted-photon method may produce both negative and implausibly high count rates. Indeed, the method of Mossoux et al. (2015a,b) produces much fewer Bayesian blocks with negative count rates and no implausibly high count rates in comparison to their weighted-photon method (see for comparison panel *h* and *f* of Fig. 12 of Worpel & Schwope 2015). This last point is crucial for flare and burst detection.

[3] The website of the Spanish Virtual Observatory is: `http://svo.cab.inta-csic.es/main/index.php`

[4] For comparison, the FWHM of the NICMOS Camera 1 is 0.″16 (3.75 detector pixels) at 1.60 $\mu$m (Yusef-Zadeh et al. 2006b), i.e., better sampled than the FWHM of the WFC3 camera.

**Table 3.** Coordinated observation log with SINFONI at ESO's VLT for the 2014 Feb.–Apr. campaign.

| Date | Start time (UT) | End time (UT) | Number of exposures [f] (Used/Total) | Total exposure (s) |
|---|---|---|---|---|
| Feb. 27[a] | 08:20:42 | 09:48:55 | 4/4 | 1600 |
| Feb. 28[b] | 08:34:58 | 09:54:37 | 0/7 | 0 |
| Mar. 01[b,d] | 08:00:14 | 10:17:59 | 0/12 | 0 |
| Mar. 02[b] | 07:49:06 | 08:18:54 | 0/3 | 0 |
| Mar. 11[a] | 08:03:55 | 10:03:28 | 11/11 | 4400 |
| Mar. 12[a] | 07:44:35 | 10:07:45 | 13/13 | 5200 |
| Apr. 02[c,e] | 06:31:39 | 09:53:52 | 16/18 | 6400 |
| Apr. 03[c,e] | 06:20:46 | 09:45:02 | 18/18 | 7200 |
| Apr. 04[c] | 05:58:19 | 09:47:58 | 21/21 | 8400 |

**Notes.** [(a)] ESO program 092.B-0920(A) (PI: N. Grosso); [(b)] ESO program 091.B-0183(H) (PI: A. Eckart); [(c)] ESO program 093.B-0932(A) (PI: N. Grosso); [(d)] partially-simultaneous observation with *XMM-Newton*; [(e)] simultaneous observation with *XMM-Newton*; [(f)] each exposure has a duration of 400 s.

extinction correction was derived from $A(H) = 4.35 \pm 0.12$ mag and $A(K_s) = 2.46 \pm 0.03$ mag (Schödel et al. 2010) with $\lambda_{\rm eff}$(NACO $H$) = 1.63725 $\mu$m and $\lambda_{\rm eff}$(NACO $K_s$) = 2.12406 $\mu$m (from the Spanish Virtual Observatory), respectively, assuming a power law leading to $A(\lambda) \propto \lambda^{-2.19 \pm 0.06}$. Thus, the computed extinction for the effective wavelength of the WFC3 F153M filter ($\lambda_{\rm eff}$ = 1.53157 $\mu$m) used is 5.03 ± 0.20 mag, which corresponds to a multiplicative factor of 103.2 ± 19.0 to correct the observed flux density for extinction.

### 2.3. VLT observations

Near-infrared integral-field observations of the Galactic Center were performed using SINFONI at the VLT in Chile (Eisenhauer et al. 2003; Bonnet et al. 2004). Sgr A* was monitored nine times in 2014 Feb.–Apr.. Table 3 summarizes the observing log, including the amount of exposures that were selected for the analysis. The selection criteria is described below. These observations were planned to be coordinated with those carried out with *XMM-Newton*. Two of these observations were simultaneous with *XMM-Newton* observations and one was partially simultaneous. They are part of the ESO programs 092.B-0183(H) (PI: A. Eckart), 093.B-0932(A) (PI: N. Grosso), and 092.B-0920(A) (PI: N. Grosso) presented in Valencia-S. et al. (2015) for the DSO/G2 study.

The SINFONI instrument is an integral-field unit fed by an adaptive optics (AO) module. The AO module was locked on a bright star 8″.85 east and 15″.54 north of Sgr A*. The $H + K$ grating used in these observations covers the 1.45 $\mu$m–2.45 $\mu$m range and exhibits a spectral resolution of $R \sim 1500$ (which corresponds to approximately 200 km s$^{-1}$ at 2.16 $\mu$m). The smallest SINFONI field of view (0″.8 × 0″.8) was jittered around the position of S2. Observations of different B- and G-type stars were performed for further telluric corrections.

Exposure times of 400 s were used to observe the Galactic center region, followed or preceded by observations on a dark cloud located about 12′45″ west and 5′36″ north of the Sgr A* sky position. These integration times were chosen to fully sample the variations of Sgr A* flux density over typical flare lengths, while optimizing the quality of the data.

The data processing and calibration was performed as described in Valencia-S. et al. (2015) and it is outlined here for completeness. First, bad lines were corrected using the procedure suggested in the SINFONI user manual. Then, a rough cosmic-ray correction in the sky and target exposures was performed using the algorithm of Pych (2004). Some science and calibration files showed random patterns that were detected and removed following the algorithms proposed by Smajić et al. (2014). Afterwards, the SINFONI pipeline was used for the standard reduction steps (e.g., flat fielding and bad pixel corrections) and for the wavelength calibration. A deep correction of cosmic rays and the atmospheric refraction effects were done using our own DPUSER routines (Thomas Ott, MPE Garching; see also Eckart & Duhoux 1991).

The quality of individual exposures was judged based on the point-spread function (PSF) at the moment of the observation. The PSF was estimated by fitting a 2D Gaussian to the bright star S2. Data cubes where the full width at half maximum of the Gaussian was higher than 96 mas (or 7.65 detector pixels) were discarded in the analysis. The 2014 Feb. 28, Mar. 1, and Mar. 2 observations are thus not used because of their poor quality. On 2014 Apr. 2 two data cubes of larger field-of-view were used for pointing. They were not included in the light curves since they map regions just beside the central S-cluster. Flux calibration on individual data cubes was performed using aperture photometry on the deconvolved $K$-band image. The deconvolution was done using the Lucy–Richardson algorithm in DPUSER. For calibration we used the stars S2 ($K_s$ = 14.13), S4 ($K_s$ = 14.61), S10 ($K_s$ = 14.12), and S12 ($K_s$ = 15.49), and adopted the $K_s$-band extinction correction $A(K_s) = 2.46 \pm 0.03$ mag (Schödel et al. 2010). Additional information on the flux estimation is given by Witzel et al. (2012). The final flux densities were extracted by fitting a 2D Gaussian to the calibrated continuum images for all time steps.

**Table 4.** VLA observation log for the 2014 Feb.–Apr. campaign.

| Date | Start time (UT) | End time (UT) | Band[a] |
|---|---|---|---|
| 2014 Mar. 01 | 11:22:08 | 18:01:07 | *X* |
| 2014 Mar. 10 | 11:17:00 | 17:25:24 | *Ku* |
| 2014 Apr. 02 | 10:00:15 | 15:52:48 | *C*, *L* |

**Notes.** [(a)] We report in this paper the *X*-, *Ku*-, *C*-, and *L*-band observations obtained only at 8.56, 13.37, 5.19 and 1.68 GHz, respectively.

### 2.4. VLA observations

Radio continuum observations were carried out with the *Karl G. Jansky* Very Large Array (VLA) on 2014 March 1, March 10 and April 2 (observing program 14A-231). The VLA was in its A-configuration during these three days of observations, with start and stop times reported in Table 4. In all observations, we used 3C 286 to calibrate the flux density scale, both 3C286 and NRAO530 to calibrate the bandpass, and J1744-3116 to calibrate the complex gains.

On 2014 Mar. 1 we observed Sgr A* at 8–10 GHz (*X*-Band) using the 8-bit sampler system with 2 GHz total bandwidth, each consisting of 64 channels each 2 MHz wide. On 2014 Mar. 10 we used the same correlator setup as 2014 Mar. 1, except using the *Ku*-Band between 13 and 15 GHz. On 2014 Apr. 2 we used the two bands 5–7 GHz (*C*-band) and 1–2 GHz (*L*-band), and alternated between these bands every 7 minutes. The *C*-band correlator was set-up similarly to that of *X*-band. The *L*-band correlator, however, used 1 GHz of bandwidth, which consisted of 16 IFs with channel widths of 1 MHz each. After primary calibration using OBIT (Cotton 2008), a self-calibration procedure

A&A 589, A116 (2016)

**Table 5.** CARMA 95 GHz observation log for the 2014 Feb.–Apr. campaign.

| Date | Start time (UT) | End time (UT) |
|---|---|---|
| 2014 Mar. 10 | 11:14:46 | 16:29:42 |
| 2014 Apr. 02 | 09:54:18 | 15:14:31 |
| 2014 Apr. 03 | 10:52:01 | 15:10:17 |

was applied using AIPS in phase only, to remove atmospheric phase errors.

### 2.5. CARMA observations

Observations of Sgr A* at 95 GHz (corresponding to 3.2 mm) were obtained with CARMA on 2014 Mar. 10, Apr. 2, and Apr. 3 (see Table 5). The array was in the C-configuration, with antenna separations ranging from 30–350 meters. The correlator processed frequencies range was 88.76−93.24 GHz in the lower sideband of the receivers and 96.76−101.24 GHz in the upper sideband. The spectral resolution was 25 MHz after Hanning smoothing. Channels corresponding to strong absorption lines of $HCO^+$ (89.19 GHz), HNC (90.65 GHz), and CS (97.98 GHz) were dropped from Sgr A* data before averaging to get the continuum flux density. Only visibility data corresponding to telescope separations larger than 20 k$\lambda$ were used for the flux measurements, to reduce contamination from extended emission near Sgr A*.

Observations of 3C279 were used to calibrate the instrumental passband. The flux density scale was established from observations of Neptune, assuming it is a 2.″2 diameter disk with brightness temperature 123 K (consistent with the Butler-JPL-Horizons 2012 model shown in ALMA memo 594). Observations of a secondary flux calibrator (the blazar 1733−130, a.k.a. NRAO 530) were interleaved with the Sgr A* observations every 15 minutes to monitor the antenna gains. The flux density of 1733−130 was measured to be 2.7 ± 0.3 Jy on 2014 Mar. 10, and 2.5 ± 0.3 Jy on Apr. 2 and Apr. 3, relative to Neptune.

The data on Mar. 10 were obtained in turbulent weather and are of poor quality, therefore we do not use it in this work. On 2014 Apr. 2 we only use the data before the beginning of the snow at about 12:30 UT.

## 3. Data analysis

### 3.1. XMM-Newton data

Figure 2 shows the *XMM-Newton*/EPIC (pn+MOS1+MOS2) background-subtracted light curves of Sgr A* binned to 300 s in the 2−10 keV energy range. The non-flaring level (i.e., the longest interval of the Bayesian blocks) during 2014 Feb.−Apr. is about 3 times the typical value of 0.18 count $s^{-1}$ (e.g., Porquet et al. 2008; Mossoux et al. 2015a). This is due to the flaring magnetar SGR J1745-29 located only 2.″4 from Sgr A* (Rea et al. 2013). Because the radius enclosing 50% of the energy for EPIC/pn at 1.5 keV on-axis is about 10″ (Ghizzardi 2002), we extract the events from a 10″-radius circle centered on Sgr A* as done in previous studies. This extraction region therefore includes events from SGR J1745-29, which artificially increases the non-flaring level of Sgr A* (Fig. 2).

#### 3.1.1. Impact of the magnetar on the flare detection

Degenaar et al. (2013) reported a large flare towards Sgr A* detected by Swift on 2013 Apr. 24. The detection of a hard X-ray burst by BAT near Sgr A* on 2013 Apr. 25 led Kennea et al. (2013) to attribute this flux increase to a new Soft Gamma Repeater unresolved from Sgr A*: SGR J1745-29. The X-ray spectrum of this magnetar is an absorbed blackbody with $N_{\rm H} = 13.7^{+1.3}_{-1.2} \times 10^{22}$ cm$^{-2}$ and $kT_{\rm BB} = 1.06 \pm 0.06$ keV (Kennea et al. 2013). But the *Chandra* X-ray Observatory (CXO) results between 1 and 10 keV from Coti Zelati et al. (2015) show that the temperature of the blackbody emitting region decreases with time: $kT_{\rm BB}/{\rm keV} = (0.85 \pm 0.01) - (1.77 \pm 0.04) \times 10^{-4}(t - t_0)$ with $t_0$ the time of the peak outburst (i.e., 2013 Apr. 24 or 56 406 in MJD). They show that before 100 d from outburst, the magnetar luminosity between 1 and 10 keV is characterized by a linear model plus an exponential decay whose $e$-folding time is 37 ± 2 d. After 100 d from the burst activation, the magnetar flux is well fitted by an exponential with an $e$-folding time of 253 ± 5 d. This flux decay is one of the slower decays observed for a magnetar. Thanks to 8 months of observations with the Green Bank Telescope and 18 months of observations with the Swift's X-Ray Telescope, the evolution of the X-ray flux and spin period of the magnetar have been well constrained by Lynch et al. (2015). The X-ray flux between 2 and 10 keV in a 20″-radius extraction region centered on the magnetar decreases as the sum of two exponentials: $F(t) = (1.00 \pm 0.06)\,{\rm e}^{-(t-t_0)/(55\pm7\ {\rm d})} + (0.98 \pm 0.07)\,{\rm e}^{-(t-t_0)/(500\pm41\ {\rm d})}$ in unit of $10^{-11}$ erg $s^{-1}$ cm$^{-2}$ with $t_0$ the same as in Coti Zelati et al. (2015).

We determined the exponential decay of the magnetar flux between 2 and 10 keV by applying a chi-squared fitting of the non-flaring level of each observation computed using the Bayesian-blocks algorithm: on Feb. 28, Mar. 10, and Apr. 2 and 3 the non-flaring level is 0.562 ± 0.003, 0.528 ± 0.004, 0.489 ± 0.003 and 0.499 ± 0.002 EPIC count $s^{-1}$, respectively. The magnetar flux variation can be described as $N(t) = N_0\,{\rm e}^{-(t-t_0)/\tau}$ with $t$ the time corresponding to the middle of each observation, $t_0$ and $N_0$ the time and count rate of the non-flaring level of the first observation, and $\tau$ the decay time scale. Our best fit parameters with corresponding $1\sigma$ uncertainties are: $N_0 = 0.558 \pm 0.003$ count $s^{-1}$ and $\tau = 281 \pm 15$ days. The decay time scale is about 2 times shorter than those computed from the formula of Lynch et al. (2015) for this date. However, as we can see in Fig. 2 of Lynch et al. (2015), the magnetar flux is not a perfect exponential decay and has some local increase of the flux, in particular during our observing period. This is seen in the last *XMM-Newton*/EPIC pn observation on 2014 Apr. 3, which is characterized by two blocks whose change point is at 16:27:48 (UTC). The corresponding count rates for the first and second blocks are 0.254 ± 0.03 and 0.299 ± 0.03 pn count $s^{-1}$. By folding light curves for each block on this date with the magnetar spin period of 3.76398106 s computed in Appendix B, we see that the pulse shape has not changed, but the flux increased by a factor of about 1.2, as determined by the Bayesian-blocks algorithm. Moreover, the *Chandra* monitoring of DSO/G2 shows that there is no significant increase of Sgr A* flux on 2014 Apr. 4 (Haggard et al. 2014).

This contamination of the non-flaring level implies a decrease of the detection level of the faintest and shortest flares, as explained in details in Appendix A. Comparing the detection probability of an *XMM-Newton* observation with the distribution of flares during the 2012 *Chandra XVP* campaign (Neilsen et al. 2013), we estimate that we lost no more than one

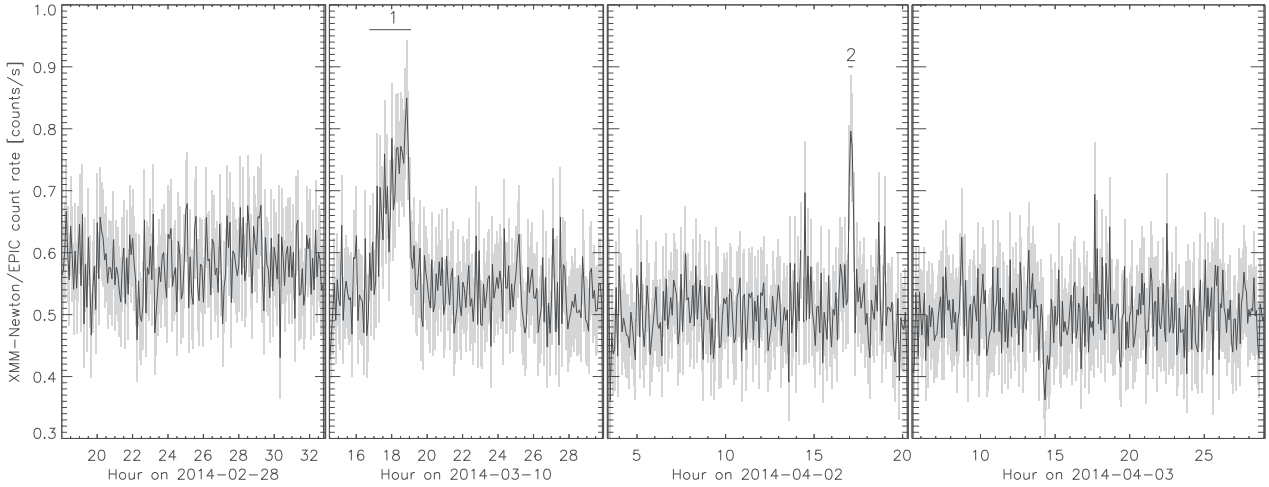


**Fig. 2.** *XMM-Newton*/EPIC (pn+MOS1+MOS2) light curves of Sgr A* in the 2−10 keV energy range obtained 2014 Feb.−Apr. The time interval used to bin the light curve is 300 s. The X-ray flares are labeled with Arabic numerals. The horizontal lines below these labels indicate the flare durations.

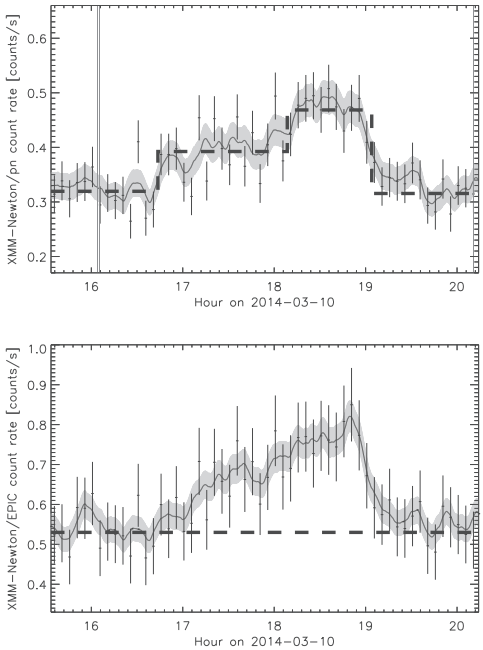


**Fig. 3.** *XMM-Newton* light curve binned on 500 s of the 2014 Mar. 10 flare from Sgr A* in the 2−10 keV energy range. *Top panel*: the crosses are the data points of the EPIC/pn light curve. The dashed lines represent the Bayesian blocks. The solid line and the gray curve are the smoothed light curve and the associated errors ($h$ = 500 s). *Bottom panel*: the total (pn+MOS1+MOS2) light curve. The horizontal dashed line and the solid line are the sum of the non-flaring level and the smoothed light curve for each instrument. The vertical gray stripe is the time during which the camera did not observe.

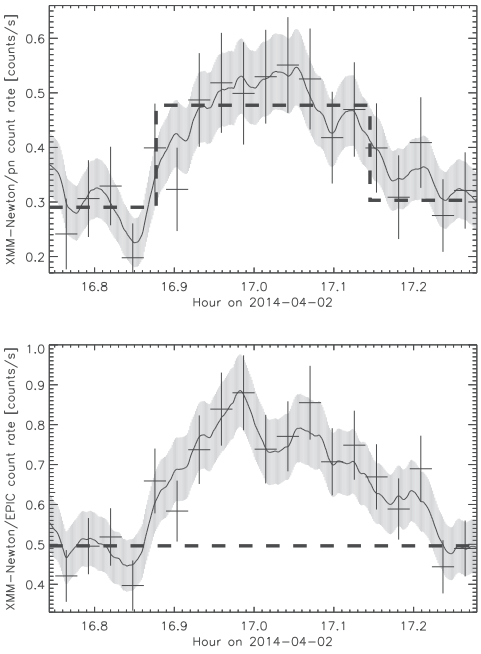


**Fig. 4.** *XMM-Newton* light curve binned on 100 s of the 2014 Apr. 2 flare from Sgr A* in the 2−10 keV energy range. The window width of the smoothed light curve is 100 s. See caption of Fig. 3 for panel description.

flare during our four *XMM-Newton* observations due to the magnetar contribution.

### 3.1.2. X-ray flare detection

By applying the Bayesian-blocks analysis on the EPIC event lists, we are able to detect two flares: one on 2014 Mar. 10 and one on 2014 Apr. 2. These flares are labeled 1 to 2 in Fig. 2. Figures 3 and 4 focus on the EPIC (pn+MOS1+MOS2) and EPIC/pn flare light curves with a bin time interval of 500 and 100 s, respectively. The comparison of the flare light curves observed by each EPIC cameras can be found in Appendix C. The second flare is detected by the Bayesian-blocks algorithm in pn, but not in MOS1 or MOS2. This is explained by the lower sensitivity of the MOS cameras, resulting in a lower detection level of the algorithm (see Fig. A.1). Table 6 gives the temporal characteristics of these X-ray flares.

We removed the magnetar contribution from the Sgr A* EPIC/pn event list in order to increase the detection level of the flares. This was done by computing the period and period derivative of SGR J1745-29 and filtering out time intervals where the magnetar flux is less than 50% of its total flux (see Appendix B for details). We only work with EPIC/pn, because it has a better temporal resolution (73.4 ms) than the EPIC/MOS

**Table 6.** Characteristics of the X-ray flares observed by *XMM-Newton* in 2014 after removing the magnetar contribution.

| Flare (#) | Date (yy-mm-dd) | Start time[a] (hh:mm:ss) | End time[a] (hh:mm:ss) | Duration (s) | total[b] (cts) | Peak[c] (count $s^{-1}$) |
|---|---|---|---|---|---|---|
| 1 | 2014-03-10 | 16:44:48 | 19:05:07 | 8418.44 | $900 \pm 60$ | $0.159 \pm 0.032$ |
| 2 | 2014-04-02 | 16:52:38 | 17:08:42 | 964.91 | $180 \pm 12$ | $0.252 \pm 0.058$ |

**Notes.** [(a)] Start and end times (UT) of the flare time interval defined by the Bayesian-blocks algorithm (Scargle et al. 2013b) on the EPIC/pn data; [(b)] Total EPIC/pn counts in the 2–10 keV energy band obtained in the smoothed light curve during the flare interval (determined by Bayesian blocks) after subtraction of the non-flaring level obtained with the Bayesian-blocks algorithm; [(c)] EPIC/pn count rate in the 2–10 keV energy band at the flare peak (smoothed light curves) after subtraction of the non-flaring level.

cameras (2.6 s; ESA: XMM-Newton SOC 2013). By applying the Bayesian-blocks analysis on the filtered pn event lists, we find no additional flares, and the start and end times of the already detected flares do not change significantly.

The flare detected on 2014 Mar. 10 is characterized by a long rise (~7700 s) and a rapid decay (~844 s). This is one of the longest flares ever observed in X-ray, with a duration of about 8.5 ks. For comparison, the largest flare observed during the *Chandra XVP* 2012 campaign has a duration of 7.9 ks and the first flare detected from Sgr A* observed by Baganoff et al. (2001) had a duration of ~10 ks. In EPIC/pn, the Bayesian-blocks algorithm divides the flare into two blocks, but in EPIC/MOS1 and MOS2 this flare is described with only one Bayesian block.

To localize the origin of this flaring emission we focus on the MOS observations, which provide a good sampling of the X-ray PSF (*FWHM* $\sim$ 4.″3) thanks to their 1.″1 × 1.″1 pixels. We first compute sky images that match the detector sampling for the flaring and non-flaring periods, and then we look for any significant excess counts during the flaring period compared to the non-flaring one, using the Bayesian method of Kraft et al. (1991).

We have suppressed the randomization of the event position inside the detector pixel during the production of the event list, therefore the event is assigned to the center of the detector pixel and its sky coordinates are reconstructed from the spacecraft attitude with an angular resolution of 0.″05. We filter the X-ray events using the (softer) `#XMMEA_EM` flag (e.g., bad rows are filtered out, keeping adjacent rows) and we select only events with the best positioning (single-pixel events, corresponding to `pattern=0`) and 2–10 keV energy. We first assess the mean sky position of the detector pixel that was the closest to Sgr A* by comparing the event sky positions with the pattern of the spacecraft offsets from the mean pointing that we derived from the attitude history file (`*SC*ATS.FIT`). We then compute images and exposure maps centered on this sky position with 1.″1 × 1.″1 sky-pixels for the flaring and non-flaring periods (see Appendix C for the definition of the Bayesian blocks). There is no moiré effect in these images, because the mean position-angle of the detector (90.°78) is very close to 90°. Panels a and b of Fig. 5 show the MOS1 and MOS2 count numbers during the flaring period. Following Kraft et al. (1991) we denote this image *N*. The horizontal row with no counts in the MOS1 image is due to a bad row. Panels c and d of Fig. 5 show the MOS1 and MOS2 count numbers during the non-flaring period, scaled-down to the flaring-period exposure using the exposure map ratios. This image is our estimate of the mean count numbers during the non-flaring period. Following Kraft et al. (1991) we denote this image *B*, as

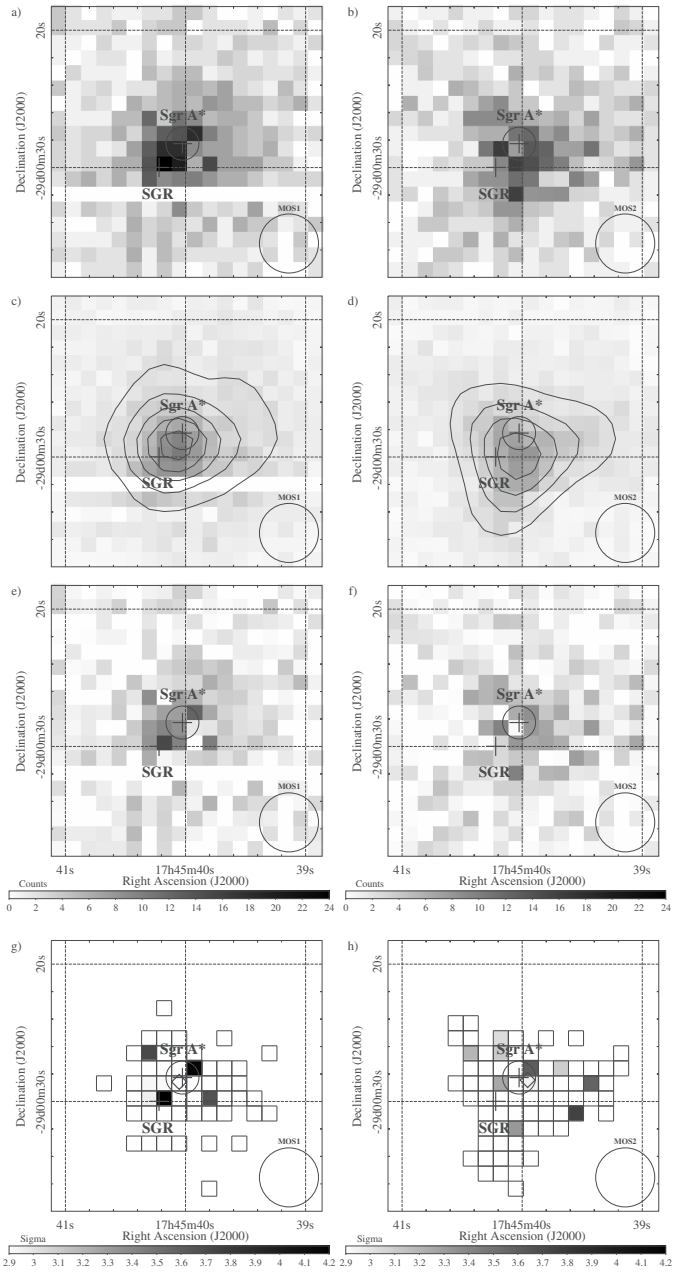


**Fig. 5.** *XMM-Newton*/MOS1 (*left column*) and MOS2 (*right column*) images of Sgr A* on 2014 Mar. 10. The energy range is 2–10 keV. The field of view is 20″ × 20″, the pixel size is 1.″1 × 1.″1. The same linear color-scale is used for panels **a)**–**f)** and **g)**–**h)**. In all panels, the black circle in the right-bottom corner is the instrument angular-resolution (FWHM); the crosses are the positions of SGR J1745-2900 (Bower et al. 2015b) and Sgr A* (Petrov et al. 2011), surrounded by a circle giving the absolute-astrometry uncertainty of EPIC ($1\sigma$ = 1.″2; Guainazzi 2013). Panels **a)** and **b)**: count numbers observed during the flaring period. Panels **c)** and **d)**: count numbers observed during the non-flaring period scaled-down to the flaring-period exposure. The contour map shows count numbers smoothed on four pixels with a Gaussian, starting from 2 counts with step of 1 count. Panels **e)** and **f)**: count excesses during the flaring period. Panels **g)** and **h)**: statistically significant count excesses ($\geq 3\sigma$; computed on the boxed-pixel area with the Bayesian method of Kraft et al. 1991), the diamond is the corresponding count-weighted barycenter of these detections.

background. Panels e and f of Fig. 5 show the difference between the previous panels, shown only for potential count excesses ($N - B > 0$). Following Kraft et al. (1991) we denote

**Table 7.** Spectral properties of the X-ray flares observed by *XMM-Newton*.

| Flare day (yy-mm-dd) | $N_H$[a] ($10^{22}$ cm$^{-2}$) | $\Gamma$[b] | $F^{unabs}_{2-10\,keV}$[c] ($10^{-12}$ erg s$^{-1}$ cm$^{-2}$) | $L^{unabs}_{2-10\,keV}$[d] ($10^{34}$ erg s$^{-1}$) | $\chi^2_{red}$[h] |
|---|---|---|---|---|---|
| 2014-03-10[e] | 23.7 (14.5–37.5) | 3.1 (2.1–4.5) | 10.1 (4.9–33.5) | 7.7 (3.7–25.6) | 1.65 |
| 2014-04-02[e] | 9.8 (2.0–23.5) | 2.2 (0.7–4.7) | 6.3 (3.5–25.7) | 4.8 (2.7–19.7) | 1.72 |
| 2002-10-03[f] | 16.1 (13.9–18) | 2.3 (2.0–2.6) | 26.0 (22.5–30.6) | 19.8 (17.1–23.3) | |
| 2007-04-04[g] | 16.3 (13.7–19.3) | 2.4 (2.1–2.8) | 16.8 (13.8–21.4) | 12.8 (10.5–16.3) | |

**Notes.** [(a)] Hydrogen column density; [(b)] Photon index of the power law; [(c)] Unabsorbed average flux between 2 and 10 keV; [(d)] Unabsorbed average luminosity between 2 and 10 keV assuming a distance of 8 kpc; [(e)] Spectral properties of the EPIC/pn spectrum computed using the MCMC method. The range given between parenthesis represents the 90% confidence interval; [(f)] Spectral properties of the EPIC (pn+MOS1+MOS2) spectrum. See Porquet et al. (2003) and Nowak et al. (2012); [(g)] Spectral properties of the EPIC (pn+MOS1+MOS2) spectrum. See Porquet et al. (2008) and Nowak et al. (2012); [(h)] Reduced $\chi^2$ for 3 degrees of freedom.

this image $S$, as source. Poisson statistics are required due to the low number of counts, hence we have to carefully determine the confidence limits of the observed count excesses to select only pixels that exclude null values at the confidence level $CL$.

Since the Bayesian method of Kraft et al. (1991) requires that the background estimate is close to the true value (see also Helene 1983), we limit our statistical analysis to the pixels where the count number during the non-flaring period is larger or equal to 20, in order to reduce the Poisson noise (see the boxed pixel areas in panels g and h of Fig. 5). We compute the confidence level for each count excess using Eq. (9) of Kraft et al. (1991)[5] and convert it to a Gaussian equivalent in units of $\sigma$. Panels g and h of Fig. 5 show pixels with confidence levels that are larger or equal to $3\sigma$. The barycenters of these pixels weighted by their count excesses (diamonds in panels g and h of Fig. 5) are consistent with the position of Sgr A* when considering the absolute astrometry uncertainty of EPIC, which confirms that the flaring emission detected on 2014 Mar. 10 came from Sgr A*.

### 3.1.3. Spectral analysis of the X-ray flares

To analyze the spectrum of the two flares seen by *XMM-Newton* on 2014 Mar. 10 and 2014 Apr. 2, we extracted events from a circle of 10″ radius centered on the Sgr A* radio position, as we did for the temporal analysis. The X-ray photons were selected with `PATTERN`≤ 4 and `FLAG==0` for the pn camera. We did not work with photons from MOS1 and MOS2, because the number of events is too small to constrain the spectral properties. The source+background time interval is the range between the beginning and the end of the flare computed by the Bayesian-blocks algorithm (see Table 6). The background time interval is the whole observation minus the time range during the flare. We also rejected 300 s on either side of the flare to avoid any bias. This extraction is the same as used in Mossoux et al. (2015a). We computed the spectrum, ancillary files, and response matrices with the SAS task `especget`.

[5] Following Kraft et al. (1991), we first determine the confidence interval $[s_{min}, s_{max}]$ of $S \equiv N - B$ at the confidence level $CL$ where, for a count excess, $s_{max}$ is defined as $f_{N,B}(s_{max}) \equiv f_{N,B}(s_{min})$ and $s_{min} = 0$, with $f_{N,B}(S) \equiv \exp(-(S+B))\,(S+B)^N/(N!\,\Sigma_{n=0}^{N} \exp(-B)B^n/n!)$ is the posterior probability distribution function. We then compute $CL = \int_{s_{min}}^{s_{max}} f_{N,B}(s)\,ds$ and its Gaussian equivalent in units of $\sigma$ given by $\phi^{-1}((1-CL)/2)$, with $\phi^{-1}$ being the reciprocal of the cumulative distribution function of the normal distribution.

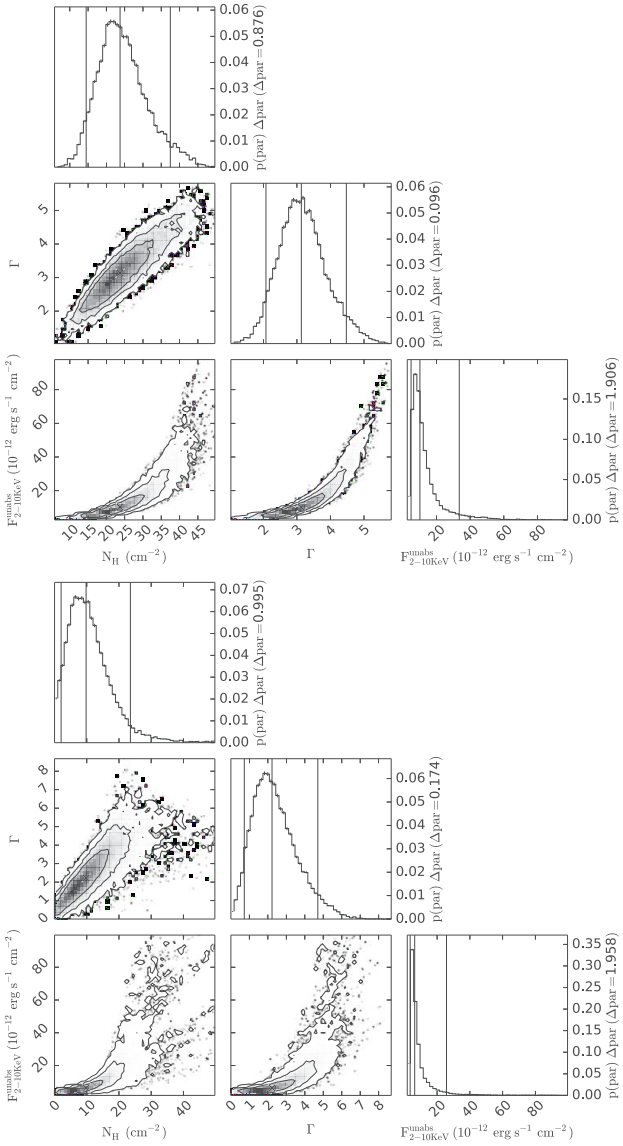


**Fig. 6.** Best-fit parameters of the 2014 Mar. 10 (*top*) and 2014 Apr. 2 (*bottom*) flares. The diagonal plots are the marginal density distribution of each parameter. The median values of each parameter are represented by the vertical dotted lines in diagonal plots and by a cross in other panels; the vertical dashed lines define the 90% confidence interval (see Table 7 for the exact values). The contours are 68%, 90% and 99% of confidence levels.

The model used to fit the spectrum with XSPEC (version 12.8.1o) is the same as that in Mossoux et al. (2015a): an absorbed power law created using *TBnew* (Wilms et al. 2000) and *pegpwrlw* with a dust scattering model from *dustscat* (Predehl & Schmitt 1995). *TBnew* uses the cross-sections from Verner et al. (1996). Interstellar medium abundances of Wilms et al. (2000) imply a decrease of the column density by a factor of 1.5 (Nowak et al. 2012). The extracted spectrum was grouped using the SAS task `specgroup`. The spectral binning begins at 2 keV with a minimum signal-to-noise ratio[6] of 4 and 3 for the first and second flares, respectively. The number of net counts during the first flare is 900 (see Table 6)

[6] The equation computing the signal-to-noise ratio is the same as in `specgroup` and in ISIS (Houck 2013). We therefore use the same grouping as in Mossoux et al. (2015a).

A&A 589, A116 (2016)

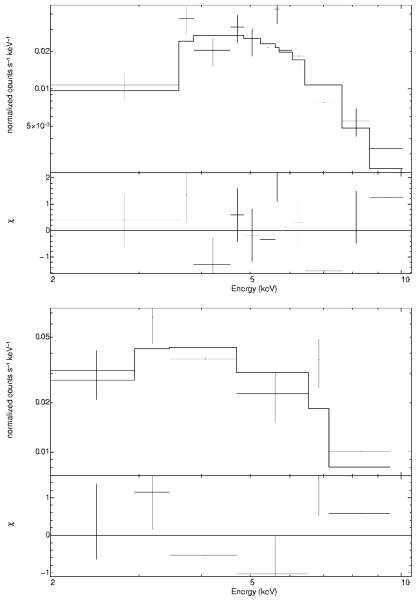


**Fig. 7.** *XMM-Newton*/EPIC pn spectrum of the 2014 Mar. 10 (*top*) and 2014 Apr 2 (*bottom*) flares. The model is the best spectrum obtained with MCMC (see text for details). The *lower panel* in the two graphs is the residual. The horizontal and vertical lines are the spectral bins and the error on the data, respectively.

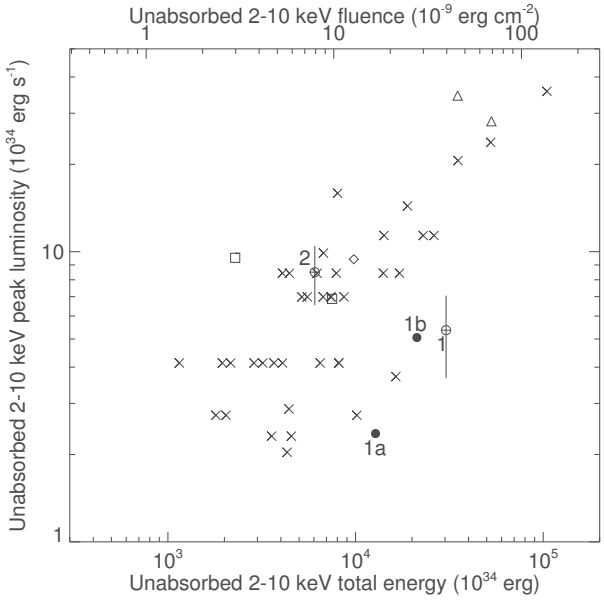


**Fig. 8.** Unabsorbed total energy vs. unabsorbed peak luminosity of the X-ray flares (adapted from Mossoux et al. 2015a). The top $x$-axis is the unabsorbed fluence. The crosses represent the X-ray flares from the *Chandra XVP* campaign (Neilsen et al. 2013), the triangles are the two brightest flares seen with *XMM-Newton* (Porquet et al. 2003, 2008), the diamond and the two squares are the 2011 March 30 flare and its subflares, respectively (Mossoux et al. 2015a). The empty circles are X-ray flares 1 and 2 of this work with their $1\sigma$ error bars. The filled circles are the components 1a and 1b of flare 1 (see Sect. 4.1.2).

and the number of spectral bins is 12. This gives an average of about 75 counts in each spectral bin. If we perform the same computation for the second flare, which has 180 net counts for 6 spectral bins, we have 31 counts per spectral bin.

We used the Markov Chain Monte Carlo (MCMC) algorithm to constrain the three parameters of the model: the hydrogen column density ($N_{\rm H}$), the photon index of the power law ($\Gamma$), and the unabsorbed flux between 2 and 10 keV ($F^{\rm unabs}_{2-10\ {\rm keV}}$). The MCMC makes a random walk of *nstep* steps in parameter space for several walkers (*nwalkers*), which evolve simultaneously. The position of each walker at a step in the parameter space is determined by the positions of the walker at the previous step. Convergence was achieved using the probability function of the parameters. The resulting MCMC chain reports all these steps. This method give us a complete view of the spectral parameters distribution and correlation.

We use Jeremy Sanders' `XSPEC_emcee`[7] program that allows MCMC analyses of X-ray spectra in XSPEC using `emcee`[8] (Foreman-Mackey et al. 2013), an extensible, pure Python implementation of Goodman & Weare (2010)'s affine invariant MCMC ensemble sampler. We follow the operating mode explained in the `XSPEC_emcee` homepage to find the optimal value for the MCMC sampler parameters. Two criteria must be fulfilled to have a good sampling in the chain: the chain length must be greater than the autocorrelation time and the mean acceptance fraction must be between 0.2 and 0.5 (Foreman-Mackey et al. 2013). We created a chain containing 30 walkers. The Python function `acor` computes the auto-correlation time ($\tau_{\rm acor}$) needed to have an independent sampling of the target density. The burn-in period (*nburn*) and chain length (*nstep*) are defined as $20 \times \tau_{\rm acor}$ (Sokal 1997) and $30 \times nburn$ (Foreman-Mackey et al. 2013), respectively. For the spectral model used here, $\tau_{\rm acor} = 5.1$ and 5.3 for the 2014 Mar. 10 and 2014 Apr. 2 flares, respectively. Thus we used $nburn = 102$, $nwalkers = 30$, and $nstep = 3060$ for the March 10 flare and $nburn = 106$, $nwalkers = 30$, and $nstep = 3180$ for the April 2 flare. The mean acceptance fraction is around 0.6 for the two flares, which is a reliable value.

The diagonal plots in Fig. 6 are the marginal distribution of each parameter (i.e., the probability to have a certain value of one parameter independently from others). The other panels in Fig. 6 represent the joint probability for each pair of parameters. The contours indicate the parameter region where there are 68%, 90% and 99% of the points (i.e., $nwalkers \times nstep$). The best-fit parameter values are the median (i.e., 50th percentile) of each parameter obtained from the marginal distribution. We also define a 90% confidence range for each parameter as the 5th and 95th percentile of the marginal distribution. These numbers are reported in Table 7. The corresponding best spectrum is overplotted on the data in Fig. 7.

We can compare the spectral parameters of this flare with those of the two brightest flares detected with *XMM-Newton*, which have the better constrained spectral parameters thanks to the high throughput and no pileup (Porquet et al. 2003, 2008). Their spectral properties are reported in Table 7. The magnetar has a soft spectrum, which implies that the soft part (0.5−3 keV) of the background is very high. Thus we have only one spectral bin in this energy band (see Fig. 7), implying that the hydrogen column density is not well constrained. The hydrogen column density and the photon index of the two brightest flares are well within the 90% confidence range of the 2014 Mar. 10 and 2014 Apr. 2 flares even if the parameters of the latter are less constrained than the former.

Assuming the typical spectral parameters of the X-ray bright flares, i.e., $\Gamma = 2$ and $N_{\rm H} = 14.3 \times 10^{22}$ cm$^{-2}$ (Porquet et al. 2003, 2008; Nowak et al. 2012), we determined with XSPEC and the pn response files in the 2−10 keV energy range an unabsorbed-flux-to-count-rate ratio of $4.41 \times 10^{-11}$ erg s$^{-1}$ cm$^{-2}$/pn count s$^{-1}$

[7] https://github.com/jeremysanders/xspec_emcee
[8] http://dan.iel.fm/emcee/current/user/line/

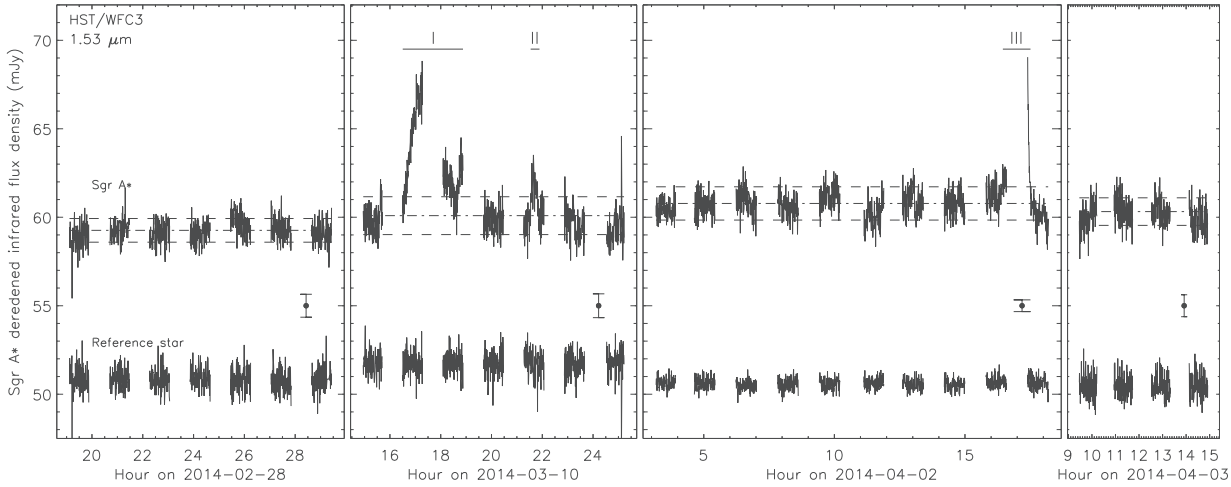


**Fig. 9.** Light curves of Sgr A* obtained with WFC3 on board HST during 2014 Feb.−Apr. The NIR flares are labeled with Roman numerals. The horizontal lines below these labels indicate the flare durations. The error bar in each panel is standard deviation of the photometry.

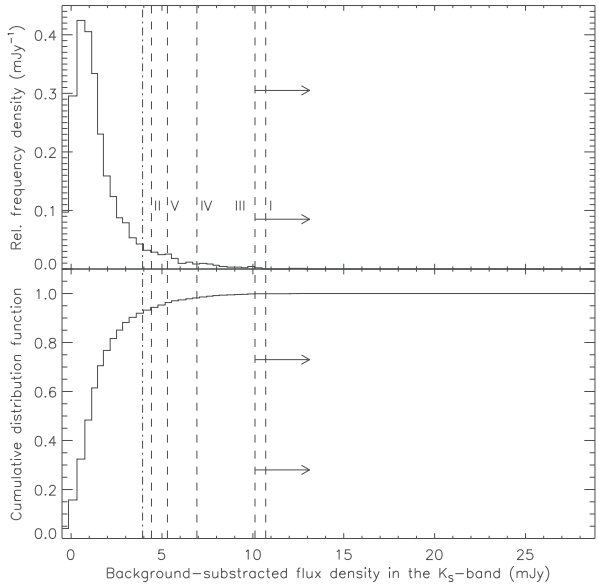


**Fig. 10.** Histogram of the NIR flux densities from Sgr A* observed in the $K_s$-band with NACO at ESO's VLT (adapted from Fig. 3 of Witzel et al. 2012). *Top panel*: the solid line is the normalized distribution of the NIR flux densities corrected from the background emission. The dashed lines are the amplitude of the HST flares I, II and the lower limit of the amplitude of the flare III extrapolated to the $K_s$-band. We also represented the amplitude above the $3\sigma$ limit of the VLT flares IV and V extrapolated to the $K_s$-band. The dot-dashed line is the detection limit corresponding to 3 times the standard deviation of the quiescent flux density of HST on 2014 Mar. 10. *Bottom panel*: the cumulative distribution function of the NIR flux densities from Sgr A* corrected from the background emission.

(corresponding to an absorbed-flux-to-count-rate ratio of $2.01 \times 10^{-11}$ erg s$^{-1}$ cm$^{-2}$/pn count s$^{-1}$). From the 8 kpc distance and the total number of counts (Table 6), we determine a total energy of $30.4 \pm 1.9 \times 10^{37}$ and $6.0 \pm 0.4 \times 10^{37}$ ergs ($1\sigma$ error) for the 2014 Mar. 10 and Apr. 2 flares, respectively. These values can be compared to flares previously observed with *Chandra* and *XMM-Newton*. Figure 8 shows the total energy of these flares versus the unabsorbed peak luminosity. Flare 1 is one of the most energetic flares, due to its very long duration. The peak amplitude and total energy of flare 2 is close to the median values observed for this flare sample.

### 3.2. HST data

The HST light curves of Sgr A* and a reference star for the four visits are shown in Fig. 9. The error bar in each panel represents the typical uncertainty on the photometry derived for the reference star (standard deviation of the photometry). The deredened non-flaring flux density of Sgr A* and the corresponding error, computed using a $1\sigma$-clipping method, are $59.3 \pm 0.7$, $60.1 \pm 0.9$, $60.8 \pm 1.1$ and $60.3 \pm 0.8$ mJy on 2014 Feb. 28, Mar. 10, Apr. 2, and Apr. 3, respectively (horizontal dot-dashed line of Fig. 9). The beginning and end of each flare is set by the $1\sigma$ limit on the flux density whose maximum amplitude is larger than $3\sigma$. We only considered flux-density increases that lasted longer than 25 s, in order to discard any calibration glitchs. All observed NIR flares are labeled with Roman numerals.

The ∼10 h visit on 2014 Mar. 10 detected two NIR flares. The first one (labeled I) peaks at $8.2\sigma$ and has an X-ray counterpart. It lasts from 16:29:51 to 18:52:36 ($1\sigma$ limit). We can see in Table 6 that it begins and ends ∼14 min before the X-ray flare. As for the X-ray flare, its shape is not a Gaussian, as it has a dip during the third HST orbit. Two interpretations can be made to explain this shape. First, this flare could be a single flare and the variation from Gaussian shape during the third orbit can be seen as substructures, as is the case for some NIR flares (Dodds-Eden et al. 2009). The second interpretation is that this NIR flare is in fact two distinct flares with a return below the $1\sigma$ limit between ∼18:30 and ∼18:39. The time delay between the two maxima in this scenario would be about 90 min. From 21:32:33 to 22:02:58 on 2014 Mar. 10, we can see that there is a second NIR flare (labeled II), which has no X-ray counterpart. Its maximum is about $3.4\sigma$.

On 2014 Apr. 2 we caught the end of a NIR flare (labeled III), lasting until 17:31:15. Its amplitude is larger than $8.8\sigma$, since its maximum occured during the Earth occultation of Sgr A*. Its beginning could correspond with the small increase in flux density seen just before the start of the Earth occultation of Sgr A*, which would lead to an upper limit on its duration of 3360 s. The

A&A 589, A116 (2016)

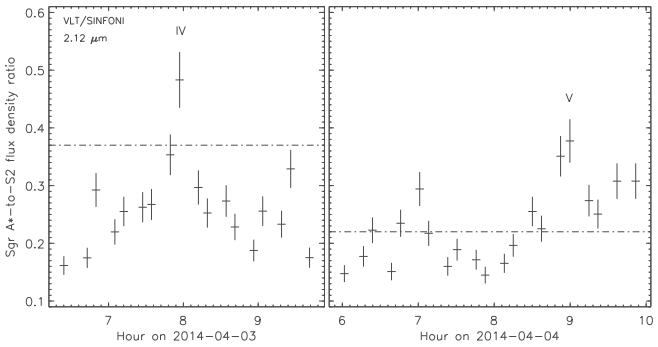


**Fig. 11.** Light curves of Sgr A* obtained with SINFONI at ESO's VLT during 2014 Apr. 3 and 4. The dash-dotted lines represent the $3\sigma$ detection level of Sgr A*. The horizontal segments indicate the exposure length of 400 s. The NIR flares are labeled with Roman numerals.

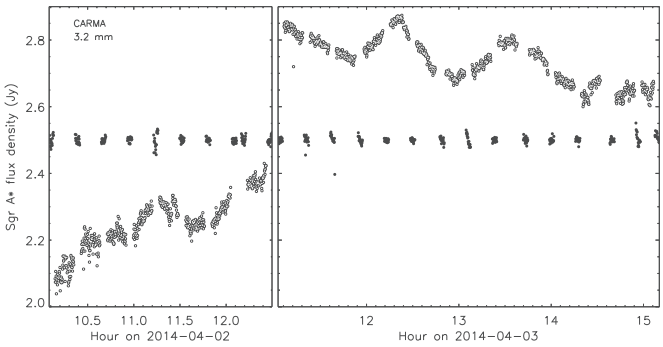


**Fig. 12.** CARMA light curves at 3.2 mm (95 GHz) of Sgr A* (white circle) and 1733-130 (black circle) in April 2014. The dash-dotted line represents the mean flux density.

duration of this NIR flare III and its possible relation with X-ray flare 2 will be discussed in Sect. 4.

The amplitudes of these flares can be compared to the sample of flux densities from Sgr A* observed in the $K_s$-band with NACO at ESO's VLT and reported by Witzel et al. (2012). They constructed a histogram of all flux densities from the light curves, without distinction between the quiescent and flaring periods. This observed distribution of the flux density has a relative maximum at 3.57 mJy. Below this amplitude the distribution decreases, because of the detection limit of NACO. Above 3.57 mJy, the distribution is highly asymmetric, with a rapid decay of the frequency density followed by a long tail to 32 mJy. Figure 10 compares the amplitude of the flares detected with HST during this campaign with the relative frequency density given in Witzel et al. (2012, Fig. 3). The normalized distribution of the NIR flux densities observed with NACO (top panel of Fig. 10) is corrected for the background emission of 0.6 mJy (Witzel et al. 2012). The amplitude of the flares detected with HST are extrapolated to the $K_s$-band using the $H - L$ spectral index of Sgr A* computed in Witzel et al. (2014b), which is $\alpha = -0.62$.

The detection threshold of HST, which we define as the $3\sigma$ limit (dot-dashed line in Fig. 10), corresponds to 8% of the amplitude sample observed with NACO (bottom panel of Fig. 10). The amplitude of NIR flare II is about 7 times smaller than the amplitude of the brightest flare observed with NACO, whereas the amplitude of flare I is only 3 times smaller than the amplitude of this event. We can only measure a lower limit on the amplitude of NIR flare III, since its maximum occured during the Earth occultation. This lower limit is nearly as large as those of flare I.

### 3.3. VLT data

Figure 11 shows the ratio between Sgr A* and S2 flux densities for the observations where a NIR flare was detected. Making a very conservative estimation, the $3\sigma$ detection levels of Sgr A* in the 2014 Apr. 3 and 4 data yield flux density ratios of $F(\mathrm{Sgr\ A^*})/F(\mathrm{S2}) \approx 0.37$ and 0.22, respectively (dash-dotted lines of Fig. 11). A flare (labeled IV) is observed on 2014 Apr. 3 with a peak amplitude of $\sim 3.9\sigma$. We clearly see its rise and decay phase below the $3\sigma$ detection level. On 2014 Apr. 4, a smaller flare (labeled V) is seen around 9:00 UT with a peak amplitude of $\sim 5.1\sigma$.

Using Eq. (2) of Witzel et al. (2012), with $K_s(\mathrm{S2}) = 14.13 \pm 0.01$ and $A(K_s) = 2.46 \pm 0.03$ (Schödel et al. 2010), we have $F(\mathrm{S2}) = 14.32 \pm 0.26$ mJy. The amplitude of the two NIR flares detected with SINFONI are thus $6.92 \pm 0.13$ and $5.30 \pm 0.09$ mJy for 2014 Apr. 3 and 4, respectively. We consider that all the SINFONI light curve variations above our $3\sigma$ detection limit can be attributed to Sgr A* activity. We can therefore compare these flux densities with the sample of flux densities observed with NACO after the background subtraction of 0.6 mJy (Fig. 10). The 2014 Apr. 3 and 4 flares are within 4% of the largest amplitude, and are 5 and 6 times smaller than the brightest amplitudes observed with NACO, respectively. The $3\sigma$ detection level corresponds to $3.15 \pm 0.06$ mJy, which is comparable to the 11% of the largest flux density observed with NACO (Fig. 10).

### 3.4. CARMA data

The flux densities at 95 GHz (3.2 mm) of Sgr A* and 1733−130 shown in Fig. 12 are computed for each 10 s integration on 2014 Apr. 2 and 3. On 2014 Apr. 2 the flux density of Sgr A* increases slowly. A bump is seen at 11.3 h, but it could not be associated with the observed NIR or X-ray flares, since the CARMA observation occurred before the flares observed with HST and *XMM-Newton*.

On 2014 Apr. 3 the flux density decreases slowly, with two bumps occuring at 12.4 and 13.6 h. The maximum of the NIR flare IV observed with VLT occurred at 7.9 h on the same date. One of these episodes of radio flux density variation could be the delayed emission from this NIR flare, which would indicate a time delay of 4.4 or 5.6 h for the first and second bumps, respectively. The delays previously measured between the X-rays and the 850 $\mu$m light curves range between 1.3 and 2.7 h (e.g., Yusef-Zadeh et al. 2006b, 2008; Marrone et al. 2008). Assuming the expanding plasmon model, the delay between the NIR and the longer wavelength (3.2 mm) emission must be larger than these values, leading to a time delay consistent with those measured for these two bumps. One time-delay measurement was made between the X-rays and the 7 mm light curve, leading to a delay of about 5.3 h (Yusef-Zadeh et al. 2009). This measure seems to reject the second bump as being the delayed sub-mm emission from the VLT flare, since the delay is too long. The first bump, therefore, could be the delayed millimeter emission of the NIR flare IV. The second bump could then be the delayed millimeter emission of a NIR flare whose peak is lower than the $3\sigma$ detection level of VLT or which occurred after the end of the VLT observation and during Earth occultation for HST.

The flux density of Sgr A* during these observations increases with frequency as $S_\nu \propto \nu^{0.2}$. For comparison, previous observations of Sgr A* between 43.3, 95.0, and 151 GHz

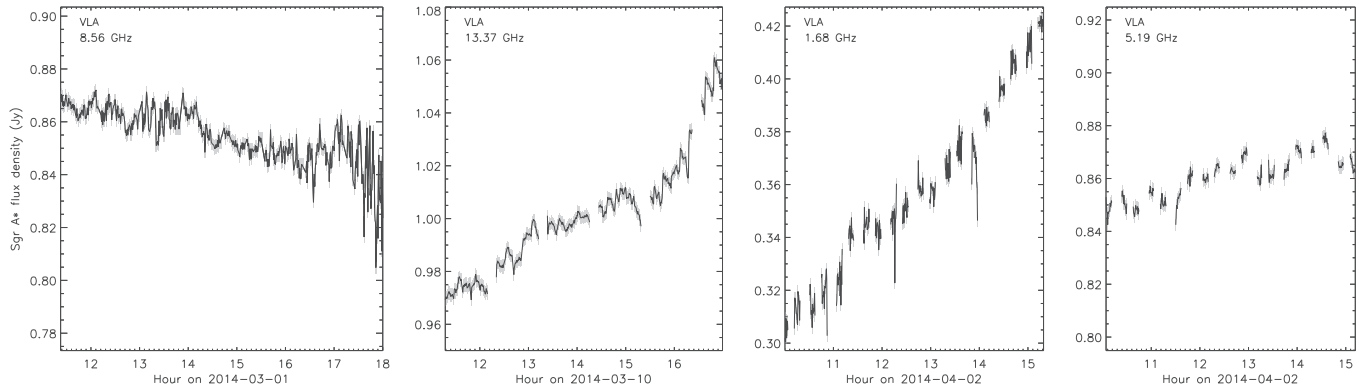


**Fig. 13.** VLA light curves of Sgr A* obtained on 2014 Mar. 1 (8.56 GHz), Mar. 10 (13.37 GHz) and Apr. 2 (1.68 and 5.19 GHz). The $y$-axis covers the same range of flux density for all observation and is centered on the mean of the minimum and maximum flux density in each panel.

(corresponding to 7.0, 3.2, and 2.0 mm; Table 2 of Falcke et al. 1998) give a similar spectra index of 0.58 ± 0.23.

### 3.5. VLA data

We obtained light curves of Sgr A* from all three days of VLA observations, selecting (for the purpose of simplification) only one intermediate frequency channel with 30 s of averaging (analysis of the full radio dataset will be given elsewhere). In all observations we selected visibilities greater than 100 k$\lambda$ in order to minimize contamination from extended thermal emission from Sgr A West. The radio light curves for the frequencies obtained with the VLA in configuration A on 2014 Mar.−Apr. are shown in Fig. 13.

We interleaved the CARMA and VLA *L*- and *C*-band observations from 2014 Apr. 2 in order to search for a time delay between the 1.68 GHz and 5.14 GHz, and the 1.68 GHz and 95 GHz light curves, using the z-transformed discrete correlation function (ZDCF; Alexander 1997). The cross-correlation graphs show no significant maximum of the likelihood function, implying that we can not derive any time delay between these light curves.

The light curves on 2014 Mar. 1 and Apr. 2 display a steady decrease and increase of flux density. The light curve on 2014 Mar. 10 shows an obvious break in its rising flux density around 16 h, with a clear increase of the rising slope. To better constrain the time of this slope change, we fit the VLA light curve with a broken line. The break is located at 15.7 ± 0.2 h with a slope increasing from 9.7 ± 0.1 to 27 ± 1 mJy h$^{-1}$ ($\chi^2_{\rm red}$ = 2828 with 508 d.o.f.), which is significant. We therefore tentatively attribute it to the onset of a radio flare, since we have only partial temporal coverage of this radio event. For comparison purposes, the light curves of the 2014 Mar. 10 flare observed with VLA, WFC3, and *XMM-Newton* are shown in Fig 14.

The radio flare observed at 13.37 GHz (2.2 cm) could be the delayed emission from a NIR/X-ray flare that occurred either at the beginning of the observation with an amplitude lower than the detection limits of WFC3 and *XMM-Newton*, or before the start of our HST and *XMM-Newton* observations. The latter would imply a delay larger than 2.2h. As explained previously in Sect. 3.4, the largest time delay that has been measured between X-ray and sub-mm flares is 5.3 h (Yusef-Zadeh et al. 2009). Considering the expanding plasmon model (Yusef-Zadeh et al. 2006a), the delay between the X-ray and centimeter light curves must be larger than 5.3 h, and therefore the possibility of a non-detected NIR/X-ray flare is likely excluded.

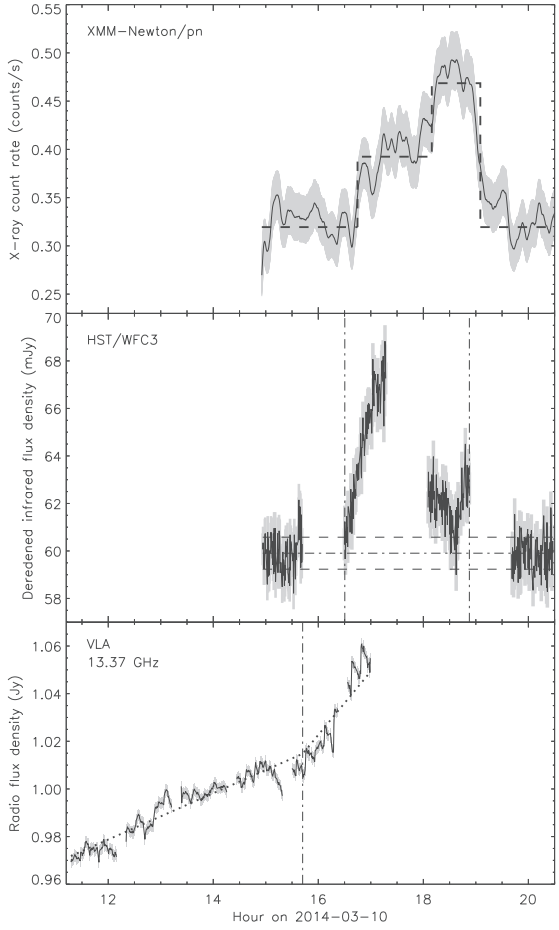


**Fig. 14.** Simultaneous X-ray, NIR and radio observations of flare I/1 from Sgr A* on 2014 Mar. 10. *Top panel*: the EPIC/pn smoothed light curve computed with a window width of 500 s and its error in gray. The dashed lines are the Bayesian blocks. *Middle panel*: the deredened HST light curve and its error in gray. The vertical dot-dashed lines are the beginning and the end of the flares. *Bottom panel*: the VLA light curve at 13.37 GHz. The vertical dot-dashed line is the time of the change of slope. The dashed broken line is the fit.

A&A 589, A116 (2016)

## 4. Determination of the X-ray emission related to the NIR flares

In the following subsections we determine the X-ray emission related to each NIR flare observed with HST or VLT, with which we associate either one of the X-ray flares detected with *XMM-Newton* or an upper limit on the amplitude of a non-detected X-ray flare.

### 4.1. The NIR flare I on 2014 Mar. 10

To compare the NIR and X-ray light curves of the 2014 Mar. 10 flare, we express the NIR and X-ray flux in the same units. To convert the X-ray count rate to flux, we use the unabsorbed-flux-to-count-rate ratio derived in Sect. 3.1.3.

The NIR flux of Sgr A* is obtained from the flux density $S_\nu$ by integrating over the F153M filter, using the filter profile $T$ (Spanish Virtual Observatory). To be consistent with the HST photometric calibration (Vega system), we assume a Rayleigh-Jeans regime ($S_\nu \propto \nu^2$):

$$\frac{F_{\rm IR}}{\rm erg\,s^{-1}\,cm^{-2}} = \int T\,S_\nu \left(\frac{\nu}{\nu_{\rm eff}}\right)^2 {\rm d}\nu, \quad (1)$$

with $\nu_{\rm eff}$ the effective frequency given by the Spanish Virtual Observatory.

The ratio between the X-ray and NIR flux during the flare is shown in Fig. 15 (the error bars are on the order of the symbol size). The NIR flux is always lower than the X-ray flux, but during the third orbit of the HST visit the X-ray contribution increased by a factor of 10 compared to the NIR. We can test two interpretations: a single flare with non-simultaneous X-ray and NIR peaks, or two distinct flares with simultaneous NIR and X-ray peaks.

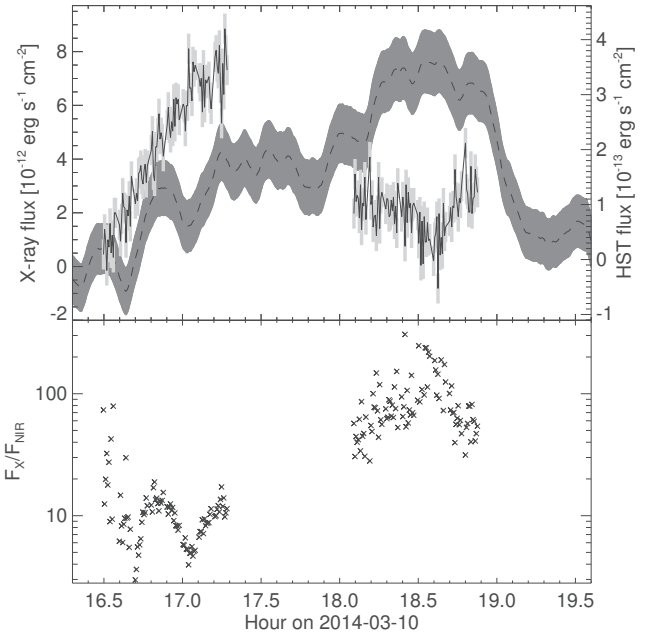


**Fig. 15.** Evolution of the ratio between NIR and X-rays during flare I/1 on 2014 Mar. 10. *Top panel*: the dashed line surrounded by the dark gray error bars corresponds to the smoothed light curve of the X-ray flare and its flux can be seen on the left $y$-axis. The solid line and the light gray error bars is the NIR light curve whose flux is read on the right $y$-axis. *Bottom panel*: the flux of the X-ray light curve divided by the NIR one.

#### 4.1.1. A single flare with non-simultaneous peaks in NIR and X-rays

Considering that the NIR flare is produced by synchrotron emission, there are three radiative processes that can explain the X-ray flare production: synchrotron (SYN; Dodds-Eden et al. 2009; Barrière et al. 2014), inverse Compton (IC; Yusef-Zadeh et al. 2006b, 2012; Wardle 2011), and synchrotron self-Compton (SSC; Eckart et al. 2008) emission. In this section, we discuss whether each process can explain the entire observed NIR/X-ray light curve on 2014 Mar. 10.

**The synchrotron–synchrotron process (SYN-SYN)**

For synchrotron emission of NIR and X-ray photons by accelerated electrons in the flaring region, the electron acceleration has to be high enough to directly emit X-ray photons. It is difficult, however, to explain how to reach the required Lorentz factor of $\gamma = 10^6$ (Marrone et al. 2008; Yusef-Zadeh et al. 2012; Eckart et al. 2012b). Moreover, the synchrotron cooling time scale $\tau_{\rm sync} = 8 \times (B/30\,{\rm G})^{-3/2} \times \left(\nu/10^{14}\,{\rm Hz}\right)^{-1/2}$ min (Dodds-Eden et al. 2009) is very short for X-ray photons (≈1 s for $B = 100$ G and $\nu = 4 \times 10^{17}$ Hz). Thus, we must have continuous injection of accelerated electrons to maintain the X-ray flare during the decay phase, which lasts ∼30 min. If the NIR and X-ray flares are created by the same population of electrons, whose energy distribution is described by a powerlaw as $N(E) = K\,E^{-p}$, the difference between the NIR and X-ray flux can be explained if the synchrotron spectrum has a cooling break frequency between the NIR and X-rays (Dodds-Eden et al. 2009). In this scenario, the X-ray spectrum has a spectral index of $\alpha = p/2$, whereas the NIR spectral index is $\alpha = (p-1)/2$ (with $S_\nu \propto \nu^{-\alpha}$; Dodds-Eden et al. 2009). Knowing that the X-ray photons are produced by the electrons from the tail of the power law distribution, during the first part of the flare there are many more electrons that create NIR photons than those creating X-ray photons. Then, the acceleration mechanism has to become more efficient, accelerating more electrons to the tail (and thus increasing $p$) of the distribution and thus changing the ratio between the NIR and the X-ray flux. Hence the production of X-ray photons increases, which explains the second part of the flare.

**The synchrotron–synchrotron self-Compton process (SYN-SSC)**

During synchrotron self-Compton emission, X-ray photons are produced by the scattering of the synchrotron radiation from radio to NIR on their own electron population. If we compare the fluxes produced by the synchrotron and SSC emissions, the variation of the X-ray/NIR ratio constrains the size evolution of the flaring source. Let us consider a spherical source of radius $R$ with a power law energy distribution of relativistic electrons. Following Van der Laan (1966), the radiative transfer for the synchrotron radiation can be computed as

$$S_{\rm SYN} = \int_0^R \frac{\epsilon_\nu}{\kappa_\nu}\left(1 - {\rm e}^{-\tau_\nu(r)}\right) 2\pi r\,{\rm d}r, \quad (2)$$

with $\kappa_\nu \propto B^{(p+2)/2}\,\nu^{-(p+4)/2}$ the absorption coefficient, $\epsilon_\nu \propto B^{(p+1)/2}\nu^{-(p-1)/2}$ the emission coefficient, $B$ the magnetic field (Lang 1999) and $\tau_\nu(r)$ the optical depth, which can be computed

at each distance $r$ from the sphere center as:

$$\tau_\nu(r) = \int_0^{2\sqrt{R^2-r^2}} \kappa_\nu \mathrm{d}l. \quad (3)$$

Assuming that we are in the optically thin regime (i.e., $\tau_\nu(r) \ll 1$), we utilize formula 3 of Marrone et al. (2008): $S_{\rm SYN} \propto B^{(p+1)/2}\, \nu^{-(p-1)/2}\, R^3$. For synchrotron radiation, we have $B \propto R^4\, \nu_{\rm m}^5\, S_{\rm m}^{-2}$ with $S_{\rm m}$ the maximum flux density of the spectral energy distribution occurring at frequency $\nu_{\rm m}$ (Marscher 1983). Finally, the synchrotron radiation can be expressed using $p = 2\alpha + 1$ as

$$S_{\rm SYN} \propto R^{4\alpha+7}\, \nu_{\rm m}^{5(\alpha+1)}\, S_{\rm m}^{-2(\alpha+1)}\, \nu^{-\alpha}. \quad (4)$$

The SSC radiation of X-ray photons is (formula 4 of Marscher 1983):

$$S_{\rm SSC} \propto R^{-2(2\alpha+3)}\, \nu_{\rm m}^{-(3\alpha+5)}\, S_{\rm m}^{2(\alpha+2)}\, \ln\left(\frac{\nu_2}{\nu_{\rm m}}\right) \nu^{-\alpha}. \quad (5)$$

The natural logarithm in this equation could be approximated by $c_1\,(\nu_2/\nu_{\rm m})^{c_2}$ with $c_1 = 1.8$ and $c_2 = 0.201$ (Eckart et al. 2012b). The synchrotron-to-SSC flux ratio is

$$\frac{S_{\rm SSC}}{S_{\rm SYN}} \propto R^{-(8\alpha+13)}\, \nu_{\rm m}^{-(8\alpha+10+c_2)}\, S_{\rm m}^{4\alpha+6}. \quad (6)$$

We therefore have three parameters that may vary during the flare to explain the increased ratio of X-ray and NIR flux (Fig. 15). Considering the plasmon model, for which a spherical source of relativistic electrons expands and cools adiabatically, we have (Van der Laan 1966): $\nu_{\rm m} \propto R^{-(8\alpha+10)/(2\alpha+5)}$ and $S_{\rm m} \propto R^{-(14\alpha+10)/(2\alpha+5)}$. Thus, $S_{\rm SSC}/S_{\rm SYN} \propto R^{-\beta}$ with $\beta \equiv (8\alpha^2 + (30 - 8\,c_2)\alpha + 25 - 10\,c_2)/(2\alpha + 5)$. We first consider the adiabatic expansion. For our observation, the ratio between the X-ray and the NIR flux increases during the 2014 Mar. 10 flare, implying that $R^{-\beta}$ must increase as the radius $R$ increases. This condition is satisfied if the exponent $\beta$ is negative and thus if the $\alpha$ value is lower than $-2.5$ or is between $-2.3$ and $-1.25$, which is inconsistent because $\alpha$ must be positive. The expansion case is thus likely to be rejected under the hypothesis of an optically thin plasmon that expands adiabatically. We can also consider the case where the plasmon is compressed during its motion through a bottle-neck configuration of the magnetic field. We can still use the equations of Van der Laan (1966), since the conservation of the magnetic flux is explicitly taken into account. The compression case is thus preferred, because it allows positive values of $\alpha$ for $\beta > 5.4$. Thus, for the SYN-SSC process, the plasmon must be adiabatically compressed with at least $S_{\rm SSC}/S_{\rm SYN} \propto R^{-5.4}$. Therefore, the observed increase of the X-ray-to-NIR flux ratio by a factor of 10 in 1.2 h implies a decrease of the radius by a factor of about 0.6. The average compression velocity is estimated as $V_{\rm comp} = \Delta R/\Delta t$, leading to $|V_{\rm comp}|/c < 0.0034\, R/R_{\rm s}$ with $R_{\rm s}$ the Schwarzschild radius ($R_{\rm s} = 1.2 \times 10^{12}$ cm for Sgr A*, which corresponds to 0.08 au). For comparison, the expansion velocities computed with this model in the literature range between 0.0028 and $0.15c$ (Yusef-Zadeh et al. 2006a, 2009; Eckart et al. 2008), which is of the same order as the compression velocity computed here. Thus, the model of an adiabatic compression of a plasmon is the likely hypothesis to explain the variation of the ratio between X-ray and NIR flux, in the context of the SYN-SSC process.

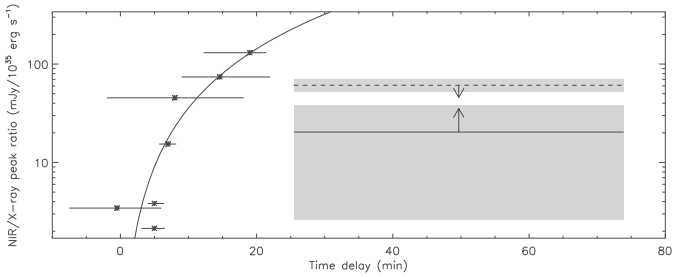


**Fig. 16.** NIR/X-ray peak ratio vs. time delay for the synchrotron-inverse Compton process. The asterisks are the results reported by Yusef-Zadeh et al. (2012), the solid line is a parabolic fit. The horizontal solid line and gray box are the lower limit and error bar on the NIR/X-ray peak ratio of the flare I/1 on 2014 Mar. 10 and the corresponding time-delay range. The dashed line is the ratio between the maximum NIR amplitude reported by Witzel et al. (2012) and the X-ray peak of flare 1, with the gray box being the corresponding error bar (see text for details).

### The synchrotron–inverse Compton process (SYN-IC)

In the case of inverse Compton emission, X-ray photons are produced by the scattering of either the NIR photons produced by synchrotron emission from the thermal electron population associated with the accretion flow that produces the sub-millimeter photons, or the sub-millimeter photons of the accretion flow on the electron population of the external source that produces the NIR photons by synchrotron radiation.

For the former process, the accretion flow is optically thin in the NIR, allowing all of the thermal electron population of the accretion flow to upscatter the NIR photons. Yusef-Zadeh et al. (2012) estimated the X-ray to NIR time delay for seven NIR/X-ray flares, which is due to upscattering of the NIR photons in the accretion flow. They identified a trend between increasing time delay and the increase of the NIR/X-ray peak ratio that is consistent with the SYN-IC process. The X-ray peak of flare 1 is defined as the maximum of the pn smoothed light curve (Table 6). We have only a lower limit on the NIR peak of flare I, which results in an estimated time delay of 25.5–73.9 min, because we have an observational gap in the HST data. Figure 16 shows a comparison of the peak ratio lower limit and time delay range of flare I/1 (horizontal solid line) with those reported in Table 2 of Yusef-Zadeh et al. (2012). This peak ratio lower limit is located below the observed trend. Assuming that the actual NIR peak can not be larger than the maximum observed amplitude (i.e., 32 mJy; Witzel et al. 2012), the actual peak ratio (dashed line) would be at least four times smaller than the value predicted by the SYN-IC process. If the actual NIR peak corresponds to this predicted value, this NIR flare would be four times brighter than the brightest flare ever observed and its shape would be completely unusual. We therefore consider this process to be very unlikely.

For the latter process, the accretion flow is optically thick in sub-millimeter, reducing the number of available sub-millimeter photons produced by the thermal electron population to be upscattered (Yusef-Zadeh et al. 2006b, 2012; Wardle 2011). If the sub-millimeter flux of the accretion flow is constant, the X-ray flare should have the same shape as the NIR flare. But in flare I/1 the X-ray flux increases while the NIR flux decreases. Since the decay of the NIR flux can only be due to the decrease of the number of accelerated electrons, the rise of the X-ray flux would require a simultaneous large increase of the sub-millimeter flux, which appears rather fine tuned. Therefore, we do not favor the SYN-IC process to explain the variation of the NIR/X-ray flux of flare I/1.

A&A 589, A116 (2016)

#### 4.1.2. Two distinct flares with simultaneous NIR and X-ray peaks

The 2014 Mar. 10 flare could be decomposed into two flaring components (called Ia/1a and Ib/1b). Each NIR/X-ray flaring component is produced by its own population of accelerated electrons. We introduce here a general model that will be used in the next subsections to fit the NIR and X-ray light curves. The model is composed of a linear part (if needed), representing the non-flaring level, plus one or two Gaussian flares:

$$F(t) = F_0 + F_1\,(t - t_0) + \sum_{i=1}^{2} A_{\rm i}\,{\rm e}^{-(t-t_{\rm i})^2/2\,\sigma_{\rm i}^2}\,, \qquad (7)$$

with $A_{\rm i}$ the amplitude above the non-flaring level and $t_{\rm i}$ and $\sigma_{\rm i}$ the center and the standard deviation of each Gaussian. For the X-rays, the non-flaring level is fixed to the Bayesian-block value. The results of the fit are given in Table 8 and the corresponding light curves and residuals are shown in Fig. 17 (top panels).

The time of the first and second peaks of the NIR and X-ray flares are consistent with each other within the $1\sigma$ errors. Flare 1b appears broader in X-rays than in the NIR, but their widths are consistent with each other within $1.5\sigma$. The delay time between the two X-ray maxima is about 5000 s, which is longer than the time between two X-ray flares observed during the 2012 *Chandra XVP* campaign (about 4000 s; see Fig. 1 of Neilsen et al. 2013). This argument, in addition to the change of flux ratio between the two flares, favors the interpretation of two distinct flares.

From the unabsorbed-flux-to-count-rate ratio derived in Sect. 3.1.3, we compute the unabsorbed total energy of these flares using the total number of counts in each Gaussian. The start and stop times of the flares are defined as the $3\sigma$ distance from the time of the maximum, i.e., 16.0 and 17.6 h for flare 1a, and 17.4 and 19.8 h for flare 1b. The unabsorbed total energy is $(12.7 \pm 6.7) \times 10^{37}$ and $(21.2 \pm 6.5) \times 10^{37}$ ergs ($1\sigma$ error) for flares 1a and 1b, respectively. The unabsorbed total energy of flare 1 is thus split nearly equally between its two components. The peak amplitude of flare 1a is close to the smallest amplitudes of flares observed (Fig. 8).

### 4.2. The NIR flare II on 2014 Mar. 10

This flare is only detected in the NIR with HST. We therefore fit the NIR light curve with a single Gaussian above a constant non-flaring level using Eq. (7). The best fit parameters are reported in Table 8.

The upper limit on the amplitude of the undetected X-ray counterpart was computed using the Bayesian method for the determination of the confidence limits described by Kraft et al. (1991, see also Helene 1983). We use the notations and equations of Sect. 3.1.2. We first define a confidence limit $CL = 0.95$ and the source $N$ as the number of counts during the time interval of the flare maximum (i.e., between $t_{\rm i} - 3\sigma$ and $t_{\rm i} + 3\sigma$ with $\sigma$ the error on $t_{\rm i}$ reported in Table 8). The background $B$ is the number of counts in the non-flaring Bayesian-block at the time of the NIR flare peak. We then determine $s_{\rm min}$ and $s_{\rm max}$ (see footnote 5 in Sect. 3.1.2) resolving the equation of $CL$. For flare II, $N = 62$ counts and the non-flaring level is defined by the Bayesian blocks as 0.315 counts s$^{-1}$ between 21.65 and 21.71 h, leading to $B = 68$ counts and $S = -6$ counts. Since $S$ is negative, $s_{\rm min} = 0$, leading to $s_{\rm max} = 6$. The upper limit on the amplitude is thus 0.028 counts s$^{-1}$ at a confidence level of 95%. The value of this upper limit is also reported in Table 8.

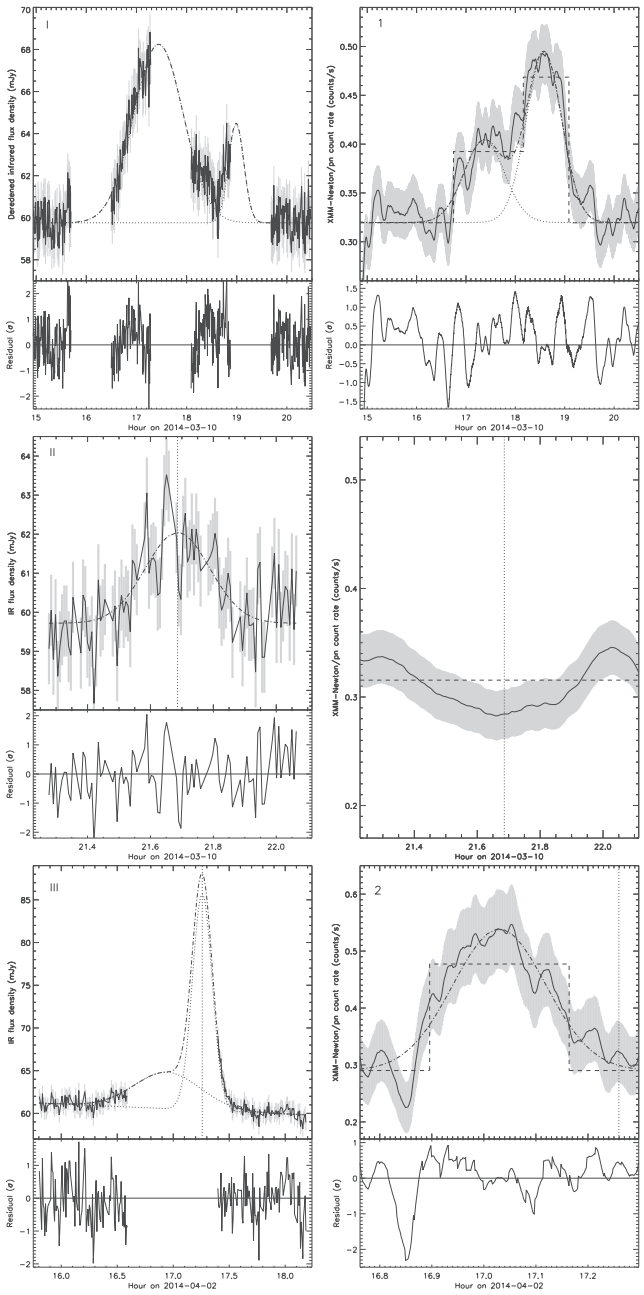


**Fig. 17.** Light curve fitting of the HST NIR flares (*left panels*) and the X-ray (*right panels*) counterparts. The solid lines are the observed light curves with the error bars in gray. The dashed lines in *right panels* are the Bayesian blocks. The X-ray light curves are smoothed with a window width of 500 s and 100 s for 2014 Mar. 10 and Apr. 2, respectively. The dotted lines are the individual Gaussians and the dot-dashed line is the sum of the Gaussians. The vertical dotted lines are the time of the NIR flare peak when there is no detected X-ray counterpart. The residuals are in units of $\sigma$.

### 4.3. The NIR flare III on 2014 Apr. 2

We consider that two NIR flares happened during the occultation of Sgr A* by the Earth. We thus fit the NIR light curve with two Gaussians (labeled IIIa and IIIb) above a linear component, which is used here to take into account the change in the non-flaring level between the last two HST orbits (Eq. (7)). The $F$-test strongly supports two Gaussian components, since this significanlty increases the goodness-of-fit ($p$-value of $3 \times 10^{-4}$). The best-fit parameters for the X-ray and NIR flares are given in

**Table 8.** Gaussian fitting of the NIR and X-ray flares observed during the 2014 campaign.

| Flare | | | Non-flaring level | | | Gaussian flare | | | | $\chi^2_{red}$ (d.o.f) |
|---|---|---|---|---|---|---|---|---|---|---|
| Date | Type | # | $F_0$ | $F_1$ | $t_0$ | $A_i$ | | $t_i$ | $\sigma_i$ | |
| 2014 | | | (mJy) | (mJy h$^{-1}$) | (h) | ([a]) | (mJy) [b] | (h) | (h) | |
| Mar. 10 | IR | Ia | 59.8 ± 0.5 | ..... | ..... | 8.64 ± 0.03 | 10.58 ± 0.03 | 17.4 ± 0.1 | 0.49 ± 0.09 | 1.52 (648) |
| – | IR | Ib | – | ..... | ..... | 4.05 ± 0.06 | 4.97 ± 0.06 | 18.9 ± 0.1 | 0.2 ± 0.1 | – |
| – | X | 1a | [BB] | ..... | ..... | 0.08 ± 0.02 | $(2.8 \pm 0.8) \times 10^{-4}$ | 17.37 ± 0.09 | 0.3 ± 0.1 | 0.39 (10796) |
| – | X | 1b | [BB] | ..... | ..... | 0.17 ± 0.02 | $(6.7 \pm 0.8) \times 10^{-4}$ | 18.58 ± 0.07 | 0.36 ± 0.07 | – |
| Mar. 10 | IR | II | 59.7 ± 0.1 | ..... | ..... | 2.3 ± 0.2 | 2.8 ± 0.2 | 21.68 ± 0.01 | 0.10 ± 0.01 | 0.67 (96) |
| – | X | ... | ..... | ..... | ..... | <0.028 | $<1.1 \times 10^{-4}$ | [21.67] | ..... | ..... |
| Apr. 2 | IR | IIIa | 61.21 ± 0.05 | −0.577 ± 0.003 | [15.8] | 4.3 ± 0.4 | 4.6 ± 0.4 | 16.94 ± 0.01 | 0.29 ± 0.02 | 0.48 (192) |
| – | IR | IIIb | – | – | – | 25.3 ± 1.4 | 27.5 ± 1.4 | 17.2 ± 0.1 | 0.09 ± 0.03 | – |
| – | X | 2 | [BB] | ..... | ..... | 0.25 ± 0.01 | $(8.4 \pm 0.5) \times 10^{-4}$ | 17.03 ± 0.04 | 0.09 ± 0.03 | 1.11 (1365) |
| – | X | ... | ..... | ..... | ..... | <0.030 | $<1.2 \times 10^{-4}$ | [17.2] | ..... | ..... |
| Apr. 3 | IR | IV | ..... | ..... | ..... | [6.9 ± 0.1] | [6.9 ± 0.1] | [7.89] | ..... | ..... |
| – | X | ... | ..... | ..... | ..... | <0.042 | $<1.7 \times 10^{-4}$ | – | ..... | ..... |
| Apr. 4 | IR | V | ..... | ..... | ..... | [5.30 ± 0.09] | [5.30 ± 0.09] | [8.82] | ..... | ..... |
| – | X | ... | ..... | ..... | ..... | <0.0093 | $<3.7 \times 10^{-5}$ | – | ..... | ..... |

**Notes.** [BB] means that the value is fixed to the count rate level of the Bayesian block. [(a)] The units are counts s$^{-1}$ for X-rays and mJy for NIR; [(b)] in the $K_s$-band.

Table 8 and the resulting graphs are shown in the bottom panels of Fig. 17.

We then fit the X-ray flare 2 with a Gaussian above a quiescent level equal to the Bayesian-block value. The maximum of the X-ray flare has no time delay relative to the NIR flare IIIa above the $3\sigma$ error bars, as usually observed for X-ray flares with NIR counterparts (Eckart et al. 2006; Yusef-Zadeh et al. 2006a; Dodds-Eden et al. 2009). Moreover, the FHWM of the NIR flare IIIa (2458 s) is about 3 times larger than that of the X-ray flare (762 s), which is reminiscent of the FWHM ratio of ∼2 observed by Dodds-Eden et al. (2009) for the 2007 Apr. 4 NIR/X-ray flare. The NIR flare IIIa is thus probably the counterpart of the X-ray flare 2. This conclusion is based on our Gaussian fitting of flare III, but a more complex shape cannot be excluded due to the NIR observational gap. However, since the X-ray flare 2 and the previously observed NIR/X-ray flares also have a Gaussian shape (Eckart et al. 2006; Yusef-Zadeh et al. 2006a; Dodds-Eden et al. 2009), we consider that this conclusion is the simplest and thus the most likely.

The amplitude of the flare IIIb is one of the largest observed when compared with the sample obtained with NACO (Witzel et al. 2012). No X-ray counterpart is detected for this flare. We thus obtain an upper limit on the X-ray amplitude using the same method as flare II with $N = 763$ counts between 16.9 and 17.5 h. The background is defined as the sum of the number of counts in non-flaring Bayesian-block values (626.4 counts) and the number of counts in the Gaussian fit of flare 2 during the maximum of the flare (121.7 counts). We thus have $B = 748.1$ counts, leading to $S = 14.9$ counts. The resulting $s_{min}$ is 0, with $s_{max} = 65$ counts. The upper limit on the amplitude of the undetected X-ray counterpart is thus 0.030 counts s$^{-1}$ at the confidence level of 95%. This value is reported in Table 8.

### 4.4. The NIR flare IV on 2014 Apr. 3

The VLT light curves consist of bins of 400 s exposures. The number of bins is too small and the bin size too large to fit a Gaussian to the VLT light curves. We thus consider only the bin with the largest flux density as the peak of the flare IV. This value and the time of the maximum are reported in Table 8.

No X-ray counterpart is detected with *XMM-Newton* on Apr. 3. We thus deduce an upper limit to the putative simultaneous X-ray flare using the same method that was used for flare II. The time interval of the maximum of flare IV is defined as the bin length of the light curve, i.e., 400 s centered on 7.89 h. The number of counts in this interval is $N = 127$ counts and the background is $B = 119.1$ counts, leading to $S = 7.9$ counts. The resulting $s_{min}$ is 0, with $s_{max} = 17$ counts, leading to an upper limit on the amplitude of 0.042 counts s$^{-1}$.

### 4.5. The NIR flare V on 2014 Apr. 4

For flare IV, we do not fit the light curve with a Gaussian and we consider the maximum of the light curve as the peak flux density of the NIR flare (Table 8).

We have no *XMM-Newton* observation on 2014 Apr. 4. However, as shown in Fig. 1, there is a simultaneous legacy *Chandra* observation (ObsID: 16212; PI: D. Haggard) on this date. We used the *Chandra* Interactive Analysis of Observations (CIAO; version 4.6) to analyze these data. We worked with the level = 2 event list of the *ACIS-S* camera (Garmire et al. 2003), available in the primary package of the *Chandra* archive. We extracted the source+background events in the 2–8 keV energy range in a 1.″25-radius circle centered on the radio coordinates of Sgr A* using the `dmcopy` task. We used the Bayesian-blocks analysis with a false detection probability of $e^{-3.5}$ to detect any flaring event. No X-ray counterpart to the NIR flare was detected during this observation. Based on $N = 1$ counts between 8.71 and 8.93 h and a non-flaring level of 0.0065 counts s$^{-1}$, we compute $B = 3$ counts and $S = -2$ counts. The resulting $s_{min}$ is 0 with $s_{max} = 4$ counts. The upper limit to the putative simultaneous X-ray amplitude is thus 0.01 counts s$^{-1}$ at the confidence level of 95% (see flare II for explanations).

## 5. Constraining the physical parameters of the flaring region

In this section we constrain the physical parameters of the flaring region by considering three radiative models for the NIR

A&A 589, A116 (2016)

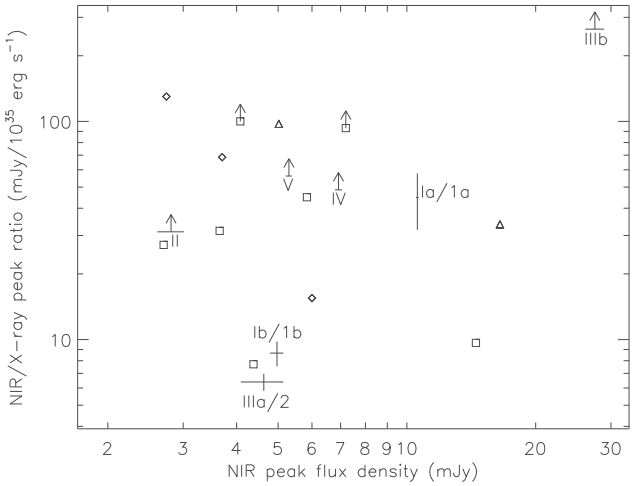


**Fig. 18.** NIR-to-X-ray peak ratio vs. amplitude of the NIR flares. Squares refer to the flares reported in Table 3 of Eckart et al. (2012b). Triangles are the simultaneous NIR/X-ray flares detected on 2007 Apr. 4 and labeled *D* and *E* in Table 2 of Trap et al. (2011). Diamonds are the delayed flares of 2004 Jul. 7, 2008 Jul. 26+27 and 2008 May 5 reported in Table 2 of Yusef-Zadeh et al. (2012). The labeled points are the NIR and X-ray flares observed during this campaign.

and X-ray emission. After computing the NIR-to-X-ray simultaneous peak ratio sample detected during the 2014 campaign, we investigated the synchrotron-synchrotron (SYN-SYN), synchrotron Self-Compton-synchrotron Self-Compton (SSC-SSC), and the synchrotron-synchrotron Self-Compton (SYN-SSC) radiation mechanisms. These processes are called "local", because these emissions are produced only by the electrons accelerated in the flaring region. The last subsection is dedicated to the Inverse Compton mechanism, which involves external electrons.

### 5.1. The sample of NIR flares and the corresponding X-ray emission

We compute the flux densities of the NIR and X-ray flare peaks to constrain the physical parameters of the flaring region needed to produce such fluxes. We extrapolate the amplitude of each NIR peak to the $K_s$-band using the $H-L$ spectral index computed in Witzel et al. (2014b). The flux density of the X-ray flare peaks is computed from the spectral fitting in `ISIS`, using the typical spectral parameters of the X-ray bright flares (see Sect. 3.1.3). The resulting conversion factor is 1 pn count $s^{-1}$ = 3.935 $\mu$Jy at 4 keV. The NIR peak flux density and corresponding values of the X-ray peaks (or upper limits) are reported in Table 8.

Figure 18 shows the NIR-to-X-ray peak ratio as a function of the amplitude of the NIR flares observed during the 2014 campaign. The unabsorbed X-ray peak luminosities are computed using the conversion factor reported in Sect. 3.1.3. The X-ray upper limit of NIR flare V was obtained from *Chandra* data. The corresponding unabsorbed-flux-to-count-rate ratio of $1.97\times10^{-10}$ erg $s^{-1}$ $cm^{-2}$/count $s^{-1}$ was computed with the same spectral parameters as for *XMM-Newton*.

We also show the flares reported by Eckart et al. (2012b), the two simultaneous flares on 2007 Apr. 4 (Porquet et al. 2008; Nowak et al. 2012) labeled *D* and *E* in Table 2 of Trap et al. (2011), and the delayed flares of 2004 Jul. 7, 2008 Jul. 26+27, and 2008 May 5 reported in Table 2 of Yusef-Zadeh et al. (2012).

The flare Ia/1a lies within the bulk of NIR flare amplitudes and peak ratio, whereas the flare IIIa/2 has the lowest NIR-to-X-ray ratio ever observed. The NIR flare IIIb is amongst the largest NIR flares (e.g., Dodds-Eden et al. 2009; Witzel et al. 2012) and has the largest NIR-to-X-ray ratio ever observed.

### 5.2. Investigation of the local radiative processes

With the peak flux density of the flares in X-rays and NIR, we use the formalism developed by Eckart et al. (2012b) to constrain the range of four physical parameters of the flaring emission: the size of the source region, the magnetic field, the density, and the maximum of the flux density spectrum. Eckart et al. (2012b) considered three cases, invoking the two radiative processes, implying the local electrons from the flaring source region: the SYN-SYN, SSC-SSC, and SYN-SSC emissions. A radiative process is considered as dominant when the alternative emission processes are lower than 10%. For example, the SYN-SYN case is dominant if both SSC contribution for NIR and X-rays are lower than 10% of the synchrotron contribution. Considering different values for the turnover frequency ($\nu_m$), which defines the frequency at which the source becomes optically thin, we have four free physical parameters for each value of the spectral index ($\alpha$): the size of the emitting region ($\theta$), peak flux density at $\nu_m$ ($S_m$), number density of relativistic particles ($\rho$), and the magnetic field ($B$). The spectral index is given by the ratio between the NIR and X-ray amplitudes for the SYN-SYN and SSC-SSC cases, and by seven different values of $\alpha$ from 0.3 to 1.5 for the SYN-SSC case. Computing the SYN or SSC flux density with the equations given by Eckart et al. (2012b), we can constrain the values of the four physical parameters for each value of $\alpha$ and $\nu_m$.

The resulting graphs for the flares detected in NIR and X-rays (labeled Ia/1a, Ib/1b and IIIa/2) are shown in Fig. 19. Each line corresponds to one value of $\alpha$. The red dots are the turnover frequencies from 50 to 3000 GHz in steps of 200 GHz. The constraint on the MIR amplitude limit observed during the bright $L'$-band and X-ray flare on 2007 Apr. 4 of 57 mJy at 11.88 $\mu$m (Dodds-Eden et al. 2009) is also used: the lines are dashed if this limit is exceeded. This happens only for the SYN-SSC emission mechanism and for high values of $\alpha$.

The physical parameters are more constrained for flare IIIa/2, since the X-ray-to-NIR amplitude ratio is high. For this flare, the SYN-SSC emission mechanism leads to a size of 0.03−7 times the Schwarzschild radius and an electron density of $10^{8.5}$–$10^{10.2}$ $cm^{-3}$ for a synchrotron spectral-index of 0.3−1.5.

From the magnetic field values deduced for these flares, one can infer the presence of sustained heating during the decay phase of the X-ray or NIR flares for the SYN-SYN and SYN-SSC case. Indeed, if the synchrotron cooling timescale, defined as $\tau_{sync} = 8\,(B/30\ \mathrm{G})^{-3/2}\,(\nu/10^{14}\ \mathrm{Hz})^{-1/2}$ min (Dodds-Eden et al. 2009), is shorter than the duration of the decay phase then sustained heating is needed. We define the decay phase from the time of the maximum of the Gaussian fit (see Table 8) to the time leading to 10% of the flare amplitude (corresponding to 2.1$\sigma$ after the maximum) in order to still have a detectable emission of the flare.

For the SYN-SYN case, the synchrotron cooling timescale is shorter for the X-ray photons, leading to more constraints on the presence of sustained heating. We thus consider the X-ray frequency ($\nu = 10^{18}$ Hz) in the computation of the synchrotron cooling timescale. The synchrotron cooling timescale is shorter than the decay time of flare 2 (695 s) for $B$ larger than 1 G, implying that sustained heating must be present during the decay phase for these values of magnetic field. A sustained heating is always needed for flares Ia/1a and Ia/1b, since they have a minimum

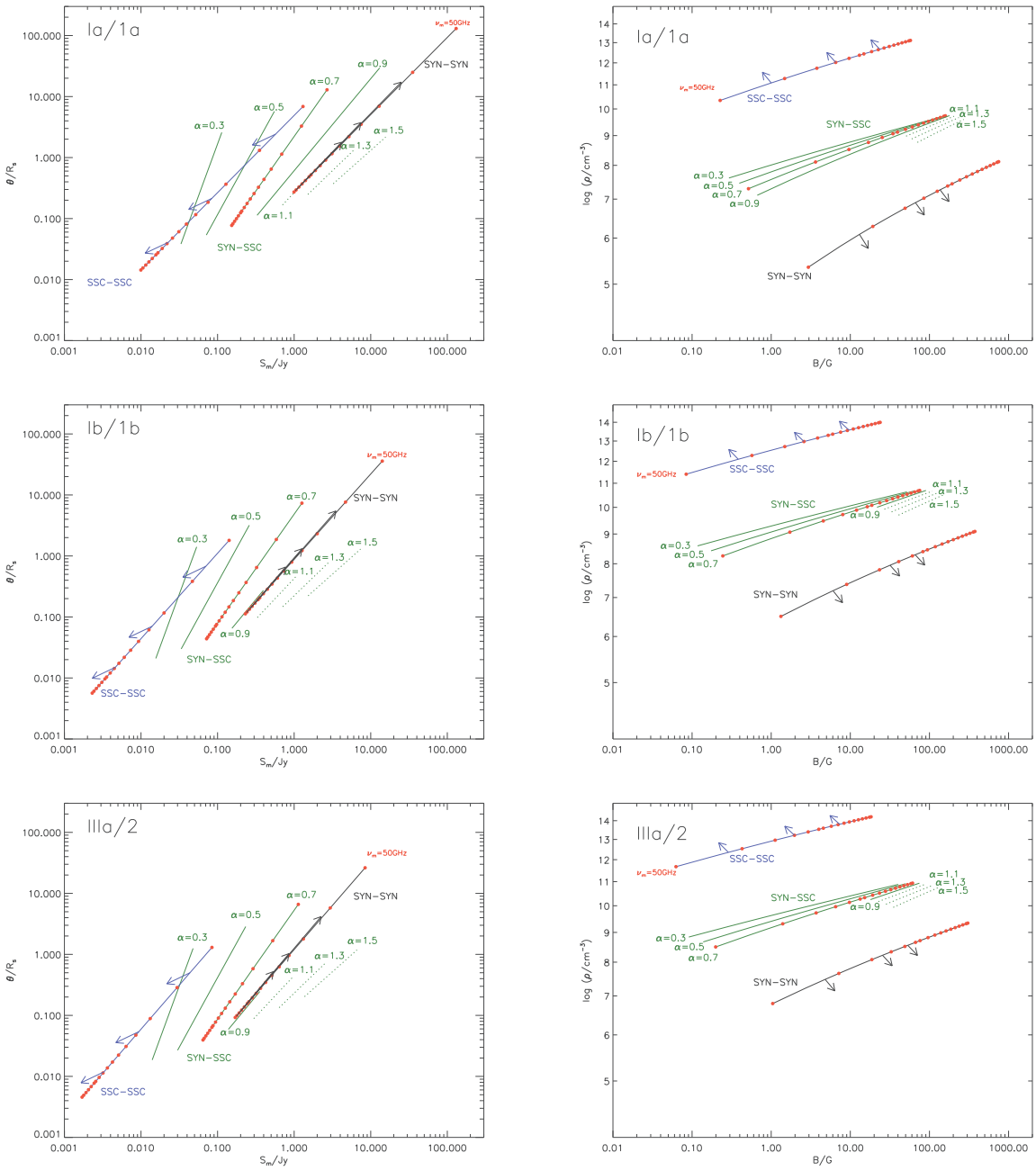


**Fig. 19.** Physical parameters of the flares observed simultaneously in X-rays and NIR for the three emission models. The flare Ia/1a, Ib/1b and IIIa/2 are in the *upper*, *middle* and *bottom panels*, respectively. *Left panels* are the size of the flaring-source region ($\theta$) vs. the peak of the spectrum ($S_{\rm m}$) at the frequency $\nu_{\rm m}$. *Right panels* are the density of the relativistic electrons vs. the magnetic field. The locii where the Synchrotron Self-Compton−Synchrotron Self-Compton (SSC-SSC), Synchrotron-Synchrotron Self-Compton (SYN-SSC) and Synchrotron-Synchrotron (SYN-SYN) are dominant are shown in black, blue and green, respectively. The red dots represent the turnover frequencies from 50 to 3000 GHz by step of 200 GHz. The arrows show the direction of the curves if the limit on the alternative emission processes is lowered. Dotted lines are locii of SYN-SSC where the MIR emission is larger than the observed upper-limit values (see text for details).

value of the magnetic field and a decay time larger than those of flare 2 (2318 and 2781 s, respectively).

For the SYN-SSC case, we consider the NIR frequency ($\nu = 10^{14}$ Hz) in $\tau_{\rm sync}$ that we have to compare to the decay time of the NIR flares. Sustained heating is now needed for flare IIIa (whose decay time is 2240 s) with a magnetic field of greater than 11 G, corresponding to an electron density larger than $10^{10.1}$ cm$^{-3}$. For flares Ia and Ib (whose decay times are 1545 and 3785 s, respectively), sustained heating is needed for magnetic fields larger than 13 and 7 G, respectively. The corresponding electron density is thus larger than $10^{8.4}$ and $10^{9.5}$ cm$^{-3}$.

We also apply the study of Eckart et al. (2012b) to constrain the physical parameters of the flaring emission for the NIR flares that have no detected X-ray counterpart (flares II, IIIb, IV and V). The resulting graphs are shown in Fig. 20. The necessary electron density and magnetic field ranges lie within lower values compared to those needed to produce detectable X-ray flares, since the efficiency of the production of X-ray photons is

smaller. Moreover, for flare IIIb, the SYN−SYN process is only dominant for small values of $\nu_m$. This is explained by the small X-ray-to-NIR amplitude ratio, since at large $\nu_m$ the synchrotron process is too efficient for the production of a small number of X-ray photons.

We can also deduce the presence of sustained heating during the decay phase of NIR flares II and IIIb for the SYN-SYN and SYN-SSC case. The synchrotron cooling timescale is shorter than the decay time of flare II (772 s) if $B$ is larger than 22 G, requiring sustained heating during the decay phase for these values of magnetic field. For flare IIIb (whose decay times are 695 s), sustained heating is required for $B$ larger than 1 G.

However, as argued by Eckart et al. (2012a), alternative models such as different spectral indexes for the NIR and X-ray, due to inhomogeneities of the accretion disk, can also explain the data with larger numbers of free parameters.

### 5.3. Investigation of the external radiative process

As reported in Sect. 4.1.1, Yusef-Zadeh et al. (2012) investigated the upscattering of the NIR photons produced in the flaring region on electrons of the accretion flow. The ratio between the Inverse Compton and the synchrotron emission is

$$\frac{L_{IC}}{L_{SYN}} \propto \frac{U_{ph}}{U_B}, \tag{8}$$

with $U_{ph}$ the photon energy density and $U_B = B^2/8\pi$ the magnetic energy density. Given the variation of $B$ with the distance from Sgr A* ($B = B_0\,(r/R_s)^{-1}$ with $B_0$ of several hundred of Gauss; Eatough et al. 2013), it is possible to create NIR and X-ray flares with a large range of NIR-to-X-ray ratio. Thus, we cannot identify the IC radiation by only considering the NIR-to-X-ray ratio.

However, using the estimation of the time delay between X-ray and NIR flare peaks as a function of the NIR-to-X-ray peak ratio reported in Yusef-Zadeh et al. (2012) and shown in Fig. 16, we can estimate the time delays that we would observe during our 2014 campaign. For the detected X-ray flares, the NIR-to-X-ray peak ratio ranges between 6 and 45 mJy/$10^{35}$ erg s$^{-1}$ (see Fig. 18) leading to a time delay less than 10 min, which is smaller than the error bars on the time of the maximum of the Gaussians. The IC emission, therefore, is still a possible radiative process for the production of the X-ray flares observed during this campaign.

For the undetected X-ray flares II, IIIb, IV and V, the NIR-to-X-ray ratio is larger than 32, 269, 48, and 55 mJy/$10^{35}$ erg s$^{-1}$, respectively. The corresponding time delays are thus greater than 9, 26, 11, and 12 min, respectively. These time delays are larger than the events with detected X-ray flares. The efficiency of the flare detection with *XMM-Newton* and *Chandra*, however, does not allow us to detect such faint X-ray flares, which may have the largest delay in the inverse Compton framework.

Thus, the flares observed during the 2014 campaign leave the IC process as a possible emission mechanism for producing X-ray flares from the NIR photons.

## 6. Discussing the X-ray flaring rate

We can compare the X-ray flare frequency during our observations (three flares over 255.644 ks) to the one derived from the *Chandra XVP* campaign in 2012: 45 flares detected by Bayesian-block algorithm over 2983.93 ks (1.5 flare per day). Considering a sample of 45 flares having the same amplitude and duration distribution as those observed during the *Chandra XVP* campaign superimposed on the non-flaring level observed with *XMM-Newton* during our campaign, the Bayesian-blocks algorithm detects 36 flares over 2983.93 ks. If we sum the number of flares that we can detect during the exposure time corresponding to each observation during the *XMM-Newton* 2014 campaign, we arrive at a prediction of 3.1 flares during this campaign. We compare the flare rate observed during the *Chandra XVP* campaign to those observed during this campaign (36 flares over 2983.93 ks and 3 flares over 255.644 ks), assuming a Poisson process (Gehrels 1986; Fay 2010). The $p$-value for the null hypothesis that the flaring rate we have to observe and the rate we currently observe is the same, is 1, which implies that the flaring rate observed close to the pericenter passage of the DSO/G2 is consistent with that observed during the *Chandra XVP* campaign. The conclusion is the same if we consider only two X-ray flares instead of three ($p$-value = 0.54). To conclude that the measured flaring rate is statistically different from those observed during the *Chandra XVP* campaign, we would have to detect at least 8 flares during our campaign ($p$-value = 0.04), which corresponds to an increase of the flaring rate by a factor of 2.6 (95% confidence interval of 1.0−5.7).

Since the beginning of the observation of Sgr A* in X-rays, two temporary episodes of higher flaring rate were observed (Porquet et al. 2008; Neilsen et al. 2013). Porquet et al. (2008) detected four flares on 2007 Apr. 04 with *XMM-Newton*. Three of these flares happened during the last 39.6 ks of the observation, corresponding to a flaring rate of 8.8 flares per day. We can compare this flaring rate to the 38 flares that should be detected by the Bayesian-block algorithm. The ratio between the two rates is 5 and the 95% confidence interval is 1.3−20 ($p$-value = 0.03). Neilsen et al. (2013) detected 4 flares during 23.6 ks with *Chandra*, which corresponds to a flaring rate of 14.6 flares per day. We can directly compare this flaring rate to that computed during the 2012 *Chandra XVP* campaign if we remove these 4 flares from the sample of 45 flares detected by the Bayesian-blocks algorithm. Thus, we have to compare 41 flares over 2960.33 ks and 4 flares over 23.6 ks. The ratio between the two rates is 13 and the 95% confidence interval is 3.3−33.3 ($p$-value = $9 \times 10^{-4}$). This implies that some temporary increase of Sgr A* activity in X-ray may have been observed without an increase of the quiescent level due to an increase of the accretion rate.

The radio monitoring of Sgr A* with VLA between 2012 and 2014 May showed no change in the flux density or the spectrum (Bower et al. 2015a; Yusef-Zadeh et al. 2015). Observations of Sgr A* after the DSO/G2 pericenter passage show that there is no increase of the flaring activity in radio/submm (Tsuboi et al. 2015; Park et al. 2015). The 2014 Feb.−June *Chandra* X-ray monitoring of Sgr A* shows no rise of the quiescent flux (Haggard et al. 2014). The compactness of the object can explain the absence of any increase in the Sgr A* accretion rate during pericenter passage at 2014.39 ± 0.14 (Valencia-S. et al. 2015), which corresponds to 2014 Apr. 20 (2014 Mar. 1−2014 Jun. 10). Five flares with an absorbed fluence greater than $5 \times 10^{-9}$ erg cm$^{-2}$ (corresponding to an unabsorbed fluence of $10.9 \times 10^{-9}$ erg cm$^{-2}$ when using $\Gamma = 2$ and $N_H = 14.3 \times 10^{22}$ cm$^{-2}$) were observed with *XMM-Newton* and *Chandra* between 2014 Aug. 30 and Oct. 20, implying an increase in the rate of energetic flares, but the overall flaring rate did not change (Ponti et al. 2015).

To assess the typical timescale for the accretion of fresh matter from the DSO/G2 object onto Sgr A* at pericenter, we compute the disk accretion timescale ($\tau_{acc}$) for Sgr A*. It is governed by the viscous timescale, which is computed for an ADAF using

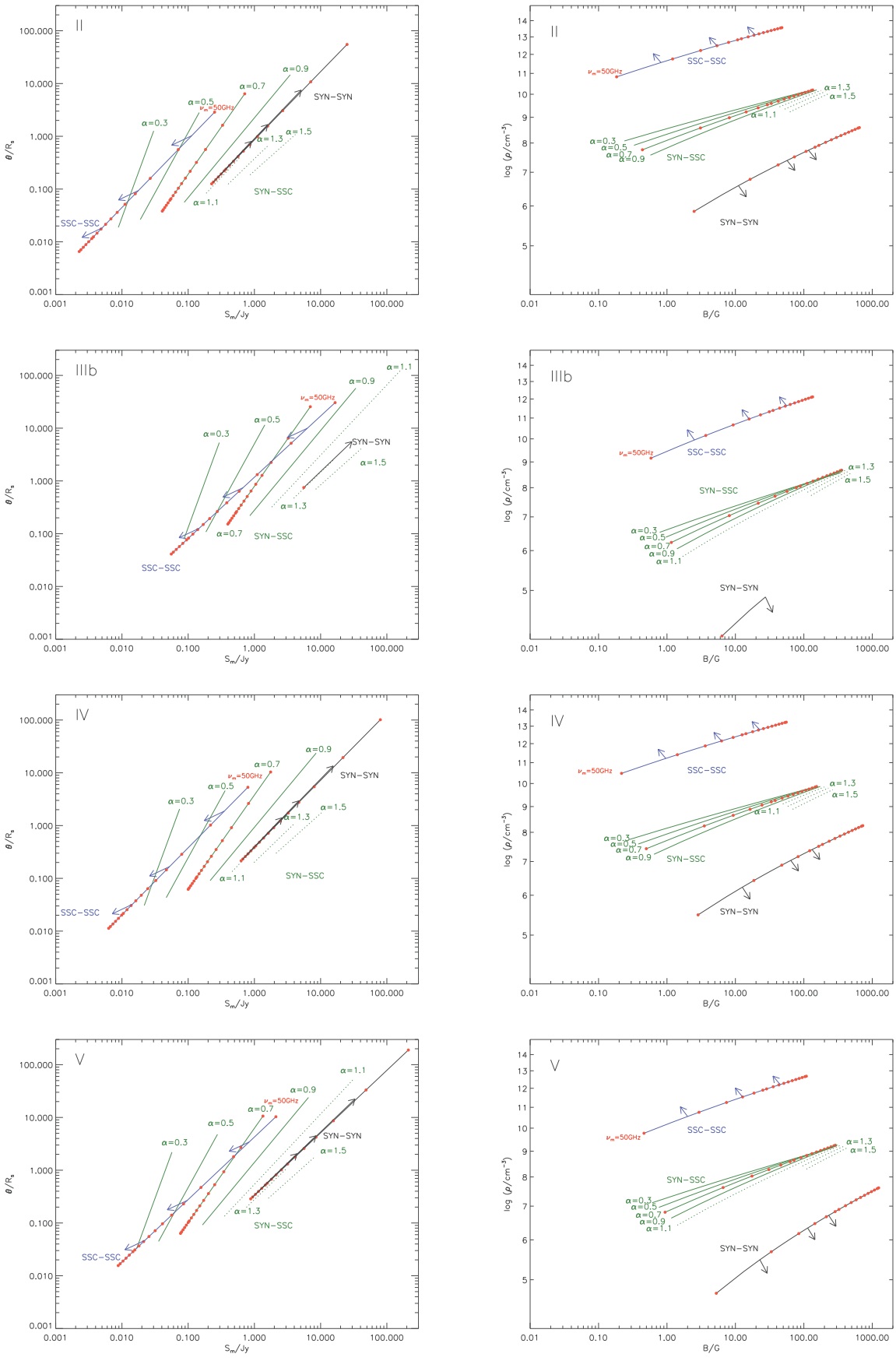


**Fig. 20.** Physical parameters of the flares only observed in NIR for the three emission models. The NIR flare II, IIIb, IV and V are in the *upper*, *second*, *third* and *bottom panels*, respectively. See Fig. 19 caption for the panel description.

the self-similar solution derived by Yuan & Narayan (2014, and references therein). At the distance $r$ of the SMBH, $\tau_{\rm acc}$ is defined as $r/V_{\rm rad}$ with $V_{\rm rad}$ the radial velocity for the self-similar solution, which gives us: $\tau_{\rm acc} \sim 3.0\,(r/2000R_{\rm s})^{1.5}\,(\alpha/0.1)^{-1}$ yrs with $\alpha \in [0,1]$ the efficiency of the mechanism of angular momentum transport introduced by Shakura & Sunyaev (1973). For a pericenter distance of about 2000 $R_{\rm s}$ (Pfuhl et al. 2015; Valencia-S. et al. 2015) and $\alpha = 0.1$, we should not see any increase of the flux from Sgr A* before 2017. Moreover, the large angular momentum of the gas and dust from DSO/G2 likely increases the true accretion timescale.

Some numerical simulations of the accretion of gas in a RIAF model were made, leading to a time range for the gas accretion of some months to several ten of years after the pericenter passage (Burkert et al. 2012; Schartmann et al. 2012). However, these simulations modeled DSO/G2 as a gas cloud or a spherical shell of gas, but not as a young star with circumstellar material. The accretion time when there is no central star may thus be lower than $\tau_{\rm acc}$, since the gas cloud is partially tidally disrupted before the pericenter passage.

Zajaček et al. (2014) modeled the DSO/G2 as an intermediate mass star of 2 $M_{\odot}$ moving in a RIAF. They studied the tidal effects on a circumstellar dusty envelope and on a circumstellar accretion disk. They showed that if the test particles are distributed in a disk-like structure, the number of particles that remain gravitationally bound to the star after the pericenter passage is larger than that for a spherical distribution of particles. From their Fig. 13, we can also infer that the accretion onto Sgr A* begins earlier for a spherical distribution than for a disk-like model. However, in these simulations, no circumstellar gas was taken into account.

## 7. Conclusions

The pericenter passage of the DSO/G2 object at the beginning of 2014 was predicted to produce an increase of the flaring activity of Sgr A* in several wavelengths. This 2014 Feb.−Apr. campaign was designed to follow an increase of its flaring activity simultaneously in X-rays, NIR, and radio/sub-mm.

Three NIR flares were detected with WFC3 on board HST: two on 2014 Mar. 10 (I and II) and one on Apr. 2 (III). Two additional NIR flares were detected with SINFONI at ESO's VLT on 2014 Apr. 3 (IV) and 4 (V). All of these NIR flares are within the top 8% of the largest amplitude flares observed with NACO at ESO's VLT (Witzel et al. 2012). Since the detection limit of WFC3 and SINFONI correspond to the 8 and 11% amplitude levels of this sample, the fact that the observed NIR flares belong to the most luminous NIR flares is statistically expected and can not be taken as any indication for an increase of NIR activity.

Two X-ray flares were detected on 2014 Mar. 10 (1) and Apr. 2 (2) using the Bayesian-blocks method on the *XMM-Newton* observations. The spectral parameters of these X-ray flares fitted with the MCMC method are consistent with those of the two brightest flares detected with *XMM-Newton* (Porquet et al. 2003, 2008).

The flare I/1 observed on 2014 Mar. 10 presents a change in the NIR to X-ray flux ratio, with an increase of the X-ray flux contribution during the second half of the flare. We tested the three radiative processes that can explain the NIR/X-ray flares from Sgr A* as a single flare, considering energetic arguments. The most likely interpretation is that the NIR and X-ray photons are produced in a plasmon in adiabatic compression by synchrotron and SSC emission mechanisms, respectively. However, the flares I and 1 can also be decomposed into two Gaussian flares with a time separation of only 1.2 h. We can thus associate the NIR flares Ia and Ib to the X-ray flares 1a and 1b, respectively. They reproduce the characteristics observed in other simultaneous NIR/X-ray flares, i.e., no apparent delay between the maxima and a similar FWHM. The flares Ia/1a lie within the bulk of NIR flare amplitudes and peak ratio, but the flare Ib/1b lies within the lowest peak ratio ever observed.

The NIR flare III is actually composed of two close Gaussian flares (IIIa and IIIb). The X-ray flare 2 is the counterpart of the NIR flare IIIa. It has the lowest NIR-to-X-ray ratio ever observed.

The NIR flares II, IIIb, IV, and V have no detectable X-ray counterpart in our *XMM-Newton* observation or the legacy *Chandra* observation. The upper limits on the X-ray amplitude were computed using the Bayesian method for the determination of the confidence limits described by Helene (1983) and Kraft et al. (1991). The flare IIIb lies within the largest NIR fluxes (e.g., Dodds-Eden et al. 2009; Witzel et al. 2012) and has the largest NIR-to-X-ray ratio ever observed.

In total, we detected seven NIR flares and three X-ray flares during the 2014 campaign.

On 2014 Mar. 10 we also identified an increase in the rising radio flux density at 13.37 GHz with the VLA, which could be the delayed radio emission from a NIR/X-ray flare that occurred before the start of our observation.

On 2014 Apr. 2 we identified a bump of the flux density on the rising 3.2-mm light curve observed with CARMA. The time range of this observation does not allow us to associate this millimeter bump to a NIR/X-ray flare. Moreover, we found no significant delay between the CARMA light curve and VLA *L*- and *C*-band data.

On 2014 Apr. 3 two millimeter flares were identified above the decaying 3.2-mm light curve. The former could be the delayed emission of the NIR flare IV.

We derived physical parameters of the flaring emission for local radiative processes, as done previously by Eckart et al. (2012b), for each NIR/X-ray flare, and also for NIR flares with no detected X-ray counterpart. Physical parameters for the flare IIIa/2 are better constrained when asssuming synchrotron and SSC emission mechanisms for the NIR and X-ray flares, respectively. This flaring region has a size of 0.03−7 times the Schwarzschild radius and an electron density of $10^{8.5}$–$10^{10.2}$ cm$^{-3}$, for a synchrotron spectral-index of 0.3−1.5. The derived physical parameters of the flaring emission associated with the undetected X-ray counterpart are poorly constrained, since the X-ray photon production efficiency is smaller.

We also tested the SYN-IC process using the NIR-to-X-ray peak amplitude ratio and the predicted time delay between the NIR and X-ray peaks. This external radiative process is also a possible emission model for the emission of the flares observed during this campaign.

No significant increase in the X-ray flaring rate has been detected during this campaign, but continuous monitoring of Sgr A* is still important to detect any steady increase of its flaring activity that could be due to accreting material from the DSO/G2. This may put some constrains on the physical properties of the G2 object and the ambient medium inside the Bondi radius of this SMBH.

*Acknowledgements.* This work has been financially supported by the Programme National Hautes Énergies (PNHE). The research leading to these results has received funding from the European Union Seventh Framework Program (FP7/2007-2013) under grant agreement No. 312789. The *XMM-Newton* project is an ESA Science Mission with instruments and contributions directly funded by ESA Member States and the USA (NASA). This work is based on observations

made with the NASA/ESA *Hubble* Space Telescope obtained at the Space Telescope Science Institute, which is operated by the Association of Universities for Research in Astronomy, Inc., under NASA contract NAS 5-26555. These HST observations are associated with programs 13403 and 13316. This work is based on observations made with ESO Telescopes at the Paranal Observatory under programs 091.B-0183(H), 092.B-0920(A) and 093.B-0932(A). *Karl G. Jansky* Very Large Array (VLA) of the National Radio Astronomy Observatory is a facility of the National Science Foundation, operated under a cooperative agreement by Associated Universities, Inc. Support for CARMA construction was derived from the states of California, Illinois, and Maryland, the James S. McDonnell Foundation, the Gordon and Betty Moore Foundation, the Kenneth T. and Eileen L. Norris Foundation, the University of Chicago, the Associates of the California Institute of Technology, and the National Science Foundation. Ongoing CARMA development and operations are supported by the National Science Foundation under a cooperative agreement, and by the CARMA partner universities.

## References

Alexander, T. 1997, in Astronomical Time Series, eds. D. Maoz, A. Sternberg, & E. M. Leibowitz, Astrophys. Space Sci. Libr., 218, 163
Baganoff, F. K., Bautz, M. W., Brandt, W. N., et al. 2001, Nature, 413, 45
Baganoff, F. K., Maeda, Y., Morris, M., et al. 2003, ApJ, 591, 891
Barrière, N. M., Tomsick, J. A., Baganoff, F. K., et al. 2014, ApJ, 786, 46
Bonnet, H., Abuter, R., Baker, A., et al. 2004, The Messenger, 117, 17
Bower, G. C., Deller, A., Demorest, P., et al. 2015a, ApJ, 798, 120
Bower, G. C., Markoff, S., Dexter, J., et al. 2015b, ApJ, 802, 69
Brinkerink, C. D., Falcke, H., Law, C. J., et al. 2015, A&A, 576, A41
Burkert, A., Schartmann, M., Alig, C., et al. 2012, ApJ, 750, 58
Coti Zelati, F., Rea, N., Papitto, A., et al. 2015, MNRAS, 449, 2685
Cotton, W. D. 2008, PASP, 120, 439
Degenaar, N., Reynolds, M., Miller, J. M., Kennea, J., & Wijnands, R. 2013, The Astronomer's Telegram, 5006, 1
Dodds-Eden, K., Porquet, D., Trap, G., et al. 2009, ApJ, 698, 676
Dressel, L. 2012, Wide Field Camera 3 Instrument Handbook for Cycle 21 v. 5.0 (Baltimore: STScI)
Eatough, R. P., Falcke, H., Karuppusamy, R., et al. 2013, Nature, 501, 391
Eckart, A., & Duhoux, P. R. M. 1991, in ASP Conf. Ser. 14, ed. R. Elston, 336
Eckart, A., Baganoff, F. K., Schödel, R., et al. 2006, A&A, 450, 535
Eckart, A., Schödel, R., García-Marín, M., et al. 2008, A&A, 492, 337
Eckart, A., García-Marín, M., Vogel, S. N., et al. 2012a, J. Phys. Conf. Ser., 372, 012022
Eckart, A., García-Marín, M., Vogel, S. N., et al. 2012b, A&A, 537, A52
Eckart, A., Mužić, K., Yazici, S., et al. 2013, A&A, 551, A18
Eisenhauer, F., Abuter, R., Bickert, K., et al. 2003, in Instrument Design and Performance for Optical/Infrared Ground-based Telescopes, eds. M. Iye, & A. F. M. Moorwood, SPIE Conf. Ser., 4841, 1548
Eisenhauer, F., Genzel, R., Alexander, T., et al. 2005, ApJ, 628, 246
ESA: XMM-Newton SOC 2013, *XMM-Newton* Users Handbook, issue 2.11
Falcke, H., & Markoff, S. B. 2013, Class. Quant. Grav., 30, 244003
Falcke, H., Goss, W. M., Matsuo, H., et al. 1998, ApJ, 499, 731
Fay, M. P. 2010, The R Journal, 2, 53
Feigelson, E. D., & Babu, G. J. 2012, Modern statistical method for astronomy with R applications (Cambridge, UK: Cambridge University Press)
Foreman-Mackey, D., Hogg, D. W., Lang, D., & Goodman, J. 2013, PASP, 125, 306
Garmire, G. P., Bautz, M. W., Ford, P. G., Nousek, J. A., & Ricker, Jr., G. R. 2003, in X-Ray and Gamma-Ray Telescopes and Instruments for Astronomy, eds. J. E. Truemper, & H. D. Tananbaum, SPIE Conf. Ser., 4851, 28
Gehrels, N. 1986, ApJ, 303, 336
Genzel, R., Schödel, R., Ott, T., et al. 2003, Nature, 425, 934
Genzel, R., Eisenhauer, F., & Gillessen, S. 2010, Rev. Mod. Phys., 82, 3121
Ghez, A. M., Salim, S., Weinberg, N. N., et al. 2008, ApJ, 689, 1044
Ghizzardi, S. 2002, In flight calibration of the PSF for the pn camera (EPIC-MCT-TN-012)
Gillessen, S., Eisenhauer, F., Fritz, T. K., et al. 2009, ApJ, 707, L114
Gillessen, S., Genzel, R., Fritz, T. K., et al. 2012, Nature, 481, 51
Gillessen, S., Genzel, R., Fritz, T. K., et al. 2013a, ApJ, 763, 78
Gillessen, S., Genzel, R., Fritz, T. K., et al. 2013b, ApJ, 774, 44
Goodman, J., & Weare, J. 2010, Comm. Appl. Math. Comput. Sci., 5, 65
Guainazzi, M. 2013, *XMM-Newton* Calibration Technical Note; XMM-SOC-CAL-TN-0018, ESA-ESAC
Haggard, D., Baganoff, F. K., Rea, N., et al. 2014, ATel, 6242, 1
Helene, O. 1983, Nucl. Inst. Meth. Phys. Res., 212, 319
Houck, J. C. 2013, ISIS 1.0 Technical Manual, Chandra X-Ray Observatory Center, MIT Center for Space Research One Hampshire St. Building NE80 Cambridge, MA 021394307 USA
Kaspi, V. M., Archibald, R. F., Bhalerao, V., et al. 2014, ApJ, 786, 84
Kennea, J. A., Burrows, D. N., Kouveliotou, C., et al. 2013, ApJ, 770, L24
Kraft, R. P., Burrows, D. N., & Nousek, J. A. 1991, ApJ, 374, 344
Lang, K. R. 1999, Astrophysical Formulae, 3rd edn., Vol. 1 (Springer)
Lynch, R. S., Archibald, R. F., Kaspi, V. M., & Scholz, P. 2015, ApJ, 806, 266
Marrone, D. P., Baganoff, F. K., Morris, M. R., et al. 2008, ApJ, 682, 373
Marscher, A. P. 1983, ApJ, 264, 296
Mori, K., Gotthelf, E. V., Zhang, S., et al. 2013, ApJ, 770, L23
Morris, M. 2012, Nature, 481, 32
Mossoux, E., Grosso, N., Vincent, F. H., & Porquet, D. 2015a, A&A, 573, A46
Mossoux, E., Grosso, N., Vincent, F. H., & Porquet, D. 2015b, A&A, 580, C2
Narayan, R., Mahadevan, R., Grindlay, J. E., Popham, R. G., & Gammie, C. 1998, ApJ, 492, 554
Neilsen, J., Nowak, M. A., Gammie, C., et al. 2013, ApJ, 774, 42
Nowak, M. A., Neilsen, J., Markoff, S. B., et al. 2012, ApJ, 759, 95
Park, J.-H., Trippe, S., Krichbaum, T. P., et al. 2015, A&A, 576, L16
Petrov, L., Kovalev, Y. Y., Fomalont, E. B., & Gordon, D. 2011, AJ, 142, 35
Pfuhl, O., Gillessen, S., Eisenhauer, F., et al. 2015, ApJ, 798, 111
Ponti, G., De Marco, B., Morris, M. R., et al. 2015, MNRAS, 454, 1525
Porquet, D., Predehl, P., Aschenbach, B., et al. 2003, A&A, 407, L17
Porquet, D., Grosso, N., Predehl, P., et al. 2008, A&A, 488, 549
Predehl, P., & Schmitt, J. H. M. M. 1995, A&A, 293, 889
Pych, W. 2004, PASP, 116, 148
Rauch, C., Ros, E., Krichbaum, T. P., et al. 2016, A&A, 587, A37
Rea, N., Esposito, P., Pons, J. A., et al. 2013, ApJ, 775, L34
Reid, M. J., Readhead, A. C. S., Vermeulen, R. C., & Treuhaft, R. N. 1999, ApJ, 524, 816
Scargle, J. D. 1998, ApJ, 504, 405
Scargle, J. D., Norris, J. P., Jackson, B., & Chiang, J. 2013a, ApJ, 764, 167
Scargle, J. D., Norris, J. P., Jackson, B., & Chiang, J. 2013b, in The Bayesian Block Algorithm, 2012 Fermi Symp. Proc. – eConf C121028 (version 1) [arXiv:1304.2818]
Schartmann, M., Burkert, A., Alig, C., et al. 2012, ApJ, 755, 155
Schödel, R., Ott, T., Genzel, R., et al. 2002, Nature, 419, 694
Schödel, R., Najarro, F., Muzic, K., & Eckart, A. 2010, A&A, 511, A18
Shakura, N. I., & Sunyaev, R. A. 1973, A&A, 24, 337
Silverman, B. W. 1986, Density Estimation for Statistics and Data Analysis, ed. C. Hall (Chapman & Hall)
Smajić, S., Moser, L., Eckart, A., et al. 2014, A&A, 567, A119
Sokal, A. 1997, in Functional Integration, eds. C. DeWitt-Morette, P. Cartier, & A. Folacci (Springer US), NATO ASI Ser., 361, 131
Strüder, L., Briel, U., Dennerl, K., et al. 2001, A&A, 365, L18
Trap, G., Goldwurm, A., Dodds-Eden, K., et al. 2011, A&A, 528, A140
Tsuboi, M., Asaki, Y., Kameya, O., et al. 2015, ApJ, 798, L6
Turner, M. J. L., Abbey, A., Arnaud, M., et al. 2001, A&A, 365, L27
Valencia-S., M., Eckart, A., Zajaček, M., et al. 2015, ApJ, 800, 125
Van der Laan, H. 1966, Nature, 211, 1131
Verner, D. A., Ferland, G. J., Korista, K. T., & Yakovlev, D. G. 1996, ApJ, 465, 487
Wardle, M. 2011, in The Galactic Center: a Window to the Nuclear Environment of Disk Galaxies, eds. M. R. Morris, Q. D. Wang, & F. Yuan, ASP Conf. Ser., 439, 450
Wilms, J., Allen, A., & McCray, R. 2000, ApJ, 542, 914
Witzel, G., Eckart, A., Bremer, M., et al. 2012, ApJS, 203, 18
Witzel, G., Ghez, A. M., Morris, M. R., et al. 2014a, ApJ, 796, L8
Witzel, G., Morris, M., Ghez, A., et al. 2014b, in IAU Symp. 303, eds. L. O. Sjouwerman, C. C. Lang, & J. Ott, 274
Worpel, H., & Schwope, A. D. 2015, A&A, 578, A80
Yuan, F., & Narayan, R. 2014, ARA&A, 52, 529
Yuan, F., Quataert, E., & Narayan, R. 2003, ApJ, 598, 301
Yusef-Zadeh, F., Roberts, D., Wardle, M., Heinke, C. O., & Bower, G. C. 2006a, ApJ, 650, 189
Yusef-Zadeh, F., Wardle, M., Roberts, D. A., et al. 2006b, BAAS 38, 1062
Yusef-Zadeh, F., Wardle, M., Heinke, C., et al. 2008, ApJ, 682, 361
Yusef-Zadeh, F., Bushouse, H., Wardle, M., et al. 2009, ApJ, 706, 348
Yusef-Zadeh, F., Wardle, M., Dodds-Eden, K., et al. 2012, AJ, 144, 1
Yusef-Zadeh, F., Roberts, D. A., Bushouse, H., et al. 2014, ApJ, 792, L1
Yusef-Zadeh, F., Diesing, R., Wardle, M., et al. 2015, ApJ, 811, L35
Zajaček, M., Karas, V., & Eckart, A. 2014, A&A, 565, A17
Zhao, J.-H. 2003, Astron. Nachr. Suppl., 324, 355

A&A 589, A116 (2016)

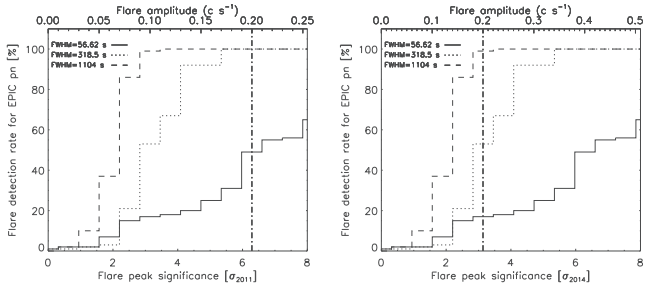


**Fig. A.1.** Comparison of the flare detection level with the non-flaring level corresponding to those of the 2011 (*left panel*) and February 2014 (*right panel*) observations. The vertical doted-dashed line represents an example flare with the same amplitude above the non-flaring level for a 2011 and 2014 Feb.−Apr. observations.

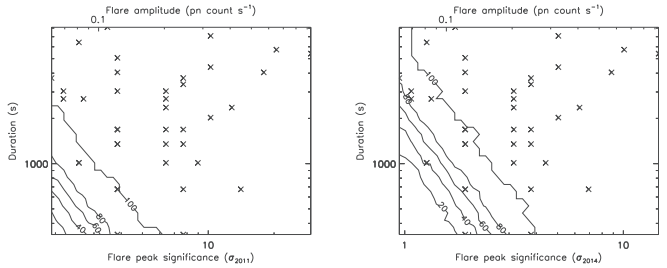


**Fig. A.2.** Flare distribution seen by *Chandra* and the detection probability of the Bayesian-blocks algorithm during an observation with *XMM-Newton*. The crosses are the X-ray flares detected during the *Chandra XVP* campaign of 2012. *Left panel*: the flare amplitude above the non-flaring level seen by EPIC/pn during the 2011 campaign. *Right panel*: the flare amplitude above the non-flaring level seen by EPIC/pn during the 2014 Feb. 28 observation.

## Appendix A: The magnetar impact on the flare detection efficiency

The contamination of the non-flaring level of Sgr A* by the Galactic center magnetar implies a decrease of the detection level of the faintest and shortest flares. To assess the impact on our flare detection efficiency, we examine the flare detection rate (Fig. B.1. of Mossoux et al. 2015a) versus the flare peak significance, i.e., the amplitude of the flare expressed in units of the standard deviation of the non-flaring level. This scaling allows the comparison of observations with different non-flaring levels. The flares used in these simulations have a Gaussian shape whose the Full Width at Half Maximum (FWHM) corresponds to the shortest, mean, and longest duration flares observed during the *Chandra XVP* campaign of 2012 (Neilsen et al. 2013). In Fig. A.1, we show the flare detection rate for the 2011 (left panel) and 2014 Feb. 28 (right panel) non-flaring levels for a false detection probability of $p_1 = \exp(-3.5)$.

We can see that because the non-flaring level in the 2014 Feb. 28 light curve has increased by a factor of about three by comparison with the 2011 campaign, the standard deviation is increased by a factor of about $\sqrt{3}$. For example, if we consider a flare with an amplitude of 0.2 count s$^{-1}$ above the non-flaring level, this corresponds to a peak significance of 6.3$\sigma$ for the 2011 light curves and this Gaussian shape flare is always detected if its duration is ∼320 s (FWHM). A flare with the same amplitude in the 2014 Feb. 28 light curve corresponds to 3.2$\sigma$ and is only detected with a probability of 53%.

In order to assess how many flares we cannot detect due to the magnetar contamination, we create a trial sample of flares following the duration and amplitude distribution determined during the *Chandra XVP* campaign of 2012 (Neilsen et al. 2013). We first compute a grid of 30 flare amplitudes and 30 flare durations in the range [0.06−0.4] count s$^{-1}$ and [337.5−8100] s, respectively, regularly distributed in the logarithmic scale. For each point of the grid, we create 300 Gaussian flares characterized by the corresponding amplitude and duration (which is two times the standard deviation of the Gaussian). We then apply the Bayesian blocks algorithm on all these flares superimposed above a non-flaring level corresponding to those of the 2011 *XMM-Newton* campaign seen with pn and each 2014 pn observation. By computing how many flares are detected among the 300 simulated flares, we estimate the probability to detect a flare with a certain amplitude and duration.

Because Neilsen et al. (2013) detect 45 flares during a total time of 2983.93 ks using the Bayesian-blocks method, we randomly select 100 sets of 45 flares following the amplitudes and durations distribution given by Neilsen et al. (2013), i.e, $\mathrm{d}N/\mathrm{d}CR_{\rm Ch} = 0.7\,CR_{\rm Ch}^{-1.9}\mathrm{e}^{-CR_{\rm Ch}/0.3}$ and $\mathrm{d}N/\mathrm{d}T = 0.05T^{-0.1}\mathrm{e}^{-T/3000}$ with $CR_{\rm Ch}$ the peak count rate as observed by *Chandra* and $T$ the flare duration[9]. In order to convert the *Chandra* count rate to the *XMM-Newton* count rate ($CR_{\rm XMM}$), we can use the relation derived in Mossoux et al. (2015a) between the Chandra HETG count rate (zero and first order) of the flare peak and the unabsorbed luminosity at the peak flare, i.e., $L^{\rm unabs}_{2-10\,\rm keV}/10^{34}\,\mathrm{erg\,s^{-1}} = -0.031 + 136.7CR_{\rm Ch}$. This unabsorbed luminosity is obtained with the spectral index $\Gamma = 2$ and the hydrogen column density $N_{\rm H} = 14.3 \times 10^{22}$ cm$^{-2}$ (Neilsen et al. 2013). We determine with the arf and rmf files of pn a count rate to unabsorbed luminosity ratio of $2.96 \times 10^{-36}$ pn count s$^{-1}$/erg s$^{-1}$. We can thus convert the *Chandra* count rate to the pn count rate assuming the same spectral parameters. Since each flare can be associated to a detection probability between 0 and 1, the sum of the probability for the 45 flares give us the total number of flares that can be detected in average by the Bayesian-blocks method during a pn observation with an exposure time of $2.98393 \times 10^6$ s. The distribution of the flare duration and amplitude seen during the *Chandra XVP* campaign and the detection probability of the Bayesian-blocks algorithm is shown in Fig. A.2. The left and right panels if this figure represents the detection probability corresponding to the mean non-flaring level seen by *XMM-Newton* during the 2011 campaign and to those observed during the 2014 Feb. 28 observation, respectively.

The mean of the number of detected flares for the 100 sets shows that considering the non-flaring level of the 2011 campaign, we can detect 85.4% of the flares detected during the *Chandra XVP* campaign. The non-detected flares are the faintest and shortest ones. For the 2014 Feb. 28, Mar. 10, Apr. 2 and Apr. 3, we detect 79.2%, 79.4%, 80.1% and 79.8% of the flares detected during the *Chandra XVP* campaign, respectively. Therefore, we estimate that we missed about 20.4% of the flares from Sgr A*. Since we detected three flares this means that we lost no more than one flare.

[9] The cutoff value is given as a lower limit in Neilsen et al. (2013) but the specific value does not influence the result of our flare distribution because we are interested by flares characterized by small amplitude and short duration since these flares may suffer of the small detection rate.

**Table B.1.** Period and period derivative taken from the literature and from this work.

| References | Period (s) | Period derivative (s s$^{-1}$) | Period second derivative (s$^{-1}$) | Epoch[a] (MJD) | Period on 56716 (MJD)[b] (s) | Period derivative on 56716 (MJD)[c] (s s$^{-1}$) |
|---|---|---|---|---|---|---|
| Mori et al. (2013) | $3.76354455 \pm 7.1 \times 10^{-7}$ | $6.5 \times 10^{-12} \pm 1.4 \times 10^{-12}$ | | 56409.2657 | $3.7637 \pm 6.18 \times 10^{-2}$ | |
| Rea et al. (2013) | $3.7635537 \pm 2 \times 10^{-7}$ | $6.61 \times 10^{-12} \pm 4 \times 10^{-14}$ | | 56424.55 | $3.76372 \pm 1.78 \times 10^{-3}$ | |
| Kaspi et al. (2014) | $3.76363824 \pm 1.3 \times 10^{-7}$ | $1.385 \times 10^{-11} \pm 1.5 \times 10^{-13}$ | $3.9 \times 10^{-19} \pm 6 \times 10^{-20}$ | 56513 | $3.7639871 \pm 6.2 \times 10^{-6}$ | $2.05 \times 10^{-11} \pm 1.1 \times 10^{-12}$ |
| Coti Zelati et al. (2015) A | $3.76363799 \pm 7 \times 10^{-8}$ | $1.360 \times 10^{-11} \pm 6 \times 10^{-14}$ | $3.7 \times 10^{-19} \pm 2 \times 10^{-20}$ | 56513 | $3.7639903 \pm 1.1 \times 10^{-6}$ | $2.089 \times 10^{-11} \pm 3.5 \times 10^{-13}$ |
| Coti Zelati et al. (2015) B | $3.7639772 \pm 1.2 \times 10^{-6}$ | $3.27 \times 10^{-11} \pm 7 \times 10^{-13}$ | | 56710 | $3.7639942 \pm 1.3 \times 10^{-6}$ | |
| This work[d] | $3.76398106^{+2.0\times10^{-7}}_{-2.1\times10^{-7}}$ | $3.7684 \times 10^{-11}{}^{+9.9\times10^{-14}}_{-1.6\times10^{-13}}$ | | 56716 | $3.76398106^{+2.0\times10^{-7}}_{-2.1\times10^{-7}}$ | $3.7684 \times 10^{-11}{}^{+9.9\times10^{-14}}_{-1.6\times10^{-13}}$ |

**Notes.** [(a)] Reference epoch for computing the parameters. MJD = TJD+40 000 days = JD-2 400 000.5 days. [(b)] The period on $t$ = 56 716 (MJD) is computed using $P = P_0 + \dot{P}_0(t - t_0) + \ddot{P}_0(t - t_0)^2$ with $P_0$, $\dot{P}_0$, $\ddot{P}_0$ the period, period derivative and period second derivative given in the literature, $t_0$ the reference epoch in the literature. Errors are propagated until $t$ = 56 716 (MJD) thanks to $\mathrm{d}P^2 = \sum(\partial P/\partial p)^2\,\mathrm{d}p^2$. [(c)] The period derivative on $t$ = 56 716 (MJD) is computed using $\dot{P} = \dot{P}_0 + \ddot{P}_0(t - t_0)$ with the definitions given above. [(d)] The errors are the 90% confidence interval (see left panel of Fig. B.2).

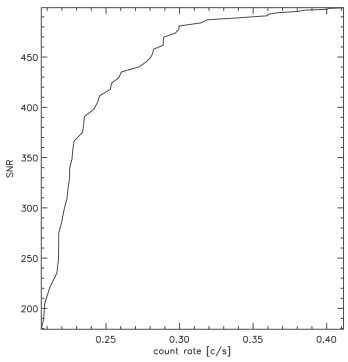


**Fig. B.1.** Evolution of the $S/N$ as a function of $CR_{\mathrm{th}}$.

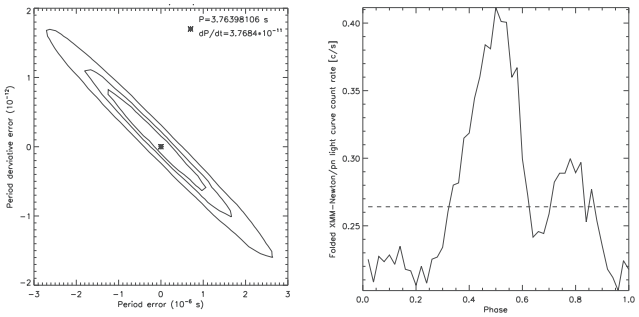


**Fig. B.2.** *Left panel*: $\chi^2$ distribution of the period and period derivative of the magnetar. The contours are the 68%, 90% and 99% of confidence level on the parameters. *Right panel*: folded light curve on the four *XMM-Newton* observations with our best fit parameters (see Table B.1).

## Appendix B: Filtering out of the magnetar pulsed emission

To filter out the magnetar contamination, we first computed the period ($P$) and period ($\dot{P}$) derivative of SGR J1745-29 by folding the light curve of all *XMM-Newton* observations of this campaign in which gaps between observations, GTI and exposure correction were taken into account. The relation between events arrival times $t$ in the barycentric referential (computed using the SAS task `barycen`) and the magnetar phase can be written as a Taylor series on the time:

$$\phi(t) = \phi_0 + \frac{t - t_0}{P} - 0.5\,\frac{(t - t_0)^2}{P^2}\,\dot{P}\,, \tag{B.1}$$

with $t_0$ the start time of the first *XMM-Newton* observation and $\phi_0$ an arbitrary phase. We choose $\phi_0$ in order to have the maximum of the pulse at $\phi$ = 0.5. A $\chi^2$ fitting with a constant function was applied on the folded light curve. The maximum $\chi^2$ give us the better period and period derivative and the corresponding $1\sigma$ errors which are reported on Table B.1. The confidence level of the $\chi^2$ distribution for these two parameters is given in Fig. B.2 (left panel). A comparison with the parameters derived from the literature is also shown. For this comparison, we use the period and period derivative given in Table B.1. The folded light curve for these parameters is represented in Fig. B.2 (right panel). We consider only the EPIC/pn camera because it has a better time resolution (73.4 ms) than EPIC/MOS (2.6 s) (ESA: XMM-Newton SOC 2013).

We use this folded light curve to compute the count rate threshold which maximizes the signal-to-noise ratio. As the magnetar flux is an additional noise on the Sgr A* light curve, magnetar flux contribution at each phase ($\tau$) of the folded light curve is $N_{\mathrm{magnetar}}(\tau) = \int_0^{\tau}(CR_{\mathrm{fold}}(t) - CR_{\mathrm{Sgr\ A^*}})\,\mathrm{d}t$ with $CR_{\mathrm{fold}}$ the count rate of the folded light curve and $CR_{\mathrm{Sgr\ A^*}} = 0.10$ count s$^{-1}$ the non-flaring level of Sgr A* seen with pn (e.g., Mossoux et al. 2015a). The signal-to-noise ratio is

$$S/N = \frac{CR_{\mathrm{Sgr\ A^*}}\,\tau}{\sqrt{N_{\mathrm{magnetar}}(\tau)}}. \tag{B.2}$$

The phase $\tau$ which maximizes the *S/N* allows us to compute the corresponding count rate threshold ($CR_{\mathrm{th}}$). Figure B.1 shows that there is no optimum value of the count rate threshold maximizing the *S/N*. Thus, we consider a count rate threshold which filters out 50% of the magnetar flux. This threshold is 0.27 count s$^{-1}$ and keeps 50% of the observation time. Then, from $P$ and $\dot{P}$, the time interval during which the count rate of the folded light curve is lower than $CR_{\mathrm{th}}$ can be computed for all observations from Eq. (B.1). Thus we can construct a new GTI file which is the combination of the GTI file from the event list of pn (which contains the time interval during which the cameras do not observe) and the GTI file created by removing the magnetar pulse using the SAS task `gtimerge`.

## Appendix C: The two X-ray flares seen in EPIC/pn, MOS1 and MOS2 cameras

Figures C.1 shows the flare light curves obtained with EPIC on board *XMM-Newton* on 2014 Mar. 10 (left panels) and Apr. 2 (right panels). The Bayesian-blocks algorithm characterizes the 2014 Mar. 10 flare with two blocks in the pn light curve but only with one block in the MOS1 and MOS2 light curves. Moreover, the duration of the flares seen in each camera is different (see Table C.1). This can be explained by the lower number counts in

A&A 589, A116 (2016)

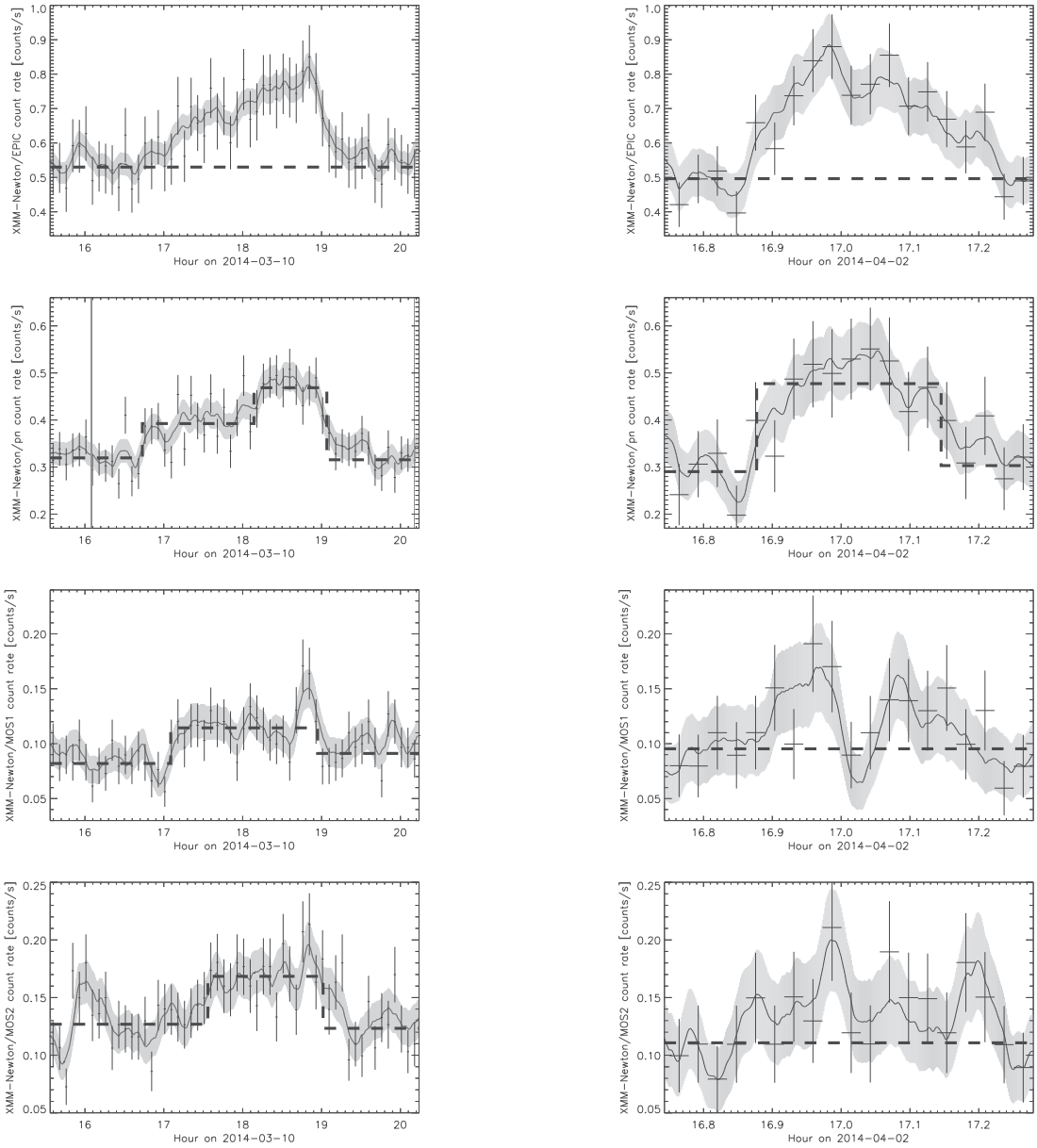


**Fig. C.1.** *XMM-Newton* light curve of the X-ray from Sgr A* in the 2−10 keV energy range. *Left panels*: the light curve of flare 1 on 2014 Mar. 10 flare binned on 500 s. *Right panels*: the light curve of flare 2 on 2014 Apr. 2 flare binned on 100 s. The total (pn+MOS1+MOS2) light curve is shown in the *top panel*. The light curves of EPIC/pn, MOS1 and MOS2 are shown in the *second, third and bottom panels*. The crosses are the data points of the total light curve. The horizontal dashed line and the solid line are the sum of the non-flaring level and the smoothed light curve for each instrument. The dashed lines represent the Bayesian blocks. The solid line and the gray curve are the smoothed light curve and the associated errors ($h$ = 500 and 100 s for flare 1 and 2, respectively). The vertical gray stripe is the time during which the camera did not observe.

MOS1 and MOS2 because of the RGS: the number of photons recorded by pn during the flare is larger and thus the accuracy on the determination of the beginning and end of the flare is better.

The flare on 2014 Apr. 2 is not detected by the Bayesian-blocks algorithm in MOS1 and MOS2 because the amplitude and the number of counts in this flare is rather small.

**Table C.1.** Characteristics of the X-ray flare observed by EPIC/MOS on 2014 Mar. 10.

| Instrument | Start time[a] (hh:mm:ss) | End time[a] (hh:mm:ss) | Duration (s) | Total[b] (counts) | Peak[c] (count $s^{-1}$) |
|---|---|---|---|---|---|
| MOS1 | 17:05:14 | 18:56:59 | 6705 | 780 ± 28 | 0.06 ± 0.02 |
| MOS2 | 17:33:32 | 19:01:11 | 5258 | 880 ± 30 | 0.07 ± 0.02 |

**Notes.** [(a)] Start and end times (UT) of the flare time interval defined by the Bayesian-blocks algorithm. [(b)] Total counts in the 2−10 keV energy band obtained in the smoothed light curve during the flare interval after subtraction of the non-flaring level obtained with the Bayesian-blocks algorithm. [(c)] Peak count rate in the 2−10 keV energy band at the flare peak (smoothed light curves) after subtraction of the non-flaring level.

The Astrophysical Journal, 800:125 (21pp), 2015 February 20 doi:10.1088/0004-637X/800/2/125
© 2015. The American Astronomical Society. All rights reserved.

# MONITORING THE DUSTY S-CLUSTER OBJECT (DSO/G2) ON ITS ORBIT TOWARD THE GALACTIC CENTER BLACK HOLE

M. Valencia-S.[1], A. Eckart[1,2], M. Zajaček[1,2,3], F. Peissker[1], M. Parsa[1], N. Grosso[4], E. Mossoux[4], D. Porquet[4], B. Jalali[1], V. Karas[3], S. Yazici[1], B. Shahzamanian[1], N. Sabha[1], R. Saalfeld[1], S. Smajic[1], R. Grellmann[1], L. Moser[1], M. Horrobin[1], A. Borkar[1], M. García-Marín[1], M. Dovčiak[3], D. Kunneriath[3], G. D. Karssen[1], M. Bursa[3], C. Straubmeier[1], and H. Bushouse[5]

[1] I. Physikalisches Institut der Universität zu Köln, Zülpicher Strasse 77, D-50937 Köln, Germany; mvalencias@ph1.uni-koeln.de
[2] Max-Planck-Institut für Radioastronomie, Auf dem Hügel 69, D-53121 Bonn, Germany
[3] Astronomical Institute of the Academy of Sciences Prague, Boční II 1401/1a, CZ-141 31 Praha 4, Czech Republic
[4] Observatoire Astronomique de Strasbourg, Université de Strasbourg, CNRS, UMR 7550, 11 Rue de l'Université, F-67000 Strasbourg, France
[5] Space Telescope Science Institute, Baltimore, MD 21218, USA
*Received 2014 October 30; accepted 2014 December 27; published 2015 February 18*

## ABSTRACT

We analyze and report in detail new near-infrared (1.45–2.45 $\mu$m) observations of the Dusty S-cluster Object (DSO/G2) during its approach to the black hole at the center of the Galaxy that were carried out with the ESO Very Large Telescope/SINFONI between 2014 February and September. Before 2014 May we detect spatially compact Br$\gamma$ and Pa$\alpha$ line emission from the DSO at about 40 mas east of Sgr A*. The velocity of the source, measured from the redshifted emission, is $2700 \pm 60$ km s$^{-1}$. No blueshifted emission above the noise level is detected at the position of Sgr A* or upstream of the presumed orbit. After May we find spatially compact Br$\gamma$ blueshifted line emission from the DSO at about 30 mas west of Sgr A* at a velocity of $-3320 \pm 60$ km s$^{-1}$ and no indication for significant redshifted emission. We do not detect any significant extension of the velocity gradient across the source. We find a Br$\gamma$ line FWHM of $50 \pm 10$ Å before and $15 \pm 10$ Å after the peribothron transit, i.e., no significant line broadening with respect to last year is observed. Br$\gamma$ line maps show that the bulk of the line emission originates from a region of less than 20 mas diameter. This is consistent with a very compact source on an elliptical orbit with a peribothron time passage in $2014.39 \pm 0.14$. For the moment, the flaring activity of the black hole in the near-infrared regime has not shown any statistically significant increment. Increased accretion activity of Sgr A* may still be upcoming. We discuss details of a source model according to which the DSO is a young accreting star rather than a coreless gas and dust cloud.

*Key words:* astrometry – black hole physics – Galaxy: center – line: identification – line: profiles – techniques: imaging spectroscopy

## 1. INTRODUCTION

Recently, the Galactic center region has attracted a lot of attention owing to the fact that a dusty object has been detected (Gillessen et al. 2012, 2013a; Eckart et al. 2013) that is approaching the central supermassive black hole (SMBH) associated with the radio source Sgr A*. As a result of its infrared (IR) excess and as indicated through nomenclature (G2) it has been speculated that the source consists of a dominant fraction of gas and dust (Gillessen et al. 2012, 2013a; Pfuhl et al. 2015). By now the object is expected to have passed through its peribothron and tidal disruption, and intense accretion events have been predicted. Eckart et al. (2013) show a possible spectral decomposition of this source using the *M*-band measurement by Gillessen et al. (2012). Depending on the relative stellar and dust flux density contributions, the *M*-band measurement is consistent with a dust temperature of 450 K and an integrated luminosity of up to $\sim 10\ L_{\odot}$. This allows for a substantial stellar contribution in mass and reddened stellar luminosity. A stellar nature is also favored by many other authors (see also Murray-Clay & Loeb 2012; Scoville & Burkert 2013; Ballone et al. 2013; Phifer et al. 2013; Zajaček et al. 2014). We will therefore refer to it in the following as a Dusty S-cluster Object, or DSO (Eckart et al. 2013). Hence, although the Br$\gamma$ line emission may be dominated by optically thin emission, a contribution from more compact optically thick regions cannot be excluded. Also, it is uncertain how large the extinction toward the center of the gas cloud really is. Therefore, the total mass of the object is very uncertain but is presumably less than that of a typical member of the high-velocity S-star cluster (i.e., $\lesssim 20\ M_{\odot}$; Ghez et al. 2003; Eisenhauer et al. 2005; Martins et al. 2006). The compactness of the DSO is also supported by the recent *L*-band detection close to peribothron (Ghez et al. 2014; Witzel et al. 2014).

Gillessen et al. (2013a, 2013b) and Pfuhl et al. (2015) report that the Br$\gamma$ luminosity of the DSO has remained constant over the entire time range covered by spectroscopy from 2004 to 2013. Figures 1 and 5 in Pfuhl et al. (2015) show that in their 2014 April data set the blue line emission is approximately as spatially compact as the red side and has a significantly stronger peak emission than the red line emission. Their derived integrated Br$\gamma$ luminosities for the blue side are about 1.14 times brighter than those for the red side (Section 3.2 in Pfuhl et al. 2015).

During the past year we have obtained a substantial, independent imaging spectroscopy data set using SINFONI at the ESO Very Large Telescope (VLT). In addition, we have re-reduced a large number of data sets available from the ESO archive and have used our own and published positional data to reestimate the orbit of the DSO. Here we present the results of this detailed investigation. The paper is organized in the following way: in Sections 2 and 3 we present the observations and data reduction, including the analysis of the spectral line properties of the DSO. In Section 4 we discuss the results, including the orbit (Section 4.1), the tidal interaction of the DSO with Sgr A*

(Section 4.2) and the ambient medium (Section 4.3), consequences for the flare activity (Section 4.4), and the interpretation of the DSO as a possible pre-main-sequence star (Section 4.5). After discussing the origin and fate of the DSO in Section 5, we summarize and conclude in Section 6.

## 2. OBSERVATIONS AND DATA REDUCTION

Here we present the data sets we are using in the study of the DSO. The procedures for data reduction and data quality selection are also described. We report mainly on the observations[6] we conducted from 2014 February to September. We use earlier archive data to discuss general properties like the DSO orbit.

### 2.1. The 2014 Data Set

We performed near-IR (NIR) integral field observations of the Galactic center using SINFONI at the VLT in Chile (Eisenhauer et al. 2003; Bonnet et al. 2004). The instrument is an image-slicer integral field unit fed by an adaptive optics (AO) module. The AO system uses an optical wavefront sensor that was locked on a bright star 15.″54 north and 8.″85 east of Sgr A*. We employed H+K grating that covers the 1.45–2.45 $\mu$m range with a spectral resolution of $R \sim 1500$ (i.e., approximately 200 km s$^{-1}$ at 2.16 $\mu$m). The 0.″8 × 0.″8 field of view was jittered around the position of the star S2, in such a way that the star remained within the upper half zone of the detector. This was done in order to avoid a region with possible nonlinear behavior of the detector. Observations of different B- and G-type stars were taken to obtain independent telluric templates.

The Galactic center region was observed in intervals of 400 s or 600 s, followed or preceded by time slots of equal length on a dark cloud 5′36″ north and 12′45″ west of Sgr A*. The integration times were chosen of that length in order to be able to also monitor the flux density of Sgr A* for time intervals of typical flare lengths and to provide a higher flexibility in data selection to optimize the quality of the data. Although this observational strategy reduces the effective integration time on source to about a third when compared with parsed sky observations at a rate of about once per hour, it ensures better control of the noise in the frames. Because of the variable weather conditions, the point-spread function (PSF) changed along the observing nights. The quality of individual exposures was judged based on the PSF at the moment of the observation, as measured from the shape of the stars in the field of view. For the analysis presented here, we have created two final data cubes, one from the combination of the best-quality exposures, and another including also medium-quality data, as described below. Table 1 shows the list of the observing dates, including the number of exposures that fulfilled the selection criteria. Note that (for both pre- and post-peribothron) our observations are bracketing and preceding those presented by Pfuhl et al. (2015).

### 2.2. Calibration

In the data reduction process, we first followed the SINFONI reduction manually to correct for the bad lines created by the data processing at the detector level. We used the suggested IDL procedure, adjusting the identification threshold (two times the background noise $\sigma_{\rm background}$) whenever necessary. A first cosmic-ray correction to the sky and target files was performed using the algorithm developed by Pych (2004). The random pattern introduced by some detector amplifiers was detected and removed in science and calibration files following the algorithms proposed by Smajić et al. (2014). Then we used the SINFONI pipeline for the standard reduction steps (like flat-fielding and bad pixel corrections) and wavelength calibration. We obtained one data cube for each on-source exposure.

DPUSER routines (Thomas Ott, MPE Garching; see also Eckart & Duhoux 1991) were used to flag remaining bad pixels and cosmic rays on the plane of the slitlets in the detector ($x$–$z$, which corresponds to declination–wavelength), in each data cube. The combined effects of the atmospheric refraction were appreciable as a spatial displacement of the stars by a couple of pixels when going from short to long wavelengths. Fixing the position of the center of a bright source at a particular wavelength and making a spatial subpixel shift at all other wavelengths could correct the problem, but the shape of the resulting spectrum in each pixel would depend on the interpolation algorithm. Therefore, to preserve the integrity of the spectrum in the narrow spectral regions where emission lines are present, the spatial image shift was done in steps of 0.045 $\mu$m.

A two-dimensional Gaussian, fitted to the bright star S2, was taken as an indication of the PSF. Cubes where the FWHM of the fitted Gaussian is less than 83 mas (or 6.65 pixels) were categorized as best-quality cubes, while those with FWHM values between 83 and 96 mas (or 7.65 pixels) were classified as medium-quality cubes. The combination of the selected data cubes was done by averaging every spatial and spectral pixel after a proper alignment of the images. The combination of the 63 best-quality cubes produced a final data cube with a total of 7.2 hr of on-source integration time. When including the 30 medium-quality exposures, the resulting data cube covers a total of 10.8 hr of integration time on-source. This second data cube was used to evaluate the effects of the data quality in the signal-to-noise ratio (S/N) of the measured quantities, and unless it is specifically mentioned in the text, all measurements and plots are derived from the higher-quality data cube.

Flux calibration was done using aperture photometry on a deconvolved $K$-band image created from the final data cube. The deconvolution was performed using the Lucy–Richardson algorithm incorporated in DPUSER, while the PSF was estimated using the IDL-based StarFinder routine (Diolaiti et al. 2000). We used as calibration stars S2 ($K_{\rm s} = 14.1$), S4 ($K_{\rm s} = 14.6$), S10 ($K_{\rm s} = 14.1$), and S12 ($K_{\rm s} = 15.2$) and adopted the $K$-band extinction correction $m_{A_K} = 2.46$ of Schödel et al. (2010); see also Witzel et al. (2012) for the flux estimation.

The NIR spectrum of the inner ∼0.″5 around Sgr A* is dominated by the stellar continuum of hundreds of stars fainter than $K_{\rm s} = 18$ mag that are part of the central cluster and that are unresolved with the current instrumentation (Sabha et al. 2012). Several absorption features from the stellar atmospheres can be recognized in the $HK$-band data. Line emission of ionized species (hydrogen and helium) at the position of the S-stars and all across the field is also substantial. We refer to the aggregate of all these components as background, and we show how it affects the detection of the faint emission of the DSO.

## 3. RESULTS

In summary, we find that both the line shape and line intensity in 2014 are very similar to those of the previous years. Before 2014 May we find no blue line emission from hydrogen or helium above the noise level. The red line center has shifted to a

[6] ESO programs 092.B-0009 (PI: A. Eckart), 093.B-0092 (PI: A. Eckart), and 092.B-0920 (PI: N. Grosso).

**Table 1**
Summary of the Galactic Center Observations

| Date | Start Time | End Time | Number of On-source Exposures | | | Exp. Time |
|---|---|---|---|---|---|---|
| (YYYY.MM.DD) | (UT) | (UT) | Total | Medium Quality | High Quality | (s) |
| 2014.02.28 | 08:34:58 | 09:54:37 | 7 | 0 | 0 | 400 |
| 2014.03.01 | 08:00:14 | 10:17:59 | 12 | 0 | 0 | 400 |
| 2014.03.02 | 07:49:06 | 08:18:54 | 3 | 0 | 0 | 400 |
| 2014.03.11 | 08:03:55 | 10:03:28 | 11 | 5 | 8 | 400 |
| 2014.03.12 | 07:44:35 | 10:07:45 | 13 | 5 | 9 | 400 |
| 2014.03.26 | 06:43:05 | 09:58:12 | 11 | 8 | 8 | 600 |
| 2014.03.27 | 06:32:50 | 10:04:12 | 18 | 1 | 7 | 400 |
| 2014.04.02 | 06:31:39 | 09:53:52 | 18 | 0 | 5 | 400 |
| 2014.04.03 | 06:20:46 | 09:45:02 | 18 | 14 | 17 | 400 |
| 2014.04.04 | 05:58:19 | 09:47:58 | 21 | 14 | 17 | 400 |
| 2014.04.06 | 07:51:42 | 08:43:15 | 5 | 4 | 1 | 400 |
| 2014.06.09 | 04:48:49 | 09:51:47 | 14 | 14 | 0 | 400 |
| 2014.06.10 | 04:54:21 | 09:49:49 | 5 | 5 | 0 | 400 |
| 2014.08.25 | 23:57:46 | 04:34:49 | 4 | 4 | 0 | 400 |
| 2014.09.07 | 00:11:08 | 04:20:07 | 2 | 2 | 0 | 400 |

**Notes.** List of start and end times and number and quality of exposures. ESO program 092.B-0009 for 2014.02.28, 2014.03.01, 2014.03.02, 2014.03.26, 2014.03.27, and 2014.04.06; ESO program 092.B-0920 for 2014.03.11, 2014.03.12, 2014.04.02, 2014.04.03, and 2014.04.04; and ESO program 093.B-0092 for 2014.06.09, 2014.06.10, 2014.08.25, and 2014.09.07. Pre- and post-peribothron measurements are separated by a horizontal line.

higher velocity of about $2700 \pm 60\,\mathrm{km\,s^{-1}}$ about 40 mas east of Sgr A*. In addition, we measure the Pa$\alpha$ 1.875 $\mu$m line between atmospheric absorption bands but find that the sky-subtracted He I (2.05 $\mu$m) is very weak, i.e., less than a fifth of the Br$\gamma$ line emission. In 2014 June our data do not allow us to detect the He I or Pa$\alpha$ line emission. Peribothron happened in 2014 May, and after that we see in 2014 June a blueshifted Br$\gamma$ line about 16 mas west of Sgr A* at $-3320\,\mathrm{km\,s^{-1}}$ and no red line emission. In 2014 June we find no blue line emission helium, Br$\gamma$, or Pa$\alpha$ above the noise level.

### 3.1. Redshifted Pre-peribothron Lines

In 2014, the Br$\gamma$ line emission from the DSO shifted to a spectral region where the emission and absorption features of the surroundings are very prominent. Moreover, the Pa$\alpha$ and the possible He I lines lie in a wavelength range where the atmospheric absorption plays a main role. Therefore, a proper background estimation and subtraction, as well as an adequate fitting and correction of the tellurics, are critical to detect and measure any emission from the DSO. The latter is expected to change from one day to the next, and also during one observing night if the weather conditions are unstable, but it is approximately the same across the field of view. The former, on the other hand, varies strongly across the field and significantly in periods of about 6 months, because of the high stellar proper motions. This means that, while the telluric absorption can be, in principle, fitted and corrected using extra observations of stars or sources in the field, the exact shape of the background spectrum at the position of the DSO cannot be known, but only approximated by using apertures in the field. A carefully calculated approximation to the background leads to a reliable estimation of the spectral properties of the source's line emission, as well as the spatial position and extension of the DSO emission.

#### 3.1.1. The Br$\gamma$ Emission Line

Figure 1 shows the spectrum integrated over apertures of radius 0.″05 at the position where the redshifted Br$\gamma$ emission from the DSO is strongest. It also shows the background spectra constructed from four different surrounding regions, as well as the resulting line emission after subtracting them from the source spectrum. In the left panels, the spatial pixels from which the spectra of the source and the background have been extracted are marked with blue crosses and pink filled squares, respectively. The Sgr A* position is marked with the big cross. The middle panels display the integrated spectrum at the DSO position (thick blue line) in comparison with the background spectra (thin pink line). The vertical dashed line at 2.166 $\mu$m marks the spectral position of the zero-velocity Br$\gamma$ line. Arrows at 2.076 $\mu$m and 2.185 $\mu$m indicate the approximate location of the DSO redshifted He I and Br$\gamma$ emission lines. The inset panel corresponds to the dashed-line box, which is a zoom-in to the spectra in the 2.18–2.20 $\mu$m range. The arrow in the inset panel marks again the position of the redshifted Br$\gamma$ line and highlights the importance of the background subtraction to recover the spectral properties of the emission. Because of the change of the spectral slope across the field of view, the overall shape of the spectrum extracted from the background area has to be slightly modified to better fit the continuum in the DSO aperture. To do that, we divide it by a third-order polynomial fitted to the ratio between the source spectrum and the spectrum of the background aperture. This is done using only the spectral windows marked with (green) crosses in the top panel of the middle column. Then, the background was scaled to best match the continuum emission around the spectral location of the Br$\gamma$ redshifted emission (i.e., at 2.173–2.183 $\mu$m and 2.195–2.220 $\mu$m). These spectra, with modified slope and scaled continuum, are used as an approximation of the background emission at the DSO position. They reproduce well most of the features in the source spectrum, as can be seen in the middle panels. Given that at wavelengths shorter than $\sim 2.08\,\mu$m the emission is highly absorbed by tellurics, we did not include this spectral region in the fit of the overall background spectral shape, but used only the selected spectral windows as described above. For this reason, the background continuum in the source aperture at $\lambda \lesssim 2.08\,\mu$m cannot be fitted properly and produces an excess of emission in the background-subtracted DSO spectra,

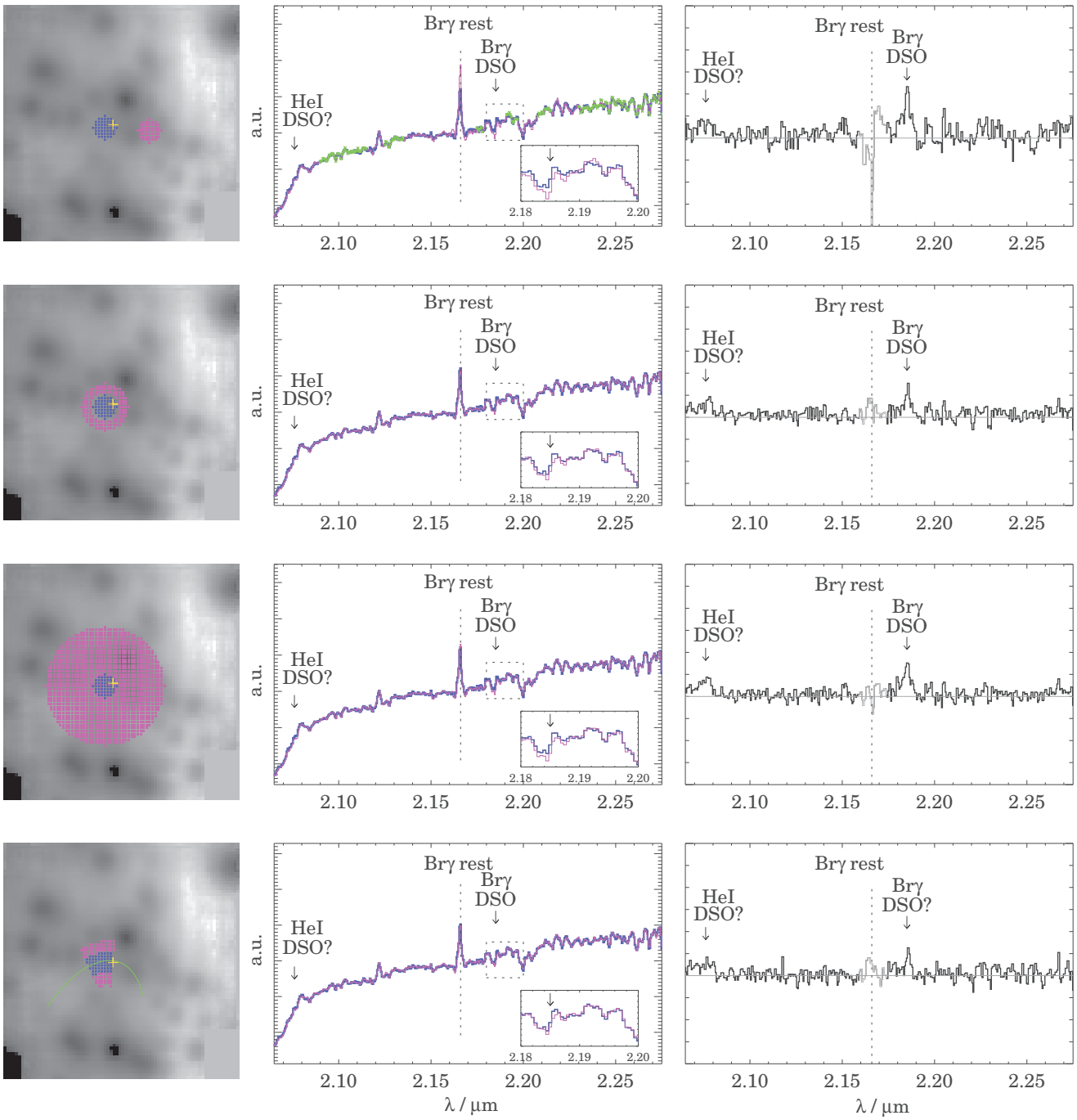


**Figure 1.** Br$\gamma$ redshifted emission of the DSO before May at 43 mas east and 5 mas south of Sgr A*. Left panels: 1 × 1 arcsec$^2$ SINFONI mosaic of the Galactic center region in 2014 February to April. DSO (blue crosses) and background (pink squares) apertures are shown. Middle panels: comparison between the DSO (thick line) and the background (thin line) spectra. Arrows mark the expected location of the redshifted He I and Br$\gamma$ lines. Right panels: results of the subtraction of the background from the DSO spectrum. The baseline is shown in gray. The vertical range of the plots corresponds to one unit in the middle panels; see details in the text.

which can be seen in the right panels. There, the large mismatch observed in the spectra in a range of 0.82 $\mu$m around the zero-velocity Br$\gamma$ line is due to strong variations of the ionized hydrogen emission in the central $r \sim 1''$ region. Lines within the telluric absorption region are treated differently to improve their signal strength; see Section 3.1.3.

The four examples shown in Figure 1 correspond to the cases when (1) the background is created from an aperture of the same size and shape as that of the source, and it is located just beside it. (2) Iris photometry is applied, i.e., the background aperture is a ring around the source aperture. In this case, the inner radius was chosen to be 0.″06, and the outer radius, 0.″11. (3) An averaged background is created from a region of radius 0.″25 at the source position that includes the DSO aperture. (4) The source emission is integrated in a segment of 0.″075 width taken along the best-fit elliptical orbit with a length of ∼0.″10 (see Section 4.1). The background is integrated from the 0.″048 width stripes above and below the source area. In all cases the

redshifted Br$\gamma$ line is detected with S/Ns between 3.9 (in the second case) and 4.7 (in the third one).

Fitting a Gaussian to the line emission in each case, we find a rather robust determination of the line peak at 2.185 $\mu$m, i.e., 2700 km s$^{-1}$ on average with a variation of 60 km s$^{-1}$. However, as can be noticed from Figure 1, the line profile changes depending on the subtracted background. The FWHM of the Br$\gamma$ line, corrected for instrumental broadening, is 730 km s$^{-1}$ in the first and third cases, 560 km s$^{-1}$ in the second one, and only 240 km s$^{-1}$ in the fourth one. Averaging over a dozen background-subtracted source apertures, the FWHM(Br$\gamma$) $\approx$ 720 $\pm$ 150 km s$^{-1}$, i.e., the line width is 50 $\pm$ 10 Å. The line flux changes, in general, by a factor of two owing to the background subtraction. In the first three examples shown in Figure 1, it is in the range 3.1–6.0 $\times$ 10$^{-16}$ erg s$^{-1}$ cm$^{-2}$, while in the last case it only reaches 1.7 $\times$ 10$^{-16}$ erg s$^{-1}$ cm$^{-2}$. For a distance of 8 kpc to the Galactic center, the average luminosity of the observed redshifted Br$\gamma$ line is 1.0 $\times$ 10$^{-3}$ $L_\odot$, and twice this value when integrating over a larger aperture of radius $r = 0\farcs075$.

In the last example in Figure 1 the recovered properties of the emission line are quite different from those of any other case, although the bulk of the source emission seems to be well within the aperture placed along the orbit, and it covers a very similar area to the circular aperture used in the first three cases: e.g., the line width in the last case is narrower and the line flux is only ~35% of that measured in any other background-subtracted spectrum. From this analysis, we call for precaution when measuring line properties along predetermined areas in the field of view.

#### 3.1.2. Position of the DSO

To confirm the position of the Br$\gamma$ emission, we removed the background emission in every pixel of the field of view following the procedure described above using the spectrum shown in the second example of Figure 1 as a background—as classical iris photometry makes unbiased and efficient use of the background in the immediate surrounding of the source. Then we integrated the residual flux in the range 2.181–2.193 $\mu$m. The result, shown in the top left panel of Figure 2, is an image of the excess flux, compared to the continuum, emitted by the source in this wavelength range. Fitting a Gaussian to this emission in every spatial pixel allows us to mask the areas where the flux within the line is less than 2$\times$ the noise level. When such a mask is applied (Figure 2, top right), the location of the DSO shown by its redshifted Br$\gamma$ emission is clearly revealed. The position of the DSO as indicated by the position of the brightest Br$\gamma$ peak in Figure 2 is 8.6 mas south and 41.5 mas east of Sgr A*.

#### 3.1.3. The He I and Pa$\alpha$ Emission Lines

The detection of Pa$\alpha$ 1.875 $\mu$m and He I 2.058 $\mu$m emission requires modeling of the atmospheric absorption. Although we observed some standard stars during the different runs to use them for the telluric modeling, the sky variation throughout the nights was large and the corrections unsatisfactory. The alternative is to use a bright star in the field, or a combination of some of them, as tracers of the telluric absorption. Figure 3 shows the case where the star S2 is used for this purpose. In the top panel, a comparison between the DSO spectrum and that of S2 is shown. The absorption features in the source spectrum around 1.9 $\mu$m are well approximated, but the overall shapes of both spectra differ from each other, as expected from the earlier discussion.

Following the common telluric correction procedure, the DSO spectrum is divided by the normalized telluric spectrum (in the case of Figure 3, that of S2). The same correction is applied to the background spectrum. Here we selected without preference the background shown in the third example of Figure 1. The resulting DSO spectrum, after the background correction, is still very noisy around 1.9 $\mu$m, but hints of the redshifted Pa$\alpha$ and He I are visible. The lines are observed with an S/N of about 2 in the case of helium and just above 1 in the case of Pa$\alpha$. The fact that Pa$\alpha$ is not observed with the expected strength (approximately 12 times brighter than Br$\gamma$, after extinction correction) is probably due to the low elevation of the Galactic center region in February–April, which resulted in stronger telluric absorption in this region. We fit the redshifted He I with a Gaussian to obtain the line properties. It peaks at 2.076 $\pm$ 0.078 $\mu$m, i.e., ~2650 $\pm$ 100 km s$^{-1}$ within the uncertainties at the same receding velocity as indicated by the Br$\gamma$ line. It also exhibits a similar width ~750 km s$^{-1}$. After correcting for extinction assuming $A_V \approx 26.8$ mag, we find He I/Br$\gamma$ ~ 0.6, consistent with models in which the emission is dominated by optically thin material (Gillessen et al. 2013b; Shcherbakov 2014).

However, this value must be taken with caution, given the low S/N of the lines and the high influence of the tellurics and background corrections in the measured line fluxes.

### 3.2. Blueshifted Pre-peribothron Lines

The blue side of the line emission would be extremely diluted if we observed the source very close to its peribothron position, and the radial velocity range would span almost 6000 km s$^{-1}$, significantly broadening the emission line and making it virtually impossible to detect. Only if the time span for such an event were of the order of a week (depending on the exact orbit) would observations immediately after our measurements have picked up significant blue line emission.

#### 3.2.1. No Detected Blue Br$\gamma$ Emission

Using a variety of apertures, we conducted a systematic search of the DSO blueshifted Br$\gamma$ emission along the portion of the orbit that lies upstream of the red emission. As we did not find blueshifted emission at the pre-peribothron position of the DSO, we extended our search to consecutive positioned apertures upstream of the 2014 April pre-peribothron position. Corresponding to the findings of Pfuhl et al. (2015), the blue line emission should have been the brightest line component in our data. If the blueshifted emission is compact, and at least half as bright as the redshifted one, we should be able to detect it with an S/N ~ 2.5 or higher.

Following the same approach presented in Section 3.1.1., i.e., subtracting background spectra created in different ways from the source spectrum, we aimed to find hints of the blueshifted component. The DSO spectrum was integrated from an aperture with the PSF size ($r = 0\farcs05$) that was placed several times in a grid mapping a squared area of 200 mas $\times$ 200 mas with Sgr A* at the northeast corner.

In this way we covered the large area to the west and to the south of Sgr A* where the approaching side of the DSO is expected to be found. We also searched for the blueshifted emission using slightly larger apertures to account for a possibly more extended emission that could be expected in case the source was not as compact as before the peribothron passage.

Figures 4 and 5 show two attempts at finding the Br$\gamma$ DSO emission in two different positions upstream of the best-fit

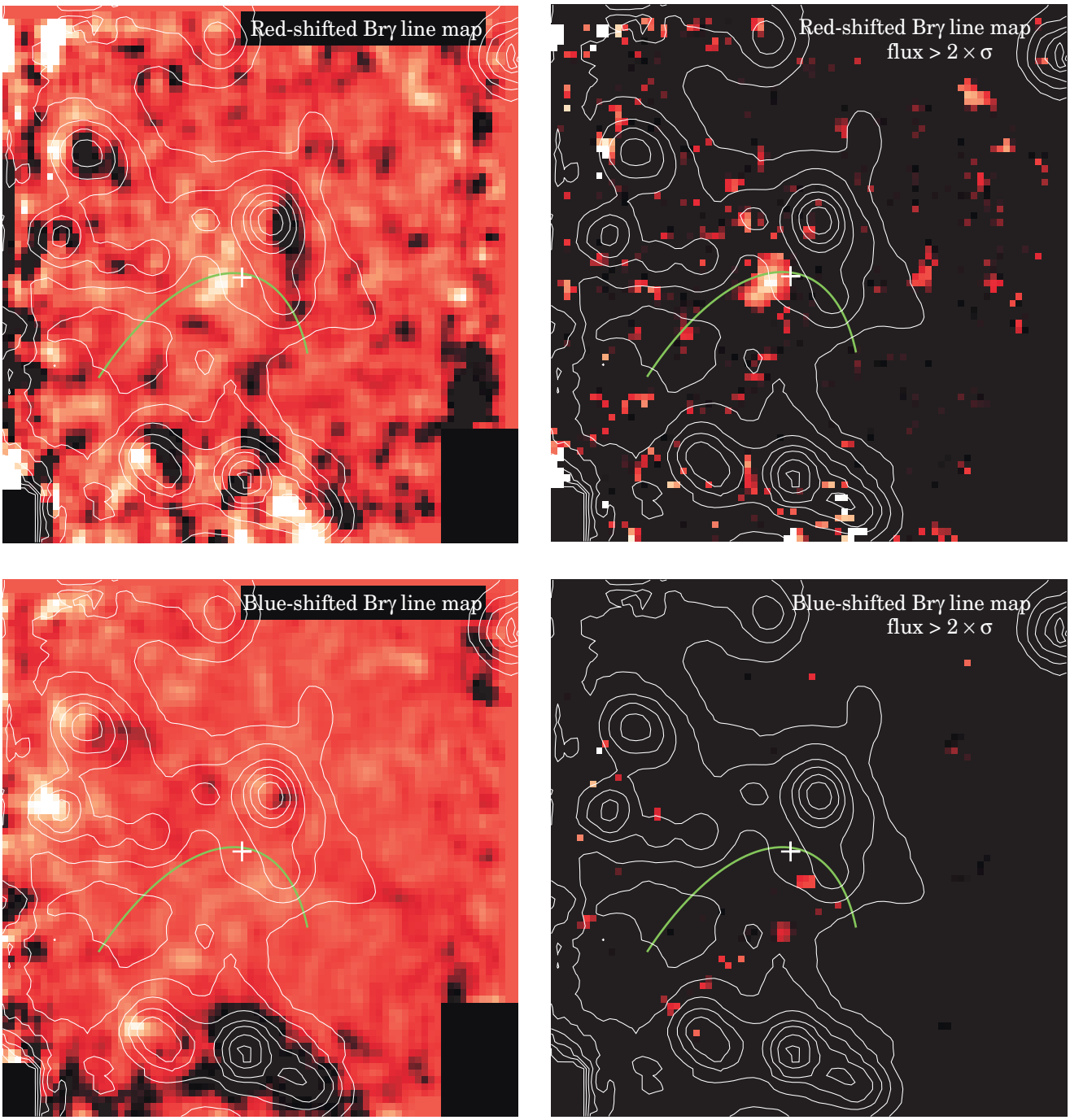


**Figure 2.** Br$\gamma$ line maps. Panels show $1.0 \times 1.0$ arcsec$^2$ of the Galactic center region in 2014 February–April. The cross marks the position of Sgr A*. The thick green line corresponds to the best-fit elliptical orbit. The *K*-band continuum contours depict the brightest S-cluster members. Top panels: DSO redshifted Br$\gamma$ line map. Left: integrated emission in a range of 120 Å around 2.185 $\mu$m after subtracting the background in every spatial pixel of the field of view. Right: same as left panel, but showing only emission that is brighter than $2\times$ the noise level. Bottom panels: blueshifted Br$\gamma$ line map. Left: integrated emission in a range of 120 Å around 2.147 $\mu$m, i.e., around the expected blueshifted Br$\gamma$ line emitted by a source approaching us at a speed of 2700 km s$^{-1}$. The background has been subtracted in every spatial pixel of the field of view. The color scale is the same as in the top panels. Right: same as left panel, but showing only emission brighter than $2\times$ the noise.

elliptical orbit. These are examples of the systematic search for the DSO Br$\gamma$ emission south/west of Sgr A*. The apertures are placed at the position (and one consecutive position) along the orbit at which Pfuhl et al. (2015) and earlier Gillessen et al. (2013b) had reported the detection of blueshifted line emission.

As in Figure 1, left panels show the size and position of the background and source apertures, middle panels compare the spectra extracted from them, and right panels present the subtraction of the two. The expected spectral positions of the blueshifted Br$\gamma$ and He I are derived assuming the emitting source to approach us after peribothron with a similar speed as the still receding part. The vertical range in the right panels is the same as the one used in Figure 1 and therefore can be directly compared. In case there is a source emitting a blueshifted line at any of these two positions, the line should be clearly visible in all four rows displayed within one figure. This is because, in

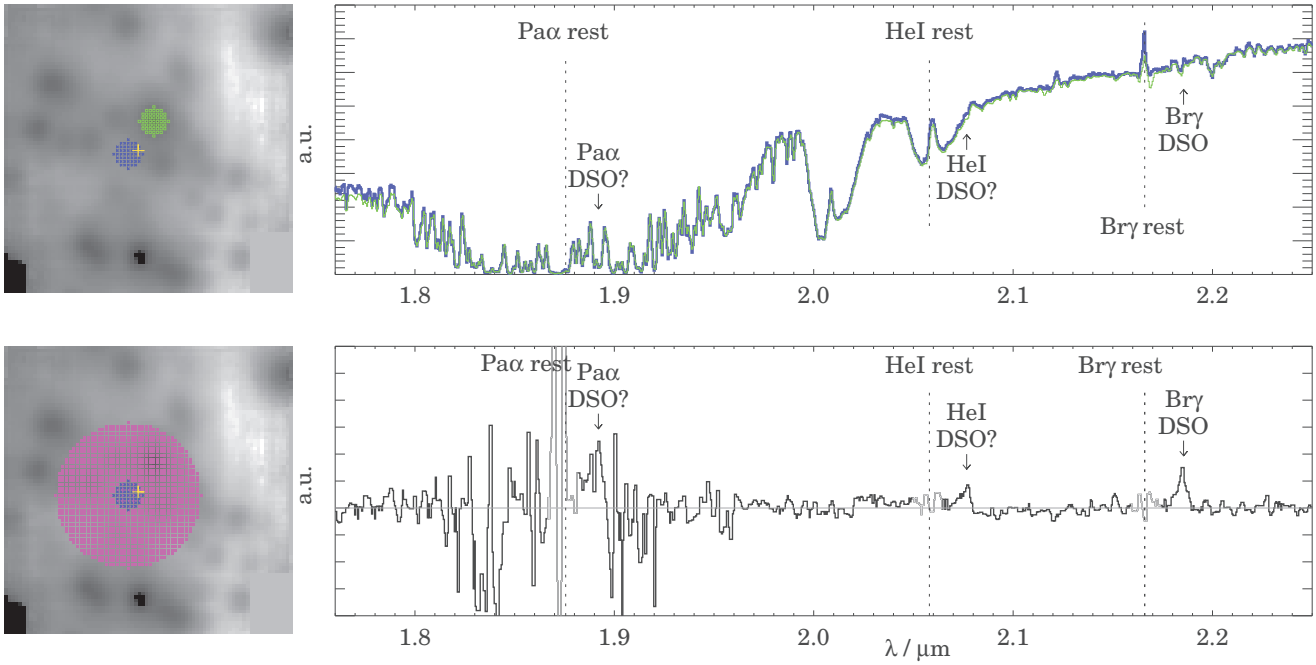


**Figure 3.** He I and Paα redshifted emission of the DSO before May. Top left: $1 \times 1$ arcsec$^2$ SINFONI mosaic of the Galactic center region in 2014 February–April. The DSO aperture is marked with blue crosses. The spectrum extracted from the aperture placed on S2, marked with empty green squares, is used to model the telluric absorption. Top right: comparison between the DSO spectrum (thick blue line) and the telluric model (thin green line). The positions of the zero-velocity hydrogen and helium lines are signaled with vertical dashed lines, while the expected positions of the redshifted emission lines from the DSO are indicated with the arrows. Bottom left: same as in left panels of Figure 1. Bottom right: results of the subtraction of the background from the DSO spectrum, after correcting both spectra for tellurics. Dashed lines and arrows are the same as above.

these four examples, the source spectrum is extracted from the same region and the only difference must be the S/N of the line, which depends on the subtracted background (we come back to this point in Section 3.2.3). Hence, we can rule out that there is a blue line similar to that seen on the redshifted side, despite the fact that the source should be similarly compact (see Figures 1 and 5 in Pfuhl et al. 2015 and comments in our introduction section).

### 3.2.2. Upper Limit for the Blueshifted Br$\gamma$ Line

Another strategy for searching a line emission is, as we did in previous sections, to subtract a background spectrum from the entire data cube and then integrate the remaining flux within narrow spectral windows around the expected wavelength. For this search we used different background spectra and integrated the residual flux in the range 2.143–2.151 $\mu$m. Figure 2 (bottom left) shows one example. We fitted a Gaussian to every spatial pixel to create a mask that selects those places where the flux is less than 2× the noise level. In the right panel of Figure 2 (bottom right), such a mask has been applied. We see possible hints of a spatially compact source at 37.5 mas west and 68.8 mas south of Sgr A* that is not located on the expected DSO orbit. Looking at the line properties, we find that on average the emission is very broad, with FWHM $> 2000$ km s$^{-1}$ (i.e., larger than 0.015 $\mu$m) and centroid at $\sim$2.149 $\mu$m. Assuming that the blueshifted Br$\gamma$ line emission is as wide as the redshifted one, i.e., 720 km s$^{-1}$, and with a noise in that spectral range of $\sim 2.9 \times 10^{-14}$ erg s$^{-1}$ cm$^{-2}$ $\mu$m$^{-1}$, we obtain an upper limit for the line flux of $\sim 4.7 \times 10^{-16}$ erg s$^{-1}$ cm$^{-2}$, i.e., a luminosity $L(\mathrm{Br}\gamma_{\mathrm{blue}}) < 1.0 \times 10^{-3}\, L_{\odot}$. Whether this emission is real, considering the multiple sources of noise, and whether it has some relation with the DSO is unknown. For the apertures placed along the orbit, the upper limit of a blueshifted Br$\gamma$ line flux is $\sim 2.8 \times 10^{-16}$ erg s$^{-1}$ cm$^{-2}$, which is about half of that of the redshifted line.

### 3.2.3. Influence of the Selected Background

There is no doubt that the subtraction of the background emission plays an important role in the detection of faint line emission. The usage of different background spectra from regions close to the position of interest is an effective tool to discriminate between a source line emission and the unlucky presence of a background feature at the studied wavelength. In the first row of Figures 6(a) and (b) we present examples of background that produce a spurious blueshifted Br$\gamma$ emission at positions far away from the expected orbit. The panels in the second row of each example show how, after selecting different background spectra, a very good overlap with the source spectrum is obtained and only noise remains after the subtraction. The aperture shown in Figure 6(a) is located at the position of the bright blob closest to Sgr A* in the bottom panels of Figure 2. The background-subtracted spectrum of this aperture was used above to estimate the upper limit for the blueshifted line. In this case, the S/N of the feature at $\sim$2.15 $\mu$m depends strongly not only on the background selected but also on the way it is scaled and subtracted. As we were not able to produce spurious detections on the red side, we conclude that those in the blue may result from an enhanced local variation of the background in this particular spectral range. Based on this analysis, we call for caution when studying line emission properties of faint sources in crowded fields.

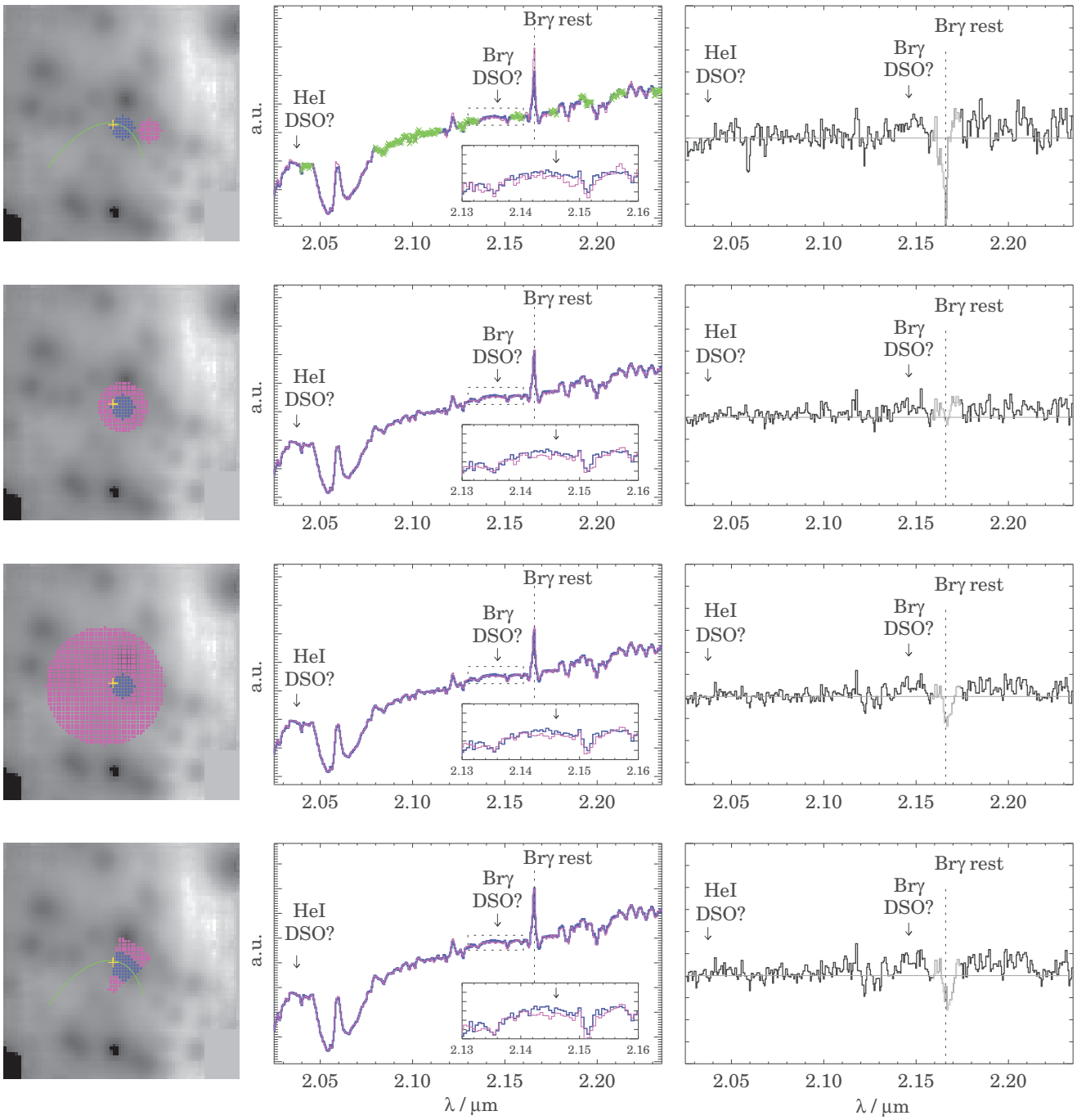


**Figure 4.** Nondetection of Br$\gamma$ blueshifted emission before May at a first upstream position at 43 mas east and about 11 mas south of Sgr A*. Left panels: same as Figure 1. Middle panels: comparison between the DSO (thick blue line) and the background (thin pink line) spectra. Arrows at 2.037 $\mu$m and 2.146 $\mu$m indicate the approximate location of the expected DSO blueshifted He I and Br$\gamma$ emission lines, in case the speed of the approaching component was the same as that of the receding one. The inset panel corresponds to the dashed-line box, which is a zoom-in to the spectra in the 2.13–2.16 $\mu$m range. The arrow in the inset panel marks again the position of the blueshifted Br$\gamma$ line. The spectral windows marked with crosses in the top panel are used to fit the slope of the background spectrum to that of the DSO. Right panels: results of the subtraction of the background from the DSO spectrum. The vertical range of the plots corresponds to one unit in the middle panels and spans the same range as in the right panels of Figure 1. The zero line is shown in gray.

### *3.3. Blueshifted Post-peribothron Br$\gamma$*

Figure 7 shows the spectrum integrated over an aperture of radius 0.″05 at the post-peribothron in 2014 June at a position of 16 mas west and about 6 mas south of Sgr A* at an S/N of 2.5–3.1 depending on the background subtraction. The line has a blueshifted center velocity of $-3320 \pm 60$ km s$^{-1}$ and, after correcting for spectral resolution, an FWHM of $15 \pm 10$ Å. Line flux and width were derived using several background corrections similar to what is shown in Figure 1. The Br$\gamma$ line luminosity is about $0.4 \times 10^{-3}\ L_{\odot}$. The narrow line estimate could be a result of the weak line detection; it could also point to a stellar nature of the source (see below).

The excess line emission can clearly be seen even before background subtraction in the inset of the middle top plot in Figure 7. Based on the post-peribothron observing dates

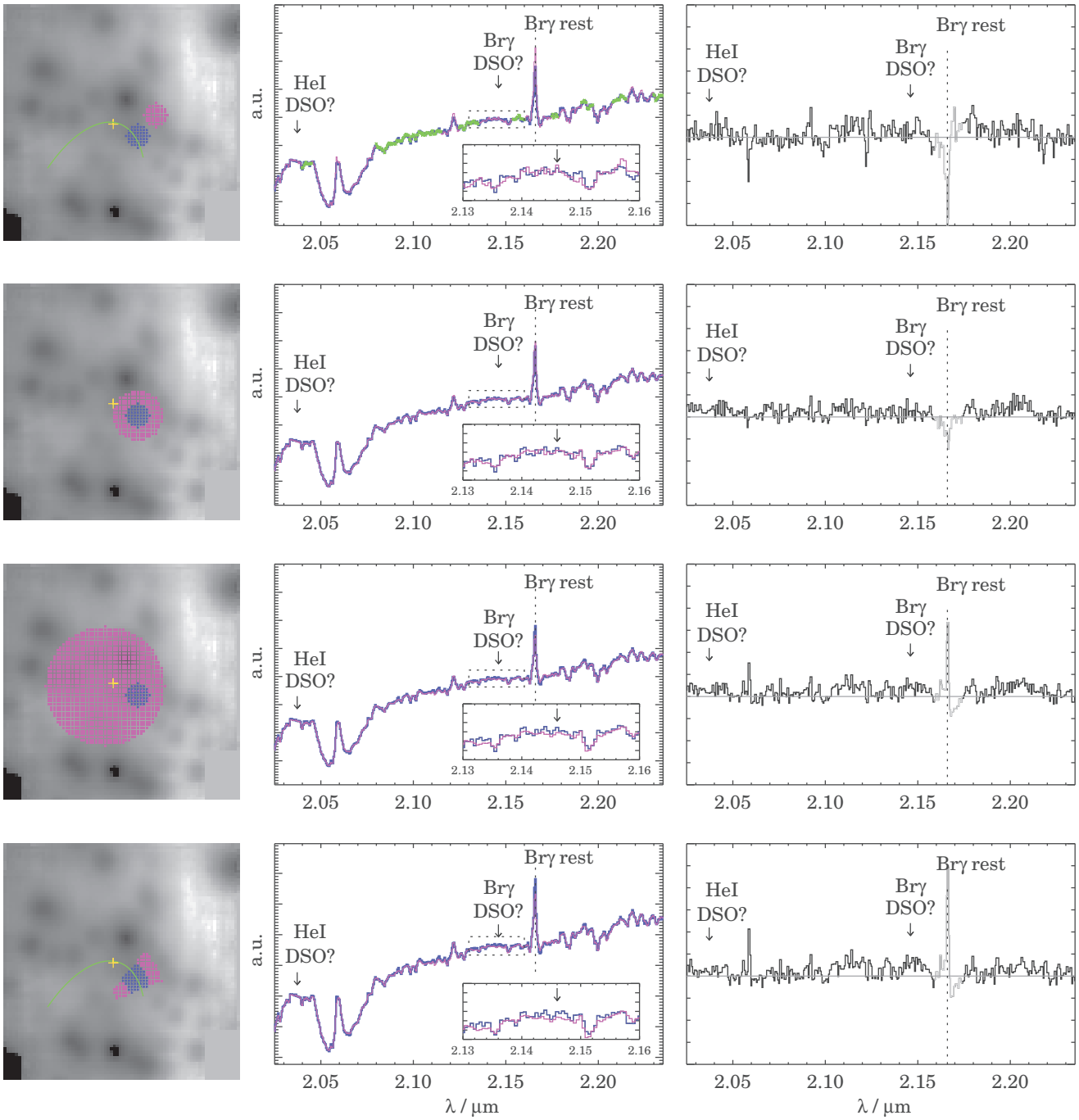


**Figure 5.** Nondetection of Br$\gamma$ blueshifted emission before May at a second upstream position 103.8 mas west and 50 mas south of Sgr A*. Panels and symbols are the same as in Figure 4.

listed in Table 1, we assigned an integration time weights epoch of 2014.55 to this measurement. No red line emission can be claimed for this epoch at this position. In the lower plots of Figure 7 we show that at that epoch neither red- nor blueshifted Br$\gamma$ line emission can be seen at our pre-peribothron position (see also the inset of the middle bottom plot). The excess line emission can clearly be seen even before background subtraction in the inset of the middle top plot. The baseline used for this spectrum excludes the region around blueshifted (2.138–2.146 $\mu$m) and redshifted Br$\gamma$ and He line emission (2.175–2.190 $\mu$m and 2.070–2.080 $\mu$m) we used at the pre-peribothron position. No redshifted emission was detected at the post-position. No redshifted line emission was detected at any position downstream of the post-peribothron position. In Figure 8 we show summary spectra at the pre- and post-peribothron positions for 2014. We obtained the spectra using a 0.″050 radius source and a 0.″25 radius background aperture centered on the DSO. We subtracted a high-pass-filtered version of the spectra that we obtained by replacing the range over which detectable line emission is present (indicated by the three lines at the bottom of the graph) by the mean in the neighboring spectral elements and smoothed the resulting spectrum with a

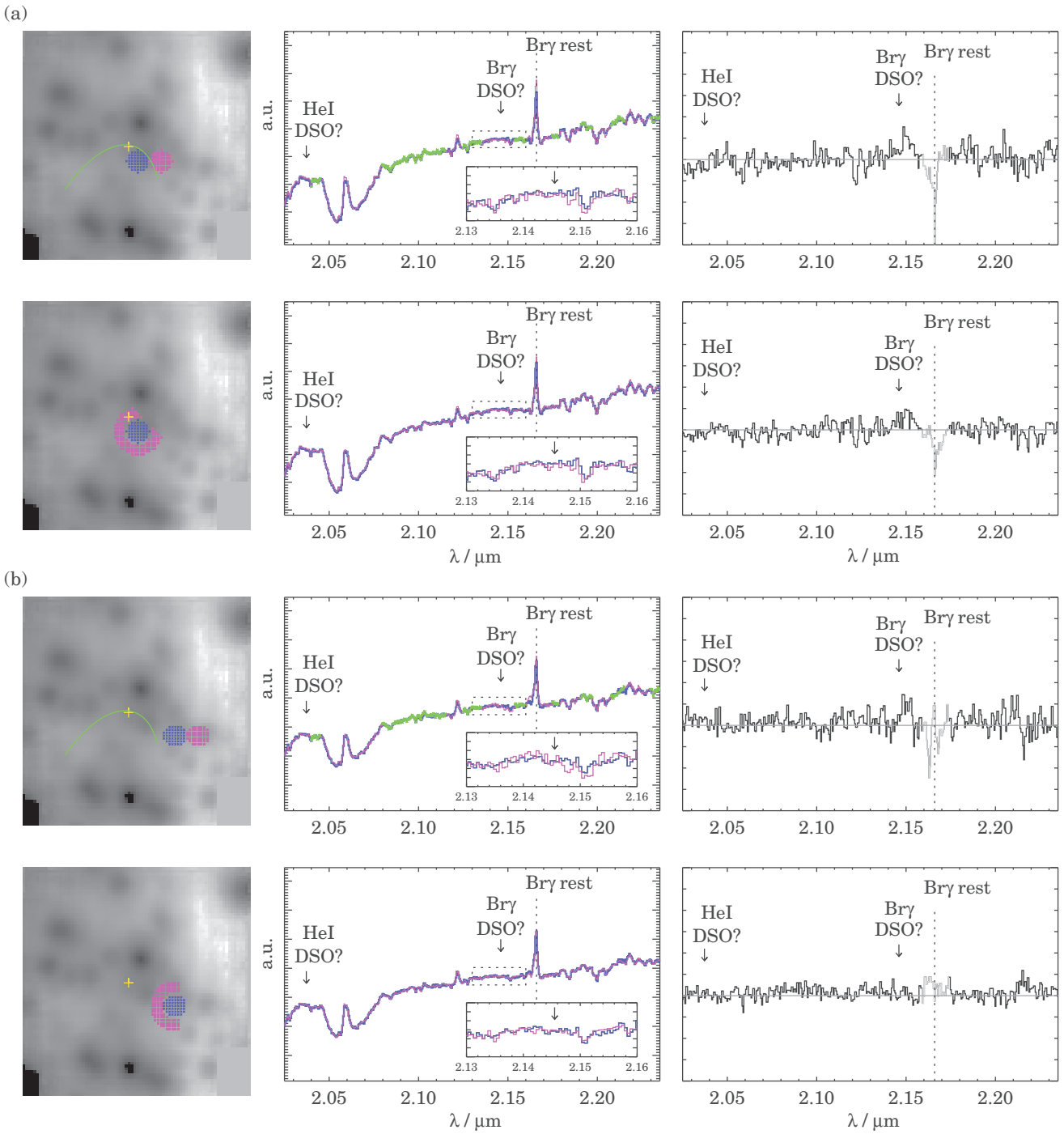


**Figure 6.** Spurious blueshifted Br$\gamma$ emission due to background selection. Panel descriptions are the same as in Figure 4. The two shown cases correspond to sources at (a) 37.5 mas west and 68.8 mas south of Sgr A*, and (b) 200 mas west and 100 mas south of Sgr A*.

Gaussian having an FWHM of 10 spectral resolution elements. The location of the Br$\gamma$ rest emission is indicated by a vertical dashed line.

An important question is that of the size of the line emission region and possible velocity gradients across the DSO. To investigate this, we obtained line maps of the Br$\gamma$ emission. In Figure 9 we show maps of the DSO in its Br$\gamma$ line emission for the times before (epoch 2010.45 May[7] and 2014.32 April) and after (epoch 2014.55) the peribothron. For the brightest and least confused Br$\gamma$ line maps for 2010 May (Figure 9) we find a geometrical mean FWHM of 6.5 pixels. For the star S2 we find an FWHM of 6.2 pixels. With 12.5 mas per pixel this gives an upper limit on the deconvolved FWHM source size of 24 mas. The centroid positions of the emission-line maps of the left half, right half, and full line in milliarcseconds relative to the position of the full line map centroid position are given in Table 2. Under the assumption that differences in the relative positions of the red and blue half of the single-line Br$\gamma$

[7] SINFONI data from ESO program 183.B-100.

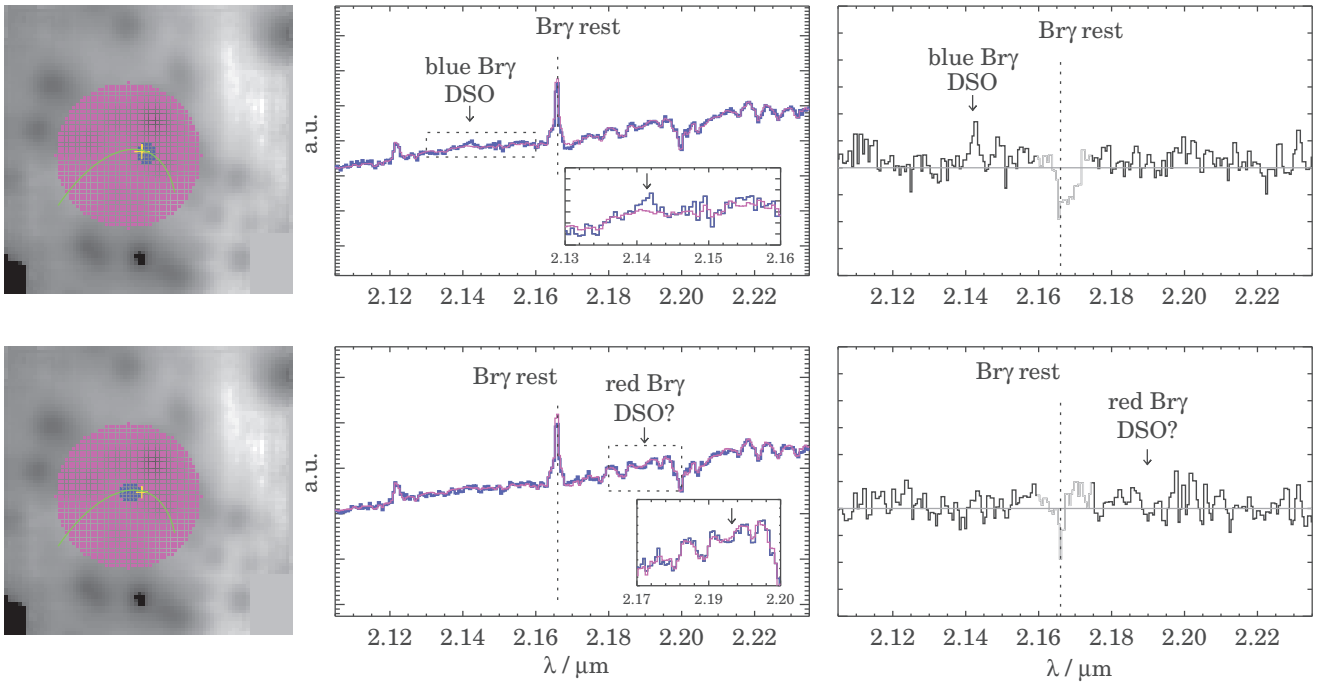


**Figure 7.** Br$\gamma$ line emission after peribothron passage: Top: blueshifted Br$\gamma$ emission detected at 12 mas west and about 5 mas north of Sgr A*. Bottom: no red- or blueshifted Br$\gamma$ emission detected at our pre-peribothron position at 43 mas east and about 5 mas south of Sgr A*.

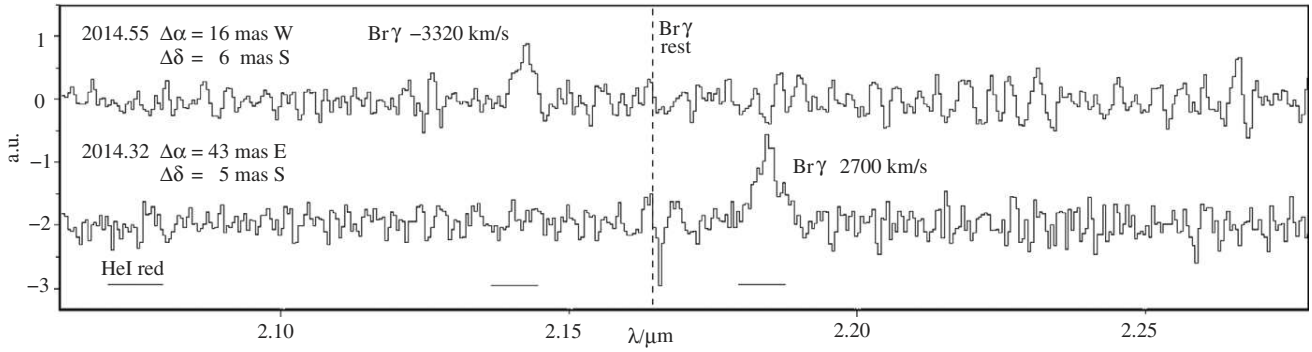


**Figure 8.** Summary spectra at the pre- and post-peribothron positions for the 2014 April and June epoch; see details in text.

**Table 2**
Centroids of DSO Line Maps

| Epoch | Blue Half | | Full Line | | Red Half | | Red–Blue Half | |
|---|---|---|---|---|---|---|---|---|
| | (mas) | (mas) | (mas) | (mas) | (mas) | (mas) | (mas) | (mas) |
| 2014 Apr | −6.75 | −7.63 | 0.0 | 0.0 | +6.25 | +6.00 | +13.0 | +13.6 |
| 2014 Jun | −0.25 | +4.25 | 0.0 | 0.0 | +4.50 | −3.88 | −4.75 | −8.13 |
| 2010 May | −4.63 | −6.00 | 0.0 | 0.0 | +4.13 | +4.63 | +8.75 | +10.63 |

**Notes.** For the single emission line we measured at both the 2014 and 2010 May epochs we list the line map right ascension and declination centroids for the blue and red half of the corresponding single line in milliarcseconds with respect to the full line position. In the last two columns we list the positional difference between the red- and blue-half centroid positions. One pixel corresponds to 12.5 mas.

emission-line map can be interpreted as being due to a velocity gradient of a tidally stretched source, we find for all epochs an upper limit of the corresponding source size of 15 mas. This implies that the source emitting the bulk of the Br$\gamma$ line is very compact, and we adopt the value of 15 mas as an upper limit on the line-emitting FWHM source size. This is consistent with the analysis of $L'$-band continuum images by Eckart et al. (2013) showing that >90% of the DSO emission at 3.8 $\mu$m wavelength is compact (FWHM $\leqslant$ 20 mas) and only up to 10% of the flux density of the DSO can be extended on the scale size of the PSF. Our size limit is also consistent with the upper limit of 32 mas presented by Witzel et al. (2014). These size estimates are all smaller than or at the lower bound of the 2008–2013 size estimate of 42 $\pm$ 10 mas Gillessen et al. (2013b). Our adopted Br$\gamma$ source size corresponds to 120 AU at a distance of 8 kpc, i.e., it is close to the peribothron distance of the source. However, it is still

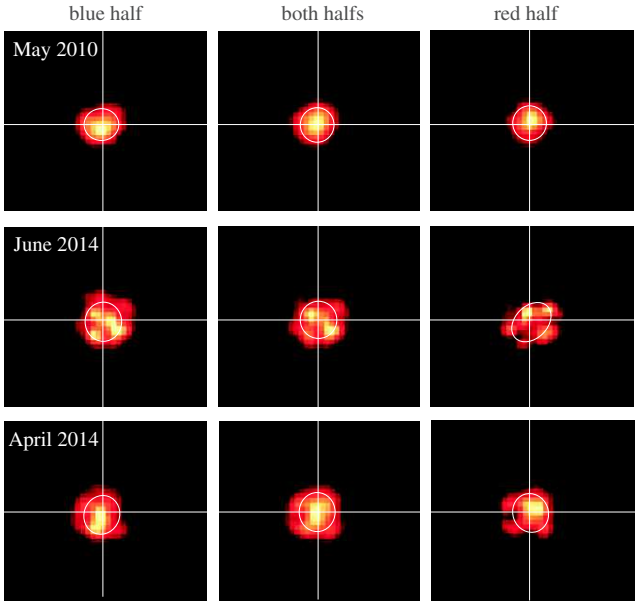


**Figure 9.** Maps of the DSO in its Br$\gamma$ line emission for the 2014.32 April, 2014.55 June, and 2010.45 May epochs. The maps are 0.″5 × 0.″5 in size. The centroid data are given in Table 2.

about 50 times larger than the estimated size of an optically thick dust shell of a 2 $M_{\odot}$ star of about 2.6 AU Witzel et al. (2014).

## 4. DISCUSSION

The fact that we found redshifted Br$\gamma$ emission at the pre-peribothron position but did not detect any blueshifted emission upstream (in Sections 3.2.2 and 3.2.1 we only show two examples—we probed several positions along the orbit) and vice versa (Section 3.3) has implications on the orbit and on the DSO model.

### *4.1. The Orbit*

Based on *L*-band imaging, an IR excess source within the central cluster of high-velocity S-stars was found to approach the immediate vicinity of Sgr A* (Gillessen et al. 2012). In addition, Br$\gamma$ line emission was reported by Gillessen et al. (2013a) and Phifer et al. (2013). In Eckart et al. (2013) we report the identification of *K*-band emission from a source at the position of the *L*-band identifications. Gillessen et al. (2013b) report a marginally spatial extension of the Br$\gamma$ line emission in their SINFONI data and find an intrinsic Gaussian FWHM size of 42 ± 10 mas (using 2008–2013 data). Given the peculiar orientation of the source estimated orbit, precise estimates of the source elongation along the orbit are difficult to obtain. Combining these observational facts indicated that a dusty object—possibly associated with a stellar object—is on an elliptical orbit around Sgr A*. The observational data were also used to derive the orbit of this object and to predict its peribothron transition. Owing to the presumably high ellipticity of the orbit, only very weakly curved sections of the orbit were available, and first predictions of the peribothron transition time in 2013 (Gillessen et al. 2012) proved to be incorrect. The inclusion of (or even restrictions to) the Br$\gamma$ line emission resulted in new predictions for early 2014 (Gillessen et al. 2013a; Phifer et al. 2013). The fact that the telescope PSF in the *L* band is intrinsically larger and therefore more susceptible to

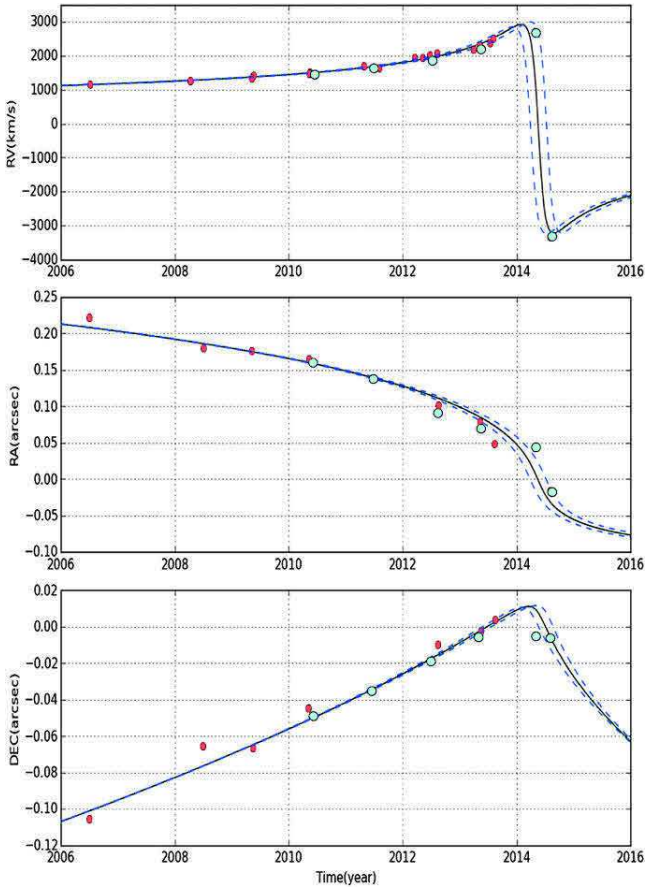


**Figure 10.** Right ascension, declination, and radial velocity of the DSO together with the best orbital fit we obtained; see details in text.

diffuse extended emission is probably the main reason for this discrepancy.

However, the predicted interactions of the gas and dust with the strong gravitational field of Sgr A* have shown that the gas itself may also not be a good probe of the exact orbital motion. This is supported by the spatial extent and the velocity gradient across the Br$\gamma$ line emission. It is also highlighted by the expected interaction of the DSO with the ambient medium and the gravitational field. Therefore, even though the recently derived Br$\gamma$-based orbital solutions are in reasonable agreement (Meyer et al. 2014a, 2014b), the orbital elements may still be uncertain.

Using results from our measurements with SINFONI obtained between 2014 February and September, SINFONI archive data, and the published Keck data (Meyer et al. 2014a, 2014b), we revisited the determination of the DSO orbit. Given that the red emission is only about 40 mas east of Sgr A* and at a radial velocity of about 2700 ± 60 km s$^{-1}$ and blue emission about 30 mas west of Sgr A* at −3320 km s$^{-1}$, we obtained a new orbital solution that places the peribothron passage at 2014.39 ± 0.14, a bit later than but close to 2014.2 as derived earlier (Meyer et al. 2014a, 2014b). Otherwise, the orbital elements are very similar to the ones derived earlier. In Figure 10 we show the fit to the data we used. The formal statistical uncertainties of the positional measurements are of the order of a few milliarcseconds. However, the systematic effects probably limit the uncertainties to a value closer to ±10 mas (see Figure 9 in Eckart et al. 2012a). For the 2014 data presented here the exact

**Table 3**
Orbital Parameters for the DSO

| $e$ | $a$ (mpc) | $i$ (deg) | $\Omega$ (deg) | $\omega$ (deg) | $T$ (yr) | $P$ (yr) |
|---|---|---|---|---|---|---|
| $0.976 \pm 0.001$ | $33.0 \pm 3$ | $113 \pm 1$ | $76 \pm 8$ | $94 \pm 8$ | $2014.39 \pm 0.14$ | $262 \pm 38$ |

**Notes.** The orbital parameters and their uncertainties have been derived on the basis of the UCLA measurements and the 2014 April data point we obtained using SINFONI at the VLT. We assume a distance of 8 kpc and a black hole mass of $4 \times 10^6\ M_\odot$.

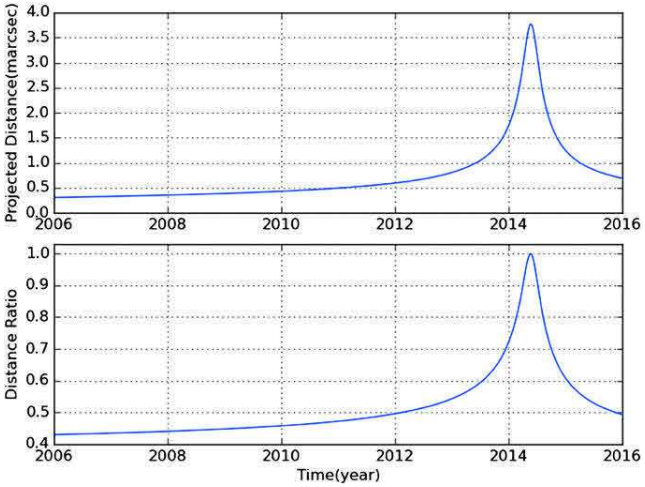


**Figure 11.** Orbital projection effects. Top: evolution of the projected separation between two neighboring points of arbitrary 0.5 units in 2011. Bottom: foreshortening factor of any structure along the orbital extent as a function of time.

positioning of the Br$\gamma$ line emission critically depends on the transfer of the Sgr A* position as obtained during a 3 mJy flare we observed in March to all the other 2014 epochs. This was done using the known position and velocity of the southward moving bright star S2 that is currently about 0.″11 north and 0.″06 west of Sgr A*. For the radial velocities we assume the value of 60 m s$^{-1}$ we adopted for the SINFONI data. The light-blue filled circles indicate our per- and post-peribothron 2014 data points we obtained using SINFONI at the VLT. The other light-blue filled circles show the results from our re-reduction of earlier SINFONI VLT archive data. Red filled circles represent data as obtained with the Keck Telescope and published by Meyer et al. (2014a, 2014b). The dashed lines indicate the approximate 1$\sigma$ uncertainty of the fit. The orbital elements are given in Table 3. With the ellipticity $e = 0.976$ and the half-axis length of 33 Mpc, we obtain a pericenter distance of about 163 AU, which is comparable to previous estimates (Pfuhl et al. 2015; Phifer et al. 2013; Meyer et al. 2014b) and indicates that even if the DSO is an embedded star, its outer shell may very well be subject to tidal disruption (see also Section 5 and Eckart et al. 2013; Witzel et al. 2014).

In Figure 11 we show the size evolution of structures along the orbit under the assumption of freely moving neighboring points. In the case of the DSO the shapes of the two graphs by chance look very similar. We verified that they are indeed very different for other orbital configurations, i.e., lower inclination or the apobothron pointing toward the observer. The top graph shows the evolution of the projected size of a source moving along the orbit. The bottom graph shows the same quantity divided by the actual three-dimensional size of the source, i.e., the amount of foreshortening that the observer needs to correct for. Both graphs demonstrate that close in time to the peribothron passage the foreshortening correcting is close to unity and that the DSO can be seen close to its full extent along the orbit.

### 4.2. Tidal Interaction with Sgr A*

The way in which the gas cloud will get disrupted depends on the exact orbit and the nature of the DSO, i.e., whether there is a stellar core or not. If there is a central star, then higher-mass (typically 10 solar masses) objects may retain more of the gas and dust mass in their corresponding Roche lobe than low-mass objects (one solar mass and below). This is discussed in Eckart et al. (2013). Recent model calculations for cases with a stellar core or even a binary core have been published by Zajaček et al. (2014).

A tail that is physically connected to the DSO has been reported by Gillessen et al. (2012, 2013a, 2013b). Eckart et al. (2013, 2014b), Phifer et al. (2013), and Meyer et al. (2014b) have questioned this physical association of the DSO with the extended Br$\gamma$ and dust continuum emitting filament about 0.″3 southeast of Sgr A*. The rather extended shape of this emission close to rest-frame velocities may very well be associated with the Galactic center fore/background features, which are numerous in this region. It also does not follow precisely the orbital track of the DSO. Especially at velocities close to rest-frame velocities, the general central cluster region is very crowded. Hence, despite an indication of very faint emission pointing toward this general region 0.″3 southeast of Sgr A*, a physical association of the bright tail emission is still questionable.

If the DSO is a pure, very compact and solitary gas and dust cloud, then it formed through a special process at a very special place and time. As speculated by Pfuhl et al. (2015), it must have formed between 1990 and 2000. Unless one claims, as a further special feature of this source, that it has been formed at 100% efficiency, some relics and further similarly compact dust filaments or bullets must have been formed along that process. These have not been identified yet. It also must be noted that during the 1990–2000 time interval the entire Galactic center region was under detailed investigation in the entire NIR/mid-IR (MIR) and radio wavelength band with observing runs closely placed in time. No special event in the mini-spiral to the southeast of Sgr A* had been reported then.

It has been noted that the thermal instability can explain in a natural way the pressure equilibrium between the hot and the cold plasma in the mini-spiral region (Czerny et al. 2013; Różańska et al. 2014).

Hence, this process is relevant for the possibility of survival of the infalling clouds in the region, and it also allows us to estimate the typical size of clouds. In fact, clouds as large as $10^{14}$–$10^{15}$cm (0.001–0.01 lt-yr) can persist. From the dominating optically thin DSO line emission a total mass of the clouds of $\simeq$10 Earth masses can be derived, depending on the strength of the ambient radiation field. This agrees with recent results (Shcherbakov

2014) suggesting the mass of the DSO/G2 cloud to be within the range 4–20 $M_{\oplus}$. Naturally, this would be upon the assumption of a coreless cloud scenario, whereas the mass estimates do not apply if a star is embedded within the cloud. It turns out that clouds located a distance exceeding ∼0.05 pc from Sgr A* can survive a few hundred years, which means that the cooling and evaporation time is shorter than the free-fall time onto the black hole.

Gillessen et al. (2013b) and Pfuhl et al. (2015) suggest that 13 years prior to the DSO peribothron passage the source G1 went through its peribothron on an orbit connected to the current DSO orbit. Dust heating of G1 would then explain the moderate IR excess of 0.3 *K*-band magnitudes of the star S2 in 2002 (Appendix in Pfuhl et al. 2015) as it passed close to Sgr A* and G1. However, with Sabha et al. (2012) we have shown that over timescales of a few months to a few years—especially close to the center—serendipitous sources can frequently be formed owing to density fluctuations of the background stars in the central arcsecond.

The DSO is supposed to be on a similar orbit to the G1 source (Pfuhl et al. 2015). However, up to this point, as it is approaching peribothron, the DSO has not shown any increase in *K*- or even *L*-band flux density that could be attributed to dust heating. In fact, while approaching Sgr A* in 2013, the *L*-band identification of the DSO was lost (Pfuhl et al. 2015). This can in part be attributed to confusion. To some extent diffusion or destruction of dust as the source entered the immediate surroundings of Sgr A* may be responsible as well, but certainly no brightening of the source in its *K*- or *L*-band emission has been observed.

Until now several models have placed a star at the center of the DSO (Murray-Clay & Loeb 2012; Eckart et al. 2013; Scoville & Burkert 2013; Ballone et al. 2013; Phifer et al. 2013; Zajaček et al. 2014). An at least partial tidal disruption is also expected if the DSO is an embedded star. A Roche description of the Sgr A*/DSO system (Eckart et al. 2013) suggests that a more massive central star will lose less of the gas and dust from the central few AU than a solar-mass-type star or a dwarf. Simulations of compact systems by Zajaček et al. (2014) support this finding as well (see also Section 4.5).

For source sizes that are much smaller than the peribothron distance with Jalali et al. (2014) we have shown that at the peribothron position the gaseous source volume is compressed by at least a factor of two owing to gravitational focusing. This results in the fact that before and after peribothron the source stays relatively compact despite the influence of possible turbulences and shocks that may be induced owing to shearing gas streams close to peribothron. Depending on the density of the overall environment, hydrodynamic interactions with the ambient material set in well past peribothron. This is consistent with all hydrodynamic and particle simulations that have been used to predict the future development of the DSO or similar sources (e.g., Zajaček et al. 2014; Burkert et al. 2012; Schartmann et al. 2012; Jalali et al. 2014).

### 4.3. Interactions with the Ambient Medium

If the DSO passes through an accretion wind from Sgr A*, it may develop a bow shock. In case it is indeed a dusty star, then one may expect to see cometary source structures quite similar to the sources X3 and X7, which are in the overall mini-cavity region just south of Sgr A* at a projected distance of 0.″8 and 3.″4 (Mužić et al. 2010). In mid-2014 the DSO is well within a sphere of hot gas surrounding Sgr A* out to approximately the Bondi radius ($\approx 10^5 R_S$). As a dusty source, the DSO can therefore be regarded as an obvious probe for strong winds possibly associated with Sgr A*. However, there is no clearly resolved structure that can be considered as a bow shock, although the DSO is already closer to Sgr A* than X3 and X7. This may indicate that the wind from Sgr A* is highly non-isotropic, possibly directed toward the mini-cavity (Mužić et al. 2010), and that the DSO has not yet passed through that wind. However, the mass load of such a wind (due to the radiatively inefficient accretion mechanism) may not be high enough to allow for the formation of a prominent cometary tail structure. The detailed density profile for the central region of the radiatively inefficient accretion flow is difficult to obtain. Methods are rather indirect and accretion model dependent (Baganoff et al. 2003; Marrone et al. 2007; Wang et al. 2013). However, Eckart et al. (2014a) have pointed out that the smaller size compared to X3 and X7 may be due to the higher particle density within the accretion stream close to Sgr A* (e.g., Shcherbakov & Baganoff 2010).

### 4.4. Flare Activity

A possibly efficient probe of the interaction of the DSO with its ambient environment or with the black hole itself is monitoring the flux density originating from the central few tenths of an arcsecond. However, the results of these efforts have not been very revealing so far.

The NIR flare activity we observed through SINFONI during the peribothron approach in 2013/2014 is in full agreement with the statistical expectations as we described them with Witzel et al. (2012). There was no exceptional activity, with three flares of a few milli-Jansky strength.

If the DSO were to develop a bow shock while approaching the immediate environment of Sgr A*, then this event might lead to shock accelerations of electrons and to correspondingly strong excursions in the radio emission. However, the strength of these emission peaks depends critically on the size of the bow shock, and early estimates on the order of 1–20 Jy in the decimeter to short centimeter wavelength range had to be revised to values on the order of 0.01–0.2 Jy (Narayan et al. 2012; Sądowski et al. 2013; Crumley & Kumar 2013). Despite a dense monitoring program with the Very Large Array (Sjouwerman & Chandler 2014), strong radio flares have not yet been reported and the now-predicted strength of the variability would be in the normal range of the flux density variations observed toward Sgr A* (e.g., Markoff et al. 2001, 2007; Eckart et al. 2012b).

So far in the X-ray observable $\geqslant$2 keV band no elevated continuum flux density level or extraordinary X-ray variability has been reported (Haggard et al. 2014). Such an extra emission would have been expected to originate from the shock-heated gas (Gillessen et al. 2012).

Although Sgr A* is extremely faint in the X-ray bands, it is strongly variable in this domain of the electromagnetic spectrum (Baganoff et al. 2001, 2003; Porquet et al. 2003, 2008; Eckart et al. 2012b; Nowak et al. 2012; Degenaar et al. 2013; Barrière et al. 2014; Mossoux et al. 2015; Neilsen et al. 2013). The statistical investigation of the NIR variability by Witzel et al. (2012) suggests that the past strong X-ray variations are potentially linked with the origin of the observed X-ray echoes (Revnivtsev et al. 2004; Sunyaev & Churazov 1998; Terrier et al. 2010; Capelli et al. 2012). Assuming an underlying synchrotron self-Compton process, the NIR variability can in fact explain the required X-ray flare fluxes as a natural and nonexceptional phenomenon of the source. Therefore, Sgr A* is the ideal extremely low accretion rate target that allows us to study this particular phase, in which apparently most SMBHs

spend their lifetime. Phenomena like the passage of the DSO may dominate the variability of objects in this phase throughout the electromagnetic spectrum.

While the DSO is a very compact continuum and line-emitting source (see Section 3.3 and Eckart et al. 2013), its peribothron distance is rather small (see Section 4.1). Hence, it is still an open question whether and when some activity of Sgr A* is triggered by the DSO fly-by.

### 4.5. The DSO as a Young Accreting Star

Large line widths are common among pre-main-sequence stars, including both T Tauri stars (with an age of about $10^5$–$10^6$ yr) and protostars (with an age of about $10^4$–$10^5$ yr), with an infalling envelope that forms a disk close to the star. Bertout (1994) already pointed out that Doppler broadening from pre-main-sequence stars may range roughly from 50 to 500 km s$^{-1}$ in the course of the accretion phase. As an example, hydrogen recombination and Na D line profiles of several hundred kilometers per second in a number of pre-main-sequence stars (e.g., T Tau, DG Tau, DR Tau, AS205, and SCrA) are shown. The M0V classical T Tauri star LkCa-8 (IP Tau) (Wolk & Walter 1996; Moto'oka & Itoh 2013) has a 600–700 km s$^{-1}$ Br$\gamma$ line width (Edwards et al. 2013), quite comparable to the width currently found for the DSO. Another case of a low-mass star with exceptionally large line widths is DK Tau A, with an 800 km s$^{-1}$ wide line (Eisner et al. 2007). It is listed by Herczeg & Hillenbrand (2014) as a K8.5 star with a mass of 0.68 $M_\odot$.

Without doubt the Br$\gamma$ line traces high-excitation regions; however, in the case of young embedded protostars it is currently unclear whether these regions are associated with accretion funnel flows, the jet base (Davis et al. 2011), or less collimated ionized winds. All of these elements can contribute to the emission and the large observed line width. In the case of the DSO there are several mechanisms that can contribute to a large line width.

1. *Contribution from collisional ionization in a bow shock.* A possible origin of a broad wide Br$\gamma$ emission line was discussed by Scoville & Burkert (2013) on the basis of the bow shock model that is relevant for the supersonic motion of the object through the hot ambient interstellar medium (ISM) emitting X-rays. They show that Br$\gamma$ emission may arise from the collisional ionization and the gas cooling in the narrow but dense cold ($\sim 10^5$–$10^6$ K) and shocked layer of the stellar wind. The high densities ($\sim 10^8$ cm$^{-3}$) in this layer can explain the observed emission measure.

2. *Contribution from wind drag in a bow shock.* The large increase in FWHM line width from 137 km s$^{-1}$ in 2006 to 730 km s$^{-1}$ in 2014 could also be related to the increase in orbital velocity from about 1200 km s$^{-1}$ to almost 9000 km s$^{-1}$ at peribothron. Discussing the emission from photoionized stellar wind bow shocks, Cantó et al. (2005) calculate the change of velocity in the thin shocked layer that develops while the source is moving through the ISM. In the context of the DSO this effect has not yet been discussed before. In their Equations (19) and (33) they approximate the dependence of that velocity as $v_{\rm sl} \propto v_w \times f(v_a, R, \theta, \phi)$. Here $v_{\rm sl}$ is the velocity in the shock layer, $v_w$ is the stellar wind velocity, and $v_a$ is the velocity relative to the ISM. The radius $R$ and the angles $\theta$ and $\phi$ describe the geometry of the shock front. It is the change of $v_{\rm sl}$ across the shock front that may contribute to the observed Br$\gamma$ line width. The analytic solution of Wilkin (1996) for the thin steady-state bow shock layer yields the estimate for the shock layer velocity $v_{\rm sl} \approx 2v_a\theta/[3(1 + v_a/v_w)]$ close to the symmetry axis, where the angle $\theta$ is small. The ratio of this velocity at the same $\theta$, but different epochs, 2006 and the peribothron crossing, yields $v_{\rm sl}^{\rm per}/v_{\rm sl}^{2006} \approx 1.07$–$1.26$ for the terminal wind velocities of 100–400 kms$^{-1}$, respectively. Thus, the increase in velocity by about 10% could be contributed by wind drag in a bow shock layer.

3. *Contribution from stellar or disk winds.* There can also be a contribution to Br$\gamma$ emission from the gaseous inner disk, stellar wind, stellar-field-driven wind (X-wind), or disk wind (Lima et al. 2010) that can originate from the corotation radius to several astronomical units (see Kraus et al. 2008 for discussion and their Figure 1). Günther (2011) shows that for classical pre-main-sequence stars, wind velocities of a few hundred kilometers per second can occur.

4. *Tidal contribution*. The increase in FWHM of DSO would then be caused by the tidal stretching and perturbation of the accretion disk, especially close to the peribothron, which would consequently lead to larger velocity dispersions of inflow and outflow streams. Simple considerations analogous to the computation of tidal compression presented by Jalali et al. (2014) show the increase of velocity deviation. There are several ways to assess the importance of tidal stretching of the DSO along its orbit from our data:

$\alpha$—if the total pre-peribothron line width of about 720 km s$^{-1}$ was dominated by tidal stretching, then a minimum source size of about 65 mas is expected based on the mean slope of 1000 km s$^{-1}$ over a projected orbital path of about 90 mas (i.e., $\sim$11 km s$^{-1}$ mas$^{-1}$) within the past 2 yr.

$\beta$—attributing the 2008–2013 size estimate of 42 $\pm$ 10 mas Gillessen et al. (2013b) to the year 2013 and assuming a free gas cloud subjected to orbital stretching along the orbit, we find that the source should be 5–8 times larger, i.e., 210–336 mas, close to peribothron. We cannot confirm such a large size from our Br$\gamma$ line maps in Figure 9 (see also Table 2).

$\gamma$—the separation of apparently simultaneously observed extreme velocity components of G2 close to the peribothron passage (Figures 1 and 15 in Gillessen et al. (2013b); Pfuhl et al. (2015), which is consistent with a cut through their *pv*-diagram in Figure 1) implies a size between 90 mas and 150 mas along the orbit. With our data we only see a single-lined DSO either red- or blueshifted with a diameter of <20 mas, and, given the low foreshortening (Section 4.1 and Figure 11), we cannot confirm the presence of multiple sources or a large source extent (see Section 3.3 and Figure 9).

$\delta$—we measured very close to the points at which extreme orbital velocities in the red and blue can be observed. At these positions for an extended tidally stretched source the emission previously blue of the source center will become redshifted and blueshifted, respectively. Hence, a line width that can be up to a factor of two narrower is expected. However, the post-peribothron line width is about a third of the pre-peribothron value, and the small source sizes are in conflict with an extended tidally stretched source. In addition, the orbital compression expected for such a scenario would imply a larger line width and a higher line flux density owing to the increased density of the emitting gas volume. Instead, for a dust-enshrouded accreting stellar object line variability in integrated line flux density and line shape is expected.

5. *Contributions from accretion.* However, there can also be a contribution from the gas accretion of the circumstellar envelope onto the stellar surface if the DSO is a young stellar object as

has already been proposed and discussed (Murray-Clay & Loeb 2012; Eckart et al. 2013; Scoville & Burkert 2013; Zajaček et al. 2014; De Colle et al. 2014). In this framework an increase of the Br$\gamma$ line width as a function of time could result from an increased perturbation of the envelope or disk that leads to an enhanced velocity dispersion in the accretion stream onto the central star as it gets closer to the peribothron.

In the following we investigate whether the infalling gas that is approximately in free fall and is being shocked upon reaching the stellar surface can explain the observed large line width of the DSO Br$\gamma$ line, which evolved from FWHM(Br$\gamma$) $\sim$ 200 km s$^{-1}$ in 2006 to FWHM(Br$\gamma$) $\sim$ 700 km s$^{-1}$ in 2014, as laid out in Section 3.1.1 (see also Phifer et al. 2013; Gillessen et al. 2013b). This corresponds to radial velocities $v_r$ of infalling material that range from about 100 km s$^{-1}$ to several hundred kilometers per second.

#### 4.5.1. The Model Geometry

For simplicity, we consider an *axisymmetric magnetospheric accretion model* (see Bouvier et al. 2007 for review) for the accretion on pre-main-sequence stars where the gas moves ballistically along the magnetic field lines from the innermost orbit of the disk and gains large infall velocities of the order of $\sim$100 kms$^{-1}$ (Hartmann et al. 1994). Unlike the boundary layer model, the magnetospheric accretion scenario can indeed explain observed redshifted absorption minima at free-fall velocity and blueward asymmetry in emission lines (Muzerolle et al. 1998a, and references therein).

The presence of a magnetic field around pre-main-sequence stars is justified by the observation of the Zeeman broadening of photospheric lines (Johns-Krull et al. 1999, 2001), as well as by the measurement of the electron cyclotron maser emission (Smith et al. 2003). The inferred field strength is $\sim$1–3 kG. In the context of the dipole magneto-accretion model, in which the gas is in free fall, the truncation radius in terms of stellar radii is (e.g., Bouvier et al. 2007)

$$\frac{R_T}{R_\star} \approx 6.5 B_3^{4/7} R_2^{5/7} \dot{M}_{-8}^{-2/7} M_1^{-1/7}, \quad (1)$$

where the strength of the dipole magnetic field at the equator $B_3$ is in kG, the stellar radius $R_2$ is in units of 2 $R_\odot$, the accretion rate $\dot{M}_{-8}$ is expressed in $10^{-8}$ $M_\odot$ yr$^{-1}$, and the stellar mass $M_1$ is in units of 1 $M_\odot$. The truncation radius in Equation (1) is derived for gas in free fall in the spherical symmetry. For disk accretion it may serve as an upper limit, since the ram gas pressure is higher in that case and the truncation radius is thus shifted inward.

For stable accretion to proceed, the truncation radius expressed by Equation (1) has to be smaller than the corotation radius $R_{co}$, $R_T \lesssim R_{co}$, at which the Keplerian angular velocity is equal to the rotational angular velocity of the star,

$$R_{co} \approx 4.2 M_1^{1/3} P_1^{2/3} R_\odot, \quad (2)$$

where $M_1$ is the stellar mass in units of 1 $M_\odot$ and $P_1$ is the stellar rotation period in units of 1 day (see Bouvier et al. 2007, for discussion). The inner portion of the disk is purely made up of gas up to the dust sublimation radius, which, according to simulations by Whitney et al. (2004), may be expressed in terms of the dust sublimation temperature and the stellar effective temperature as

$$R_{sub} = R_\star \left( \frac{T_{sub}}{T_\star} \right)^{-2.085}, \quad (3)$$

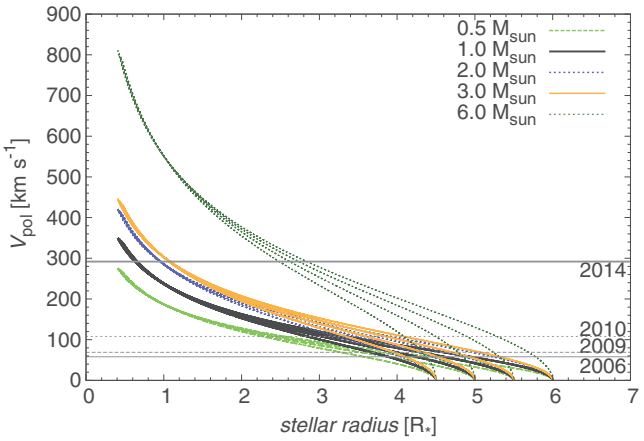


**Figure 12.** Poloidal velocity profile as a function of the distance from the pre-main-sequence star in a magnetospherical accretion model (Hartmann et al. 1994) for different masses of pre-main-sequence stars at $\sim$1 Myr (Siess et al. 2000). The gray horizontal lines represent the observed radial velocity for years 2006, 2009, 2010, and 2014 with an increasing tendency (Phifer et al. 2013; Gillessen et al. 2013b; this work).

which for typical values of $T_\star$ (spectral types K, M: 3000–4500 K) and $T_{sub} \approx 1500$ K has values of $\sim$4–10 $R_\star$. Beyond the dust sublimation radius, dust can coexist with the gaseous phase. The emerging radiation from the accretion flow is reprocessed by the circumstellar dust, giving rise to the IR excess.

For the calculation of the velocity profiles of the accretion flow we assume the truncation radius to be at $R_T = 5$ $R_\star$ (Gullbring et al. 1998; Alcalá et al. 2014), which is close to the estimate in Equation (1). We compute the poloidal velocity profiles in the framework of the magnetospheric accretion model (see Equations (1) and (3) of Hartmann et al. 1994) for 0.5, 1.0, 2.0, and 3.0 $M_\odot$ pre-main-sequence stars with a stellar radius of 2.1, 2.6, 3.6, and 4.8 $R_\odot$, respectively, at 1 Myr (Siess et al. 2000) for solar metallicity and no overshooting; see Figure 12 for the comparison of the poloidal velocity for the observed radial velocity, which is observed to increase with the approach of the DSO to the peribothron. For earlier epochs the observed FWHM is consistent with the accretion onto a low-mass object of $\sim$0.5–1 $M_\odot$. To explain the higher FWHM in 2014, a massive pre-main-sequence star of Herbig Ae/Be type is needed at the first glance, since for lower-mass stars only the upstream parts reach comparable velocities; see the poloidal velocity profile of the 6 $M_\odot$ star with a radius of 2.9 $R_\odot$ in Figure 12. However, such a massive stellar core having a luminosity of $\gtrsim$100 $L_\odot$ is inconsistent with the luminosity constraint on the DSO ($\leqslant$10 $L_\odot$), and the pre-main-sequence stage is also very short (Siess et al. 2000).

The physics of circumstellar material of pre-main-sequence stars is generally more complex, especially close to the SMBH, where the disk surrounding the star is expected to be warped and perturbed by tidal effects. Although basic observational signatures of pre-main-sequence stars (strong stellar magnetic fields, truncation radius, accretion shocks observed mainly for classical pre-main-sequence stars) are in accordance with the magnetospheric accretion model (Bouvier et al. 2007) and suggest that Br$\gamma$ originates in gas infall rather than outflow (Najita et al. 1996), it is plausible that there is a contribution to Br$\gamma$ emission from stellar or disk winds.

We note that the line profile may be generally nonsymmetric and its width dependent on the inclination, at which the emerging

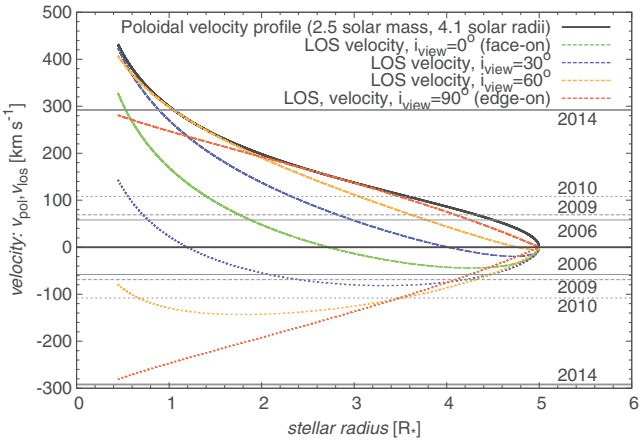


**Figure 13.** Profiles of maximum line-of-sight velocity as a function of the distance from the star in a magnetospherical accretion model (Hartmann et al. 1994) for a 2.5 $M_\odot$ pre-main-sequence star for a different inclination of the view of emerging radiation. The receding flow (nearer to the observer, mostly redshifted, positive velocities) is labeled by dashes, while the approaching flow (farther away, mostly blueshifted, negative velocities) is represented by dots. The gray horizontal lines represent the observed radial velocity $v \sin i$ for years 2006, 2009, 2010, and 2014 with an increasing tendency (Phifer et al. 2013; Gillessen et al. 2013b, this work):

emission is viewed. This is demonstrated by the profiles of the maximum line-of-sight velocity in Figure 13, where we plot separately approaching (mostly blueshifted) and receding (mostly redshifted) accretion streams for 2.5 $M_\odot$ pre-main-sequence stars (at ∼1 Myr; Siess et al. 2000). The separation between the dashed and the dotted lines for each stellar radius and inclination is an approximate measure of the observed line width. The line broadening is generally bigger for a larger inclination (see also Muzerolle et al. 1998a, for detailed radiative transfer modeling). The results in Figure 13 clearly show that with a star of about 2 $M_\odot$ the observed Br$\gamma$ line widths, covering the full range from about 200 km s$^{-1}$ to 700 km s$^{-1}$, can be reproduced. From the range of maximum and minimum velocities it is also evident that the line profile can be asymmetric and skewed to one side.

#### 4.5.2. Accretion Luminosity and Rate

In fact, the broad hydrogen Br$\gamma$ line with the FWHM of the order of ∼100 km s$^{-1}$ is frequently observed in the spectra of accreting pre-main-sequence stars (detection rate 70%–74%; Folha & Emerson 2001; Ilee et al. 2014) and appears to be a useful tracer of magnetospheric accretion on embedded pre-main-sequence stars (Muzerolle et al. 1998a, 1998b; Folha & Emerson 2001; Calvet et al. 2004). Here the star is assumed to accrete matter from its envelope or the inner edge of an accretion disk. Accretion from the surrounding ISM can be considered as insignificant.

The correlation between Br$\gamma$ emission-line luminosity and accretion luminosity is found to be tight (Muzerolle et al. 1998b; Calvet et al. 2004). The empirical relation between emission-line and accretion luminosities is based on various signatures of accretion luminosity (H$\alpha$ luminosity, optical, and UV excess). The recent fit is as follows (Alcalá et al. 2014):

$$\log (L_{\rm acc}/L_\odot) = \zeta_1 \log [L({\rm Br}\gamma)/L_\odot] + \zeta_2, \qquad (4)$$

with $\zeta_1 = 1.16 \pm 0.07$ and $\zeta_2 = 3.60 \pm 0.38$. This correlation may then be extended to heavily extincted protostars that are enshrouded in a dusty envelope.

If we naively apply this relation to the DSO and its Br$\gamma$ emission-line luminosity of $L({\rm Br}\gamma) = f_{\rm acc} \times 10^{-3}\, L_\odot$, where $f_{\rm acc}$ is a factor of the order of unity, we get a reasonable range for the accretion luminosity, $\log (L_{\rm acc}/L_\odot) \approx 1.16 \log f_{\rm acc} + 0.12$; $L_{\rm acc} = 1.3 \times 14.5^{\log f_{\rm acc}}\, L_\odot$, and for $f_{\rm acc} = \{1, 2, 3, 4\}$ yielding $(1.3, 3.0, 4.7, 6.6)\, L_\odot$.

For the assumption of the innermost radius of $R_{\rm in} = 5\, R_\star$, the accretion rate is given by (Gullbring et al. 1998)

$$\dot{M}_{\rm acc} \cong \frac{L_{\rm acc} R_\star}{G M_\star} \left(1 - \frac{R_\star}{R_{\rm T}}\right)^{-1}, \qquad (5)$$

which can be written as

$$\dot{M}_{\rm acc} \approx \xi \left(\frac{L_{\rm acc}}{L_\odot}\right) \left(\frac{R_\star}{R_\odot}\right) \left(\frac{M_\star}{M_\odot}\right)^{-1} M_\odot\ {\rm yr}^{-1}, \qquad (6)$$

with $\xi = 4.1 \times 10^{-8}$.

Inserting the estimated values for mass, radius, and the accretion luminosity, we obtain an accretion rate of the order of $\lesssim 10^{-7}\, M_\odot\ {\rm yr}^{-1}$, which is about 10 times larger than the median value observed for pre-main-sequence stars in the Taurus and Chameleon I regions (Hartmann et al. 1998). It is, however, consistent with the span of pre-main-sequence accretion rates, which seem to evolve with the age of the pre-main-sequence star as $\dot{M}_{\rm acc} \propto t^{-2.1}$ (Baxter et al. 2008).

The gas outflow rate was shown to correlate with the accretion in pre-main-sequence systems. The ratio of rates was established approximately as $\dot{M}_{\rm w}/\dot{M}_{\rm acc} \sim 0.1$ (Edwards et al. 2006, and references therein), which corresponds to the order of $\dot{M}_{\rm w} \lesssim 10^{-8}\, M_\odot\ {\rm yr}^{-1}$. This order of magnitude for the wind outflow rate was discussed by Scoville & Burkert (2013) for the wind–wind bow shock origin of Br$\gamma$ emission.

The estimates of accretion luminosity and accretion and mass-loss rates are upper limits since there may be contribution to Br$\gamma$ flux from sources other than accretion flows, namely, stellar wind or disk outflows (Kraus et al. 2008).

#### 4.5.3. Density and Emission Measure

The radial density profile of the accretion flow may be inferred based on the estimated values of pre-main-sequence star mass, radius, mass accretion rate, and the assumed size of the magnetosphere. Assuming an axisymmetric steady flow of matter along the streamlines, the following relation holds for the hydrogen number density (Hartmann et al. 1994),

$$n_{\rm H}(r) = \frac{\dot{M}_{\rm acc}}{4\pi m_{\rm H} \left(\frac{1}{r_{\rm mi}} - \frac{1}{r_{\rm mo}}\right)} \frac{r^{-5/2}}{(2GM_\star)^{1/2}} \frac{(4-3y)^{1/2}}{(1-y)^{1/2}}, \qquad (7)$$

where the magnetic streamlines are described by $r = r_{\rm m} \sin^2\theta$, where $\theta$ denotes the angle between the magnetic dipole axis and the radius vector $\mathbf{r}$; in Equation (7) $y = r/r_{\rm m} = \sin^2\theta$ and $r_{\rm mi}$ and $r_{\rm mo}$ stand for the radius of the innermost and the outermost streamline intersecting the accretion disk, respectively; we take $r_{\rm mi} = 5\, R_\star$ and $r_{\rm mo} = 7\, R_\star$ for definiteness. The mass accretion rate is held fixed at $\dot{M}_{\rm acc} = 10^{-7}\, M_\odot\ {\rm yr}^{-1}$ in accordance with Equation (6). The density profiles for the same set of stars as in Figure 12 are plotted in Figure 14.

The density profile in Figure 14 enables us to estimate the emission measure, ${\rm EM} \propto n_{\rm e}^2 V$, under the assumption $n_{\rm e} \approx n_{\rm H}$; see Equation (7). The computation is performed for the distance range where the poloidal velocity, Figure 12, reaches the values

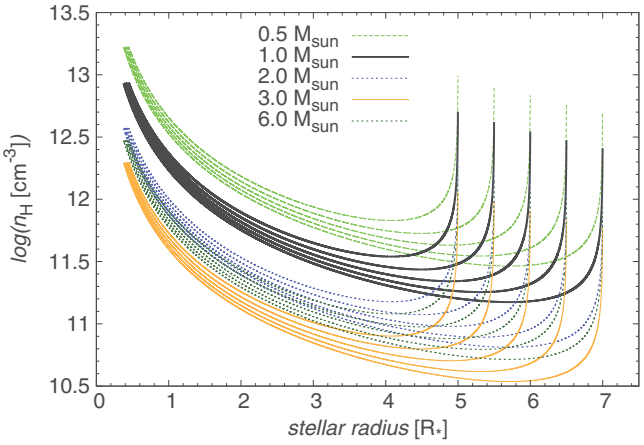


**Figure 14.** Radial number density profile as a function of the distance from the star in units of stellar radii. The computed profile is valid for the steady axisymmetric accretion on a pre-main-sequence star. Individual lines correspond to accretion flows along magnetic streamlines for a particular mass of a star (see the labels). The radius of a star is adopted from the evolutionary tracks of Siess et al. (2000) at ∼1 Myr.

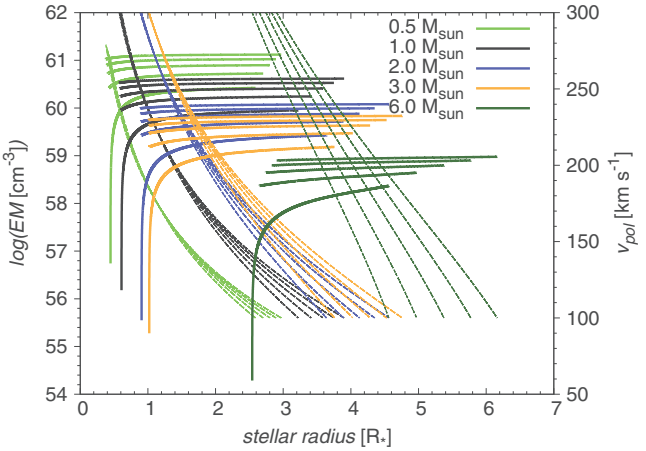


**Figure 15.** Logarithm of emission measure, EM (solid lines, with labels on the left vertical axis) and poloidal velocity profile $v_{\rm pol}$ (dot-dashed lines, with labels on the right vertical axis) as a function of the distance from the star in units of stellar radii. The computed profile is valid for the steady axisymmetric accretion on a pre-main-sequence star. Individual lines correspond to accretion flows along magnetic streamlines for a particular mass of a star (see the key). The radius of a star is adopted from the evolutionary tracks of Siess et al. (2000) at ∼1 Myr.

of $v_{\rm pol} = 200 \pm 100\,{\rm km s^{-1}}$, which roughly corresponds to the observed FWHM of the Br$\gamma$ line. Finally, we get the profiles of cumulative emission measure for a different mass of a pre-main-sequence star according to the evolutionary tracks by Siess et al. (2000) at ∼1 Myr; see Figure 15. The emission measure is of the order of $10^{58}$–$10^{61}$ cm$^{-3}$, being higher for lower-mass stars, and these values originate from close to the star, on the scale of ∼1–3 $R_\star$. This implies that luminous line emission at the observed high velocities can originate from close to a few solar mass star.

One should consider these values highly estimative because of the uncertain values of mass accretion rate and the size and character of the magnetosphere. The temperature of the accretion flow was also not discussed. However, models of the accretion on pre-main-sequence stars show that the infalling gas is shock heated and the Br$\gamma$ line can be effectively produced close to the stellar surface (Bouvier et al. 2007). In principle, it is possible to reproduce the emission measure of $\sim 10^{57}$ cm$^{-3}$ that is obtained in the cold bow shock model by Scoville & Burkert (2013) and that corresponds to the observed flux of Br$\gamma$ emission. Thus, both mechanisms, wind–wind interaction and gas infall, can contribute in case the DSO is a young stellar object.

Given the accretion rate of $\lesssim 10^{-7}\,M_\odot\,{\rm yr}^{-1}$, the star associated with the DSO would be embedded within the hot accretion flow surrounding the star with a probably complex geometry. On the length scale of one stellar radius the density profiles in Figure 10 imply large IR $K$ band and visible extinction of $A(K) \sim 0.1 \times A(V) \approx 0.1 \times (1.8 \times 10^{21})^{-1} \int n_{\rm e}(l) dl$, which is ∼59, 37, 20, and 16 mag for a 0.5 $M_\odot$, 1.0 $M_\odot$, 2.0 $M_\odot$, and 3.0 $M_\odot$ star, respectively. Combined with the possible contribution of an extended outer dust shell and a warped or inflated outer disk, this is plenty of extinction to dim the light from the central star and produce the observed continuum characteristics of the DSO (Eckart et al. 2013, 2014a, 2014b; Phifer et al. 2013; Gillessen et al. 2012).

The material within the accretion flow is certainly not homogeneous. To first order we assume that it consists of cloudlets, sheets, or filaments that have a dense, optically thick core surrounded by a shell of optically thin material. Since the overall line emission is dominated by optically thin material, and given the uncertainties in the Pa$\alpha$/Br$\gamma$ and He I/Br$\gamma$ line ratios, the maximum contribution of the optically thick material to the line fluxes can only be of the order of 0.05. Since the dense material is bright, the ratio $\eta$ between the mean emission measure of the optically thin and thick material needs to be involved. Hence, a volume filling factor around $0.05 \times \eta$ will reproduce the optically thin line ratios and give a substantial contribution to the observed velocity profile. In addition, there will be a temperature gradient from the start of the accretion stream near the dust sublimation radius and the contact point on the stellar surface, leading to an enhanced contribution of the higher-velocity material.

The observed accreting pre-main-sequence stars generally have a lower accretion rate than the time-averaged infall rate (Audard et al. 2014). As a result, the gas from an infalling envelope is thought to be accumulated first in the quasi-Keplerian circumstellar disk. The accumulation of matter continues until the instability causes an increase in the mass transfer by about three to four orders of magnitude from the disk to the star, the so-called episodic accretion (Audard et al. 2014). If the DSO is indeed an embedded accreting pre-main-sequence star, the tidal effects from the SMBH lead to a gravitational instability that, combined with magnetorotational instability (Zhu et al. 2009), can cause a continual mass transfer from the disk, especially close to the peribothron, where the tidal radius shrinks to $\lesssim$1 AU for a 1 $M_\odot$ star; see also the tidal radius discussion related to Figure 16.

Let us sum up that the observed emission up to now is not in contradiction with the scenario of a pre-main-sequence star that is surrounded by a dusty envelope and accretes matter from an accretion disk inside the dust sublimation radius. Hot accretion flows as discussed here, possibly combined with disk winds (Günther 2011), can indeed produce emission lines with FWHM of several hundred kilometers per second. Hence, we find that for a 1–2 $M_\odot$ embedded pre-main-sequence star these two effects can already fully account for the observed Br$\gamma$ line widths. However, in general the observed Br$\gamma$ line profile and flux may result from the combination of hydrogen recombination

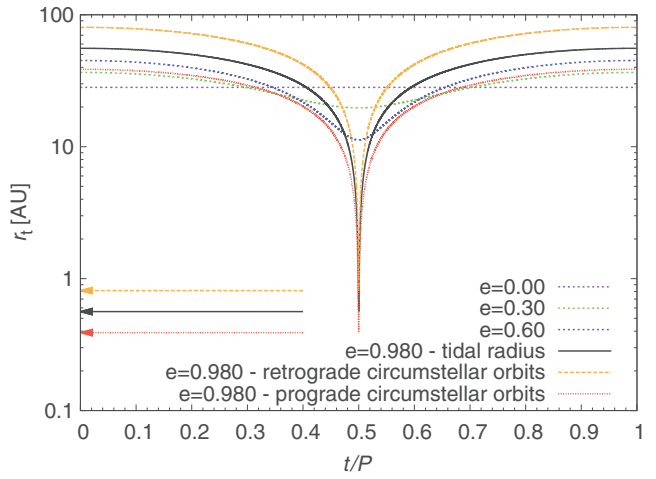


**Figure 16.** Temporal evolution of the tidal Hill radius for the orbits of a 1 $M_\odot$ star around the SMBH with a different orbital eccentricity. At $t/P = 0.5$ the pericenter passage occurs. For the inferred orbit of the DSO, tidal radii for prograde as well as retrograde orbits are depicted. Actual values of the tidal radii at the peribothron are depicted by corresponding arrows. The current orbital solution implies a considerable tidal stripping for distances from the star $\gtrsim$1 AU.

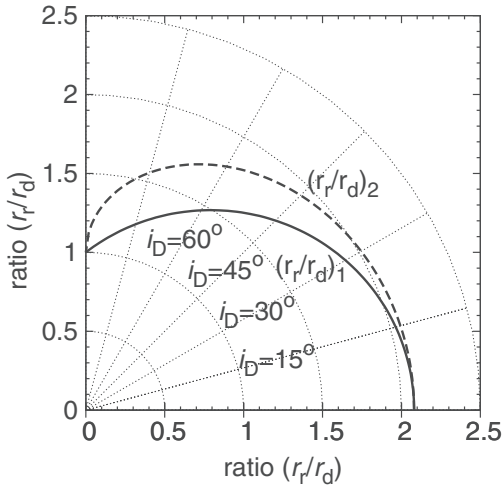


**Figure 17.** Polar plot of the dependence of the ratio of critical tidal radii of retrograde ($r_r$) and prograde ($r_d$) disks on the inclination of the accretion disk around a pre-main-sequence star with respect to the orbital plane of the star around the SMBH. In this plot the vertical and horizontal axes represent the same quantity—the ratio between retrograde and prograde tidal radii. The ratio dependence on the inclination was derived by Innanen (1980). The plotted relations have the form of $(r_r/r_d)_{1,2} = \{1 + f_{1,2}/2 + [f_{1,2} + (f_{1,2}/2)^2]^{1/2}\}^{2/3}$, where $f_1 = 4(\cos^2 i)/3$ and $f_2 = 4\cos i/(2 + \cos i)$. The relation $(r_r/r_d)_1$ dominates the second one. The largest difference between the critical tidal radii of a factor of ~2 is for low-inclination orbits with respect to the orbital plane of DSO.

emission of the gaseous dusty envelope photoionized by nearby stars (Shcherbakov 2014), the collisionally ionized cold bow shock layer (Scoville & Burkert 2013), and the hot accretion flow on a pre-main-sequence star, as is discussed here. Whether and to what extent each of these processes contributes to the final emission will be constrained by further observations and modeling during the post-peribothron phase.

## 5. POSSIBLE ORIGIN, STABILITY, AND FATE OF THE DSO

There is evidence of both young and more evolved stars in the Galactic center (Genzel et al. 2010) that lie in the sphere of influence (~2 pc) of the SMBH. Mutual interactions among stars cause the oscillations of their orbital eccentricity via the mechanism of resonant relaxation (Hopman & Alexander 2006) or the Kozai oscillations (Karas & Šubr 2007; Chen & Amaro-Seoane 2014). These can set some stars on a plunging trajectory toward the SMBH (Zajaček et al. 2014). Similarly, with Jalali et al. (2014) we have shown that young stellar objects can efficiently be formed on plunging orbits in the vicinity of SMBHs as a consequence of orbital compressing of infalling gas clumps. An embedded young star/protostar is surrounded by an accretion disk whose orbit orientation can be any (direct, retrograde, or perpendicular) with respect to the orbit of the host star around the SMBH. These DSOs (Eckart et al. 2013) have an IR excess, and the currently observed DSO may indeed serve as a paradigm of these objects.

The restricted three-body problem may be used to obtain the approximations for critical stability (Hill) radii of disks. Using the restricted circular three-body problem, the equation of motion for a mass element in the rotating frame of star–SMBH becomes (i.e., Innanen 1979, 1980)

$$\frac{d^2r}{dt^2} \simeq \left(\Omega^2 - \frac{d^2V}{dR^2} - \frac{GM_\star}{r^3}\right) r \pm 2\Omega v_r\,, \qquad (8)$$

where $r$ is the distance of a mass element from the star and $R$ labels the distance of the star from the SMBH, $r \ll R$. For $R \gg R_g$, the gravitational potential of the black hole is approximately equal to the Newtonian $V \equiv V(R)$, hence $-d^2V/dR^2 = 2GM_\bullet/R^3$. The angular frequency of the circular motion for the star is $\Omega^2 = GM_\bullet/R^3$, and for the minor body $\omega^2 = GM_\star/r^3$. The difference between direct and retrograde orbits arises from the different signs of the Coriolis term $\pm 2\Omega v_r$, where $v_r = \omega r$.

When generalized for orbits with eccentricity $e$, one gets the following ratio of critical tidal radii for retrograde and direct disks, $r_{H,r}$ and $r_{H,d}$, respectively (Innanen 1979):

$$\frac{r_{H,r}}{r_{H,d}} = \left[\frac{5 + e + 2(4 + e)^{1/2}}{3 + e}\right]^{2/3}. \qquad (9)$$

In terms of the critical tidal radius,

$$r_t = R(t)(M_\star/(3M_\bullet))^{1/3}, \qquad (10)$$

the critical Hill radius for prograde orbits $r_d$ and retrograde orbits $r_r$ may be expressed as $r_r = 3^{1/3} r_t$ and $r_d = 3^{-1/3} r_t$. Since the mass of the SMBH $M_\bullet$ is larger by at least five orders of magnitude than the mass of any star $M_\star$, the tidal Hill radius $r_t$ expressed by Equation (10) extends up to Lagrangian points L1 and L2, beyond which the circumstellar matter is strongly tidally perturbed and may escape the Roche lobe of the star (see Figure 18 of Eckart et al. 2013). The temporal evolution of the tidal radii for the current orbital elements and the stellar mass of $m_\star = 1\ M_\odot$ is shown in Figure 16.

The ratio $r_{H,r}/r_{H,d}$ acquires values of (1.9, 2.1) for eccentricities $e \in (1, 0)$. Therefore, retrograde orbits are expected to be stable for larger distances from the host star, approximately by a factor of two for low-inclination orbits; see Figure 17 for the polar plot of the dependence of the ratio of tidal Hill stability radii $r_{H,r}/r_{H,d}$ on the inclination $i_D$ between a putative circumstellar accretion disk and the orbital plane of DSO.

## 6. CONCLUSIONS

In our sensitive imaging spectroscopy data set we measured prominent line emission from the DSO and determined new orbital parameters based on data from 2014 February to September. The source appeared to be single lined at all times. Before the peribothron, we detected redshifted Br$\gamma$ line emission (at 2700 km s$^{-1}$) but no blueshifted emission above the noise level at the position of Sgr A* or upstream of the presumed orbit. After the peribothron, we detected blueshifted Br$\gamma$ line emission (at $-3320$ km s$^{-1}$) but no redshifted emission above the noise level at the position of Sgr A* or downstream of the presumed orbit. We find a Br$\gamma$ line FWHM of $50 \pm 10$ Å before and $15 \pm 10$ Å after the peribothron transit, i.e., no significant line broadening with respect to last year is observed. Such a broadening would be expected in the case of significant tidal interaction. This is a further indication for the fact that the DSO is spatially rather compact.

We show that for a 1–2 $M_\odot$ embedded pre-main-sequence star hot accretion streams close to the star, possibly in combination with disk winds, can fully account for the luminous observed Br$\gamma$ emission with line widths covering the full range from about 200 km s$^{-1}$ to 700 km s$^{-1}$. The accretion material and the surrounding shell/disk provide enough extinction to explain the IR colors of the DSO (Eckart et al. 2013). The resulting line profile can be asymmetric and skewed to one side, calling for precaution when using the line emission to derive orbital parameters. Following the pre-main-sequence evolutionary tracks of low- and intermediate-mass stars by Siess et al. (2000), we find that after an initial phase of a few $\times 10^5$ yr 1–2 $M_\odot$ stars can stay for a major portion of their T Tauri stage with a luminosity of less than 10 $L_\odot$ (see also Chen & Amaro-Seoane 2014). This is consistent with a dust temperature of 450 K and a possible spectral decomposition of the NIR/MIR spectrum (Eckart et al. 2013) of the DSO using the $M$-band measurement by Gillessen et al. (2012). Higher stellar masses would not comply with this luminosity limit and are not required to explain the Br$\gamma$ line widths. An embedded pre-main-sequence star can also explain the increase of the Br$\gamma$ line width assuming that tidal stretching and perturbation of the envelope lead to an enhancement of the velocity dispersion in the accretion stream onto the central star as the DSO approaches the peribothron. An identification of the DSO with a dust-embedded star also puts the interpretation of a common history of the DSO/G2 and G1 at risk (Pfuhl et al. 2015). Owing to the higher mass (1–2 $M_\odot$ instead of 3 Earth masses), a much higher drag force than the one provided by the small source size would be required to connect the DSO orbit to that of G1.

We also find that the NIR flaring activity of Sgr A* has not shown any statistically significant increment. This points to the fact that the DSO had not yet reached its peribothron before 2014 May. Even if the source has a stellar core, a major part of the enshrouding cloud may be dissolved during the peribothron passage. Therefore, increased accretion activity of Sgr A* may still be upcoming. The Sgr A*/DSO system can be looked upon as a binary system, and the Roche lobe picture can be adopted in which the Lagrange point L1 between the two objects is of special importance if mass transfer between the two objects needs to be considered. If the central star has around one solar mass, the L1 will get very close ($\sim$1 AU) and may allow the dominant part of the gas and dust to transit into the Sgr A*-dominated Roche lobe. As a result, the low-mass stellar core may be even less luminous after the transit than the matter in its immediate vicinity (i.e., 1 AU) before the transit. This will, however, be only for a very short time, and it is not clear whether the gas close to the star will remain in the Roche lobe of the star after peribothron or not. For higher-mass stellar cores that were heavily extincted before peribothron, most of the material closer to the stars (i.e., a few AU) may be largely unaffected by the transition, and the stellar core may by even cleared from extincting material and brighter in the NIR bands than before the peribothron.

In the near future it will become increasingly difficult to measure the strength and spatial extent of the line emission on the blue side of the orbit. This is due to a high-velocity star that is moving into this field from the northwest. It will then be followed by S2 going though peribothron around $2017.9 \pm 0.35$ (Gillessen et al. 2009; Eisenhauer et al. 2003) and S0–102 around $2021.0 \pm 0.3$ (Meyer et al. 2014a, 2014b). Strong continuum contributions and residual line features in the stellar atmospheres may make sensitive observations very difficult and time-consuming.

The research leading to these results received funding from the European Union Seventh Framework Program (FP7/2007-2013) under grant agreement n312789. This work has been financially supported by the Programme National Hautes Energies (PNHE). This work was supported in part by the Deutsche Forschungsgemeinschaft (DFG) via the Cologne Bonn Graduate School (BCGS), the Max Planck Society through the International Max Planck Research School (IMPRS) for Astronomy and Astrophysics, as well as special funds through the University of Cologne. M.Z., B.S., S.S., and A.B. are members of the IMPRS. Part of this work was supported by fruitful discussions with members of the European Union funded COST Action MP0905: Black Holes in a Violent Universe and the Czech Science Foundation—DFG collaboration (No. 13-00070J). This work was co-funded under the Marie Curie Actions of the European Commission (FP7-COFUND). M.G.-M. is supported by the German federal department for education and research (BMBF) under project number 50OS1101. We are grateful to all members of the ESO PARANAL team.

## REFERENCES

Alcalá, J. M., Natta, A., Manara, C. F., et al. 2014, A&A, 561, A2
Audard, M., Ábrahám, P., Dunham, M. M., et al. 2014, arXiv:1401.3368
Baganoff, F. K., Bautz, M. W., Brandt, W. N., et al. 2001, Natur, 413, 45
Baganoff, F. K., Maeda, Y., Morris, M., et al. 2003, ApJ, 591, 891
Ballone, A., Schartmann, M., Burkert, A., et al. 2013, ApJ, 776, 13
Barrière, N. M., Tomsick, J. A., Baganoff, F. K., et al. 2014, ApJ, 786, 46
Baxter, E., Corrales, L., Yamada, R., & Esin, A. A. 2008, ApJ, 689, 308
Bertout, C. 1994, LNP, 431, 49
Bonnet, H., Abuter, R., Baker, A., et al. 2004, Msngr, 117, 17
Bouvier, J., Alencar, S. H. P., Harries, T. J., Johns-Krull, C. M., & Romanova, M. M. 2007, in Protostars and Planets V, ed. B. Reipurth, D. Jewitt, & K. Keil (Tucson, AZ: Univ. Arizona Press), 479
Burkert, A., Schartmann, M., Alig, C., et al. 2012, ApJ, 750, 58
Calvet, N., Muzerolle, J., Briceño, C., et al. 2004, AJ, 128, 1294
Cantó, J., Raga, A. C., & González, R. 2005, RMxAA, 41, 101
Capelli, R., Warwick, R. S., Porquet, D., Gillessen, S., & Predehl, P. 2012, A&A, 545, A35
Chen, X., & Amaro-Seoane, P. 2014, ApJL, 786, L14
Crumley, P., & Kumar, P. 2013, MNRAS, 436, 1955
Czerny, B., Kunneriath, D., Karas, V., & Das, T. K. 2013, A&A, 555, A97
Davis, C. J., Cervantes, B., Nisini, B., et al. 2011, A&A, 528, A3
De Colle, F., Raga, A. C., Contreras-Torres, F. F., & Toledo-Roy, J. C. 2014, ApJL, 789, L33
Degenaar, N., Miller, J. M., Kennea, J., et al. 2013, ApJ, 769, 155
Diolaiti, E., Bendinelli, O., Bonaccini, D., et al. 2000, A&AS, 147, 335
Eckart, A., Britzen, S., Horrobin, M., et al. 2012a, http://pos.sissa.it/cgi-bin/reader/conf.cgi?confid=169, id.4

Eckart, A., & Duhoux, P. R. M. 1991, in ASP Conf. Ser. 14, Astrophysics with Infrared Arrays, ed. R. Elston (San Francisco, CA: ASP), 336
Eckart, A., García-Marín, M., Vogel, S. N., et al. 2012b, A&A, 537, A52
Eckart, A., Horrobin, M., Britzen, S., et al. 2014a, in IAU Symp. 303, The Galactic Center: Feeding and Feedback in a Normal Galactic Nucleus, ed. L. O. Sjouwerman, C. C. Lang, & J. Ott (Cambridge: Cambridge Univ. Press), 269
Eckart, A., Mužić, K., Yazici, S., et al. 2013, A&A, 551, A18
Eckart, A., Valencia-S., M., Peissker, F., et al. 2014b, ATel, 6285, 1
Edwards, S., Fischer, W., Hillenbrand, L., & Kwan, J. 2006, ApJ, 646, 319
Edwards, S., Kwan, J., Fischer, W., et al. 2013, ApJ, 778, 148
Eisenhauer, F., Abuter, R., Bickert, K., et al. 2003, Proc. SPIE, 4841, 1548
Eisenhauer, F., Genzel, R., Alexander, T., et al. 2005, ApJ, 628, 246
Eisner, J. A., Hillenbrand, L. A., White, R. J., et al. 2007, ApJ, 669, 1072
Folha, D. F. M., & Emerson, J. P. 2001, A&A, 365, 90
Genzel, R., Eisenhauer, F., & Gillessen, S. 2010, RvMP, 82, 3121
Ghez, A. M., Duchêne, G., Matthews, K., et al. 2003, ApJL, 586, L127
Ghez, A. M., Witzel, G., Sitarski, B., et al. 2014, ATel, 6110, 1
Gillessen, S., Eisenhauer, F., Fritz, T. K., et al. 2009, ApJL, 707, L114
Gillessen, S., Genzel, R., Fritz, T. K., et al. 2012, Natur, 481, 51
Gillessen, S., Genzel, R., Fritz, T. K., et al. 2013a, ApJ, 763, 78
Gillessen, S., Genzel, R., Fritz, T. K., et al. 2013b, ApJ, 774, 44
Gullbring, E., Hartmann, L., Briceño, C., & Calvet, N. 1998, ApJ, 492, 323
Günther, H. M. 2011, AN, 332, 448
Haggard, D., Baganoff, F. K., Rea, N., et al. 2014, ATel, 6242, 1
Hartmann, L., Calvet, N., Gullbring, E., & D'Alessio, P. 1998, ApJ, 495, 385
Hartmann, L., Hewett, R., & Calvet, N. 1994, ApJ, 426, 669
Herczeg, G. J., & Hillenbrand, L. A. 2014, ApJ, 786, 97
Hopman, C., & Alexander, T. 2006, ApJ, 645, 1152
Ilee, J. D., Fairlamb, J., Oudmaijer, R. D., et al. 2014, MNRAS, 445, 3723
Innanen, K. A. 1979, AJ, 84, 960
Innanen, K. A. 1980, AJ, 85, 81
Jalali, B., Pelupessy, F. I., Eckart, A., et al. 2014, MNRAS, 444, 1205
Johns-Krull, C. M., Valenti, J. A., & Koresko, C. 1999, ApJ, 516, 900
Johns-Krull, C. M., Valenti, J. A., Piskunov, N. E., Saar, S. H., & Hatzes, A. P. 2001, in ASP Conf. Ser. 248, Magnetic Fields Across the Hertzsprung–Russell Diagram, ed. G. Mathys, S. K. Solanki, & D. T. Wickramasinghe (San Francisco, CA: ASP), 527
Karas, V., & Šubr, L. 2007, A&A, 470, 11
Kraus, S., Hofmann, K.-H., Benisty, M., et al. 2008, A&A, 489, 1157
Lima, G. H. R. A., Alencar, S. H. P., Calvet, N., Hartmann, L., & Muzerolle, J. 2010, A&A, 522, A104
Markoff, S., Bower, G. C., & Falcke, H. 2007, MNRAS, 379, 1519
Markoff, S., Falcke, H., Yuan, F., & Biermann, P. L. 2001, A&A, 379, L13
Marrone, D. P., Moran, J. M., Zhao, J.-H., & Rao, R. 2007, ApJL, 654, L57
Martins, F., Trippe, S., Paumard, T., et al. 2006, ApJL, 649, L103
Meyer, L., Ghez, A. M., Witzel, G., et al. 2014a, in IAU Symp. 303, The Galactic Center: Feeding and Feedback in a Normal Galactic Nucleus, ed. L. O. Sjouwerman, C. C. Lang, & J. Ott (Cambridge: Cambridge Univ. Press), 264
Meyer, L., Witzel, G., Longstaff, F. A., & Ghez, A. M. 2014b, ApJ, 791, 24
Mossoux, E., Grosso, N., Vincent, F. H., & Porquet, D. 2015, A&A, 573, 46
Moto'oka, K., & Itoh, Y. 2013, RAA, 13, 1189
Murray-Clay, R. A., & Loeb, A. 2012, NatCo, 3, 1049
Muzerolle, J., Calvet, N., & Hartmann, L. 1998a, ApJ, 492, 743
Muzerolle, J., Hartmann, L., & Calvet, N. 1998b, AJ, 116, 2965
Mužić, K., Eckart, A., Schödel, R., et al. 2010, A&A, 521, A13
Najita, J., Carr, J. S., & Tokunaga, A. T. 1996, ApJ, 456, 292
Narayan, R., Özel, F., & Sironi, L. 2012, ApJL, 757, L20
Neilsen, J., Nowak, M. A., Gammie, C., et al. 2013, ApJ, 774, 42
Nowak, M. A., Neilsen, J., Markoff, S. B., et al. 2012, ApJ, 759, 95
Pfuhl, O., Gillessen, S., Eisenhauer, F., et al. 2015, ApJ, 798, 111
Phifer, K., Do, T., Meyer, L., et al. 2013, ApJL, 773, L13
Porquet, D., Grosso, N., Predehl, P., et al. 2008, A&A, 488, 549
Porquet, D., Predehl, P., Aschenbach, B., et al. 2003, A&A, 407, L17
Pych, W. 2004, PASP, 116, 148
Revnivtsev, M. G., Churazov, E. M., Sazonov, S. Y., et al. 2004, A&A, 425, L49
Różańska, A., Czerny, B., Kunneriath, D., et al. 2014, MNRAS, 445, 4385
Sabha, N., Eckart, A., Merritt, D., et al. 2012, A&A, 545, A70
Sądowski, A., Sironi, L., Abarca, D., et al. 2013, MNRAS, 432, 478
Schartmann, M., Burkert, A., Alig, C., et al. 2012, ApJ, 755, 155
Schödel, R., Najarro, F., Muzic, K., & Eckart, A. 2010, A&A, 511, A18
Scoville, N., & Burkert, A. 2013, ApJ, 768, 108
Shcherbakov, R. V. 2014, ApJ, 783, 31
Shcherbakov, R. V., & Baganoff, F. K. 2010, ApJ, 716, 504
Siess, L., Dufour, E., & Forestini, M. 2000, A&A, 358, 593
Sjouwerman, L. O., & Chandler, C. J. 2014, in IAU Symp. 303, The Galactic Center: Feeding and Feedback in a Normal Galactic Nucleus, ed. L. O. Sjouwerman, C. C. Lang, & J. Ott (Cambridge: Cambridge Univ. Press), 327
Smajić, S., Moser, L., Eckart, A., et al. 2014, A&A, 567, A119
Smith, K., Pestalozzi, M., Güdel, M., Conway, J., & Benz, A. O. 2003, A&A, 406, 957
Sunyaev, R., & Churazov, E. 1998, MNRAS, 297, 1279
Terrier, R., Ponti, G., Bélanger, G., et al. 2010, ApJ, 719, 143
Wang, Q. D., Nowak, M. A., Markoff, S. B., et al. 2013, Sci, 341, 981
Whitney, B. A., Indebetouw, R., Bjorkman, J. E., & Wood, K. 2004, ApJ, 617, 1177
Wilkin, F. P. 1996, ApJL, 459, L31
Witzel, G., Eckart, A., Bremer, M., et al. 2012, ApJS, 203, 18
Witzel, G., Ghez, A. M., Morris, M. R., et al. 2014, ApJ, 796, L8
Wolk, S. J., & Walter, F. M. 1996, AJ, 111, 2066
Zajaček, M., Karas, V., & Eckart, A. 2014, A&A, 565, A17
Zhu, Z., Hartmann, L., & Gammie, C. 2009, ApJ, 694, 1045

Enmanuelle MOSSOUX

# ETUDES MULTI-LONGUEURS D'ONDE DE L'ACTIVITÉ DU TROU NOIR SUPERMASSIF SGR A* AU CENTRE DE NOTRE GALAXIE


## Résumé

Sgr A*, le trou noir supermassif le plus proche de nous, émet une luminosité quiescente très faible ainsi que des éruptions en infrarouge proche (NIR), rayons X et radio.

Cette thèse a pour but d'étudier l'effet du passage de DSO/G2 près de Sgr A* sur les éruptions.

J'ai utilisé et amélioré trois méthodes pour l'étude en rayons X: les blocs Bayésiens en deux passes pour détecter les éruptions avec une certaine probabilité, le lissage des courbes de lumières pour diminuer le bruit de Poisson et la méthode de Monte Carlo par chaînes de Markov pour l'ajustement des spectres des éruptions.

J'ai contraint les paramètres physiques de la source pour une des 3 éruptions détectées en rayons X en 2011 et pour 3 éruptions détectées en rayons X et NIR durant la campagne multi-longueurs d'onde de février-avril 2014.

L'activité en rayons X et NIR de février-avril 2014 correspond à celle observée avant le passage de DSO/G2 près de Sgr A*.

J'ai calculé le taux d'éruption intrinsèque en rayons X de Sgr A* en 1999-2015 et détecté une plus faible activité à partir du 28 octobre 2013. L'énergie stockée pendant cette période peut expliquer la plus forte activité observée du 30 août au 9 septembre 2014.


**Mots clés : Centre galactique, Sgr A*, accrétion, mécanismes radiatifs, multi-longueurs d'onde, XMM-Newton**


## Résumé en anglais

Sgr A*, the closest supermassive black hole, is an extremely low luminosity black hole emitting flares in near-infrared (NIR), X-rays and radio.

The goal of this Ph.D. is to study the impact of the pericenter passage of the Dusty S-cluster Object DSO/G2 close to Sgr A* on the flaring activity.

I used and improved three methods for the study in X-rays: the two-steps Bayesian blocks method to detect flares with a given false detection probability, the light curve smoothing to reduce the Poisson noise and the Monte Carlo Markov chains method for the fitting of the flare spectra.

I constrained the physical parameters of the flaring region for one of the three X-ray flares detected in 2011 and for three NIR/X-ray flares detected during the 2014 Feb.-Apr. multiwavelength campaign.

The X-ray and NIR activity during the 2014 Feb.-Apr. is not different from those observed before the DSO/G2 pericenter passage.

I computed the intrinsic flaring rate in X-rays from Sgr A* in 1999-2015 and I detected a smaller flaring activity beginning on 2013 Oct. 28. The energy saved during this time period could explain the largest activity observed from 2014 Aug. 30 to Sept. 9.


**Keywords : Galactic Center, Sgr A*, accretion, radiation mecanisms, multiwavelengths, XMM-Newton**